UNIVERSITE BRETAGNE LOIRE

UNIVERSITÉ DE NANTES

Thèse de Doctorat

Boris GOUILLEUX

Mémoire présenté en vue de l'obtention du
grade de Docteur de l'Université de Nantes
sous le sceau de l'Université Bretagne Loire

École doctorale : Matière, Molécules Matériaux en Pays de la Loire

Discipline : Chimie
Spécialité : Chimie analytique
Unité de recherche : Laboratoire CEISAM (UMR CNRS 6230)

Soutenue le 18 Octobre 2017

Gradient-based methods on a benchtop spectrometer. New perspectives for low-field NMR spectroscopy

JURY

Président du jury	**Myriam MALET-MARTINO**, **Professeur, Université Paul Sabatier**
Rapporteurs :	**Philippe LESOT**, Directeur de recherche, Université de Paris-Sud **Myriam MALET-MARTINO**, Professeur, Université Paul Sabatier
Examinateurs :	**Jean-Nicolas DUMEZ,** Chargé de recherche, CNRS-ICSN **Bernhard BLÜMICH**, Professor, RWTH Aachen University **Ville-Veikko TELKKI**, Associate Professor, University of Oulu
Invité(s) :	**Serge AKOKA**, Professeur, Université de Nantes **François-Xavier FELPIN**, Professeur, Université de Nantes
Directeur de Thèse :	**Patrick GIRAUDEAU**, Professeur, Université de Nantes
Co-encadrante de Thèse :	**Mireia RODRIGUEZ I ZUBIRI**, Chargée de recherche, Université de Nantes

Acknowledgments

Dear Jury Members,

First and foremost I would like to thank Prof. Myriam Malet-Martino and Dr. Philippe Lesot for considering my request to review my thesis work.

I would also extend my humble gratitude to Prof. Bernhard Blümich, Dr. Jean-Nicolas Dumez and Dr. Ville-Veikko Telkki for accepting to be an examiner of my thesis, as well as Prof. Serge Akoka and Prof. François-Xavier Felpin for accepting to be a member of the jury.

Obviously, I would like to warmly thank Prof. Patrick Giraudeau, Dr. Mireia Rodriguez I Zubiri my supervisor and co-supervisor, respectively, for their commitment and their support in PhD work.

Boris Gouilleux

Remerciements

Ce travail de thèse a été réalisé au sein de l'équipe EBSI (Elucidation de Biosynthèses et Spectrométries Isotopiques) du laboratoire CEISAM (Chimie et Interdisciplinarité : Synthèse, Analyse, Modélisation). Je souhaiterais remercier vivement Messieurs Bruno Bujoli et Jean-Michel Bouler, directeurs successifs, de m'avoir accueilli au sein de leur laboratoire.

Je remercie également la région Pays de la Loire d'avoir financé ce projet de recherche via le pari scientifique « ResoNantes ».

Je tiens tout particulièrement à remercier Monsieur Patrick Giraudeau, directeur de cette thèse pour m'avoir choisi comme doctorant afin de conduire ce projet et bien évidemment pour son encadrement. Merci pour tout le savoir que tu as pu me transmettre et pour m'avoir communiqué le goût de la recherche. Je tenais également à te remercier pour ta confiance et tous ces congrès auxquels tu m'as permis de participer. De même, je remercie beaucoup Madame Mireia Rodriguez I Zubiri pour son encadrement et son soutien dans les applications en chimie organique ainsi que pour sa bonne humeur au quotidien.

Je souhaite également remercier Monsieur François-Xavier Felpin pour ses nombreuses idées et collaborations qui ont permis de tester nos développements de méthodes sur des cas concrets en chimie organique et en flux. Dans cette lignée, je remercie également Daniel Cortes et Lubna Goulamaly, cela a été un plaisir de travailler à vos côtés.

Un grand merci à Benoît Charrier pour son aide précieuse au cours de mes travaux de thèse, pour sa bonne humeur, et les bons moments passés à Aix la Chapelle. Merci également à Monsieur Jonathan Farjon pour son coup de main dans la rédaction du manuscrit, ses nombreuses idées et les francs moments de rigolade devant le spectro.

Je tiens à remercier vivement Monsieur Serge Akoka pour l'ensemble des discussions enrichissantes, son support dans de nombreux travaux ainsi que son soutien pour mes projets d'après thèse. Egalement, je tiens à remercier Monsieur Jean-Nicolas Dumez pour m'avoir reçu au sein de son laboratoire au début de ma thèse et m'avoir transmis de nombreuses notions qui m'ont été par la suite très utiles dans mon projet. Je le remercie également pour ses précieux conseils et son soutien pour mes projets d'après thèse.

Je remercie également Monsieur Lucio Frydman de m'avoir accueilli au sein de son laboratoire en Israël en février 2017. Ce séjour a été un plaisir et très enrichissant.

Il me semble également opportun de remercier Messieurs Ernesto Danieli et Juan Perlo (Magritek) pour leur aide plus que déterminante dans la réalisation de mon projet de thèse.

Je remercie Monsieur Gérald Remaud, notre responsable d'équipe, pour sa disponibilité et ses conseils. Et plus généralement, je remercie l'ensemble de l'équipe EBSI que j'ai eu la chance de côtoyer: Estelle Martineau, Virgine Silvestre, Denis Loquet, Mathilde Grand, Anne-Marie Schiphorst et tous les autres… Je remercie également les stagiaires qui sont passés ces trois dernières années et tout particulièrement Damien Nouaux que j'ai eu le plaisir d'encadrer.

Je remercie maintenant ma splendide équipe de bureau. Laetitia et Jérémy, un grand merci pour la décoration du bureau aussi surprenante que cinéphile… Laetitia, merci pour ces trois années passées dans ce même bureau et ton aide dans les nombreux projets que l'on a eu en commun. Jérémy, merci pour tous ces jeux de mots que je garderai secret et ta culture audio-visuelle si enrichissante. Merci Tangi pour m'avoir fait découvrir le Finistère en long, en large et en travers même si je n'y ai toujours pas mis les pieds. Cela a été un vrai régal de partager ces moments de thèse avec toi. Dans cette lignée, je remercie Valentin pour tous les bons moments passés au labo et en soirée.

Je remercie tous les autres doctorants Florian, Titouan, Antoine, David… ou maintenant anciens doctorants Maxime, Renaud, Martin, Yoann… La liste est bien trop longue.

Je remercie mes amis très chers et de longues dates : Nicolas, Rémy, Gaspard, Triple et Jim pour votre amitié, votre soutien si particulier et pour tous ces moments incroyables et improbables que j'ai pu passer à vos côté.

Je remercie ma famille : ma mère Martine, mon père Thierry et mes frères Damien et Théo pour votre soutien depuis le début.

Pour finir, mille mercis à toi Mathilde, pour ton soutien de tous les jours, ton optimisme puis pour ces merveilleux moments passés à tes côtés et à venir.

List of Acronyms

1D, 2D and nD	One, two, n-dimensional
$\Delta\nu$	Frequency difference between two spins
Δf	Frequency dispersion induced by a pulse field gradient
δ^{π}	Duration of a 180° chirp pulse
δt_G	Step duration within the gradient ramp.
$\phi(z)$	z-dependent dephasing arising from the spatial encoding
γ	Gyromagnetic ratio
Ω	Spin offset
ψ	Wave function
τ	Residence time
τ_G	Duration of a pulse field gradient
AM	Amplitude-modulated
B_0	Static magnetic field
B_1	Magnetic field of the radio frequency pulse
BW	Band Width of the chirp pulse
C	Spatial encoding constant
COSY	Correlation Spectroscopy
CT	Constant time
DEPT	Distortionless Enhancement by Polarization Transfer
DQ	Double Quantum
DQS	Double Quantum Spectroscopy
DW	Dwell Time
EPSI	Echo-planar Spectroscopic-imaging
FBW	Band Width of the digital Filter
FT	Fourier Transform
FT-IR	Fourier-transform Infrared
FWHM	Full Width at Half Maximum

G_a	Acquisition Gradient
GC	Gas Chromatography
G_e	Encoding Gradient
G_f	Final gradient amplitude
G_i	Initial gradient amplitude
GLY	Glycerol
G_p	Pre-phasing gradient
G_{ramp}	Ramp delay between initial and final gradient amplitudes
HETCOR	Heteronuclear Correlation
HF	High-Field
HMBC	Heteronuclear Multiple Bond Correlation
HMQC	Heteronuclear Multiple Quantum Coherence
HPLC	High Performance Liquid Chromatography
HSQC	Heteronuclear Single Quantum Coherence
INEPT	Insensitive Nuclei Enhanced by Polarization Transfer
L	Characteristic length of the sensitive volume
LF	Low-Field
LOD	Limit of detection
M3S	Multi-scan Single-shot
NdFeB	Neodymium-iron-boron
n_g	Number of steps in a gradient ramp
NIR	Near Infrared
N_L	Number of pairs of bipolar gradients during the EPSI block
NMR	Nuclear Magnetic Resonance
PAT	Process Analytical Tool
PCA	Principal Component Analysis
PEEK	Polyetheretherketone
PFG	Pulse Field Gradient
PLS	Partial Least Square

PM	Phase-modulated
PTFE	Polytetrafluoroethylene
PUFA	Polyunsaturated fatty acid
Q_v	Volume flow rate
Q_{max}	Maximal volume flow rate to allow full thermal polarization
RF	Radio Frequency
RSD	Relative Standard deviation
SmCo	Samarium–cobalt
SNR	Signal-to-noise-ratio
SW	Spectral Width
SW_{conv}	Spectral Width along the conventional dimension
SW_{UF}	Spectral Width along the ultrafast dimension
T	Total time spent by spins into the transverse plane
t_1	Evolution time to sample the indirect dimension
T_1	Longitudinal relaxation time
T_1^{flow}	Effective longitudinal relaxation time
t_2	Detection time to sample the direct dimension
T_2	Transverse relaxation time
T_2^{flow}	Effective transverse relaxation time
T_a	Duration of an acquisition gradient
TD	Time-domain
TOCSY	Total Correlation Spectroscopy
UF	Ultrafast
UFA	Unsaturated fatty acid
UV	Ultra-violet
v	Velocity of volume elements of the fluid
V_s	Sensitive volume
V_p	Pre-polarization volume

General Introduction

Nuclear magnetic resonance (NMR) spectroscopy is a powerful analytical tool, used in a wide range of applications, from the elucidation of (bio)-chemical structures, to pharmaceutical, biomedical or food sciences. NMR provides valuable structural, conformational, quantitative and dynamic information on molecules and furthermore enables the determination of the purity, the yield of enantiomeric excesses, isotopic ratios etc. Since the early days of NMR, the pursuit of a better sensitivity and spectral resolution has led to higher and higher super-conducting magnets, providing nowadays stable magnetic fields of up to 23.5 T (*i.e.*, 1 GHz), and higher values announced for the future. Combined with the development of cryogenic probes, modern high-field (HF) spectrometers provide amazing analytical performances, which enable the analysis of biological macromolecules as well as complex mixtures and low concentrated substances.

The downside of this technological effort is a bulky and constraining instrumentation operated by a specialized staff within a dedicated laboratory. Moreover, HF NMR is associated with a heavy financial investment and with the need for cryogenic fluids (N_2 and He), involving a high operating and environmental cost. Overall, these economic and practical drawbacks drastically hamper the use of HF NMR in production sites and synthetic laboratories at the expense of other more accessible analytical tools such as liquid and gas chromatography, Fourier-Transform Infrared (FT-IR), Near Infrared (NIR), Raman etc.

Recently, a new generation of low-field (LF) spectrometers, more compact, relatively low cost and cryogen-free, has emerged as an alternative to high-field NMR, with practical NMR devices capable of probing small and medium-sized molecules in a real-life working environment. Indeed, these so-called “benchtop NMR” spectrometers provide numerous practical assets such as the opportunity to work directly under a fume-hood and without deuterated solvents thanks to an external lock-system. LF NMR devices now deliver multi nuclear spectra whose quality has been greatly improved over the last few years. This has recently enabled successful applications, especially in the fields of process monitoring and quality control [1, 2].

Obviously, the use of a low static magnetic field B_0 - typically 1 – 2 T - involves a significant reduction of the performance in terms of sensitivity and spectral resolution. The spectral width in frequency is indeed reduced leading to overcrowded spectra with numerous peak-overlaps. Furthermore, strong couplings - commonly encountered in LF NMR - and the use of protonated solvents make the identification and quantification of chemical compounds far more complicated. In turn, two-dimensional (2D) NMR, has already been set up on LF spectrometers to outmatch this inherent limitation of the 1D ^{1}H experiments. Unfortunately, the potential of 2D NMR is associated with an intrinsic long acquisition duration, arising from the need to sample the frequencies involved in the indirect dimension through numerous 1D experiments in a time-incremented fashion. This long duration makes 2D NMR ill-suited for most of the benchtop NMR applications where kinetic monitoring and high-throughput analyses are required. Some modern NMR methodologies, well-known from HF NMR, would be relevant in such a context. Counting among them, Ultrafast (UF) 2D NMR, which is capable of delivering an arbitrary 2D spectrum within a sub-second experiment, makes 2D experiments compatible with the time constraints of benchtop NMR appliances. Moreover recent solvent suppression tools simplifies the spectra by selectively reducing the huge and bulky solvent signal(s). While these methodologies are well-recognized at high field, they have never been reported on a benchtop spectrometer, as they require specific hardware and substantial work for the implementation at low-field.

The aim of this thesis – positioned within the “ResoNantes” project funded by Région Pays de la Loire – is the implementation of these aforementioned modern NMR methods on such a compact NMR apparatus to improve its analytical performance and to extend its scope of applications. These experiments are performed on the first benchtop spectrometer equipped with a gradient coil, a crucial prerequisite to the implement of modern NMR experiments. The introductory part A reports the current state-of-the-art of LF NMR spectroscopy in terms of instrumentation, methodology, performance along with examples of applications. In addition, two reviews are proposed: one on fast multidimensional NMR methods in general, followed by a second one focused on UF 2D NMR . Part B deals with the objectives of this three-years PhD and the framework in terms of soft/hardware resources to conduct this project. In part C, we discuss about the implementation of UF NMR and gradient-based solvent suppression methods on a 43 MHz compact NMR spectrometer. These methodological efforts enabled

various applications in the fields of reaction monitoring and quality control, which are highlighted in part D.

The present thesis is based on a compendium of research and review articles written in the course of the three-year PhD. The published and accepted ones have been evaluated by expert researchers in the field of NMR spectroscopy from well-recognized peer-reviewed international scientific journals. Some of them are not present inside the body of the manuscript but are available in appendix. Complementary bibliographic sections, descriptions and commentaries have been introduced to tie these articles together into a coherent ensemble.

A. Literature Review

1. State-of-the-art of compact NMR spectroscopy

1.1. Why using compact NMR spectrometers?

HF NMR spectrometers, relying on stable superconducting magnets provide invaluable chemical insights in a variety of situations and play a central role in analytical chemistry. However, the size of these magnets and safety requirements keep HF NMR away from the synthetic laboratories and from production settings. As a result, NMR users waste a large amount of time due to the queue before measurement and by bringing their sample to the machine in the dedicated room. The use of NMR would be more convenient if the NMR spectrometer was directly located in the working chemistry laboratory, for instance, close to the UV-visible spectrometer or to the gas chromatograph (GC). The great and recent improvements on the cryogen-free permanent magnets meet this need for NMR devices on the workbench. These new compact spectrometers provide B_0 magnetic field with a sufficient homogeneity to resolve the chemical shifts thus providing significant advantages. First of all, such benchtop NMR devices can be used in situation where the resolution and the sensitivity of a superconducting magnet is not required. This would take a part of the workload of the overbooked HF spectrometers. Moreover, being compact enough to be placed under a fume-hood, this technology opens new opportunities for NMR analysis of hazardous compounds, reaction and process monitoring [1-3], product control [1, 4] and even for teaching [5].

1.2. Technological and Methodological developments

Originally, permanent magnets were as large as superconducting magnets are today, and the attempt to reduce their size systematically led to magnets with very poor homogeneity and resolution. It turns out that benchtop NMR systems commercially available for more than three decades, also known as time-domain spectrometers or relaxometers, have only been used for applications based on relaxation time measurements referred as time-domain (TD) NMR in contrast to NMR spectroscopy or Fourier transform (FT) NMR. This situation has

changed during the last few years thanks to huge efforts addressed to improve magnet design and field shimming strategies, which have led to the successful measurement of sub-parts-per-million resolution spectra with compact instruments [6].

1.2.1. Permanent Benchtop magnet configurations

There are two main arrangements that are commonly encountered for compact and permanent magnets. The first design consists of two parallel plates as magnetic poles, which are mounted within an iron yoke. The amount and type of magnetic material used in the parallel plates combined with the pole gap, determines the static field strength B_0 between the two poles (figure A.1a). The sample is located in a solenoid radio frequency (RF) coil so that a B_1 field is generated along a direction perpendicular to the B_0-direction [4]. Another arrangement that has become more and more popular in the field of benchtop NMR is the cylindrical Halbach design [7, 8]. In this design, the two poles are replaced by a series of small polarized magnetic blocks, which are placed in a circular pattern. The direction of polarization of each block is rotated slightly relative to its immediate neighbors. Similar rings of polarized block are built and then stacked in order to achieve a cylindrical magnet (figure A.1b). The working volume allows the insertion of a 5 mm NMR tube within the magnet where the static B_0 field is transverse to the tube. A solenoid RF coil is located inside the cylindrical magnet, generating a B_1 field perpendicular to B_0. Recently, great improvements in shimming this magnet design were reported [9]. The central ring provides the main static field while the displacement of the outer rings along the z-axis is used to shim B_0 along the axial direction. Thanks to this mechanical solution combined with fine corrections performed by electrical shim coils, these improved Halbach magnets lead to a highly homogeneous field [6, 10].

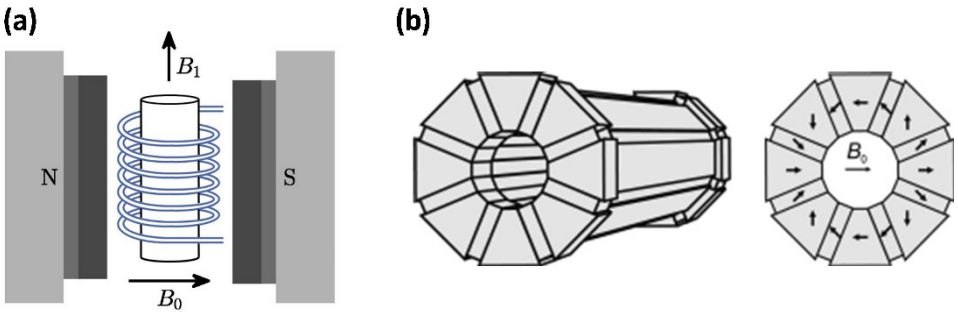

Figure A.1. Permanent magnet configurations. (a): Parallel plate magnet in which, B_0 magnetic field is generated on the z-axis between the pole pieces (light gray). Shim and gradient plates (medium/dark gray) can be included. The sample is placed in a solenoid rf coil (blue) which generates a B_1 field perpendicular to B_0. Figure 1a reproduced from Ref. 4**. (b)** Cylindrical Halbach design combining magnet blocks with trapezoidal and rectangular cross sections. Left: 3D sketch of the magnet array. Right: Cross section of the cylindrical magnet showing the different geometries of the pieces mounted with their corresponding polarization directions, indicated by black arrows, required to generate a homogeneous magnetic field B_0 in the magnet bore. Figure 1b reproduced from Ref. 6**.**

1.2.2. Overview of the technical characteristics and market situation

Today's benchtop NMR systems share common features. All the systems rely on permanent magnets, which are cryogen-free, compact (with varying degrees), generating homogenous fields with a strength between 1 – 2 T (i.e. from 43 to 82 MHz). Moreover, based on thermosensitive materials such as neodymium-iron-boron (NdFeB) or samarian–cobalt (SmCo), these permanent magnets suffers from poor temporal field stability arising from the temperature variations. Even if SmCo provides a weaker temperature coefficient compared to NdFeB, an efficient control of this parameter is required and set up by the different manufacturers. Besides the temperature control, they offer the capability of correcting the residual temporal magnetic drift without the need of deuterated solvents by either an external lock system or via intern algorithms. Nowadays, these modern benchtop systems are commercialized essentially by four companies: Magritek, Oxford instruments, Nanalysis and Thermo Scientific (figure A.2). Nevertheless, the compact spectrometers proposed by the different manufacturers provide a different analytical performance and can be distinguished in terms of weight, field homogeneity, probes, lock systems, NMR tubes and accessories. These technical characteristics are overviewed in the following references [1, 11].

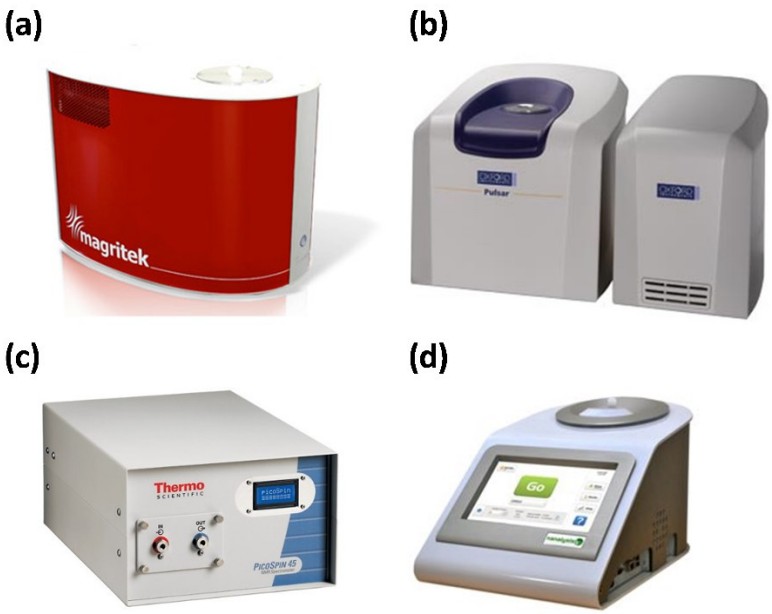

Figure A.2. Overview of the main benchtop NMR spectrometers currently available in 2017. **(a)**: "Spinsolve" (Magritek) [12] ; **(b)**: "Pulsar" (Oxford instrument) [13]; **(c)** "picoSpin" (Thermo Scientific) [14] and **(d)**: "NMReady" (Nanalysis) [15].

1.2.3.1D and 2D NMR experiments

Benefiting from the capability of resolving the chemical shift, compact NMR spectrometers provide different choices for 1D and 2D experiments and different probed nuclei such as ^{1}H, ^{2}H, ^{19}F, ^{13}C, ^{31}P and even more "exotic" nuclei such as ^{7}Li and ^{11}B [1]. Moreover, experiments performed on ^{15}N – a nucleus in very low natural abundance - were reported by hyphenating LF NMR spectroscopy and para-hydrogen hyperpolarization with reversible exchange (SABRE) [16, 17]. This plurality of probed nuclei makes compact NMR spectroscopy a versatile tool in different research areas (figure A.3). Indeed, nuclei such as ^{19}F (figure A.3c) and ^{31}P experiments (figure A.3d) - well recognized in HF NMR in pharmaceutic industry, metabolism studies and phospholipids analysis - provide alternative solutions thanks to their 100 % natural abundance and their higher spectral widths compared to ^{1}H while the crowded ^{1}H spectra suffer from overlaps [18].

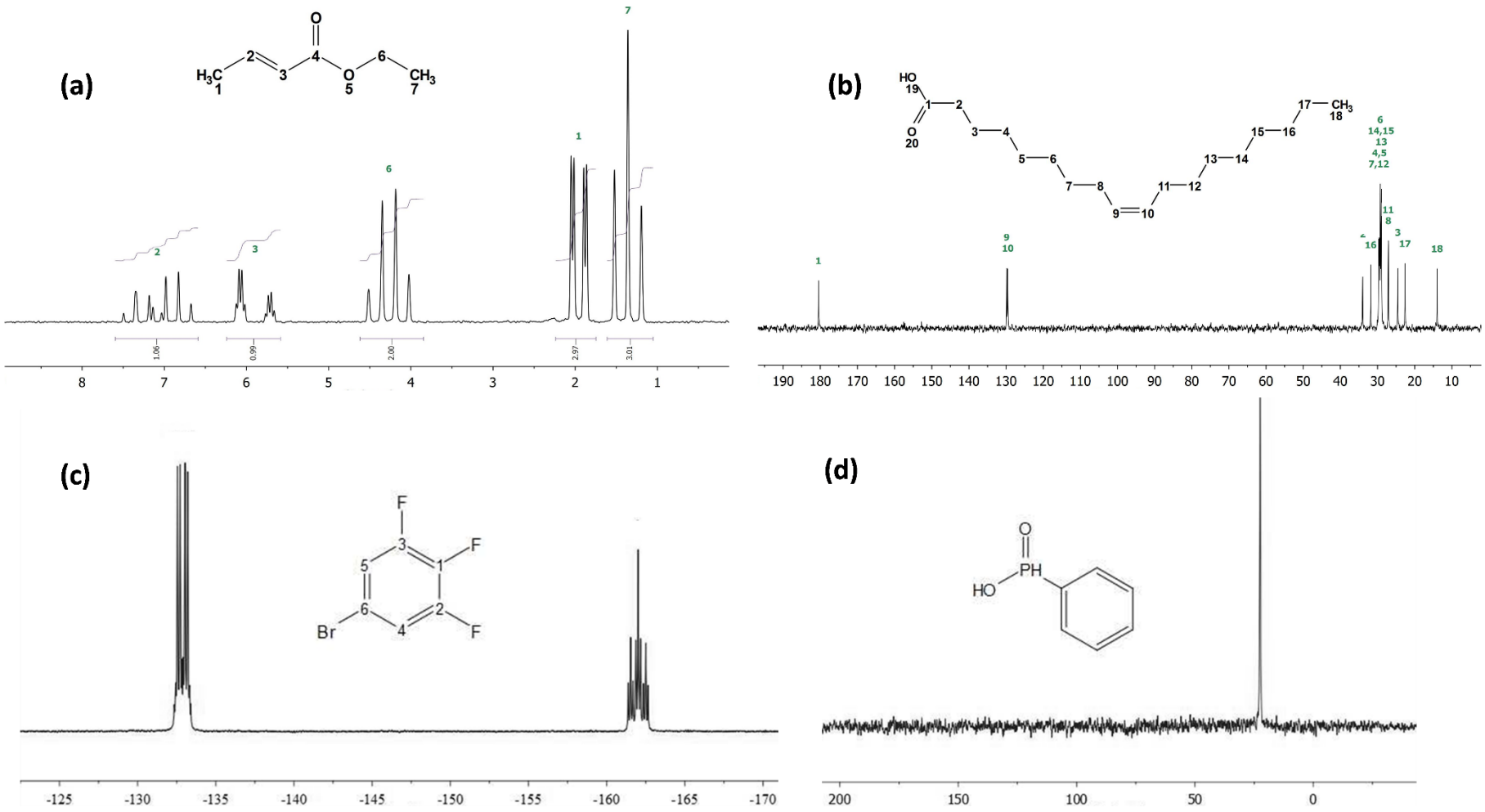

Figure A.3. Panel of 1D spectra of different nuclei obtained with compact spectrometers. **(a)**: ^{1}H spectrum of ethyl crotonate recorded in a single scan at 43 MHz (i.e. 1 T), 250 mM in $CDCl_3$. **(b)**: ^{13}C spectrum of oleic acid recorded at 15 MHz (i.e. 1.4 T) in 34 min, 1 M in $CDCl_3$. **(c)**: ^{19}F spectrum of neat 5-bromo-1,2,3-trifluorobenzene recorded at 41 MHz (i.e. 1 T) in a single scan. **(d)**: ^{31}P spectrum of phenyl phosphinic acid recorded at 17.5 MHz (i.e. 1 T) in 2.7 min, 300 mM in D_20. All these spectra are available online via this webpage [19].

Numerous multi-pulsed NMR experiments, well-known from HF NMR spectroscopy have been implemented on compact spectrometers [1]. Compact devices, including multichannel probes, provide useful 1D hetero-nuclear experiments such as insensitive nuclei enhanced by polarization transfer (INEPT), distortionless enhancement by polarization transfer (DEPT), especially valuable in ^{13}C NMR for sensitivity enhancement and J-edited spectra. Furthermore, the improved temporal stability of the magnetic field allows the acquisition of proper 2D interferograms. The resulting 2D spectra, which can be acquired in routine on the most recent LF spectrometers, provide structural insights and potentially alleviate the peak-overlaps generally encountered in the low-field ^{1}H spectra. For instance, the J-resolved sequence leads to a significant simplification of a crowed spectrum by 45° tilting the multiplets centered at the different chemical shifts for separating J_{H-H} and chemical shifts along each dimension. This enables an accurate measurement of couplings generally hard to decipher from 1D data. For instance, this approach was applied to measure the residual dipolar coupling at 1 T for differentiation of enantiomers [20]. In addition, 2D homonuclear correlations as COSY (COrrelation SpectroscopY) and TOCSY (Total COrrelation SpectroscopY) are nowadays available on compact spectrometer both in ^{1}H and ^{19}F. In 2D heteronuclear, a large panel of experiments are nowadays implemented screening different range of scalar correlations: HETCOR (HETeronuclear Correlation), HSQC (Heteronuclear Single Quantum Coherence), (Heteronuclear Multiple Quantum Coherence) HMQC and HMBC (Heteronuclear Multiple Bonds Correlation) as illustrated in figure A.4.

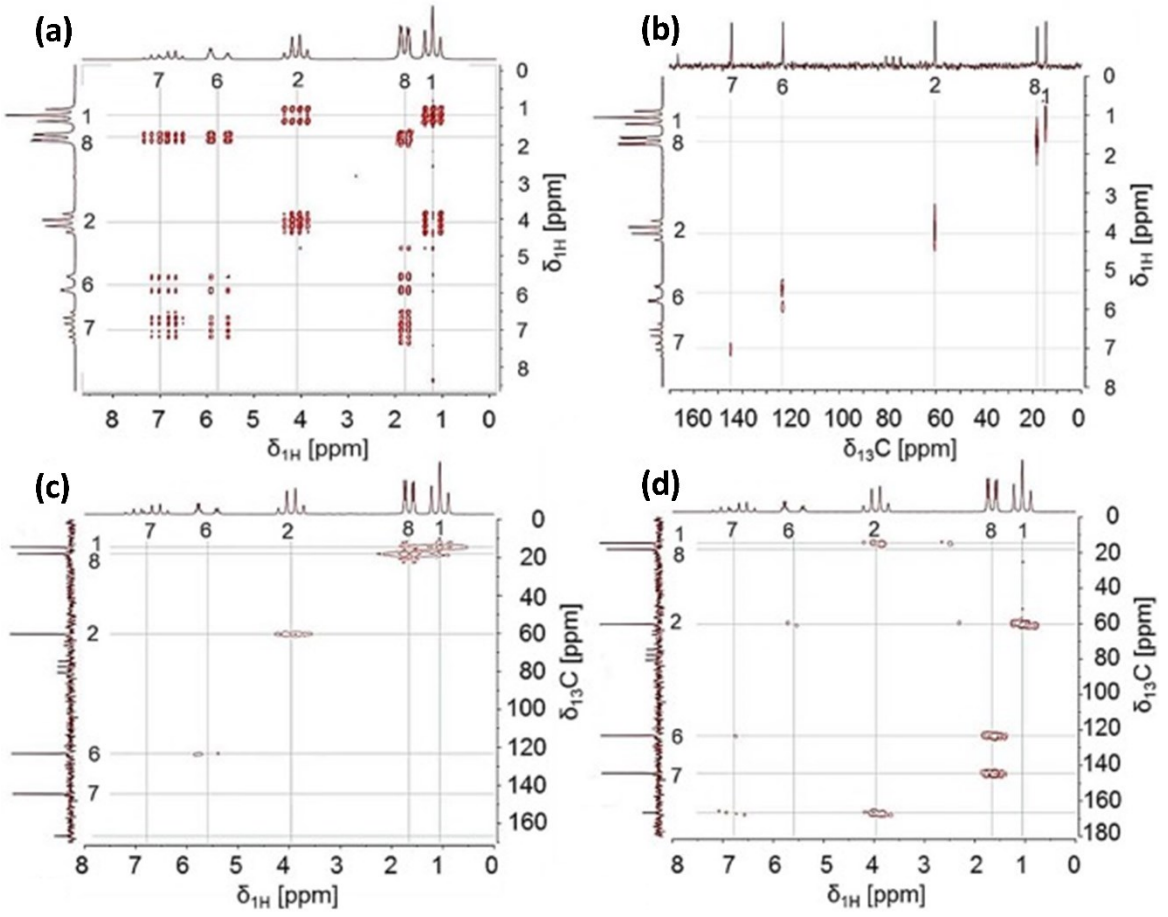

Figure A.4. 2D spectra of 1.75 M ethyl crotonate in $CDCl_3$ acquired at 43 MHz. For the peak assignments see figure A.3a. **(a)** Homo-nuclear ^{1}H-^{1}H COSY spectrum recorded in 10 min. **(b)** ^{1}H-^{13}C HETCOR spectrum recorded in 5.6 h. **(c)** ^{1}H-^{13}C HSQC spectrum recorded in 10 min. **(d)** ^{1}H-^{13}C HMBC recorded in 67 min. The figure is reproduced from Ref. 1.

1.3. Performance and limits of LF NMR spectroscopy

1.3.1. Sensitivity and Resolution

The technological improvements of permanent magnets open exciting opportunities. However, working with a low B_0 field involves an inherent reduction of the analytical performance. First, the amplitude of the NMR signal is reduced when the magnetic field strength decreases. Besides the reduction of the sensitivity, the resolution is also altered. Indeed, while the frequency differences of resonances are field dependent and decrease with magnetic field strength, the spin coupling leads to line splitting independent of the magnetic field strength. In turn, multiplets centered at different chemical shifts are clearer separated at high-field than at low-field so that LF spectra are more difficult to interpret. Yet, the high homogeneity of the modern permanent magnets leads to sharp peaks (full width

at half maximum (FWHM) typically < 1 Hz), thereby balancing the intrinsic low spectral width in Hz and enabling the characterization of small molecules (figure A.5b). In terms of sensitivity, the recent Halbach magnet described in section 1.2.1 deliver a signal-to-noise-ratio (SNR) of a single scan measured for neat water about 200 000 and a limit of detection of few mM measured on a small molecule is reported [6]. Overall, LF NMR spectrometers deliver a sufficient sensitivity and resolution to elucidate the structure of pharmaceutical compounds such as ibuprofen, aspirin, lidocaine etc. in reasonable concentrations. Along with this statement, Figure A.3a shows how a 1 T compact magnet is able to characterize properly in a single scan a sample of ethyl crotonate at 250 mM. Nevertheless, the situation becomes more complex in the case of mixtures of compounds or higher sized molecules where there is a high probability for encountering strong overlaps making the identification unsuitable. In addition, medium-sized molecules, especially the ones with straight aliphatic chains involve tricky ^{1}H spectra (figure A.6d). This is further emphasized by the presence of strong coupling as described in the following section.

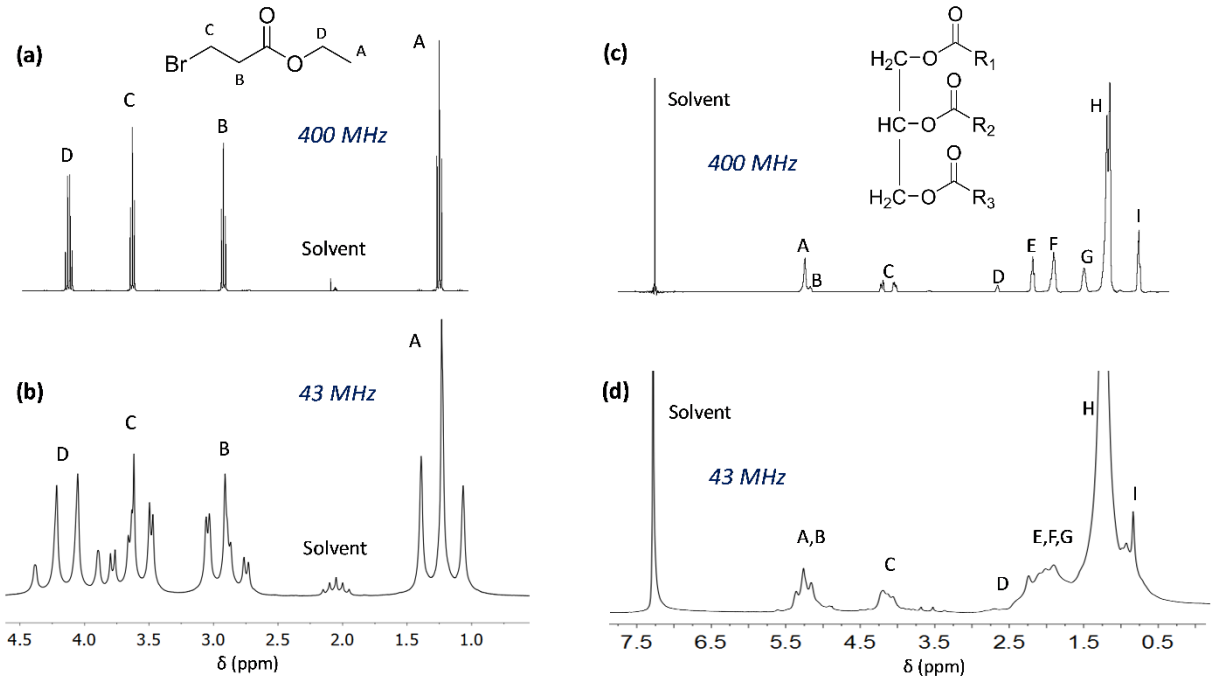

Figure A.5. **Left panel**: Comparison of LF and HF spectra of a small molecule. ^{1}H spectra of 3-bromo-ethylpropionate in acetone-d6 recorded in a single scan at 400 MHz **(a)** and at 43 MHz **(b)**. **Right panel**: Comparison of LF and HF spectra of medium-sized molecules. On the top: scheme of triglycerides present in edible oils, R_i corresponds to the fatty chains. ^{1}H spectra of a peanut oil sample dissolved in $CHCl_3$ recorded at 400 MHz **(c)** and at 43 MHz **(d)**.

1.3.2. Strong coupling

When the frequency difference $\Delta\nu$ between two coupled nuclei has the same magnitude as the scalar coupling constant, i.e. $\Delta\nu \approx J$, second order coupling – usually called "strong coupling" - appears. For a given spin system, as the frequency difference decreases with the reduction of the field strength while scalar coupling constants remain unchanged, strong couplings are commonly encountered in LF NMR spectroscopy. This leads to tricky effects, which are misleading for structural characterization and involves "strong coupling artifacts" in 2D experiments containing 180° refocusing pulse within the t_1-evolution [21].

In order to reveal the most important features of this phenomenon, we start with a brief theoretical description based on the energy levels applied to a strongly coupled two spin-system, noted AB. If the weak coupling condition does not hold, the simple product wave functions are no longer the eigenfunctions of the system. It turns out that in the AB system, the two levels (2) and (3) where the total magnetic quantum number (m) is equal to zero, are slightly shifted in energy and acquire the following mixed wave functions:

$$\psi_2 = |\alpha\beta> \cos\theta + |\beta\alpha> \sin\theta \qquad \text{(A.1)}$$

$$\psi_3 = |\beta\alpha> \cos\theta - |\alpha\beta> \sin\theta \qquad \text{(A.2)}$$

The angle θ is called the strong coupling parameter and is defined as:

$$\sin 2\theta = \frac{J_{AB}}{D} \quad ; \quad D = \sqrt{(\nu_A + \nu_B)^2 + J_{AB}^2} \qquad \text{(A.3)}$$

As the D value could be tedious to calculate, in practice the "strength" of the coupling is estimated with $\tan 2\theta = \left| {}^{J_{AB}}/_{\nu_A - \nu_B} \right|$. The stage where strong coupling effects become appreciable may be taken where $\tan 2\theta \geq 0.1$. For instance, a two spin system split by 1 ppm and coupled 7 Hz lead to a value of 0.02 at 400 MHz (no appreciable effect) and 0.16 at 43 MHz (consequent effect).

The table I gives the frequencies and intensities of the four allowed transitions in the strong coupling case.

Table I: Frequencies and intensities of the allowed transitions for an AB spin system. $\Sigma = \nu_A + \nu_B$. (1) and (4) corresponds to spin states whose m = +1 and -1 respectively, while (2) and (3) are spin states whose m = 0.

Spin	Transitions	Frequency	Intensity
A	(1) – (3)	$-1/2\,D - \ 1/2\,\Sigma - 1/2\,J_{AB}$	$1 - \sin 2\theta$
A	(2) – (4)	$-\ 1/2\,D - \ 1/2\,\Sigma + 1/2\,J_{AB}$	$1 + \sin 2\theta$
B	(1) – (2)	$+1/2\,D - \ 1/2\,\Sigma - 1/2\,J_{AB}$	$1 + \sin 2\theta$
B	(3) – (4)	$+\ 1/2\,D - \ 1/2\,\Sigma + 1/2\,J_{AB}$	$1 - \sin 2\theta$

The expressions of frequency and intensity allow us describing the way the two-spin spectrum changes as we go from the weak case AX trough the strong case AB. Indeed, the stronger is the coupling, the higher are the inner lines whereas the outer ones gradually decrease (see intensity columns of the table I. This well-called “roof effect” could be a clue to identify coupling partners, but it may rapidly evolve in a strong distortion making multiplet analysis far more complex, as illustrated in the aromatic region of the spectra in figure A.6. Moreover, although the outer splittings remain equal to J_{AB}, the center of this doublet do not match with the exact chemical shift value anymore. Therefore, a special care must be taken when extracting chemical shift values from strongly coupled spectra.

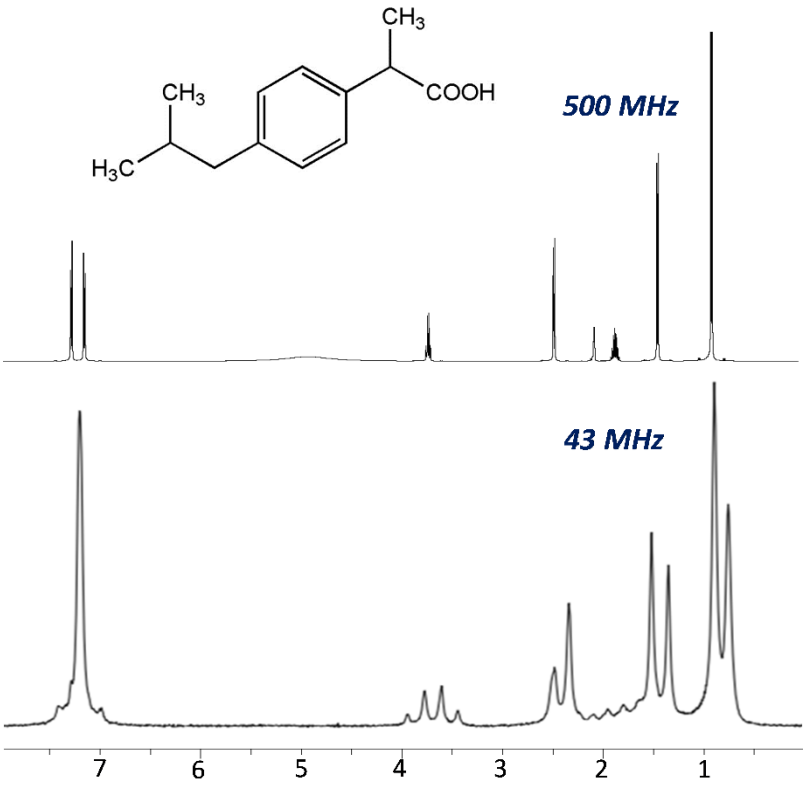

Figure A.6. ^{1}H spectra of ibuprofen recorded at 500 (top) and 43 MHz (bottom). It worth noting how the strong coupling effect at 43 MHz makes unsuitable the analysis of the aromatic signals while structural insights in this region are still provided at 500 MHz.

Even more spurious is the phenomenon of "virtual coupling" in which apparently first-order multiplets contain false coupling information. In some cases, protons that are not actually coupled will exhibit splitting. This phenomenon is involved in higher strongly spin systems than AB and can be summarized as follows: when two or more protons are strongly coupled, then any protons coupled to them will lead to multiplets with false coupling information on the spectrum and/or unexpectedly complex multiplet structure. This phenomenon was discovered as soon as the 60's where low-field magnet were used [22]. Since then, virtual coupling has been a source of complications for structural characterization [23]. This complex feature is well illustrated by the potential impact of virtual coupling on the signal of methyl groups. Indeed, methyl groups usually provide reliable simple multiplets in NMR spectra. Unfortunately, if such a methyl group is coupled to a proton which is part of a strongly-coupled system, then its NMR signal can become a more complex multiplet generating misleading information (figure A.7).

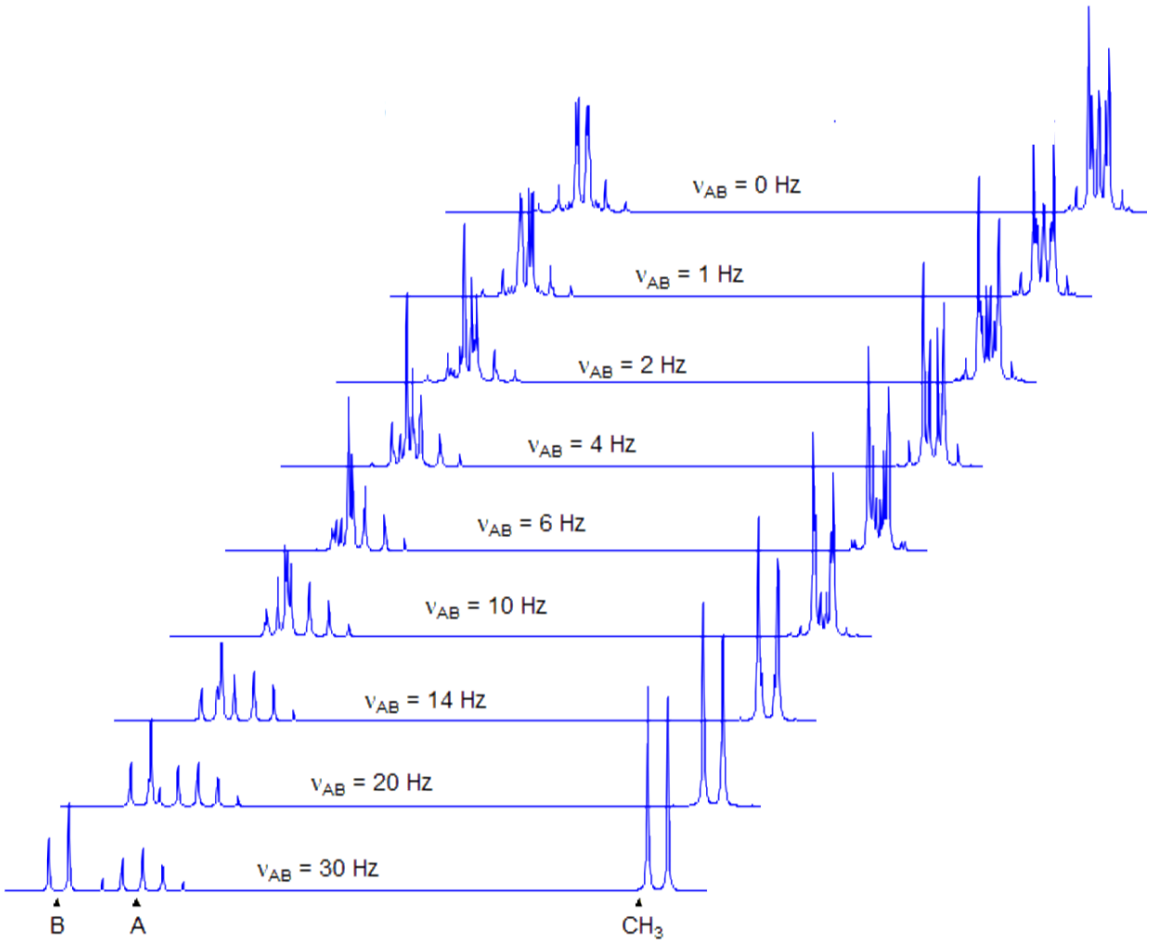

Figure A.7. Virtual coupling in an ABX_3 spin-system where X_3 is a methyl group. Evolution of the methyl signal in function of frequency difference ν_{AB} between A and B. $J_{AB} = 10$; $J_{BX} = 7$; $J_{AX} = 0$. Note that the CH_3 seems to be coupled with A as of $\nu_{AB} = 14$ Hz while J_{AX} is null. The figure is available online via this webpage [24].

A last feature that should be addressed is related to the strong coupling artifacts encountered in J-Resolved experiment as well as in constant time (CT) 2D experiments. Strong coupling potentially leads to additional peaks in those 2D spectra making their interpretation ambiguous [21]. Strong coupling artefacts arise from a mixing effect occurring when a 180° pulse is applied within the evolution period. Indeed, besides the coherence inversion, a 180° pulse causes a partial coherence transfer in a strongly coupled spin-system. The resulting artefacts cannot be suppressed by phase cycling or pulsed field gradients, as the artefact signals originate from the same coherence transfer pathway as the required signals.

In summary, the strong coupling effect commonly encountered at low-field involves potential drawbacks that should be taken into account when analyzing a LF spectrum:

i. This makes predicting or analyzing the spectra much more difficult than in the case of weak coupling.

ii. Both chemical shift values and scalar coupling constants measured on the spectrum potentially do not match with the real ones from the electronic structures. This spurious spectroscopic values can hamper the use of databases (generally built from HF spectra) to signal identification.

iii. In contrast to the weak coupling case, 180° pulses cause a partial coherence transfer so that strong coupling artifacts occur in 2D J-Resolved and in 2D CT experiments.

iv. Since the coupling and the chemical shift Hamiltonian do not commute anymore, strong coupling makes harder a rapid analysis of pulse-sequences, even if a product operator description of AB and ABX spin systems has been reported [25].

2. Applications of low-field NMR spectroscopy

Compact NMR is widely applied in food science, technology and industry. The applications and studies of low field NMR can be classified into the different great themes of NMR, namely relaxation, diffusion measurement, spectroscopy and imaging. In the following section, we focus on the recent application in LF NMR spectroscopy reported in the field of process monitoring and quality control.

2.1. Reaction monitoring and Process Control

Reaction monitoring based on analytical spectroscopy provides essential kinetic and speciation information in a variety of application fields, from organic and inorganic synthesis to biochemistry and bioengineering [26]. It is therefore a major tool of interest for kinetic studies as well as for the understanding of reaction mechanisms. Besides these academic and fundamental applications, process monitoring through the use of process analytical tools (PAT) has a growing relevance for chemical production and manufacture, especially in the pharmaceutical, food and (petro-) chemical industries [2]. Counting among the PAT, NMR has the great advantage of being non-specific, non-destructive and it does not require elaborated sample preparations and calibration procedures [27]. Moreover, NMR spectroscopy exhibits a strict linearity between the absolute signal area and the sample concentration, which is also valid in complex matrices [3]. Based on all these assets, HF NMR has been successfully used in (bio)-organic and pharmaceutical applications for monitoring chemical processes [28-31], either directly inside the NMR tube [31-33] or by using a flow-NMR setting [27, 30, 34-40]. Moreover, the recent work for reaction monitoring performed in flow synthesis should be highlighted [40-42]. Yet, it is striking to see that HF NMR spectroscopy – based on a bulky and expensive equipment - has not reached the degree of compactness required for use in the chemistry laboratory and in the production sites whereby safe, practical and cryogen free systems are preferred to control the manufacturing processes. In this framework, there is a huge need to develop tools based on compact NMR spectroscopy. The new generation of benchtop spectrometers meets these economic and practical demands in bringing NMR directly onto the work bench of the organic chemist or in being integrated within industrial process lines. The present section aims at emphasizing the central features of reaction

monitoring through compact NMR spectroscopy as well as the successful applications that have been reported so far in 2017.

2.1.1. Working with non-deuterated solvents

Deuterated solvents are widely used in NMR since they are convenient for locking and shimming the system as well as for calibrating the spectra. Unfortunately, their use becomes unsuitable for almost all the studies in the framework of process monitoring. Indeed, even a short percentage of deuterated solvent is not acceptable since deuterium can cause unwanted isotope effects especially for solvents with exchangeable ^{2}H that may confuse the kinetics of the studied process. Besides this fundamental aspect, a more detrimental reason is the increase in the cost of the monitoring for large volume reactions. Nowadays, modern benchtop spectrometers include an external lock-system, which is able to balance the drift of magnetic field in the course of time while pure protonated solvent are used. These technological effort makes these compact spectrometers well-suited for process monitoring.

The other side of the coin to the exclusive use of protonated solvents is that the solvent signals become dramatically intense relative to the solutes. Such big signals obscure the spectral features of the interesting analytes for several reasons: (i) the dynamic range of the receiver limits the simultaneous detection of signals with orders of magnitude differences; (ii) the broad solvent signal can overlap the lines of interest; (iii) analog receiver overflow potentially leads to baseline distortions, which can make the integration of relevant signals far more difficult. Further details on these features as well as a review of the different solvent suppression methods are described in the section C.3.2. In this context, solvent suppression methods are vital tools to cope with this overall effect, especially in LF NMR where the overlapping issue becomes more stringent due to the reduced spectral width in frequency.

2.1.2. Monitoring set up

Monitoring chemical reactions can be achieved through different settings, each one having its specific advantages and disadvantages. An obvious way is to collect amounts of the reactional mixture from the reactor at different instants in the course of the reaction. This “at-line” or “off-line” methodology – often encountered in organic chemistry – involves quenching the collected samples and it is hardly compatible with automation. To circumvent this tedious periodic sampling, one may carry out the chemical reaction directly inside the NMR tube. This

method exhibits the best NMR performance in terms of sensitivity, shimming and available pulse-sequences so that it is valuable for structural characterization in the context of understanding reaction mechanism [42]. However, monitoring inside the NMR tube suffers from major drawbacks regarding the experimental conditions while the time lag imparted for mixing reactants and inserting the NMR tube into the spectrometer makes the beginning of the reaction difficult to follow, unless specific settings are introduced to add reactants directly into the probe. Moreover, as permanent magnet are thermosensitive, only a limited range of temperatures can be admitted, further reducing the scope of applications.

On the contrary, monitoring chemical processes through a bypass system, whereby the reactor is connected to the NMR apparatus, exhibits a greater flexibility regarding the experimental conditions: regulated temperature, mechanical stirring, inert atmosphere, etc. In this type of monitoring – commonly referred to as “on-line monitoring” - a pump generates a continuous flow to refresh the sensitive volume of the magnet with the reaction mixture in the course of the studied process; afterward the mixture returns to the reaction vessel [27]. Inert materials such as PEEK or PTFE can be used for the connections between the reactor and the NMR flow probe. All transfer lines could also be thermostatted to maintain a constant temperature of the flowing mixture [43]. It is worth mentioning that this higher flexibility regarding experimental conditions provides more relevant kinetic data compared to the monitoring directly inside the NMR tube [44]. Despite its obvious advantages, particular features needs to be considered when a bypass is used. First, the detection of a change in the reactor by the NMR spectrometer is delayed because of the bypass set-up [2, 3, 45]. Hence, the time spent into the tubing should be short enough to minimize the error in a subsequent analysis of the reaction kinetics. Furthermore, the NMR experiment performed on flowing systems involves specific considerations – discussed in details in a dedicated section – so that the choice of the flow rate becomes a special tradeoff between time-resolution and NMR performance.

The availability of compact LF NMR spectrometer enables on-line monitoring directly in chemical laboratories as well as in production sites. Especially, these flow-through measurements can be achieved under a fume hood, which is an important asset for safety requirements. Moreover, the smaller size of compact spectrometers allows the use of shorter bypass setups providing a better time resolution. Nonetheless, as sensitivity is a long-standing

concern, especially in LF NMR, the design of a flow-cell, which maximizes the sensitive volume is strongly recommended. Such a design has been investigated with numerical simulations and experimentally by ^{1}H NMR spectroscopy and imaging to determine the characteristics of flow cells such as residence time distribution and mixing effects [46]. Nowadays, most of the benchtop NMR systems can be purchased with a kit for flow-measurement consisting of the flow-cell and the necessary tubing, and potentially a peristaltic pump.

2.1.3. Examples of monitoring with compact NMR spectroscopy

Recently, the number of publications and conference papers on reaction monitoring with LF NMR spectroscopy has been increasingly growing. Reaction monitoring with a compact NMR spectrometer started with a prototype based on a commercial device usually applied for relaxometry, which was adapted for spectroscopy [47, 48]. Guthausen and coworkers monitored the emulsion polymerization of butyl acrylate via a bypass system whereby ^{1}H spectra were collected every 60 s. To follow the progress of the reaction, the olefinic signal was integrated with a Gaussian line-fitting. Moreover, as the sterical arrangement of the produced polymer evolved in the course of the reaction, involving a reduction of the transverse relaxation, the line width was also used for the monitoring. Afterwards, experimental data from both integrals and line widths were analyzed with kinetic models for free-radical polymerization. This monitoring led to the determination of entry and termination rate coefficients [47]. The authors pointed out some complications arising from the overlap between the olefinic region and the solvent signal, a recurring problem in LF NMR monitoring.

In a similar framework, the hydrogenation of toluene to methyl cyclohexane in lab-scale reactor was monitored with a similar customized benchtop system in an on-line fashion [48]. The NMR spectra were recorded in a single scan experiment and the resulting data were analyzed with chemometric tools to cope with huge overlaps in the aliphatic region arising from the reduced spreading of chemical shifts at 20 MHz. Furthermore, the results were compared with success to off-line gas chromatography pointing out the potential of compact LF NMR spectroscopy as a processing analytical device. A few years later, Dalitz *et al* integrated a similar 20 MHz spectrometer in a more appropriate setting in an industrial context [43]. Particular attention was paid to the temperature regulation. A heating circulator maintained a constant temperature within a bypass system while a flow probe using a glass dewar limited the temperature loss in the spectrometer.

The first reaction monitoring with a benchtop spectrometer under the fume hood was reported by Casanova and coworkers in 2011. A fist-sized Halbach magnet, operating at 0.7 T, i.e. 27 MHz, enabled the monitoring of the indium trichloride catalyzed trimerization of propionaldehyde [10]. The reaction mixture was flowing through the bore of the magnet in a closed loop with the help of the peristaltic pump. The experiment was controlled by a console placed outside of the fume hood. The progress of the reaction was followed by integration of the aldehyde peak of the reactant.

The recent development of longer Halbach magnets equipped with a set of shim coils, provided higher and more homogenous B_0 fields leading to a better sensitivity and a sub-Hertz line width. This amazing technological effort enabled more challenging applications such as the monitoring of standard reactions at concentrations lower than 1 M. In 2014, Danieli *et al* probed a transfer hydrogenation reaction on-line with a 43 MHz benchtop system placed next to the reactor [6]. Different kinetic curves were measured as a function of the catalyst concentration (figure A.8c); both direct integration and line fitting were used. A linear dependence of the kinetic constant on the catalyst concentration was observed in good agreement with a gas chromatographic data. The authors reported a detection and quantification limits of 3 and 10 mM, respectively, for a single scan experiment. This study showed how these recent compact magnets (figure A.8a) used with optimized flow parameters are suitable to probe chemical reactions even at realistic low concentrations and paved the way of further real-time monitoring.

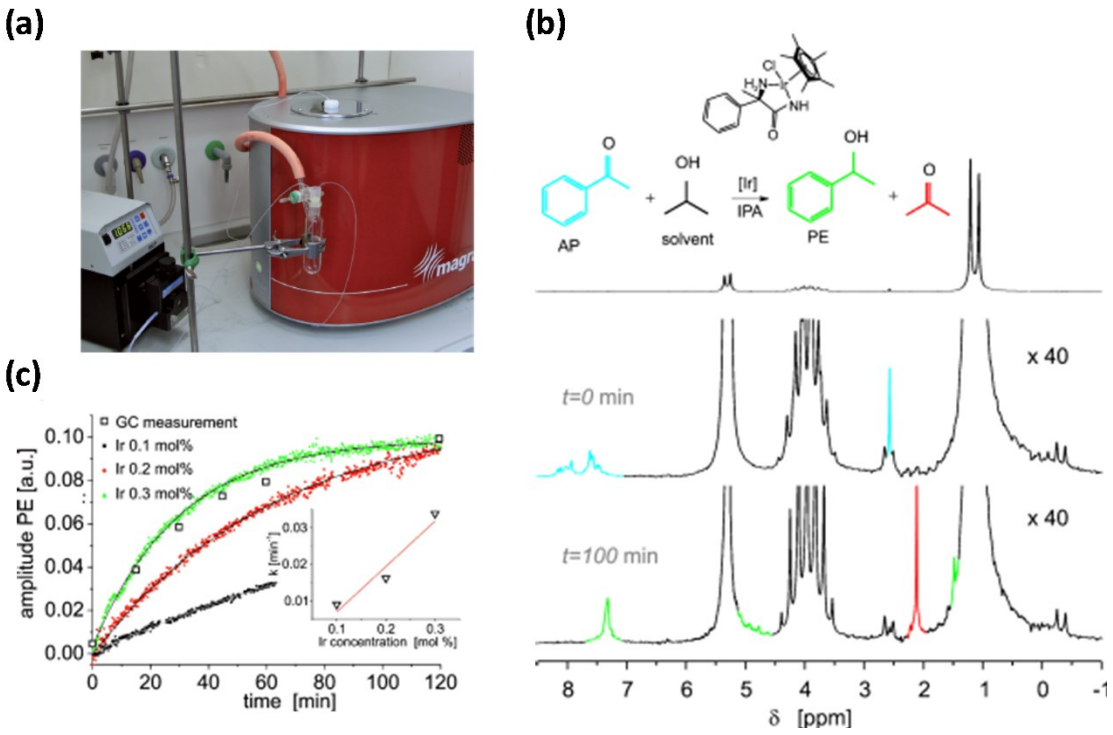

Figure A.8. On-line monitoring of a chemical reaction under the fume hood by using compact NMR spectrometer. **(a)**: 43 MHz benchtop NMR system (Spinsolve, Magritek) located inside a chemical fume hood. The Schlenk reactor is closed to the spectrometer and the peristaltic pump can be seen on the left. **(b)**: Scheme of the studied reaction and two NMR spectra recorded at the beginning and the end of the monitoring. **(c)**: Kinetic curves for different catalyst concentrations. The bigger opened squares over the fastest reaction curve correspond to the GC measurements of reference samples taken from the reactor at particular times. The inset shows the characteristic rates for the three curves as a function of the Iridium concentration. Figures reproduced from Ref. 6.

In this field, Blümich and collaborators investigated the potential of LF NMR spectroscopy to probe in real-time a transesterification reaction for biodiesel production [49]. The reaction mixture was stirred and passed through a bypass system integrating the magnet of a 43 MHz spectrometer. Single-scan spectra were recorded in continuous flow mode at 10 s intervals. A multivariate calibration model relying on partial least squares regressions was previously built to analyze the measured data and to obtain the biodiesel conversion ratio with errors on the order of 1 %. Afterwards, this information was used in combination with a Lorentzian deconvolution of the spectra to evaluate the relative concentrations of methanol present in the ester-rich phase in comparison with the one in the glycerol phase. Beyond the promising potential for process control in biodiesel production, this study points out the capability of monitoring biphasic reactions.

Although the real time monitoring of chemical process occurring on short timescales is an important challenge, probing complex reactions over long periods of time is also an issue. Indeed compact and permanent magnets potentially suffer from drifts of the static magnetic field so that one may question their stability for such applications. In this context, the long fermentation processes in slurries of the two microbial cultures *Hansenula polymorpha* and *Ustilago maydis* were monitored in continuous flow mode over 23 h. ^{1}H NMR spectra were recorded every 15 s with a 43 MHz benchtop system located close to the bioreactor [50]. Gas bubbles generated in the multiphase mixture were removed with a bubble trap during the continuous-flow fermentation process. It is worth mentioning that such a setting including gas recycle and circulation pumps, bubble trap and stirred tank reactor is strongly facilitated by the compact size of the benchtop device. The data recorded at low-field in an on-line manner for the *Hansenula polymorpha* fermentation were then compared with results obtained at 400 MHz from samples collected in the course of the reaction. During this fermentation, glycerol consumption could accurately be evaluated within the resulting complex mixture. In addition, the quantification of glucose, itaconic acid, and the relative amount of glycolipids could be performed during the cultivation of *Ustilago maydis*, despite the formation of several by-products.

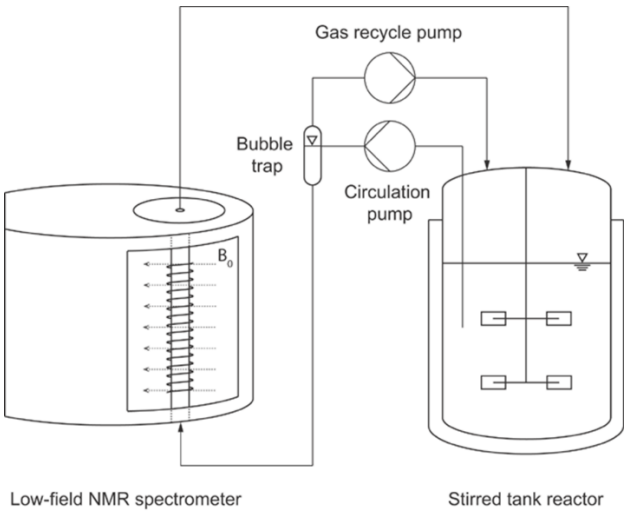

Figure A.9. Schematic diagram of the experimental setup used for fermentation monitoring. Cultivation broth was pumped through a 43 MHz LF NMR spectrometer (Spinsolve, Magritek) via the external bypass and was then aseptically recycled to the bioreactor. Air bubbles were removed with a bubble trap and a peristaltic gas recycle pump. Inside of the NMR spectrometer a polyurethane tube with an inner diameter of 3mm was used. B_0 indicates magnetic field strength for NMR measurements. Figure reproduced from Ref. 50.

Alongside these studies achieved with bypass systems, Elipe *et al.* explored the pros and cons of capillary-sized sample volumes for reaction monitoring [51]. Three different types of chemical reactions were followed with a compact NMR spectrometer at 45 MHz in injection mode (figure A.10a): a Fischer esterification inside the NMR flow cell, the Suzuki coupling performed in a small reaction vessel and finally the formation of an oxime in a larger scale jacketed reactor. In the Fisher esterification, methanol, acetic acid and a small amount of sulfuric acid were mixed in a vial, and an aliquot of the reaction was immediately injected into the flow cell of the benchtop instrument through a HPLC filter. The spectra were collected over a period of time without stirring at 42°C. The kinetic curves were obtained by integrating the peaks of the methoxy group of methanol at 3.42 ppm and the methoxy group of methylacetate at 3.68 ppm. Next, the Suzuki coupling reaction allowed to evaluate the impact of protonated solvents on the spectra and the potential overlapping of the proton signals of the solutes (figure A.10b). The reaction was carried out in a small reaction vessel under stirring and probed by collecting small aliquots from the reactor in regular intervals for analysis by injecting them into the spectrometer through a filter. Each experiment was performed with 50 scans to reach a sufficient sensitivity. To face the overlap between starting and final materials, integration was achieved with global spectral deconvolution. The last mentioned reaction involved a biphasic system whereby reactants were contained exclusively in the aqueous layer to react and give the product, which was extracted into the organic layer. The reaction was carried out in a large scale jacketed reactor to optimize the reaction parameters. Samples were taken from the organic phase every 15 minutes, centrifuged, filtered and then injected into the spectrometer for NMR analysis. This work demonstrated the feasibility of at-line monitoring with capillary-size samples in the cases of reactions involving concentrated materials.

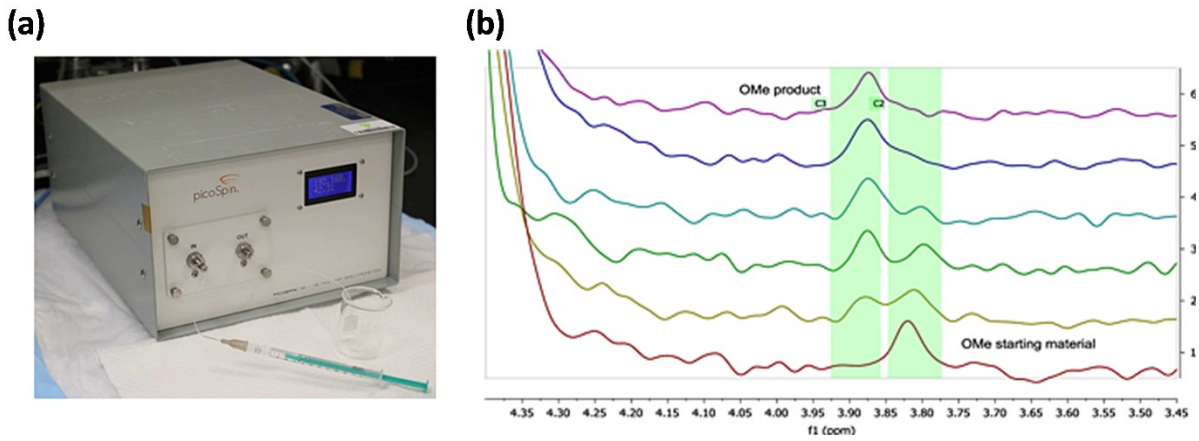

Figure A.10. **(a)**: Benchtop system (picoSpin-45 NMR, Thermo Scientific). Reaction monitoring is carried out by simple injection of aliquots in the inlet port through an HPLC filter. **(b)**: ^{1}H NMR stacked spectra of the methoxy region for the time course array of the Suzuki coupling reaction of 5-bromo-2-methoxypyridine and phenylboronic acid catalyzed with PdCl2 in DMF-H2O 1:1. Figures reproduced from Ref. 51.

These recent applications have witnessed how the inherent low ^{1}H chemical shift dispersion at low-field could be a limiting factor, especially when non-deuterated solvents are used. Hence, one may consider the opportunity to probe other nuclei providing a higher chemical shift dispersion. ^{13}C NMR is a common solution, however, its low natural abundance leads to time-consuming experiments making it unsuitable for reaction monitoring. ^{19}F exhibits a sensitivity close to ^{1}H as well as an appealing spectral width limiting potential overlaps. Maiwald and coworkers described an automated procedure for successive ^{1}H – ^{19}F NMR experiments to monitor an esterification reaction, in which one reactant includes a $–CF_3$ group, in an on-line manner [52]. In the same study, the experimental data are automatically processed and an accurate comparison of different analyzing methods: direct integration, line fitting, PLS (Partial Least Square) calibration and indirect hard modelling, is described.

Hitherto the monitored reactions in the aforementioned applications were carried out inside a vessel. It is worth reporting the recent in-line integration of compact NMR within flow chemistry systems. Continuous-flow chemistry is gaining interest in industry and research laboratories due to the inherent efficiency of the reactor configuration which is superior to batch reactors [53]. Integrating analytics in-line enables obtaining a large amount of insights in real-time about the reaction progress, catalytic activity or stability [41]. Furthermore, such a process monitoring allows controlling the reaction progress and selectivity via manual or automated feedback optimization. In this framework, Cronin and coworkers described a

synthetic flow chemistry platform consisting of a flow reactor, an in-line benchtop NMR spectrometer as well as an automatic control system, which analyzes NMR data and carries out self-optimization relying on a Nelder–Mead algorithm [54] (figure A.11). They performed a range of reactions including imine formation, electrophilic fluorinations and Diels–Alder reactions. This platform enabled kinetic studies, structural characterization and self-optimization of flow conditions. The use of different NMR experiments such as DEPT ^{13}C, ^{19}F NMR and 2D NMR was reported in this study.

Again in this background, Duchateau and coworkers recently achieved the in-line monitoring of the production of widely used Grignard reagents from magnesium metal under continuous flow in integrating a 43 MHz compact spectrometer within their flow setup [55]. This monitoring allowed the quick optimization of working conditions for this process.

A last example of the use of NMR as an integrating PAT in flow synthesis was reported by Ley and coworkers. In this work, a continuous flow process that is fully integrated with a 43 MHz benchtop device for a hypervalent iodine (III) mediated cyclization to generate substituted cyclopropanes was developed [56]. An interesting point was the proposed solutions to circumvent the overlapping situation as well as the use of non-deuterated solvent to perform the reaction. First, a solvent evaporation device was incorporating together with a solvent switching system between the flow outlet and the benchtop instrument so that the NMR date were recorded with a deuterated solvent while the reaction was continued with a protonated one. Then, to overcome the remaining overlaps between the reactants, COSY spectra recorded in around 10 min allowed tracking the consumption of starting material and the formation of products in the overcrowded region, otherwise unsolvable by 1D ^{1}H NMR.

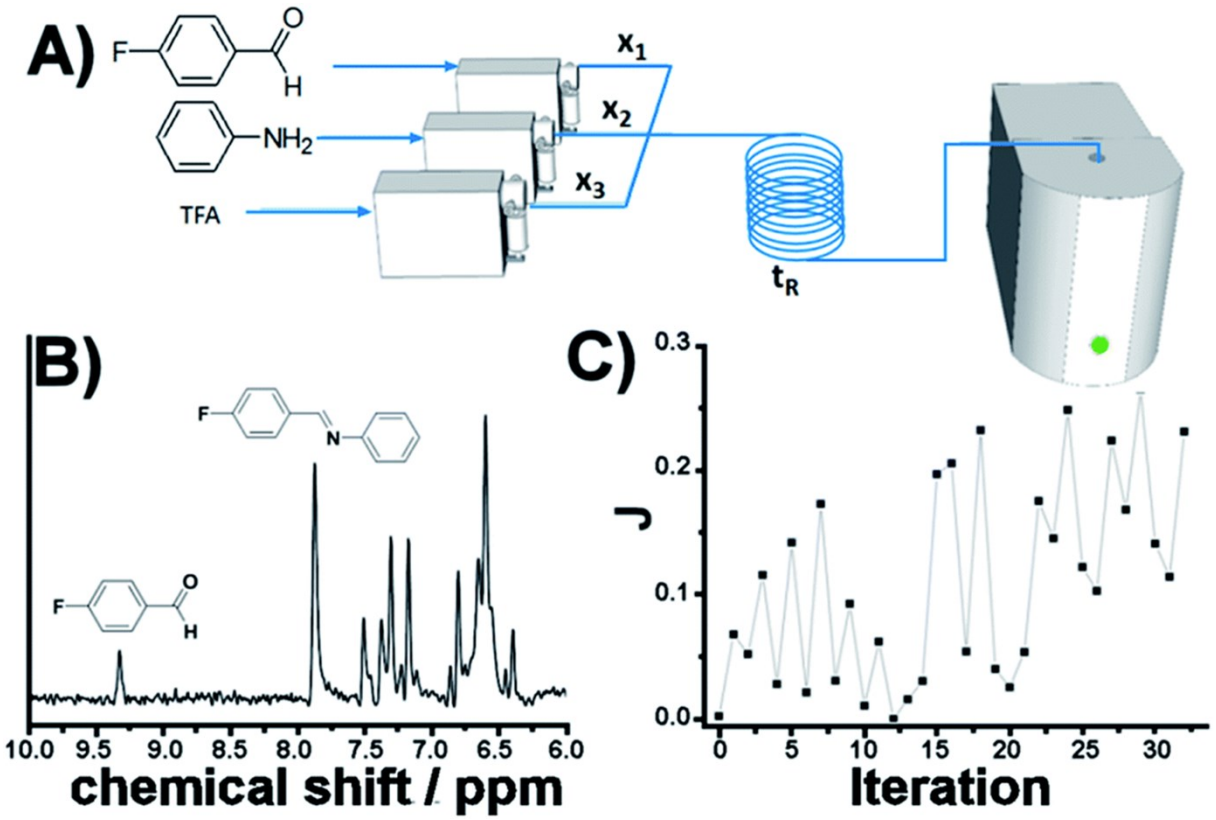

Figure A.11. Self-optimization reaction of an imine synthesis under flow employing in-line NMR to feedback the signal. TFA: trifluoroacetic acid; t_R: residence time; xi: volumetric fractions and J: space-time yield of the reaction. Figures reproduced from Ref. 54.

Finally, compact NMR spectrometers have also been shown to enable hyphenation with other techniques such as size exclusion chromatography (SEC) [57, 58]. Table II gives an overview of the recent reaction monitoring and process control achieved by LF NMR spectroscopy from 2009 to 2017.

.

Table II: Overview of the recent reaction monitoring and process control achieved by LF NMR spectroscopy from 2009 to 2017.

First author (year)	Applications	Setups	Frequency / apparatus	NMR experiments	Data analysis	Process timescale
Guthausen et al (2009) Ref.48	Monitoring of hydrogenation of toluene to methylcyclohexane	On-line with a bypass system.	20 MHz / Prototype mq 20 minispec (Bruker) adapted for spectroscopy	1D 1H	Direct intergration and PLS	Several hours
Vargas et al (2010) Ref. 47	Monitoring of emulsion polymerization of butyl acrylate	On-line with a bypass system.	20 MHz / Prototype mq 20 minispec (Bruker) adapted for spectroscopy	1D 1H	Intergration by line-fitting and peak-width	Around 2 hours
Cudaj et al (2011) Ref. 57	Analysis of synthetic polymers and a block co-polymer	On-line setup hyphenated to size exclusion chromatography	20 MHz / Prototype mq 20 minispec (Bruker) adapted for spectroscopy	1D 1H	na	Around 20 min
Küster et al (2011) Ref. 10	Monitoring of the trimerization of propionaldehyde catalyzed by indium trichloride	On-line with a bypass system.	27 MHz magnet opereted by a Kea spectromter (Magritek) placed outside the fume hood	1D 1H	Direct intergration	Several hours
Dalitz et al (2014) Ref. 43	Monitoring of an esterification reaction	On-line with a bypass system adapted for high temperatures. Fed lines and pump heads were thermostated. Flow probe with a glass dewar	20 MHz / Prototype mq 20 minispec (Bruker) adapted for spectroscopy	1D 1H	Integration by Lorentz-Gaussian line fitting	Around 2 h
Danieli et al (2014) Ref. 6	Monitoring of a transfer hydrogenation reaction	On-line with a bypass system.	43 MHz / Spinsolve (Magritek)	1D 1H	Both direct integration and Lorentzian line fitting	Around 2 h
Killner et al (2015) Ref. 49	Monitorig of a transesterification for a biodiesel production	On-line with a bypass system.	43 MHz magnet opereted by a Kea spectromter (Magritek) placed outside the fume hood	1D 1H	Integration by Lorentzian line fitting and PLS	Around 1h30

Table II: (continued)

First author (year)	Applications	Setups	Frequency / apparatus	NMR experiments	Data analysis	Process timescale
Kreyenschulte et al (2015) Ref. 50	Monitoring of fermentation processes	On-line with a bypass system including including gas recycle and circulation pumps, bubble trap	43 MHz / Spinsolve (Magritek)	1D 1H	Direct Integration	Around 24 h
Sans et al (2015) Ref. 54	Process control and self optimiatization of a flow chemistry platform	In-line/ On-line integrated within a flow synthesis setting	60 MHz / Spinsolve (Magritek)	1D: 1H, 19F,13C, DEPT and 2D: COSY and HSQC	Directect Integration and deconvolution	na
Elipe et al (2015) Ref. 51	Assessment of LF monitoring of three different reactions	At-line with injection mode	45 MHz / picoSpin (Thermo Scientific)	1D 1H	Directect Integration and deconvolution	na
Zientek et al (2015) Ref. 52	Simultaneous 1H and 19F monitoring of an esterification	On-line with a bypass system adapted for high temperatures. Fed lines and pump heads were thermostated. Flow probe with an evcuated dewar tube	43 MHz / Spinsolve (Magritek)	1D 1H and 19F	Direct integration, line fitting and indirect hard modelling	3 h
Goldbach et al (2016) Ref. 55	Optimizing the preparation of Grignard reagents from magnesium metal under continuous flow conditions	In-line/ On-line integrated within a flow synthesis setting	43 MHz / Spinsolve (Magritek)	1D 1H	Direct integration	2 h
Ahmed-Omer et al (2016) Ref. 56	Monitoring of a hypervalent iodine(III) mediated cyclopropanation in a continuous flow process	In-line/ On-line integrated within a flow synthesis setting	43 MHz / Spinsolve (Magritek)	1D: 1H 2D: COSY and J-Res	Direct integration	na

2.2. Authentication and quality control

One major application of NMR spectroscopy in industry is product and quality control. HF NMR has proved to be an efficient tool in such applications, as highlighted by numerous studies in food sciences [59]. However, HF NMR is not generally seen as a good candidate technique for routine applications due to the aforementioned practical and economic reasons. Based on the recent technological improvements, benchtop NMR spectroscopy can now compete with and complement other routine analytical techniques such as GC, high performance liquid chromatography (HPLC), Raman and FT-IR in delivering valuable insights without the need of elaborated sample preparation.

The last years have witnessed the use of LF NMR spectroscopy as a screening tool in different matrices: food, emulsions, pharmaceutics as well as raw rubber and biodiesel samples. Table III gives an overview of this promising potential. The driving idea can be summarized as follows: is the HF NMR performance needed to achieve quality control? Otherwise, might it be possible to balance the resolution losses in LF NMR by subsequent chemometric analysis? Following this question, the studies presented above rely on two approaches: *(i)* identification and quantification of key markers. This is possible if LF NMR provides enough resolution; *(ii)* "profiling approach", based on the comparison of LF NMR fingerprints and supported by statistical methods.

Malet-Martino and coworkers demonstrated the potential of a 60 MHz benchtop spectrometer for uncovering adulteration of "100% natural" sexual enhancement and weight loss dietary supplements [60]. After a very simple and rapid sample preparation, around 20 min of recording was sufficient to detect the adulterants at a concentration of 0.9 mM. Furthermore, the quantification by the internal standard method could be achieved with the LF NMR spectrometer in a reasonable period of time (45 min) and led to data similar to those obtained with HF NMR (500 MHz) for concentrations near 2 mM.

Blümich and coworkers investigated the potential of compact NMR spectroscopy as a reliable method for biodiesel quality control. The ^{1}H spectra of rapeseed oil, rapeseed biodiesel as well as of methanol and glycerol could be clearly differentiated at 43 MHz. Despite several peak-overlaps, spectra of biodiesel samples produced from different feedstocks enabled the

estimation of the unsaturated fatty acid methyl esters percentages for each of the samples by integrating relevant resolved signals [61]. The obtained results were in good agreement with those provided by HF NMR measurements. This practical and rapid analytical method (two scan acquisitions) are advantageous for further standard tests at production sites.

The same research group described a suitable approach for quality control of solutions from raw rubber in the rubber manufacturing industry [62]. Samples collected from oil-extended styrene-butadiene rubber (SBR), solution polymerized SBR, emulsion polymerized SBR, and SBR from different lots and the same lots are analyzed at 43 MHz. ^{1}H and ^{13}C spectra recorded in 10 s and more than one hour, respectively, exhibited differences not only between SBR samples polymerized in different ways but also between the same type of SBR from the same and from different lots from the same manufacturer (figure A.12).

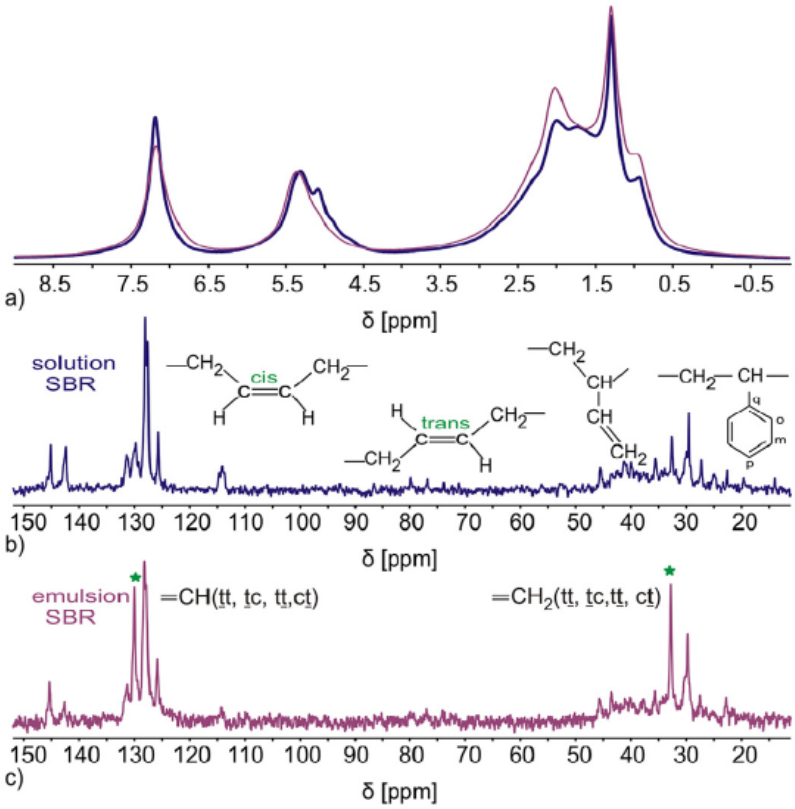

Figure A.12. NMR spectra of oil-extended solution-polymerized SBR (blue) and emulsion-polymerized SBR (red). **(a)** Superposed 1H NMR spectra. ^{13}C spectra of solution-polymerized SBR **(b)** and emulsion-polymerized SBR **(c)**.Figures reproduced from Ref. 63.

Very recently, a new screening protocol to address the issue of coffee authenticity was reported relying on NMR analysis operated at 60 MHz [63]. After a simple chloroform-based extraction, the low-field NMR experiments performed on the lipophilic fraction were shown to be sensitive and selective enough to monitor a key marker compound: 16-Omethylcafestol, found only in robusta coffees. This compound gives rise to an isolated peak at 3.16 ppm. By analyzing an assortment of laboratory-prepared coffee mixtures, the effective limit of detection was estimated to be 10–20% w/w robusta in arabica for approximatively 40 min experiments.

Other relevant studies related to the authentication issue in food science have been recently reported. Nevertheless, the ^{1}H spectra generated by low-field devices do not provide in some instances a sufficient resolution and sensitivity to detect and quantify a key marker capable of discriminating samples from different sets. Such a situation is encountered in the analysis of triglycerides of food samples whose spectra suffer from numerous and severe peak overlaps (figure A.13). Thus, a screening approach considering the most abundant fatty acids to characterize the overall lipid fingerprint is preferred at low-field. Such a profiling approach – nowadays popular in food authentication [64] – combined with chemometric tools has been described to screen edible oil adulteration. In this study, Kemsley and coworkers combined 1D ^{1}H experiments in 16 scans with PLS regression to detect olive oil with hazelnut oil samples within an adulteration level of 11 % [65]. In the same vein, ^{1}H NMR experiments at 60 MHz were performed on samples of beef and horse meat after a simple chloroform-based extraction yielding their respective triglyceride fingerprints. Subsequent statistical analysis of the LF NMR data allowed to differentiate between beef and horse meat with no more than a 10 min spectral acquisition time [66]. This highlights the real potential of LF-NMR spectroscopy as a rapid and efficient screening tool.

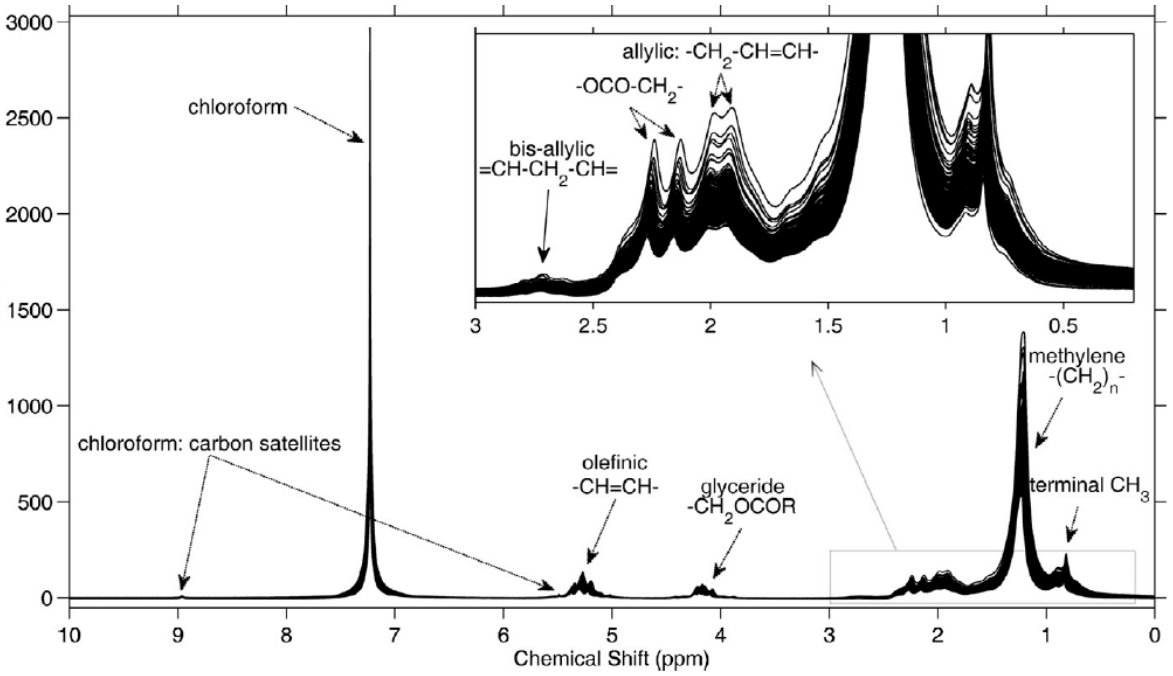

Figure A.13. 60 MHz ^{1}H spectroscopy for the detection of olive oil adulteration. Annotated 60 MHz 1H NMR spectra for 20 extra virgin olive oils, 10 hazelnut oils and 144 olive oil–hazel nut oil mixtures. The inset shows an expansion of the chemical-shift region 0.2–3 ppm. Figure reproduced from Ref. 66.

Table III: Overview of the recent product control and screening applications achieved by LF NMR spectroscopy.

Matrices	Applications	First author (year)	Frequency (MHz) / apparatus	Sample preparations	Methods
Pharmaceutics	Adulterarion of sexual enhancement and weight loss dietary supplements	Pages et al (2014) Ref.60	60 MHZ / Pulsar (Oxford Instrument)	samples dissolved in CD_3OD	1D ^{1}H
Raw rubber	Quality control of raw rubber	Singh et al (2016) Ref.62	43 MHz / Spinsolve (Magritek)	samples dissolved in $CDCl_3$	1D ^{1}H and ^{13}C
Biodiesel	Quality control of biodiel production	Linck et al (2013) Ref.61	43 MHz / coupled with Kea2 NMR spectrometer (Magritek)	extraction of organic phase, washed, centrifiged and dried. No dilution in solvent	1D ^{1}H ; T1 with inversion-recovery
Edible oil	Adulteration of olive oil with hazelnu oil	Parker et al (2014) Ref.65	60 MHZ / Pulsar (Oxford Instrument)	samples dissolved in non-deuterated CHCl3	1D ^{1}H ; PLS regression
Meat	Adulteration of beef meat with horse meat	Jakes et al (2015) Ref.66	60 MHZ / Pulsar (Oxford Instrument)	Chloroform-based extraction	1D ^{1}H ; PCA and Naïve Bayes classification
Coffees	Authentication of aribica versus robusta ground roast coffees	Defernez et al (2017) Ref.63	60 MHZ / Pulsar (Oxford Instrument)	Chloroform-based extraction	1D ^{1}H

References

[1] K. Singh, B. Blümich, NMR spectroscopy with compact instruments, Trends Anal. Chem. TrAC, 83 (2016) 12-26.
[2] K. Meyer, S. Kern, N. Zientek, G. Guthausen, M. Maiwald, Process control with compact NMR, Trends Anal. Chem. TrAC, 83 (2016) 39-52.
[3] F. Dalitz, M. Cudaj, M. Maiwald, G. Guthausen, Process and reaction monitoring by low-field NMR spectroscopy, Prog. Nucl. Magn. Reson. Spectrosc., 60 (2012) 52-70.
[4] J. Mitchell, L.F. Gladden, T.C. Chandrasekera, E.J. Fordham, Low-field permanent magnets for industrial process and quality control, Prog. Nucl. Magn. Reson. Spectrosc., 76 (2014) 1-60.
[5] S.D. Riegel, G.M. Leskowitz, Benchtop NMR spectrometers in academic teaching, Trends Anal. Chem. TrAC, 83 (2016) 27-38.
[6] E. Danieli, J. Perlo, A.L.L. Duchateau, G.K.M. Verzijl, V.M. Litvinov, B. Blümich, F. Casanova, On-Line Monitoring of Chemical Reactions by using Bench-Top Nuclear Magnetic Resonance Spectroscopy, ChemPhysChem, 15 (2014) 3060-3066.
[7] K. Halbach, Design of permanent multipole magnets with oriented rare earth cobalt material, Nucl. Instr. Meth., 169 (1980) 1-10.
[8] H. Raich, P. Blümler, Design and construction of a dipolar Halbach array with a homogeneous field from identical bar magnets: NMR Mandhalas, Concepts Magn. Reson., 23B (2004) 16-25.
[9] E. Danieli, J. Perlo, B. Blümich, F. Casanova, Small Magnets for Portable NMR Spectrometers, Angew. Chem. Int. Edit., 49 (2010) 4133-4135.
[10] S.K. Kuster, E. Danieli, B. Blumich, F. Casanova, High-resolution NMR spectroscopy under the fume hood, Phys. Chem. Chem. Phys., 13 (2011) 13172-13176.
[11] E. Auguste, E. Lucas, L. Poigniez, D. Ramamurthy, H. Vaneeckhoutte, P. Lesot, RMN de paillasse à transformée de Fourier: le renouveau de la résonance magnétique nucléaire à bas champ, Spectra Analyse, 315 (2017) 32-64.
[12] Magritek, Spinsolve, http://www.magritek.com/products/spinsolve/, accessed online 12 August 2017.
[13] Oxford Instrument, Pulsar, https://www.oxford-instruments.com/products/spectrometers/nuclear-magnetic-resonance-nmr/pulsar, accessed online 12 August 2017.
[14] Thermo Scientific, picoSpin, https://www.thermofisher.com/order/catalog/product/912A0832, accessed online 12 August 2017.
[15] Nanalysis, NMReady, http://www.nanalysis.com/products-overview/, accessed online 12 August 2017.
[16] S. Gloggler, M. Emondts, J. Colell, R. Muller, B. Blumich, S. Appelt, Selective drug trace detection with low-field NMR, Analyst, 136 (2011) 1566-1568.

[17] J.F.P. Colell, M. Emondts, A.W.J. Logan, K. Shen, J. Bae, R.V. Shchepin, G.X. Ortiz, P. Spannring, Q. Wang, S.J. Malcolmson, E.Y. Chekmenev, M.C. Feiters, F.P.J.T. Rutjes, B. Blümich, T. Theis, W.S. Warren, Direct Hyperpolarization of Nitrogen-15 in Aqueous Media with Parahydrogen in Reversible Exchange, J. Am. Chem. Soc., 139 (2017) 7761-7767.
[18] R.K. Harris, E.D. Becker, S.M. Cabral de Menezes, R. Goodfellow, P. Granger, NMR nomenclature. Nuclear spin properties and conventions for chemical shifts (IUPAC recommendations 2001), Pure Appl. Chem., 73 (2001) 1795-1818.
[19] Magritek, Examples of NMR spectra, http://www.magritek.com/products/spinsolve/nmr-spectra-examples/, accessed online 12 August 2017.
[20] M.R.M. Koos, E. Danieli, F. Casanova, B. Blümich, B. Luy, Differentiation of enantiomers by 2D NMR spectroscopy at 1 T using residual dipolar couplings, Magn. Reson. Chem., 54 (2016) 527-530.
[21] M.J. Thrippleton, R.A.E. Edden, J. Keeler, Suppression of strong coupling artefacts in J-spectra, J. Magn. Reson., 174 (2005) 97-109.
[22] J.I. Musher, E.J. Corey, Virtual long-range spin-spin couplings in NMR, Tetrahedron, 18 (1962) 791-809.
[23] J.R. Brisson, J.P. Carver, Virtual coupling in the 1H NMR spectrum of N,N'-diacetyl chitobioside. Application to glycopeptides, J. Biol. Chem., 257 (1982) 11207-11209.
[24] H.J. Reich, Virtual coupling https://www.chem.wisc.edu/areas/reich/nmr/05-hmr-16-virt-coupl.htm, accessed online 12 August 2017.
[25] L.E. Kay, R.E.D. McClung, A product operator description of AB and ABX spin systems, J. Magn. Reson. , 77 (1988) 258-273.
[26] J. Workman, M. Koch, B. Lavine, R. Chrisman, Process Analytical Chemistry, Anal. Chem., 81 (2009) 4623-4643.
[27] M. Maiwald, H.H. Fischer, Y.-K. Kim, K. Albert, H. Hasse, Quantitative high-resolution on-line NMR spectroscopy in reaction and process monitoring, J. Magn. Reson., 166 (2004) 135-146.
[28] H. Weber, L. Brecker, Online NMR for monitoring biocatalysed reactions, Curr. Opin. Biotechnol., 11 (2000) 572-578.
[29] M. Maiwald, O. Steinhof, C. Sleigh, M. Bernstein, H. Hasse, Quantitative high-resolution online NMR spectroscopy in pharmaceutical reaction and process monitoring, Elsevier, Oxford2008.
[30] M.A. Bernstein, M. Štefinović, C.J. Sleigh, Optimising reaction performance in the pharmaceutical industry by monitoring with NMR, Magn. Reson. Chem., 45 (2007) 564-571.
[31] F. Susanne, D.S. Smith, A. Codina, Kinetic Understanding Using NMR Reaction Profiling, Org. Process Res. Dev., 16 (2012) 61-64.
[32] T.R. Hoye, B.M. Eklov, T.D. Ryba, M. Voloshin, L.J. Yao, No-D NMR (No-Deuterium Proton NMR) Spectroscopy: A Simple Yet Powerful Method for Analyzing Reaction and Reagent Solutions, Org. Lett., 6 (2004) 953-956.

[33] I.M. Clegg, C.M. Gordon, D.S. Smith, R. Alzaga, A. Codina, NMR reaction monitoring during the development of an active pharmaceutical ingredient, Anal. Methods, 4 (2012) 1498-1506.
[34] M. Khajeh, M.A. Bernstein, G.A. Morris, A simple flowcell for reaction monitoring by NMR, Magn. Reson. Chem., 48 (2010) 516-522.
[35] D.A. Foley, C.W. Doecke, J.Y. Buser, J.M. Merritt, L. Murphy, M. Kissane, S.G. Collins, A.R. Maguire, A. Kaerner, ReactNMR and ReactIR as Reaction Monitoring and Mechanistic Elucidation Tools: The NCS Mediated Cascade Reaction of α-Thioamides to α-Thio-β-chloroacrylamides, J. Org. Chem., 76 (2011) 9630-9640.
[36] J.Y. Buser, A.D. McFarland, Reaction characterization by flow NMR: quantitation and monitoring of dissolved H2via flow NMR at high pressure, Chem. Commun., 50 (2014) 4234-4237.
[37] D.A. Foley, E. Bez, A. Codina, K.L. Colson, M. Fey, R. Krull, D. Piroli, M.T. Zell, B.L. Marquez, NMR Flow Tube for Online NMR Reaction Monitoring, Anal. Chem., 86 (2014) 12008-12013.
[38] A. Brächer, R. Behrens, E. von Harbou, H. Hasse, Application of a new micro-reactor 1H NMR probe head for quantitative analysis of fast esterification reactions, Chem. Eng. J., 306 (2016) 413-421.
[39] A.C. Barrios Sosa, R.T. Williamson, R. Conway, A. Shankar, R. Sumpter, T. Cleary, A Safe and Efficient Synthetic Route to a 2,5-Dimethyl-1-aryl-1H-imidazole Intermediate, Org. Process Res. Dev., 15 (2011) 449-454.
[40] K.A. Farley, U. Reilly, D.P. Anderson, B.P. Boscoe, M.W. Bundesmann, D.A. Foley, M.S. Lall, C. Li, M.R. Reese, J. Yan, Utilizing on- and off-line monitoring tools to follow a kinetic resolution step during flow synthesis, Magn. Reson. Chem., 55 (2017) 348-354.
[41] V. Sans, L. Cronin, Towards dial-a-molecule by integrating continuous flow, analytics and self-optimisation, Chem. Soc. Rev., 45 (2016) 2032-2043.
[42] M.V. Gomez, A. de la Hoz, NMR reaction monitoring in flow synthesis, Beilstein J. Org. Chem., 13 (2017) 285-300.
[43] F. Dalitz, L. Kreckel, M. Maiwald, G. Guthausen, Quantitative Medium-Resolution NMR Spectroscopy Under Non-Equilibrium Conditions, Studied on the Example of an Esterification Reaction, Appl. Magn. Reson., 45 (2014) 411-425.
[44] D.A. Foley, A.L. Dunn, M.T. Zell, Reaction monitoring using online vs tube NMR spectroscopy: seriously different results, Magn. Reson. Chem., 54 (2016) 451-456.
[45] N. Zientek, C. Laurain, K. Meyer, M. Kraume, G. Guthausen, M. Maiwald, Simultaneous 19F–1H medium resolution NMR spectroscopy for online reaction monitoring, J. Magn. Reson., 249 (2014) 53-62.
[46] F. Dalitz, M. Maiwald, G. Guthausen, Considerations on the design of flow cells in by-pass systems for process analytical applications and its influence on the flow profile using NMR and CFD, Chem. Eng. Sci., 75 (2012) 318-326.
[47] M.A. Vargas, M. Cudaj, K. Hailu, K. Sachsenheimer, G. Guthausen, Online Low-Field 1H NMR Spectroscopy: Monitoring of Emulsion Polymerization of Butyl Acrylate, Macromolecules, 43 (2010) 5561-5568.

[48] G. Guthausen, A.v. Garnier, R. Reimert, Investigation of Hydrogenation of Toluene to Methylcyclohexane in a Trickle Bed Reactor by Low-Field Nuclear Magnetic Resonance Spectroscopy, Appl. Spectrosc., 63 (2009) 1121-1127.
[49] M.H.M. Killner, Y. Garro Linck, E. Danieli, J.J.R. Rohwedder, B. Blümich, Compact NMR spectroscopy for real-time monitoring of a biodiesel production, Fuel, 139 (2015) 240-247.
[50] D. Kreyenschulte, E. Paciok, L. Regestein, B. Blümich, J. Büchs, Online monitoring of fermentation processes via non-invasive low-field NMR, Biotechnol. Bioeng., 112 (2015) 1810-1821.
[51] M.V. Silva Elipe, R.R. Milburn, Monitoring chemical reactions by low-field benchtop NMR at 45 MHz: pros and cons, Magn. Reson. Chem., DOI 10.1002/mrc.4189(2015) n/a-n/a.
[52] N. Zientek, C. Laurain, K. Meyer, A. Paul, D. Engel, G. Guthausen, M. Kraume, M. Maiwald, Automated data evaluation and modelling of simultaneous 19F–1H medium-resolution NMR spectra for online reaction monitoring, Magn. Reson. Chem., 54 (2016) 513-520.
[53] J. Wegner, S. Ceylan, A. Kirschning, Flow Chemistry – A Key Enabling Technology for (Multistep) Organic Synthesis, Adv. Synth. Catal., 354 (2012) 17-57.
[54] V. Sans, L. Porwol, V. Dragone, L. Cronin, A self optimizing synthetic organic reactor system using real-time in-line NMR spectroscopy, Chem. Sci., 6 (2015) 1258-1264.
[55] M. Goldbach, E. Danieli, J. Perlo, B. Kaptein, V.M. Litvinov, B. Blümich, F. Casanova, A.L.L. Duchateau, Preparation of Grignard reagents from magnesium metal under continuous flow conditions and on-line monitoring by NMR spectroscopy, Tetrahedron Lett., 57 (2016) 122-125.
[56] B. Ahmed-Omer, E. Sliwinski, J.P. Cerroti, S.V. Ley, Continuous Processing and Efficient in Situ Reaction Monitoring of a Hypervalent Iodine(III) Mediated Cyclopropanation Using Benchtop NMR Spectroscopy, Org. Process Res. Dev., 20 (2016) 1603-1614.
[57] M. Cudaj, G. Guthausen, T. Hofe, M. Wilhelm, SEC-MR-NMR: Online Coupling of Size Exclusion Chromatography and Medium Resolution NMR Spectroscopy, Macromol. Rapid Commun., 32 (2011) 665-670.
[58] V. Räntzsch, M. Wilhelm, G. Guthausen, Hyphenated low-field NMR techniques: combining NMR with NIR, GPC/SEC and rheometry, Magn. Reson. Chem., 54 (2016) 494-501.
[59] L. Mannina, A.P. Sobolev, S. Viel, Liquid state 1H high field NMR in food analysis, Prog. Nucl. Magn. Reson. Spectrosc., 66 (2012) 1-39.
[60] G. Pagès, A. Gerdova, D. Williamson, V. Gilard, R. Martino, M. Malet-Martino, Evaluation of a Benchtop Cryogen-Free Low-Field 1H NMR Spectrometer for the Analysis of Sexual Enhancement and Weight Loss Dietary Supplements Adulterated with Pharmaceutical Substances, Anal. Chem., 86 (2014) 11897-11904.
[61] Y. Garro Linck, M.H.M. Killner, E. Danieli, B. Blümich, Mobile Low-Field 1H NMR Spectroscopy Desktop Analysis of Biodiesel Production, Appl. Magn. Reson., 44 (2013) 41-53.
[62] K. Singh, B. Blümich, Desktop NMR Spectroscopy for Quality Control of Raw Rubber, Macro. Mol. Symp., 365 (2016) 191-193.

[63] M. Defernez, E. Wren, A.D. Watson, Y. Gunning, I.J. Colquhoun, G. Le Gall, D. Williamson, E.K. Kemsley, Low-field 1H NMR spectroscopy for distinguishing between arabica and robusta ground roast coffees, Food Chem., 216 (2017) 106-113.
[64] E. Cubero-Leon, R. Peñalver, A. Maquet, Review on metabolomics for food authentication, Food Res Int., 60 (2014) 95-107.
[65] T. Parker, E. Limer, A.D. Watson, M. Defernez, D. Williamson, E.K. Kemsley, 60 MHz 1H NMR spectroscopy for the analysis of edible oils, TrAC, Trends Anal. Chem., 57 (2014) 147-158.
[66] W. Jakes, A. Gerdova, M. Defernez, A.D. Watson, C. McCallum, E. Limer, I.J. Colquhoun, D.C. Williamson, E.K. Kemsley, Authentication of beef versus horse meat using 60 MHz 1H NMR spectroscopy, Food Chem., 175 (2015) 1-9.

3. Flow NMR measurements

Flow NNR measurements has been a cross-cutting subject in the previous section. Whether working in a bypass system or within a flow chemistry platform, benchtop NMR monitoring involves NMR measurements on flowing mixtures. Yet, NMR experiments on flowing systems are associated to some special features which significantly impact the sensitivity and the resolution. These points are discussed in the present section.

NMR on flowing liquids has been reported as early as in the 50's. In a pioneer study, the intensity of the NMR signal was found to be proportional to the flow rate and the effects of the flow on T_1 and T_2 were also evaluated [1]. Over the next two decades numerous investigations were made, resulting in a comprehensive description of the effects involved by flowing liquids through the sensitive volume V_s of the flow-cell [2, 3]. Next, studies were undertaken to either improve the signal to- noise of the resulting spectra, reach quantitative conditions with a shorter repetition time [4] or to use NMR to measure aspects of the flow itself [5]. The capability of performing NMR on flowing systems also enabled hyphenated techniques such as LC-NMR [6].

In flow NMR, three essential effects should be taken into account, depending on the velocity of the flow and the characteristic length scales of the flow cell: the "in-flow" effect, the olarization build-up and the "out-flow" effect.

3.1. "In-flow effect"

The first of these effects is commonly reported as 'inflow effect'. During the repetition time of the NMR experiment, excited volume elements are flowing out of the sensitive volume while the unexcited ones are flowing into it (figure A.14). Since the repetition time of an NMR experiment is usually much longer than the pulse sequence and acquisition times, the effect is to replace saturated volume elements by fresh ones during the repetition time. This continuous replenishment leads to a potential intensity enhancement per time unit. Assuming the replenishment is achieved under full thermal polarization, this effect can be regarded as an effective longitudinal relaxation time T_1^{flow} defined as follows [7]:

$$\frac{1}{T_1^{flow}} = \frac{1}{T_1^{static}} + \frac{1}{\tau} \qquad \text{(A.4)}$$

τ is the residence time, i.e. the time spent by a volume element flowing with a volume flow rate Q_v in the sensitive volume V_s. This parameter can be computed as the ratio of the length of the sensitive volume l_s by the fluid velocity v.

$$\tau = \frac{l_s}{v} = \frac{V_s}{Q_v} \qquad \text{(A.5)}$$

3.2. Polarization build-up

Relying on this in-flow effect, increasing the flow rate reduces the residence time and in turn leads to an effective T_1^{flow} shorter than T_1^{static}. This provides potential advantages such as sensitivity enhancement per time unit as well as preserving quantitative conditions with shortened reparation times [4]. Unfortunately, this opportunity should be considered with caution since this bonus effect is true as long as the excited spins are refreshed by fully polarized ones. This polarization build-up occurs when the sample flows through the pre-polarization volume V_p (figure A.14). A sufficient time – typically five times the T_1 measured in static condition - within the pre-polarization volume is required to exhibit full thermal polarization. Thus, there is a maximum flow rate Q_{max} to hold this condition:

$$Q_{max} = \frac{V_p}{5 \, . \, T_1} \qquad \text{(A.6)}$$

In this context, a careful consideration should be given to the polarization volume of the hardware. In the case of magnets severely restricted in size, which does not provide a

sufficient polarization build-up time even at relatively low flow rate, one solution is to introduce longer polarization regions in the experimental setup which can be achieved by the use of a specially designed a flow probe incorporating spiral units, leading to a longer path for the fluid within the magnetic field [8-10]. This approach, however, leads to additional mixing of the fluid and to a significant reduction of the time resolution in the case of reaction monitoring.

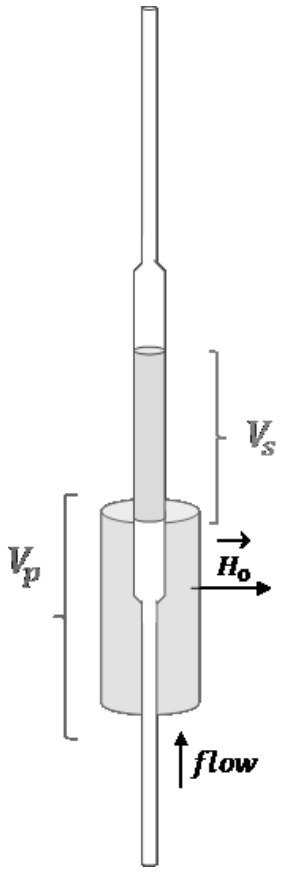

Figure A.14. Scheme of a typical flow-cell used for benchtop NMR monitoring. V_p: pre-polarization volume; V_s : sensitive volume and $\overrightarrow{H_0}$: static magnetic field.

3.3. "Out-flow effect"

A last feature, commonly referred to as "out-flow effect" in the literature must be mentioned as it impacts significantly the resolution of the NMR spectra. During pulse sequence and acquisition, the fluid moves according to the local velocity. There is a certain probability that volume elements, which were polarized and excited and therefore exhibit transverse

magnetization, leave the sensitive volume before the acquisition is finished. This leads to a higher effective transverse relaxation rate $1/T_2^{flow}$, which is given in analogy to the longitudinal effective relaxation rate:

$$\frac{1}{T_2^{flow}} = \frac{1}{T_2^{static}} + \frac{1}{\tau} \qquad \text{(A.7)}$$

This higher effective transversal relaxation rate involves severe line-broadening. Obviously, this effect depends again on the velocity field, polarization state, and geometry of the sensitive volume, i.e. the length along the flow direction.

3.4. Practical considerations

The aforementioned phenomena leads to an overall effect, which results in a special tradeoff concerning the choice of the flow rate. The compromise between the in-flow effect and the polarization build-up is well illustrated in figure A.15 extracted from reference [11]. This figure shows the signal area as function of the flow rate. As expected the curve has a maximum: first, the in-flow effect improve the sensitivity in continuously refreshing the spins; next, over a certain value of flow rate, the replenishment is done with partially polarized spin so that the curve vanishes. Along with this, the signal becomes broader and broader as the flow rate increases. Overall, there is an optimal range of flow rates, which compromise sensitivity per time unit and resolution.

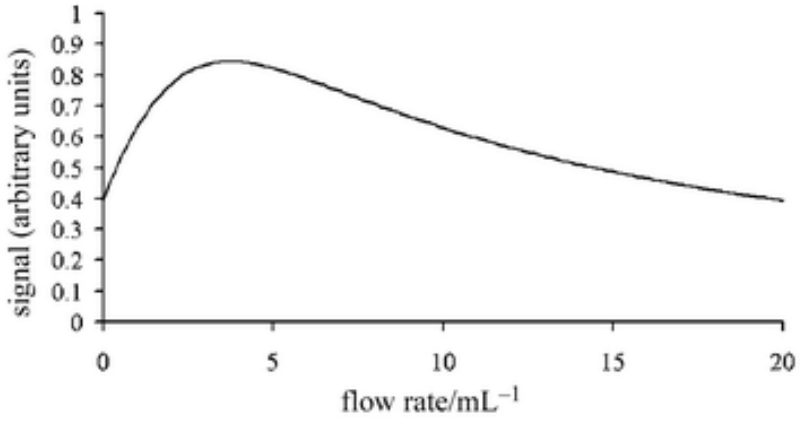

Figure A.15. Signal intensity in function of the flow rate. The sensitivity increase as the spins spend enough time in the pre-polarization volume to be fully polarized. Figure reproduced from Ref. 11.

In setups whose pre-polarization volume is short, this compromise leads to a relative low flow regime, which might be in conflict with the use of bypass systems whereby a fast sample transfer from the reactor to the NMR flow-cell is required to improve the time resolution of the on-line monitoring. This issue can be circumvented by using a split valve prior to the NMR probe so that the sample can be transferred with a larger flow rate up to this point. The main part is fed back to the reactor, while only a small amount is transferred into the probe at lower velocities to tune the flow rate as described above [12, 13].

References

[1] G. Suryan, Nuclear magnetic resonance and the effect of the methods of observation, Curr. Sci., 6 (1949) 203-204.
[2] D.W. Arnold, L.E. Burkhart, Spin-Echo NMR Response from a Flowing Sample, J. Appl. Phys., 36 (1965) 870-871.
[3] L.R. Hirschel, L.F. Libelo, Nuclear Magnetic Resonance in Flowing Fluids, J. Appl. Phys., 32 (1961) 1404-1405.
[4] J.F. Haw, T.E. Glass, H.C. Dorn, Conditions for quantitative flow FT-1H NMR measurements under repetitive pulse conditios, J. Magn. Reson., 49 (1982) 22-31.
[5] A. Caprihan, E. Fukushima, Flow measurements by NMR, Phys. Rep., 198 (1990) 195-235.
[6] P. Keifer, Flow techniques in NMR spectroscopy, Annu. Rep. NMR Spectrosc., 62 (2007) 1-47.
[7] F. Dalitz, M. Cudaj, M. Maiwald, G. Guthausen, Process and reaction monitoring by low-field NMR spectroscopy, Prog. Nucl. Magn. Reson. Spectrosc., 60 (2012) 52-70.
[8] C.A. Fyfe, L. Van Veen Jr, Flow nuclear magnetic resonance investigation of the intermediates formed during the bromination of phenols in acetic acid, J. Am. Chem. Soc., 99 (1977) 3366-3371.
[9] J.F. Haw, T.E. Glass, D.W. Hausler, E. Motell, H.C. Dorn, Direct coupling of a liquid chromatograph to a continuous flow hydrogen nuclear magnetic resonance detector for analysis of petroleum and synthetic fuels, Anal. Chem., 52 (1980) 1135-1140.
[10] A. McGill, A. Nordon, D. Littlejohn, Potential applications of process analysis by NMR spectrometry, J. Proc. Anal. Chem, 6 (2000) 36-38.
[11] A. Nordon, C.A. McGill, D. Littlejohn, Process NMR spectrometry, Analyst, 126 (2001) 260-272.
[12] M. Maiwald, H.H. Fischer, Y.-K. Kim, K. Albert, H. Hasse, Quantitative high-resolution on-line NMR spectroscopy in reaction and process monitoring, J. Magn. Reson., 166 (2004) 135-146.
[13] F. Dalitz, L. Kreckel, M. Maiwald, G. Guthausen, Quantitative Medium-Resolution NMR Spectroscopy Under Non-Equilibrium Conditions, Studied on the Example of an Esterification Reaction, Appl. Magn. Reson., 45 (2014) 411-425.

4. Speeding up 2D NMR

Despite the high homogeneity of the recent compact magnets, LF NMR ^{1}H spectroscopy involves complex and crowded spectra when mixtures or medium-sized molecules are probed. 2D NMR alleviates this inherent issue by offering an orthogonal dimension leading to a resolution enhancement. However, it is worth noting that 2D NMR is not widely used at low-field in practical situations (see table II and III in section A.2) whilst 2D experiments are nowadays available on modern benchtop systems and easily usable even by non-experts. The main reason is probably the long experiment duration, which becomes a significant handicap for the most popular applications of benchtop NMR such as reaction monitoring and high-throughput screening. Therefore, the implementation of fast 2D NMR experiments would be a relevant tool in the LF NMR context.

Fortunately, the NMR community has made strong efforts toward reducing the experiment duration of these 2D acquisitions at high-fields. The present section aims at emphasizing these methodological developments that have been realized in the last decades. First, an overview of the different approaches to speed up 2D NMR is given. Afterwards, a particular emphasis is placed on ultrafast 2D NMR, which is capable of delivering 2D spectra in single scan. A first picture of key principles and popular applications of this sub-second methodology is proposed, followed by a more comprehensive review of methods and applications.

Fast n-Dimensional Data Acquisition Methods

Laetitia Rouger, Boris Gouilleux and Patrick Giraudeau

(Original book chapter published in Encyclopedia of Spectroscopy and Spectrometry, 3rd Edition (2017) 588-596)

Abstract

This article describes the principles and the main features of the numerous methods which have been developed to overcome the time limitation of multi-dimensional NMR. They are classified into four main categories: the first one contains strategies aiming at reducing the repetition time between successive scans, while the methods consisting in reducing the number of t_1 increments belong to the second category. The third family of approaches contains more exotic approaches departing from the conventional Jeener-Ernst scheme: Hadamard and Ultrafast spectroscopy. Finally, the methods relying on parallel receivers are presented.

Abbreviations

2D: two-dimensional

ALSOFAST: alternate SOFAST

ASAP: acceleration by sharing adjacent polarization

BEST: band-selective short transient

bPR: back projection-reconstruction

COSY: correlation spectroscopy

CS: compressed sensing

D-DNP: dissolution dynamic nuclear polarization

DFT: discrete Fourier transform

FDM: filter diagonalization method

FID: free induction decay

FM: forward maximum entropy

nD: multi-dimensional

HMBC: heteronuclear multiple-bond correlation

HMQC: heteronuclear multiple-quantum correlation

HPLC: high-performance liquid chromatography

HSQC: heteronuclear single-quantum correlation

IMPACT: improved and accelerated constant time

INADEQUATE: incredible natural abundance double quantum transfer experiment

INEPT: insensitive nuclei enhanced by polarization transfer

LP: linear prediction

MaxEnt: maximum entropy

MDD: multi-dimensional decomposition

MINT: maximum entropy interpolation

NUS: non-uniform sampling

PANACEA: parallel acquisition NMR, an all-in-one combination of experimental applications

PANSY: parallel acquisition NMR spectroscopy

rMDD: recursive MDD

SMART: small recovery time

SNR: signal-to-noise ratio

SOFAST: band-selective optimized flip-angle short-transient

UF: ultrafast

Speeding up n-dimensional NMR

The emergence of two-dimensional (2D) spectroscopy in the 1970s has literally revolutionized the field of NMR, offering an almost infinite number of experiments capable of yielding valuable information for structural analysis of small molecules. Later on, the development of higher dimensionality experiments has been decisive in understanding the structure and dynamics of macromolecules. The basic scheme for multi-dimensional (nD) NMR experiments was proposed by Jeener in 1971 and further developed by Ernst and co-workers. It consists in repeating the following sequence:

Preparation – Evolution (t_1) – Mixing – Acquisition (t_2)

while incrementing the evolution time to indirectly monitor the evolution of spin interactions during t_1. The second dimension (t_2) corresponds to the direct detection of the free induction decay (FID), while the preparation and mixing periods enable spin manipulations capable of yielding the desired coherence pathway. The strength of this generic scheme is that it can lead, after Fourier Transforming the data along the two time dimensions, to a variety of two dimensional spectra correlating the chemical shift and/or coupling information of two nuclei along orthogonal dimensions. The incorporation of further evolution and mixing periods makes it possible to increase the dimensionality of the experiment to 3D, 4D spectra or even more. But the Jeener-Ernst scheme also comes with long experiment times as a major drawback. The experiment time is given by $T_{exp} = T_{scan} \cdot NS \cdot \prod_{i=1}^{n-1} N_i$ where N_i represents the number of increments in the n-1 indirect dimensions, T_{scan} the repetition time separating two successive acquisitions, and NS the number of scans (or transients). N_i has a direct impact on the spectral resolution in the corresponding dimension. It results in long experiment durations: from a few tens of minutes to a few hours for 2D experiments, and up to several days for 3D or 4D spectra. This duration has several consequences: *i)* the overload of spectrometer schedules, *ii*) the impossibility to monitor fast kinetic or dynamic processes and *iii*) the sensitivity to hardware instabilities between the successive increments, which reduces the signal-to-noise ratio (SNR) in the indirect dimension(s).

The last decades have witnessed considerable research efforts geared towards reducing this experiment duration. A number of valuable solutions have been described and applied to a variety of situations where conventional nD NMR fails. The description of these approaches is the aim of this article, where the various time-reduction approaches are categorized as described in Table 1. The first family of methods consists in reducing the time separating two successive increments, most of the time by a clever optimization of pulse angles and delays. The second category focuses on the methods that reduce the number of increments in the indirect dimension, the subsequent resolution losses being compensated by adapted signal processing methods. Then, more exotic alternatives are described that completely depart from the classical scheme: Hadamard spectroscopy and Ultrafast NMR. Finally, recent hardware-based developments capable of speeding up the acquisition of nD data are described, as well as some fruitful combinations of the methods mentioned above.

Table 1. Classification of the main fast n-dimensional acquisition methods in NMR

Reduction of TR		• Fast-HMQC • SOFAST-HMQC • ALSOFAST-HMQC • 3D BEST experiments • IMPACT-HMBC • ASAP-HSQC • SMART
Reduction of N_i	**Uniform Sampling**	• Reduction of N_i • Spectral Aliasing
	Non-uniform sampling	• Off-grid (Radial sampling) • On-grid (Random, exponential, Poisson-Gap sampling)
Non-Jeener methods		• Hadamard Spectroscopy • Ultrafast spectroscopy and hybrid approaches
Simultaneous acquisitions		• PANSY

Combined strategies	• SOFAST + NUS • NUS + aliasing • UltraSOFAST • Ultrafast + CS • Ultrafast + aliasing • Ultrafast + Hadamard • Ultrafast + PANSY

Increasing the repetition rate

The speed of multidimensional experiments can be significantly improved by shortening the duration of each scan required to sample the whole nD FID. This duration, T_{scan}, consists of the length of the pulse sequence T_{rf}, plus the acquisition period T_a, plus the recovery delay T_{rec} inserted between scans to let the spin system relax back to equilibrium (Figure 1a). Of all these delays, T_{rec} is clearly the longest one (typically several seconds) and appears to be the only one which can be reduced without losing resolution. As the signal available at the beginning of each scan is related to the amount of polarization that the spins have reached during the relaxation period, reducing T_{rec} involves a deep understanding of how the sensitivity depends on the recovery delay. The equation presented in Figure 1b makes the essential link between the sensitivity, the excitation angle and the recovery delay T_{rec}, highlighting the need to balance repetition rate and sensitivity.

Ernst and co-workers developed a sensitivity optimization in the case of simple pulse-acquire 1D experiments with high repetition rates by a fine tuning of the excitation angle. Figure 1c shows the optimal flip angle (Ernst angle) as a function of T_{rec}. While the 90° excitation is the best choice when the recovery delay is fixed at least to four times the longitudinal relaxation time constant T_1, other flip angles are actually more efficient to take incomplete magnetization recovery into account. The optimization of the flip angle provides significant improvement of sensitivity within the context of the fast-pulsing regime.

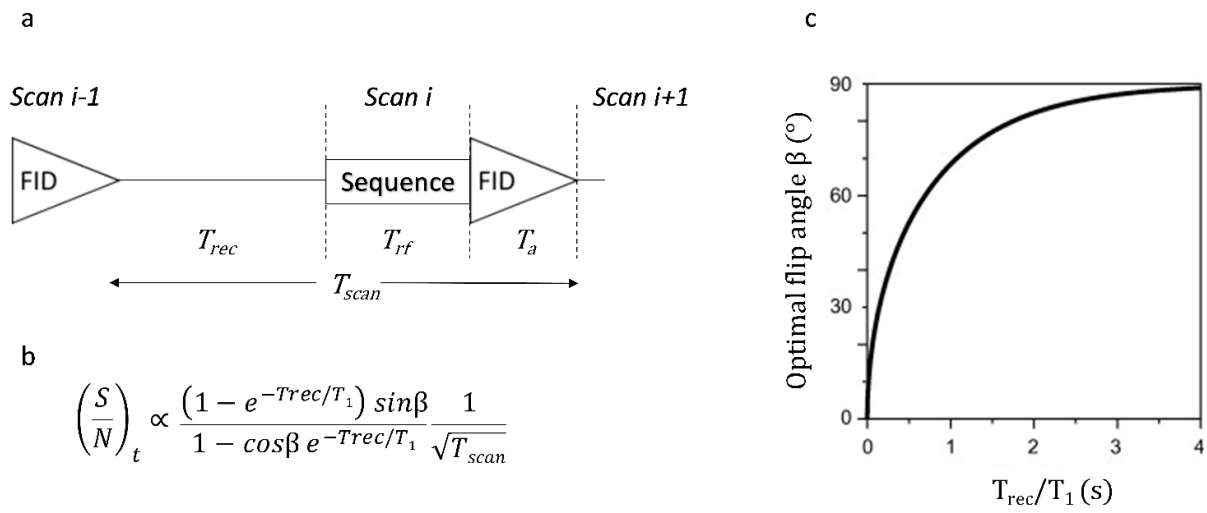

Figure 1. (a) Schematic representation of fast-pulsing experiments. (b) Signal-to-noise ratio (SNR) for a multi-scan experiment expressed as a function of pulse sequence delays and flip angle excitation. (c) Optimal flip angle as a function of relative recovery delay T_{rec}/T_1. (c) Reprinted from Prog. Nucl. Magn. Reson. Spectrosc., 55, P. Schanda, Fast-pulsing longitudinal relaxation optimized techniques: Enriching the toolbox of fast biomolecular NMR spectroscopy, 238-265, Copyright (2009), with permission from Elsevier.

This methodology becomes more difficult to set up for complex pulse sequences of the kind used in multidimensional experiments. However in HMQC (Heteronuclear Multiple-Quantum Correlation), applying an Ernst angle excitation is relatively straightforward, which has led to the first optimized fast-pulsing sequence, called FAST-HMQC. In this experiment a flip angle higher than 90° is applied to the initial pulse, leading to a 25% gain in sensitivity compared to the conventional version. In addition to the Ernst optimization, fast-pulsing 2D experiments generally use a longitudinal ^{1}H relaxation enhancement in order to further improve the sensitivity when short repetition delays are applied. Spin relaxation depends on its own deviation from thermal equilibrium, e.g. auto-relaxation, but also on the state of the other spins, e.g. cross-relaxation. The key idea is to excite only protons of interest thanks to shaped and band-selective pulses, while all the other protons remain unperturbed, e.g. along the z-axis. As the non-perturbed neighboring protons cross-relax with the protons of interest via dipole-dipole interactions, they provide a significant acceleration of the proton longitudinal relaxation.

The combination between the Ernst optimization and the reduction of longitudinal ^{1}H relaxation has led to a myriad of fast-pulsing sequences. In the context of macromolecules

such as proteins, the band-Selective Optimized Flip-Angle Short-Transient Heteronuclear Multiple Quantum Coherence (SOFAST-HMQC) (Figure 2a) has become a central pulse sequence, yielding 2D HMQC spectra in a few seconds only. The ALSOFAST (alternate SOFAST) experiment was also proposed, yielding similar results but with a non-selective INEPT scheme instead of selective pulses. Fast-pulsing experiments have also been extended to 3D via the BEST (Band Selective Short Transient) method. The 3D BEST HNCO/CA pulse sequences are capable of recording 3D H-N-C correlated spectra on a small protein in a few minutes only, with enough sensitivity to detect all expected cross-peaks.

Fast-pulsing experiments have also been adapted for small molecules. Contrary to macromolecules, dipole-induced cross relaxation is almost inefficient, and the addition of a spin-lock period between scans provides an efficient exchange of z-polarization via scalar interactions. This approach (Figure 2b) named ASAP (Acceleration by Sharing Adjacent Polarization), was applied to HMQC and HSQC (Heteronuclear Single-Quantum Correlation) experiments, while a version adapted to long-range couplings was also developed, named IMPACT-HMBC (IMProved and Accelerated Constant Time Heteronuclear Multiple-Bond Correlation). The gain of sensitivity compared to conventional 2D NMR is illustrated in Figure 2c. All these optimized experiments have become fast and efficient tools, even though they are quite hardware-demanding.

A last approach worth mentioning is the SMART (SMAll Recovery Time), recently proposed by Pelupessy *et al.* This strategy, inspired from fast MRI, consists in quenching residual coherences stemming from previous scans by applying random inter-scan gradients along the 3 spatial directions. This strategy enables a drastic reduction of the recovery delay (0.1 s), yielding COSY (Correlation spectroscopy) spectra in *ca.* 1 min. Nevertheless, this approach requires a triple-axis gradient probe, which limits its general use.

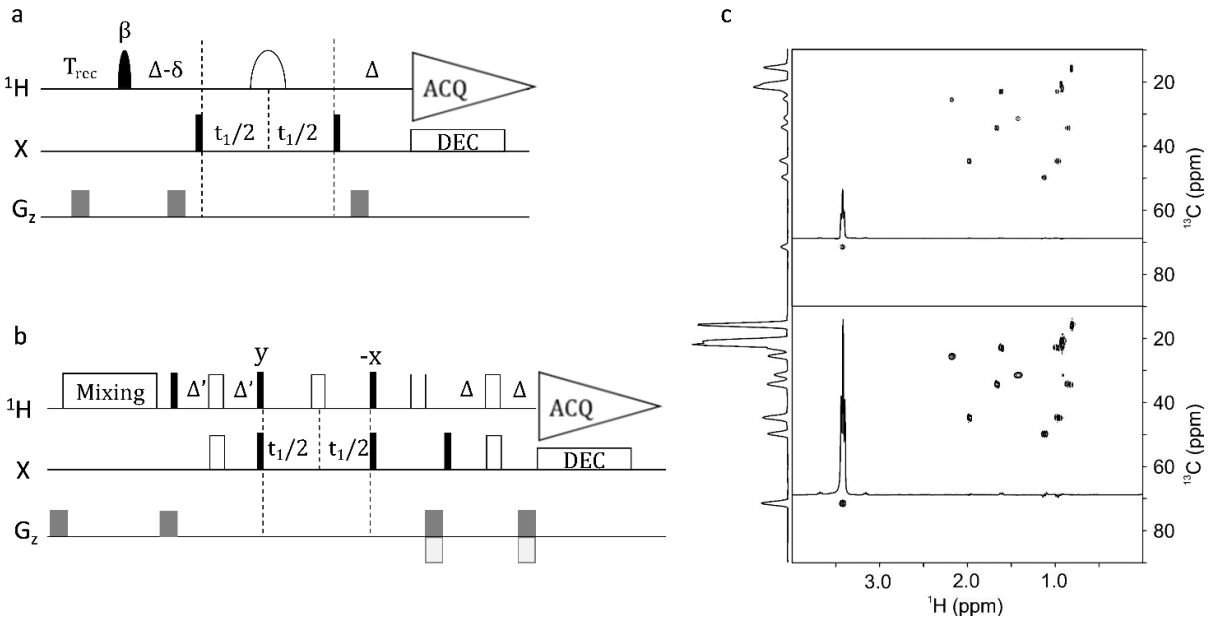

Figure 2. Schematic representations of SOFAST-HMQC (a) and ASAP-HSQC (b) pulse sequences, designed to record ^{1}H-X (X=^{13}C or ^{15}N) 2D spectra in a reduced time. Filled and open boxes indicate 90° and 180° rf pulses, respectively, pulse phases are x unless indicated otherwise. The delay Δ is usually set to ($1/2J_{HX}$). The combination of grey and open boxes indicates the switching gradient for every other scan. For SOFAST-HMQC (a), T_{rec} represents the recovery delay before the first selective pulse with a flip angle of β, the delay δ takes into account the spin evolution during this pulse. For ASAP-HSQC (b), an isotropic mixing block is added prior to each scan. (c) Comparison of conventional HSQC (top) and ASAP-HSQC (bottom) spectra of menthol in $CDCl_3$ with equivalent overall measurement time. For an equivalent spectral quality, a gain in sensitivity of 3-4 is observed in the case of the ASAP experiment. (c) Reprinted with permission from J. Am. Chem. Soc. 136, 1242-1245. Copyright (2014) American Chemical Society.

Reducing the number of increments

Numerous sampling schemes and signal processing methods have been proposed to compensate the resolution losses subsequent to the reduction of the number of increments in the indirect dimension. There are two categories of sampling schemes: uniform or non-uniform sampling (NUS).

Using uniform sampling, the number of increments can be reduced in two ways: by reducing either the sampling rate or the maximum evolution time in the indirect dimension. On the one hand, reducing the sampling rate leads to spectral aliasing or folding, as the Nyquist sampling theorem is no longer respected. However, algorithms may be used to reconstruct the unfolded spectrum. On the other hand, reducing the maximum evolution time in the indirect dimension

leads to truncation and to subsequent artefacts on the spectrum. To minimize these ones, linear prediction (LP) is nowadays widely used. This signal reconstruction method relies on the hypothesis that at any time, the signal can be described as a linear combination of past values. It also assumes an exponential decay of the signal; a small deviation from this model leads to incorrect reconstruction of peak positions. This method is especially useful for spectra with a limited number of resonances. An alternative to LP is the Filter Diagonalization Method (FDM), which reduces the problem into the diagonalization of a small matrix by constructing a matrix where the off-diagonal elements represent the correlations between resonances. Thus, the output is not a spectrum, but a list of parameters describing it. The main drawback of the FDM is its sensitivity to low SNR and overlapping.

The use of the Discrete Fourier Transform (DFT) to process NMR signals implicitly relies on the periodicity of the sampling, and appears to be unsuited for non-uniform sampling schemes. Nevertheless, DFT can be applied to zero-augmented data, *ie.* NUS data supplemented by zero values for the times of the uniformly-spaced scheme that are not sampled. The resulting spectrum contains strong sampling artifacts, as it is a convolution of the DFT spectrum of the uniformly sampled data with the DFT of the sampling vector. Thus, non-FT methods are needed to reduce these sampling artifacts.

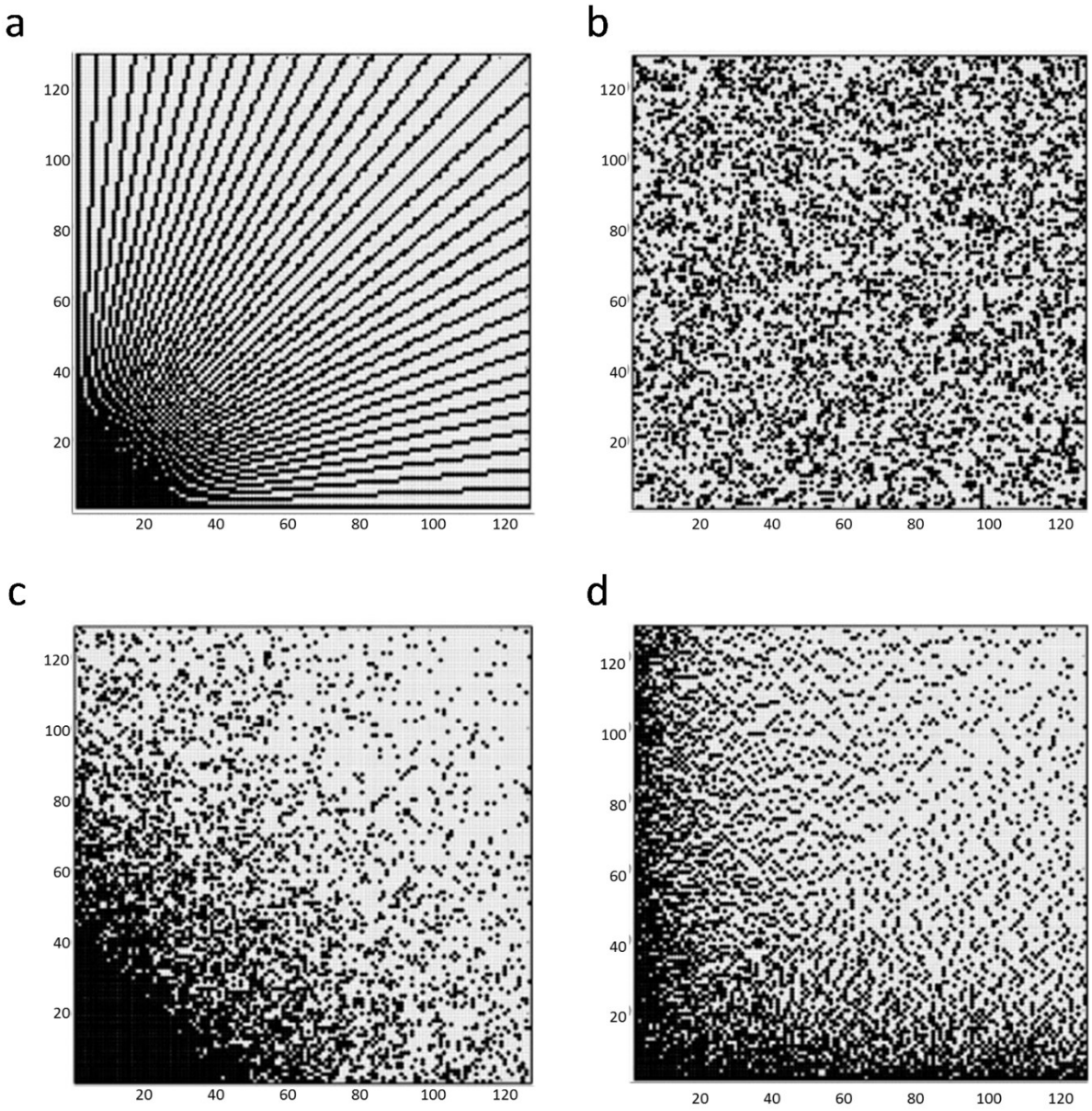

Figure 3. Non uniform sampling schemes for 30% sampling coverage of the underlying Nyquist grid: radial sampling (a), random sampling (b), exponentially weighted random (c) and Poisson gap (d). Reproduced from Phys. Chem. Chem. Phys. 14 (2012) 10835-10843 with permission of the Royal Society of Chemistry.

NUS schemes can be classified into two categories, on-grid and off-grid sampling schemes. The former are subsets of the uniformly-sampled Nyquist grid, the latter rely on uniform sampling along radial vectors in the t_1-t_2 space. Indeed, in the so-called radial sampling (Figure 3a), the evolutions of the two time dimensions are coupled. The spectra can be retrieved using specific reconstruction methods such as radial Fourier transform or a method inspired from tomography: the back Projection Reconstruction (bPR). Due to its specific sampling artifacts

and reconstruction methods, radial sampling is unsuited for high dynamic ranges or complex spectra.

On-grid NUS schemes have been widely investigated, and numerous sampling schemes and reconstruction algorithms have been designed. Historically, the first NUS approaches applied to nD NMR were purely random and exponentially biased random sampling (Figure 3b and c). In these sampling schemes, the distribution of the gaps is Gaussian. Later on, a Poisson gap sampling was developed. As the distribution of the gaps follows a Poisson distribution, this schedule avoids long gaps between the samples. Therefore, this strategy shows a better repeatability than random and biased random sampling.

The following processing strategies can be applied on datasets acquired with any sampling scheme. The Maximum Entropy (MaxEnt) iterative optimization follows two constraints: maximize the entropy in the frequency domain and minimize the difference between reconstructed and experimental data in the time domain. As the linearity of this processing is relatively poor, it is unsuitable for quantitative applications. In this case, Forward Maximum entropy (FM) or Maximum entropy INTerpolation (MINT), both derived from MaxEnt, are preferred as they are highly linear. Contrary to MaxEnt where the regularization functional is the entropy, Compressed Sensing (CS) explicitly seeks to maximize the sparseness of the reconstructed spectrum, using l_1-norm. This widely used method is mainly applied to 2D data. To process higher dimensionality data, Multi-Dimensional Decomposition (MDD) is a valuable tool. This processing strategy is based on multivariate analysis. A recursive variation, called rMDD, needs less data, but the assumption of Lorentzian shapes has to be verified. Finally, in the Covariance processing method the Fourier transform is only performed in one dimension, followed by the calculation of the correlations between frequencies. This strategy leads to an equivalent frequency resolution in the indirect dimension as in the direct dimension, regardless the number of data points in the indirect dimension. An equivalent processing is available for heteronuclear experiments, known as indirect covariance.

The approaches based on a reduction of the number of t_1 increments not only allow to speed up the acquisition of nD spectra, but can also be used to increase the spectral resolution for a given acquisition time. Numerous sampling schemes and processing algorithms are available, and must be chosen carefully according to the studied system and to the type of spectrum to be recorded.

Hadamard spectroscopy

Hadamard spectroscopy is an alternative non-FT method inspired by the continuous-wave slow passage technique which was widely used before the advent of FT-NMR. It relies on the sampling of the discrete frequency domain thanks to an array of narrow independent frequency channels. Instead of applying hard excitation pulses, selective radiofrequency pulses with an effective bandwidth from 1 to 100 Hz are employed. The main feature of Hadamard spectroscopy is the introduction of an encoding/decoding scheme based on Hadamard matrices. One scan, recorded with a combination of frequencies (e.g. excitation of different regions of the spectrum), matches with one row of the Hadamard matrix. For each row, signals from the different regions of the spectrum can be positive or negative according to the sign of the matrix coefficients, in order to complete the Hadamard encoding. The whole information is next decoded thanks to the same matrix, where the different peaks are obtained by performing additions/subtractions from the columns. Note that the completion of all scans of the Hadamard-matrix is necessary to achieve the encoding/decoding process. An example of such Hadamard matrix is proposed on the Figure 4a.

The processing of this strategy becomes very interesting in the context of nD NMR experiments. Indeed, the Hadamard encoding actually replaces the common t_1 incrementation, resulting in a significant time saving since the number of scans related to the size of the Hadamard matrix is generally lower than the number of increments for the conventional nD FT-NMR. In practice, as NMR spectra are often relatively sparse, recording an initial 1D spectrum can be useful to determine the regions of interest before the Hadamard encoding. Standard 2D pulse sequences are then employed but without an evolution period. Such a workflow to acquire Hadamard 2D spectra is illustrated in Figure 4a. As shown in Figure 4b and 4c, Hadamard spectroscopy can significantly accelerate nD NMR experiments. Nonetheless, some drawbacks arise from this methodology such as the need to obtain prior knowledge of the sample, and the relaxation losses induced by the length of the encoding pulses, especially when narrow frequency bands are chosen.

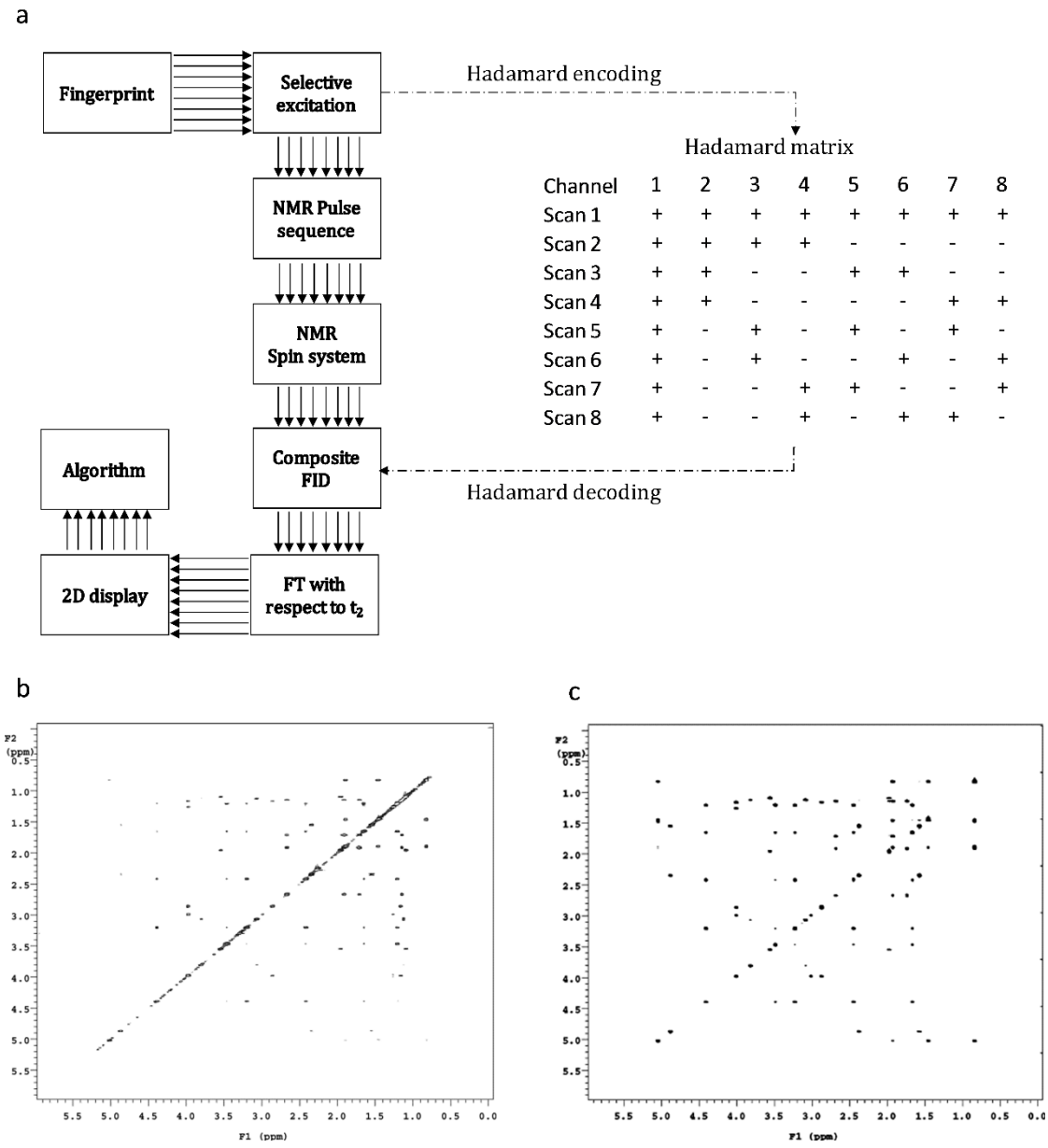

Figure 4. (a) Schematic workflow to obtain a 2D spectrum by Hadamard Spectroscopy. (b) Conventional 800 MHz TOCSY spectrum recorded on a sample of erythromycin; 256 increments were required for a total experiment time of 2 h 53 min 50 s. (c) 800 MHz TOCSY spectrum recorded on erythromycin by a Hadamard approach in 2 min 33s (around 68 times faster). Twenty two protons sites were selected from the preliminary fingerprint for direct excitation. A Hadamard matrix of order 28 was also required for encoding and decoding. Reprinted from Prog. Nucl. Magn. Reson. Spectrosc., 42, E. Kupce, T. Nishida, R. Freeman, Hadamard NMR spectroscopy, 95-122, Copyright (2003), with permission from Elsevier.

Ultrafast nD NMR and hybrid methods

Ultrafast (UF) NMR, also known as single-scan, is the fastest and the most recent of the methods described in this article. The main feature of UF NMR (Figure 5a) is that instead of repeating the N_1 experiments of the conventional 2D NMR scheme, the sample is divided into N_1 slices undergoing different evolution periods, all within a single scan. Proposed by Frydman and co-workers in 2002, this sub-second method is inspired from imaging and relies on a spatial-encoding block, where the spins located at different *z* coordinates are treated as independent sub-ensembles. This spatial encoding is generally carried out in a continuous fashion, as described in Figure 5b. The key element in the UF pulse sequences (here on the example of COSY) is the application of linear frequency-swept pulses together with gradients along the z axis. After a conventional excitation, the two successive pulses applied with bipolar gradients generate a z-dependent phase of the form $\phi = C \cdot \Omega_1 \cdot z$ where Ω_1 is the resonance frequency and *C* an adjustable constant dependent on the spatial-encoding scheme. After a conventional mixing period, the linear dephasing is refocused during signal detection by a linear gradient,[1] yielding a series of echoes at times proportional to the corresponding resonance frequencies. This series of echoes is similar to a 1D spectrum obtained without FT, and forms the first dimension of the UF 2D spectrum. The second dimension is then obtained in an Echo-Planar Spectroscopic Imaging (EPSI) fashion, by alternating positive and negative gradients yielding a series of 1D sub-spectra while the transverse magnetizations evolve in a conventional way. The rearrangement of this series of 1D spectra, followed by their Fourier Transform along the time dimension, leads to a 2D spectrum in a single-scan.

[1] The expression "linear gradient" is not exact, although commonly encountered in the NMR literature. In fact, the gradient is a constant value, and the magnetic field which results from the application of this gradient has a linear dependance with z. Footnote added in the thesis after publication of the article.

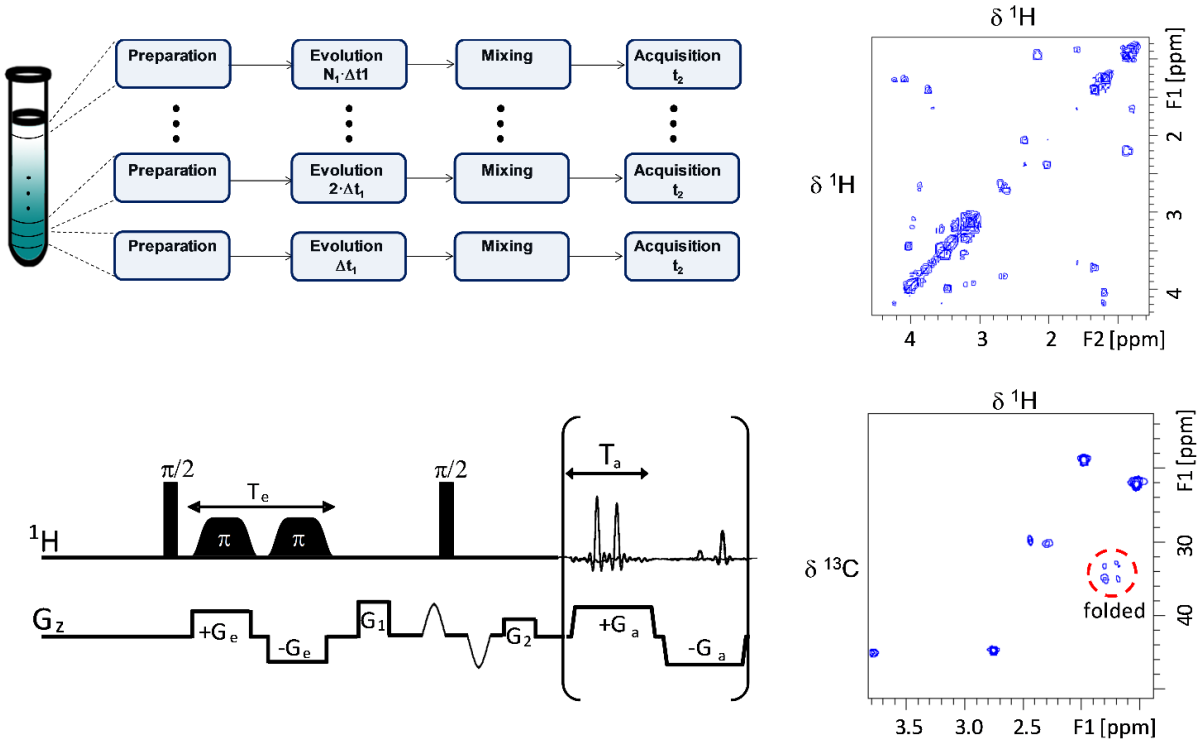

Figure 5. Principle of Ultrafast 2D NMR. (a) Generic scheme for the acquisition of UF spectra; (b) shows –on the example of an UF COSY pulse sequence– how this spatial encoding is made possible by simultaneously applying frequency-swept pulses together with gradients along the *z* axis. (c) Example of the UF COSY spectrum of a mixture of small molecules (metabolites, 100 mmol.L^{-1}in D_2O), recorded in *ca*. 110 ms on a 400 MHz spectrometer with a conventional probe; (d) Example of the UF HSQC spectrum of an ibuprofen sample (2 mol.L^{-1} in aceton-d_6), recorded in *ca*. 110 ms spectrometer with a cryogenic probe. The peaks circled in red are folded and correspond to the aromatic part of the spectrum.

The strength of UF NMR is its general character, which makes it applicable to any kind of 2D NMR correlation. Examples of homo- and hetero-nuclear 2D spectra recorded in a single-scan are given in Figure 5. UF NMR is even extendable to 3D or 4D single-scan experiments, by spatially encoding the sample along two or three orthogonal dimensions. Still, UF NMR is characterized by the need to compromise between sensitivity, resolution and accessible spectral width. This is mainly due to limitations in the gradient system and to the need to acquire the signal with high filter bandwidths. But the performance of UF NMR has been remarkably increased during the last decade, thanks to clever pulse sequence developments. Moreover, large efforts have been made to improve the accessibility of UF NMR: while not commercially available at the time of writing, a number of web-available protocols may help potential users to set this experiment on their own hardware.

While UF NMR is certainly the fastest 2D method, it still suffers from low sensitivity: typically, for a single-scan homonuclear 2D acquisition, limits of detection of a few mM have been reported under favorable configurations (high field and cryogenic probe). Consequently, single-scan applications have been mainly oriented towards concentrated samples. The most exciting of these applications include the real-time monitoring of fast (bio)chemical processes, where UF NMR offers a unique opportunity to characterize short-lifetime reaction intermediates. It also shows great promises when NMR is coupled with another analytical technique, as the hyphenated character of the experimental setting is often incompatible with multi-scan acquisitions. UF NMR has been successfully coupled to high-performance liquid chromatography (HPLC) and to dissolution dynamic nuclear polarization (D-DNP).

However, sensitivity is often an issue, and single-scan experiments are not always adapted to the study of diluted samples such as mixtures of biological interest. Moreover, the detection of large spectral widths in a single-scan leads to significant resolution and sensitivity penalties. Therefore, when time permits, a much higher performance can be reached via hybrid UF acquisition strategies which consist of repeating and/or combining several UF scans. These methods result in substantial sensitivity, resolution and/or spectral width improvements, while the experiment time remains quite short. Figure 7 summarizes the three main families of hybrid strategies. The most basic hybrid approach (Figure 7) consists in simply accumulating several UF scans, separated by a recovery delay, to increase the SNR and/or for phase cycling purposes. Figure 3b illustrates the principle of interleaved acquisitions, consisting in repeating several UF scans while incrementing a pre-acquisition delay τ in order to increase the spectral width, improve the resolution or reduce the demand on gradient amplitudes. Finally, Figure 3c illustrates how hybrid acquisitions can yield spectra with n dimensions in the time required to record a (n-1)D conventional spectrum, by coupling conventional time-encoding with ultrafast spatial-encoding strategies. For an equivalent overall experiment time, these hybrid methods are generally more efficient than their conventional counterparts. In particular, they are much more immune to hardware instabilities, resulting in improved analytical performances in terms of sensitivity, robustness and repeatability. Promising applications to fast quantitative metabolomics have been demonstrated by Giraudeau and co-workers.

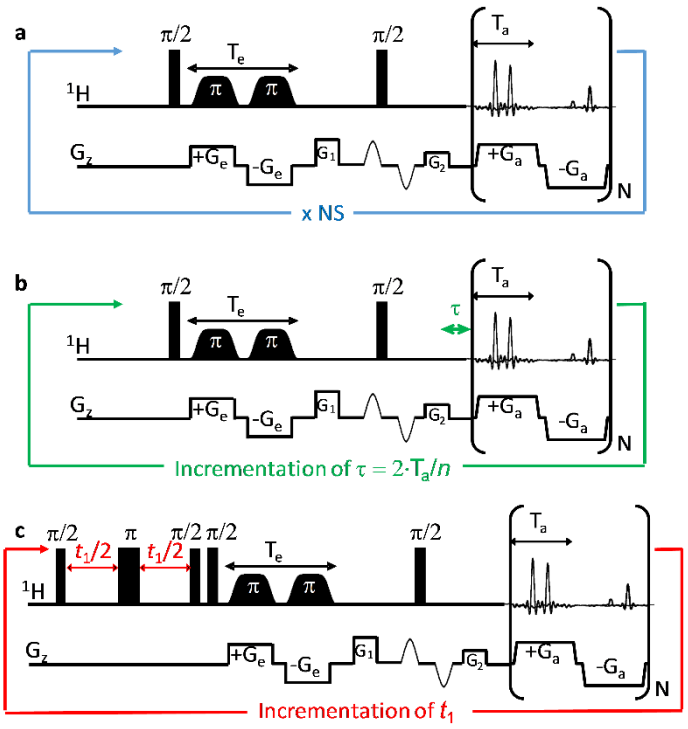

Figure 6. Principle of the main hybrid strategies based on UF 2D NMR. (a) Multi-scan single-shot (M3S) approach, consisting in accumulating several UF scans for sensitivity or phase cycling purposes. (b) Interleaved UF acquisition procedure, consisting in repeating several UF scans while incrementing the pre-acquisition delay τ in order to increase the spectral width, improve the resolution or reduce the demand on gradient amplitudes. (c) Fast hybrid 3D approach, illustrated on the example of Jres-COSY, capable of recording 3D spectra with a single time incrementation coupled to a spatially-encoded 2D pulse sequence. Reproduced from Magn. Reson. Chem. (2015) doi: 10.1002/mrc.4237 with permission from John Wiley and Sons

Multiple receivers

Parallel Acquisition NMR SpectroscopY (PANSY) allows the acquisition of multiple types of spectra in the same sequence, using multiple receivers. The principal aim of this hardware-based approach is to elucidate the whole structure of a molecule with a single experiment, as illustrated in the PANACEA pulse sequences (parallel acquisition NMR, an all-in-one combination of experimental applications). Figure 7 illustrates one of these sequences, which leads to the acquisition of a 1D ^{13}C, a 2D ^{13}C INADEQUATE, a 2D ^{1}H-^{13}C HSQC, and a 3D ^{13}C-^{1}H J-HMBC spectra within the same experiment. This pulse sequence has also been modified by adding the capability to acquire the corresponding ^{15}N correlation spectra.

As all the spectra are acquired simultaneously, the use of this methodology not only speeds up structural elucidation, but it also avoids the influence of slow variations such as temperature or sample degradation. Nevertheless, this powerful tool is not adapted to fast-relaxing systems such as macromolecules, due to the length of the pulse sequences; moreover it requires specific hardware.

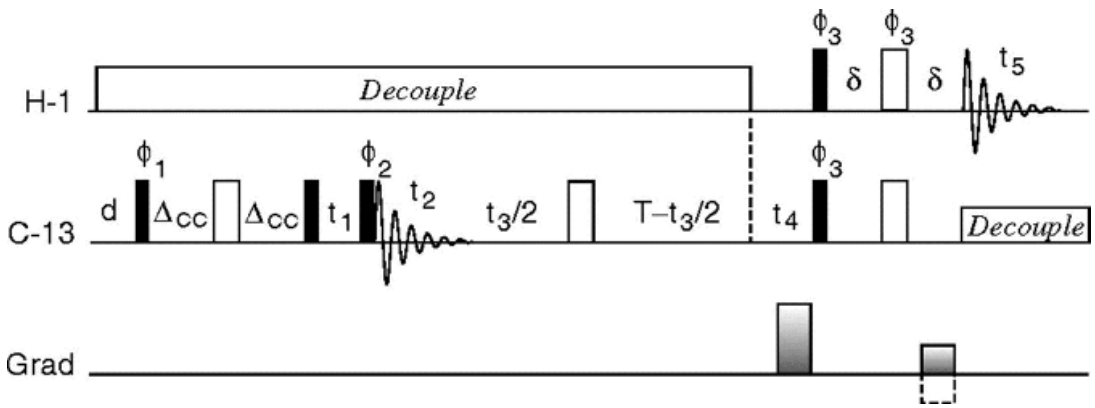

Figure 7. PANACEA pulse sequence designed for the simultaneous observation of a decoupled one-dimensional ^{13}C spectrum, a two-dimensional ^{13}C-^{13}C INADEQUATE spectrum, a two-dimensional multiplicity-edited ^{13}C-^{1}H HSQC spectra, and a three-dimensional ^{13}C-^{1}H J-HMBC spectrum on a spectrometer equipped for parallel acquisition of ^{1}H and ^{13}C signals. Reprinted with permission from J. Am. Chem. Soc. 130, 10788-10792. Copyright (2008) American Chemical Society.

Combined strategies

The methods described in this article illustrate how the researchers' imagination has helped shortening the duration of 2D experiments by innovative strategies. Of course, each method has its pros and cons, and there is no universal fast nD method. The choice of the most adapted strategy should therefore be made depending on the targeted question. Nevertheless, these methods are not independent and further progress in speed, sensitivity or resolution can be expected by combining them. Among the experiments described in Table 1, almost any combination is conceivable, especially those between methods from different categories. Many combinations have already been proposed in the recent literature, with the main leitmotiv that the combination of two methods can bring much more than the sum of their parts. As an example, non-uniform sampling has already been combined with SOFAST or

spectral aliasing, in order to reduce the number of increments while avoiding resolution losses. Ultrafast NMR has been combined with almost all the other methods such as SOFAST, aliasing/folding, compressed sensing, Hadamard spectroscopy and even with parallel acquisition methods. And further combinations will certainly arise in the near future, in a permanent quest towards higher performances in the shortest possible time.

The NMR community is also aware of the need to make these developments available to a broad community of end-users. While some of the methods described above are already available in major commercial software, web available protocols greatly help in the implementation of others. Moreover, NMR spectroscopists are still very active in this field, and new methods will certainly emerge from NMR labs in the years to come. While fast methods often have to pay a price in sensitivity, promising perspectives arise from their combination with hyperpolarization techniques, suggesting exciting new developments and applications in the near future.

Further reading

Ernst, R. R., Bodenhausen, G., Wokaun, A. (1987). *Principles of nuclear magnetic resonance in one and two dimensions*. Oxford: Oxford Science Publications edn.

Frydman, L., Scherf, T., Lupulescu, A. (2002). The acquisition of multidimensional NMR spectra within a single scan. *Proceedings of the National Academy of Sciences USA* **99**, 15858-15862

Giraudeau, P., Frydman, L. (2014). Ultrafast 2D NMR: An Emerging Tool in Analytical Spectroscopy. *Annual Reviews of Analytical Chemistry* **7**, 129-161

Akoka, S., Giraudeau, P. (2015). Fast hybrid multi-dimensional NMR methods based on ultrafast 2D NMR. *Magnetic Resonance in Chemistry* in press, doi: 10.1002/mrc.4237.

Mobli, M., Hoch, J. (2014). Nonuniform sampling and non-Fourier signal processing methods in multidimensional NMR. *Progress in Nuclear Magnetic Resonance Spectroscopy* **83**, 21-41

Jeannerat, D. (2007). Computer optimized spectral aliasing in the indirect dimension of 1H-13C heteronuclear 2D NMR experiments. Anew algorithm and examples of applications to small molecules. *Journal of Magnetic Resonance* **186**, 112-122

Kupče, E., Freeman R. (2007). Fast multidimensional NMR by polarization sharing. *Magnetic Resonance in Chemistry* **45,** 2–4

Kupče, E., Nishida T., Freeman R. (2003). Hadamard NMR spectroscopy. *Progress in Nuclear Magnetic Resonance Spectroscopy* **42,** 95–122

Kupče, E., Freeman, R. (2008). Molecular structure from a single NMR experiment. *Journal of the American Chemical Society* **130**, 10788-10792

Schanda, P. (2009). Fast-pulsing longitudinal relaxation optimized techniques: Enriching the toolbox of fast biomolecular NMR spectroscopy. *Progress in Nuclear Magnetic Resonance Spectroscopy* **55,** 238–265

Schanda, P., Kupce, E., Brutscher R. (2005). SOFAST-HMQC experiments for recording two-dimensional heteronuclear correlation spectra of proteins within a few seconds. *Journal of Biomolecular NMR* **33**, 199–211

4.2. Ultrafast NMR: an overview of principles and applications

Ultrafast multi-dimensional NMR: principles and recent applications

Boris Gouilleux, Laetitia Rouger and Patrick Giraudeau

(Original book chapter published in eMagRes, 5 (2016) 913-922)

Abstract

Multi-dimensional NMR (nD NMR) spectroscopy is widely used in chemical and biochemical analyses. Conventional nD NMR experiments, however, are affected by inherently long acquisition durations, arising from their need to record numerous 1D experiments in a time-incremented fashion. Proposed in 2002 by Frydman and co-workers, ultrafast (UF) 2D NMR is capable of yielding arbitrary nD homo- or hetero-nuclear NMR spectra in a single scan. The performance of this sub-second 2D NMR methodology has been greatly improved in the last decade, and UF NMR has become a powerful analytical tool witnessing an expanded scope of applications. Recent developments also gave birth to a new generation of multi-scan hybrid methods which offer an appealing alternative to conventional NMR for a variety of applications where the sensitivity of single-scan methods is limited. This article summarizes the principles and the recent developments which have contributed to the success of this method, and focuses on applications which have been recently demonstrated in various areas of analytical chemistry –from the real-time monitoring of kinetic or dynamic processes to high-throughput metabolomics. Promising perspectives arising from the association of UF NMR with other techniques (such as hyperpolarization methods) are also highlighted.

1 Introduction

Multidimensional (nD) spectroscopy has played a central role in the development of NMR methods for a broad range of applications, from chemistry to biology and medicine. nD spectroscopy brings invaluable correlation information as well as a considerable resolution enhancement, which are both essential to elucidate complex molecular structures. However, conventional nD NMR suffers from long acquisition durations due to the need to sample the indirect dimension(s) through the repetition of numerous experiments. These long experiment times have several consequences: *i)* the overload of spectrometer schedules, *ii*) the impact of instabilities on the signal-to-noise ratio (SNR), leading to t_1 noise and *iii*) the incompatibility of nD experiments with samples whose composition is evolving with time, and with most hyphenated techniques.

Numerous strategies have been developed to overcome this limitation.[1] A first family of approaches consists in optimizing pulse angles to minimize the inter-scan delay. Several other strategies, such as Non-Uniform Sampling (NUS) consist in reducing the number of time increments by a sparse sampling of the indirect dimension(s), associated with non-linear reconstruction methods. Other developments are based on alternatives to Fourier Transform (FT) NMR, such as Hadamard spectroscopy.

A decade ago, a new generic multidimensional approach was designed by Frydman and co-workers,[2] allowing the acquisition of homo- or heteronuclear 2D NMR spectra within a single scan. The so-called "ultrafast" (UF) method provides analogous information to its conventional counterpart, but in a fraction of a second only.

In this article, the principles and specificities of UF 2D NMR are first summarized, as well as the specificities of this methodology and its extension to 3D NMR. Then, applications of this methodology are illustrated in a variety of fields in which the experiment duration plays a crucial role, such as real-time monitoring of fast processes, coupled techniques or high-throughput metabolomics.

2 Principles and Characteristics of Ultrafast NMR

2.1 Principles

The key feature of the UF methodology is the replacement of the time-incremented period in the conventional 2D NMR scheme by a spatially-dependent evolution period. Figure 1 illustrates how spatial encoding enables spins throughout the sample to undergo spatially distinct t_1 evolution periods within a single scan.

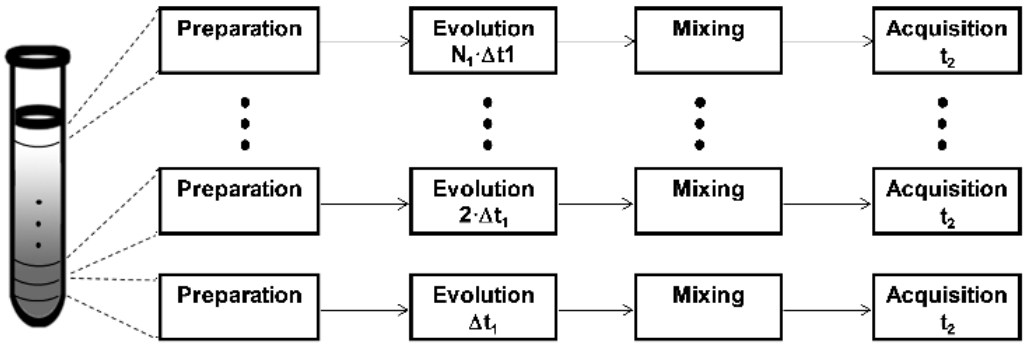

Figure 1. General scheme for ultrafast 2D NMR experiments. Instead of repeating experiments with an incremented t_1 evolution period, the sample is subdivided into N_1 slices which undergo different t_1 evolution periods within a single scan. This discrete spatial encoding approach can be extended to a continuous one by considering an infinite number of infinitesimal slices, *i.e.* $N_1 \rightarrow \infty$.

Spatio-temporal encoding can be achieved in different ways. The initially proposed pulse sequence relied on a discrete scheme where a train of frequency selective pulses was applied in combination with a pair of bipolar gradients.[2] Since this technically demanding procedure suffered from several drawbacks such as the presence of "ghost peaks", it was replaced in 2003 by a continuous scheme which can be achieved either in real-time or in constant time (Figure 2b).[3] Whichever the continuous encoding pattern, an encoding gradient G_e is applied along the B_0 axis, leading to a *z*-dependent resonance frequency. A chirp pulse with a linear frequency sweep is applied simultaneously so that the spins located at different *z* positions are excited at different times $t(z)$ (Figure 2a). This gradient/pulse combination yields a non-linear dephasing $\varphi(\Omega_i, z)$ which is then changed into a linear –and much easier to manipulate–

form through an additional spin manipulation, by applying an identical chirp pulse together with an opposite gradient. The resulting dephasing is of the form $\varphi(z) = C \cdot \Omega_i \cdot z$, where C is an adjustable constant depending on the encoding pattern (Figure 2b). It can be viewed as a sum of helices –each resonance frequency being characterized by a different winding. As in conventional 2D NMR, this generic encoding period is preceded by a preparation period and followed by a mixing period, identical to those applied in conventional 2D pulse sequences.

A whole 2D NMR signal can be retrieved from the encoded information if the spin evolution during a time t_2 is collected in a way that refocuses the magnetization windings obtained through the spatial encoding process. To this end, an acquisition gradient G_a is applied while the receiver is open, which refocuses the dephasing $\varphi(\Omega_i, z)$ induced by the spatial encoding. The magnetization helices are successively unwound, leading to a series of echoes in the *k* space, where *k* is a wave number depending on the acquisition gradient: $k = \gamma_a \int_0^t G_a(t')dt'$ (γ_a is the gyromagnetic ratio of the detected nuclei). Echoes occur when the refocusing induced by the acquisition gradient exactly compensates the dephasing imparted by spatial encoding, *i.e.* $k = -C\Omega_i$. This series of echos resembles a 1D spectrum, though obtained without Fourier transformation, yielding the first dimension of the UF 2D spectrum (Figure 2c). This indirect domain is generally called the "ultrafast dimension". The additional dimension is obtained through a detection block based on Echo-Planar Spectroscopic Imaging EPSI. In this scheme, the classical free evolution of the spins is monitored during a time t_2 through a train of bipolar gradient pairs which are capable of mapping the spatial dimension k and the time dimension t_2 (Figure 2c). This leads to a series of mirror-image 1D spectra along the ultrafast dimension while the system evolves during t_2 under the influence of the conventional NMR parameters such as J-couplings, chemical shift and transverse relaxation (Figure 2c). This t_2 evolution will eventually lead to the second dimension of the 2D spectrum after FT. As this additional dimension arises from a conventional evolution during the signal detection, it is referred to as "conventional dimension".

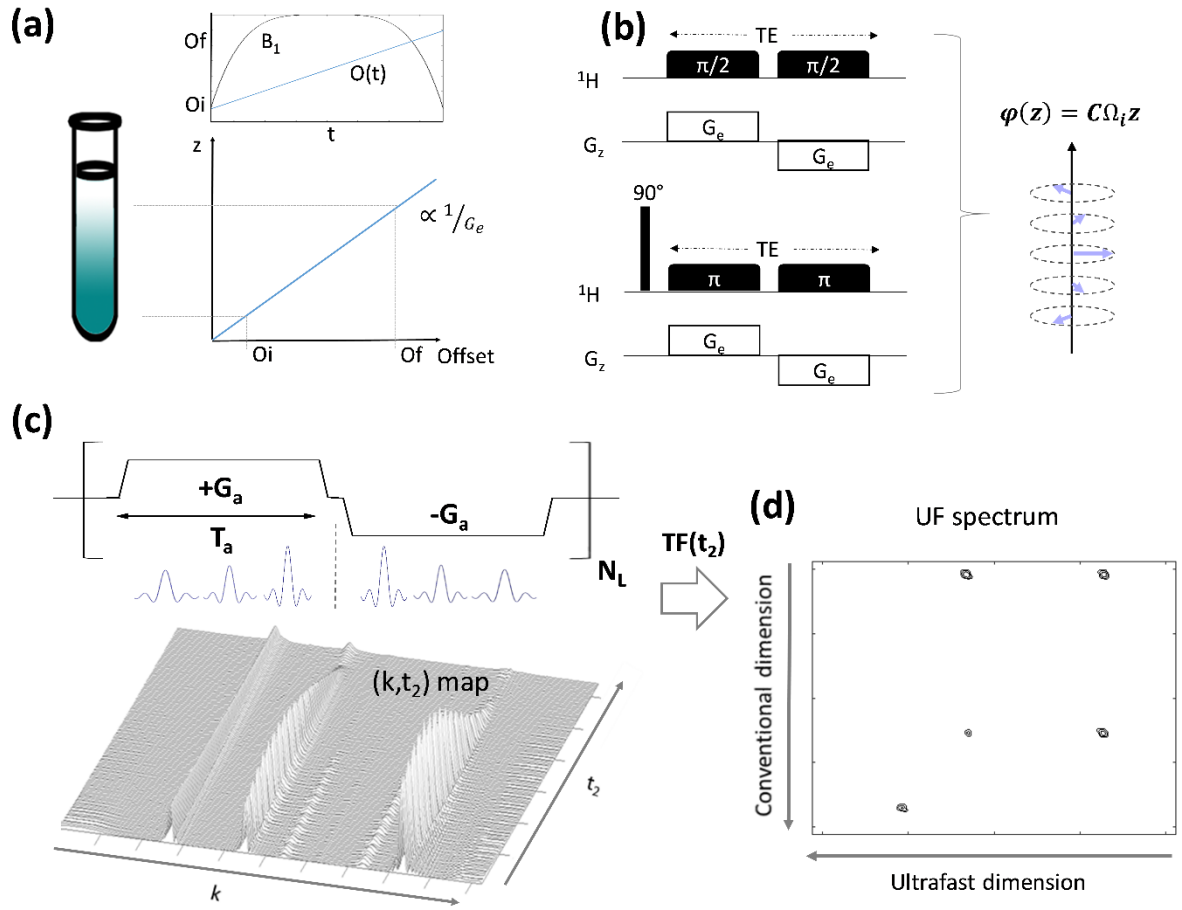

Figure 2. Overview of the main features characterizing ultrafast NMR experiments. **(a)** Principle of continuous spatial encoding. The action of an encoding gradient G_e is combined with a chirp pulse whose frequency is linearly swept, so that spins located at different *z* positions in the sample are excited at different times. It induces a z-dependent dephasing φ of the transverse magnetization, which also depends on the resonance frequency Ω_i. **(b)** Typical pulse sequences capable of achieving this continuous spatial encoding, in a real-time (top) or constant time fashion (bottom). Both encoding patterns lead to a linear dephasing of the form $C \cdot \Omega_i \cdot z$, where *C* is a spatio-temporal constant depending on the duration of spatial encoding *TE*. **(c)** Principle of EPSI-based detection in UF NMR. An acquisition gradient G_a is applied to refocus the z-dependent dephasing, leading to several echoes (as illustrated at the top). The timing of these echoes in the *k* space is directly proportional to the resonance frequency Ω_i, leading to a 1D spectrum without FT. To record the second dimension, a train of bipolar gradients is continuously applied in order to map the (k, t_2) space. The bottom figure shows such a 2D map recorded at 400 MHz on a sample of ethanol. **(d)** shows the resulting UF 2D spectrum after FT along t_2.

This particular data acquisition procedure requires a specific processing to obtain the 2D spectrum. This processing first consists in splitting and rearranging the echoes detected during the successive acquisition gradients, leading to two mirror-image $S(k, t_2)$ maps akin to the

$S(F_1,t_2)$ interferogram resulting from a conventional 2D dataset after FT along the indirect dimension. The FT of these maps along t_2 yields two symmetric $S(F_1, F_2)$ maps, which are added after inverting one of them along the ultrafast dimension, leading to the final 2D spectrum (Figure 2d). Additional corrections are generally applied, such as shearing the two mirror-maps to cope with a potential positive/negative gradient offset of the gradients, or the application of a spatial apodization in the *k* domain to remove the effect of non-linearities on the edge of the detection coil.

2.2 Examples

Contrary to other fast 2D methods which target a specific pulse-sequence, one of the main assets of UF NMR is its generic nature that makes it suitable for any kind of 2D NMR correlation. In principle, any conventional 2D experiment can be converted into its UF variant, by applying a spatial encoding scheme instead of the incremented evolution period and by replacing the classical acquisition by an EPSI block. Figure 3 shows representative examples of UF spectra obtained using commercial spectrometers, together with the corresponding pulse sequences. Although not comprehensive, this figure illustrates the versatility of UF 2D NMR, pointing out some of its characteristic features, such as the possibility to record homo- or – hetero-nuclear spectra or to perform single- or double-quantum experiments, relying on a single- or multi-scan approach.

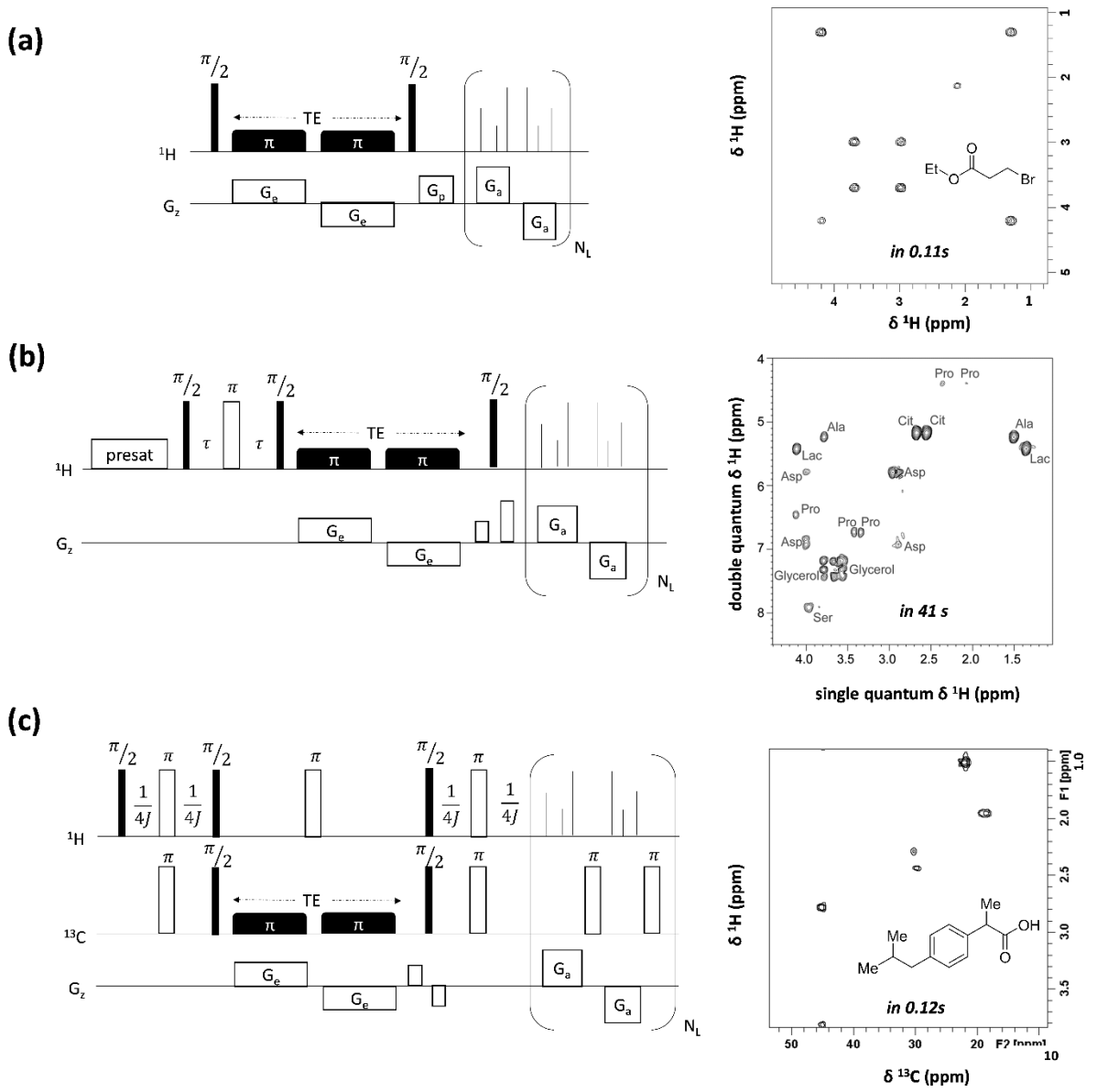

Figure 3. Examples of UF pulse sequences and spectra illustrating the versatility of the UF approach. **(a)** UF COSY pulse-sequence applied to a sample of ethyl-3-bromopropionate in acetone-d_6. The spectrum was recorded in 0.11 s at 400 MHz. **(b)** UF DQS (Double-Quantum Spectroscopy) pulse-sequence applied to a mixture of 7 metabolites in H_2O/D_2O (90/10). The spectrum was recorded at 600 MHz with four interleaved scans to increase the observable spectral width, resulting in an acquisition time of 41 s. The build-up delay was τ = 25 ms. Reproduced from Ref. [37] with permission from The Royal Society of Chemistry. **(c)** UF ^{1}H-^{13}C HSQC pulse-sequence applied to a sample of ibuprofen in acetone-d_6, and recorded in 0.12 s at 500 MHz with a cryogenic probe (aliphatic range only). In all these schemes, TE refers to the duration of spatial encoding; the open rectangle without annotations refer to conventional coherence-selection gradients.

2.3 Specificities of UF NMR

Ultrafast NMR obviously suffers from an intrinsically low sensitivity owing to its single-scan nature, when compared to multi-scan acquisitions characterizing conventional nD NMR. In addition, the SNR is also impacted by several factors arising from the spatially-encoded nature of UF NMR:[4]

- Translational molecular diffusion during spatial encoding leads to the need of a compromise between resolution and sensitivity. In fact, a better resolution requires a longer spatial encoding duration; however the latter leads to SNR losses arising from the effects of diffusion in the presence of magnetic field gradients.
- Due to the constant time nature of the spatial encoding scheme which is employed in most UF experiments, the SNR is significantly modulated by spin-spin couplings. These J-modulation effects, if not taken into account, can lead to missing peaks on the UF 2D spectra.
- The SNR is also impacted by the need to acquire the signal with large filter bandwidths (several hundreds of kHz) to account for the gradient-induced spread in resonance frequencies from spins over the whole sample volume.

Additionally, a compromise has to be found between the resolution ($\Delta\nu_{UF}$) and the spectral widths (SW_1 and SW_2) accessible within a single-scan as they are related by the following equation:

$$\gamma_a \cdot G_a \cdot L = 2 \cdot \frac{SW_1 \cdot SW_2}{\Delta\nu_{UF}}$$

where L is the height of the detection coil. The maximum acquisition gradient amplitude available is thus a major limiting factor. Moreover, the typical sensitivity, resolution and spectral widths that can be achieved in a single-scan are dependent on the hardware (probe and magnetic field). Table 1 illustrates these typical performances of UF 2D pulse sequences for two different hardware configurations, so that users can extrapolate what can be expected on their own system. Table 1 shows that for a constant resolution, increasing the magnetic field leads to a better sensitivity, albeit at the cost of a reduced spectral width. Therefore, the optimum configuration depends on the targeted application.

Table I. Analytical performance of ultrafast 2D NMR under two typical commercial configurations (400 MHz spectrometer, direct room temperature (RT) probe and 700 MHz spectrometer, inverse cryogenic probe). The performance of sub-second single-scan experiments is compared to the one of a 60 s hybrid approach consisting in accumulating UF experiments (here, 16 accumulations consisting of 4 interleaved scans x 4 transients, with a 3.5 s interscan delay). Typical values are given for small molecule samples analyzed in a 5 mm tube.

	UF experiment (0.2 s)		**Hybrid experiment (60 s)**	
	400 MHz RT probe	**700 MHz Cryoprobe**	**400 MHz RT probe**	**700 MHz Cryoprobe**
LOD	100 mM	1 mM	50 mM	0.5 mM
SW for COSY (^{1}H x ^{1}H)	6 x 6 ppm	2.5 x 2.5 ppm	12 x 12 ppm	5 x 5 ppm
SW for HSQC (^{13}C x ^{1}H)	40 x 4 ppm	15 x 3 ppm	80 x 8 ppm	30 x 6 ppm
FWHM (UF dim.)	50 Hz	50 Hz	50 Hz	50 Hz
FWHM (Conv. dim.)	35 Hz	25 Hz	35 Hz	25 Hz

LOD: Limit Of Detection; SW: Spectral Width; FWHM: Full Width at Mid-Height in the spatially-encoded dimension (UF dim.) or in the conventional FT dimension (Conv. dim.).

2.4 New generation of UF experiments

During the last decade, numerous strategies have been developed to overcome the limitations mentioned above. To reduce translational molecular diffusion effects, two approaches have been proposed. The first one consists in reducing the diffusion coefficient by relying on low temperatures, viscous solvents, or on the encapsulation of the analytes in phospholipidic vesicules.[5] The second one is a multi-echo encoding scheme[6] which makes UF experiments more immune to such diffusion effects.

As regards J-modulation effects during constant time spatially-encoded experiments, they have been characterized very recently through numerical simulations.[7] Thanks to an in-depth understanding of this effect, several strategies of J-modulation control are now available to maximize the SNR arising from UF experiments.

Several approaches were developed to alleviate the compromise between resolution and spectral widths. Most of them rely on folding methods to recover the peaks lying outside the detected spectral window, such as gradient-controlled folding[8], spatial/spectral encoding[9] or

reverse detection.[10] UF datasets can also be recorded in a non-uniform sampling fashion to reach higher resolutions or larger spectral widths.[11] The use of interlaced FT has been proved to double the accessible spectral width along the direct-acquisition domain.[12]

There are, however, many applications where a single-scan experiment is not needed. In such cases, significant improvements can be achieved through multi-scan hybrid approaches, capable of yielding 2D spectra whose quality is comparable to the one of conventional experiments, but in a much shorter time (from a few tens of seconds to a few minutes). For example, the multi-scan single-shot (M3S) method, consisting of a classical signal accumulation, leads to an increase of the SNR and to a better repeatability compared to the single-scan approach.[13] Another multi-scan approach based on interleaved acquisitions was also optimized to increase the accessible spectral widths or to ease the gradient demand. [14] These two strategies can be easily combined, resulting in 2D spectra whose performance is significantly improved compared to single-scan acquisitions. Table 1 illustrates this feature for a one minute experiment –still much shorter than conventional 2D NMR.

Thanks to the numerous improvements mentioned above, which can be combined, UF NMR has become a powerful analytical tool capable of delivering high-resolution 2D spectra with a drastically reduced acquisition time compared to conventional 2D NMR.

2.5 UF spectroscopy at arbitrary dimensions

Multi-dimensional spectra can also be acquired within a single-scan –at least in principle– by spatially encoding the sample along independent spatial dimensions.[15] Shrot and Frydman have shown how 3D and 4D experiments can be recorded in a single scan, by replacing the indirect dimensions of conventional nD experiments by spatial encoding along two or three orthogonal directions. Decoding the complex resulting magnetization windings requires applying rapidly oscillating gradients along two or three dimensions during the detection. However, these experiments require a probe with triple axis gradients and put a high demand on the associated hardware. Moreover, they accumulate the drawbacks of UF 2D NMR along additional dimensions, leading to a very limited sensitivity and resolution.

An alternative approach consists of a hybrid method allowing the recording of a 3D spectrum in the time of a conventional 2D experiment.[16] In this “fast spatially encoded 3D NMR”, one

of the indirect dimensions is spatially encoded while the other one results from a conventional time incrementation. Although the durations of these experiments are longer than those of the fully spatially encoded one, this method does not require any specific hardware. Moreover, the limitations arising from the spatially-encoded nature of the experiment are counterbalanced by the signal accumulation arising from the conventional dimension.

3 Applications

3.1 Real-time monitoring

Monitoring chemical or biochemical processes via analytical spectroscopies plays a central role in kinetic and dynamic studies, and in the elucidation of reaction mechanisms. Among spectroscopic techniques, NMR has the great advantage of being non-specific and non-destructive; it does not require any prior knowledge on the analyzed compounds and delivers both structural and quantitative information. In this context, UF 2D experiments have considerably extended the potential of reaction monitoring by NMR, making it possible to study, in real time, complex (bio)chemical processes involving multiple analytes whose 1D spectra are overlapped.[17] For instance, Herrera *et al.* applied the UF methodology to study the mechanisms leading to the formation of pyrimidines.[18] They recorded 525 UF TOCSY spectra (every 10 s during a 1h 30 min reaction) to monitor the reaction between an aliphatic ketone with an amount of trifluoromethanesulfonic acid anhydride (Tf_2O) in the presence of deuterated-acetonitrile (Figure 4). More recently, the same authors described an interleaved and excitation-optimized approach capable of recording up to 2500 2D NMR heteronuclear data sets within 100 min, thus considerably increasing the potential of these real time methods.[19] These successful results have then inspired the implementation of 2D real-time monitoring for other applications like *in situ* electrochemistry coupled to NMR. Boisseau *et al.* implemented an electrochemical cell inside a 5 mm NMR tube, to follow electrochemical reactions in real time by UF 2D NMR, in order to elucidate unstable reaction intermediates.[20] Again, this example highlights the potential of UF NMR to study fast chemical reactions.

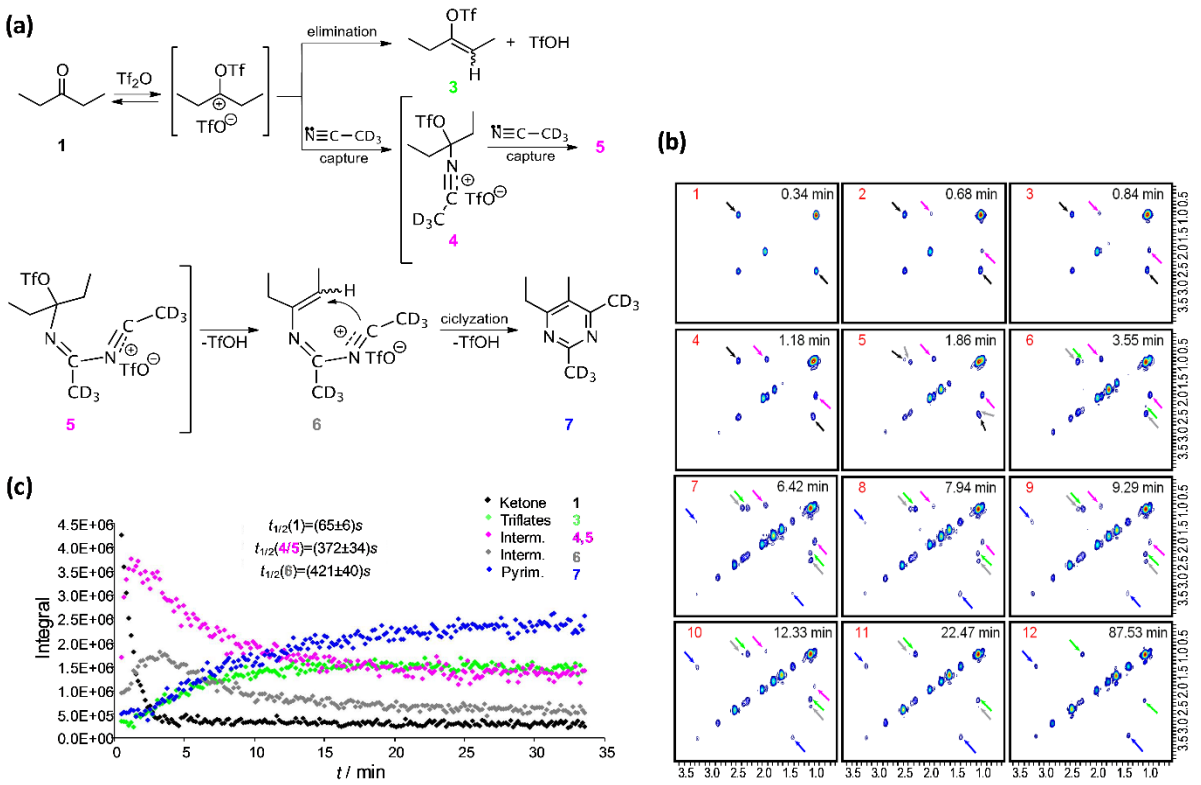

Figure 4. Monitoring of the formation of pyrimidine by UF TOCSY, illustrating the potential of UF NMR for real-time reaction monitoring. **(a)** Proposed mechanism for the reaction between a symmetric pentanone, triflic anhydride, and acetonitrile-d_3. This scheme was established according to the reactant and product cross-peaks detected by UF TOCSY. **(b)** Some of the 525 TOCSY spectra recorded in the course of the reaction every 10 s, over 87.53 min at 37 °C. **(c)** Graph of the averaged integrated peak intensity as a function of time for the different species. Reproduced with permission from Ref. [18]

2D NMR is also widely applied to study dynamic phenomena in biochemistry, as it brings valuable structural and dynamic insight on complex macromolecules. The study of short-lived excited states is very important for understanding molecular folding/misfolding, binding interactions or other dynamic phenomena. These fast dynamic processes require analytical techniques operating on a second's timescale, such as UF NMR. To enable the fast repetition of UF experiments, Gal *et al.* combined UF NMR with the SOFAST methodology (Selective Optimized-Flip-Angle Short Transient), resulting in a Ultra-SOFAST pulse sequence which can be repeated at a Hz rate. [21] This UF SOFAST approach was recently applied to understand central features of the function of RNAs by monitoring conformational transitions and structural rearrangements in real time.[22]

3.2 Coupled techniques

Coupling NMR with other analytical techniques can significantly improve its performance, either in terms of discriminating capacity (when coupled to chromatographic techniques) or in terms of sensitivity (when associated with hyperpolarization methods). NMR coupled to liquid chromatography (LC-NMR) is a hyphenated technique combining the separation power of LC with the quantitative and structural insights provided by NMR acquisitions. However, when these experiments are carried out in an on-line mode, the design of a fast and efficient detection tool is essential to characterize the eluted compounds in real-time. UF NMR responds to this double time and characterization constraint, and its coupling with a chromatographic technique was reported by Shapira *et al*.[23] In a more recent work Queiroz *et al*. implemented this approach on a commercial high-performance liquid-chromatography system coupled to NMR (HPLC-NMR), to detect and characterize aromatic compounds in mixtures within the course of a chromatographic run.[24]

The main limitation of NMR remains its relatively low sensitivity, and several approaches based on hyperpolarization have been proposed to deal with this drawback. In liquid-state NMR, the most efficient strategies are dissolution dynamic nuclear polarization (D-DNP) or signal amplification by reversible exchange (SABRE) based on para-hydrogen. These methods offer a great sensitivity enhancement –up to orders of magnitude– but the hyperpolarized signals are short-lived, and consequently incompatible with the signal accumulation characterizing conventional 2D NMR experiments. UF NMR offers an appealing solution to this limitation, and it was successfully coupled to the D-DNP [25] and SABRE [26] methods, yielding single-scan 2D spectra of hyperpolarized substrates at sub-millimolar concentrations. The application of these methods to biological mixtures –such as those studied in metabolomics– is particularly promising. Very recently, heteronuclear 2D correlation spectra of hyperpolarized breast cancer cell extracts have been obtained in a single scan after a 30 min polarization step, with a sufficient sensitivity to characterize metabolites whose conventional detection required hours of acquisition at high field (Fig. 5) [27].

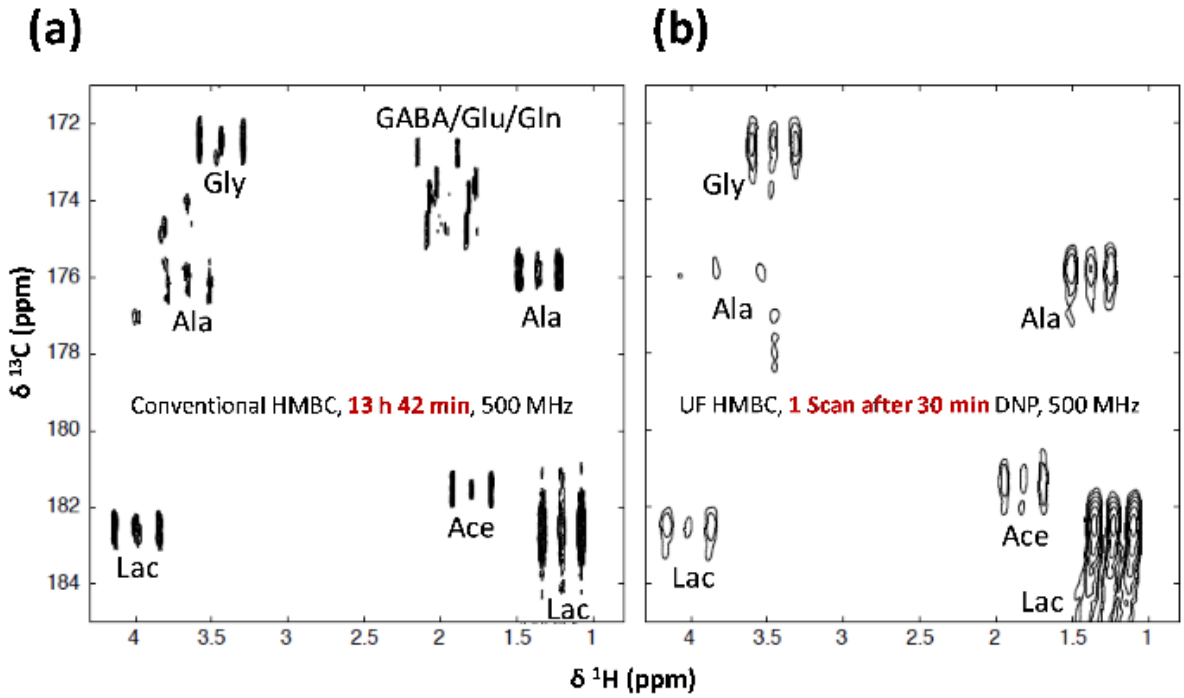

Figure 5. ^{1}H-^{13}C HMBC spectra of partially ^{13}C-enriched extracts from human breast cancer cell lines. **(a)** Conventional HMBC spectrum, recorded in 13 h 42 min at 500 MHz with a cryogenic probe. **(b)** Hyperpolarized single scan HMBC spectrum at 500 MHz after 30 min of polarization. Reproduced from Ref. [27] with permission from The Royal Society of Chemistry

3.3 Metabolomics and fluxomics

2D NMR is increasingly used in metabolomics, a field where NMR is one of the major analytical tools to determine the metabolic content of samples from biological origin. In such complex samples characterized by strong peak overlaps, 2D spectroscopy is highly relevant to improve the identification of putative biomarkers, but also to increase the accuracy of quantitative analysis.[28] However, conventional 2D NMR is barely compatible with the high-throughput needs characterizing metabolomics studies which involve large sample collections. UF 2D NMR is therefore a valuable alternative to conventional 2D methods in this field. Single-scan experiments, however, are generally not adapted to samples from biological origin, due to their intrinsic low-sensitivity. But an alternative is offered by hybrid methods, consisting in accumulating several UF experiments to improve the sensitivity, the resolution and/or the spectral width.[29] These experiments offer an interesting compromise between single-scan and conventional 2D acquisitions. Furthermore, hybrid methods, such as M3S are characterized by a better repeatability than their conventional counterparts, owing to their better immunity

vis-à-vis hardware instabilities during the experiment. In particular, the hybrid COSY experiment has been proved efficient to provide homonuclear correlation spectra of biological samples within only a few minutes. Le Guennec *et al.* have shown that this method offers an easier and less ambiguous biomarker identification than 1D pulse sequences which are generally used in metabolomics.[13] Moreover, the high repeatability of fast hybrid COSY makes it particularly appropriate for the targeted quantitative analysis of complex metabolite mixtures, as recently shown on breast cancer cell extracts (Fig. 6 a) or plant extracts (Fig. 6 b).[13, 30] In a similar vein, another recent quantitative application of UF NMR pertains to the field of fluxomics. 2D NMR is an efficient tool for studying metabolic fluxes by measuring ^{13}C enrichments in complex mixtures of ^{13}C-labeled metabolites. However, the methods reported so far have been hindered by long experiment durations, thus limiting their use in fluxomics studies. To take advantage of the time saving and higher precision offered by UF experiments, several acquisition strategies have been proposed, consisting in recording homonuclear ^{1}H 2D spectra where ^{13}C couplings are expressed in one dimension only. [31] The signal overlap is significantly reduced while quantitative site-specific information can be extracted from lines of the 2D map (Fig. 6 c). Even more, the overlap can be further reduced by tilting the ^{1}H-^{13}C isotopic pattern along a third dimension.[32] This approach requires a 3D acquisition, which can be achieved in a few minutes only via a hybrid strategy based on UF NMR (Fig. 6 d).

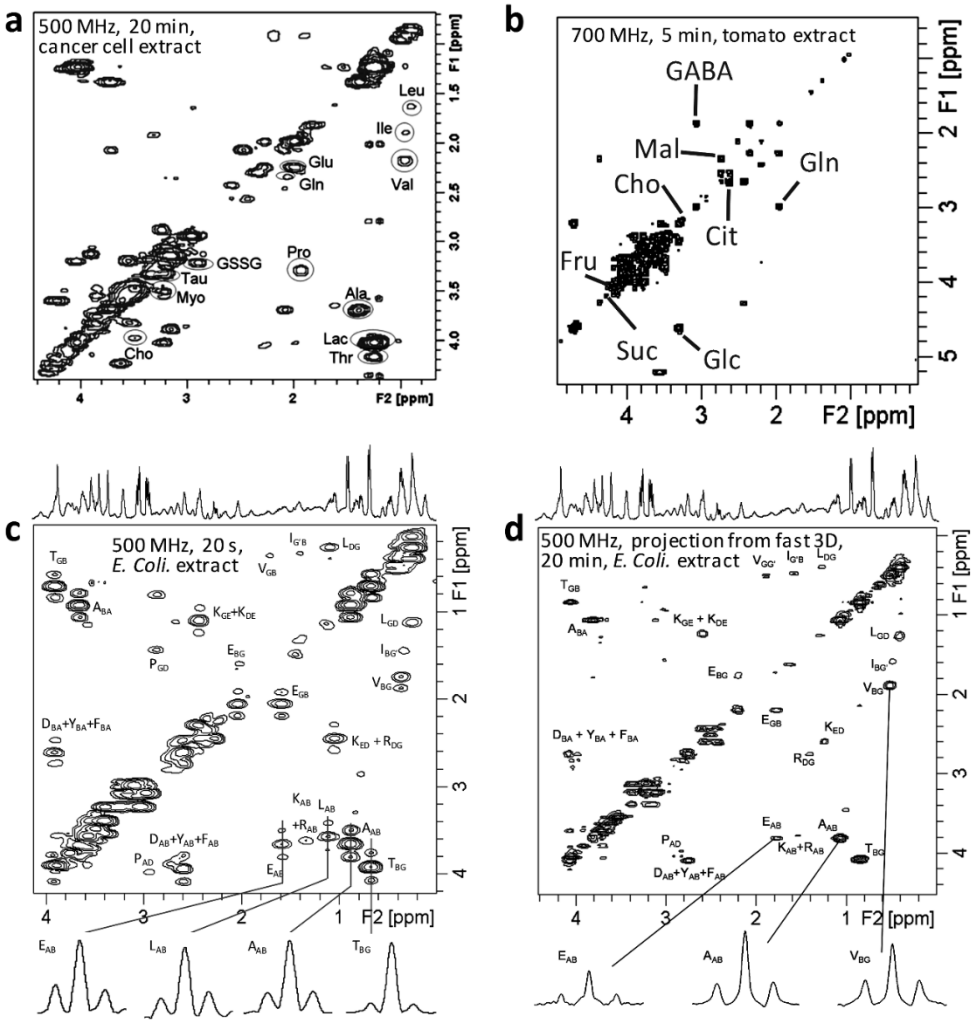

Figure 6. Examples from recent literature showing the potential of fast hybrid nD NMR techniques based on ultrafast nD spectroscopy in the fields of metabolomics and fluxomics. **(a, b)** Fast COSY spectra recorded on metabolic extracts for absolute quantification purposes; major metabolites (indicated on the figure) were quantified with an accuracy of a few percent relying on standard addition **(a)** or external calibration **(b)** approaches. **(a)** Spectrum obtained in 20 min at 500 MHz with a cryogenic probe using a multi-scan single-shot (M3S) strategy on a breast cancer cell extract. Reprinted with permission from Ref.[13]; Copyright 2012 American Chemical Society **(b)** Spectrum obtained in 5 min at 700 MHz with a cryogenic probe using a hybrid interleaved and M3S strategy on a tomato fruit pericarp extract. Reprinted from Ref. [30] with kind permission from Springer Science and Business Media **(c, d)** Spectra recorded on a biomass hydrolysate from *E. Coli.* cells grown in a partially ^{13}C-enriched glucose environment, used in the field of fluxomics to measure site-specific ^{13}C enrichments. **(c)** Ultrafast COSY spectrum recorded in 4 scans (20 s) at 500 MHz with a cryogenic probe. Reproduced from P. Giraudeau and L. Frydman, Ref.[4] **(d)** F_1F_2 plane from a 3D J-resolved-COSY spectrum recorded in about 20 minutes at 500 MHz with a cryoprobe, with a hybrid pulse sequence based on ultrafast 2D NMR, where the spatio-temporal encoding of two dimensions is associated with the conventional temporal encoding of the third one. Reproduced with permission from Ref.[16]

3.4 Towards UF *in vivo* spectroscopy

Localized 2D spectroscopy is a powerful tool to disentangle the overlapping resonances resulting from the acquisition of *in vivo* 1D spectra. However, the long experiment times are ill-suited for *in vivo* applications where the effect of motion is particularly critical, leading to large noise ridges along the indirect dimension. Extending the UF approach to *in vivo* spectroscopy would therefore be extremely promising, and a first step was taken by Roussel *et al.*, who proposed an approach capable of recording UF 2D J-resolved localized spectra on *in vitro* phantoms placed in a small animal imaging system.[33] Unfortunately, the extension of this approach to an *in vivo* setting would inevitably suffer from the inhomogeneity of the voxel where the acquisition is performed. But Pelupessy *et al.* have designed a new class of spatially-encoded experiments, based on UF 2D NMR and capable of recording high-resolution 2D NMR spectra in inhomogeneous fields.[34] Based on this methodology, Wei *et al.* reported the acquisition of *ex vivo* localized 2D spectra in inhomogeneous biological tissues.[35] While not yet applied to *in vivo* spectroscopy, these developments have paved the way towards promising developments and applications. In a parallel magnetic resonance community, UF 2D NMR has recently inspired extremely promising developments in the field of MRI. Frydman *et al*. developed a new class of "SPEN" (spatiotemporal encoding) experiments, capable of delivering single-scan 2D images in an inhomogeneous environment, an approach which was successfully applied in a hyperpolarized context.[36]

4 Conclusion

Thanks to recent methodological and analytical developments, ultrafast multi-dimensional NMR has become a method of choice for a variety of applications, offering a valuable alternative to conventional nD spectroscopy. It is of particular interest for applications requiring short experiment times associated with a high spectral dispersion, such as the monitoring of fast kinetic or dynamic processes. Furthermore, while single-scan experiments are not as sensitive as their conventional analogues, their performance has been significantly enhanced by the development of multi-scan hybrid techniques. The latter offer –within a reasonable time– numerous application perspectives in the field of analytical chemistry,

particularly for high-throughput applications such as metabolomics. But one of the most exciting research avenues currently explored concerns the coupling of UF spectroscopy with dissolution-DNP. Associating these two techniques results in a powerful tool that should find applications in a broad array of domains. Finally, promising perspectives also arise in the extension of the UF methodology to an *in vivo* context, a field where the coupling with hyperpolarization could also open new research avenues.

The widespread use of ultrafast multidimensional spectroscopy among a broad community of users will also depend on its implementation on commercial NMR equipment. Large efforts have recently been devoted to improve the accessibility of UF NMR, and hopefully it is just a matter of time before manufacturers begin to implement it systematically on commercial spectrometers.

Acknowledgments

The authors acknowledge the members of the EBSI group at the CEISAM laboratory. We also thank our numerous collaborators, as well as funding sources (ANR, Région Pays de Loire, Biogenouest and IUF) and Michel Giraudeau for linguistic assistance.

5 References

1. L. Rouger, B. Gouilleux, and P. Giraudeau, 'Fast n-dimensional data acquisition methods'. In Encyclopedia of Spectroscopy and Spectrometry, 3rd edition, Lindon, J. C.; Tranter, G. E.; Koppenaal, D., Elsevier, 2016; in press.
2. L. Frydman, T. Scherf, and A. Lupulescu, *Prod. Natl. Acad. Sci. USA*, 2002, **99**, 15858-15862.
3. P. Pelupessy, *J. Am. Chem. Soc.*, 2003, **125**, 12345-12350.
4. P. Giraudeau, and L. Frydman, *Annu. Rev. Anal. Chem.*, 2014, **7**, 129-161.
5. L. Rouger, D. Loquet, S. Massou, S. Akoka, and P. Giraudeau, *ChemPhysChem*, 2012, **13**, 4124-4127.
6. P. Giraudeau, and S. Akoka, *J. Magn. Reson.*, 2008, **190**, 339-345.
7. B. Gouilleux, L. Rouger, B. Charrier, I. Kuprov, S. Akoka, J.-N. Dumez, and P. Giraudeau, *ChemPhysChem*, 2015, in press, doi: 10.1002/cphc.201500514.
8. P. Giraudeau, and S. Akoka, *J. Magn. Reson.*, 2010, **205**, 171-176.
9. Y. Shrot, and L. Frydman, *J. Chem. Phys.*, 2009, **131**, 224516.
10. Z. Wei, J. Yang, L. Lin, G. Liu, Y. Lin, and Z. Chen, *Magn. Reson. Chem.*, 2014, **52**, 680-685.
11. Y. Shrot, and L. Frydman, *J. Magn. Reson.*, 2011, **209**, 352-358.
12. M. Mishkovsky, and L. Frydman, *J. Magn. Reson.*, 2005, **173**, 344-350.
13. A. Le Guennec, I. Tea, I. Antheaume, E. Martineau, B. Charrier, M. Pathan, S. Akoka, and P. Giraudeau, *Anal. Chem.*, 2012, **84**, 10831-10837.
14. L. Rouger, B. Charrier, M. Pathan, S. Akoka, and P. Giraudeau, *J. Magn. Reson.*, 2014, **238**, 87-93.
15. Y. Shrot, and L. Frydman, *J. Am. Chem. Soc*, 2003, **125**, 11385-11396.
16. P. Giraudeau, E. Cahoreau, S. Massou, M. Pathan, J. C. Portais, and S. Akoka, *ChemPhysChem*, 2012, **13**, 3098-3101.
17. A. Herrera, E. Fernández-Valle, R. Martínez-Álvarez, D. Molero-Vílchez, Z. D. Pardo-Botero, and E. Sáez-Barajas, *Magn. Reson. Chem.*, 2015, in press, DOI: 10.1002/mrc.4240.
18. A. Herrera, E. Fernández-Valle, R. Martínez-Álvarez, D. Molero, Z. D. Pardo, E. Sáez, and M. Gal, *Angew. Chem. Int. Edit.*, 2009, **48**, 6274-6277.
19. Z. D. Pardo, G. L. Olsen, M. E. Fernández-Valle, L. Frydman, R. Martínez-Álvarez, and A. Herrera, *J. Am. Chem. Soc.*, 2012, **134**, 2706-2715.
20. R. Boisseau, U. Bussy, P. Giraudeau, and M. Boujtita, *Anal. Chem.*, 2015, **87**, 372-375.
21. M. Gal, P. Schanda, B. Brutscher, and L. Frydman, *J. Am. Chem. Soc.*, 2007, **129**, 1372-1377.
22. A. Corazza, E. Rennella, P. Schanda, M. C. Mimmi, T. Cutuil, S. Raimondi, S. Giorgetti, F. Fogolari, P. Viglino, L. Frydman, M. Gal, V. Bellotti, B. Brutscher, and G. Esposito, *J. Biol. Chem.*, 2010, **285**, 5827-5835.
23. B. Shapira, A. Karton, D. Aronzon, and L. Frydman, *J. Am. Chem. Soc.*, 2004, **126**, 1262-1265.

24. L. H. K. Queiroz Junior, D. P. K. Queiroz, L. Dhooghe, A. G. Ferreira, and P. Giraudeau, *Analyst*, 2012, **137**, 2357-2361.
25. L. Frydman, and D. Blazina, *Nat. Phys.*, 2007, **3**, 415-419.
26. V. Daniele, F.-X. Legrand, P. Berthault, J.-N. Dumez, and G. Huber, *ChemPhysChem*, 2015, in press, DOI: 10.1002/cphc.201500535.
27. J.-N. Dumez, J. Milani, B. Vuichoud, A. Bornet, J. Lalande-Martin, I. Tea, M. Yon, M. Maucourt, C. Deborde, A. Moing, L. Frydman, G. Bodenhausen, S. Jannin, and P. Giraudeau, *Analyst*, 2015, **140**, 5860-5863.
28. P. Giraudeau, and S. Akoka, *Adv. Bot. Res.*, 2013, **67**, 99-158.
29. S. Akoka, and P. Giraudeau, *Magn. Reson. Chem.*, 2015, in press, DOI: 10.1002/mrc.4237.
30. T. Jézéquel, C. Deborde, M. Maucourt, V. Zhendre, A. Moing, and P. Giraudeau, *Metabolomics*, 2015, **11**, 1231-1242.
31. P. Giraudeau, S. Massou, Y. Robin, E. Cahoreau, J.-C. Portais, and S. Akoka, *Anal. Chem.*, 2011, **83**, 3112-3119.
32. R. Boisseau, B. Charrier, S. Massou, J. C. Portais, S. Akoka, and P. Giraudeau, *Anal. Chem.*, 2013, **85**, 9751-9757.
33. T. Roussel, P. Giraudeau, H. Ratiney, S. Akoka, and S. Cavassila, *J. Magn. Reson.*, 2012, **215**, 50-65.
34. P. Pelupessy, E. Renella, and G. Bodenhausen, *Science*, 2009, **324**, 1693-1697.
35. Z. Wei, L. Lin, Y. Lin, S. Cai, and Z. Chen, *Chem. Phys. Lett.*, 2013, **581**, 96-102.
36. R. Schmidt, C. Laustsen, J.-N. Dumez, M. I. Kettunen, E. M. Serrao, I. Marco-Rius, K. M. Brindle, J. H. Ardenkjaer-Larsen, and L. Frydman, *J. Magn. Reson.*, 2014, **240**, 8-15.
37. A. Le Guennec, P. Giraudeau, S. Caldarelli, and J.-N. Dumez, *Chem. Commun.*, 2015, **51**, 354-357.

4.3. Ultrafast NMR: a comprehensive review of methods and applications

Ultrafast 2D NMR: Methods and applications

Boris Gouilleux, Laetitia Rouger and Patrick Giraudeau

(Original review article accepted

in Annual Reports on NMR Spectroscopy, 2017)

Abstract:

Multidimensional NMR (nD NMR) has become one of the most powerful spectroscopic tools to deliver diverse structural and functional insights into organic and biomolecules as well as on raw materials. A long-standing concern of nD NMR is related to its long experiment duration, arising from the need to sample the indirect dimension(s) in a multi-step fashion. For decades, the NMR community has been developing numerous strategies to speed up nD NMR experiments and therefore extend their scope of applications. Among them is the ultrafast (UF) NMR methodology, capable of delivering arbitrary homo- or heteronuclear multidimensional spectra in a single scan. Since the initial concept was published in 2002, the performance of this sub-second 2D NMR approach has been greatly improved so that UF NMR is nowadays a relevant analytical tool used in broad variety of situations whereby the experiment duration is crucial. Following a description of the principles of UF NMR, the present review aims at emphasizing the numerous methodological developments that this approach has undergone so far in 2017. Thereafter, the high versatility of UF NMR is highlighted through the review of the applications that have been reported in a variety of settings and disciplines, in isotropic as well as anisotropic media.

1. Introduction

Nuclear magnetic resonance (NMR) is a highly versatile spectroscopic technique with applications in a large range of disciplines, from chemistry and physics to medicine including organic chemistry, natural products research, metabolic studies, structural biology, drug discovery and environmental sciences, owing to its wealth of information about structural, quantitative and dynamic features. The development of 2D NMR by Jeener in the 1970's enabled a true "revolution" in the world of NMR as it brings invaluable correlation information together with resolution enhancement, which are both determining for the fields of application that we know today [1]. Later on, the development of higher dimensionality (nD NMR) experiments has been decisive in understanding the structure and dynamics of bio-macromolecules. The downside of conventional nD NMR is mainly the long acquisition durations arising from the need to sample the indirect dimension(s) through the repetition of numerous transients. This long experiment time involves several drawbacks such as the overload of spectrometer schedules, the impact of hardware instabilities in the indirect dimension(s) and obviously, the incompatibility of nD experiments with samples whose composition is evolving over time and with most hyphenated techniques. The NMR community has invested considerable research efforts geared towards reducing this experiment duration [2]. A first strategy is directed at reducing the time separating two successive increments through i) a decrease of the relaxation times for the relevant nuclei by relying on a reservoir of longitudinal magnetization and ii) an optimization of the pulse angles. In this vein, the selective optimized flip-angle short-transient (SOFAST) and the acceleration by sharing adjacent polarization (ASAP) methods have proved to be effective in the analysis of bio-macromolecules and small organic molecules, respectively [3]. A second approach focuses on the methods that reduce the number of increments in the indirect dimension. Numerous sampling schemes and signal processing algorithms have been proposed to compensate the subsequent resolution losses such as spectral aliasing [4] and non-uniform sampling methods (NUS) [5]. Other developments are based on alternatives to Fourier transform (FT) NMR, such as Hadamard spectroscopy [6].

The present review deals with one of the most recent fast multi-dimensional methods: the so-called ultrafast (UF) NMR experiment, first proposed in 2002 by Frydman and co-workers for the sake of collecting 2D NMR spectra in a single scan [7]. The basic scheme of UF NMR

spectroscopy enables the collection of arbitrarily high multidimensional homo or heteronuclear NMR spectra within a single transient. By contrast to Jeener's concept, the central feature of UF NMR is the replacement of the time-incremented period in the conventional 2D scheme by a spatiotemporal manipulation, whereby spins undergo spatially distinct t_1-evolution periods throughout the sample within the same transient. Subsequent gradient-based methods – based on imaging principles – were proposed to read out this spatially encoded information and to retrieve multidimensional correlation into patterns that are identical to those afforded by conventional techniques. Several reviews about UF NMR have already been published, the reader could refer to ones proposed by the Frydman's research group for a deep understanding of theoretical matters [8,9] while the one written in 2014 by Giraudeau & Frydman deals with this topic from the point of view of analytical chemistry [10]. The present review claims to pursue these endeavors by reporting the methodological improvements that UF NMR has undergone so far in 2017 and providing an overview of its multidisciplinary scope of practical and fundamental applications.

In a first part, the principles and the characteristics of UF NMR are described, as well as methodological developments concerning spatial encoding, detection, processing, hybrid and combined methods. The extension to UF nD NMR is also discussed. Besides this methodological review, a comprehensive work-flow to implement UF NMR is proposed including pulse-programs and processing routines. In a second part, applications of UF NMR are illustrated in a variety of settings and disciplines, both in liquid state and in oriented media. First, applications in which the experiment duration plays a crucial role are reported: the real-time 2D NMR monitoring of samples whose composition evolves over time, in the field of organic and bio-chemistry; the coupling of UF 2D NMR with chromatography and hyperpolarization techniques, where the single-scan nature offers an appealing solution to the irreversibility issue of the separation/preparation processes. Then, promising applications in the field of quantitative NMR (qNMR) are also reported, especially in "omics" disciplines. Furthermore, the high versatility of this generic approach is highlighted by the development of pseudo-2D UF experiments, which dramatically speed up diffusion experiment, relaxation measurement and even the study of chemical exchange saturation transfer (CEST). Finally, the potential of the UF methodology in the context of inhomogeneous B_0 magnetic fields is described, as well as applications to localized 2D NMR spectroscopy.

2. Methods

2.1. Principle

2.1.1. General

The key feature of ultrafast 2D NMR experiments is the replacement of the conventional time incrementation by a spatial encoding, as illustrated in Figure 1. Thanks to this substitution, the spins located at different z positions undergo distinct t_1 evolution periods according to their position in the tube, and these different evolution periods take place simultaneously within the course of a single scan. While the preparation and mixing steps are similar to the ones encountered in conventional experiments, a specific detection scheme is required to decode the information encoded in the evolution step.

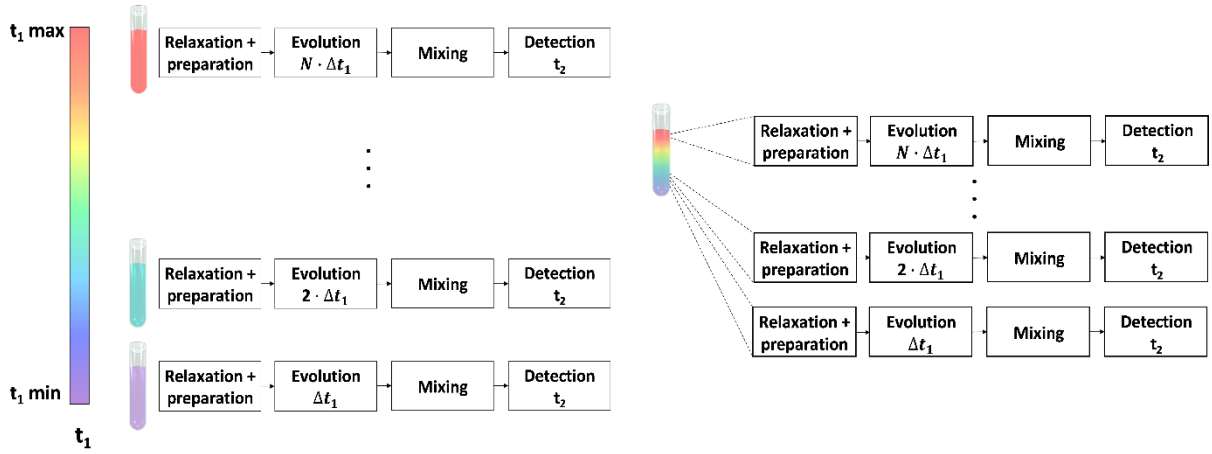

Figure 1. General diagram for conventional 2D experiments (left) and for ultrafast 2D NMR experiments (right). Whereas in conventional experiments the pulse sequence is repeated with an incremented t_1 evolution period, in ultrafast experiments each slice of the sample undergoes different t_1 evolution periods within a single scan.

2.1.2. Spatial encoding

The spatial encoding method initially used in ultrafast NMR was based on a discrete scheme [7], but it was quickly replaced by continuous schemes [11–13]. Whichever the encoding scheme, a magnetic field gradient (noted G_e) is applied along the encoding axis so that spins at different locations in the tube experience different effective magnetic fields, thus

undergoing different resonance frequencies. It results in different rotation times in the transverse plane according to the frequency, directly related to the *z*-position of the spins. The induced spatial dependence of the phase is of the form:

$$\phi(z) = C \cdot \Omega_i \cdot z \qquad \text{Equation 1}$$

where C is a constant depending on the encoding scheme, Ω_i is the frequency of the chemical site *i* and *z* the position in the tube. In the initial discrete encoding scheme, this result is obtained by applying a series of selective pulses with incremented offset applied in combination with pairs of bipolar gradients, as illustrated in Figure 2a. This approach is technically demanding, moreover it is characterized by the occurrence of ghost peaks and a limited resolution [13].

Soon after the emergence of the ultrafast methodology, different types of continuous encoding schemes were proposed. Shrot and Tal suggested two different real-time encoding schemes [11,12], thereafter named $\left(\frac{\pi}{2}-\frac{\pi}{2}\right)$ and $\left(\frac{\pi}{2}-\pi\right)$. On the other hand, a constant time phased-modulated scheme was proposed by Pelupessy [13], thereafter named $(\pi-\pi)$. In these continuous encoding schemes, the sample is virtually divided into an infinite number of infinitesimal slices, unlike the discrete way.

In the real-time encoding schemes, this infinitesimal division is performed thanks to the application of a $\frac{\pi}{2}$ chirp pulse simultaneously to the encoding gradient (G_e, Figure 2b). Again, spins are excited at different times according to their *z*-position in the tube. The spatial dependence of the phase induced by this gradient - $\frac{\pi}{2}$ chirp pulse pair is [12]:

$$\phi^{\pi/2}(z) = \frac{\delta^{\pi/2}}{2} \cdot \left(\Omega_1 + \frac{\gamma_e G_e^{\pi/2} L}{4}\right) + \frac{\delta^{\pi/2}}{L} \cdot \left(\frac{\gamma_e G_e^{\pi/2} L}{2} - \Omega_1\right) \cdot z - \frac{\gamma_e G_e^{\pi/2} \delta^{\pi/2}}{2L} \cdot z^2 \qquad \text{Equation 2}$$

In this equation, $\delta^{\pi/2}$ is the duration of the $\frac{\pi}{2}$ chirp pulse, $G_e^{\pi/2}$ the amplitude of the gradient applied simultaneously to this chirp pulse, γ_e the gyromagnetic ratio of the encoded nucleus, L the length of the sensitive volume and Ω_1 the chemical sift precession of the considered

spin. A *z* –dependent phase is obtained, but the z^2 quadratic evolution term prevents the refocusing of the magnetizations by a linear magnetic field gradient.

A first solution to refocus this quadratic term is to apply a second similar $\frac{\pi}{2}$ chirp pulse together with an opposite gradient ($-G_e^{\pi/2}$). This second $\frac{\pi}{2}$ chirp pulse also flips back the magnetizations along the *z*-axis, and a non-selective $\frac{\pi}{2}$ pulse is needed prior to detection. This $\left(\frac{\pi}{2}-\frac{\pi}{2}\right)$ encoding scheme, illustrated in Figure 2c, leads to an amplitude-modulated signal.

In order to achieve phase-modulated experiments such as correlation spectroscopy (COSY) or J-resolved spectroscopy, Tal *et al.* proposed to replace the second $\frac{\pi}{2}$ chirp pulse by a π chirp pulse. The spatial dependence of the phase induced by this gradient - π chirp pulse pair is [12]:

$$\phi^{\pi}(z)=\frac{\delta^{\pi}\gamma_e G_e^{\pi} L}{4}-\left(2\delta^{\pi}\gamma_e G_e^{\pi}-\frac{2\delta^{\pi}}{L}\cdot\Omega_1\right)\cdot z+\frac{\delta^{\pi}\gamma_e G_e^{\pi}}{L}\cdot z^2 \qquad \text{Equation 3}$$

In this equation, δ^{π} is the duration of the π chirp pulse and G_e^{π} the amplitude of the gradient applied simultaneously to this chirp pulse. The optimization of this parameters allows to compensate the z^2 dephasing induced by the first chirp pulse while keeping magnetizations in the tranverse plane. This $\left(\frac{\pi}{2}-\pi\right)$ encoding scheme is illustrated in Figure 2d.

Additionally to these two real-time encoding scheme, the constant time $(\pi-\pi)$ scheme (Figure 2e) starts with a non-selective $\frac{\pi}{2}$ excitation of all the spins, and the evolution time is spatially modulated thanks to the presence of a π chirp pulse together with an encoding gradient G_e^{π}. The spatial dependence of the phase induced by this gradient - π chirp pulse pair, as described above, includes a quadratic term which prevents the refocusing of the magnetizations by a linear magnetic field gradient. A second π chirp pulse is thus applied together with an opposite gradient $-G_e^{\pi}$, in order to cancel this quadratic dephasing. As for

the real-time $\left(\frac{\pi}{2}-\pi\right)$ scheme, magnetizations end in the transverse plane, leading to phase-modulated experiments.

Regardless of the encoding scheme used, a linear spatial dependence of the phase is obtained (Equation 1). The spatial encoding constant C which characterizes the resulting magnetization winding for each scheme is defined in Table 1 depending on the overall duration T_e of the spatial encoding, i.e. the time spent by the spins in the transverse plane. One should note that a different magnetization winding is obtained for each resonance frequency in the sample, leading to a specific spatial encoding for each chemical shift.

Table 1. Description of the main continuous spatial encoding schemes in UF NMR.

encoding scheme	real/constant time	modulation	T_e	C
$\left(\frac{\pi}{2}-\frac{\pi}{2}\right)$	real-time	amplitude	$\delta^{\pi/2}$	$\frac{2T_e}{L}$
$\left(\frac{\pi}{2}-\pi\right)$	real-time	phase	$\frac{\delta^{\pi/2}}{2}+\delta^{\pi}$	$\frac{2T_e}{L}\cdot\frac{1-G_e^{\pi/2}/G_e^{\pi}}{1+G_e^{\pi/2}/G_e^{\pi}}$
$(\pi-\pi)$	constant time	phase	$2\delta^{\pi}$	$\frac{2T_e}{L}$

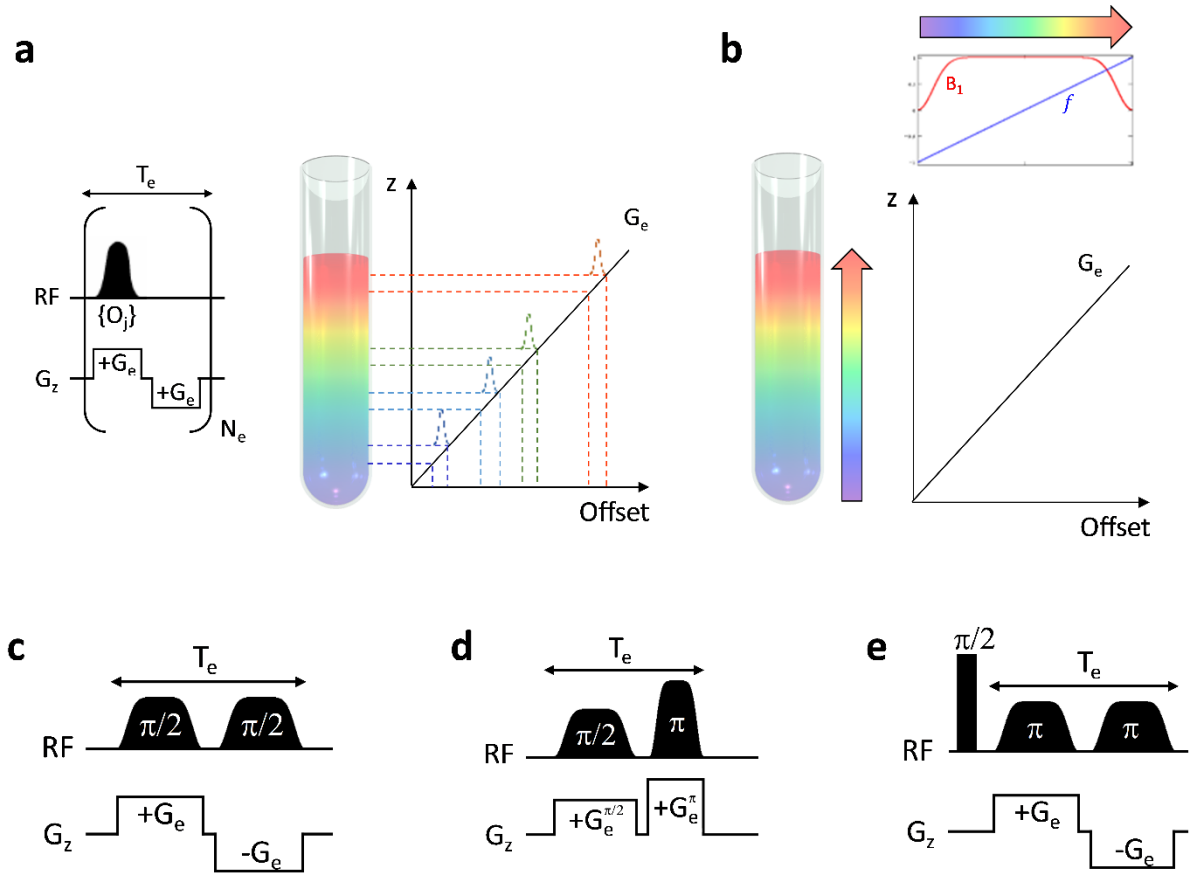

Figure 2. (a) Principle of discrete spatial encoding. The action of an encoding gradient G_e is combined with a selective pulse so that spins located in a particular slice of the sample are excited. This combination is repeated while varying the offset of the selective pulse so that the different slices of the sample are excited at different times. (b) Principle of continuous spatial encoding. The repetition of selective pulses is replaced by a chirp pulse whose frequency is linearly swept. By combining this pulse with the encoding gradient, spins located at different z positions in the sample are excited at different times. (c - e) Typical pulse sequences capable of achieving this continuous spatial encoding, in a real-time (c and d) or constant time manner (e).

Following this encoding step, the mixing period is similar to the one of conventional 2D NMR experiments.

2.1.3. Detection

Once the receiver opened, a reading gradient (G_a) is applied to refocus the linear dephasing created during the spatial encoding. Since the spatio-temporal encoding step leads to a different magnetization winding for each resonance frequency, the application of G_a generates a series of gradient echoes occurring when:

$$k = -C \cdot \Omega_1 \qquad \text{Equation 4}$$

where

$$k = \gamma_a \int_0^t G_a(t')\,dt' \qquad \text{Equation 5}$$

is a wave number in the *k* space (Figure 3a). Therefore, the resulting signal is equivalent to a 1D spectrum, obtained without Fourier transform. The dimension created this way will be called the "ultrafast" dimension in the rest of the manuscript, and is also reported as "spatially-encoded dimension" in the literature. It corresponds to the indirect dimension in the corresponding conventional experiment.

To obtain the second dimension, a technique analogous to EPSI (Echo-Planar Spectroscopic Imaging [14,15]) is used. It consists in a series of bipolar gradient pairs which replaces the normal free evolution. This train of gradients leads to periodic refocusings and defocusings of the signal, giving rise to a series of mirror-image 1D spectra along the UF dimension (Figure 3b). Meanwhile, the system evolves under conventional NMR parameters, according to the experiment type (chemical shift, couplings …). After FT along the detection time t_2, this leads to the second dimension, called "conventional dimension", corresponding to the direct dimension in conventional 2D experiments.

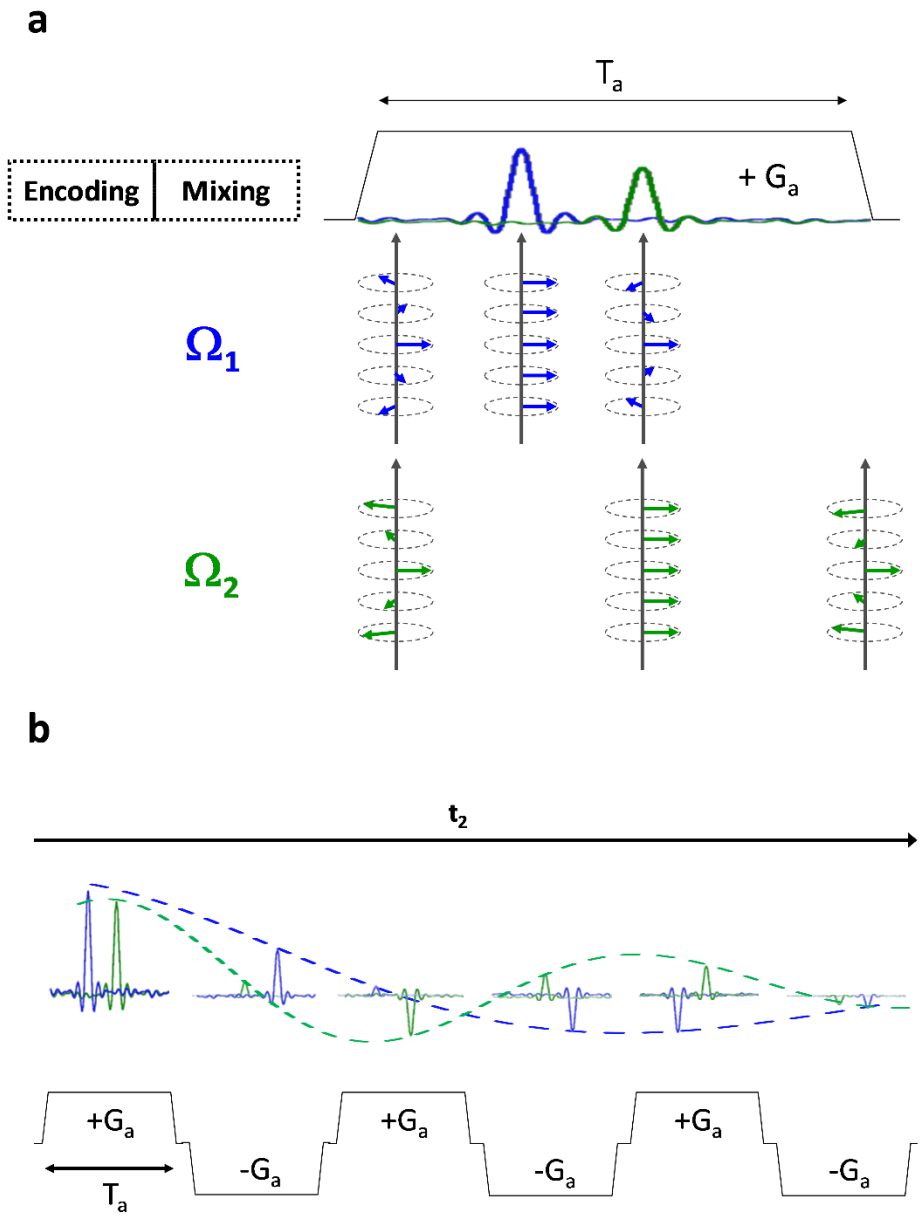

Figure 3. Principle of EPSI-based detection in UF NMR. (a) An acquisition gradient G_a is applied to refocus the *z*-dependent dephasing, leading to several echoes. The timing of these echoes in the k space is directly proportional to the resonance frequency Ω_i, leading to a 1D spectrum without FT. (b) To record the second dimension, a train of bipolar gradients is continuously applied in order to map the (k , t_2) space.

2.1.4. Data processing

The processing workflow specific to UF experiments is illustrated in Figure 4. As a first step, data arising from positive and negative gradients are split and rearranged, leading to two mirror-image S(k, t_2) maps. A FT is subsequently applied along the t_2 dimension, leading to

symmetric S(F_1, F_2) maps. The map arising from negative gradients is then inverted, and added to the other one to give the ultrafast spectrum.

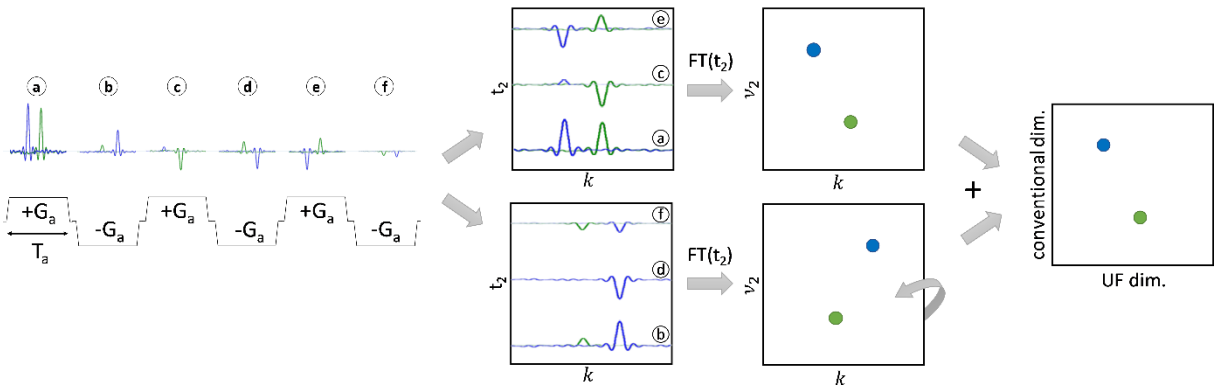

Figure 4. Diagram of the data processing for UF 2D experiments. Series of echoes acquired during positive and negative gradients are divided and organized in two $\nu_1 - t_2$ maps. Two mirror-image spectra are obtained after FT along t_2. One of them is inversed and added to the other, leading to the UF 2D spectrum.

2.2. Main characteristics of the UF methodology

The ultrafast methodology is characterized by several compromises, described in the following lines. However, in the past fifteen years, numerous solutions were developed to circumvent those limitations, of which an overview is given thereafter.

2.2.1. Spectral width and resolution considerations

A first characteristic of UF experiments is that spectral widths cannot be adjusted independently, contrary to conventional experiments. Accessible spectral widths and resolution in the ultrafast domain depend on experimental parameters and are linked to each other according to the following relation:

$$\gamma_a \cdot G_a \cdot L = 2 \cdot \frac{SW_{UF} \cdot SW_{conv}}{\Delta \nu_{UF}} \qquad \text{Equation 6}$$

where γ_a is the gyromagnetic ratio of the detected nucleus, G_a is the acquisition gradient amplitude, L is the length of the coil for the encoded nucleus, SW_{UF} and SW_{conv} are the

spectral widths in the ultrafast and conventional dimensions respectively, and $\Delta\nu_{UF}$ is the peak width at half maximum in the ultrafast dimension.

Giraudeau and Akoka demonstrated that independently of the spatial encoding scheme, the resolution in the ultrafast dimension is inversely proportional to the spatial encoding constant C [16]:

$$\Delta\nu_{UF} \propto \frac{1}{LC} \qquad \text{Equation 7}$$

Consequently, a better resolution should be achieved by increasing the duration of the spatial encoding T_e, as C is directly related to T_e for each encoding scheme (see Table 1). However, the next paragraphs show that increasing T_e leads to sensitivity losses and that a compromise has to be set between resolution and sensitivity.

Finally, the resolution in the conventional dimension ($\Delta\nu_{conv}$), equivalent to the direct dimension in conventional 2D experiments, is determined by the number of acquisition gradient pairs N in the EPSI train:

$$\Delta\nu_{conv} \propto \frac{1}{2N} \qquad \text{Equation 8}$$

2.2.2. Compromises / limits

One of the key issues of the ultrafast methodology is its low sensitivity. The latter is not only due to the single-scan nature of such experiments, but is also related to different effects which have been widely described in the literature, such as J-modulation (in the case of constant time encoding), the need to use large filter bandwidths, and the effects of translational molecular diffusion.

The use of strong gradients during the detection is actually the main source of sensitivity losses in UF experiments. It induces a large frequency dispersion, forcing to set a large digital filter bandwidth. This augmented digital bandwidth leads to a lower signal-to-noise ratio (SNR) as noise increases, and this is even more critical when large spectral widths are targeted. Under

typical conditions, this results in a per-scan sensitivity reduced by a factor between 5 and 10 compared to a one-scan 1D acquisition.

During the spatial encoding, and particularly during the application of the chirp pulse together with a gradient, translational molecular diffusion can be detrimental to sensitivity [17]. Indeed, the motion of the spins induces a loss of information as their evolution is imperfectly spatially encoded. Furthermore, the longer the spatial encoding, the higher the effects of diffusion; but as mentioned above (Equation 7), the resolution in the ultrafast domain is inversely proportional to the duration of the spatial encoding T_e. Thus, a compromise has to be found between sensitivity and resolution in the ultrafast domain. Giraudeau and Akoka showed that regarding this compromise, the $(\pi - \pi)$ encoding scheme is the most favourable [17]. For this particular encoding scheme, a value of T_e = 30 ms was found to be the best compromise for most small molecules samples.

Finally, when the $(\pi - \pi)$ spatial encoding scheme is used, ultrafast experiments can be considered as constant time experiments, leading to J-modulation effects as it is the case for conventional constant time experiments. This J-modulation induces sensitivity losses and possible missing peaks, depending on the nature of the spin system and J-coupling values [18].

Equation 6 highlights the need to set another compromise, as the maximum gradient amplitude available is a major limiting factor. Indeed, for an equivalent resolution in the ultrafast domain, the two spectral widths are interdependent [19]. This results in a compromise related to the maximum gradient amplitude available, and thus highly hardware dependent. The maximum gradient amplitude reached is typically 50 to 60 G/cm on conventional probes.

The quality of the gradient system also has a major influence on the ultrafast experiments. The train of alternate gradients during the acquisition has to be stable. Otherwise, it could lead to important line shape distortions and sensitivity losses. The achievable resolution in the conventional dimension thus depends on the stability of the train of acquisition gradients, as it is governed by the duration of the latter. Eddy currents could also occur during the beginning of each gradient [20], leading to the same disturbances. To prevent this, a delay of a few dozen of micro-seconds is usually inserted between consecutive acquisition gradients,

and their shape is usually trapezoidal. Typical EPSI trains that can be achieved on modern hardware are formed of 100 to 200 bipolar gradient pairs.

2.3. Ameliorations

Since the first UF experiments were suggested, numerous improvements were developed to get rid (at least partially) of the compromises mentioned above. The different pulse sequence elements of UF pulse sequences were targeted, from spatial encoding to detection including data processing.

2.3.1. Spatial encoding

2.3.1.1. Spatial/spectral encoding

The spatial/spectral encoding method is based on the partition of the ultrafast domain into relevant and irrelevant spectral regions [21,22]. The latter are excluded from the spatial encoding, whereas the former are encoded with the desired linear dephasing. This selectivity can be performed by the use of Serial Selective Encoding (SSE) or Parallel Selective Encoding (PSE).

In the SSE scheme [22], the various frequencies to be encoded are addressed sequentially. This discrete encoding suffers from long pulse durations and relaxation losses if the targeted frequencies are close to each other or when dealing with numerous sites. It is also unsuitable for samples with short T_2 transverse relaxation times.

All the targeted frequencies are simultaneously encoded in the PSE scheme [21], thanks to the use of 2D spatial-spectral pulses. Signal losses arising from T_2 relaxation effects or homonuclear J-coupling modulations during the encoding period are decreased, compared to the SSE scheme. However, this method needs complex radiofrequency (RF) waveforms and requires the use of stronger gradients than SSE.

Although information from the 1D spectrum is needed to design such a spatial/spectral encoded experiment, the use of this technique reduces the gradient demand, so that diffusion effects become negligible. Moreover, it leads to a better sensitivity and to an enhancement of the resolution.

2.3.1.2. Hadamard

As for the spatial/spectral encoding method, only regions of interest are encoded in multiscan 2D Hadamard NMR. This Hadamard encoding is performed by modifying the phases of the different regions of interest through the different scans [23]. Thus, one encoded spectral region corresponds to a line of the Hadamard matrix. In multiscan 2D Hadamard NMR, traces are obtained thanks to FT in the direct dimension (Figure 5A), which is followed by the application of Hadamard Transform (HT) in the indirect dimension, leading to the 2D spectrum.

In ultrafast 2D Hadamard NMR, each line of the Hadamard matrix is spatially encoded, thanks to the use of spatial-spectral pulses. During the EPSI detection block, spatially resolved traces are obtained as series of echoes, without FT (Figure 5B). As in its multiscan counterpart, HT is applied in the ultrafast dimension to retrieve the 2D spectrum.

The use of Hadamard spatial encoding is particularly interesting when the ultrafast domain is sparse, as the gain in sensitivity is inversely proportional to the size of the Hadamard matrix (correlated to the number of spectral regions to be encoded). This technique is thus unsuitable for crowded spectra and, as for the spatial/spectral encoded experiments, requires an *a priori* knowledge of the 1D spectrum.

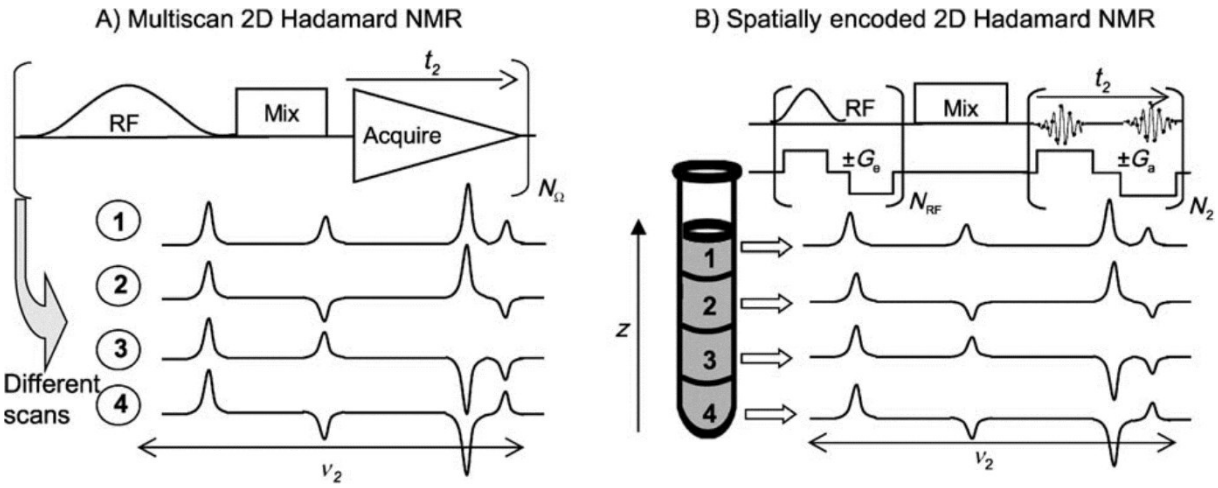

Figure 5. A) Original Hadamard-encoded scheme proposed for obtaining 2D NMR spectra. B) UF 2D Hadamard approach based on a combined spectral/spatial encoding of the indirect-domain information. Both data are processed on the basis of a Hadamard transfer which weights the spectral

set by a matrix— $\begin{pmatrix} 1 & 1 & 1 & 1 \\ 1 & -1 & 1 & -1 \\ 1 & 1 & -1 & -1 \\ 1 & -1 & -1 & 1 \end{pmatrix}$ for the illustrated example—to afford the desired site-resolved information. Reproduced from Ref. 23 with permission from John Wiley and Sons.

2.3.1.3. Gradient folding

In UF experiments, aliasing occurs in the conventional dimension, i.e. the resonances are folded with respect to the extremity of the spectral window. This feature can be used to alleviate the compromise between spectral widths. On the contrary, there is no aliasing in the ultrafast dimension since there is no FT, but "folding" gradients can be tuned to symmetrically fold the spectrum. This method, based on the $(\pi - \pi)$ spatial encoding scheme, requires the addition of "folding" gradients before and after the mixing period, named G_1 and G_2 respectively [24]. It makes use of the two symmetrical magnetization windings generated by this particular encoding scheme.

Indeed, two mirror-image echo trains are actually detected in the ultrafast dimension, where the symmetry point is:

$$k_0 = -\gamma_a G_2 \tau_2 \qquad \text{Equation 9}$$

G_2 is usually set to observe only one echo train during the acquisition gradient. By changing the amplitude and duration of G_1, the two mirror-image echo trains can be partially superimposed, so that all the signals of interest can be observed in a reduced spectral width compared to the original UF experiment.

Although this gradient-controlled folding is applicable to almost all UF 2D experiments, it proves to be particularly useful for heteronuclear ones, usually characterized by a large spectral width in the ultrafast dimension and a sparse spectrum.

2.3.1.4. Reduction of diffusion effects

As discussed in paragraph 2.2.2, translational molecular diffusion during spatial encoding can lead to significant sensitivity losses. Two different approaches can be used to alleviate this

limitation: physically reduce the translational molecular diffusion, or modify the spatial encoding to reduce the effects of this diffusion.

Simple precautions can physically reduce diffusion, like lowering the sample temperature or using a more viscous solvent. However, these are often unsuitable, particularly for biological samples. A specific sample preparation protocol has been developed for such cases, using medium-size phospholipid vesicles to encapsulate the analytes [25]. As a result, the local mobility is unchanged while limiting the motion of the analytes along the *z* dimension.

An alternative is to design pulse sequences that would be less sensitive to diffusion effects, such as the multi-echo spatial encoding scheme. It is based on the $(\pi - \pi)$ scheme, the pair of 180° chirp pulses being replaced by a succession of shorter 180° chirp pulses pairs (Figure 6) [16]. For identical durations of the whole spatial encoding scheme (T_e), the achieved resolution is the same as in the original one. However, molecular diffusion effects are reduced due to the use of shorter gradients. Consequently, the resolution can be increased thanks to multi-echo spatial encoding, while limiting the SNR losses due to molecular diffusion effects. Nevertheless, when diffusion is not predominant (i.e. when using short T_e) this technique leads to sensitivity and resolution losses, due to adiabaticity losses.

However, it should be highlighted that for most UF experiments, the typical T_e values - resulting from the need to compromise between spectral widths and resolution - do not lead to significant diffusion effects. An exception is J-resolved UF spectroscopy, where much longer T_e values can be applied due to the reduced spectral width in the conventional dimension [26].

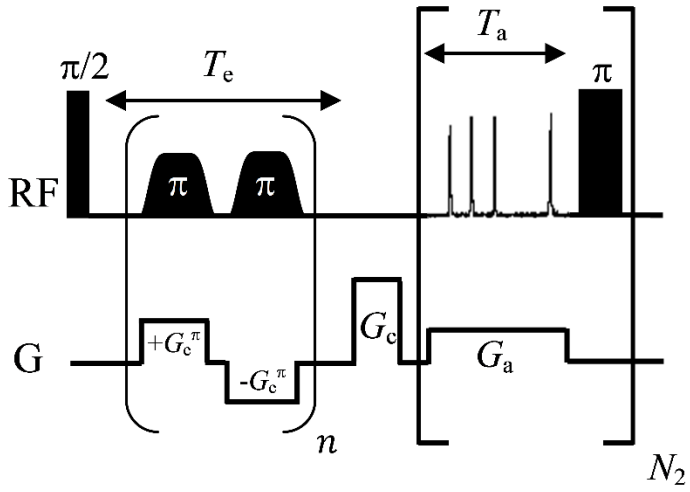

Figure 6. Pulse sequence for the acquisition of ultrafast 2D J-resolved spectra based on the $(\pi - \pi)$ phase-modulated encoding scheme, using the multiple-echo excitation scheme designed to limit diffusion effects.

J-modulation

Due to their constant time nature, UF experiments based on the $(\pi - \pi)$ encoding scheme suffer from J-modulation. The signal intensity thus depends on the nature of the spin system, the J coupling constants, and the duration of the spatial encoding (T_e). The latter can be tuned by a small delay added prior to the pair of chirp pulses, noted as t_{mix} [18]. This delay can be optimized for each spin system independently, but it can also be optimized for different spin systems by the use of selective excitation pulses. However, an *a priori* knowledge of the sample is required. These optimizations have to be performed for each sample. Another method relies on the averaging of J-modulation effects by adding UF spectra recorded with different delays t_{mix}. Although this solution requires several scans, and thus a longer acquisition duration, it is more general and does not require any *a priori* knowledge on the sample.

J-modulation effects can also be exploited to determine small J-coupling constants, e.g. ^{7}Li-^{7}Li J-couplings. To access to this information, the acquisition of numerous 2D spectra is required, leading to very long acquisition durations using conventional constant time 2D NMR experiments [27]. The acceleration provided by UF experiments is particularly beneficial for this kind of analysis [28].

2.3.2. Multi-scan strategies

When the targeted application does not require sub-second acquisition times, various multi-scan strategies can be used to overcome the limitations of UF 2D NMR such as the sensitivity or the accessible spectral widths [29]. The acquisition time of such experiments is thus extended to dozens of seconds or a few minutes, with an improved performance while still much faster than their conventional counterpart.

2.3.2.1. Multi-Scan Single-Shot acquisitions

Multi-Scan Single-Shot acquisitions (M3S) consist of the accumulation of UF experiments for signal averaging, leading to sensitivity improvements proportional to the square root of the number of experiments [29]. In addition, Pathan *et al*. proved that signal averaging in homonuclear UF NMR results in a better precision than what could be achieved by conventional 2D experiments in the same time [30]. This feature is related to a better immunity of UF experiments towards spectrometer instabilities. As a consequence, the signal-to-noise is similar in the two dimensions of UF experiments while t_1 noise occurs in conventional 2D NMR [31]. This is particularly critical in samples with large dynamic ranges.

*2.3.2.2. I*nterleaving

Interleaved UF experiments are designed to access higher spectral widths in both dimensions, but can also be used to reduce the demand on the acquisition gradient amplitude, or improve the resolution in the conventional dimension [32]. These experiments rely on the repetition of the pulse sequence along with the incrementation of the pre-acquisition delay, as illustrated in Figure 7. For n_i interleaved scans, the pre-acquisition delay is incremented by $\frac{2 \cdot T_a}{n_i}$ between each scan. The different scans form interleaved trajectories in the (k, t_2) space.

After processing these trajectories in an interleaved fashion, the spectral width in the conventional dimension thus becomes:

$$SW_{conv} = \frac{n_i}{2 \cdot T_a} \qquad \text{Equation 10}$$

and is increased by the interleaving procedure. As shown by the following relation,

$$SW_{UF} = \frac{\gamma_a \cdot G_a \cdot T_a \cdot L}{2 \cdot T_e}$$ Equation 11

the increase of T_a to reach a higher SW_{UF} can also be compensated by interleaving in order to keep SW_{conv} constant. Similarly, the gradient demand during acquisition can be reduced by increasing T_a together with interleaving. The specific interleaved processing may lead to artifacts in the conventional dimension, at a position $\frac{SW_{conv}}{n_i}$ for each peak. However, several data processing strategies were developed to correct those artifacts [33]. At the cost of few scans, this procedure allows the acquisition of a full-range UF spectrum comparable to its conventional counterpart, as illustrated in Figure 7b. Interleaved experiments were routinely used in several recent applications [34–36].

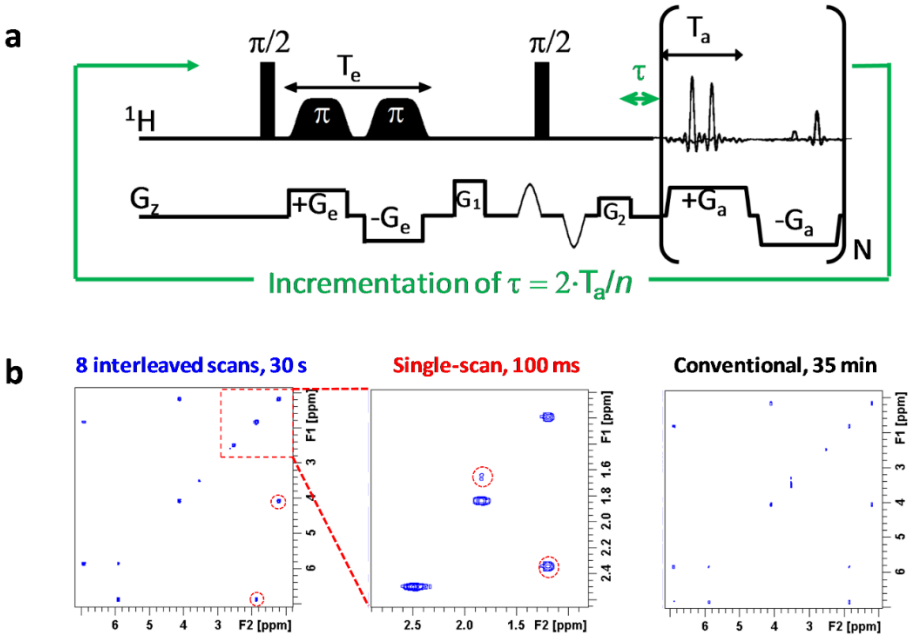

Figure 7. (a) Principle of the interleaved UF acquisition procedure, consisting in repeating several UF scans while incrementing the pre-acquisition delay in order to increase the spectral width, improve the resolution or reduce the demand on gradient amplitudes. (b) Illustration of the potential of this procedure, for ethyl crotonate COSY spectra recorded on a 700 MHz spectrometer. On the center: single-scan UF-COSY spectrum. The accessible spectral widths are limited to approximatively 2 ppm, and aliasing occurs in the conventional dimension (red circles). On the left: UF-COSY spectrum with 8 interleaved scans. The whole spectral width is retrieved, giving access to a spectrum comparable to the conventional one (on the right) 70 times faster. Reproduced from Ref. 29 with permission from John Wiley and Sons.

2.3.3. Data processing

In addition to the improvements based on modifications of the pulse sequence mentioned above, different data processing solutions were proposed to improve the performances of UF experiments, such as the application of a “spatial apodization” or the use of interlaced FT.

2.3.3.1. Apodization

In UF experiments, apodization in the conventional dimension can be applied as in conventional 2D experiments. It is particularly useful since the signal is highly truncated in this dimension due to the limited number of alternated gradients during acquisition.

Apodization can also be applied in the spatially-encoded domain, i.e. in the ultrafast dimension, in order to correct asymmetric line shape distortions [37], as shown by the comparison of Figures 8a and 8c. In addition to the line shape improvement, this processing also leads to an enhancement of the sensitivity. Simulations showed that the asymmetric lineshapes arise from gradient non-uniformities on the edge of the sample or from a non-uniform excitation on the edge of the RF pulses. This is particularly critical in cryogenically cooled probes.

To perform this “spatial apodization”, a FT is applied in the indirect dimension, transforming the time domain into spatial domain. The resulting profile (Figure 8d) is then multiplied by an apodization window, usually Gaussian, to eliminate the signals arising from the edge of the detection volume. Finally, an inverse FT is applied to the data to retrieve echoes in the time domain. Since it was suggested, this spatial apodization method has been used routinely in numerous studies [33,35,38,39].

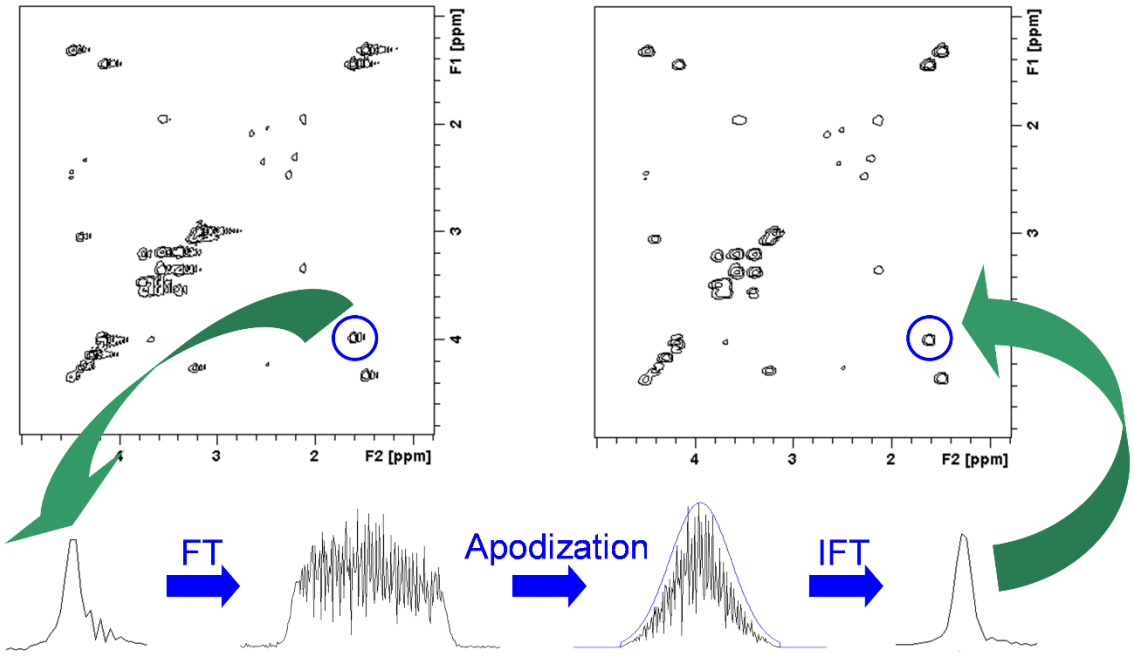

Figure 8. Spatial apodization procedure applied to an UF 2D COSY spectrum recorded in 0.1 s on a mixture of metabolites. A Fourier transform is applied in the ultrafast dimension, and the time-domain signal is multiplied by a gaussian window. After inverse Fourier transform, the resulting signal profits from a smaller linewidth and more symmetric lineshapes. Reproduced from Ref. 37 with permission from John Wiley and Sons.

2.3.3.2. Interlacing

In the usual UF data processing, signals detected during positive and negative gradients are processed independently, thus halving the signal used in the FT. This signal separation leads to an SNR loss by a factor $\sqrt{2}$ and halves the spectral width in the direct dimension. As proposed by Mishkovsky and coworkers in 2005, these losses can be avoided by the use of interlaced FT [40]. This transform exploits odd and even echoes simultaneously, leading to a better SNR and a larger spectral width in the direct dimension. However, extra experimental precaution has to be taken concerning the proper alignment of the indirect domain k-peaks in both odd and even data sets. Despite their potential in terms of sensitivity and spectral width, such interlaced ultrafast experiments are barely used in routine due to the impact of non-idealities on the resulting spectra.

2.3.4. Detection

2.3.4.1. Non-uniform sampling

A non-uniform sampling pattern can be applied in the conventional domain, thanks to the use of pseudo-random oscillating gradients [41]. In this way, the amplitude of the acquisition gradients (G_a) is reduced, thus alleviating technical issues and increasing the sensitivity, as the bandwidth of the digital filter can be reduced. The spectrum is retrieved thanks to Compressed Sensing, an iterative reconstruction algorithm. Due to this reconstruction of the spectrum, NUS-UF experiments require high SNR and sparse spectra in the direct domain.

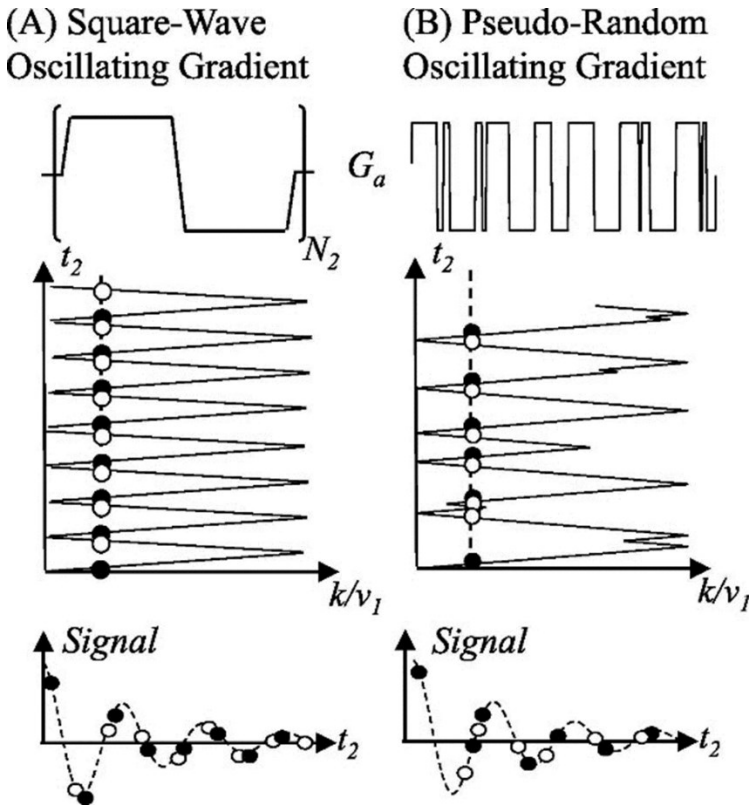

Figure 9. (A) Traditional ultrafast acquisition scheme. (B) Pseudo-random ultrafast acquisition scheme for the sake of an iterative ν_2 reconstruction. The upper and middle panels display the G_a waveforms and their corresponding k–t_2 trajectories. The bottom row considers a cross section of these trajectories for a given k - value (dashed line), and shows the sampled FID points with black and white dots denoting data recorded during positive and negative gradient, respectively. Unlike the regular sampling provided by the square-wave modulation in (A), the random sporadic sign-changes in waveform (B) provides a sampling pattern that is suitable for an iterative reconstruction that is not necessarily bound by Nyquist criteria. Reproduced from Ref. 41 with permission from Elsevier.

2.3.4.2. z^2 gradients

In magnetic resonance imaging (MRI) systems, longer switching times between acquisition gradients need to be used, due to hardware limitations. It leads to longer dwell times in the direct dimension (usually greater than 200 µs), and thus a smaller spectral width in the direct dimension. To alleviate this, sinusoidal gradients can be applied during acquisition, resulting in a non-linear sampling of the *k*-axis, i.e. the ultrafast dimension [42]. To retrieve linear *k*-axis, data must be "regridded" by unidimensional linear interpolation, without FT.

2.3.4.3. Constant gradient

The fast switching of the acquisition gradients often leads to the occurrence of eddy currents, thus creating inconsistencies in the data. One of the solutions to avoid it is to use a fixed and constant-valued throughout the entire course of the data acquisition [43]. The excitation scheme is then based on discrete spatial encoding. The latter is formed by a train of temporally overlapping selective pulses (of duration T_p), applied simultaneously to a constant gradient G_e, followed by a storage or inversion of the spin coherences thanks to a chirp pulse applied simultaneously to a gradient G_e', where $G_e' \neq G_e$.

The achievement of narrow and well separated voxels by long selective pulses leads to significant sensitivity losses. A solution to partially recover sensitivity is the use of chirp pulses instead of selective pulses, giving rise to larger voxels. As overlap occurs between the latter, constructive interferences arise with a period of $\frac{\gamma_e \cdot G_e}{\Delta O \cdot \gamma_a \cdot G_a}$. Although these experiments are potentially more affected by molecular diffusion effects, they could be useful for rapidly relaxing systems and higher-dimensional experiments.

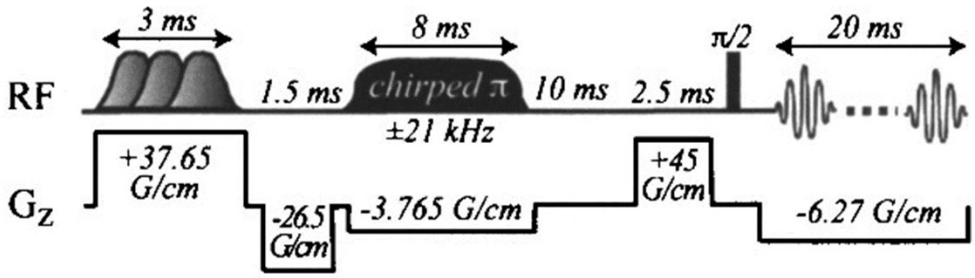

Figure 10. Ultrafast 2D COSY NMR pulse sequence using the constant-gradient acquisition protocol to record phase-modulated 2D data. Reproduced from Ref. 43 with permission from American Institute of Physics.

2.4. Protocol to implement UF 2D NMR experiments

The practical use of UF experiments is significantly different from conventional 2D NMR experiments. This difference makes UF NMR hardly accessible to non-specialists of this technique. The difficulty to implement and use UF experiments may act as a major brake on the development of this methodology. The improvement of its accessibility is thus one of the major challenges of the spreading of this technique among the NMR spectroscopy community. Several implementation protocols were proposed in recent years [44,45] but tedious parametrization is still needed. Here, we propose a simplified implementation protocol, being all integrated in the acquisition software, in which UF experiments are automatically parametrized from conventional 2D NMR acquisition parameters. At the time of writing, since Agilent has retired from the NMR business, Bruker is the only manufacturer of high field NMR spectrometers whose hardware is compatible with UF experiments; this protocol is thus dedicated to the implementation of UF experiments on Bruker spectrometers of the Avance generation.

All programs and experiments used in the following protocol were developed in the EBSI group (CEISAM laboratory) from Nantes (France). The pulse sequences are based on the $(\pi - \pi)$ continuous phase-encoding excitation scheme, as the latter was found to be the best compromise between sensitivity and resolution limitations [16]. Preliminary calibrations, designed to characterize hardware performances, are thereafter used to automatically parametrize UF experiments. This automatic parametrization of 2D UF experiments from

conventional 2D NMR parameters not only handles the acquisition of single-scan experiments, but also calculates interleaving and processing parameters (including spatial apodization). The automatization of this parametrization makes UF NMR experiments accessible to non-specialists of this technique. Only UF-COSY and UF-HSQC (UltraFast Heteronuclear Single Quantum Correlation) implementations are described here, but two other ^{1}H homonuclear ultrafast experiments can also be automatically parametrized following this protocol: UF-TOCSY (UltraFast TOtal Correlation SpectroscopY [7]) and UF-DQS (UltraFast Double-Quantum Spectroscopy [36,46]). Implementation files can be downloaded at http://madoc.univ-nantes.fr/course/view.php?id=24710, and must be copied to the folder indicated in Table 2.

Table 2. Quick description of the files used in the protocol to implement UF experiments, and in which folder they should be copied.

File:	Description:	To be placed in:
echograd	pulse program for gradient and chirp pulse calibration	\Bruker\TOPSPIN\exp\stan\nmr\lists\pp\user
ufcosy	pulse program for acquisition of UF-COSY spectra	\Bruker\TOPSPIN\exp\stan\nmr\lists\pp\user
ufhsqc	pulse program for acquisition of UF-HSQC spectra	\Bruker\TOPSPIN\exp\stan\nmr\lists\pp\user
UF-chirp-15-11	example of Chirp pulse for ^{1}H	\Bruker\TOPSPIN\exp\stan\nmr\lists\wave\user
ufset	AU program for automatic settings	\Bruker\TOPSPIN\exp\stan\nmr\au\src\user
UFfeatures1H.txt	text file of the spectrometer characterization for ^{1}H UF experiments, used by **ufset** and **ufcalauto**	\Bruker\TOPSPIN\exp\stan\nmr\au\src\user
UFfeatures13C.txt	text file of the spectrometer characterization for ^{13}C UF experiments, used by **ufset** and **ufcalauto**	\Bruker\TOPSPIN\exp\stan\nmr\au\src\user
ufproc	python processing program for ultrafast spectra, including automatic calibration	\Bruker\TOPSPIN\exp\stan\nmr\py\user
ufcalauto	python program for automatic calibration of ultrafast spectra	\Bruker\TOPSPIN\exp\stan\nmr\py\user
ufcal	python program for manual calibration of ultrafast spectra	\Bruker\TOPSPIN\exp\stan\nmr\py\user
ufsym	python program for symmetrization of ultrafast spectra	\Bruker\TOPSPIN\exp\stan\nmr\py\user

2.4.1. Preliminary calibrations

Preliminary calibrations must be done on a sample with a limited number of resonances, for example ethanol (10%) in D_2O. Run a preliminary 1D ^1H experiment, tune and match, lock and shim, and calibrate the 90° pulse angle (pw90).

The echograd pulse sequence (Figure 11a) is used for the calibration of the gradients and chirp pulse. The chirp pulse is first inactivated to calibrate the gradients. It leads to a spin echo which, after FT and phasing, shows a profile of the sample. In a second experiment, the selective pulse is activated for calibration.

Create a new experience by copying the previous one (1D ^1H spectrum), set the pulse program (echograd), and run the automatic parametrization macro: ufset. Adjust the receptor gain, and run the acquisition. The FID should look like Figure 11b. Delay d5 should be adjusted to shift the echo approximatively in the center of the acquisition window. The processing parameters have also been automatically parametrized by ufset. The apodization window used is Gaussian, and the center of the latter (parameter GB in Topspin) must be set according to the position of the echo, *i.e.,* 0.5 if the echo perfectly centered in the acquisition window. Process the free induction decay (FID), by Topspin commands GM, FT and phase the spectrum starting by first order phase correction. Due to the phase dispersion induced by the gradients, a huge first order phase correction is necessary. A symmetric image can then be obtained via a small zero order phase correction. The resulting profile should look like Figure 11d. Measure the width at the base of the dispersion profile (ΔF, in Hz – as indicated in Figure 11d); it corresponds to the frequency dispersion induced by a 10% gradient. The corresponding gradient amplitude value (in T/m) can be calculated as $\frac{2\pi \cdot \Delta F}{\gamma \cdot L}$, where γ is the gyromagnetic ratio for ^1H nucleus and L is the length of the sensitive volume.

Create a new experience by copying the previous one, in order to calibrate the chirp pulses used for spatial encoding. The pulse shape used for this calibration is UF-chirp-15-11 (already set by ufset). The GPZ0 gradient must induce a frequency dispersion equivalent to the chirp pulse bandwidth (11 kHz in this case). This value can be calculated thanks to the last experiment. Adjust the power of the chirp pulse (sp1) to obtain an effective inversion (as Figure 11e). Signal must be processed with the GFP command. There is no need for an accurate

value of sp1 as adiabatic inversion is efficient over a wide power range. However, residual oscillations may appear if sp1 is too small.

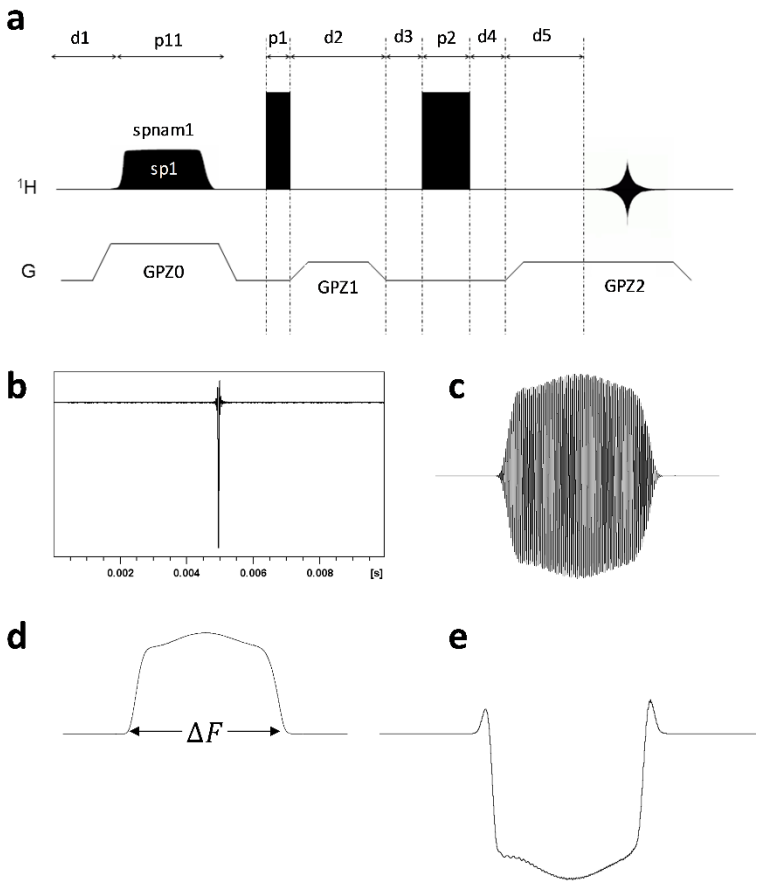

Figure 11. (a) echograd pulse sequence for the calibration of UF experiments; (b) FID obtained, centered in the acquisition window; dispersion profile obtained after FT, (c) before and (d) after phase correction; (e) dispersion profile inversed by the calibrated chirp pulse.

Open the file \Bruker\TOPSPIN\exp\stan\nmr\au\src\user\UFfeatures1H.txt in a text editor. This file is used by the ufset program to automatically parametrize UF experiments. Indeed, many parameters are hardware-dependent. The first line will be modified thereafter. On the second line, indicate the frequency dispersion induced by a 100% gradient (in Hz): ten times the ΔF value measured above. This value is used in the ufset program to calculate all gradient amplitudes in the pulse sequence according to the desired spectral widths. On the third line, indicate the calibrated power of the chirp pulse (in dB). Save and close the file.

2.4.2. Implementation of UF-COSY experiments

As for the preliminary calibrations, a simple sample such as ethanol in D_2O may be used for this implementation.

Create a conventional COSY experiment, by the use of a parameter file (rpar), and adjust the following parameters to the sample: offset, spectral widths (note the spectral width in the indirect dimension as SW_{th}), pulse durations and powers. One scan and two dummy scans are recommended for the first experiment, but these values can be adjusted as needed. Then set the pulse program to ufcosy. Run the automatic settings program ufset. The latter calculates all the necessary experimental parameters to run this experiment in an ultrafast manner, and directly set them in the Topspin experiment. The execution of the program ends with a message displaying the effective spectral width in the conventional dimension, an eventual modification of the recovery delay if the latter was too short for ultrafast experiments, or warnings concerning the experiments duration. Ultrafast settings are now applied to this experiment. Note that the command “ufset r” allows to retrieve the initial conventional parameters.

Adjust the receptor gain, and run the acquisition. Processing parameters have also been calculated and modified by the ufset program. Process the data with the ufproc command. The latter lasts a dozen of seconds while nothing must be done before the apparition of the “ultrafast processing done” message. The spectrum thus obtained is automatically calibrated, thanks to the features indicated in the file UFfeatures1H.txt. Although, as the first parameter of this file has not been adapted to the spectrometer, the automatic calibration is still inaccurate. Calibrate the spectrum with the manual calibration program (ufcal), then measure the effective spectral width in the ultrafast dimension (SW_{obs}). Change the first line of the UFfeatures1H.txt file to $2 \cdot SW_{th} / SW_{obs}$. The automatic calibration will be more accurate for the next experiments.

On any other sample, a new ultrafast experiment can be created, acquired and processed following the same procedure as above, after calibration of the 90° pulse angle in a 1D ^1H experiment.

2.4.3. Implementation of UF-HSQC experiments

The implementation of the UF-COSY experiments must be done prior to this procedure. A sample as concentrated ibuprofen in acetone-d_6 is recommended. Preliminary settings include 1D ^{1}H and ^{13}C experiments, and calibration of the pw90 for each channel.

Open the file \Bruker\TOPSPIN\exp\stan\nmr\au\src\user\UFfeatures13C.txt in a text editor. The first line will be modified thereafter, as well as the second one if needed. On the third line, indicate the power of the ^{13}C chirp pulse (in dB). In a first approximation, the latter can be considered equal to the ^{1}H one. The frequency bandwidth encoded during the spatial encoding step is usually five times larger than the desired spectral width. However, if the maximal ^{13}C spectral width needed ($SW_{UF}^{\max}$ - in Hz) is higher than $0.04 \cdot G_a^{\max}$ (where $G_a^{\max}$ is the frequency dispersion – in Hz – induced by a 100% gradient, as indicated in the UFfeatures1H.txt file), then encoding gradients will not reach the required amplitude. In this case, change the second line of the UFfeatures13C.txt file to $\frac{0.2 \cdot G_a^{\max}}{SW_{UF}^{\max}}$. Save and close the file.

Create a conventional HSQC experiment, by the use of a parameter file (rpar), and adjust the following parameters to the sample: average coupling constant (cnst2), offsets, spectral widths (note the spectral width in the indirect dimension as SW_{th}), pulse durations and powers… Eight scans and two dummy scans are recommended for the first experiment, but these values can be adjusted as needed. Then set the pulse program to ufhsqc. Run the automatic settings program ufset.

Adjust the receptor gain, and run the acquisition. Process the data with the ufproc command. The spectrum thus obtained is automatically calibrated, thanks to the features indicated in the files UFfeatures1H.txt and UFfeatures13C.txt. Although, as the first parameter of this latter file has not been adapted to the spectrometer, the automatic calibration is still inaccurate. Calibrate the spectrum with the manual calibration program (ufcal), then measure the effective spectral width in the ultrafast dimension (SW_{obs}). Change the first line of the UFfeatures13C.txt file to $2 \cdot SW_{th} / SW_{obs}$. The automatic calibration will be more accurate for the next experiments.

On any other sample, a new UF-HSQC experiment can be created, acquired and processed following the same procedure as above, after calibration of the 90° pulse angles in 1D ^{1}H and 1D ^{13}C experiments.

As mentioned above, two other experiments can be parametrized by the ufset program (UF-TOCSY and UF-DQS). Additionally, this program can be completed to include the parametrization of any other UF experiment. Other developments of UF experiments as presented in part 2.3. can be included in this program by advanced users if needed.

2.5. Higher dimensionality

All the developments mentioned above were intended for UF 2D experiments. Nevertheless, higher dimensionality spectra are accessible using the ultrafast method. Two strategies can be used for this purpose: pure single scan or hybrid experiments.

2.5.1. Pure single scan

Thanks to multiple axis gradient systems, combinations of linearly independent gradient geometries can be used to simultaneously monitor the spins' evolution along separate time axes. All indirect time domains being monitored thanks to spatial encoding, this methodology enables the acquisition of a whole 3D or even higher-dimensional spectrum in only one scan, i.e. a fraction of a second [19]. Nonetheless, its single scan nature also implies a very low sensitivity, and limitations in terms of resolution and spectral ranges in the two spatially encoded dimensions. In addition, as this technique relies on multiple axis gradients, specific hardware is required.

2.5.2. Hybrid

To reach higher-dimensional experiments, spatial encoding and conventional time incrementation can also be used simultaneously [29,47]. In a so called hybrid 3D experiment, one of the indirect dimensions is thus acquired with a conventional time incrementation, whereas the other one is acquired in an ultrafast manner. This hybrid method lowers the acquisition time of a nD spectrum to the time usually needed to acquire a (n-1)D spectrum. Even though these are long acquisition times compared to the pure single scan method, the hybrid one does not require specific hardware, and is less demanding for the latter.

Furthermore, hybrid experiments are more sensitive than their pure single scan counterparts, and limitations of the resolution and spectral range only occur in the dimensions acquired in an ultrafast manner.

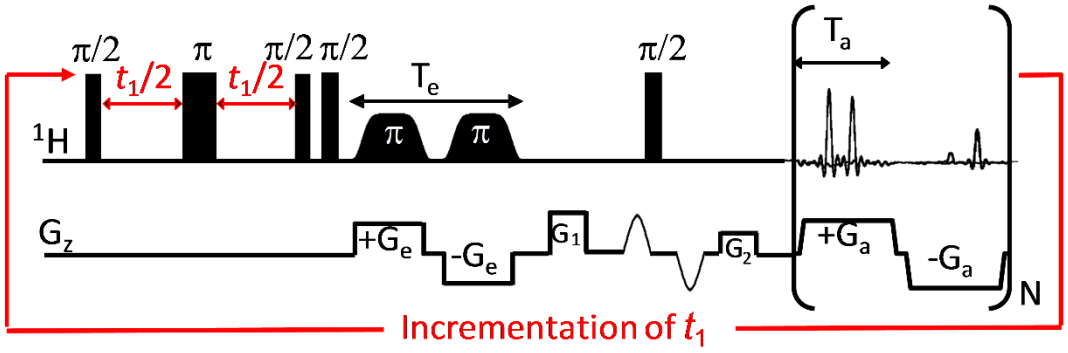

Figure 12. Principle of the fast-hybrid 3D approach, illustrated on the example of Jres-COSY, capable of recording 3D spectra with a single time incrementation coupled to a spatially encoded 2D pulse sequence. Reproduced from Ref. 29 with permission from John Wiley and Sons.

3. Applications

3.1. Real-time reaction monitoring by UF 2D NMR

Reaction monitoring relying on analytical spectroscopy plays a central role in a variety of applications, from organic and inorganic synthesis to biochemistry and bioengineering [48]. It is a determining tool for kinetic studies as well as for the deep understanding of reaction mechanisms. Among spectroscopic techniques, NMR has the great advantage of being nonspecific and nondestructive and delivers both structural and quantitative information. Although NMR is a well-recognized processing analytical tool in organic and pharmaceutical applications [49–52], one dimensional spectra can suffer from numerous overlaps and become ill-suited for the real-time monitoring of complex reactive mixtures. Unfortunately, 2D NMR is not adapted in its original form for such monitoring. This is true even in the case of slow processes compared to the 2D NMR timescale since the sample composition evolves while gathering the 2D-interferogram. This leads to incoherent chemical information between the different lines of the 2D matrix [38]. It is worth noting that time-resolved schemes based on NUS can circumvent this issue in the case of processes occurring in a relative long timescale [53,54]. More generally, fast 2D NMR experiments performed in a duration significantly shorter than the time scale of the studied process would be an appealing and more convenient

solution to extend the scope of NMR monitoring. Early after their ground-breaking publication in 2002 [7], Frydman and coworkers investigated the potential of UF 2D NMR to monitor (bio)-chemical processes on the fly. A first example was reported in 2003, where a set of mixing-incremented 2D exchange NMR experiments was collected in a ultrafast fashion to probe the interconversion of N,N-dimethylacetamide between its two rotamers [55]. Kinetic rates and the activation energy of such a dynamic process occurring on a timescale of 1 s were estimated. This UF methodology gained further interest through the real-time monitoring of an H/D exchange involved by the dissolution of a protonated protein in D_2O [56]. In this study, a series of four-scan interleaved UF ^{15}N-^{1}H HSQC spectra - recorded every 4 s - was carried out in order to monitor the kinetics of hydrogen exchange in ubiquitin at a site-resolved level. Beyond this potential of UF NMR to characterize a dynamic phenomenon, the same article highlights the capability of detecting short-lived intermediate species. This is portrayed by the real-time in situ tracking of a transient Meisenheimer complex that forms upon rapidly mixing two organic reactants inside the NMR tube (Figure 13). After the triggering of the organic reaction, UF-TOCSY experiments were performed every 2.4 s. Figure 13 shows the changes of UF spectra patterns occurring in the course of the reaction, showing a competition between thermodynamic and kinetic controls on a 2-s timescale. These pioneering works shed light on how UF NMR delivers on the fly kinetic information as well as mechanistic insights, and anticipated further exciting applications. Numerous examples are herein described highlighting the potential of UF 2D NMR for the real-time monitoring of fast organic reactions and of dynamic biomolecular processes.

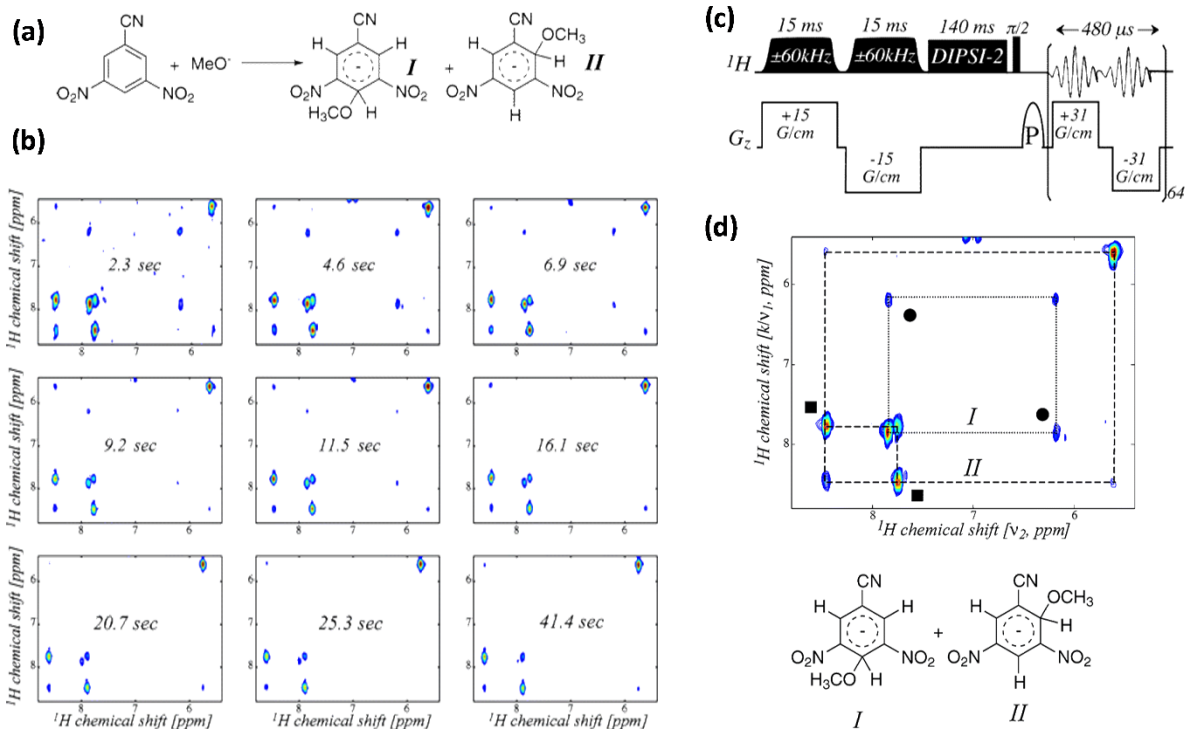

Figure 13. Example of real-time monitoring with UF 2D NMR. (a) formation of Meisenheimer complexes. (b) examples of spectra taken from a set of UF TOCSY spectra. (c) scheme of the ultrafast TOCSY pulse-sequence based on an amplitude modulated spatial encoding. (d) the different homonuclear scalar correlations that distinguish the complexes I and II. Reproduced from Ref. 56 with permission from American Chemical Society.

3.1.1 Monitoring chemical reactions

Since the aforementioned monitoring, UF 2D NMR has been used to probe complex chemical reactions involving multiple analytes whose 1D spectra were overcrowded. This is well illustrated by the work of Herrera and coworkers [57]. In a first study, the mechanisms involved in the formation of alkyl pyrimidines was investigated via homonuclear UF experiments [58]. 525 UF-TOCSY spectra were recorded - every 10 s during a 1 h 30 min reaction - to follow the reaction between an aliphatic ketone with a two-fold amount of a strong electrophile: trifluoromethanesulfonic acid anhydride (Tf_2O) in the presence of deuterated acetonitrile as both co-reactant and the solvent. The UF-TOCSY experiments delivered structural insights from well-resolved cross-peaks matching with the different species involved in the mechanism (Figure 14). The evolution of the cross-peak intensity *versus* reaction-time provided the kinetic rates of the starting material and the final products, then ensured the intermediate nature of some detected compounds.

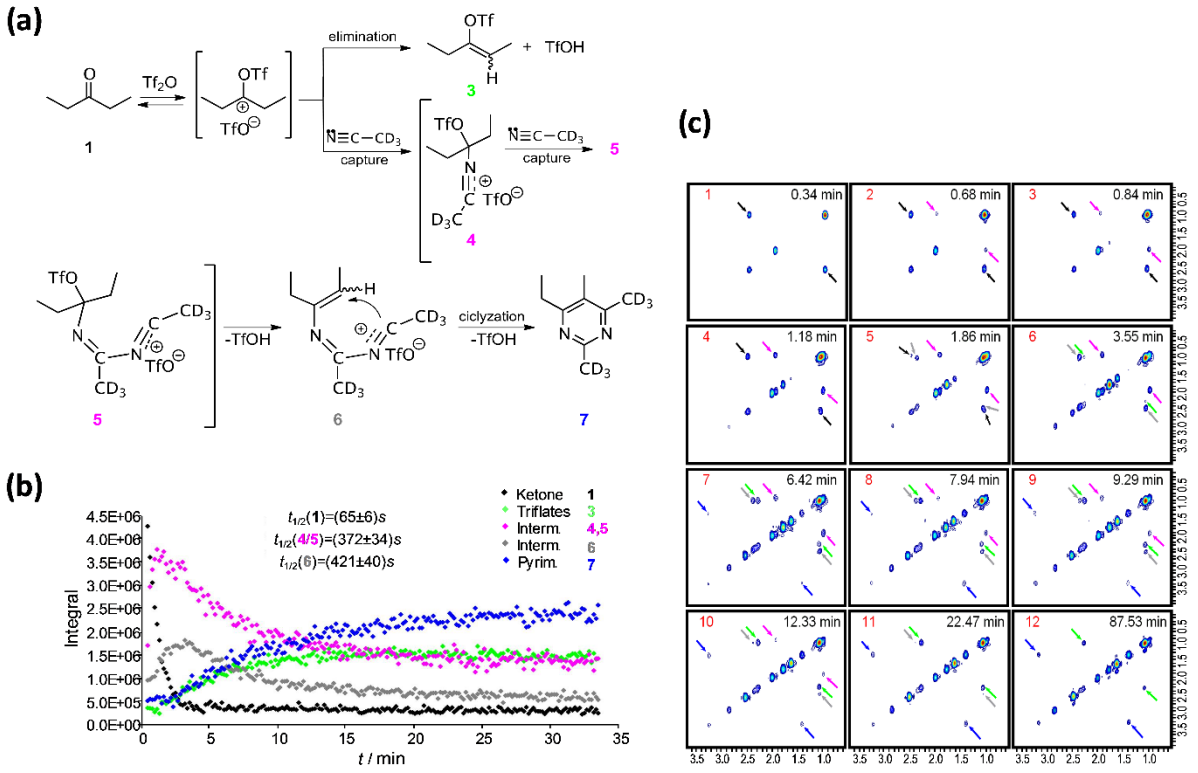

Figure 14. UF TOCSY monitoring of a complex organic reaction. (a) proposed mechanism for the reaction between a symmetric ketone (1), triflic anhydride, and deuterated acetonitrile. The mechanism was proposed according to the cross-peaks from species reactant detected by UF TOCSY. (b) plots of the averaged integrated peak intensity as a function of the reaction time. (c) UF TOCSY spectra taken from different instants in the course of the reaction. Reproduced from Ref. 58 with permission from John Wiley and Sons.

In spite of the elucidation of transient species and the obtained kinetic features, some interrogations remained open concerning the initial stage of the mechanism. A deeper understanding of the mechanism was reached by additional monitoring based on heteronuclear correlations. In this context, UF-HMBC (UltraFast Heteronuclear Multi-Bond Correlation) monitoring led to supplementary mechanistic insights, especially on the evolution of non-protonated carbons, which are important reactive sites. In addition to confirming the results previously established with UF-TOCSY experiments, structures of new transients were identified [59]. It should be mentioned that this series of UF-HMBC spectra was recorded on ^{13}C-labeled compounds for sensitivity reasons. Hopefully, recent methodological developments enhancing the sensitivity and the robustness for multi-scans experiments now make the UF approach suitable to probe the ^{13}C-^{1}H correlations at natural abundance. Such a study was reported by Giraudeau and collaborators, where UF-^{13}C-^{1}H HSQC experiments were

performed to monitor the mutarotation of glucose at natural abundance [60]. Based on the same optimizations, Herrera and coworkers applied such a UF-HSQC monitoring on the previous reaction at natural abundance in order to go even further in the details of the mechanism involved in the formation of alkyl pyrimidines. To screen the broad ^{13}C ultrafast dimension, an interleaved and excitation-optimized pulse-sequence enabled to monitor several spectral regions of interest in the course of the reaction. Up to 2 500 2D HSQC NMR data were recorded in this fashion during a 100-min reaction. This led to the detection of new transient species, which was a determining point for a whole and deep understanding of the studied reaction [61]. Furthermore, this complementarity between homo and heteronuclear monitoring have recently encouraged the authors to develop the Tandem Ultrafast TOCSY / HMBC experiments to study in details the reactivity of alicyclic ketones [62]. Still in this framework, other results should be highlighted such as the characterization of intermediates through the UF-HSQC monitoring of a hydrolysis of an acetal [63] or the comprehensive study of a Michaelis-Arbuzov reaction by UF ^{1}H-^{31}P-HMBC [64]. This series of articles highlights the versatility of the UF methodology, which enables homo or heteronuclear 2D monitoring on the fly. These great results encouraged other UF monitoring achieved on different settings and in various field of applications. For instance, Boisseau *et al* reported the use of UF NMR in the case of in-situ electrochemistry [38]. An electrochemical cell was implemented inside a 5 mm NMR tube to study in real time electrochemical reactions. Again, the UF-COSY experiments revealed the presence of unstable transients leading to new chemical insights. Moreover, the UF methodology was recently implemented on a 43-MHz benchtop spectrometer. The key idea in this strategy is to combine the time-resolution of UF 2D NMR with the versatility of a benchtop spectrometer to obtain a rapid and informative processing analytical tool operating directly under a fume hood. The proof concept was demonstrated by probing in real-time a palladium catalytic Heck-Matsuda reaction through a train of UF-COSY spectra collected at 43 MHz. This monitoring was performed in situ [65], as well as in online fashion via a by-pass system [66].

3.1.2. Monitoring biomolecular dynamic processes

Besides the control and the study of organic reactions, NMR is widely used in the field of biochemistry since it delivers structural and dynamic insights from samples of macromolecules. Probing biophysical events such as folding / misfolding of proteins or binding

interactions between ligands and receptors is a key feature in biochemistry. However, such real-time monitoring on macromolecules by NMR is far from straightforward. The short timescale of these events – typically about few seconds – combined with the complexity of the sample require fast multidimensional NMR experiments [3,67]. Even if UF 2D NMR meets this demand by delivering 2D acquisitions within a single scan, practical sensitivity in biomolecular measurements requires the signal averaging of at least a minimal number of transients in order to reach an acceptable SNR. In the protein NMR community, the development of the SOFAST excitation has dramatically reduced the inter-scan delay upon gathering a large amount of longitudinal magnetization [68]. Such a gain in sensitivity per unit time is achieved by selectively exciting a subset of protons that are of interest (typically amid groups for protein samples) while leaving all other protons unperturbed. This assists in efficiently relaxing the protons of interest, significantly decreasing their effective spin-lattice relaxation time. Therefore short recycle delays (e.g. 100 – 300 ms) can be applied allowing experiments at high-repetition rates. If possible, the flip angle is also tuned (Ernst angle) to further improve the sensitivity. ^{15}N-^{1}H UF-HMQC (UltraFast Heteronuclear Multi-Quantum Correlation) monitoring the ^{15}N dimension by a constant time phase-modulated spatial encoding was merged with this SOFAST excitation leading to an UltraSOFAST HMQC experiment. By averaging UF spectra with a recycling delay within a 100-300 ms range, this method yields 2D heteronuclear spectra in about 1 s on protein samples at 2 mM (Figure 15) enabling the real-time monitoring of protein kinetics occurring on timescales down to a few seconds [69]. Bearing in mind that the EPSI detection block is demanding for the hardware, a special care should be taken when applying such a fast-pulsing method together with ultrafast experiments. Shortly after this impressive results, Gal and coworkers further improved the signal-to-noise ratio of this methods by improving the shape of the 2D-peaks [70]. This resulting fast and sensitive tool paves the way for further biomolecular dynamic applications as highlighted by the real-time analysis of the adenine-induced folding of an adenine-sensing riboswitch, with nucleotide-resolved resolution. By following changes in 2D spectra at rates of approximately 0.5 Hz, distinct steps associated with the ligand-induced folding of the riboswitch were identified [71].

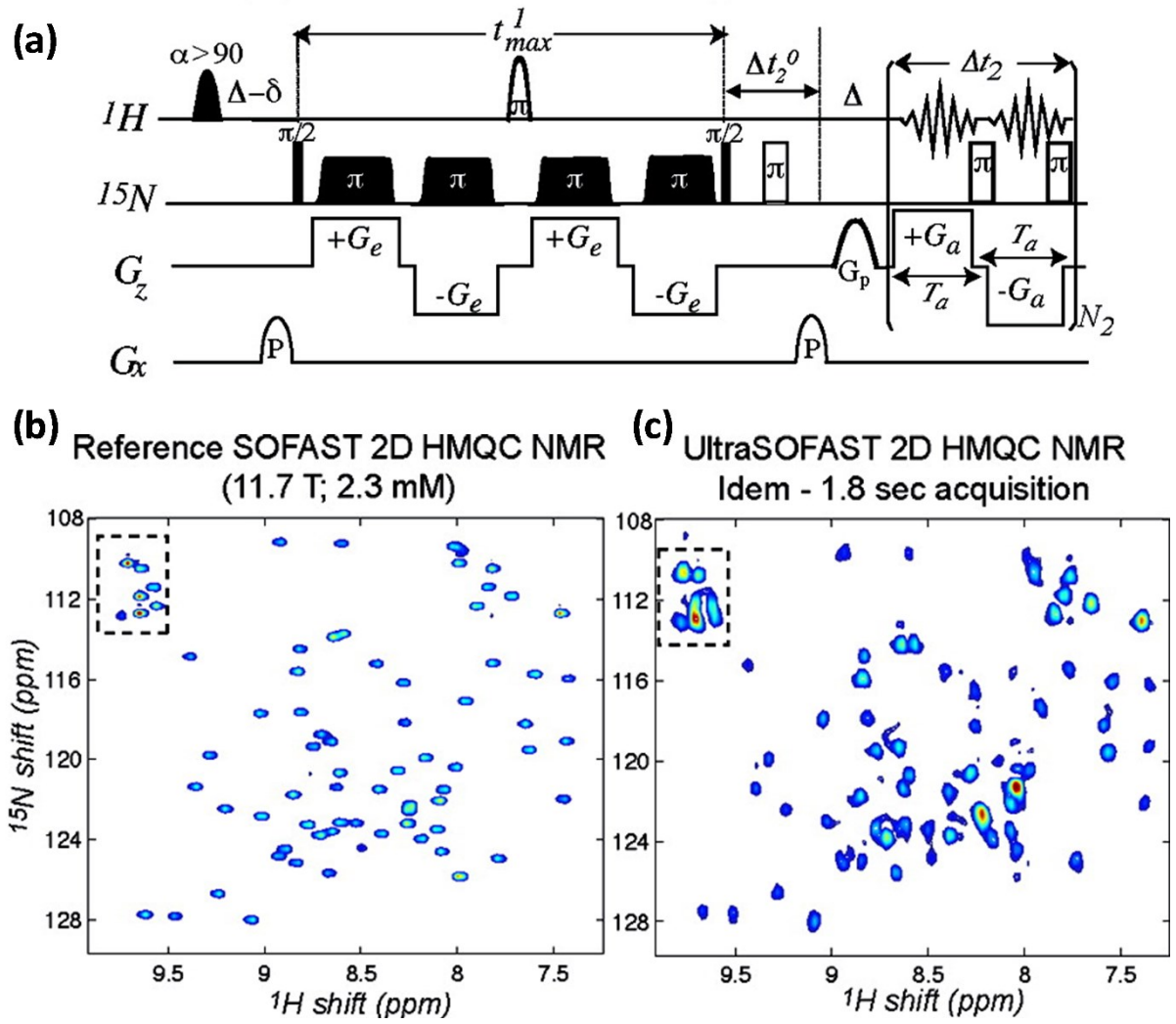

Figure 15. Real-time monitoring of protein kinetics occurring on timescales down to a few seconds. (a) scheme of the UltraSOFAST HMQC sequence. A constant time phase-modulated spatial enconding is performed to monitor the ^{15}N indirect dimension. This sequence incorporates a SOFAST excitation where both excitation and refocusing ^{1}H pulses are band-selective on the protons of interest, i.e., amide protons. Note that the selective excitation is applied with a tuned flip angle (Ernst angle) to further enhance the sensitivity per time units. (c) resulting UltraSOFAST HMQC spectrum versus (b) its reference SOFAST counterpart of ^{15}N-labeled Ubiquitin at mM concentration. Dashed boxes contain folded peaks arising from amine groups. Reproduced from Ref. 69 with permission from American Chemical Society.

3.2. UF 2D NMR coupled with liquid chromatography

Coupling liquid chromatography (LC) with high resolution NMR (LC-NMR) aims to simplify the NMR analysis of mixtures by detecting successively the analytes in the course of the elution [72]. This combination of the discrimination power of the chromatography with the wealth of information provided by NMR leads to a performant tool, so that this hyphenated technic has

become increasingly routine in pharmaceutical laboratories for drug discovering [73] and for the analysis of natural products [74]. In the “on-flow” mode, 1D NMR spectra are acquired directly on the flowing mixture after elution through the column. 2D NMR provides new vistas towards the characterization of organic and pharmaceutical compounds that are unavailable with its 1D counterpart. Nevertheless, the time constraint of conventional 2D experiments is not compatible with the on-flow procedure. Hence, an alternative mode called “stop flow mode” is applied, whereby fractions which have eluted from the column are successively collected and then inserted individually into the spectrometer allowing the desired experiment duration. The downside of this approach is a longer waiting time, axial diffusion issues and the impossibility for real-time visualization of the LC separation. In addition, this involves robot-driven devices for collecting the successive fractions. Therefore, there is a need for fast multidimensional NMR suitable with the practical and versatile on-flow procedure. Two different strategies have been carried out for coupling LC separation with fast 2D NMR detection in this continuous mode. 2D Hadamard was successfully applied within a LC-NMR setup to probe with a high time resolution a model synthetic mixture as well as human urine samples [75]. This methodology provides interesting performances in terms of sensitivity and resolution, nonetheless, it should be mentioned that prior knowledge is required to properly achieve the frequency encoding. Alternatively, the potential of UF 2D NMR was investigated and the proof of concept of LC-UF NMR was reported by Shapira *et al* in 2004 [76]. In this work, ultrafast TOCSY experiments were carried out on a mixture of model organic analytes, which were previously separated via a homemade experimental setup, consisting of a classical silica-based glass column designed specifically for this kind of experiment. Thereafter, this coupling was extended to a commercial (High Performance Liquid Chromatography) HPLC-NMR device [77]. Constant time phase-modulated UF-COSY spectra were collected every 12 s during a 12-min chromatographic run carried out on a mixture of natural aromatic compounds (Figure 16). A noticeable feature was the use of an analytical C-18 column with regular HPLC solvents, highlighting the suitability of this approach to common HPLC-NMR hardware and conditions.

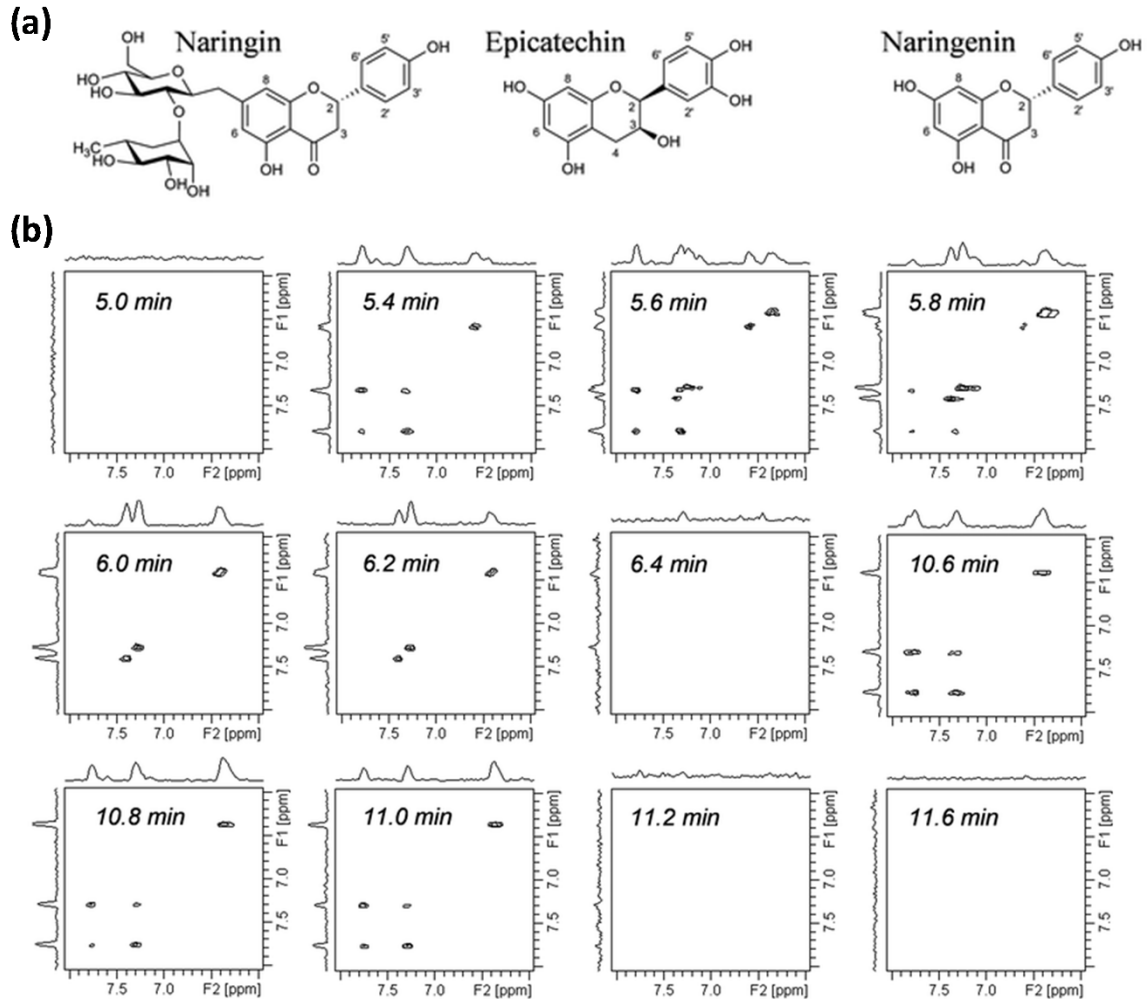

Figure 16. UF 2D NMR hyphenated with a commercial LC device. (a) schemes of the studied aromatic compounds. (b) a subset of constant time phase-modulated ultrafast COSY spectra, recorded in the course of the elution. The flow rate was fixed at 0.4 mL.min^{-1} and the sample injection volume was 100 mL. Reproduced from Ref. 77.

3.3. UF 2D NMR coupled with hyperpolarization

In spite of its incomparable wealth of information, NMR still suffers from an intrinsic low-sensitivity compared to other spectroscopies. Therefore, improving sensitivity has been a key feature since the early days of this spectroscopy. Numerous determining improvements, such as ultrahigh-field superconducting magnets (nowadays above 1 GHz) and cryogenic probes have boosted the NMR sensitivity and extended the scope of applications. Beyond this technological effort, the last decade has undergone the advent of hyperpolarization techniques, which directly deals with the root issue by replacing the weak bulk polarization arising at room-temperature (10^{-5}) with metastable spin states to reach unity values. Once

suitably prepared, the hyperpolarized sample can be exploited by the NMR spectrometer in order to yield a super-signal with an enhancement of several orders of magnitude of the SNR. Several strategies have been developed to build and exploit this hyperpolarized state in liquids, including the optical pumping of noble gases [78,79], the use of parahydrogen [80] and microwave-driven dynamic nuclear polarization (DNP) from unpaired electrons [81,82]. Whatever the method, hyperpolarization is a short lived state depending on relaxation mechanisms so that it can be exploited on a timescale dependent on the longitudinal relaxation time T_1 of the hyperpolarized nuclei. Thus, hyperpolarized NMR is best-suited for experiments performed in a single or at most a few scans. This timescale is a poor starting point to consider implementing 2D NMR on such samples. Against this background, UF 2D NMR is a well-suited approach to circumvent this limit and deliver 2D hyperpolarized NMR spectra. This potential is illustrated by the use of this spatial encoded approach as a reference method to yield 2D spectra on hyperpolarized compounds.

3.3.1. UF 2D NMR coupled with dissolution DNP

DNP refers to the mechanisms which transfer electron spin polarization to nuclear spins by resonant microwave excitation of electron spin transitions. The maximum DNP enhancement of the NMR signal is given by the electron to nuclear gyromagnetic ratios γ_e/γ_n . Several in situ [83] or ex situ [84,85] setups have been proposed to carry out DNP prior to liquid NMR analysis. Particularly promising has been dissolution DNP (D-DNP), whereby the sample is previously frozen at low temperature (1.1 – 1.5 K) and subsequently polarized through microwave irradiation in the presence of radicals. After this polarization step, the sample is rapidly melted and dissolved in a suitable hot solvent and transferred to a conventional liquid-state spectrometer. Golman and collaborators reported a gain of SNR about 10^4 via such a procedure [86]. As mentioned above, this amazing boost in sensitivity is however associated with a short-lived state so that only experiments with a single (or at most a few) scan(s) are conceivable to yield 2D hyperpolarized spectra. Hopefully, UF NMR comes to the rescue by replacing the conventional t_1-incremented evolution period by a one-step spatial encoding. This potential of D-DNP hyphenated with UF 2D NMR was demonstrated in 2007 by Frydman and Blazina [87], who showed that 2D spectra of hyperpolarized liquid samples at submicromolar concentrations could be acquired in 0.1 s. Their results shed light on the high complementarity of the two techniques: UF 2D NMR solves the irreversibility issue of D-DNP,

and hyperpolarization copes with the inherent low sensitivity of this spatial encoded experiments. A further complication related to D-DNP is the significant necessary time (e.g. 1 s) to transfer the sample from the polarizer to the spectrometer. Bearing in mind that the hyperpolarization vanishes through relaxation mechanisms, this transfer time involves that only sites with relatively long liquid states T_1 can be used to retain a sufficient amount of super-signal. Therefore, UF experiments relying on the hyperpolarization of slow relaxing low-γ nuclei as quaternary ^{13}C or ^{15}N are best-suited. UF-HMBC, exploiting long distance correlation between protons and non-protonated ^{13}C and ^{15}N was successfully coupled with D-DNP [88]. Thereafter, a band-selective version of this UF experiments were reported to measure several correlations in a single shot, a strategy that was successfully applied to mixtures of hyperpolarized natural products at millimolar concentrations (Figure 17) [22]. Along the same lines, hyperpolarized plant and cancer cell extracts were recently studied by UF 2D ^{13}C-^{1}H HMBC at natural abundance on a 500 MHz spectrometer equipped with a cryogenic probe. The 2D spectra were recorded in a single scan after a 30 min polarization step (assisted by cross-polarization [89]), with a sufficient sensitivity to characterize metabolites whose conventional 2D detection required several hours of acquisition [90]. In parallel, it was also reported that a modified DNP setting provided a faster transfer from the polarizer to the spectrometer and in turn allowed the acquisition of homonuclear UF 2D experiments [91]. Overall, these results highlight the capability of DNP coupled with UF NMR of delivering 2D spectra in fraction of second on biological substrates at millimolar concentrations and at natural abundance. This paves an exciting way towards applications such as metabolomics where sensitivity is an inevitable limitation. Furthermore, the application to large-scale metabolomics studies imply to improve and validate the reproducibility of the whole procedure. The higher the repeatability, the greater the likelihood that one can detect small biologically relevant differences between samples. A first step to this direction was very recently reported, whereby the average repeatability of a D-DNP setting applied on metabolomic samples was 3.6 % for signals above the limit of quantification (SNR > 10) [92].

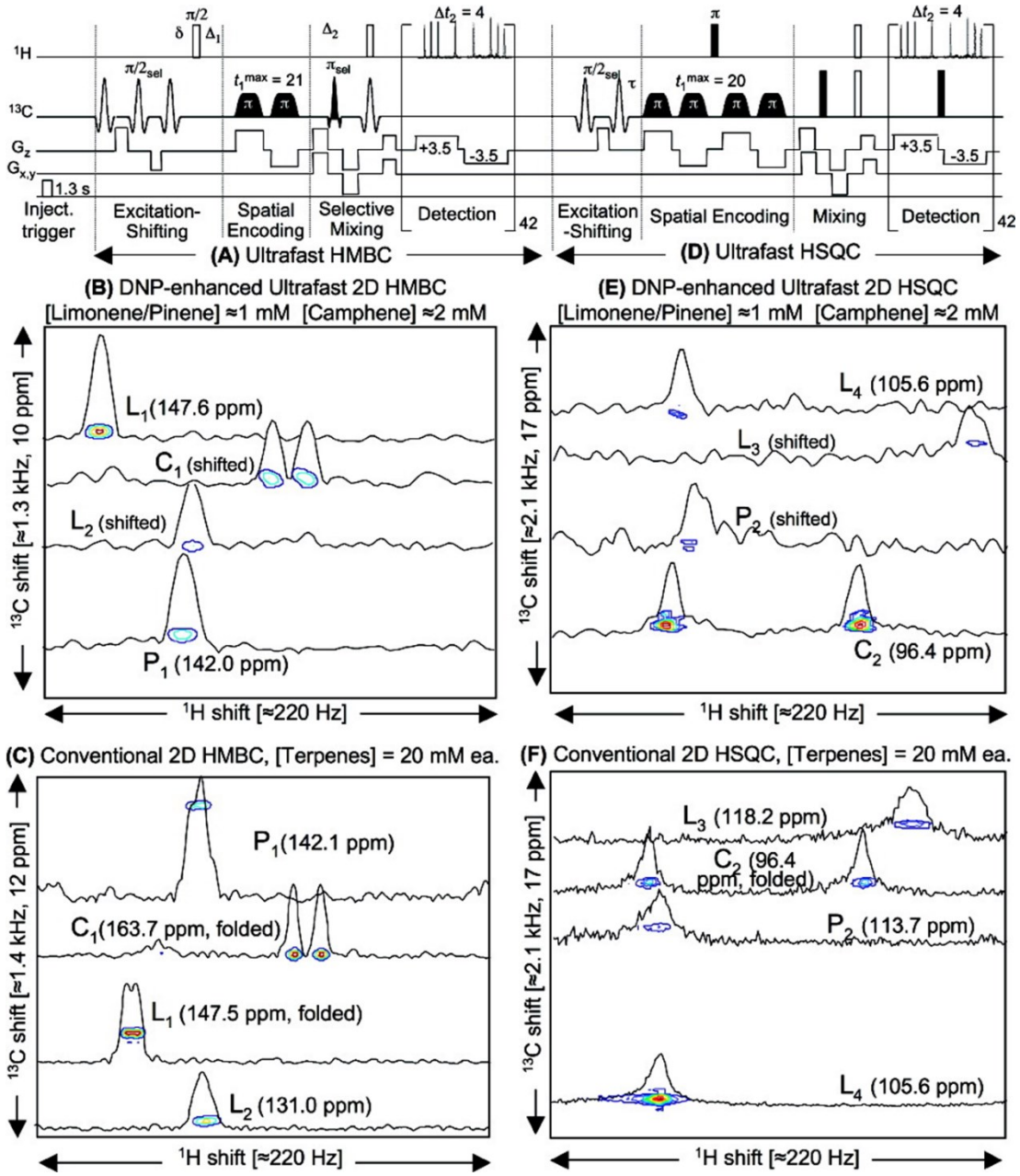

Figure 17. Examples of UF 2D heteronuclear experiments performed on hyperpolarized natural products via D-DNP. (a) and (d) Respectively 2D HMBC and HSQC ^{13}C-^{1}H performed in the ultrafast fashion, including gradient and timing parameters (in G/cm and ms) and spectral/spatial manipulations bringing the relevant signals within the spectral window. (b) and (e) Projections of UF HMBC and HSQC 2D spectra obtained after polarizing a 0.5 M limonene/α-pinene/camphene 1:1:2 solution in a toluene/toluene-d_8 1:5 mixture with 20-mM BDPA (α,γ-bisdiphenylene-β-phenylallyl). Sudden dissolution in methanol-d_4 led to a final concentration of 1 mM for limonene and α-pinene, and 2 mM for camphene. (c) and (f) Conventional HMBC and HSQC 2D NMR spectra recorded on a 20-mM equimolar terpene mixture in $CDCl_3$, obtained in 90 min using 32 scans, 64 t_1-increments, a 2 s recycle delay, and a 0.5 s acquisition time. These conventional data were acquired with the same ^{13}C spectral widths as the UF spectra, leading to the aliasing of some of the peaks. Also shown are the unfolded positions of the ^{13}C resonances characterized in each experiment (in ppm from TMS). Both HSQC and HMBC conventional pulse sequences were made spectrally selective to avoid the appearance of unwanted ^{13}C resonances. Reproduced from Ref. 22 with permission from American Chemical Society.

3.3.2. UF 2D NMR coupled with Parahydrogen techniques

Para-Hydrogen Induced-Polarization (PHIP), relying on the total spin alignment of parahydrogen (p-H_2) molecules, is another emergent hyperpolarization technique [80]. In particular, Signal Amplification By Reversible Exchange (SABRE) is a promising PHIP method based on the reversible binding of p-H_2 and the substrate of interest to a metal center, usually an iridium complex [93]. The resulting transient coupling network can transfer the spin order of p-H_2 to the nuclear spins of the substrate, thereby observable polarization is formed. SABRE has widely extended the application field of parahydrogen-based hyperpolarization and a 1000-fold ^{1}H NMR signal enhancement for free pyridine was reported [94]. SABRE is generally used to record 1D NMR spectra. In the case of complex mixtures, this leads to numerous overlaps, which can be even more server when co-substrates are used to improve the limit of detection. As the SABRE-enhanced ^{1}H signal is short-lived, the use of ultrafast 2D NMR is again an appealing way to yield 2D spectra on such hyperpolarized samples. Yet, it is worth to mention that unlike other strategies previously described, SABRE enables the production of hyperpolarized substrates in few seconds with an intensity that is reproducible to within a 5% tolerance. Based on this property, conventional 2D NMR spectra can be recorded with SABRE-enhancement by repeating the parahydrogen hyperpolarization for each t_1-transients. This involves, nevertheless, the use of a specific hardware, which periodically shuttles the sample between a polarization chamber and a NMR flow-probe. The same authors reported the use of UF-COSY experiments to detect SABRE-based hyperpolarization of quinoline at 10 Mm. Moreover, Daniele *et al* reported the use of UF-COSY coupled with SABRE, assisted with deuterated co-substrates, to yield COSY spectra in less than 1 s on a complex mixture of analytes at sub-millimolar concentrations (Figure 18) [95].

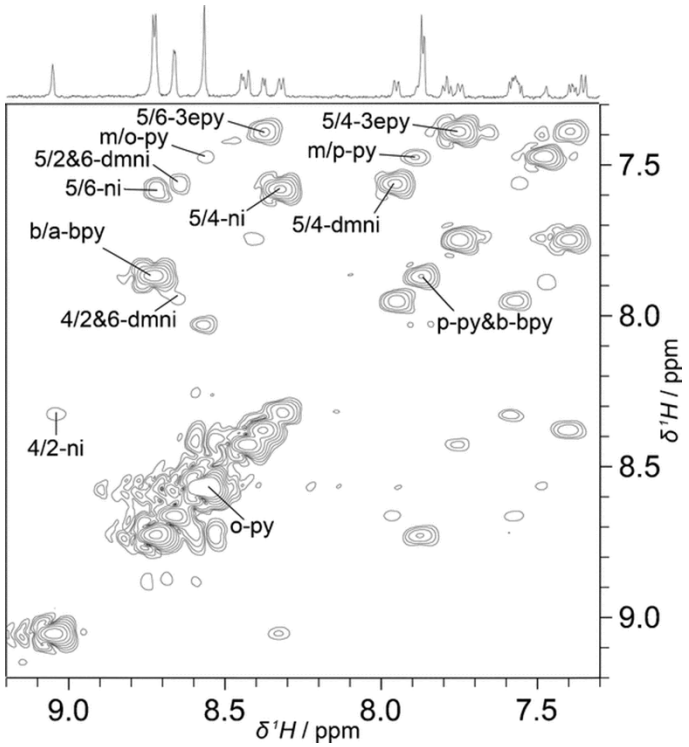

Figure 18. Illustration of UF 2D NMR coupled with SABRE-enhancement. Single-scan ultrafast COSY spectrum of a mixture composed by small molecules at concentrations on the order of 0.5 mM, with SABRE hyperpolarization. In addition to the substrates, the sample contained 0.13 mM of complex precursor [Ir(COD)(IMes)Cl], 10 mM of deuterated pyridine as a co-substrate and 4 bar of p- H_2 in methanol-d_4. Reproduced from Ref. 95 with permission from John Wiley and Sons.

3.4. UF 2D NMR for quantitative applications

Beyond the obvious potential of ultrafast 2D NMR for real-time monitoring and hyphenated techniques, it was proved to be relevant for quantitative NMR applications.

3.4.1. Principles of quantitative 2D NMR

Quantitativity has been associated with NMR spectroscopy since its early days. In the field of analytical chemistry, NMR is classified as a primary method as the measured signal of a compound S_i is directly proportional to its concentration: $S_i = k \cdot p_i \cdot C_i$, where p_i is the number of nuclei related to the measured site; C_i is the concentration of the compound and k is a proportionality constant depending on the hardware. This means that the measure of a NMR signal relatively to a reference compound provides the concentration of the probed molecule. Numerous methodological developments in qNMR have extended the measurement of analyte concentrations from pure samples to complex mixtures [96]. qNMR

is a determining tool in a variety of applications, such as pharmaceuticals [97,98], natural products [99,100], metabolomics [101–103], food science [104,105] etc. Yet, major methodological challenges are associated with quantitative NMR applied to complex mixtures. The first one is the signal overlap that becomes particularly critical when complex mixtures are analyzed by ^{1}H qNMR. The fields of metabolomics and natural products are particularly affected by this issue, because the ubiquitous peak overlap that characterizes ^{1}H NMR spectra prevents the accurate determination of peak areas. Several strategies have been used to cope with this resolution issue, such as deconvolution methods or heteronuclear analysis via nuclei providing broader ranges of chemical shift: ^{13}C, ^{15}N, ^{31}P etc. Moreover, a very efficient alternative in terms of analytical performance is multidimensional experiments, which has the advantage of offering a much better discrimination of resonances than 1D NMR, as the peaks are spread along one (or more) orthogonal dimension(s) [106–115]. Despite this asset, some features have hampered the use of multidimensional NMR as a quantitative tool. The first one is related to the long experiment duration that is ill-suited for high-throughput applications or for the analysis of unstable biological samples. Moreover, this acquisition time becomes even higher due to the necessary long recycling delay (5 x T_1) to vouch full-longitudinal relaxation between each t_1-transient. This makes such long experiments sensitive to the spectrometer instabilities over time [116,117]. This generates additional noise in the indirect dimension – commonly called "t_1-noise"- leading to a reduction of the overall 2D-peak SNR. From an analytical point of view, this reduced SNR involves a penalty in terms of repeatability, a critical point for quantitative prospects. Another feature is the complexity of the 2D-peak response that is highly site specific. Indeed, the 2D peak volumes are still proportional to the analyte concentration, but the coefficient of proportionality k become peak-dependent, as it is modulated in a complex manner by J-couplings, relaxation, pulse sequence delays, pulse angles and off-resonance effects. This issue is often circumvented by a calibration procedure –as with other analytical techniques: mass spectrometry, UV-spectroscopy etc. – consisting of recording spectra of model mixtures at different concentrations and plotting the peak volumes versus the concentrations for each peak of interest. However, such a calibration method involves the acquisition of several 2D spectra collected in quantitative conditions making this 2D qNMR method even more time-consuming. This drawback highlights the need for alternative and faster 2D NMR strategies.

By drastically reducing the duration of 2D experiments, ultrafast NMR offers promising perspectives for quantitative analysis [118]. The time saving leads to a double benefit: first, the ability to deal with large batches of samples, and furthermore a better resistance to the hardware instabilities since a whole 2D interferogram is obtained for each transient. In 2009, Giraudeau *et al*. performed an analytical evaluation of UF 2D NMR on model mixtures [119]. Two homonuclear UF sequences: J-resolved spectroscopy and TOCSY, were evaluated in terms of repeatability and linearity on model mixtures. A repeatability better than 1% for UF J-resolved spectra and better than 7% for TOCSY spectra was obtained. In addition, both methods were characterized by an excellent linearity, which is a determining property in the case of a calibration procedure. Nonetheless, the sensitivity of UF NMR should be discussed in this framework. Obviously, the single-scan nature of UF experiment does not provides a sufficient sensitivity for most quantitative applications. Since signal averaging is generally required, it is worth considering the SNR per time-unit obtained with UF experiments *versus* the one obtained with its conventional counterpart. Such an analytical comparison was performed on model mixtures of metabolites. Interestingly, M3S [29] UF homonuclear experiments yielded a better sensitivity than conventional 2D experiments for a same experimental duration [31]. This was attributed to the higher immunity of UF experiments to the temporal instabilities of the hardware. Based on this performance, ultrafast qNMR has emerged as a promising tool, especially in the field of metabolomics.

3.4.2. Quantitative UF NMR in metabolomics

NMR is widely used for metabolomics studies, where it often exploits a very standardized 1D ^{1}H NMR protocol associated with uni- or multivariate statistical analysis to compare samples from different sets [120,121]. Although this method provides efficient discrimination between samples, it does not provide the quantification of metabolites responsible for this discrimination. In order to yield such a precious quantitative insight, a targeted approach — metabolic profiling— that consists in identifying and quantifying a few tens of metabolites in unfractionated extracts is necessary [102,121,122]. The severe overlaps encountered on the 1D spectra and the need of high-throughputs analysis of large batches of metabolomic samples make ultrafast 2D NMR well suited to such applications. The high-repeatability and accuracy of this method was applied to the determination of absolute metabolite

concentrations in biological extracts. Le Guennec *et al*. collected UF-COSY spectra to measure the absolute metabolite concentration in three breast cancer cell line extracts [30]. A calibration procedure based on a standard addition protocol ensured the quantitativity of the measurements. M3S COSY spectra of such extracts were recorded in 20 min and provided the absolute concentrations of 14 major metabolites (Figure 20a and b), whereby a significant metabolic differences was revealed between cell lines. This work portrays the further use of UF 2D NMR for targeted approach in metabolomics as illustrated by the use of the same strategy for a targeted study on plant extracts (Figure 19) [35].

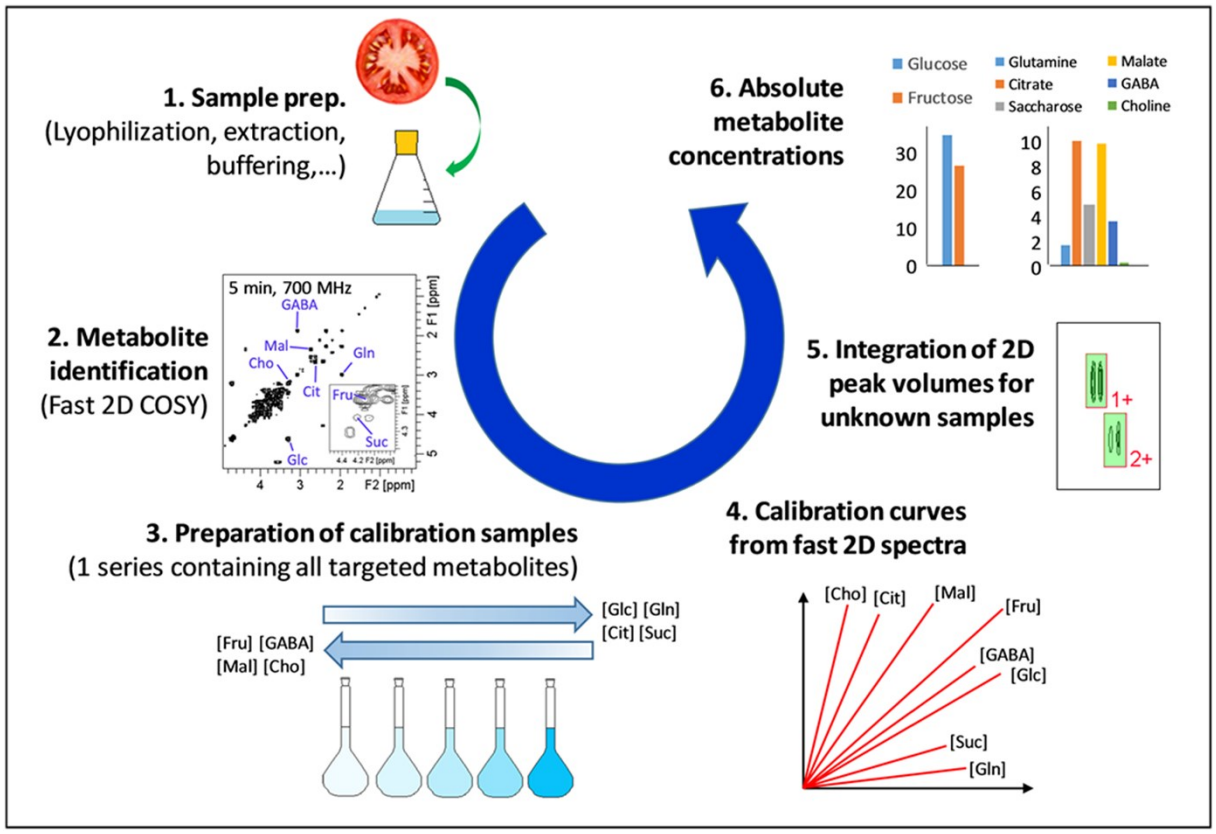

Figure 19. Analytical workflow for the determination of the absolute metabolite concentrations in biological extracts. Herein an example on tomato fruit pericarp extracts. This work-flow relies on a fast 2D NMR acquisition strategy (hybrid multi-scan COSY based on ultrafast 2D NMR) associated with a calibration protocol. This workflow is general and may be applied to any kind of biological samples with any 2D experiment. Reproduced from Ref. 96 with permission from John Wiley and Sons.

In the case of homonuclear correlation experiments, the strong and numerous diagonal peaks potentially disturb the accurate quantification through overlap with relevant correlation peaks, which is particularly critical when large dynamic ranges are involved. Fortunately, the

generic nature of UF NMR allows to perform DQS in an ultrafast fashion. The proof of concept was established by Le Guennec *et al* on a model mixture [46], and this UF-DQS proved its analytical potential through the quantification of taurine in an energy drink sample with a far better accuracy than with a UF-COSY experiment [36]. Further quantitative applications of UF 2D NMR pertain to the field of fluxomics. 2D NMR is a relevant tool for studying metabolic fluxes by measuring ^{13}C-enrichments in complex mixtures of ^{13}C-labeled metabolites [123,124]. However, this 2D approach is again hampered by its long acquisition time. In order to combine the time saving and the higher precision provided by UF 2D NMR, several acquisition strategies for measuring ^{13}C-enrichments from fast 2D spectra have been recently proposed, consisting in recording homonuclear ^{1}H 2D spectra where ^{13}C couplings are expressed in one dimension only [125]. The signal overlap is significantly reduced while quantitative site-specific information can be extracted from lines of the 2D map (Figure 20c). Furthermore, the overlap can be further reduced by tilting the ^{1}H–^{13}C isotopic pattern along a third dimension (Figure 20d). This approach requires a 3D acquisition, which can be achieved in a few minutes only via a hybrid strategy based on UF NMR [47].

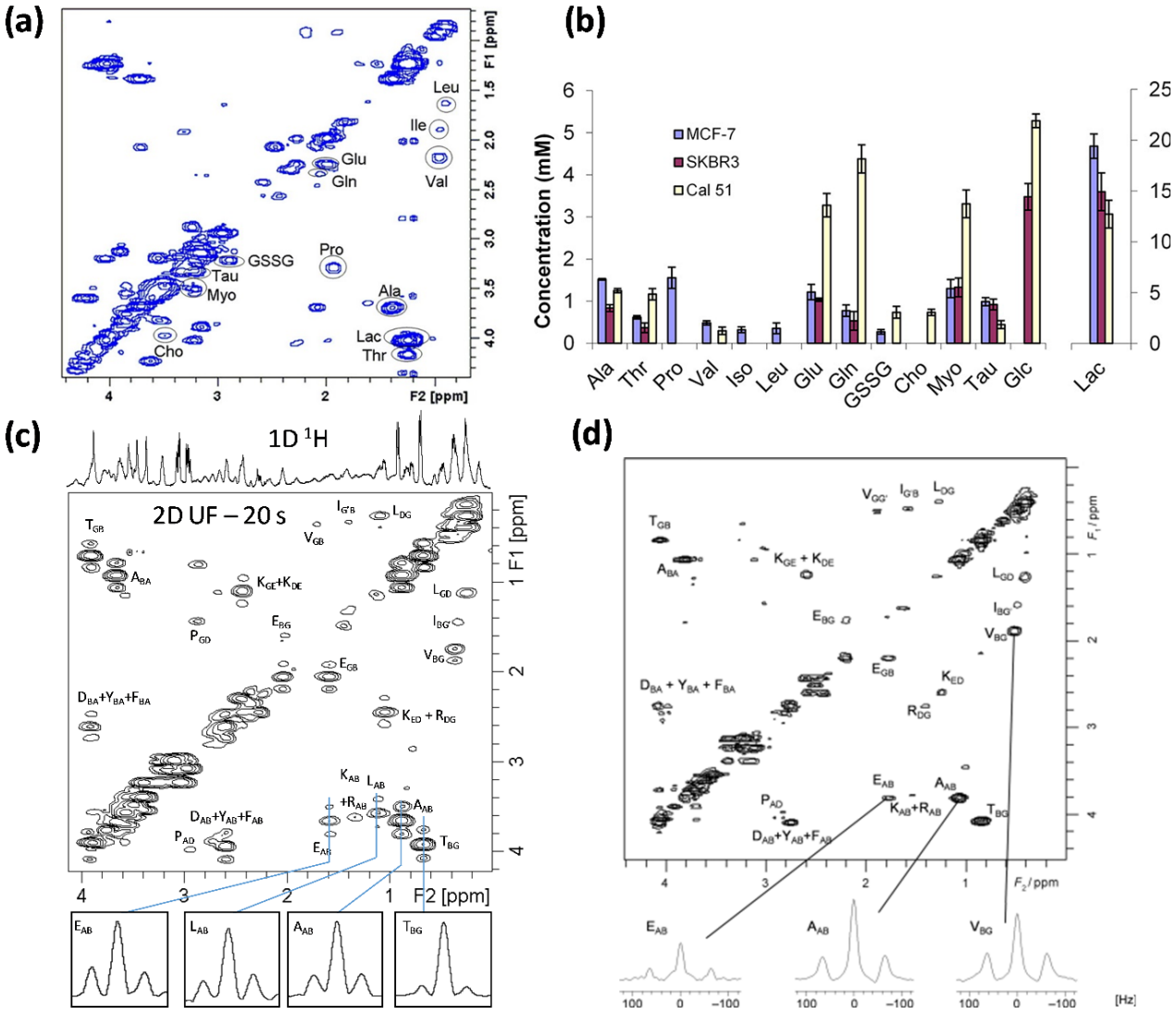

Figure 20. Illustrations of the potential of UF NMR for quantitative application in metabolomics and fluxomics. (a) ^{1}H M3S COSY spectrum recorded in 20 min of a breast cancer cell line extracts. (b) Metabolite concentrations of intracellular extracts obtained from three cell lines, by a quantitative M3S COSY protocol associated with a standard addition procedure. (c) UF zTOCSY on a sample of a biomass hydrolyzate from E. coli cells grown on 50% of [U-^{13}C]-glucose and 50% of n.a. glucose. This ultrafast spectrum - recorded in 3 min (40 scans) - is used in the field of fluxomics to measure site-specific ^{13}C-enrichments. (d) (F1, F2) plane from a 3D J-resolved-COSY spectrum recorded on a similar sample in about 12 min at 500 MHz with a cryoprobe. The hybrid pulse sequence is based on ultrafast 2D NMR, where the spatio-temporal encoding of two dimensions is associated with the conventional temporal encoding of the third one. (a) and (b) reproduced from Ref. 30 with permission from American Chemical Society, (c) reproduced from Ref. 125, (d) reproduced from Ref. 47 with permission from John Wiley and Sons.

3.5. Pseudo-UF NMR

In the methodological section, we described how the ultrafast methodology yields arbitrary homo or heteronuclear 2D spectra, departing from conventional pulse-sequences and replacing the t_1-evolution by a spatial encoding and the detection under free evolution by an EPSI block. While this approach was mainly used to spatially encode spectroscopic parameters as chemical shifts or J-couplings, this broad concept can be further applied to spatially encode dynamic parameters such as relaxation-times T_1, T_2 or diffusion coefficients D. Widely used and popular pseudo-2D experiments such as diffusion ordered spectroscopy (DOSY), Inversion Recovery (IR) or even 2D Laplace NMR, can be collected in a ultrafast manner.

3.5.1. Single-scan measurement of longitudinal relaxation

A first example of such a pseudo-UF approach relates to the development of fast methods for the measurement of longitudinal relaxation times T_1. Single-scan relaxation measurements could be determining to understand the dynamics of spin systems and to probe molecular motions over a wide range of timescales. Generally, T_1 measurements are achieved by IR [126] based on a multistep scheme where the inter-transient delay must be long enough ($> 5 \times T_1$) to vouch full longitudinal relaxation. The resulting experiment duration is of course beyond the usual scope of real-time dynamic studies. This drawback has urged strong efforts to speed up the T_1-measurment. As soon as in the 1970's, single scan schemes were proposed such as the triplet pulse-sequences [127,128]. However, the drawback of almost all these experiments is that they lack chemical shift resolution and/or return a value that reflects a combination of longitudinal and transverse relaxation. More recently, slice-selective approaches were proposed. The key feature in these experiments is to prepare the magnetization differently in different parts of the sample. The data is then acquired in such a way that the spatial modulation of the magnetization is reflected in the spectrum. Moreover, unlike previously reported single-scan methods, these kind of experiments preserve chemical shift information and are therefore applicable to samples with multiple resonances [129,130]. Although very helpful, these slice-selective methods are, nevertheless, ill-suited for the measurement of short T_1s (e.g. < 1 s), which hinders their use for probing dynamic phenomena at the molecular level. In this context, Smith *et al*. proposed a pulse sequence akin to UF 2D NMR experiments to perform single-scan IR experiments best-suited for short T_1s measurements [131]. It is

worth noting that in contrast to the standard UF processing, a 2D FT transformation is applied on the (k, t_2) maps obtained after EPSI detection. The effect of the longitudinal relaxation is reflected by the variation of magnetization along the length of the sample (Figure 21). This pseudo-ultrafast method opens new opportunities to study real-time molecular dynamics.

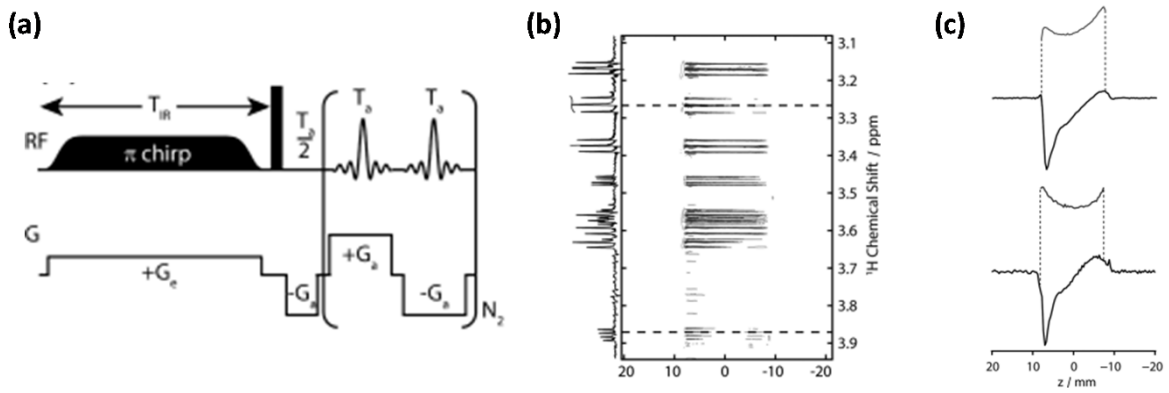

Figure 21. Single scan measurement of short T_1s (a) Ultrafast IR pulse-sequence. (b) UF-IR spectrum acquired on 100 mm D-xylose dissolved in D_2O obtained after a 2D FT transformation applied on the (k, t_2) pseudo-interferogram. (c) Slices taken at 3.3 ppm and 3.9 ppm (dashed lines) portray the variation of magnetization along the length of the sample provided by an adiabatic inversion pulse applied synchronously with a magnetic field gradient. Shown in gray are profiles arising from the same sites after full recovery. These are used as reference for an accurate reconstruction of the IR curves. Reproduced from Ref. 131 with permission from John Wiley and Sons.

3.5.2. Single-scan measurement of translational diffusion

DOSY encodes the effect of random Brownian motion in the indirect dimension while the chemical shift information is retained along the direct dimension [132]. This enables the separation of the analytes according to their diffusion coefficients within a same sample. DOSY is a powerful and popular tool for the analysis of complex mixtures. In the conventional version, this experiment relies on a series of transients recorded with incremented gradient strengths. Due to this multistep-scheme akin the other conventional 2D or pseudo-2D approaches, DOSY is associated with a significant acquisition time. Moreover, the original DOSY pulse sequence involves multiple steps of phase cycling increasing even more the experiment duration. In this context, several attempts have been made to address this time constraint. In this vein, the Oneshot DOSY [133] reduced the time-consuming phase-cycling to a single step, while Urbanczyk *et al* reduced the number of increments through a non-

uniform sampling of the diffusion dimension [134]. Alternatively, the acquisition of the DOSY data may be parallelised with a spatial encoding of the diffusion dimension. This concept, introduced by Keeler and co-workers [135], and then reintroduced by Frydman *et al* [136], makes it possible to acquired 2D DOSY data in a single scan. In this approach the incremented gradients of the classic stimulated-echo DOSY (STE-DOSY) pulse sequence are replaced with the concurrent application of linearly swept chirp pulses and magnetic field gradients. This leads to a spatial dependence of the local diffusion weighting, which may be seen as a parallel encoding of all DOSY sub-experiments. In such a spatially encoded DOSY, the diffusion information for each resonance is recovered at the acquisition stage by acquiring an ‘‘image’’ of the sample by either applying a constant read-out gradient when the receiver is open [135], or by using an EPSI scheme [136]. Furthermore, Dumez and coworkers have very recently provided optimizations of this approach based on numerical simulations (see Figure 22) and demonstrated that this spatial encoded DOSY scheme is suitable for the extension to 3D experiments [137]. They developed a 3D DOSY-COSY pulse-sequence, in which the correlation interferogram is built with a conventional t_1-incrementation while the diffusion dimension is spatially encoded, accelerating this 3D pseudo-spectra by one order of magnitude.

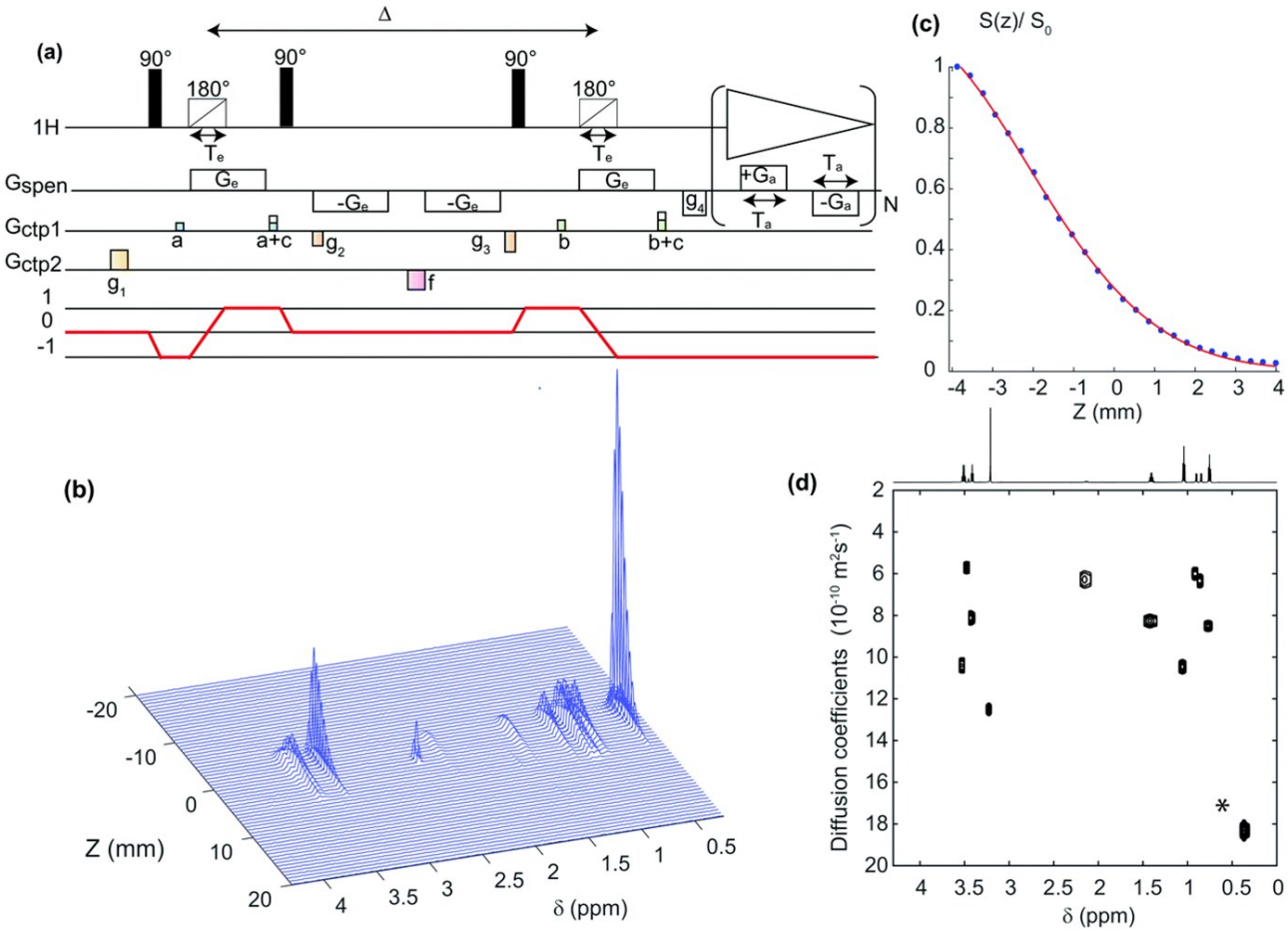

Figure 22. Illustration of the potential of the UF concept to yield DOSY spectra within a single scan. (a) Pulse sequence for spatial encoded DOSY. The selected coherence transfer pathway is shown in red. Gradients "a" and "b" are crushers surrounding the refocusing chirp pulses; gradient "c" selects the anti-echo pathway for the stimulated echo; gradient "f" is a spoiler during longitudinal storage; "g_1", "g_2" and "g_3" are compensating gradients. (b) 2D spectroscopic imaging data set obtained with the spatial encoding 2D DOSY experiment on a mixture of three alcohols (methanol, ethanol, propanol) and an amino-acid (L-valine), at a concentration of ~100 mM in D_2O. (c) Diffusion decay curve obtained from the data set shown in (b), for the methanol CH_3 resonances at 3.2 ppm. (d) 2D DOSY display obtained from the data set shown in (b). The water peak is folded and indicated by an asterisk. The ^1H pulse-acquire spectrum is shown above the DOSY display. The experiment was carried out with a 600 MHz spectrometer equipped with a triple-axis gradient high-resolution probe. Reproduced from Ref. 137 with permission from Royal Society of Chemistry.

3.5.3. Ultrafast Laplace NMR

We have described how the ultrafast methodology can be applied to correlate dynamic parameters with the chemical shift information. In some fields of applications, there is a need of mapping such dynamic constants together instead of retaining the chemical shift. These T_1-T_2 and D-T_2 correlation experiments are referred as 2D Laplace NMR due to the 2D inverse Laplace transformation involved in the process of such experiments. This approach is popular

for the investigation of porous media in food science [138] but suffers from a prohibitive experiment duration arising from the need of encoding successively the studied dynamic parameters. Recently, Telkki and coworkers applied the ultrafast concept to Laplace 2D NMR reducing the experiment time by one to two orders of magnitude for T_1-T_2 [139] and D-T_2 correlation experiments [140], as illustrated in Figure 23. The so-called ultrafast multidimensional Laplace NMR methodology was established both with high-field spectrometers [139,140] and with a low-field single-sided NMR system [141].

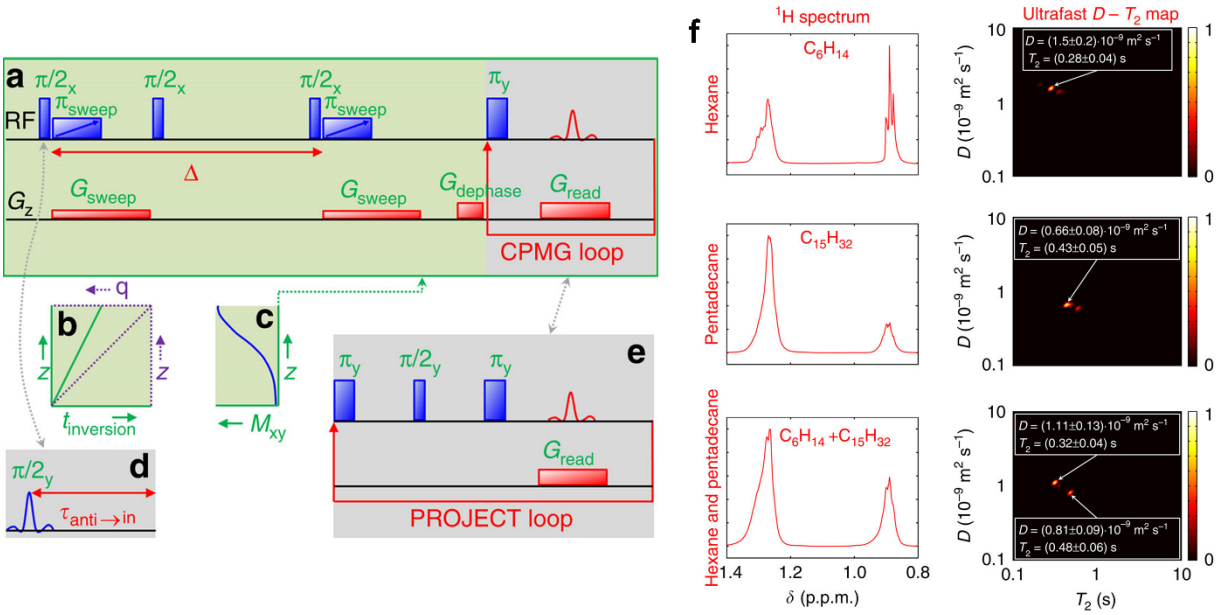

Figure 23. Ultrafast multidimensional Laplace NMR. (a) Pulse sequence of the UF D-T_2 experiment. (b) Spatial dependence of the inversion time inversion and the value of wave vector q due to the spatial encoding. (c) Transverse magnetization profile after the diffusion encoding. (d) An excitation block replacing the first 90° pulse suited for PHIP experiments. (e) PROJECT loop replacing the CPMG loop in order to eliminate J-modulation. (f): ^{1}H NMR spectra and ultrafast D–T_2 maps of 1.65 M hexane, 0.79 M pentadecane and a mixture of 1.36 M hexane and 0.65 M pentadecane in CCl_4. While the compounds are not resolved in the ^{1}H NMR spectrum of the mixture, they are resolved in the D–T_2 map. The experiments were carried out on a 600-MHz NMR spectrometer. Reproduced from Ref. 140.

3.5.4. Reducing the experiment duration of chemical exchange saturation transfer

Another example of such a UF pseudo 2D method was addressed to speed up the chemical exchange saturation transfer (CEST) experiment [142]. CEST has become a popular technique for generating enhanced MRI contrast in vivo and in vitro. To fully characterize these

phenomena and to investigate suitable candidates for contrast agents, the polarization of the reporter signal (typically water) is measured as a function of the frequency offset of the saturating radio-frequency irradiation. The resulting "Z-spectrum" is obtained point by point involving a long experiment duration. In 2013, Jerschow and collaborators proposed an ultrafast method to obtain a Z-spectrum over a large range of frequency offsets from only two scans [143]. This UF sequence consists in a saturation with radiofrequency pulse applied together with a gradient, followed by a 90° excitation and finally a read-out gradient is applied during the detection. The saturation is turned off and on for respectively the first and second scan, leading to a whole Z-spectrum by a simple comparison of the two scans (Figure 24). In order to take advantage of this time saved, this UF version – often reported as "UFZ" – has been used for the fast screening of para- and diamagnetic CEST contrast agents under different experimental conditions (saturation time and RF power). Further developments and applications have been recently reported. This ultrafast CEST strategy was applied for the monitoring of fast temperature and pH changes as well as for the high-throughput screening of CEST contrast agents [144,145]. Moreover, Döpfert and coworkers developed UF CEST experiment hyphenated with hyperpolarized Xenon [146] and with ^{129}Xe-based sensors [147]. Finally, UF-CEST combined with a point-resolved spectroscopy (PRESS) scheme was recently applied in the field of localized spectroscopy in phantoms and in-vivo [148].

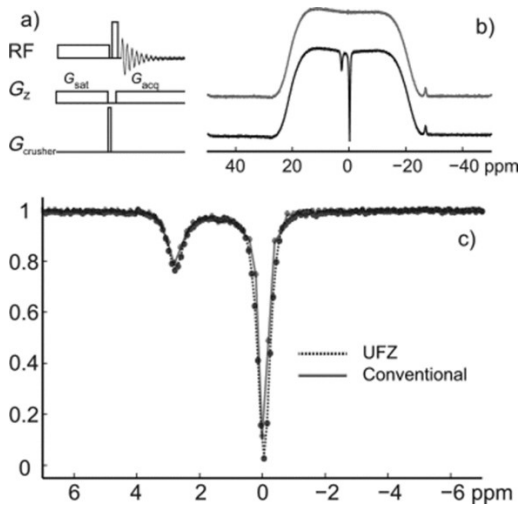

Figure 24. Principles of ultrafast CEST experiment (UFZ). (a) Pulse sequence for the UFZ spectroscopy. (b) Reference spectrum without saturation (upper curve) and raw UFZ spectrum (lower curve). (c) A comparison of the conventional Z-spectrum (solid) and the UFZ spectrum (dashed). Reproduced from Ref. 143 with permission from John Wiley and Sons.

3.6. UF 2D NMR in oriented media

In the previous sections the potential of UF NMR has been illustrated in the liquid state. Some applications have also been reported in oriented media, from the measurement of anisotropic interactions in liquid crystals to studies in High Resolution Magic Angle Spinning (HR-MAS) as well as in the solid-state.

3.6.1. UF 2D NMR in liquid crystals

NMR in oriented media provides valuable and relevant interactions such as chemical shift anisotropy, dipolar and quadrupolar couplings that are averaged to zero in liquids. Residual dipolar couplings (RDCs) are a well-known source of spatial structural and dynamic information. Their measurement by conventional 2D methods is time-consuming so that an ultrafast version of such experiments would be convenient, and the time saved could allow to probe RDC on unstable samples. Against this background, Giraudeau, Thiele and coworkers reported in 2012 the first use of UF 2D NMR in an oriented media [149]. This work demonstrated the ability of measuring RDC via a sub-minute UF-HSQC experiment on small molecules in high concentration at natural abundance, dissolved in a weak oriented media (Figure 25b). The RDC values obtained were close to the ones established with a time-consuming conventional experiment. Such a UF approach in a weak oriented media was recently reported through the measurement of another valuable order dependent parameter: the residual quadrupolar coupling (RQC). Lesot *et al* developed an anisotropic deuterium UF experiment (ADUF) - performed on deuterated analytes dissolved in lyotropic polypeptide chiral liquid crystals – which allowed the discrimination of enantiopic site (Figure 25d) [150]. This pioneering work would be particularly promising for the monitoring of chiral enzymatic transformations in oriented media, where the experiment time is critical [151].

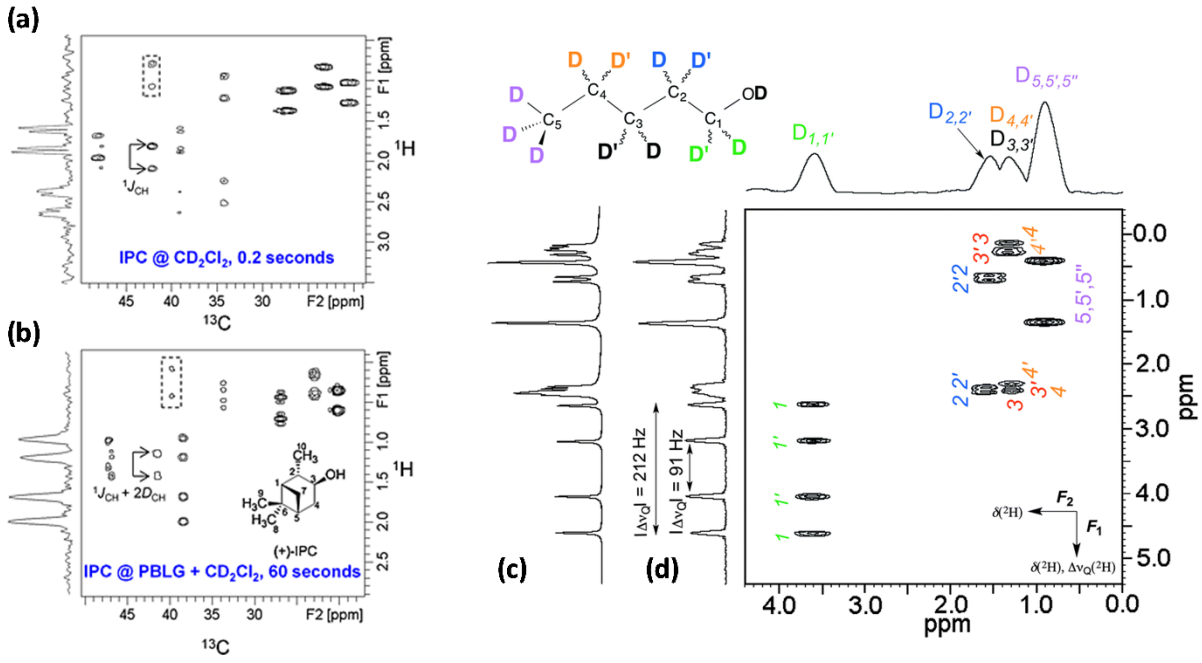

Figure 25. UF 2D experiments performed on oriented media for RDC and RQC measurement. Ultrafast ^{1}H–^{13}C-coupled HSQC spectra of isotropic (a) and anisotropic (b) (+)-isopinocampheol samples, acquired at 300 K on a 500 MHz spectrometer equipped with a cryoprobe. The peaks within the dashed box were folded along both dimensions of the 2D spectrum. The molecular structure of (+)-isopinocampheol is shown on the spectrum at the bottom. The projection shown corresponds to the column at 38.9ppm (C4). PBLG: poly-g-benzyl-L-glutamate. (c) Proton decoupled ^{2}H 1D spectrum in a PBLG mesophase. (d) Single-scan ADUF-{^{1}H} 2D map recorded in 400 ms. (a) and (b) reproduced from Ref. 149 with permission from John Wiley and Sons, (c) and (d) reproduced from Ref. 150.

3.6.2. UF 2D NMR in the solid-state

A last example relates to UF 2D NMR applied to solid-state samples. HR-MAS is a very powerful and convenient tool to analyse raw materials such as biopsies, plant tissues or foodstuffs, inaccessible to other analytical techniques. UF 2D NMR was developed on this setting to speed up the long experiment duration of 2D methods limiting the high throughput analysis of complex samples as illustrated by André *et al* [34]. In this article UF spectra were recorded on a model sample, then on banana slopes, while spinning at the magical angle (Figure 26a and b). Besides this development in HR-MAS, the UF methodology was developed in the solid-state at very high field (17.6 T), using a double resonance MAS probe together with external micro-imaging gradients [152]. In this work two popular 2D solid-state NMR sequences: double-quantum correlation and RF-driven proton spin diffusion, were applied in through an ultrafast format on elastomers under magic-angle spinning (Figure 26c and d). Such an ultrafast 2D approach is particularly convenient to expedite time-consuming arrayed 2D experiments. An

example of this time saved by UF NMR was highlighted in recording spin-diffusion build-up curves, which are a central tool for structural studies in disordered solids.

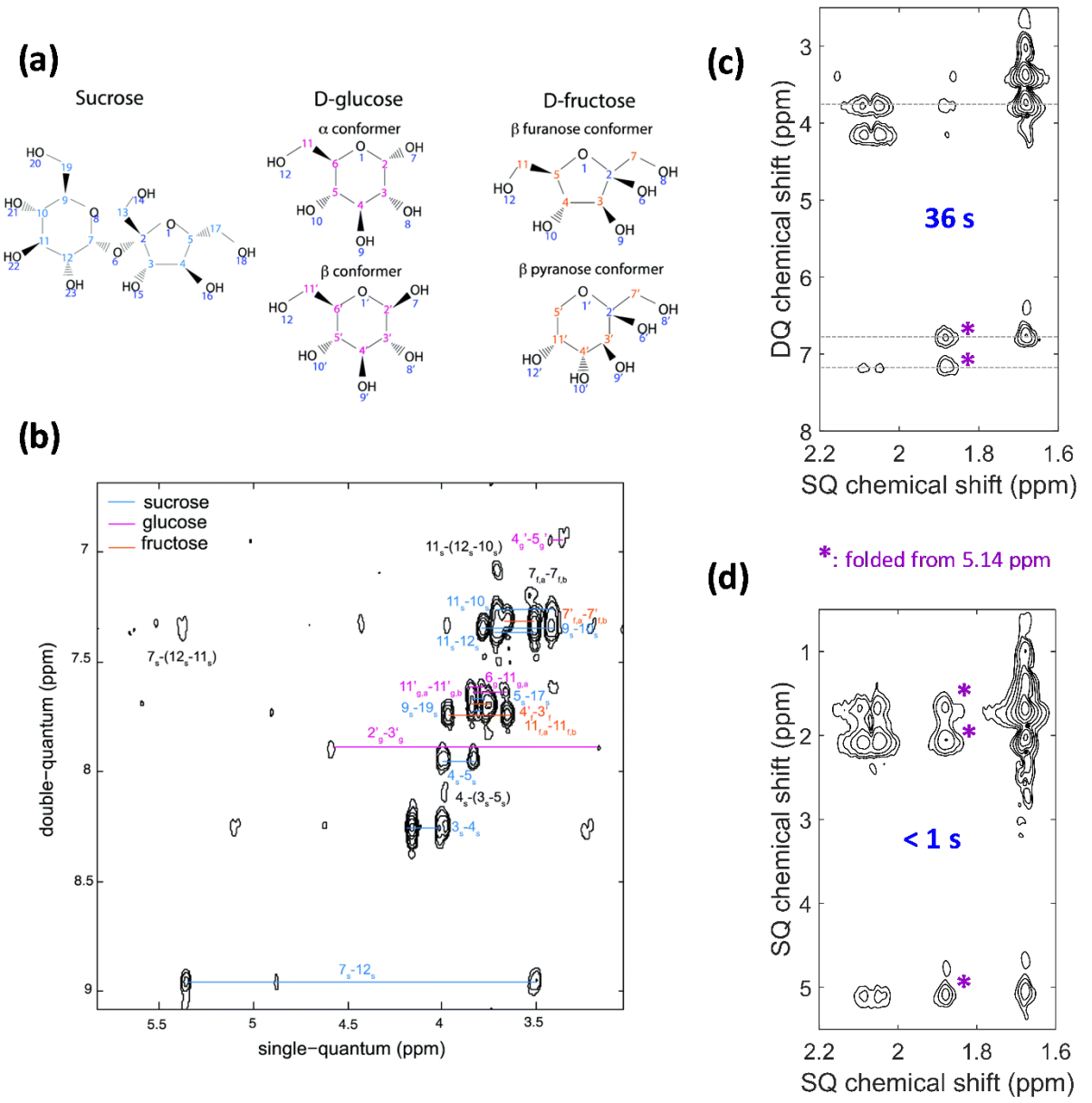

Figure 26. Ultrafast 2D NMR applied in HR-MAS and solid-state. Left panel: (b) Ultrafast experiment with two interleaved scans to increase the SQ dimension and (a) Chemical structure of sucrose, D-glucose and D-fructose. (b) Ultrafast HR-MAS DQS spectrum of a 10 mg sample of fresh banana, spinning at a frequency of 4.53 kHz. Pairs of correlation peaks for the three most abundant sugars in the sample (glucose, fructose and sucrose) are indicated by colored lines. (c) Ultrafast DQ spectra of a natural rubber sample recorded in 36 s. (d) Ultrafast PSD spectra of the same sample, recorded in less than 1 s. The folded region appears in purple. (a) and (b) reproduced from Ref. 34 with permission from Royal Society of Chemistry, (c) and (d) reproduced from Ref. 152 with permission from Elsevier.

3.7. UF 2D NMR in inhomogeneous fields

Besides the aforementioned UF applications, which were carried out with samples submitted to a homogenous B_0 magnetic field, the UF NMR concept plays a central role to record high-resolution NMR spectra in inhomogeneous fields. Many circumstances arise in which the spatial and temporal homogeneities of magnetic fields are degraded such as the study of heterogeneous biological tissues in human or animal in vivo NMR detection, food matrices, rock samples for oil exploration [153], or even in-situ NMR spectro-electrochemistry [154]. Numerous strategies have been developed to address this challenge. One relies on intermolecular multiple-quantum coherences (i-MQCs) originating from long range dipolar interactions among spins in different molecules [155], while another one is based on nutation echoes, very popular in *ex situ* NMR [156,157]. Both approaches have individual prerequisites: a concentrated component to generate the distant dipolar field for the i-MQCs techniques and a known and time-independent $B_0(r)$ profile for the second strategy [153]. Alternatively, Pelupessy *et al* proposed in 2009 a spatially encoded method to yield high-resolution 2D spectra in a single scan in inhomogeneous fields in a manner that is highly inspired from the previously described ultrafast multidimensional experiments [158]. This UF method deals with unknown spatiotemporal variations of the magnetic field profile, which is a determining advantage for practical applications such as *in vivo* experiments. The key feature of this method is to track in a single scan the differences of the precession frequencies of two coupled spins. This is achieved with two similar spatial encoding schemes localized on both sides of a mixing pulse while considering a +1 → -1 coherence transfer pathway. This leads to the differential evolution of two single-quantum coherences while the unknown spatially dependent frequency induced by the inhomogeneous B_0 field is eliminated by simple subtraction. As a result, the overall phase before detection is only dependent on the difference of precession frequency between the coupled spins and proportional to the spatial encoding constant. The J-coupling is then monitored during a UF detection scheme similar to the one used by Giraudeau *et al* for recording UF J-resolved spectra [159]. This leads to a map in which the J-coupling in F2 is correlated in F1 to the difference of chemical shifts from coupled spins. However, this F1 dimension that is reminiscent of a zero quantum (ZQ) evolution makes direct spectral assignments challenging and the uncoupled spins (singlets) are lacking. Further efforts were made to circumvent these drawbacks. In 2011, Chen and

coworkers proposed a new experiment, which combines a spatial encoding approach similar to the one described by Pelupessy with another coherence transfer scheme based on intermolecular zero-quantum coherences (i-ZQC) [160]. This leads to a 2D spectrum akin the common 2D-J-resolved with chemical shifts and J-coupling along two orthogonal dimensions (Figure 27). Relying on this strategy, Chen and collaborators applied UF NMR together with other i-MQC schemes leading to ultrafast intermolecular single-quantum coherences (UF i-SQC) [161,162] and ultrafast intermolecular double-quantum coherences (UF i-DQS) experiments [163]. Furthermore, the same research group extended this approach to 2D correlation spectroscopy. After mathematical manipulations of UF-SECSY (UltraFast Spin-Echo Spectroscopy) and SETOCSY (Spin-Echo TOCSY) data, they could obtain 2D COSY and TOCSY spectra in a single scan [164]. This method is suitable through linear inhomogeneities along the orientation of encoding and decoding gradients. Besides this work on homonuclear experiments, Zhang *et al* developed 2D heteronuclear correlation experiments based on distant dipolar field modulations and ultrafast acquisitions. This new class of pulse sequences is compatible with unknown spatial variations of the field [165].

This new set of homo or heteronuclear ultrafast 2D pulse sequences immune to B_0 heterogeneities could be combined in the near future with the 3D-localized version of UF experiments previously reported for 2D J-resolved [166] and COSY experiments [167]. This would open exciting opportunities in the field of ex / in-vivo spectroscopy. In this framework, a first step was taken by Chen and coworkers in reporting the acquisition of ex vivo localized 2D spectra in inhomogeneous biological tissues [168,169].

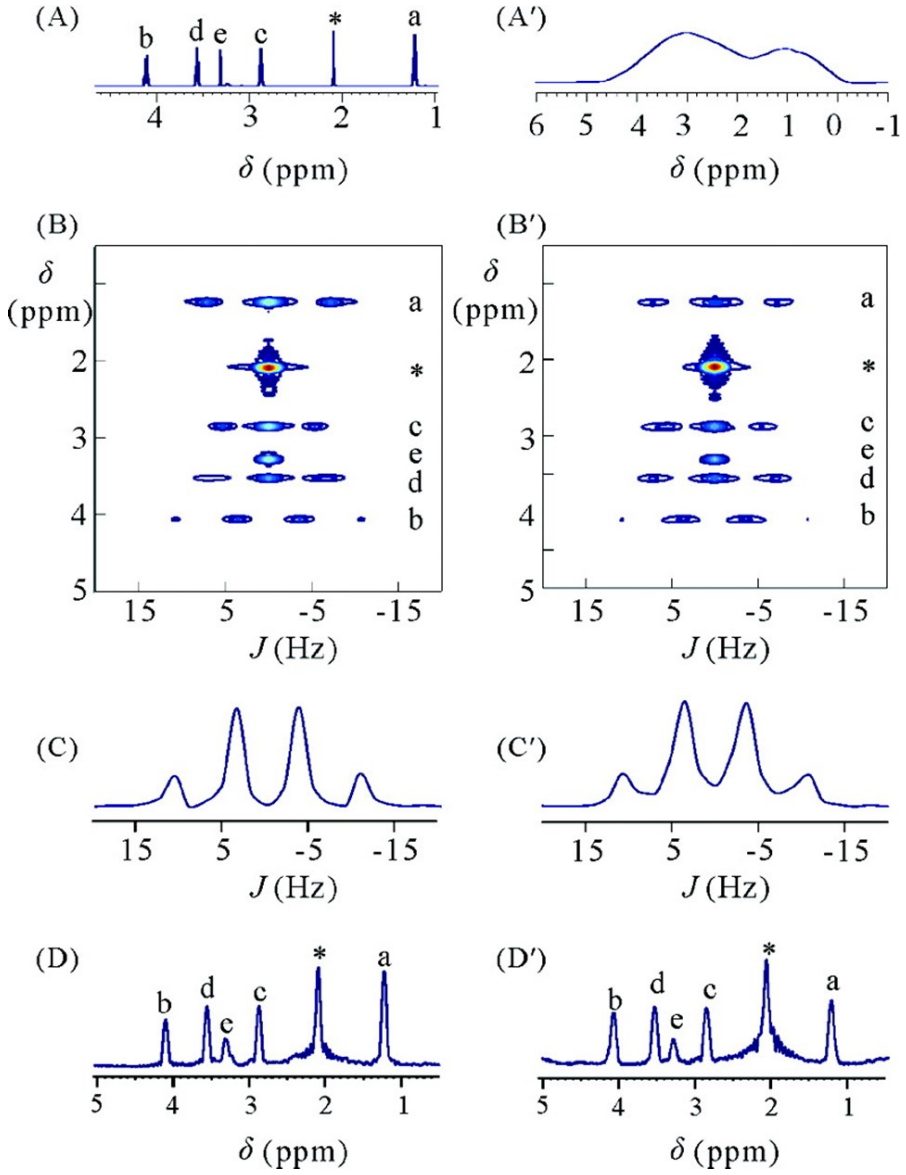

Figure 27. 2D J-resolved experiment in inhomogeneous fields combining spatial encoding and i-ZQC coherence transfer scheme. (A) Conventional 1D ^{1}H NMR spectrum of the solution of ethyl 3-bromopropionate and methanol in acetone recorded in a homogeneous field. The peaks with asterisk are solvent. (A') Same, but in the presence of ~3.6 ppm (or 1.8 kHz at 500 MHz) field inhomogeneity artificially introduced by detuning the spectrometer's $\{z_1,x_1,y_1\}$ shim coils. (B, B') 2D i-ZQC J-resolved spectra, obtained in the homogeneous and inhomogeneous B_0 fields, respectively. (C, C_0) Projections along the F2 dimension of the quadruplet at 4.16 ppm in (B) and (B_0) spectra, respectively. (D, D_0) Accumulated projections along the F1 dimension (chemical shift axis) from (B) and (B_0) spectra, respectively. The spectra are presented in magnitude mode. Reproduced from Ref. 160 with permission from American Chemical Society.

4. Conclusion

Thanks to methodological and analytical developments in the past fifteen years, the ultrafast nD NMR spectroscopy has emerged as a valuable alternative to its conventional counterpart. It has become an appealing solution for numerous applications, giving access to the monitoring of fast processes, unattainable in the conventional way. While single-scan experiments are characterized by a limited sensitivity compared to their conventional analogs and need some compromises between spectral widths, resolution and sensitivity, numerous hybrid multi-scan techniques have been developed to circumvent those limitations. Such hybrid experiments offer a reasonable acquisition time, short enough for numerous applications, particularly high throughput quantitative analysis such as metabolomics.

In addition to these developments and applications, new exciting perspectives arise from the association of ultrafast 2D experiments with D-DNP. In this case, each technique compensates for the limitations of the other: while ultrafast NMR circuvments the irreversible character of D-DNP, the latter overcomes the sensitivity limitation of the former.

Simultaneously to methodological and analytical developments, efforts have been geared towards the improvement of the UF techniques accessibility. These are essential to broaden the community of users among NMR spectroscopists and achieve a widespread use of this technique. The latest implementation protocol available proposed in this article further simplifies the implementation and use of UF experiments for non-specialists of this technique.

References:

[1] J. Jeener, Lecture Presented at Ampere International Summer School II, Basko Polje, Yugoslavia. (1971).

[2] L. Rouger, B. Gouilleux, P. Giraudeau, Fast n-Dimensional Data Acquisition Methods, in: J.C. Lindon, G.E. Tranter, D.W. Koppenaal (Eds.), Encyclopedia of Spectroscopy and Spectrometry (Third Edition), Academic Press, Oxford, 2017: pp. 588–596. doi:10.1016/B978-0-12-409547-2.12107-9.

[3] P. Schanda, Fast-pulsing longitudinal relaxation optimized techniques: Enriching the toolbox of fast biomolecular NMR spectroscopy, Prog. Nucl. Magn. Reson. Spectrosc. 55 (2009) 238–265. doi:10.1016/j.pnmrs.2009.05.002.

[4] D. Jeannerat, Computer optimized spectral aliasing in the indirect dimension of 1H-13C heteronuclear 2D NMR experiments. A new algorithm and examples of applications to small molecules., J. Magn. Reson. 186 (2007) 112–122.
[5] V.Y. Orekhov, V.A. Jaravine, Analysis of non-uniformly sampled spectra with multi-dimensional decomposition, Prog. Nucl. Magn. Reson. Spectrosc. 59 (2011) 271–292.
[6] E. Kupce, R. Freeman, Two-dimensional Hadamard spectroscopy, J. Magn. Reson. 162 (2003) 300–310.
[7] L. Frydman, T. Scherf, A. Lupulescu, The acquisition of multidimensional NMR spectra within a single scan, Proc. Natl. Acad. Sci. U.S.A. 99 (2002) 15858–15862.
[8] A. Tal, L. Frydman, Single-scan multidimensional magnetic resonance, Prog. Nucl. Magn. Reson. Spectrosc. 57 (2010) 241–292.
[9] M. Gal, L. Frydman, Multidimensional NMR spectroscopy in a single scan, Magn. Reson. Chem. 53 (2015) 971–985. doi:10.1002/mrc.4271.
[10] P. Giraudeau, L. Frydman, Ultrafast 2D NMR: An Emerging Tool in Analytical Spectroscopy, Annu. Rev. Anal. Chem. 7 (2014) 129–161.
[11] Y. Shrot, B. Shapira, L. Frydman, Ultrafast 2D NMR spectroscopy using a continuous spatial encoding of the spin interactions, J. Magn. Reson. 171 (2004) 163–170.
[12] A. Tal, B. Shapira, L. Frydman, A continuous phase-modulated approach to spatial encoding in ultrafast 2D NMR spectroscopy, J. Magn. Reson. 176 (2005) 107–114.
[13] P. Pelupessy, Adiabatic single scan two-dimensional NMR spectroscopy, J. Am. Chem. Soc. 125 (2003) 12345–12350.
[14] P. Mansfield, Multi-planar image formation using NMR spin echoes, J. Phys. C: Solid State Phys. 10 (1977) 55–58.
[15] P. Mansfield, P.G. Morris, NMR imaging in biomedicine, Academic Press, New-York, 1982.
[16] P. Giraudeau, S. Akoka, Resolution and sensitivity aspects of ultrafast J-resolved 2D NMR spectra, J. Magn. Reson. 190 (2008) 339–345.
[17] P. Giraudeau, S. Akoka, Sources of sensitivity losses in ultrafast 2D NMR, J. Magn. Reson. 192 (2008) 151–158.
[18] B. Gouilleux, L. Rouger, B. Charrier, I. Kuprov, S. Akoka, J.-N. Dumez, P. Giraudeau, Understanding J-Modulation during Spatial Encoding for Sensitivity-Optimized Ultrafast NMR Spectroscopy, ChemPhysChem. 16 (2015) 3093–3100. doi:10.1002/cphc.201500514.
[19] Y. Shrot, L. Frydman, Single-scan NMR spectroscopy at arbitrary dimensions, J. Am. Chem. Soc. 125 (2003) 11385–11396.
[20] P.D. Majors, J.L. Blackley, S.A. Altobelli, A. Caprihan, E. Fukushima, Eddy current compensation by direct field detection and digital gradient modification, J. Magn. Reson. 87 (1990) 548–553.
[21] Y. Shrot, L. Frydman, Spatial/spectral encoding of the spin interactions in ultrafast multidimensional NMR, J. Chem. Phys. 131 (2009) 224516.
[22] P. Giraudeau, Y. Shrot, L. Frydman, Multiple Ultrafast, Broadband 2D NMR Spectra of Hyperpolarized Natural Products, J. Am. Chem. Soc. 131 (2009) 13902–13903.
[23] A. Tal, B. Shapira, L. Frydman, Single-scan 2D Hadamard NMR spectroscopy, Angew. Chem. Int. Ed. 48 (2009) 2732–2736.
[24] P. Giraudeau, S. Akoka, A new gradient-controlled method for improving the spectral width of ultrafast 2D NMR experiments, J. Magn. Reson. 205 (2010) 171–176.

[25] L. Rouger, D. Loquet, S. Massou, S. Akoka, P. Giraudeau, Limitation of Diffusion Effects in Ultrafast 2D Nuclear Magnetic Resonance by Encapsulation of Analytes in Phospholipidic Vesicles, ChemPhysChem. 13 (2012) 4124–4127. doi:10.1002/cphc.201200622.
[26] P. Giraudeau, S. Akoka, Sensitivity losses and line shape modifications due to molecular diffusion in continuous encoding ultrafast 2D NMR experiments, J. Magn. Reson. 195 (2008) 9–16.
[27] G. Hamdoun, M. Sebban, V. Tognetti, A. Harrison-Marchand, L. Joubert, J. Maddaluno, H. Oulyadi, Alkyllithium Mixed Aggregates: Dynamic Behavior and Comprehensive Analysis of NMR 2J7Li–7Li Spin–Spin Coupling, Organometallics. 34 (2015) 1932–1941. doi:10.1021/acs.organomet.5b00162.
[28] G. Hamdoun, B. Gouilleux, M. Sebban, G. Barozzino-Consiglio, A. Harrison-Marchand, P. Giraudeau, J. Maddaluno, H. Oulyadi, 2D 7 Li Ultrafast CT-COSY: a new tool for the rapid measurement of tiny homonuclear lithium scalar couplings, Chem. Commun. 53 (2017) 220–223. doi:10.1039/C6CC08744B.
[29] S. Akoka, P. Giraudeau, Fast hybrid multi-dimensional NMR methods based on ultrafast 2D NMR, Magn. Reson. Chem. 53 (2015) 986–994.
[30] A. Le Guennec, I. Tea, I. Antheaume, E. Martineau, B. Charrier, M. Pathan, S. Akoka, P. Giraudeau, Fast determination of absolute metabolite concentrations by spatially-encoded 2D NMR: application to breast cancer cell extracts, Anal. Chem. 84 (2012) 10831–10837.
[31] M. Pathan, S. Akoka, I. Tea, B. Charrier, P. Giraudeau, Multi-scan single shot" quantitative 2D NMR: a valuable alternative to fast conventional quantitative 2D NMR, Analyst. 136 (2011) 3157–3163.
[32] L. Frydman, A. Lupulescu, T. Scherf, Principles and features of single-scan two-dimensional NMR spectroscopy, J. Am. Chem. Soc. 125 (2003) 9204–9217.
[33] L. Rouger, B. Charrier, M. Pathan, S. Akoka, P. Giraudeau, Processing strategies to obtain clean interleaved ultrafast 2D NMR spectra, J. Magn. Reson. 238 (2014) 87–93. doi:10.1016/j.jmr.2013.11.008.
[34] M. Andre, M. Piotto, S. Caldarelli, J.-N. Dumez, Ultrafast high-resolution magic-angle-spinning NMR spectroscopy, Analyst. 140 (2015) 3942–3946. doi:10.1039/c5an00653h.
[35] T. Jézéquel, C. Deborde, M. Maucourt, V. Zhendre, A. Moing, P. Giraudeau, Absolute quantification of metabolites in tomato fruit extracts by fast 2D NMR, Metabolomics. 11 (2015) 1231–1242. doi:10.1007/s11306-015-0780-0.
[36] L. Rouger, B. Gouilleux, M. Pourchet-Gellez, J.-N. Dumez, P. Giraudeau, Ultrafast double-quantum NMR spectroscopy with optimized sensitivity for the analysis of mixtures, Analyst. 141 (2016) 1686–1692. doi:10.1039/c6an00089d.
[37] P. Giraudeau, S. Akoka, Sensitivity and lineshape improvement in ultrafast 2D NMR by optimized apodization in the spatially encoded dimension, Magn. Reson. Chem. 49 (2011) 307–313. doi:10.1002/mrc.2746.
[38] R. Boisseau, U. Bussy, P. Giraudeau, M. Boujtita, In Situ Ultrafast 2D NMR Spectroelectrochemistry for Real-Time Monitoring of Redox Reactions, Anal. Chem. 87 (2015) 372–375.
[39] Z. Wei, J. Yang, L. Lin, G. Liu, Y. Lin, Z. Chen, Reverse detection for spectral width improvements in spatially encoded dimensions of ultrafast two-dimensional NMR spectra, Magn. Reson. Chem. 52 (2014) 680–685. doi:10.1002/mrc.4117.

[40] M. Mishkovsky, L. Frydman, Interlaced Fourier transformation of ultrafast 2D NMR data, J. Magn. Reson. 173 (2005) 344–350.
[41] Y. Shrot, L. Frydman, Compressed sensing and the reconstruction of ultrafast 2D NMR data: Principles and biomolecular applications, J. Magn. Reson. 209 (2011) 352–358.
[42] N. Sela, H. Degani, L. Frydman, Ultrafast 2D NMR spectroscopy using sinusoidal gradients: Principles and ex vivo brain investigations, Magn. Reson. Med. 52 (2004) 893–897. doi:10.1002/mrm.20204.
[43] Y. Shrot, L. Frydman, Ultrafast two-dimensional NMR spectroscopy using constant acquisition gradients, J. Chem. Phys. 125 (2006) 204507.
[44] M. Gal, L. Frydman, Ultrafast Multidimensional NMR: Principles and Practice of Single-scan Methods, in: G.A. Morris, J.W. Emsley (Eds.), Encyclopedia of Magnetic Resonance, Wiley, Chichester, 2010: pp. 43–60.
[45] L.H.K. Queiroz, A.G. Ferreira, P. Giraudeau, Optimization and practical implementation of ultrafast 2D NMR experiments, Quimica Nova. 36 (2013) 577-U143.
[46] A. Le Guennec, P. Giraudeau, S. Caldarelli, J.-N. Dumez, Ultrafast double-quantum NMR spectroscopy, Chem. Commun. 51 (2015) 354–357. doi:10.1039/c4cc07232d.
[47] R. Boisseau, B. Charrier, S. Massou, J.C. Portais, S. Akoka, P. Giraudeau, Fast Spatially Encoded 3D NMR Strategies for C-13-Based Metabolic Flux Analysis, Anal. Chem. 85 (2013) 9751–9757. doi:10.1021/ac402155w.
[48] J. Workman, M. Koch, B. Lavine, R. Chrisman, Process Analytical Chemistry, Anal. Chem. 81 (2009) 4623–4643. doi:10.1021/ac900778y.
[49] M.A. Bernstein, M. Štefinović, C.J. Sleigh, Optimising reaction performance in the pharmaceutical industry by monitoring with NMR, Magn. Reson. Chem. 45 (2007) 564–571. doi:10.1002/mrc.2007.
[50] I.M. Clegg, C.M. Gordon, D.S. Smith, R. Alzaga, A. Codina, NMR reaction monitoring during the development of an active pharmaceutical ingredient, Anal. Methods. 4 (2012) 1498–1506. doi:10.1039/c1ay05384a.
[51] F. Susanne, D.S. Smith, A. Codina, Kinetic Understanding Using NMR Reaction Profiling, Org. Process Res. Dev. 16 (2012) 61–64. doi:10.1021/op200202k.
[52] M. Maiwald, H.H. Fischer, Y.-K. Kim, K. Albert, H. Hasse, Quantitative high-resolution on-line NMR spectroscopy in reaction and process monitoring, J. Magn. Reson. 166 (2004) 135–146. doi:10.1016/j.jmr.2003.09.003.
[53] Y. Wu, C. D'Agostino, D.J. Holland, L.F. Gladden, In situ study of reaction kinetics using compressed sensing NMR, Chem. Commun. 50 (2014) 14137–14140. doi:10.1039/c4cc06051b.
[54] R. Dass, W. Koźmiński, K. Kazimierczuk, Analysis of Complex Reacting Mixtures by Time-Resolved 2D NMR, Anal. Chem. 87 (2015) 1337–1343. doi:10.1021/ac504114h.
[55] B. Shapira, L. Frydman, Arrayed acquisition of 2D exchange NMR spectra within a single scan experiment, J. Magn. Reson. 165 (2003) 320–324.
[56] M. Gal, M. Mishkovsky, L. Frydman, Real-time monitoring of chemical transformations by ultrafast 2D NMR spectroscopy, J. Am. Chem. Soc. 128 (2006) 951–956.
[57] A. Herrera, E. Fernández-Valle, R. Martínez-Álvarez, D. Molero-Vílchez, Z.D. Pardo-Botero, E. Sáez-Barajas, Monitoring organic reactions by UF-NMR spectroscopy, Magn. Reson. Chem. 53 (2015) 952–970. doi:10.1002/mrc.4240.
[58] A. Herrera, E. Fernández-Valle, R. Martínez-Álvarez, D. Molero, Z.D. Pardo, E. Sáez, M. Gal, Real-Time Monitoring of Organic Reactions with Two-Dimensional Ultrafast TOCSY NMR Spectroscopy13, Angew. Chem. Int. Ed. 48 (2009) 6274–6277.

[59] A. Herrera, E. Fernandez-Valle, E.M. Gutiérrez, R. Martinez-Alvarez, D. Molero, Z.D. Pardo, E. Saez, 2D Ultrafast HMBC : a valuable tool for monitoring organic reactions, Org. Lett. 12 (2010) 144–147.

[60] P. Giraudeau, P. Lemeunier, M. Coutand, J.-M. Doux, A. Gilbert, G.S. Remaud, S. Akoka, Ultrafast 2D NMR applied to the kinetic study of D-glucose mutarotation in solution, J. Spectrosc. Dyn. 1 (2011) 2.

[61] Z.D. Pardo, G.L. Olsen, M.E. Fernández-Valle, L. Frydman, R. Martínez-Álvarez, A. Herrera, Monitoring Mechanistic Details in the Synthesis of Pyrimidines via Real-Time, Ultrafast Multidimensional NMR Spectroscopy, J. Am. Chem. Soc. 134 (2012) 2706–2715.

[62] I. Fernández, M.E. Fernández-Valle, R. Martínez-Álvarez, D. Molero-Vílchez, Z.D. Pardo, E. Sáez-Barajas, Á. Sánchez, A. Herrera, Discovering Mechanistic Insights by Application of Tandem Ultrafast Multidimensional NMR Techniques, J. Org. Chem. 79 (2014) 8086–8093. doi:10.1021/jo5012834.

[63] L.H.K. Queiroz, P. Giraudeau, F.A.B. dos Santos, K.T. de Oliveira, A.G. Ferreira, Real-time mechanistic monitoring of an acetal hydrolysis using ultrafast 2D NMR, Magn. Reson. Chem. 50 (2012) 496–501. doi:10.1002/mrc.3827.

[64] M.E. Fernández-Valle, R. Martínez-Álvarez, D. Molero-Vílchez, Z.D. Pardo, E. Sáez-Barajas, A. Herrera, 2D Ultrafast HMBC 1H,31P: Obtaining Mechanistic Details on the Michaelis–Arbuzov Reaction, J. Org. Chem. 80 (2015) 799–805. doi:10.1021/jo502253p.

[65] B. Gouilleux, B. Charrier, E. Danieli, J.-N. Dumez, S. Akoka, F.-X. Felpin, M. Rodriguez-Zubiri, P. Giraudeau, Real-time reaction monitoring by ultrafast 2D NMR on a benchtop spectrometer, Analyst. 140 (2015) 7854–7858. doi:10.1039/c5an01998b.

[66] B. Gouilleux, B. Charrier, S. Akoka, F.-X. Felpin, M. Rodriguez-Zubiri, P. Giraudeau, Ultrafast 2D NMR on a benchtop spectrometer: Applications and perspectives, TrAC Trends Anal. Chem. 83, Part A (2016) 65–75. doi:10.1016/j.trac.2016.01.014.

[67] A. Kumar, J. Balbach, Real-time protein NMR spectroscopy and investigation of assisted protein folding, Biochim. Biophys. Acta. 1850 (2015) 1965–1972. doi:10.1016/j.bbagen.2014.12.003.

[68] P. Schanda, B. Brutscher, Very fast two-dimensional NMR spectroscopy for real-time investigation of dynamic events in proteins on the time scale of seconds, J. Am. Chem. Soc. 127 (2005) 8014–8015.

[69] M. Gal, P. Schanda, B. Brutscher, L. Frydman, UltraSOFAST HMQC NMR and the Repetitive Acquisition of 2D Protein Spectra at Hz Rates, J. Am. Chem. Soc. 129 (2007) 1372–1377. doi:10.1021/ja066915g.

[70] M. Gal, T. Kern, P. Schanda, L. Frydman, B. Brutscher, An improved ultrafast 2D NMR experiment: Towards atom-resolved real-time studies of protein kinetics at multi-Hz rates, J. Biomol. NMR. 43 (2009) 1–10. doi:10.1007/s10858-008-9284-9.

[71] M.-K. Lee, M. Gal, L. Frydman, G. Varani, Real-time multidimensional NMR follows RNA folding with second resolution, Proc. Natl. Acad. Sci. U.S.A. 107 (2010) 9192–9197.

[72] L.A. Cardoza, V.K. Almeida, A. Carr, C.K. Larive, D.W. Graham, Separations coupled with NMR detection, TrAC Trends Anal. Chem. 22 (2003) 766–775.

[73] O. Corcoran, M. Spraul, LC–NMR–MS in drug discovery, Drug Discov. Today. 8 (2003) 624–631. doi:10.1016/S1359-6446(03)02749-1.

[74] V. Exarchou, M. Krucker, T.A. van Beek, J. Vervoort, I.P. Gerothanassis, K. Albert, LC–NMR coupling technology: recent advancements and applications in natural products analysis, Magn. Reson. Chem. 43 (2005) 681–687. doi:10.1002/mrc.1632.

[75] Z. Zhou, W. Lan, W. Zhang, X. Zhang, S. Xia, H. Zhu, C. Ye, M. Liu, Implementation of real-time two-dimensional nuclear magnetic resonance spectroscopy for on-flow high-performance liquid chromatography, J. Chromatogr. A. 1154 (2007) 464–468. doi:10.1016/j.chroma.2007.04.018.

[76] B. Shapira, A. Karton, D. Aronzon, L. Frydman, Real-time 2D NMR identification of analytes undergoing continuous chromatographic separation, J. Am. Chem. Soc. 126 (2004) 1262–1265.

[77] L.H.K. Queiroz, D.P.K. Queiroz, L. Dhooghe, A.G. Ferreira, P. Giraudeau, Real-time separation of natural products by ultrafast 2D NMR coupled to on-line HPLC, Analyst. 137 (2012) 2357–2361. doi:10.1039/c2an16208c.

[78] M.S. Albert, G.D. Cates, B. Driehuys, W. Happer, B. Saam, C.S. Springer, A. Wishnia, Biological magnetic resonance imaging using laser-polarized 129Xe, Nature. 370 (1994) 199–201.

[79] G. Navon, Y.-Q. Song, T. Rõõm, S. Appelt, R.E. Taylor, A. Pines, Enhancement of Solution NMR and MRI with Laser-Polarized Xenon, Science. 271 (1996).

[80] R.A. Green, R.W. Adams, S.B. Duckett, R.E. Mewis, D.C. Williamson, G.G.R. Green, The theory and practice of hyperpolarization in magnetic resonance using parahydrogen, Prog. Nucl. Magn. Reson. Spectrosc. 67 (2012) 1–48. doi:10.1016/j.pnmrs.2012.03.001.

[81] J. Wolber, F. Ellner, B. Fridlund, A. Gram, H. Johannesson, G. Hansson, L.H. Hansson, M.H. Lerche, S. Mansson, R. Servin, M. Thaning, K. Golman, J.H. Ardenkjaer-Larsen, Generating highly polarized nuclear spins in solution using dynamic nuclear polarization, Nucl. Instr. and Meth. in Phys. Research, Section A: Accelerators, Spectrometers, Detectors and Associated Equipment. 526 (2004) 173–181.

[82] C. Griesinger, M. Bennati, H.M. Vieth, C. Luchinat, G. Parigi, P. Höfer, F. Engelke, S.J. Glaser, V. Denysenkov, T.F. Prisner, Dynamic nuclear polarization at high magnetic fields in liquids, Prog. Nucl. Magn. Reson. Spectrosc. 64 (2012) 4–28. doi:10.1016/j.pnmrs.2011.10.002.

[83] C.G. Joo, K.N. Hu, J.A. Bryant, R.G. Griffin, In Situ Temperature Jump High-Frequency Dynamic Nuclear Polarization Experiments: Enhanced Sensitivity in Liquid-State NMR Spectroscopy, J. Am. Chem. Soc. 128 (2006) 9428–9432. doi:10.1021/ja0611947.

[84] A. Krahn, P. Lottmann, T. Marquardsen, A. Tavernier, M.-T. Turke, M. Reese, A. Leonov, M. Bennati, P. Hoefer, F. Engelke, C. Griesinger, Shuttle DNP spectrometer with a two-center magnet, Phys. Chem. Chem. Phys. 12 (2010) 5830–5840. doi:10.1039/c003381b.

[85] J. Leggett, R. Hunter, J. Granwehr, R. Panek, A.J. Perez-Linde, A.J. Horsewill, J. McMaster, G. Smith, W. Kockenberger, A dedicated spectrometer for dissolution DNP NMR spectroscopy, Phys. Chem. Chem. Phys. 12 (2010) 5883–5892. doi:10.1039/c002566f.

[86] J.H. Ardenkjaer-Larsen, B. Fridlund, A. Gram, G. Hansson, L. Hansson, M.H. Lerche, R. Servin, M. Thaning, K. Golman, Increase in signal-to-noise ratio of >10,000 times in liquid state NMR, Proc. Natl. Acad. Sci. U.S.A. 100 (2003) 10158–10163.

[87] L. Frydman, D. Blazina, Ultrafast two-dimensional nuclear magnetic resonance spectroscopy of hyperpolarized solutions, Nat. Phys. 3 (2007) 415–419.

[88] M. Mishkovsky, L. Frydman, Progress in Hyperpolarized Ultrafast 2D NMR Spectroscopy, ChemPhysChem. 9 (2008) 2340–2348.

[89] A. Bornet, R. Melzi, A.J. Perez Linde, P. Hautle, B. van den Brandt, S. Jannin, G. Bodenhausen, Boosting Dissolution Dynamic Nuclear Polarization by Cross Polarization, J. Chem. Phys. Lett. 4 (2013) 111–114. doi:10.1021/jz301781t.

[90] J.-N. Dumez, J. Milani, B. Vuichoud, A. Bornet, J. Lalande-Martin, I. Tea, M. Yon, M. Maucourt, C. Deborde, A. Moing, L. Frydman, G. Bodenhausen, S. Jannin, P. Giraudeau, Hyperpolarized NMR of plant and cancer cell extracts at natural abundance, Analyst. 140 (2015) 5860–5863. doi:10.1039/c5an01203a.

[91] R. Panek, J. Granwehr, J. Leggett, W. Kockenberger, Slice-selective single scan proton COSY with dynamic nuclear polarisation, Phys. Chem. Chem. Phys. 2010 (2010) 5771–5778.

[92] A. Bornet, M. Maucourt, C. Deborde, D. Jacob, J. Milani, B. Vuichoud, X. Ji, J.-N. Dumez, A. Moing, G. Bodenhausen, S. Jannin, P. Giraudeau, Highly Repeatable Dissolution Dynamic Nuclear Polarization for Heteronuclear NMR Metabolomics, Anal. Chem. 88 (2016) 6179–6183. doi:10.1021/acs.analchem.6b01094.

[93] R.W. Adams, J.A. Aguilar, K.D. Atkinson, M.J. Cowley, P.I.P. Elliott, S.B. Duckett, G.G.R. Green, I.G. Khazal, J. López-Serrano, D.C. Williamson, Reversible Interactions with para-Hydrogen Enhance NMR Sensitivity by Polarization Transfer, Science. 323 (2009) 1708–1711. doi:10.1126/science.1168877.

[94] M.J. Cowley, R.W. Adams, K.D. Atkinson, M.C.R. Cockett, S.B. Duckett, G.G.R. Green, J.A.B. Lohman, R. Kerssebaum, D. Kilgour, R.E. Mewis, Iridium N-Heterocyclic Carbene Complexes as Efficient Catalysts for Magnetization Transfer from para-Hydrogen, J. Am. Chem. Soc. 133 (2011) 6134–6137. doi:10.1021/ja200299u.

[95] V. Daniele, F.-X. Legrand, P. Berthault, J.-N. Dumez, G. Huber, Single-Scan Multidimensional NMR Analysis of Mixtures at Sub-Millimolar Concentrations by using SABRE Hyperpolarization, ChemPhysChem. 16 (2015) 3413–3417. doi:10.1002/cphc.201500535.

[96] P. Giraudeau, Challenges and perspectives in quantitative NMR, Magn. Reson. Chem. 55 (2017) 61–69. doi:10.1002/mrc.4475.

[97] J.K. Kwakye, Use of NMR for quantitative analysis of pharmaceuticals, Talanta. 32 (1985) 1069–1071.

[98] U. Holzgrabe, Quantitative NMR spectroscopy in pharmaceutical applications, Prog. Nucl. Magn. Reson. Spectrosc. 57 (2010) 229–240.

[99] E. Tenailleau, P. Lancelin, R.J. Robins, S. Akoka, Authentication of the origin of vanillin using quantitative natural abundance 13C NMR, J. Agric. Food Chem. 52 (2004) 7782–7787.

[100] F. Le Grand, G. George, S. Akoka, Natural abundance 2H-ERETIC-NMR authentication of the origin of methyl salicylate, J. Agric. Food Chem. 53 (2005) 5125–5129.

[101] J.C. Lindon, J.K. Nicholson, E. Holmes, J.R. Everett, Metabonomics: Metabolic processes studied by NMR spectroscopy of biofluids, Concepts Magn. Reson. 12 (2000) 289–320. doi:10.1002/1099-0534(2000)12:5<289::aid-cmr3>3.0.co;2-w.

[102] D.S. Wishart, Quantitative metabolomics using NMR, TrAC Trends Anal. Chem. 27 (2008) 228–237.

[103] S. Zhang, G.A. Nagana Gowda, V. Asiago, N. Shanaiah, C. Barbas, D. Raftery, Correlative and quantitative 1H NMR-based metabolomics reveals specific metabolic pathway disturbances in diabetic rats, Anal. Biochem. 383 (2008) 76–84.

[104] L. Mannina, A.P. Sobolev, S. Viel, Liquid state 1H high field NMR in food analysis, Prog. Nucl. Magn. Reson. Spectrosc. 66 (2012) 1–39. doi:10.1016/j.pnmrs.2012.02.001.

[105] D. Castejón, I. Mateos-Aparicio, M.D. Molero, M.I. Cambero, A. Herrera, Evaluation and Optimization of the Analysis of Fatty Acid Types in Edible Oils by 1H-NMR, Food Anal. Methods. 7 (2014) 1285–1297. doi:10.1007/s12161-013-9747-9.

[106] P. Giraudeau, N. Guignard, E. Hillion, E. Baguet, S. Akoka, Optimization of homonuclear 2D NMR for fast quantitative analysis: application to tropine-nortropine mixtures, J. Pharm. Biomed. Anal. 43 (2007) 1243–8.
[107] H. Koskela, T. Väänänen, Quantitative determination of aliphatic hydrocarbon compounds by 2D NMR, Magn. Reson. Chem. 40 (2002) 705–715.
[108] H. Koskela, O. Heikkilä, I. Kilpeläinen, S. Heikkinen, Quantitative two-dimensional HSQC experiment for high magnetic field NMR spectrometers, J. Magn. Reson. 202 (2010) 24–33.
[109] H. Koskela, Quantitative 2D NMR studies, Annu. Rep. NMR Spectrosc. 66 (2009) 1–31.
[110] I.A. Lewis, S.C. Schommer, B. Hodis, K.A. Robb, M. Tonelli, W. Westler, M. Sussman, J.L. Markley, Method for determining molar concentrations of metabolites in complex solutions from two-dimensional 1H-13C NMR spectra, Anal. Chem. 79 (2007) 9385–9390.
[111] E. Martineau, P. Giraudeau, I. Tea, S. Akoka, Fast and precise quantitative analysis of metabolic mixtures by 2D 1H INADEQUATE NMR, J. Pharm. Biomed. Anal. 54 (2011) 252–257.
[112] E. Martineau, I. Tea, S. Akoka, P. Giraudeau, Absolute quantification of metabolites in breast cancer cell extracts by quantitative 2D 1H INADEQUATE NMR, NMR Biomed. 25 (2012) 985–992.
[113] E. Martineau, S. Akoka, R. Boisseau, B. Delanoue, P. Giraudeau, Fast quantitative 1H-13C 2D NMR with very high precision, Anal. Chem. 85 (2013) 4777–4783.
[114] W. Gronwald, M.S. Klein, H. Kaspar, S.R. Fagerer, N. Nurnberger, K. Dettmer, T. Bertsch, P.J. Oefner, Urinary Metabolite Quantification Employing 2D NMR Spectroscopy, Anal. Chem. 80 (2008) 9288–9297.
[115] F. Hu, K. Furihata, Y. Kato, M. Tanokura, Nondestructive quantification of organic compounds in whole milk without pretreatment by two-dimensional NMR spectroscopy, J. Agric. Food Chem. 55 (2007) 4307–4311.
[116] A.F. Mehlkopf, D. Korbee, T.A. Tiggelman, R. Freeman, Sources of t1 noise in two-dimensional NMR, J. Magn. Reson. 58 (1984) 315–323.
[117] G.A. Morris, Systematic sources of signal irreproducibility and t1 noise in high field NMR spectrometers, J. Magn. Reson. 100 (1992) 316–328.
[118] P. Giraudeau, S. Akoka, Fast and ultrafast quantitative 2D NMR: vital tools for efficient metabolomic approaches, Adv. Bot. Res. 67 (2013) 99–158.
[119] P. Giraudeau, G.S. Remaud, S. Akoka, Evaluation of Ultrafast 2D NMR for Quantitative Analysis, Anal. Chem. 81 (2009) 479–484.
[120] N.J. Kruger, M.A. Troncoso-Ponce, R.G. Ratcliffe, 1H NMR metabolite fingerprinting and metabolomic analysis of perchloric acid extracts from plant tissues, Nat. Protoc. 3 (2008) 1001–1012.
[121] G. Le Gall, I.J. Colquhoun, A.L. Davis, G.J. Collins, M.E. Verhoeyen, Metabolite Profiling of Tomato (Lycopersicon esculentum) Using 1H NMR Spectroscopy as a Tool To Detect Potential Unintended Effects Following a Genetic Modification, J. Agric. Food Chem. 51 (2003) 2447–2456.
[122] A.M. Weljie, J. Newton, P. Mercier, E. Carlson, C.M. Slupsky, Targeted Profiling: Quantitative Analysis of 1H NMR Metabolomics Data, Anal. Chem. 78 (2006) 4430–4442.
[123] S. Massou, C. Nicolas, F. Letisse, J.-C. Portais, NMR-based fluoxomics: Quantitative 2D NMR methods for isotopomers analysis, Phytochemistry. 68 (2007) 2330–2340.

[124] S. Massou, C. Nicolas, F. Letisse, J.-C. Portais, Application of 2D-TOCSY NMR to the measurement of specific 13C-enrichments in complex mixtures of 13C-labeled metabolites, Metab. Eng. 9 (2007) 252–257.
[125] P. Giraudeau, S. Massou, Y. Robin, E. Cahoreau, J.C. Portais, S. Akoka, Ultrafast Quantitative 2D NMR: An Efficient Tool for the Measurement of Specific Isotopic Enrichments in Complex Biological Mixtures, Anal. Chem. 83 (2011) 3112–3119. doi:10.1021/ac200007p.
[126] R.L. Vold, J.S. Waugh, M.P. Klein, D.E. Phelps, Measurement of spin relaxation in complex systems, J. Chem. Phys. 48 (1968) 3831–3832.
[127] R.J. Kurland, R.G. Parrish, The half-wave triplet pulse sequence for determination of longitudinal relaxation rates of single line spectra, J. Magn. Reson. 17 (1975) 295–300. doi:10.1016/0022-2364(75)90194-8.
[128] H.T. Edzes, An analysis of the use of pulse multiplets in the single scan determination of spin-lattice relaxation rates, J. Magn. Reson. 17 (1975) 301–313. doi:10.1016/0022-2364(75)90195-X.
[129] N.M. Loening, M.J. Thrippleton, J. Keeler, R.G. Griffin, Single-scan longitudinal relaxation measurements in high-resolution NMR spectroscopy, J. Magn. Reson. 164 (2003) 321–328. doi:10.1016/S1090-7807(03)00186-1.
[130] R. Bhattacharyya, A. Kumar, A fast method for the measurement of long spin-lattice relaxation times by single scan inversion recovery experiment, Chem. Phys. Lett. 383 (2004) 99–103.
[131] P.E.S. Smith, K.J. Donovan, O. Szekely, M. Baias, L. Frydman, Ultrafast NMR T1 Relaxation Measurements: Probing Molecular Properties in Real Time, ChemPhysChem. 14 (2013) 3138–3145. doi:10.1002/cphc.201300436.
[132] H. Barjat, G.A. Morris, S. Smart, A.. Swanson, S.C.R. Williams, High-resolution diffusion-ordered spectroscopy (HR-DOSY) - A new tool for the analysis of complex mixtures, J. Magn. Reson. Ser. B. 108 (1995) 170–172.
[133] M.D. Pelta, G.A. Morris, M.J. Stchedroff, S.J. Hammond, A one-shot sequence for high-resolution diffusion-ordered spectroscopy, Magn. Reson. Chem. 40 (2002) S147–S152. doi:10.1002/mrc.1107.
[134] M. Urbańczyk, W. Koźmiński, K. Kazimierczuk, Accelerating Diffusion-Ordered NMR Spectroscopy by Joint Sparse Sampling of Diffusion and Time Dimensions, Angew. Chem. Int. Ed. 126 (2014) 6582–6585. doi:10.1002/ange.201402049.
[135] N.M. Loening, J. Keeler, G.A. Morris, One-Dimensional DOSY, J. Magn. Reson. 153 (2001) 103–112. doi:10.1006/jmre.2001.2423.
[136] Y. Shrot, L. Frydman, Single-scan 2D DOSY NMR spectroscopy, J. Magn. Reson. 195 (2008) 226–231. doi:10.1016/j.jmr.2008.09.011.
[137] L. Guduff, I. Kuprov, C. van Heijenoort, J.-N. Dumez, Spatially encoded 2D and 3D diffusion-ordered NMR spectroscopy, Chem. Commun. 53 (2017) 701–704. doi:10.1039/c6cc09028a.
[138] S. Godefroy, P.T. Callaghan, 2D relaxation/diffusion correlations in porous media, Magn. Reson. Imaging. 21 (2003) 381–383. doi:10.1016/S0730-725X(03)00144-9.
[139] S. Ahola, V.-V. Telkki, Ultrafast Two-Dimensional NMR Relaxometry for Investigating Molecular Processes in Real Time, ChemPhysChem. 15 (2014) 1687–1692. doi:10.1002/cphc.201301117.

[140] S. Ahola, V.V. Zhivonitko, O. Mankinen, G. Zhang, A.M. Kantola, H.-Y. Chen, C. Hilty, I.V. Koptyug, V.-V. Telkki, Ultrafast multidimensional Laplace NMR for a rapid and sensitive chemical analysis, Nat. Commun. 6 (2015) 8363. doi:10.1038/ncomms9363.
[141] J.N. King, V.J. Lee, S. Ahola, V.-V. Telkki, T. Meldrum, Ultrafast Multidimensional Laplace NMR Using a Single-Sided Magnet, Angew. Chem. Int. Ed. 128 (2016) 5124–5127. doi:10.1002/ange.201511859.
[142] S.D. Wolff, R.S. Balaba, NMR imaging of labile proton exchange, J. Magn. Reson. 86 (1990) 164–169.
[143] X. Xu, J.-S. Lee, A. Jerschow, Ultrafast Scanning of Exchangeable Sites by NMR Spectroscopy, Angew. Chem. Int. Ed. 52 (2013) 8281–8284. doi:10.1002/anie.201303255.
[144] J. Döpfert, C. Witte, L. Schröder, Slice-selective gradient-encoded CEST spectroscopy for monitoring dynamic parameters and high-throughput sample characterization, J. Magn. Reson. 237 (2013) 34–39. doi:10.1016/j.jmr.2013.09.007.
[145] X. Xu, N.N. Yadav, X. Song, M.T. McMahon, A. Jerschow, P.C.M. van Zijl, J. Xu, Screening CEST contrast agents using ultrafast CEST imaging, J. Magn. Reson. 265 (2016) 224–229. doi:10.1016/j.jmr.2016.02.015.
[146] J. Döpfert, C. Witte, L. Schröder, Fast Gradient-Encoded CEST Spectroscopy of Hyperpolarized Xenon, ChemPhysChem. 15 (2014) 261–264. doi:10.1002/cphc.201300888.
[147] C. Boutin, E. Léonce, T. Brotin, A. Jerschow, P. Berthault, Ultrafast Z-Spectroscopy for 129Xe NMR-Based Sensors, J. Phys. Chem. Lett. 4 (2013) 4172–4176. doi:10.1021/jz402261h.
[148] Z. Liu, I.E. Dimitrov, R.E. Lenkinski, A. Hajibeigi, E. Vinogradov, UCEPR: Ultrafast localized CEST-spectroscopy with PRESS in phantoms and in vivo, Magn. Reson. Med. 75 (2016) 1875–1885. doi:10.1002/mrm.25780.
[149] P. Giraudeau, T. Montag, B. Charrier, C.M. Thiele, Fast access to residual dipolar couplings by single-scan 2D NMR in oriented media, Magn. Reson. Chem. 50 (2012) S53–S57. doi:10.1002/mrc.3856.
[150] P. Lesot, P. Berdagué, P. Giraudeau, Detection of quadrupolar nuclei by ultrafast 2D NMR: exploring the case of deuterated analytes aligned in chiral oriented solvents, Chem. Commun. 52 (2016) 2122–2125. doi:10.1039/C5CC09409G.
[151] M. Chan-Huot, P. Lesot, P. Pelupessy, L. Duma, G. Bodenhausen, P. Duchambon, M.D. Toney, U.V. Reddy, N. Suryaprakash, “On-the-Fly” Kinetics of Enzymatic Racemization Using Deuterium NMR in DNA-Based Chiral Oriented Media, Anal. Chem. 85 (2013) 4694–4697. doi:10.1021/ac4004002.
[152] L. Rouger, M. Yon, V. Sarou-Kanian, F. Fayon, J.-N. Dumez, P. Giraudeau, Ultrafast acquisition of 1H-1H dipolar correlation experiments in spinning elastomers, J. Magn. Reson. 277 (2017) 30–35. doi:10.1016/j.jmr.2017.02.005.
[153] Z. Chen, S. Cai, Y. Huang, Y. Lin, High-resolution NMR spectroscopy in inhomogeneous fields, Prog. Nucl. Magn. Reson. Spectrosc. 90 (2015) 1–31. doi:10.1016/j.pnmrs.2015.05.003.
[154] Y. Huang, S. Cao, Y. Yang, S. Cai, H. Zhan, C. Tan, L. Lin, Z. Zhang, Z. Chen, Ultrahigh-Resolution NMR Spectroscopy for Rapid Chemical and Biological Applications in Inhomogeneous Magnetic Fields, Anal. Chem. 89 (2017) 7115–7122. doi:10.1021/acs.analchem.7b01036.
[155] S. Vathyam, S. Lee, W.S. Warren, Homogeneous NMR Spectra in Inhomogeneous Fields, Science. 272 (1996) 92–96. doi:10.1126/science.272.5258.92.

[156] C.A. Meriles, D. Sakellariou, H. Heise, A.J. Moulé, A. Pines, Approach to High-Resolution ex Situ NMR Spectroscopy, Science. 293 (2001) 82–85. doi:10.1126/science.1061498.
[157] J. Perlo, F. Casanova, B. Blümich, Ex Situ NMR in Highly Homogeneous Fields: 1H Spectroscopy, Science. 315 (2007) 1110–1112. doi:10.1126/science.1135499.
[158] P. Pelupessy, E. Renella, G. Bodenhausen, High-Resolution NMR in Magnetic Fields with Unknown Spatiotemporal Variations, Science. 324 (2009) 1693–1697.
[159] P. Giraudeau, S. Akoka, A new detection scheme for ultrafast 2D J-resolved spectroscopy, J. Magn. Reson. 186 (2007) 352–7.
[160] Y. Lin, Z. Zhang, S. Cai, Z. Chen, High-Resolution 2D J-Resolved Spectroscopy in Inhomogeneous Fields with Two Scans, J. Am. Chem. Soc. 133 (2011) 7632–7635. doi:10.1021/ja1113479.
[161] H.-H. Cai, H. Chen, Y.-L. Lin, J.-H. Feng, X.-H. Cui, Z. Chen, Feasibility of Ultrafast Intermolecular Single-Quantum Coherence Spectroscopy in Analysis of Viscous-Liquid Foods, Food Anal. Methods. 8 (2015) 1682–1690. doi:10.1007/s12161-014-0046-x.
[162] Y. Lin, Z. Zhang, S. Cai, Z. Chen, Spatially-encoded intermolecular single-quantum coherence method for high-resolution NMR spectra in inhomogeneous fields, Chem. Phys. Lett. 634 (2015) 11–15. doi:10.1016/j.cplett.2015.05.030.
[163] K.-Y. Wang, H. Chen, Z.-Y. Zhang, Y.-Q. Huang, Z. Chen, Two-Dimensional J-Resolved NMR Analyses of Fish and Its Products via Spatially Encoded Intermolecular Double-Quantum Coherences, Food Anal. Methods. 9 (2016) 1502–1511. doi:10.1007/s12161-015-0334-0.
[164] Z. Zhang, H. Chen, C. Wu, R. Wu, S. Cai, Z. Chen, Spatially encoded ultrafast high-resolution 2D homonuclear correlation spectroscopy in inhomogeneous fields, J. Magn. Reson. 227 (2013) 39–45. doi:10.1016/j.jmr.2012.11.020.
[165] Z. Zhang, Y. Huang, P.E.S. Smith, K. Wang, S. Cai, Z. Chen, High-resolution heteronuclear multi-dimensional NMR spectroscopy in magnetic fields with unknown spatial variations, J. Magn. Reson. 242 (2014) 49–56. doi:10.1016/j.jmr.2014.02.009.
[166] T. Roussel, P. Giraudeau, H. Ratiney, S. Akoka, S. Cavassila, 3D localized 2D ultrafast J-resolved magnetic resonance spectroscopy: In vitro study on a 7T imaging system, J. Magn. Reson. 215 (2012) 50–65.
[167] Y. Lin, Q. Zhang, Z. Wei, S. Cai, J. Zhong, Z. Chen, Ultrafast localized two-dimensional magnetic resonance correlated spectroscopy via spatially encoded technique, Magn. Reson. Med. 71 (2014) 903–910. doi:10.1002/mrm.24731.
[168] Z. Wei, L. Lin, Y. Lin, S. Cai, Z. Chen, Ultrafast acquisition of localized two-dimensional magnetic resonance correlated spectra of inhomogeneous biological tissues with resolution improvements, Chem. Phys. Lett. 581 (2013) 96–102. doi:10.1016/j.cplett.2013.07.015.
[169] Z. Wei, L. Lin, C. Wang, J. Yang, G. Liu, J. Zhong, Y. Lin, Z. Chen, High-resolution localized spatiotemporal encoding correlated spectra under inhomogeneous magnetic fields via asymmetrical gradient encoding/decoding, NMR Biomed. 28 (2015) 210–216. doi:10.1002/nbm.3241.

B. Outline of the thesis

1. Purpose of the thesis

The new generation of compact and permanent magnets is a breakthrough in the field of LF NMR. Their high degree of homogeneity leads to sharp peaks with a line width typically < 1 Hz and thereby offering a sufficient resolution to characterize small molecules (see section A.1.2) However, the situation becomes more complex when medium-sized molecules or mixtures are probed, involving crowded ^{1}H spectra (see section A.1.3). This is even truer if a non-deuterated solvent is used. It should be noted that these current limits are intrinsic with the use of a low magnetic field and will remain as long as the permanent magnets provide magnetic fields < 2 T.

To go further and use benchtop NMR to probe reactive mixtures or relative complex samples, researchers have often hyphenated 1D ^{1}H NMR experiments with deconvolution methods and/or chemometric tools to extract relevant information from overcrowded spectra. Another way would be to improve the analytical performance at the stage of the acquisition. Indeed, a large panel of sophisticated experiments have been developed in HF NMR, which enable, for instance, the acquisition of 2D spectra with a high time resolution as described in section A.4.

Yet, these aforementioned methods were not implemented on benchtop apparatus at the beginning of this PhD work, and researchers rather use 1D ^{1}H NMR supported by post acquisition treatments (devolution, chemometric) as illustrated by tables II and III from section A.2. This may be because the implementation of these modern methods is not straightforward on a benchtop system. Indeed, many of them require a specific hardware, *i.e.* a powerful gradient coil which is not yet routinely available on benchtop spectrometers. Moreover, the implementation of tailored pulse-sequences as well as the use of selective pulses and pulse with linear frequency swept (chirp pulses) is not possible with most of commercial software provided with LF instruments.

Relying on a prototype benchtop NMR spectrometer equipped with a gradient coil, the present thesis aims to implement gradient-based methods, especially ultrafast 2D NMR (see section A.4.2 and A.4.3) and modern solvent suppression methods on such a LF instrument.

To conduct these objectives, the thesis is positioned within the “ResoNantes” project, which is described in the following section.

2. “ResoNantes” project

The “ResoNantes” project is funded by Région Pays de la Loire and carried out in the EBSI (Elucidation de Biosynthèse par Spectrométries Isotopiques) team within the CEISAM laboratory (Chimie Et Interdisciplinarités: Synthèse, Analyse et Modélisation) at the University of Nantes. This project, started in 2014, aims to implement advanced gradient-based NMR methods on benchtop apparatus to improve its analytical performance and to extend its scope of applications.

Based on a collaboration with Magritek (Aachen, Germany), the first benchtop NMR spectrometer equipped with a gradient coil has been designed. This hardware development is a cornerstone for the implementation of ultrafast 2D NMR as well as of tailored solvent suppression methods. Besides this prototype, an alternative interface to the normal Spinsolve software is provided. This programming interface, built on the Prospa language, allows, among other things, to generate chirp pulses and to code home-written scripts to process data from ultrafast experiments.

This project is conducted in three stages. The first one consists of a theoretical analysis of UF 2D NMR based on a product operator description and numerical simulations to optimize the performance of this spatially encoded method and to anticipate the spin response at low-field. This first step – carried out at high-field - has led to J-controlled UF 2D NMR, which has enabled UF sensitivity-optimized COSY and double quantum experiments as well as the accurate measurement of sub-Hertz J-couplings. The second one consists in implementing the UF methodology on the prototype benchtop device and more generally, in implementing gradient-based methods that would be relevant in the LF framework. Based on this methodological effort, practical applications are conducted in the last stage, especially in collaboration with the CORAIL team (Catalysis, ORganometallic chemistry And synthesIs of Ligands) in the CEISAM laboratory whose organic chemists are expert in catalytic chemistry and in organic synthesis with flow devices. Thus, the potential of these gradient-based

methods has been evaluated through several reaction monitoring, which have been carried out with different settings. Moreover, the ability to record fast 2D spectra has urged us to investigate their potential for high-throughput screening applications.

3. Material

3.1. Prototype benchtop NMR instrument

The experiments performed at low field were recorded on a customized Spinsolve (Magritek, Aachen, Germany) operating at a frequency of 43 MHz via a permanent magnet based on a Hallbach design (see section A.1.1). Through the collaboration with Magritek, this equipment includes a gradient coil along the B_0-axis (i.e. along the transverse plane of the NMR tube) which can generate a maximum field gradient of 0.16 $T.m^{-1}$. This compact spectrometer – total volume: 60 cm x 40 cm x 43 cm and weight: 55 kg - includes a simple channel ^{1}H, ^{19}F. This instrument is designed to work with standard 5 mm (outer-diameter) NMR tube. An external lock system is also included so that the use of deuterated solvents is not required. Finally, this benchtop device is plugged with a standard power cable and connected in USB with a computer.

3.2. Software and programming interface.

The Spinsolve commercial software is available with the benchtop instrument. This interface designed and adapted for non-expert users includes “press-button” 1D and 2D NMR experiments: 1D ^{1}H, 1D ^{19}F, ^{1}H-^{1}H COSY and ^{1}H J-resolved as well as T_1 and T_2 measurements achieved by IR and CPMG respectively. Moreover, the Spinsolve software provides automatic shimming algorithms.

This software is well suited for routine applications by non-expert users. Yet, all the acquisition parameters are not tunable and this interface does not allow pulse-programming, which is a poor starting point for methodological developments. Through the collaboration with Magritek, a programming interface has been made available to us. This interface, built on Prospa language (general purpose script based application which has been used by Magritek to provide different interfaces for its spectrometers) enables:

- Full access to pulse-program parameters
- Pulse programming capabilities
- The design of shaped pulses and chirp pulses
- A scripting language to control the experiment, process and save the data.
- 1D and 2D processing and display facilities.

The implementation of ultrafast 2D NMR (acquisition and processing) and solvent suppression methods has been achieved via this programming interface.

3.3. Shimming procedure

Besides the mechanical shimming performed on the Halbach magnet, the fine field correction required to reach sub-Hertz resolution is achieved by finely tuning the current of a set of electrical shim coils. This is automatically achieved on a reference NMR tube (H_2O/D_2O) and via algorithms available in the Spinsolve software. Different routines are proposed depending on the starting line width. In practice, we run a "Quickshim" (about 5 min) every morning and a "Powershim" (near 45 min) if the benchtop system has been moved. A line width characterized by a FWHM < 0.6 Hz has been typically obtained with such a procedure.

3.4. Flow measurements setup

Flow measurements have been carried out thanks to a kit furnished by Magritek. This consists of a specially designed glass flow cell, a peristaltic pump and PEEK tubing. The glass flow cell has an outer diameter of 5 mm at the sensitive volume of the magnet to maximize the sensitivity. To avoid the formation of vortices, the inner diameter of the glass cell increases gradually from 1 to 4 mm over a transition region of about 10 mm in length. In a similar way, the diameter of the cell gets reduced after the sensitive volume to shorten the flow time after the NMR experiment. A scheme of such a flow cell is proposed in figure A.15 (section A.3). The active sample volume V_s defined by the RF coil is about 60 µL while the pre-polarization V_p volume is roughly 370 µL. No appreciable line distortions were observed under static conditions compared with a conventional 5 mm NMR tube.

C. Methodological Developments

1. J-controlled UF 2D NMR

1.1. Constant time experiment and J-modulation

The first methodological work of this PhD was a theoretical investigation of UF experiments in order to pursue the studies already conducted in our laboratory to track the sources of sensitivity losses in UF 2D NMR and to anticipate the behaviour of UF 2D NMR at low magnetic field.

As described in the literature review, the continuous spatial encoding can be achieved in three different manners: by amplitude-modulation (AM), phase modulation (PM) or by constant time phase-modulation (CT PM) (see section A.4.3). In what follows, the latter was used to perform all the UF experiments since it offers the best compromise between sensitivity and resolution. The expression “constant time” means that all the spins spend the same evolution time in the transverse plane, alike conventional constant time experiments such as CT COSY. As a result, the UF CT PM experiments exhibit similar properties to their conventional counterparts. An important feature is the strong and complex impact of J-couplings on 2D peak intensities. This J-modulation effect had been poorly investigated in the UF CT PM experiments whilst it is a potential source of sensitivity losses. The following section - based on a research article – attempts to address this feature.

1.2. Description and optimizations of the J-modulation effect in UF 2D NMR

Understanding J-modulation during spatial encoding for sensitivity-optimized ultrafast NMR

Boris Gouilleux, Laetitia Rouger, Benoît Charrier, Ilya Kuprov, Serge Akoka,

Jean-Nicolas Dumez and Patrick Giraudeau

(Original research article)

ChemPhysChem, 16 (2015) 3093-3100.

Abstract

Ultrafast (UF) NMR is an approach yielding 2D spectra within a single scan. This methodology has become a powerful analytical tool used in a large array of applications. However, UF NMR still suffers from an intrinsic low sensitivity, and from the need to compromise between sensitivity, spectral width and resolution. In particular, the modulation of signal intensities by the spin-spin J-coupling interaction (J-modulation) impacts significantly the intensities of the spectral peaks. This effect can lead to large sensitivity losses and even to missing spectral peaks depending on the nature of the spin system. We used a general simulation package (Spinach) to describe J-modulation effects in UF experiments. The results from simulations match with experimental data and the results of product operator calculations. Several methods are proposed to optimize the sensitivity in UF COSY spectra. The potential and drawbacks of the different strategies are discussed. These approaches provide a way to adjust the sensitivity of UF experiments for a large range of applications.

Introduction

Two dimensional nuclear magnetic resonance (2D NMR) spectroscopy is a powerful analytical tool used in a wide array of applications like structure elucidation, quantitative analysis, or metabolomics.[1] Conventional 2D NMR experiments suffer from an intrinsic long experiment duration, which is necessary to obtain the indirect dimension by repeating numerous transients with incremented delays. This long acquisition duration makes conventional 2D NMR sensitive to hardware instabilities in the course of the experiment, and unsuitable for the study of fast processes or the coupling with other techniques.[2] A large number of methods have been proposed to cope with this time limitation. Some of these approaches consist in optimizing recovery delays and pulse angles, such as the SOFAST (ref. [3]), BEST (ref. [4]) or ASAP (ref. [5]) approaches. Several other strategies have been developed to improve the length of 2D experiments by reducing the number of t_1 increments, the subsequent resolution losses being compensated by adapted signal processing methods.[6] Others are based on an alternative to Fourier transform (FT) NMR, such as Hadamard spectroscopy.[7] A decade ago, Frydman and co-workers developed a new generic multidimensional approach, Ultrafast (UF) NMR, yielding homo-or heteronuclear 2D spectra within a single scan.[8] In this method, the incrementation of the evolution period t_1 is replaced by a spatial encoding scheme. After a conventional mixing period, the spatially encoded information is decoded by a detection block based on Echo Planar Spectroscopic Imaging (ESPI).[9] At the heart of this methodology, the spatial encoding step is generally performed in a continuous fashion thanks to a combination of bipolar gradients and linearly frequency-swept pulses.[10] In particular, the phase-modulated encoding block using a double spin echo scheme has been established as the optimum compromise between sensitivity and resolution.[11]

Since its performance has been significantly improved during the last decade, UF NMR is nowadays an efficient method applied in numerous fields such as metabolomics, real-time reaction monitoring or hyphenated techniques such as chromatography and dissolution DNP.[12] However, in spite of its high potential, this approach still suffers from an intrinsic low sensitivity, and from the need to compromise between sensitivity, spectral width and resolution,[13] even if several strategies have been proposed to alleviate this compromise.[14] There are several reasons for these sensitivity losses, such as the need to record the signal in the presence of strong gradients, leading to large digital filter bandwidths impacting the

signal-to-noise ratio (SNR), or the effect of translational molecular diffusion during spatial encoding.[15]

A significant source of sensitivity losses in ultrafast NMR is the effect of spin-spin scalar couplings (J couplings) during the spatial encoding step. Since most UF experiments rely on an encoding step in which all spins spend an equal amount of time in the transverse plane, a so-called "constant time" approach, the intensity of the detected signals is modulated by J couplings in a complex, spin-system-dependent way. This "J-modulation" effect is well described in the case of conventional constant time experiments[16] but it remains poorly understood for ultrafast experiments that rely on spatial encoding. Since J-modulation can lead to large SNR losses and even to missing spectral peaks, there is a motivation to develop tools for its understanding and control, which may result in ways to optimize the signal to noise ratio of UF experiments. We propose here a description of J-modulation effects in a large range of spin systems in order to predict their impact on sensitivity. For that, we first rely on a theoretical description, then on numerical simulations for more complicated spin systems with strong couplings. The calculated J-modulation effects are also compared to experimental results, and finally used to optimize the sensitivity in a variety of situations.

Theory

Pulse sequence

In order to evaluate the impact of J-modulation on the signal of constant time UF experiments, we introduce in this section a theoretical description using the product-operator formalism. We focus here on the case of the UF CT-COSY, one of the most widely used UF experiments, which relies on a CT phase-modulated spatial encoding. This double spin echo method starts with a hard 90° pulse, followed by the application of a pair of 180° chirp pulses applied during alternating gradients (Fig. 1A). The constant time nature of this scheme is due to the identical time spent in the transverse plane by all the spins regardless of theirs position along the z-axis. A theoretical description of this pulse sequence applied to a system of two coupled spins has been already proposed by Wu *et al*.[17] who established an expression of the density matrix at the beginning of detection, showing a J-modulation that is different for the diagonal peak (cosine modulation) and for the cross peak (sine modulation). It is also demonstrated

that this modulation depends on the scalar coupling constant J and on the total time T spent in the transverse plan. In practice, this J-modulation can be modified by adding a new delay called t_{mix} prior to the spatial encoding step, which allows to control the total time spent by the spins in the transverse plane (Fig. 1A). Given the trigonometric nature of the J-modulation, there is an optimal t_{mix} value, which maximizes the sensitivity depending on the spin system and on the coupling constant. As J-modulation effects in more complex spin systems is not described in the study of Wu et al., it is necessary to extend this initial description to a more general $A_N M_P X_Q$ system.

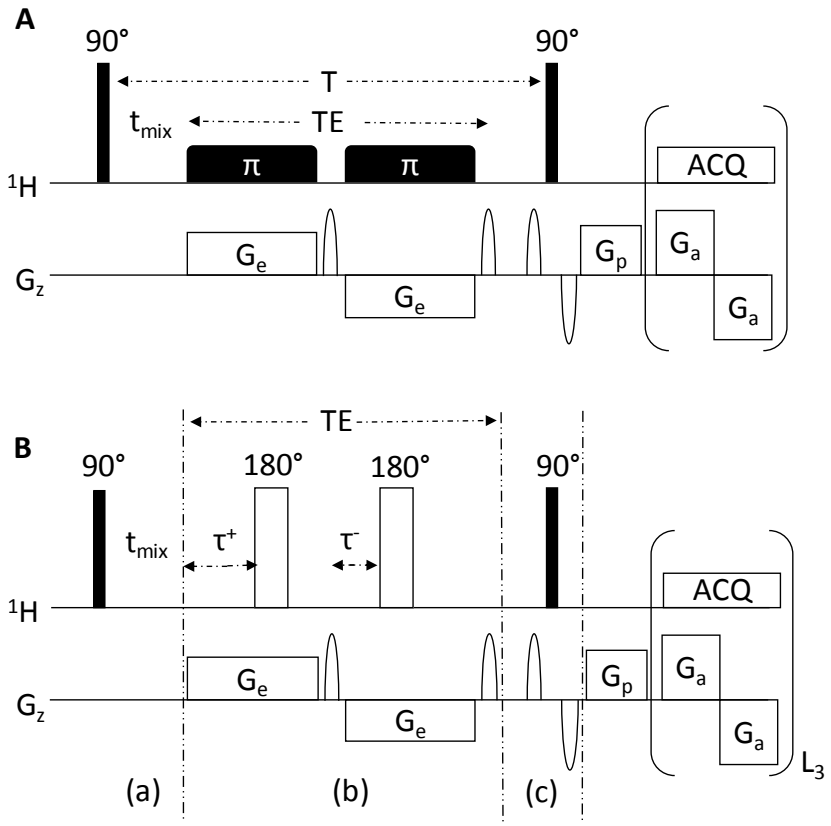

Fig. 1. Pulse sequence of UF CT-COSY **(A)**, and schematic view under the assumption of instantaneous inversion **(B)**.

Spin system and interaction

Consider three coupled spins-½ A, M and X. The propagation of the density matrix is computed with the product-operator formalism, ignoring relaxation and diffusion effects. Only the case of weak couplings is considered with analytical calculations; strong couplings will be treated

numerically. In the case of weak couplings, the free precession Hamiltonian H_{FP} for an $A_N M_P X_Q$ system is expressed as follows:

$$H_{FP} = \sum_n \Omega_A A_{nz} + \sum_p \Omega_M M_{pz} + \sum_q \Omega_X X_{qz} + 2\pi J_{AM} \sum_n \sum_p A_{nz} M_{pz} + 2\pi J_{AX} \sum_n \sum_q A_{nz} X_{qz} + 2\pi J_{MX} \sum_p \sum_q M_{pz} X_{qz}$$

Where Ω_i is the chemical-shift offset of spin i, and J_{ij} is the scalar coupling constant between spins i and j. An important feature is the response of the spins to the π-chirp pulses during the spatial encoding with alternating excitation gradients $\pm Ge$. The proposed description assumes an instantaneous rotation provided by the chirp pulse (Fig. 1B), when its carrier pulsation $O^{(\pi)}$ matches the total offset of the spin i: $O^{(\pi)} = \Omega_i \pm \gamma Gez$. This is a common assumption already proposed by Tal et al.[9b] A last point to be considered is the different rotation time of the spins included in the same spin system. As shown in the previous matching equation, for a given slice z the carrier frequency of the chirp does not match simultaneously the different total offsets of each spin. This results in small additional delays in the predicted modulation. Numerical simulations show, however that these delays can be reasonably neglected under typical experimental parameters. Therefore, they will not be considered further.

Density matrix propagation

Consider the application of the UF CT-COSY pulse sequence to a general $A_N M_P X_Q$ spin system. The effective length of the sample is L, and the z coordinate ranges from $-L/2$ to $L/2$. All the radiofrequency RF pulses are applied along the x-axis, and the density matrix is propagated under the assumptions discussed previously. The initial density matrix is:

$$\sigma_{[0]} = \boldsymbol{A}_{1z}$$

After the first 90° pulse the matrix becomes:

$$\sigma_{[0^+]} = -\boldsymbol{A}_{1y} = -\frac{1}{2i}(\boldsymbol{A}_{1+} - \boldsymbol{A}_{1-})$$

Given the coherence transfer pathway (CTP): 0; -1; +1; -1; -1, only the evolution of $\boldsymbol{A}_{1-}$ is relevant. During period (a) (Fig. 1. B), the density matrix evolves with the free precession Hamiltonian for a duration t_{mix}:

$$\sigma_{[0^+]} \xrightarrow{H_{FP} t_{mix}} \sigma_{[a]}$$

$$= \frac{1}{2i} \begin{Bmatrix} \cos(\pi J_{AM} t_{mix})^P \cos(\pi J_{AX} t_{mix})^Q \boldsymbol{A}_{1-} \\ i \cos(\pi J_{AX} t_{mix})^Q \cos(\pi J_{AM} t_{mix})^{P-1} \sin(\pi J_{AM} t_{mix}) \sum_p 2\boldsymbol{A}_{1-}\boldsymbol{M}_{pz} \\ i \cos(\pi J_{AM} t_{mix})^P \cos(\pi J_{AX} t_{mix})^{Q-1} \sin(\pi J_{AX} t_{mix}) \sum_q 2\boldsymbol{A}_{1-}\boldsymbol{X}_{qz} \end{Bmatrix} e^{i\Omega_A t_{mix}}$$

Here only operators providing signal during detection are retained, in particular, operators in "multiple anti-phase" are ignored since none of them provide in phase -1 order operators. Then spatial encoding generates a phase depending on the z position as follows:

$$\sigma_{[b]} = \frac{1}{2i} \begin{Bmatrix} \cos(\pi J_{AM} T)^P \cos(\pi J_{AX} T)^Q \boldsymbol{A}_{1-} \\ i \cos(\pi J_{AX} T)^Q \cos(\pi J_{AM} T)^{P-1} \sin(\pi J_{AM} T) \sum_p 2\boldsymbol{A}_{1-}\boldsymbol{M}_{pz} \\ i \cos(\pi J_{AM} T)^P \cos(\pi J_{AX} T)^{Q-1} \sin(\pi J_{AX} T) \sum_q 2\boldsymbol{A}_{1-}\boldsymbol{X}_{qz} \end{Bmatrix} e^{i\Omega_A t_{mix}} e^{iC\Omega_A z}$$

Where C refers to the spatio-temporal encoding constant ($C = 2TE/L$). After the mixing period, i.e. the action of the second hard 90°pulse, the coherence transfer is obtained:

$$\sigma_{[c]} = \frac{1}{4i} \begin{Bmatrix} \cos(\pi J_{AM} T)^P \cos(\pi J_{AX} T)^Q \boldsymbol{A}_{1-} \\ -\cos(\pi J_{AX} T)^Q \cos(\pi J_{AM} T)^{P-1} \sin(\pi J_{AM} T) \sum_p 2\boldsymbol{A}_{1z}\boldsymbol{M}_{p-} \\ -\cos(\pi J_{AM} T)^P \cos(\pi J_{AX} T)^{Q-1} \sin(\pi J_{AX} T) \sum_q 2\boldsymbol{A}_{1z}\boldsymbol{X}_{q-} \end{Bmatrix} e^{i\Omega_A t_{mix}} e^{iC\Omega_A z}$$

Thanks to the density matrix established at the beginning of the detection, i.e. $t_2 = 0$, the analytical expressions of the J-modulation of the diagonal peak S_{AA} and of the cross-peaks S_{AM} and S_{AX} are obtained as follows:

$$S_{AA} \propto \cos(\pi J_{AM} T)^P \cos(\pi J_{AX} T)^Q$$

$$S_{AM} \propto \cos(\pi J_{AX} T)^Q \cos(\pi J_{AM} T)^{P-1} \sin(\pi J_{AM} T)$$

$$S_{AX} \propto \cos(\pi J_{AM} T)^P \cos(\pi J_{AX} T)^{Q-1} \sin(\pi J_{AX} T)$$

These expressions show how the J-modulation depends on the scalar coupling constants and on the total time T spent in the transverse plane, impacting in a variety of ways the peak intensities. This total time may be tuned by varying the t_{mix} delay placed immediately after excitation.

Methods

Numerical simulations

Numerical simulations were performed using the Fokker-Planck theory module implemented in version 2.0 of Spinach library.[18] The calculation was carried out in the direct product $\boldsymbol{F}$ of spin state space $\boldsymbol{S}$ and the three-dimensional Cartesian space $\boldsymbol{R^3}$:

$$\boldsymbol{F} = \boldsymbol{S} \otimes \boldsymbol{R^3}$$

Matrix representations of the spin Hamiltonian $\boldsymbol{H}$, the diffusion operator $\boldsymbol{D}$ and the magnetic field gradient operators $\{\boldsymbol{G}_x, \boldsymbol{G}_y, \boldsymbol{G}_z\}$ have the following expressions in the Fokker-Planck space:

$$\boldsymbol{H}(t) = \widehat{H}(t) \otimes \mathbf{1} \qquad \boldsymbol{D} = D\left(\mathbf{1} \otimes \left[\frac{\partial^2}{\partial x^2} + \frac{\partial^2}{\partial y^2} + \frac{\partial^2}{\partial z^2}\right]\right)$$

$$\boldsymbol{G}_x = \hat{L}_\gamma \otimes x \qquad \boldsymbol{G}_y = \hat{L}_\gamma \otimes y \qquad \boldsymbol{G}_z = \hat{L}_\gamma \otimes z \qquad \hat{L}_\gamma = \sum_k \gamma_k \hat{L}_z^{(k)}$$

where D is the diffusion coefficient, $\mathbf{1}$ is a unit matrix of an appropriate dimension, $\widehat{H}(t)$ is the spin Hamiltonian commutation superoperator, γ_k are magnetogyric ratios of the spins in the system and $\hat{L}_z^{(k)}$ are the corresponding longitudinal spin operators. Finite-difference matrices[19] were used as representations of the differentiation operators. The resulting equation of motion

$$\boldsymbol{F}(t) = \boldsymbol{H}(t) + g_x(t)\boldsymbol{G}_x + g_y(t)\boldsymbol{G}_y + g_z(t)\boldsymbol{G}_Z + i\boldsymbol{D}$$

$$\frac{d}{dt}\boldsymbol{\rho}(t) = -i\boldsymbol{F}(t)\boldsymbol{\rho}(t)$$

where $g_{x,y,z}$ are gradient amplitudes, was solved for the free induction decay $f(t)$ using the standard time-ordered exponential propagation technique[20] with the initial condition $\boldsymbol{\rho_0}$ set to spatially uniform longitudinal magnetization and the detection state $\boldsymbol{\sigma}$ to spatially uniform $\hat{L}_+$ spin operator:

$$f(t) = \left\langle \boldsymbol{\sigma} \middle| \exp_{(o)}\left(-i\int_0^t \boldsymbol{F}(t)dt\right) \middle| \boldsymbol{\rho} \right\rangle$$

Trajectory-level state space restriction functionality of Spinach[21] was used to keep matrix dimensions manageable throughout the simulation. The number of points in the discretization of $\boldsymbol{R^3}$ and the finite difference stencil size were increased until convergence was achieved in the simulation result.

All simulated spectra were performed with the following features. Acquisition parameters: 512 points separated by a dwell time of 0.55 µs were used to compute the UF dimension whereas the conventional one was obtained with 128 loops in the detection block. Acquisition gradients were fixed at 0.687 T·m^{-1}. For the encoding parameters, excitation gradients of 0.020 T·m^{-1} were applied while the π-chirp pulses were performed by a WURST built with 1000 points, sweeping a bandwidth of 13 kHz in 15 ms. The second chirp of the double spin echo is flanked by two crushers. The CTP was completed in the same way as on the Fig. 1a, via gradient pulses at 0.48 T·m^{-1} applied during 1 ms. The length of the sample was fixed at 1.5 cm and the Liouvillian propagation was performed over 500 z-positions. In all simulations a B_0 field of 11.77 T·m^{-1} was considered and ideal pulses were assumed. The simulated 2D FID was then processed in the same way than the experimental spectra: sinusoidal apodisation for the conventional dimension while a Gaussian apodisation was applied in the UF dimension, including zero filling in both dimensions.

Sample preparation

The experimental UF CT-COSY spectrum of histidine (Fig. 3F) was recorded on a sample containing histidine dissolved in 1 mL of a mix of phosphate buffer (pH = 7) and D_2O (37.5 / 62.5: v/v) to obtain a concentration of 110 mmol.L^{-1}. The UF CT-COSY spectra related to Fig. 2B and Fig. 3E were respectively recorded on samples of alanine at 100 mmol·L^{-1} and taurine at 160 mmol·L^{-1}, both in D_2O. The metabolic mixture related to Fig. 4B and C was prepared with 4 metabolites alanine (Ala), lactate (Lac), threonine (Thr), and taurine (Tau), plus choline(Cho) acting as an internal relaxation reference, dissolved in a 2.4 mL mix of phosphate buffer (pH = 7) and D_2O (37.5 / 62.5: v/v) leading to a concentration of 50 mmol·L^{-1} for each metabolite. The UF CT-COSY spectra related to Fig. 5C, D and G were recorded on a 207 mmol.L^{-1} ferulic acid sample in acetone-d6.

NMR spectrometer

NMR spectra were recorded at 298 K on a Bruker Avance III 500 spectrometer, operating at a frequency of 500.13 MHz and equipped with a dual 1H/13C cryogenic probe including a z-axis gradient. Conventional 1D experiments were recorded with routine pulse sequences available within the commercial software Bruker Topspin 2.1.

UF experiments

For all the ultrafast experiments, spatial encoding was performed using a constant time spatial encoding scheme, i.e. double spin echo with 15 ms smoothed chirp encoding pulses. The sweep range for the encoding pulses was set to 13 kHz for all the spectra, and the amplitude of the encoding gradients was adapted to obtain a frequency dispersion equivalent to the frequency range of the pulses: Ge = 0.0204 T·m^{-1}. Coherence-selection gradients were added for the UF CT-COSY as indicated on Fig. 1A. The acquisition gradient parameters were set as follows: 0.688 T·m^{-1} for the sample of taurine, histidine and metabolic mixture and 0.573 T·m^{-1} for the experiments on the sample of ferulic acid. For all the experiments, the acquisition gradient duration was Ta = 281.6 µs and the detecting block used 128 detection

gradients pairs. The specific processing for ultrafast spectra was performed on MATLAB using the same method as described for the simulated spectra.

Results and discussion

We discuss here the ability to predict J-modulation effects with both numerical simulations and the analytical expressions. Several spin systems are considered, including different regimes of scalar couplings, i.e. weak and strong couplings, through comparisons between computed J-modulation and experimental results. Calculations of J-modulation are used to customize the UF CT-COSY experiments and improve its sensitivity in a variety of situations.

Predicting the effect of J-modulation with numerical simulations

Case of weak coupling.

To evaluate the ability to predict the J-modulation, the UF CT-COSY sequence was simulated for different t_{mix} increments with a step of 5 ms. All the simulations were performed with the Spinach package, which was adapted to include the simulation of spatial encoding schemes. A fixed spatial encoding duration of TE = 30 ms was used for all the simulations, corresponding to typical experimental parameters in UF CT-COSY. This series of simulations was performed on a small molecule, alanine, which provides a weak coupled system A_3X with a scalar coupling constant of 7.24 Hz (Fig. 2A and B). For each increment of t_{mix}, the peak volumes were measured by integration on the simulated spectra, leading to the evolution of intensities for the four peaks as a function of t_{mix}. The same procedure was carried out experimentally, then the results were compared to the simulated data and to the analytical expressions established in the previous section (Fig. 2C-F).

To take transverse relaxation into account, both the simulated data and analytical expressions were multiplied by a pure exponential factor with a τ decay constant. The latter was estimated experimentally from the signal decay observed as a function of t_{mix} for a peak without J-modulation, i.e. the singlet of choline which was added in all the samples described in this article and used as an internal reference for relaxation

effects. The τ decay constant was estimated at 220 ms from a series of experiments where t_{mix} ranged from 0 to 1000 ms.

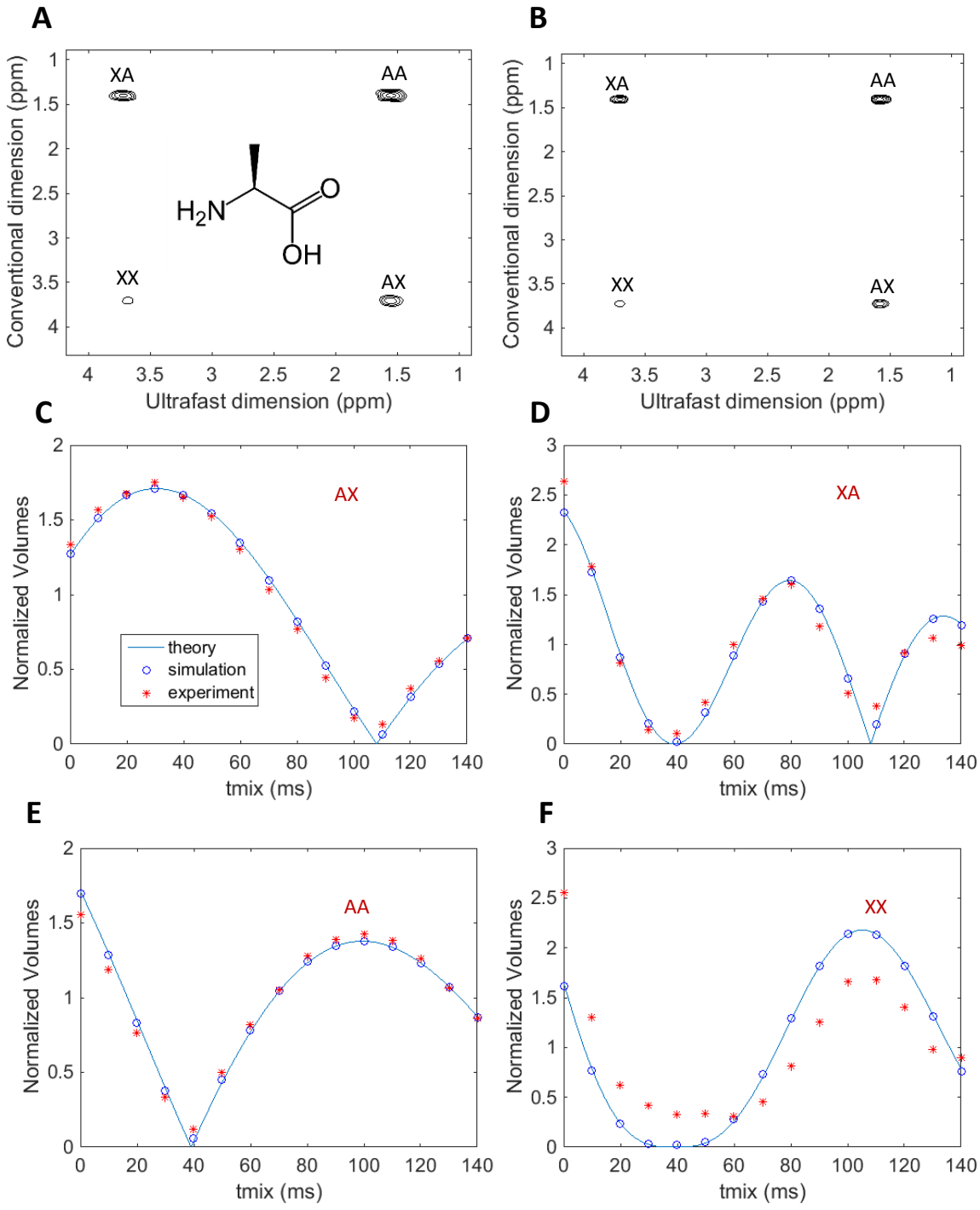

Fig. 2. J-modulation effects in a weakly coupled spin system (alanine). UF CT COSY spectra obtained experimentally **(A)** and from Spinach numerical simulations **(B)** were processed and integrated in the same way. The analytical expressions of J-modulation (blue line) are compared to results from numerical simulations (blue circles) and to experimental data (red crosses). TE was set to 30 ms. J modulation is studied as a function of t_{mix} for the cross peaks AX **(C)** and XA **(D)**, and for the diagonal peaks AA **(E)** and XX **(F)**. All the curves are normalized to their mean value.

In this study, we assume that all the small molecules studied have similar τ decay constants, an assumption which is supported a posteriori by the good match between the analytical, simulated and experimental results. The effect of the J-modulation predicted by the analytical expressions and numerical simulations matches very well with the experimental data (Fig. 2C-F). The only slight difference is observed for the XX peak, due to a small overlap of the experimental peak with the singlet of the internal relaxation reference (choline). Also noticeable is the asymmetric evolution of peak intensities for symmetric signals on each side of the diagonal, an effect that can be expected as such signals undergo different J modulation effects. These results highlight the efficiency of our simulation platform for predicting UF spectra of small molecules. Moreover these curves shows that the effect of J-modulation is highly peak-dependent, even in a simple case like alanine.

Case of strong coupling.

While the analytical expressions of J-modulation were suitable to predict the optimal t_{mix} in the case of a weakly coupled A_3X spin system, these expressions are no longer valid in the case of strongly coupled spin systems. In this context, numerical simulations are essential to analyse the J-modulation. Here we evaluated the ability to predict the optimal t_{mix} in such cases with taurine and histidine samples, which respectively provide strongly coupled A_2B_2 and ABX (geminal coupling) spins system (Fig. 3A-F).

As for the alanine sample, transverse relaxation was taken into account with a τ decay constant of 220 ms. A noticeable feature of these spectra is the excellent match between experimental and simulated spectral patterns. The effect of J-modulation is shown for the circled peaks. A good match is obtained for taurine (Fig. 3G) whereas in the case of histidine the match is only qualitative (Fig. 3H). The discrepancies between simulation and experiment can be explained by the difficulty to accurately determine the actual chemical shifts –used as input values in the simulations– in the presence of second order effects. Still, the numerical simulation platform remains efficient enough to predict the local maxima. Overall, even for strongly coupled spin systems, the

numerical simulations performed through the Spinach package appear to be a relevant tool to optimize the J-modulation for complex spin systems.

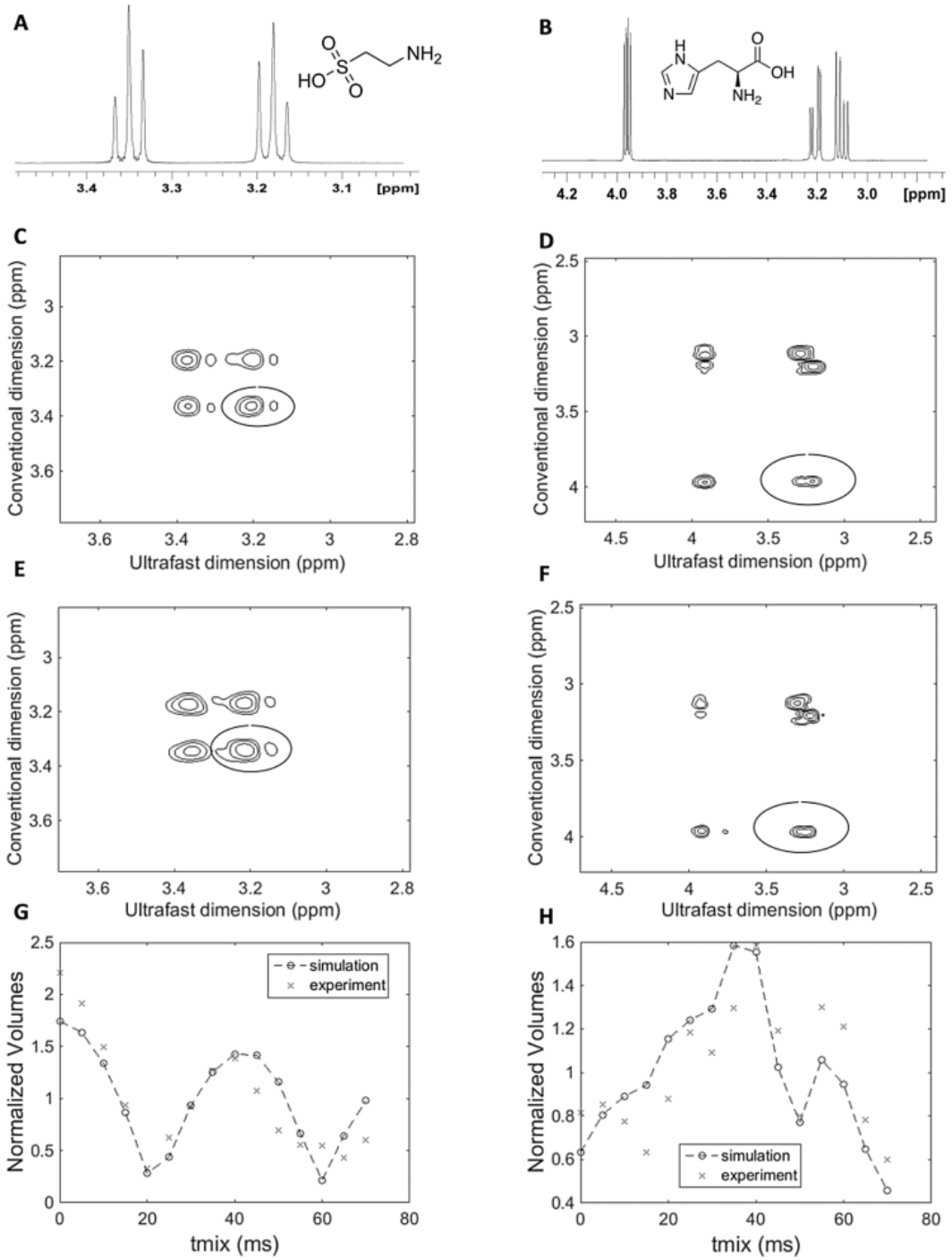

Fig. 3. 1D ^{1}H spectra of taurine **(A)** and histidine **(B)** showing strong second order coupling effects. Simulated constant time phase-modulated UF CT-COSY spectra of the A_2B_2 spin system from taurine **(C)**, and ABX spin system from histidine **(D)** performed with the Spinach package. TE was set to 30 ms in all cases. Experimental constant time phase-modulated UF CT-COSY spectra of taurine **(E)** and histidine **(F)**. Integral of the simulated versus experimental signals as a function of t_{mix} for the circled cross peaks of taurine **(G)** and histidine **(H)**.

Optimization strategies and applications

Best compromise strategy. Understanding and predicting the effects of J-modulation can prevent unnecessary sensitivity losses. However, the optimization for real-life samples containing different spin systems (either from the same compound or from different molecules) is not straightforward. A first approach consists in choosing the best compromise between the different spin systems, an approach that is well suited for spectra of complex mixtures. Let us consider, as an example, the quantification of metabolites inside a mixture, a domain where UF CT-COSY is recognized as a powerful tool.[22] We focus here on the detection of alanine (Ala), lactate (Lac), threonine (Thr) and taurine (Tau). Each of these metabolites is usually quantified, relying on a calibration procedure, through one well-resolved cross-peak: Ala (1.47, 3.78) ppm, Lac (1.32, 4.10) ppm, Thr (1.33, 4.26) ppm and Tau (3.26, 3.42) ppm (Fig. 4B).

Here, the best approach consists in avoiding situations where some peaks would be missing while others would have a maximum intensity under the influence of J-modulation effects. On the contrary, a situation where all the signals of interest have a similar response is far more preferable, the limiting factor being the peak with the lowest SNR. Simulating the intensity of the cross peaks as a function of t_{mix} can help choosing a compromise value averaging the effects of the J-modulation. Fig. 4A shows these curves for the system described above, obtained on a series of 15 simulated spectra with a t_{mix} value ranging from 0 to 140 ms. To predict the local maxima more accurately, the data from numerical simulations were multiplied by a pure exponential decay with a τ decay constant of 220 ms. From these curves, an optimum t_{mix} of 20 ms can be chosen, leading to a sensitivity improvement of about 20% for Lac, Thr and Ala cross-peaks, while the SNR of the taurine peak is decreased to match those of the other metabolites (Fig. 4B and C). This sensitivity optimization requires knowing accurately the characteristics of the detected compounds which is usually the case in a quantification issue. Regarding quantitative applications, it should be noted that the coefficient of proportionality between peak volumes and concentrations will remain peak-dependent in most cases, hence the need to rely on a calibration protocol, as it is the case in almost all quantitative 2D NMR experiments.[23]

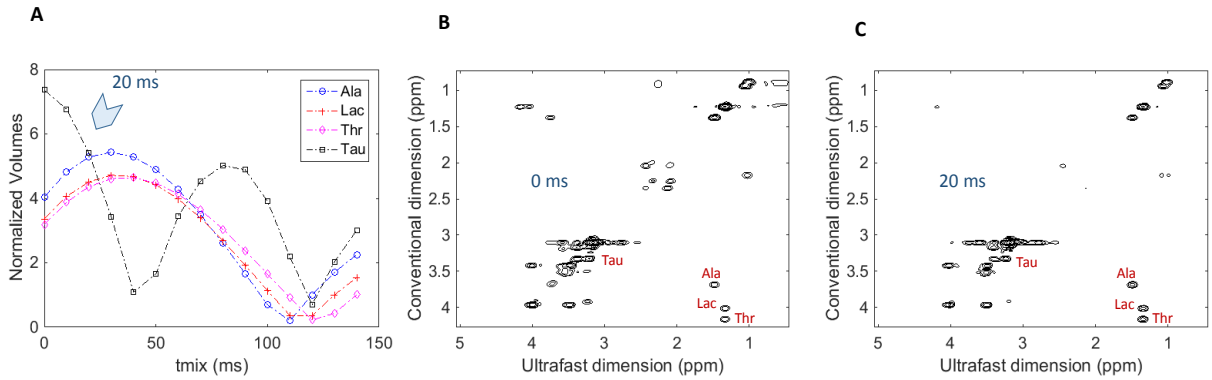

Fig. 4. Calculated signals as a function of t_{mix} (with TE = 30 ms) for the cross peaks of interest from Ala, Lac, Thr and Tau. A compromise is found at t_{mix} = 20 ms **(A)**. Experimental constant time phase-modulated UF CT-COSY spectra of a 50 mmol.L^{-1} mixture of metabolites in D_2O, recorded in a single-scan at 500 MHz with a cryoprobe for t_{mix} values at 0 ms **(B)** and 20 ms **(C)**

Recording spectra without missing peaks.

While this first example requires optimizing the sensitivity of one specific peak for each spin system, other common situations –such as structure elucidation– require the observation of all the peaks arising from a given molecule. Unfortunately, as mentioned above, J-modulation effects can lead to missing peaks in the 2D spectra. This phenomenon is clearly illustrated on the case of ferulic acid (Fig. 5A), a small molecule showing a variety of coupling patterns. Under non-optimized experimental conditions, two diagonal peaks are missing: CC at (7.16, 7.16) ppm and DD at (6.89, 6.89) ppm, while two symmetric cross-peaks: AE (6.40, 7.63), EA (7.63, 6.40) ppm show very low intensities (Fig. 5C). These occasional missing peaks become a tricky issue to check or elucidate a molecular structure, making it difficult to set up the UF constant time experiments as routine sequences. Averaging the effect of the J-modulation on all the spin systems of interest forms an appealing solution to avoid these missing peaks. As the sensitivity issues of UF experiments often require the accumulation of a few scans, adding several spectra recorded with incremented t_{mix} values is a convenient way of doing it in a reasonable time. This multi-scan approach was evaluated on the same sample of ferulic acid by adding a serial of nine spectra with t_{mix} values ranging from 0 to 40 ms. The resulting spectrum (Fig. 5D), recorded in 46.13 seconds, contains all the expected peaks, showing the efficiency of

this approach. This straightforward method has the advantage of being applicable to unknown samples.

Enhancement of cross-peak intensities for multiple spin systems.

While achieving the detection of all the expected peaks, the multi-scan approach does not maximize the peak intensity, as it results from the signal averaging of J-modulation effects. Still, several applications such as reaction monitoring require maximizing the intensity of cross-peaks, and being able to do it in a single scan would be particularly appealing. This requires, however, the simultaneous optimization of J-modulation effects for different spin systems. To achieve this goal, we propose a new excitation block where the 90° hard pulse is replaced by spectrally selective pulses followed by delays, in order to excite successively and independently each spin system of the sample (Fig. 5E). These selective pulses are separated by suitably chosen delays, calculated so that each spin system spends an optimal time in the transverse plane to optimize the effect of J-modulation. The optimum delay can be predicted from the calculated (or simulated) J-modulation curves (Fig. 5F). This single-scan approach was applied to the ferulic acid sample characterized by two different spin systems (Fig. 5A). The corresponding spin systems have very different J coupling constants (16.0 Hz for AE and 8.1 Hz for CD). Thanks to a prediction of the J-modulation for each cross-peak, the inter-pulse delay can be adjusted so that each spin system reaches the maximum of its J-modulation curve in the same experiment (Fig. 5F). In this example, p_{AE} and p_{BCD} are the durations of the selective pulses exciting spins A-E and spins B-C-D, respectively. Note that here, the pulse exciting A and E has to be polychromatic to excite two different regions at the same time. The inter-pulse delays d_1 and d_2 can be computed relying on the following equations, where T_{AE} and T_{BCD} represent respectively the total time spent in transverse plane for the spin systems AE and BCD, respectively.

$$\begin{cases} T_{AE} = \dfrac{p_{AE}}{2} + d_1 + p_{BCD} + d_2 + TE \\ T_{BCD} = \dfrac{p_{BCD}}{2} + d_2 + TE \end{cases}$$

Relying on these equations and on the calculated J-modulation curves, an UF CT-COSY spectrum using this excitation block was recorded on the ferulic acid sample with $\boldsymbol{d_1}$ = 17.5 ms and $\boldsymbol{d_2}$ = 27.8 ms. The selective pulses had a Gaussian shape with a duration of p_{AE} = 17.91 ms for the first one and p_{BCD} = 7.15 ms for the second one. The resulting spectrum (Fig. 5G) clearly shows the high cross-peak intensity reached for all the correlation peaks within a single-scan, it also results in a strong decrease of the diagonal peaks. This approach requires a fine-tuning of the pulse sequence parameters, and is therefore suitable to the study of spin systems which are a priori known.

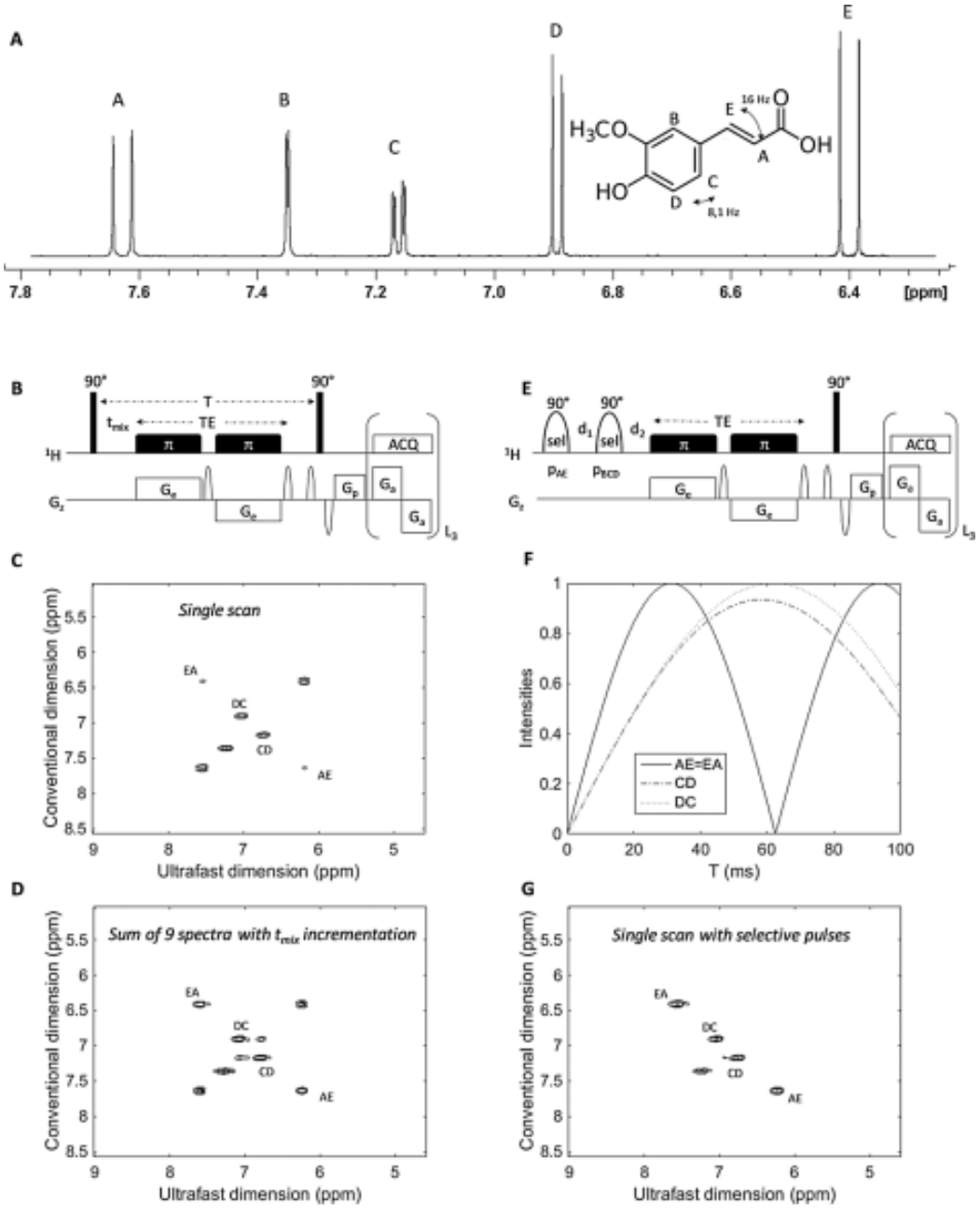

Fig. 5. 1D ^{1}H spectrum of a 207 mmol.L^{-1} ferulic acid sample in acetone-d6 **(A)**. The molecular structure is shown with the corresponding J coupling constants. Pulse sequence for constant time phase-modulated UF-COSY **(B)**, and corresponding spectrum of ferulic acid recorded in 1 scan with a t_{mix} of 30 ms **(C)**, and by adding 9 spectra acquired with a t_{mix} incrementation of 5 ms per scan from 0 to 40 ms **(D)**, with TE = 30 ms. Pulse sequence for constant time phase-modulated UF CT-COSY including a new excitation block based on spectrally selective pulses **(E)**. Calculated J-modulation as a function of T, i.e. the total time spent in the transverse plan, for the cross peaks of ferulic acid **(F)**. UF CT-COSY spectrum obtained with the pulse sequence shown in **(E)** using the new excitation block **(G)**.

Due to the use of selective pulses, it is also limited by the position of peaks in the 1D spectrum, but polychromatic pulses make it possible to excite simultaneously several

distinct spectral regions. Therefore, this approach could be useful when the intensity of targeted cross peaks needs to be optimized, such as in the monitoring of real-time dynamic phenomena which generally focus on targeted cross-peaks.

Conclusions

This paper highlights the significant role of J-modulation as a potential source of sensitivity losses in the case of the UF constant time experiments, and demonstrates how understanding J-modulation effects can lead to significant sensitivity recovery in a variety of situations. The combination of theoretical description and numerical simulations shows the possibility to predict the J-modulation effects for several spin systems, even strongly coupled. Based on this prediction, several single-scan or multi-scan strategies were designed to optimize the peak intensity in UF CT-COSY spectra. The optimal strategy depends on the targeted applications, and the potential and drawbacks of the different approaches were discussed so that the user can choose the optimal approach for a given situation. We hope that these tools will help users of the ultrafast NMR method to tune the sensitivity of their experiments for a large range of applications.

Acknowledgements

We warmly thank Prof. Malcolm H. Levitt (University of Southampton) for fruitful discussion. Funding from the Région Pays de la Loire (Grant RésoNantes) is also acknowledged.

References

[1] a) W. P. Aue, E. Bartholdi, R. R. Ernst, J. Chem. Phys. 1976, 64, 2229-2246; b) J. Jeener, Lecture presented at Ampere International Summer School II, Basko Polje, Yugoslavia 1971.

[2] G. A. Morris, J. Magn. Reson. 1992, 100, 316-328.

[3] P. Schanda, B. Brutscher, J. Am. Chem. Soc. 2005, 127, 8014-8015.

[4] P. Schanda, H. Van Melckebeke, B. Brutscher, J. Am. Chem. Soc. 2006, 128, 9042-9043.

[5] E. Kupce, R. Freeman, Magn. Reson. Chem. 2007, 45, 2-4.

[6] a) A. S. Stern, K.-B. Li, J. C. Hoch, J. Am. Chem. Soc. 2002, 124, 1982-1993; b) H. Barkhuijsen, R. De Beer, W. M. M. J. Bovée, D. Van Ormondt, J. Magn. Reson 1985, 61, 465-481; c) J. C. Hoch, J. Magn. Reson 1985, 64, 436-440.

[7] a) E. Kupce, R. Freeman, J. Magn. Reson 2003, 162, 158-165; b) E. Kupce, R. Freeman, J. Magn. Reson 2003, 162, 300-310.

[8] a) L. Frydman, T. Scherf, A. Lupulescu, Prod. Natl. Acad. Sci. USA 2002, 99, 15858-15862; b) L. Frydman, A. Lupulescu, T. Scherf, J. Am. Chem. Soc. 2003, 125, 9204-9217.

[9] a) P. Mansfield, J. Phys. C: Solid State Phys. 1977, 10, 55-58; b) A. Tal, L. Frydman, Prog. Nucl. Magn. Reson. Spectrosc. 2010, 57, 241-292.

[10] Y. Shrot, L. Frydman, J. Chem. Phys. 2008, 128, 052209.

[11] P. Pelupessy, J. Am. Chem. Soc. 2003, 125, 12345-12350.

[12] P. Giraudeau, L. Frydman, Annu. Rev. Anal. Chem. 2014, 7, 129-161.

[13] a) Y. Shrot, L. Frydman, J. Chem. Phys. 2009, 131, 224516; b) P. Pelupessy, L. Duma, G. Bodenhausen, J. Magn. Reson. 2008, 194, 169-174.

[14] a) Z. Wei, L. Lin, Q. Ye, J. Li, S. Cai, Z. Chen, J. Chem. Phys. 2015, 143, 024201; b) P. Giraudeau, S. Akoka, J. Magn. Reson. 2010, 205, 171-176.

[15] a) Y. Shrot, L. Frydman, J. Chem. Phys. 2008, 128, 164513; b) P. Giraudeau, S. Akoka, J. Magn. Reson. 2008, 192, 151-158; c) L. Rouger, D. Loquet, S. Massou, S. Akoka, P. Giraudeau, ChemPhysChem 2012, 13, 4124-4127; d) P. Giraudeau, S. Akoka, J. Magn. Reson. 2008, 190, 339-345.

[16] a) M. E. Girvin, J. Magn. Reson. Ser. A 1994, 108, 99-102; b) D. Mayer, W. Dreher, D. Leibfritz, Magn. Reson. Med. 2000, 44, 23-28; c) H. Watanabe, N. Takaya, F. Mitsumori, NMR Biomed. 2008, 21, 518–526.

[17] C. Wu, M. Zhao, S. Cai, Y. Lin, Z. Chen, J. Magn. Reson. 2010, 204, 82-90.

[18] H. J. Hogben, M. Krzystyniak, G. T. P. Charnock, P. J. Hore, I. Kuprov, Journal of Magnetic Resonance 2011, 208, 179-194.

[19] B. Fornberg, Mathematics of computation 1988, 51, 699-706.

[20] R. R. Ernst, G. Bodenhausen, A. Wokaun, Principles of nuclear magnetic resonance in one and two dimensions, Oxford Science Publications ed., Oxford, 1987.

[21] a) H.J. Hogben, P.J. Hore, I. Kuprov, J Chem Phys 2010, 132; b) I. Kuprov, J Magn Reson 2008, 195, 45-51.

[22] T. Jézéquel, C. Deborde, M. Maucourt, V. Zhendre, A. Moing, P. Giraudeau, Metabolomics 2015, In press, doi: 10.1007/s11306-015-0780-0.

[23] P. Giraudeau, Magn. Reson. Chem. 2014, 52, 259-272.

1.3. Further applications in UF double quantum spectroscopy (DQS) and J-coupling measurements.

This article showed how the control of J-modulation can lead to a sensitivity enhancement in a varieties of situations. These optimizations, here performed on UF COSY, could be applied to other UF experiments as long as a constant time spatial encoding is involved. In this context, I contributed –as second author– to two articles which can be seen as a direct application of the previous article.

First, a similar work were achieved to yield a sensitivity-optimized UF double quantum spectroscopy (DQS) experiment. Towards this end, we added a delay t_{mix} between the double quantum (DQ) building block and the CT spatial encoding in order to adjust the J-modulation effects. Still, numerical simulations offer a good prediction of the J-modulation effects so that a sensitivity enhancement can be achieved by finely tuning the t_{mix} delay. Furthermore, this optimized UF DQS experiment led to a practical application in the field of quantitative 2D NMR. This methodological work and the related application are described in a research article in Appendix 1.

Beyond its impact on sensitivity, J-modulation can also be exploited for accurate measurements of J-coupling constants. The research article previously presented pointed out the reliance of the signal intensity S on the coupling constant J and the time spent in the transverse plane T:

$$S = f(\pi.J.T) \qquad (C.1)$$

Where the function f depends on the nature of the spin-system. Thus based on prior knowledges on the J-modulations profile, the scalar coupling constant can be determined by recording a series of CT experiments like CT COSY with different values of T. In such time-consuming arrayed 2D experiments, the ultrafast version of the CT COSY seems to be an appealing solution. Such an application of UF CT PM COSY was carried out in collaboration with Oulyadi and coworkers at the University of Rouen to measure small ^{7}Li-^{7}Li scalar coupling constants (< 1 Hz). This experiments also constitute the first UF experiments on ^{7}Li. The whole study is described in the corresponding research article in Appendix 2.

2. Development of UF 2D NMR at 43 MHz

After receiving the customized benchtop NMR spectrometer in May 2015, the first methodological development at low field was the implementation of the ultrafast methodology on this apparatus. This following work has been largely inspired by the many improvements that UF 2D NMR has undergone at high field over the last fifteen years.

2.1. Description of the pulse field gradients

The main ingredient involved in UF NMR is the application of magnetic field gradients. Our customized benchtop spectrometer enables pulse field gradients (PFG) with a trapezoidal envelope, which are programmed as follows (figure C.1):

i. First a gradient ramp is programmed to reach progressively the desired gradient amplitude G_f. This progressive ramp alleviates the overshooting issues.
ii. The gradient amplitude is then maintained during a delay τ_G
iii. At the end, the gradient amplitude decrease through a similar ramp

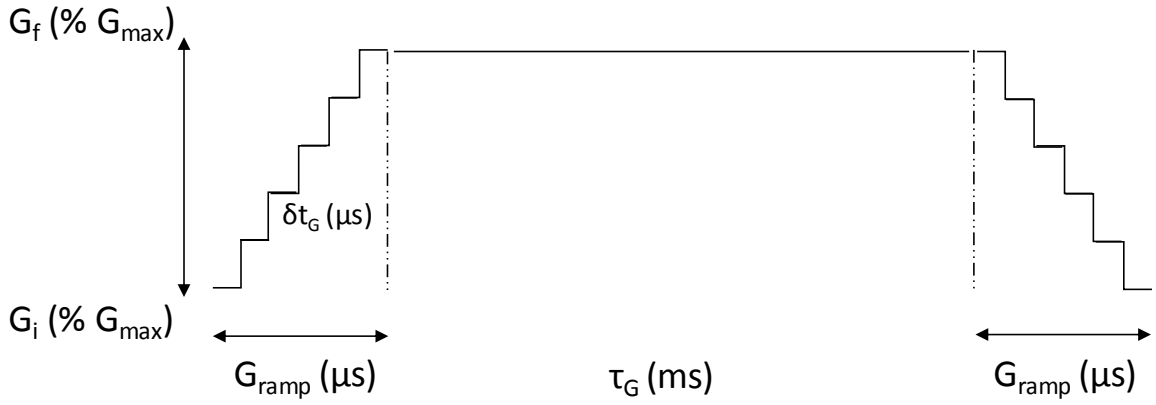

Figure C.1. Overview of the parameters required to program a PFG on the Spinsolve spectrometer. The ramp delay G_{ramp} is the transition state from the starting gradient amplitude G_i (commonly null) to the final one G_f, is the latter being defined as a percentage of the maximum gradient amplitude. This ramp consists of n_G steps with a duration δt_G. These parameters are fixed by the user.

Based on the parameters, the gradient amplitude is computed on the fly during the ramp for each step n:

$$G(n) = G_i + n\,\frac{(G_f - G_i)}{n_G - 1} \qquad \text{(C.2)}$$

Where n takes the value 0 to n_G - 1. In practice, n_G is fixed at 100 with a step duration δt_G in a range of 1 – 2 µs.

2.2. Frequency dispersion induced by a PFG

The key parameters to achieve the spatial encoding and the EPSI block are linked to the gradient strength generated by the gradient coil. Hence, the determination of the frequency dispersion induced by a pulse field gradient in our benchtop system is a prerequisite for implementing UF NMR.

To experimentally evaluate this dispersion, we used a pulse sequence – further called "echograd" – consisting of a spin echo, in which a gradient G_1 is located prior to the 180° hard pulse (figure C.2). A readout gradient G_2 is then applied to generate a gradient echo as shown in figure C.3a. A FT applied on the time domain yields the frequency response, which can be seen here as a 1D image of the sample. Following the FT, a large first order phase correction is required to visualize the profile. This tedious correction can be nonetheless circumvented in centering accurately the gradient echo within the acquisition window. The circled shape of the resulting profile in figure C.2b reminds that the gradient direction is collinear to the B_0 field, *i.e.* orthogonal to the NMR tube. This regular shape highlights the spatial homogeneity of the gradient coil.

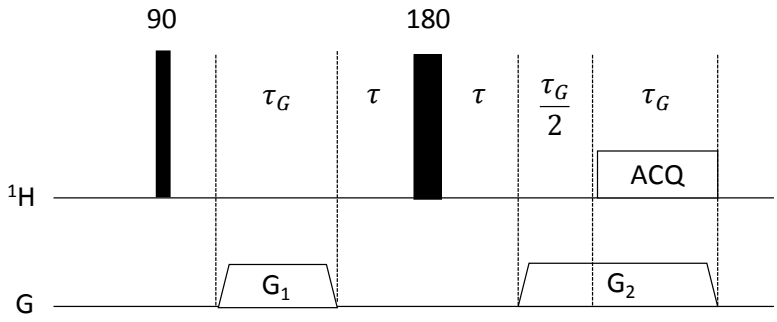

Figure C.2. Scheme of the pulse-sequence "echograd". After FT in the time domain, this experiment provides a frequency profile which corresponds to a 1D image of the sample.

It is possible to measure graphically the frequency dispersion Δf induced by the pulse field gradient. For instance, with a gradient amplitude G_1 fixed at 10 % of the maximum value, a dispersion about 2.8 kHz is measured in figure C.3b so that the maximum Δf generated by the gradient coil is around 28 kHz. Given the characteristic length L of the sample equal to 4 mm (i.e. inner diameter of the NMR tube), the strength of the PFG can be calculated as follows:

$$G = \frac{2\pi.\Delta f}{\gamma.L} \qquad \text{(C.3)}$$

This leads to a maximal gradient strength around 0.16 T.m^{-1} as described by the constructor.

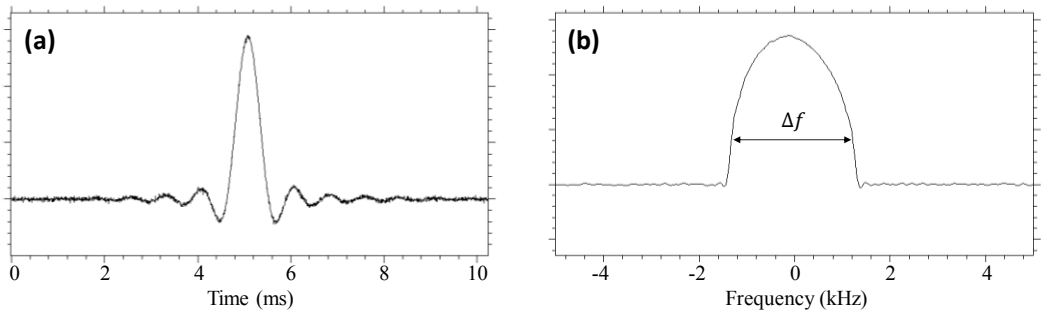

Figure C.3. **(a)**: gradient echo obtained via the pulse sequence presented in figure C.2 performed on a sample of H_2O in D_2O. G_1 and G_2 were fixed at 10 % of the maximum gradient value and applied during 10 and 15 ms, respectively. The signal is centered within the acquisition window by opening the receiver 5 ms after the application of G_2 with an acquisition time of 10 ms. **(b)**: frequency response yielded after FT. The circled shape highlights the transversal gradient direction. The frequency dispersion Δf can be directly measured on this profile.

2.3. Presentation of the UF CT PM COSY pulse-sequence

The pulse-sequence of the UF CT PM COSY experiment used in this work is presented in figure C.4. The experiment starts with a spatial encoding step, followed by a 90°mixing pulse and finally the decoding is achieved through an EPSI block. Each of these blocks are described in section A.4.3. In what follows, we consider only the continuous constant time phase-modulated (CT PM) spatial encoding. This choice was guided by prior studies at high-field which concluded that this encoding offers relevant advantages:

i. It offers the best compromise between sensitivity and resolution. The signal intensity may be doubled compared to amplitude modulated (AM) encoding. Then, for every z position, CT PM provides the longer maximal time spent by spins into the transverse plane so that it offers the finest resolution compared to AM and PM encoding.

ii. It relies on 180° chirp pulses that are easier calibrated in practice and less sensitive to RF imperfections compared to the 90° chirp pulses

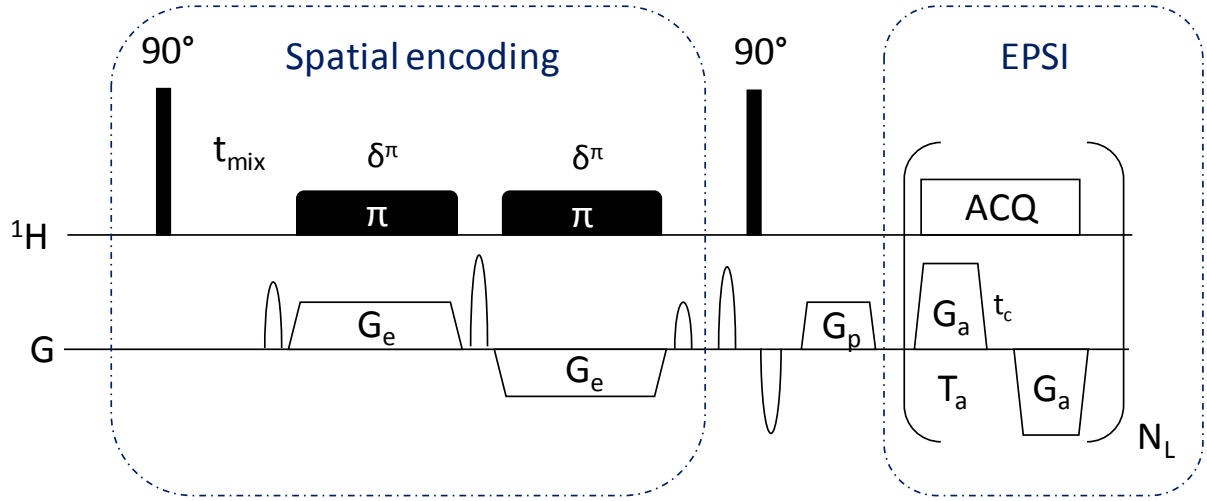

Figure C.4. Scheme of the UF CT PM COSY pulse-sequence. The spatial encoding consists of a 180° chirp pulse applied during δ^{π} together with an excitation gradient G_e and this block is repeated with a negative excitation gradient in order to suppress both quadratic and zero-order contributions leading to a pure linear dephasing $\phi(z) = C.\Omega.z$, where C is the spatial encoding constant. EPSI relies on a train of bipolar G_a gradients with a duration T_a and which are spaced by a short time t_c allowing the commutation between the positive and the negative ones. N_L pairs of bipolar gradients are repeated in the course of the detection. G_p is a pre-phasing gradient which translates the echo positions within the k-space and the delay t_{mix} tunes J-modulation. The non-designated gradients are used as crushing spoilers and for coherence selection. The pulse program is available in Appendix 3.

Tuning all the pulse sequence parameters can be relatively complex since they pertain to several compromises between, spectral widths, resolution and sensitivity. In order to get a comprehensive picture of the further choices, we remind these following equations that are valid for CT PM encoding (see section A.4.3 for more details)

$$SW_{UF} = \frac{\gamma . G_a . T_a . L}{4\delta^{\pi}} \qquad \text{(C.4)}$$

$$SW_{conv} = \frac{1}{2T_a} \qquad \text{(C.5)}$$

$$\Delta\nu_{UF} = \frac{1}{4\delta^{\pi}} \qquad \text{(C.6)}$$

$$\Delta\nu_{Conv} = \frac{1}{2N_L . T_a} \qquad \text{(C.7)}$$

2.4. Chirp pulses and excitation gradients

The linearly swept chirp pulse used in the spatial encoding are characterized by a pulse length δ^{π}, a frequency band width BW and a power γB_1. In what follows, the chirp pulses were performed with a WURST shape (figure C.5) whose analytical expression is given below:

$$\gamma B_1(t) \propto 1 - |\sin(\pi t)^{nw}| \qquad \text{(C.8)}$$

With nw is fixed at 50. The wurst shape helps smoothing the frequency response of the chirps and reduces the wiggles of the echoes in the UF dimension.

Since several parameters are involved in the optimization of a chirp pulse, this required fixing one of them prior to tuning the others. At high field, 15-ms chirp pulses are often used in UF ^{1}H NMR to have a good compromise between spectral width and resolution. Given the shorter spectral width in frequency at 43 MHz, a longer chirp pulse to improve the resolution is an appealing choice. Therefore, we decided to start with a pulse duration δ^{π} of 30 ms. Based on this value, the pulse bandwidth BW was optimized. In order to rotate all the signals, the BW must be at least superior to the SW of the 1D ^{1}H spectra. For instance, if we consider a SW of 8 ppm at 43 MHz, this leads to $BW >$ 350 Hz. It was important to investigate the spin response

through the action of the 180° chirp pulse. Indeed, an instantaneous 180° rotation is a determining feature for the quality of the spatial encoding. To evaluate this property, we considered a spin at a fixed z-position and evolving into the transverse plane with a +1 coherence order, represented by the product operator I^+. An ideal 180° chirp pulse provides a coherence inversion, *i.e.* converts instantaneously I^+ into I^-. Numerical simulations were performed to compute the trajectories of $I^+$and I^- in the course of the chirp pulse. The results are displayed in figure C.5. It turns out that the larger is the band width, the faster is the 180° rotation (figure C.5a versus figure C.5d). A $BW \geq 3500$ Hz is necessary to yield an adequate spin response.

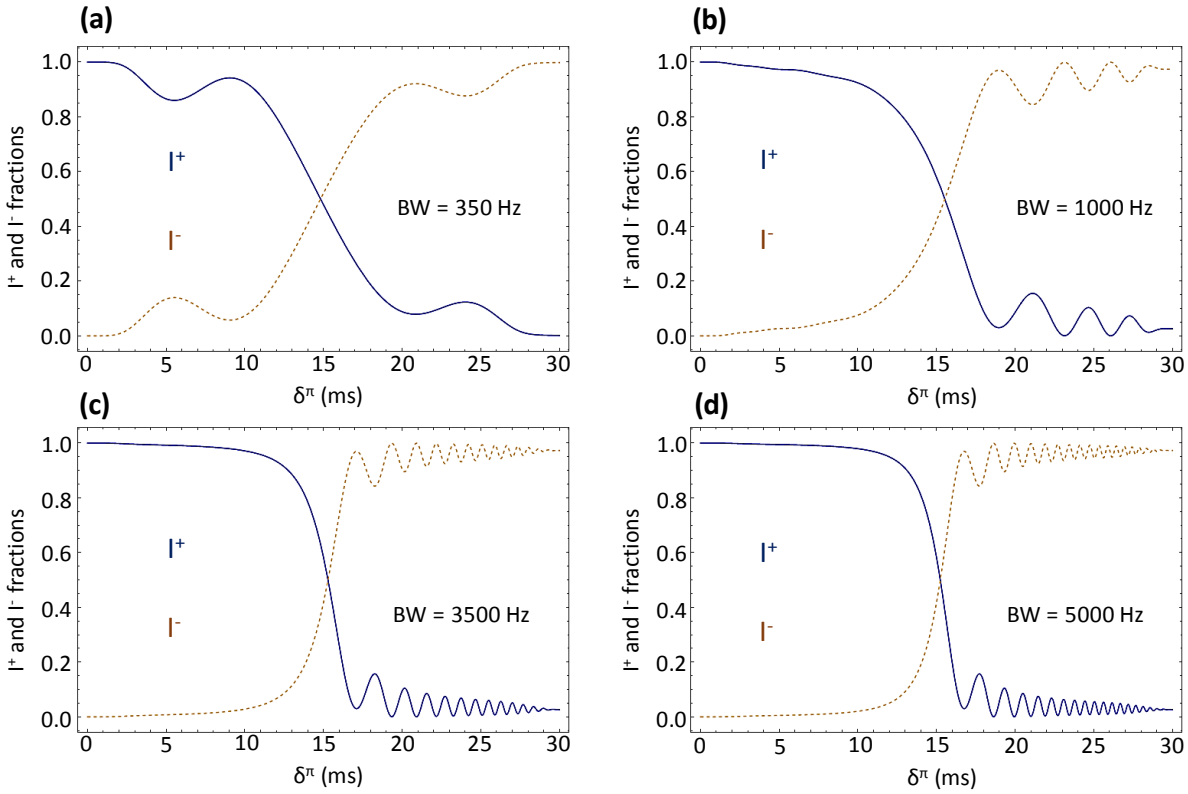

Figure C.5. Trajectories of the $I^+$and I^- product operators during a 30-ms chirp pulse applied together with a positive excitation gradient. **(a)**, **(b)**, **(c)** and **(d)** chirp pulses with respectively a BW of 350, 1000, 3500 and 5000 Hz. These simulations - performed with SpinDynamica [1] (Mathematica) – were carried out on a single spin located at the middle of the length of the sample (z=0). Theses numerical simulations highlight the necessary time to achieve the coherence inversion regarding to the band width of the chirp pulse.

At this stage, it may be tempting to increase again the band width thereby obtaining even more efficient chirp pulses. Unfortunately, it is worth keeping in mind that increasing BW involves the use of stronger excitation gradients since the frequency dispersion induced by G_e should match with BW to yield an efficient encoding: $\Delta f = BW$. The use of stronger G_e is associated with sensitivity losses due to the diffusion effects. Thereafter, to empirically determine an optimal band width value, we carried out a series of four UF diagonal spectra recorded with several values of BW whereas δ^{π} was fixed at 30 ms. These diagonal spectra are obtained simply by turning off the mixing 90° hard pulse and the coherence selection gradients of the UF CT PM COSY pulse-sequence. For each BW value, G_e is adjusted so that its frequency dispersion Δf matches with BW. The four different 180° chirp pulse are calibrated as described in the following section C.2.5. This study was performed on a sample of 3-bromo-ethylpropionate in acedtone-d_6. Figure C.6 shows the projections along the UF dimension from the methyl signal obtained with the different 30-ms chirp pulses. For low BW, *i.e.* 350 Hz, the echo suffered from distortions and was not located at the correct chemical shift (figure C.6a). This result is correlated to the spin response obtained by the numerical simulation presented in figure C.5a where the 180° rotation is not instantaneous. Higher BW enabled more efficient spatial encoding leading to echoes with a better line shapes (figure C.6b, 6c and 6d). However, a slight line broadening with a decrease of the amplitude was observed with the BW at 5 kHz compared to the echo obtained with BW = 3.5 kHz (figure C.6c versus C.6d). This is explained by the diffusion arising from the increase of G_e. This is coherent with observations and simulations made at high field [2]. A band width of 3.5 kHz was found as the best compromise between high degree of spatial encoding and diffusion effects.

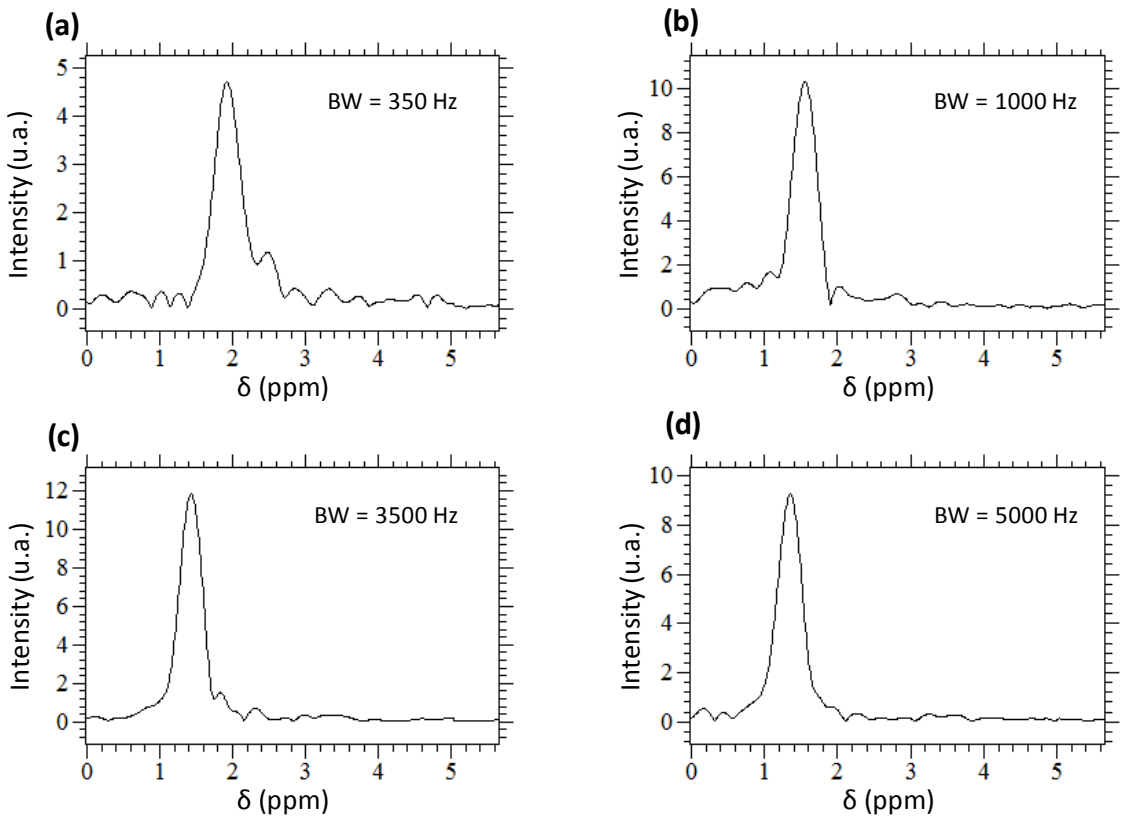

Figure C.6. Projections along the UF dimension of the methyl signal at 1.23 ppm from UF diagonal spectra recorded with several values of BW and G_e. The gradient amplitudes are defined as a percentage of the maximum value. **(a):** BW = 350 Hz and G_e = 1.16 %; **(b):** BW = 1000 Hz and G_e = 3.31 %; **(c):** BW = 3500 Hz and G_e = 11.6 %; **(d):** BW = 5000 Hz and G_e = 16.57 %. For each experiment the frequency dispersion generated by G_e corresponds to BW.

2.5. Calibration of a 180° chirp pulse

Once both the pulse duration and the band width are fixed, the power of the chirp pulse must be adjusted to perform the desired rotation. In practice, this is achieved experimentally via the pulse-sequence displayed in figure C.7a based on the echograd experiment in which the considered chirp pulse is applied together with the excitation gradient prior to the 90° hard pulse. After loading the same parameters as those used in the echograd experiment, the power in decibel of the chirp pulse is then increased step by step until yielding an inversion of the frequency profile (figure C.7c). It should be noticed that further increase of the power still leads to a 180° rotation due to the adiabatic regime.

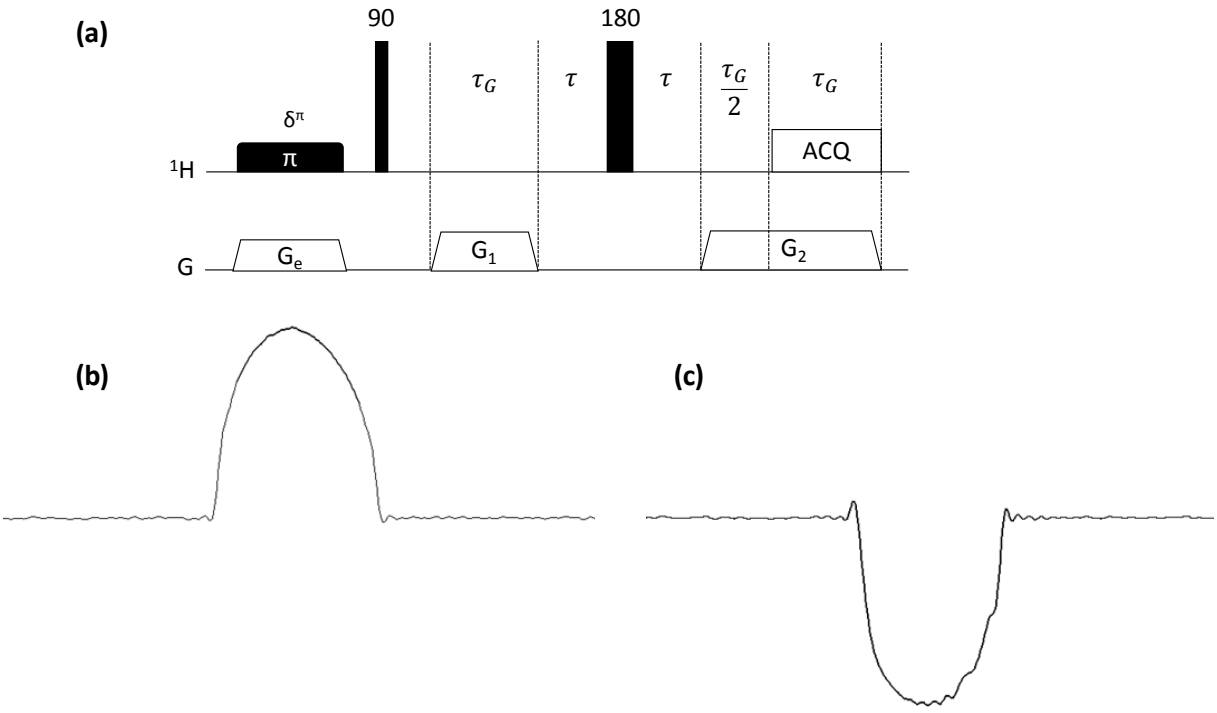

Figure C.7. (a): Scheme of the pulse sequence used for the calibration of a 180° chirp pulse. **(b)** Frequency domain obtained without active chirp pulse. **(b)**: Frequency domain when the power is sufficient to yield an inversion of the profile.

2.6. Implementation of the EPSI block

As shown in figure C.4, several parameters are involved to implement the EPSI block. A cross-cutting feature is the duration of the acquisition gradient T_a since this value pertains to the spectral widths. Increasing the duration T_a extends SW_{UF} (see equation C.4) whereas it reduces the SW_{Conv} (see equation C.5). This tradeoff is fortunately less stringent at 43 MHz so that a high value of T_a is an appealing choice.

Since the receiver is open during the application of the acquisition gradient, T_a is defined as follows: $T_a = N_k \,.DW$, where N_k is the number of points acquired during one acquisition gradient and DW is the dwell time between each point. In practice, T_a is therefore determined by the choice of N_k and DW. The latter should be short enough to digitalize properly the echoes occurring along the k-dimension. However, It is worth mentioning that the shorter is the value of DW, higher is the noise level during the detection. Indeed, the band width of the digital filter FBW – applied when the receiver is open – is automatically determined by the

software and is inversely proportional to DW. In what follows, 256 points were acquired with a DW of 5 µs.

The last parameter is the number of loops N_L, which impacts the resolution along the conventional dimension (see equation C.7). A number of 128 pairs of bipolar gradients was fixed for the further UF experiments

2.7. Apodisation along the UF dimension

In UF experiments, apodisation in the conventional dimension can be applied as in conventional 2D experiments [3]. This becomes more complex along the UF dimension since no FT is applied. As described in section A.4.3, the trick is to apply a FT along the ultrafast dimension. The resulting spatial profile is then multiplied by a filter function, usually a Gaussian, and an inverse FT is finally applied to the apodised spatial profile to retrieve echoes in the k-dimension. This procedure and the overall effect on a UF FID is illustrated in figure C.8 where a SNR enhancement is clearly visible (figure C.8a versus figure C.8d). At high field, this apodisation procedure reduces drastically the asymmetry of the line shape as shown in section A.4.3. In our benchtop system, most of the peaks do not suffer from such an asymmetric line shape (see figure C.9a). This effect is only observed for intense signal as illustrated in figure C.9c. Hence, the present spatial apodisation is mainly useful to increase the SNR (figure C.9a versus figure C.9b) while improving the line shape for intense peaks (figure C.9c versus figure C.9d).

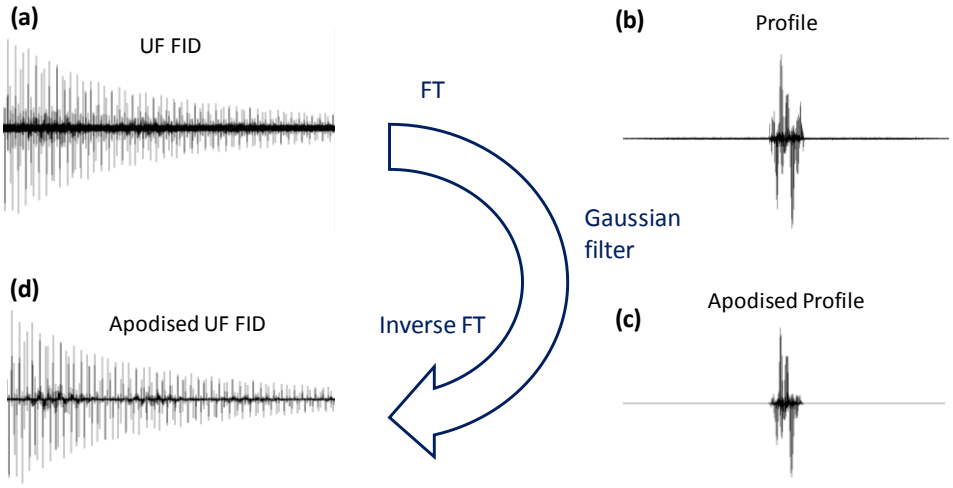

Figure C.8. Procedure of spatial apodisation along the UF dimension. **(a)**: initial UF FID. **(b)**: Resulting spatial profile after FT applied on the initial FID. **(c)**: apodised spatial profile via a Gaussian function. **(d)** Apodised FID thanks to an inverse FT applied on the apodised profile. Note how the level of noise is clearly reduced in the apodised UF FID. The data are from a UF diagonal experiment performed on a sample of ethanol in H_2O.

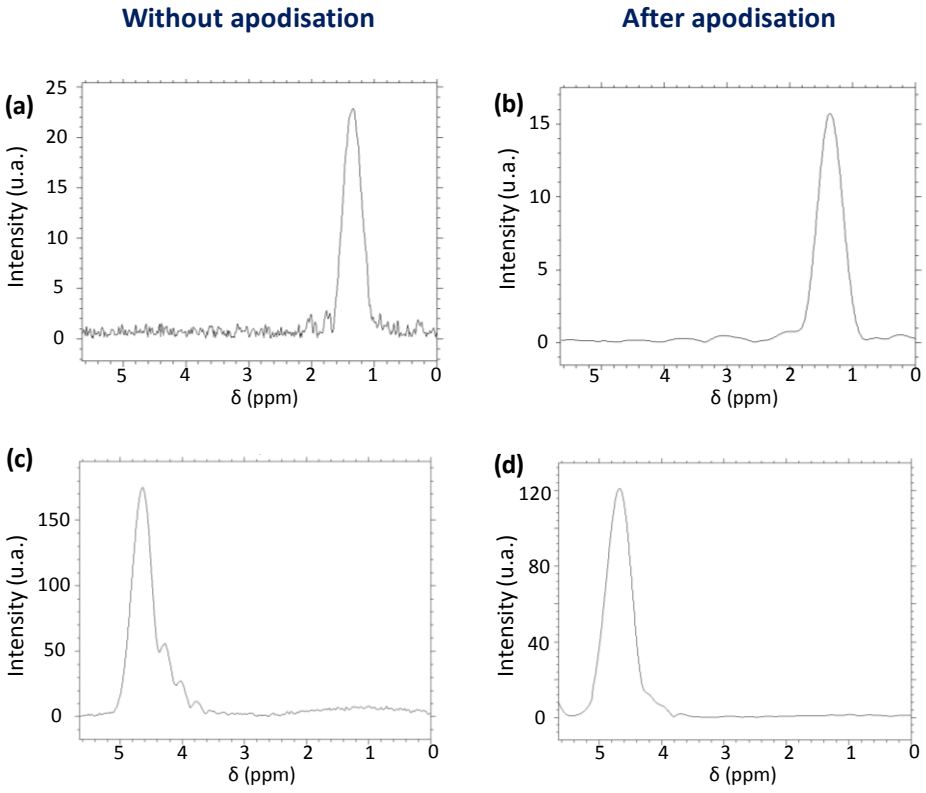

Figure C.9. Effects of the spatial apodisation on data from UF diagonal experiment performed on a sample of ethanol in H_2O. Projections along the UF dimension from the methyl signal without apodisation **(a)** and after apodisation **(b)**. It must be noted the significant SNR enhancement after the spatial apodisation. **(c)**: the intense hydroxyl signal, which suffers from an asymmetrical line shape. The spatial apodisation copes with this signal distortion **(d)**.

2.8. Correction of the acquisition gradient offsets

EPSI is demanding for the hardware. In theory, positive and negative acquisition gradients amplitudes are perfectly equal and constant from the first iteration to the last one: $G_a^+ = G_a^- = constant$. Unfortunately, this condition is not exactly hold in practice due to imperfections of the gradient coil. These potential gradient offsets lead to echoes whose positions in the k-dimension change in the course of the (k, t_2) trajectory (figure C.10b). This involves signal distortions after FT along the t_2-dimension (figure C.10a). It could be mentioned that this drift is not purely linear suggesting that the G_a^+/G_a^- offset evolves during t_2. Hence to outmatch this issue, the amplitude of one of the acquisition gradient has to become a variable in function of the index of the EPSI loop. In practice the pulse program automatically generates a list of G_a^- amplitudes as follows:

$$G_a^-(N_i) = G_a^+ + \alpha + \beta\sqrt{N_i} \qquad \text{(C.9)}$$

Where alpha and beta were adjusted experimentally to balance the gradient offset (figure C.10d). After the FT along t_2, this adjustment offers UF spectra with a significant improvement of the line shape (figure C.10c). It is worth mentioning that this optimization was carried only once to correct the hardware imperfections. The resulting couple (α, β) has always been efficient so far.

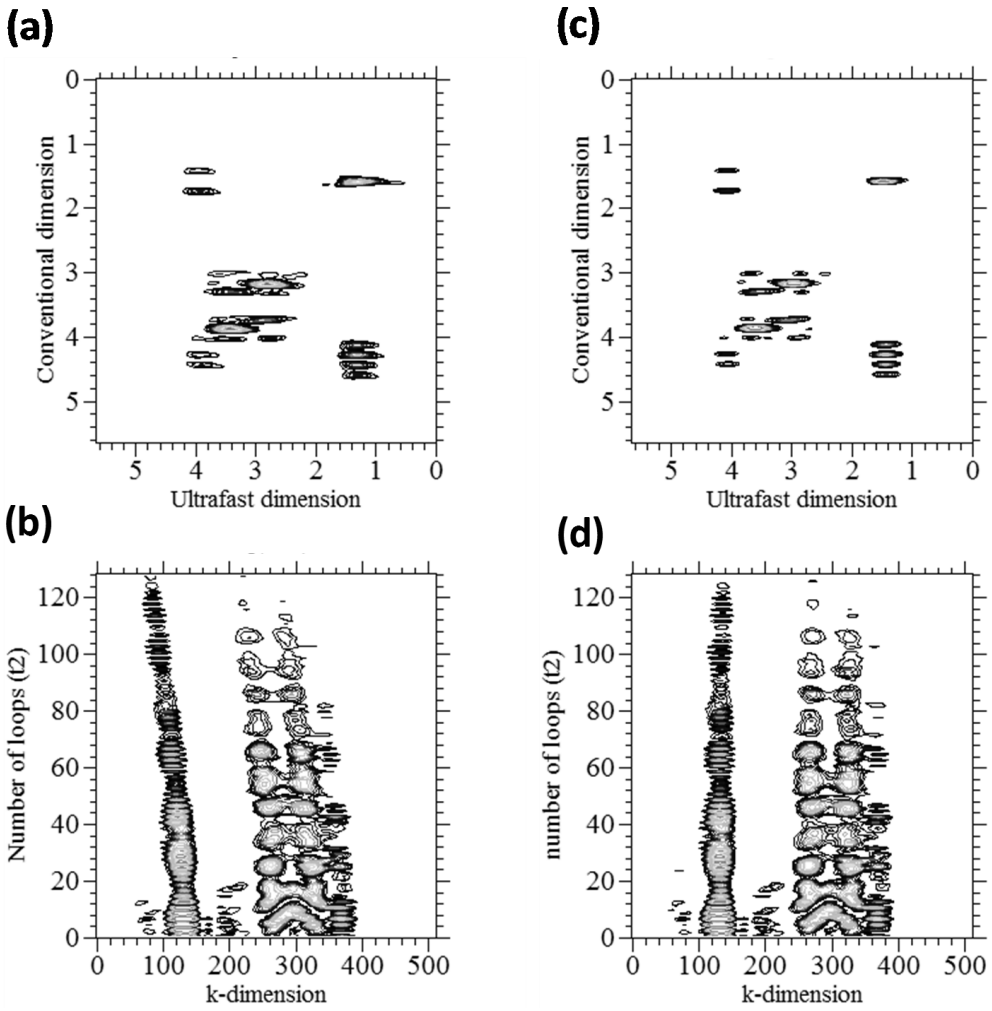

Figure C.10. (a): UF COSY spectra suffering from acquisition gradient offset and **(b)** the corresponding (k, t_2) map. **(c)** UF COSY spectra recorded without offsets and the corresponding (k, t_2) map **(d)**. Data from a UF COSY experiment performed on a sample of 3-bromo-ethylpropionate in acedtone-d_6.

2.9. Data processing

The principle of the data processing is described in the literature review: section A.4.3. We wrote a procedure in Prospa language that enables an automatic data treatment from the UF FID (Appendix 6). This consists of the following steps:

i. A spatial apodisation is applied on the UF FID including zero-filling
ii. Data arising from positive and negative gradients are split and rearranged, leading to two mirror-image S(k, t_2) maps.
iii. FT with zero-filling and sinusoidal apodisation is subsequently applied along the t_2 dimension, leading to symmetric S(F1, F2) maps plotted in magnitude mode.

iv. One of the map is inverted and added to the other one (correction of an eventual shift between the two data set is performed prior to the addition)

It is worth mentioning that the choice of the magnitude mode is justified by the 2D-peak shape in ultrafast spectra. Unlikely conventional 2D experiments - where the line shape is a product of two Lorentzian functions – the 2D peak shape is the product of a Lorentzian with a function $f(k/v)$ depending on the spatial encoding scheme and on the gradient encoding direction. As demonstrated by Frydman and collaborators, the CT PM spatial encoding provides real, purely-absorptive line shapes along the ultrafast dimension in contrast to the other schemes whereby a combination of echo and anti-echo, i.e $k > 0$ and $k < 0$, is required [4]. Therefore, this property makes the magnitude mode less critical in UF NMR compared to the same situation in non-phase sensitive conventional 2D experiments.

References

[1] C. Bengs, M.H. Levitt, SpinDynamica: Symbolic and numerical magnetic resonance in a Mathematica environment, Magn. Reson. Chem., DOI 10.1002/mrc.4642 n/a-n/a.
[2] P. Giraudeau, S. Akoka, Resolution and sensitivity aspects of ultrafast *J*-resolved 2D NMR spectra, J. Magn. Reson., 190 (2008) 339-345.
[3] P. Giraudeau, S. Akoka, Sensitivity and lineshape improvement in ultrafast 2D NMR by optimized apodization in the spatially encoded dimension, Magn. Reson. Chem., 49 (2011) 307-313.
[4] Y. Shrot and L. Frydman, Spatial encoding strategies for ultrafast multidimensional nuclear magnetic resonance, J. Chem. Phys., 128 (2008), 052209.

3. Gradient-based solvent suppression methods

3.1. A vital need in benchtop NMR

After the implementation of UF 2D NMR on our 43 MHz compact spectrometer, it appeared relevant to investigate the potential of the gradient coil to implement solvent suppression methods.

Indeed, the modern benchtop NMR spectrometers have been designed to circumvent the use of deuterated solvents for locking the static magnetic field. This is a determining advantage in many applications, especially in the field of reaction monitoring (see section A.1.1.2). Obviously, the downside of this feature is the associated huge and broad solvent peak, which often obscures the signals of interest. This is particularly the case at low-field where 1D ^{1}H spectra are already crowded. Beyond the strong overlaps located near the solvent resonance, other ones can be observed involving the ^{13}C satellite lines from carbonated solvents. Taken together with the drawbacks already mentioned in section A.1.1.2, it turns out that efficient solvent suppression methods, suitable with flow measurements, become a vital need to extend the potential of LF NMR spectroscopy.

The research article in the following section deals with the implementation of gradient based-solvent suppression methods on our benchtop device. First, a description of the features making solvent suppression a tricky task is given as well as a review of the different strategies to do this. Then, the implementation of such methods as well as an analytical evaluation both in static and flowing conditions are reported.

3.2. Implementation at 43 MHz. Evaluation both in static and flowing conditions

Gradient-based solvent suppression methods on a benchtop spectrometer

Boris Gouilleux, Benoît Charrier, Serge Akoka and Patrick Giraudeau

(Original research article)

Magnetic Resonance in Chemistry, 55 (2017) 91-98.

Abstract

Benchtop NMR emerges as an appealing alternative to widely extend the scope of NMR spectroscopy in harsh environments and for on-line monitoring. Obviously, the use of low-field magnets induces a dramatic reduction of the spectral resolution leading to frequent peak overlaps. This issue is even more serious since applications such as chemical process monitoring involve the use of non-deuterated solvents, leading to intense and broad peaks overlapping with the signals of interest. In this article, we highlight the need for efficient suppression methods compatible with flowing samples, which is not the case of the common pre-saturation approaches. Thanks to a gradient coil included in our benchtop spectrometer, we were able to implement modern and efficient solvent suppression blocks such as WET or excitation sculpting to deliver quantitative spectra in the conditions of the on-line monitoring. While these methods are commonly used at high-field, this is the first time that they are investigated on a benchtop setting. Their analytical performance is evaluated and compared under static and on-flow conditions. The results demonstrate the superiority of gradient-based methods, thus highlighting the relevance of implementing this device on benchtop spectrometers. The comparison of major solvent suppression methods reveals an optimum performance for the WET-180-NOESY experiment, both under static and on-flow conditions.

Introduction

In the pursuit of a better sensitivity and resolution, modern NMR spectrometers are based on stronger and stronger superconducting magnets, whose performance makes NMR spectroscopy essential for a wide range of applications, from the elucidation of (bio) chemical structures, to pharmaceutical, biomedical or food sciences. Unfortunately, the incompatibility of high-field NMR with harsh environments, the associated maintenance costs as well as the need for a dedicated laboratory involving specialized staff, have hampered the use of high field NMR (HF NMR) in production and industrial sites.

A new generation of compact and cryogen-free low-field spectrometers has emerged as a relevant alternative to extend the scope of NMR in harsh environments.[1] These benchtop spectrometers are no longer restricted to relaxometry, and they now deliver NMR spectra of sufficient quality to enable promising applications in fields such as chemical process monitoring [1-9] or food screening [10-12]. However, the analytical performance at low-field is significantly reduced compared to its high field counterpart. As a major drawback, the resolution is dramatically reduced since the frequency dispersion decreases with the static magnetic field while the scalar coupling constants remain unchanged. Peak overlaps between signals of interest are therefore ubiquitous. This is particularly true for applications such as reaction monitoring –the most reported application of benchtop NMR– where non-deuterated solvents are preferentially used to avoid potential isotope effects and for economic reasons. A consequence of using protonated solvents is that the intense and broad solvent signals will hamper the detection and/or quantification of the solute peaks. On top of that, strong solvent peaks lead to digitization issues since the dynamic range of the receiver limits the simultaneous detection of signals with large amplitude differences.[13] The resulting baseline distortions strongly impact the signal-to-noise ratio (SNR) and the areas of the peaks of interest. In this context, a suitable and efficient solvent suppression pulse sequence is crucial. Numerous and continuous efforts have been made at high field to suppress the solvent signal and to circumvent the issues mentioned above. From the first pre-saturation methods,[14] several tens of sophisticated suppression blocks have been designed in order to reach stronger and cleaner solvent suppressions. Some of them are efficient both inside an NMR tube and on flowing samples, as reported in the literature on hyphenated techniques.[15] This last point is of

particular interest for benchtop NMR, where a wide range of applications are carried out on flowing systems. In spite of their promising potential for low-field NMR, these modern suppression methods have not yet been implemented on benchtop spectrometers, since the implementation of a gradient coil in commercial models is extremely recent.[8]

Relying on a benchtop spectrometer (designed by Magritek, Aachen, Germany, a version of the commercial Spinsolve benchtop spectrometer) including a gradient coil, we evaluated the relevance of gradient-based solvent suppression methods, both on static and flowing samples. We first present an overview of the major building blocks of solvent suppression pulse sequences, then the specific features associated with flowing systems are discussed in the context of solvent signal suppression. Finally, an analytical evaluation of the major methods is presented through different criteria in terms of residual signal, trueness and robustness.

1. Overview of the solvent suppressions methods

1-1. Specificities of the solvent signal suppression

Efficiently reducing a strong solvent signal is not straightforward, as highlighted by the numerous articles dedicated to this topic in the last decades. Indeed three main physical and chemical phenomena make the solvent signal suppression difficult: the radiation damping (RD), the “faraway solvent” effect and the frequency instabilities.

Radiation damping is a well-known effect, well reported and described in the literature.[16] This physical phenomenon may be basically explained as follows: once excited, the strong solvent transverse magnetization leads to an oscillating current in the receiver coil, which generates a transverse magnetic field at the same frequency. As a result, the solvent relaxation is dominated by the short characteristic time of RD rather than by the longer transverse relaxation time T_2. Therefore, the solvent signal becomes much broader with potential phase distortions, and consequently more difficult to suppress. Since the radiation damping rate is proportional to B_0,[17] its impact is limited at low field compared to the two other effects described below.

The “faraway solvent” effect arises from the spins located at the edges of the sensitive volume, which experience a different radiofrequency and magnetic field compared to the bulk region.[18] These spins mostly contribute to the signal detected at the edge of the solvent peak, facilitating the peak overlaps with the nearby resonances. Some pulse sequences have been specifically designed to limit the effect of faraway water.[19]

The solvent frequency instabilities are detrimental to the efficiency of the solvent suppression. This is especially the case for applications like reaction monitoring where the position of the solvent peak is shifted as the composition of the sample evolves in the course of the reaction. In practice, a drift of the order of 6 Hz (*i.e.*, 0.14 ppm) is commonly observed on our benchtop spectrometer, which is detrimental to the quality of the solvent signal suppression.

1-2. Solvent suppression building blocks

Whatever the solvent suppression method used, it can be subdivided into three steps consisting of a preparation, an excitation and a readout block. For each of these steps, the different blocks mostly encountered in the literature are described below.

1-2-1 Preparation blocks

Among the panel of preparation blocks, the continuous wave saturation (Sat) (figure 1a) is probably the most used suppression block on high-field spectrometers.[14] This popularity is due to its ease of use and its efficiency for solvent signals located relatively far from the peaks of interest. Nonetheless, the approach remains sensitive to the various frequency shifts with a significant risk to impact the signals nearby the solvent peak. Moreover, this block is not efficient against the faraway solvent effect.

The WET block[20] (water suppression enhanced through T1 effects) (figure 1b) has emerged as a robust and versatile approach. It combines a train of selective shaped pulses applied together with gradient spoilers to selectively disperse the longitudinal component of the solvent magnetization. It enables an efficient selective suppression in a reduced time compared to the Sat-block with no need for signal averaging. The WET block is popular in hyphenated technics such as LC-NMR since its compactness and its single-scan character make it ideally suited for on-flow NMR.[15] Since the first publication, new WET schemes have been designed to improve the initial WET block.[18, 21] In particular, the WET-180[18] – including a

toggled 180° (adiabatic or hard) pulse with a modification of the last selective pulse (figure 1c)– yields a narrower solvent signal with a cleaner phase than the classical WET block.

1-2-2 Excitation blocks

The basic 90° hard pulse (figure 1d) is inherently sensitive to the faraway solvent leading to a broad solvent peak. Numerous excitation blocks have been developed to overcome the faraway solvent effect and therefore obtain a narrower residual signal. The first approach is the use of a composite 90° pulse[22] (CP) instead of the common 90° hard pulse. This is achieved by a train of four 90° hard pulses (figure 1e) with the following phases: x, y, -x, -y. By combining the inefficiency of each hard pulse on the edge of the sensitive volume, the faraway solvent is thus less excited while the region of interest experiences an effective 90°. Another strategy to cope with the faraway solvent is the Sat-180 block .[19] It is formed by a 90° pulse preceded by either an adiabatic or a hard 180° pulse, which is toggled on and off together with a change of 180° in the receiver phase (figure 1f). The water is first saturated by the appropriate preparation block, while the solute magnetizations and the faraway solvent are left intact along z. The 180° adiabatic pulse then inverts the solute magnetizations from +z to -z, while the faraway water magnetization is mainly unaffected and remains along +z. As a consequence, the 90° detection pulse generates a faraway water signal with an opposite phase compared to the signals of interest. The experiment is then repeated with the inversion pulse turned off, resulting in a signal where the solute and faraway water magnetizations have the same phase. The addition of these two transients cancels the faraway water signal while those of the solute magnetizations are co-added. It should be noted that this approach needs at least two scans.

The nuclear Overhauser effect spectroscopy sequence (NOESY-1D) is a widely used excitation block (figure 1g), especially in the field of metabolomics.[23, 24] This block is a 1D version of the 2D NOESY pulse sequence. It is well-recognized for reducing the effect of the faraway solvent by combining several contributions. The first one is a T_1-descrimination between the solutes and the solvent. This aspect is adjusted by tuning the mixing delay between the second and third 90° pulses. A continuous saturation could be further added if the optimized delay is long enough for a selective irradiation. The second contribution is related to the phase cycling and

is actually equivalent to a Sat-180 block without delay between the first two 90° pulses. This approach also requires two scans.

1-2-2 Readout blocks

The most common readout block is the simple observation of a free induction decay (FID) (figure 1h), ensuring that all the signals are detected except the solvent peak which has been suppressed through the use of the preparation and/or excitation blocks previously described. It is also possible to selectively suppress the solvent resonance at this stage thanks to pulse sequence elements inspired from the WATERGATE scheme,[25] the most widely used being excitation sculpting.[26] This readout block consists in a spin echo flanked by identical spoiler gradients including a selective 180° pulse prior to the 180° hard pulse. The solute signal is refocused by the 180° hard pulse while the solvent signal –previously inverted by the selective pulse– actually experiences a 360° rotation and its magnetization remains dispersed. The most efficient version –excitation sculpting– is based on a double spin echo (figure 1i).[26] These suppression methods are widely used in the field of protein NMR since they enable to observe exchangeable protons.[27] Nevertheless, these blocks generate signal distortions arising from the J-modulation during the echo time, making it difficult to quantify the solutes. A solution to cope with this drawback has been proposed, where the effect of J-modulation is reduced thanks to the application of a “perfect echo” flanked by spoiler gradients (figure 1j).[28]

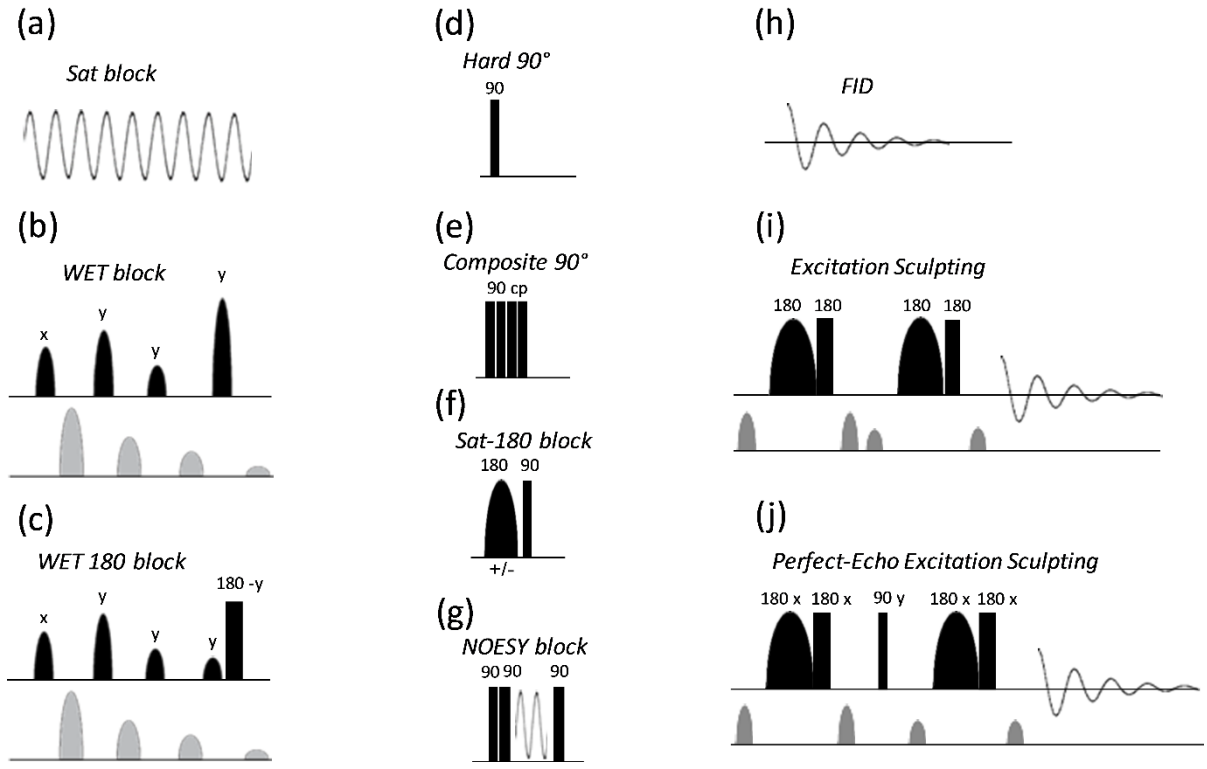

Figure 1. Basic building blocks used for solvent suppression methods and considered in this manuscript. From left to right the columns match with preparation, excitation and readout blocks

2. Specific feature of the on-flow NMR

The emergence of benchtop spectrometers extends the scope of NMR spectroscopy for chemical process monitoring. Performed in an on-line fashion, NMR provides a time resolved monitoring of the reaction progress, which is non-destructive and suitable for almost all compounds in contrast with commonly used spectroscopies such as UV-visible, FT-IR or Raman. Among the different methodologies, the on-line system in continuous flow is the most attractive one, especially compared to the case where the NMR tube is used as a reactor, which is too restrictive for numerous chemical processes.[29]

Yet, NMR experiments on flowing systems are associated to some special features which significantly impact the sensitivity, the resolution and the efficiency of the solvent suppression methods. NMR experiments on flowing liquids have been reported as early as in the 50's. Numerous investigations were made subsequently, resulting in a comprehensive description

of the effects involved by flowing liquids trough the sensitive volume V_s of the flow-cell.[30, 31] The first of these effects is commonly reported as "inflow effect",[3] which can be summarized as follows: during the NMR experiments, the excited spins are flowing out of the sensitive volume while the unexcited ones are flowing into it. The sensitive volume is therefore refreshed by unsaturated spins between two repetitions of the pulse sequence. This "inflow effect" leads to an intensity enhancement and allows shorter repetition times (TR) to reach quantitative conditions.[32] If the replenishment is achieved with fully polarized spins, this effect can be regarded as a change of the longitudinal relaxation rate T_1^{static} value by an effective T_1^{flow} expressed as follows:

$$\frac{1}{T_1^{flow}} = \frac{1}{T_1^{static}} + \frac{1}{\tau}$$

where τ is the residence time, *i.e.*, the time spent by the spins in the volume V_s. Obviously, the impact of this phenomenon on the NMR signal depends on the flow rate Q and on the characteristic lengths of the flow-cell, *i.e.*, the length of the sensitive V_s and pre-polarization V_p volumes (figure 2a). Assuming a laminar flow – which is usually the case in applications of online NMR – the mean velocity v is time-independent and can be directly calculated via the flow rate and section area of the sensitive volume. The residence time is in turn computed as the ratio of length of the sensitive volume l_s by the fluid velocity v:

$$\tau = \frac{l_s}{v} = \frac{V_s}{Q} = \frac{\pi\, l_s \left({}^{d}/_{2}\right)^2}{Q};$$

where d is the inner diameter of the flow-cell.

In this context, increasing the flow rate limits the residence time and in turn leads to an effective T_1^{flow} lower than T_1^{static}. Therefore, a higher flow rate enhances the signal sensitivity per time unit, then TR can be shortened while preserving quantitative conditions. Unfortunately, this opportunity should be considered with caution, since this "inflow effect" enhances the signal intensity as long as the excited volume elements are refreshed by fully

polarized spins.[3, 32] Therefore, this requires a sufficient time spent by the flowing sample in the pre-polarization volume V_p to allow the spins to reach their full thermal polarization. This necessary time is usually fixed at five times the T_1 measured in static conditions. Therefore, there is a maximum flow rate Q_{max} to remain in such conditions:

$$Q_{max} = \frac{V_p}{5 \, . T_1}$$

Typically this maximum flow rate is about 2 mL/min for a T_1 of 2 s in our experimental setup. Another feature involved by on-flow NMR, referred as "outflow effect", makes the use of high flow regimes even more problematic. Indeed, when the receiver is open, there is a probability that some polarized and excited spins leave the sensitive volume before the end of the acquisition. This translates into an effective transverse relaxation rate T_2^{flow}

$$\frac{1}{T_2^{flow}} = \frac{1}{T_2^{static}} + \frac{1}{\tau}$$

This effect is even more pronounced for short residence times and leads to significant line broadening. The overall effect results in a compromise between the two effects mentioned above, leading to an optimum sensitivity for a flow rate Q_{max} depending on the TR/T_1 ratio. We performed experiments at different flow rates and for different TR/T_1 ratios on a model sample –ethanol at 40% in H_2O– to illustrate this compromise in the case of our benchtop spectrometer (Figure 2b). The intensity S_0 is here monitored through the area of the ethanol triplet (1.05 ppm). For this signal, a T_1^{static} of 2.60 s was experimentally measured at 43.6 MHz. Each point was computed as the mean value of three successive experiments performed with 4 scans and an acquisition time of 3.28 s. The results clearly show the existence of an optimal flow rate, with a relatively flat curve close to this maximum. For common values of TR/T_1 the optimal flow rates range from 0.8 to 2.0 mL/min, therefore the evaluation of the solvent suppression methods will be performed at these two extrema.

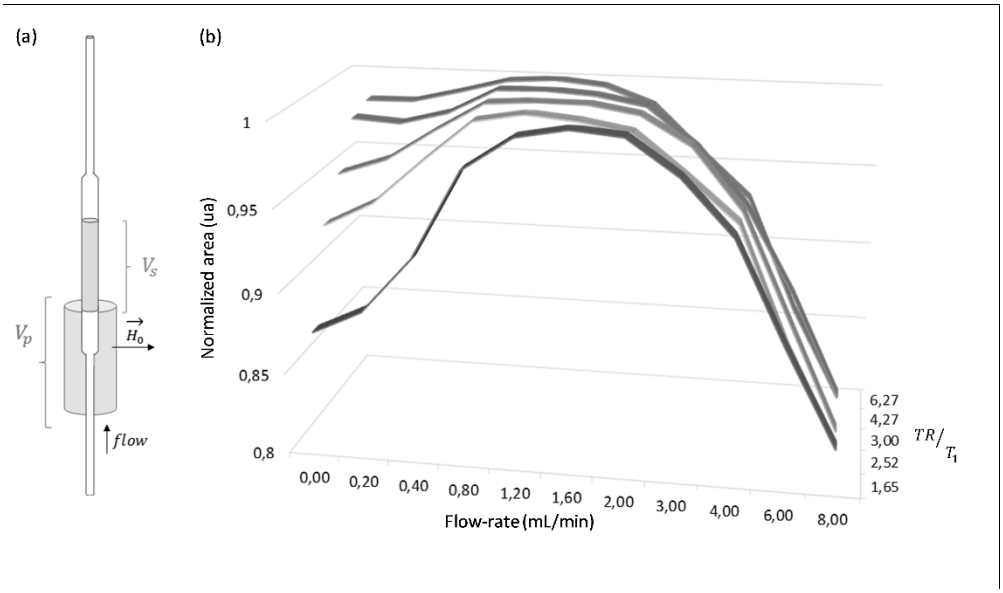

Figure 2. (a) Scheme of the flow cell implemented inside the benchtop NMR spectrometer. $\overrightarrow{H_0}$ represents the static magnetic field vector which is perpendicular to the axis of the tube in the Hallbach design. V_s and V_p are the sensitive and pre-polarization volumes. (b) Curves of Intensity S_0 as a function of the flow rate displayed for different TR/T_1 ratios. Each value of intensity matches with the mean value of three successive experiments performed on a sample of ethanol at 40% in H_2O. The intensity is measured by the area of the ethanol triplet located at 1.05 ppm.

3. Evaluation of solvent suppression methods

3-1 Evaluation criteria

According to the aforementioned aspects, the ideal suppression method on a benchtop spectrometer should meet the following requirements: i) reduce the solvent signal as much as possible; ii) be highly selective since the spectral width is dramatically reduced at low field, while avoiding baseline distortions; iii) be robust *vis-à-vis* the instabilities of the carrier frequency in order not to impact the peaks close to the solvent resonance. iv) be adapted to on-flow conditions, which means that the method should be fast enough to account for the refreshment of spins, even for short residence times.

We evaluate the solvent suppression methods described in Part 1 through several analytical criteria such as trueness and robustness. Moreover, these criteria are evaluated at two flow rates: 0.8 and 2.0 mL/min, and also in static conditions. For this purpose we rely on simple protocols,[33] applied to samples of lactate and alanine in non-deuterated H_2O. The alanine sample provides a common situation with a quadruplet shifted by 1.1 ppm (50 Hz) from the water signal. The lactate sample provides a more challenging case with a quadruplet located

at 4.1 ppm, at only 30 Hz from the water signal. The experimental conditions used for these measurements, both for static and flowing samples, are given in the experimental section.

3-2 Overview of the solvent residual signals

Figure 3 shows an overview of the residual water signal obtained with the different methods on the lactate sample. In the absence of solvent suppression, there is a strong overlap between the water and lactate signals. This overlap, combined with a high dynamic range, makes the spectrum unsuitable for identification and quantification. The different solvent suppression methods may be divided into two categories. The first one is based on saturation blocks whereas the second one relies on methods applying gradient-pulses such as WET and excitation sculpting schemes. The reduction of the water signal is limited with the use of saturation blocks since the continuous wave power should remain low enough to avoid impacting the nearby peaks. On the contrary, methods including WET or excitation sculpting blocks provides a stronger reduction of the solvent resonance. Therefore, the approaches based on gradient pulses emerge as the best choice according to the first evaluation criterion mentioned in 3.1. But as mentioned before, the reduction of the solvent peak is not sufficient to yield spectra suitable for quantification. Indeed these methods have different impacts on the baseline and on the multiplet close to water resonance. Figure 4 illustrates this impact on the lactate quadruplet at only 30 Hz from the water resonance. The Sat, Sat-CP, and WET methods are not efficient since they lead to overlaps between a part of the residual water signal and the closest peaks of interest. The methods including a scheme dedicated to the suppression of the faraway water as Sat-180, WET-CP and WET-180 lead to narrower residual water signals, and the quadruplet at 4.1 ppm is entirely resolved. In terms of baseline, the NOESY excitation block limits the potential distortions and provides a flat baseline compared to the other excitation schemes. This result is highlighted, for instance, through the comparison between Sat-180 and Sat-NOESY, or even between WET-180 and WET-180-NOESY. The best results are actually obtained by pulse-sequences combining the advantages of several suppression blocks like WET-180-NOESY, which yields a very narrow residual signal with a flat baseline. Finally, while the methods based on excitation-sculpting provide an efficient solvent suppression, they lead to strong signal distortions due to the J-modulation

arising from the spin echoes. The resulting distorted shapes are detrimental to quantification. This well-known effect is further aggravated at low-field, since long echo times are imposed by the long duration of selective pulses due to the very narrow spectral width. A “perfect echo” version of this suppression method was recently developed to overcome this issue by cancelling the J-modulation effect through the use of a perfect echo instead of the classical spin echo. Reported at high-field,[28] the PE-ES-Sel appears less suitable at low-field due to the second order nature of the couplings (figure 4). Beyond this first overview, the specific case of the exchangeable protons in equilibrium with the solvent should be mentioned. Obviously, the saturation blocks are not suitable in such a case but both WET and excitation sculpting schemes could be used with different features. At high field, the WET block preserves the signal of movable protons as long as the block duration remains short. This property should be taken with care at low-field. Indeed, the required selectivity involves longer selective pulses increasing the duration of the WET blocks and could impact the signal from exchangeable protons. Another solution is the excitation sculpting since it does not saturate the solvent during the preparation step. However, this method leads to some drawbacks at low-fields as described above.

To sum up this overview, WET-CP, WET-180, WET-180-NOESY and Sat-NOESY emerge as promising suppression methods. Therefore, these methods were selected for a more quantitative study, described in the next paragraphs. In particular, WET-180-NOESY appears very promising compared to the other approaches as it copes with the faraway water issue while limiting the baseline distortions.

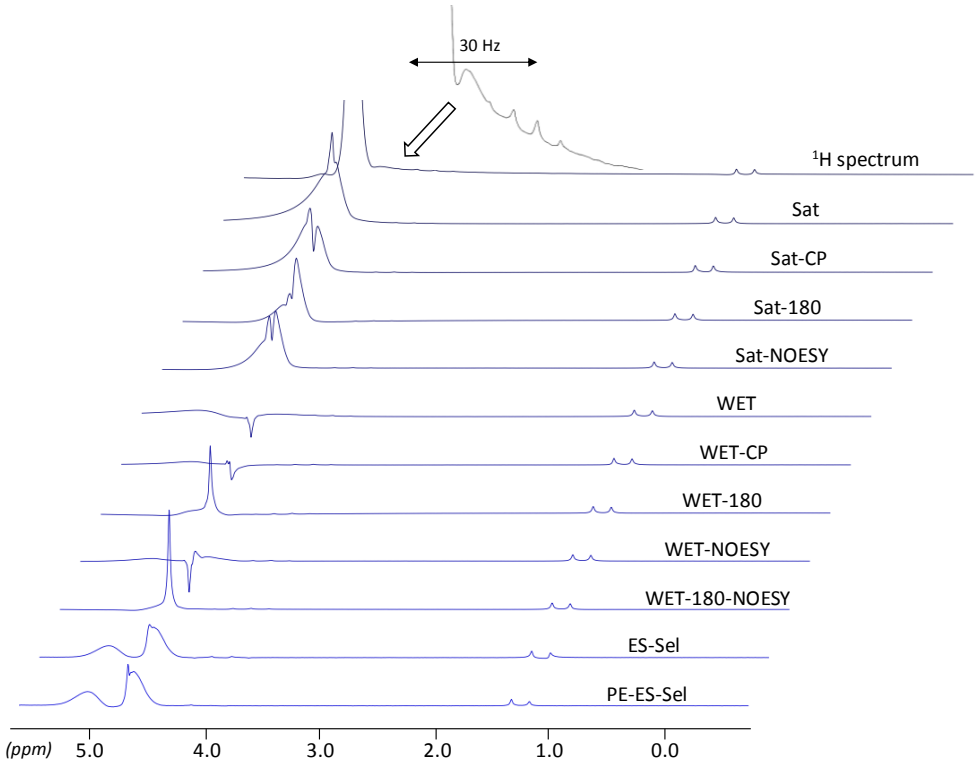

Figure 3. Overview of the residual water signals with various solvent suppression methods. The spectra were recorded from a sample of lactate at 0.2 mol/L in H_2O. To facilitate the comparison, the same receiver gain and vertical scale were applied for all these experiments.

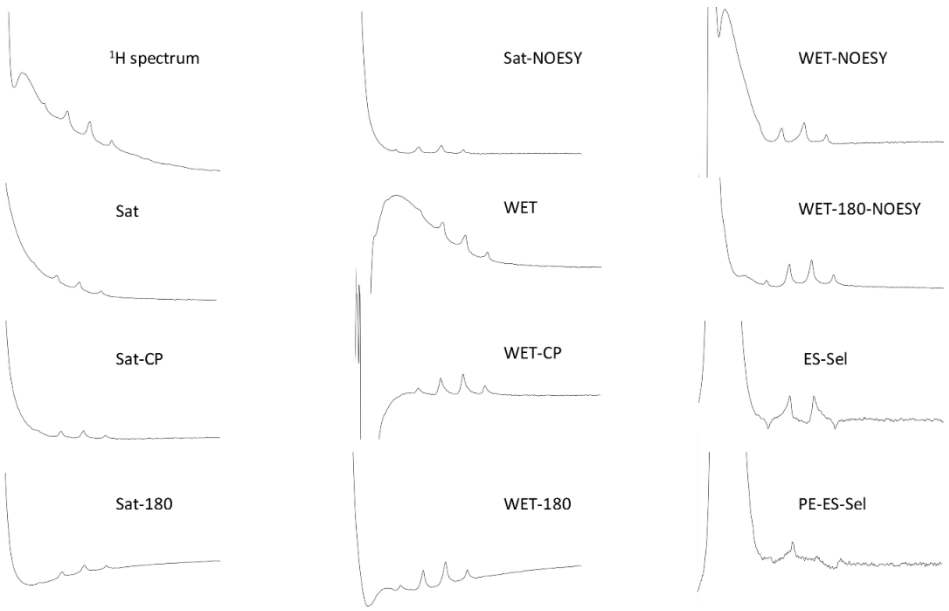

Figure 4. Impact of the water suppression on the nearby protons for various solvent suppression methods (zoom of Figure 3). These spectra were obtained from a sample of lactate at 0.2 mol/L in H_2O.

3-3 Evaluation of the trueness

As described above, WET-CP, WET-180, Sat-NOESY and WET-180-NOESY enable a clean and efficient solvent suppression. However, it is important to evaluate if the resulting spectra remain quantitative given the potential impacts of the suppression methods on the nearest resonances and on the baseline. We chose to evaluate this feature based on trueness. To this end, we compare the area of the quadruplet divided by the area of the doublet located faraway the peak of water, in the case of alanine and lactate samples. We define the parameter Δ to evaluate the trueness:

$$\Delta = 100 \, . \, \frac{\alpha_{exp} - \alpha_{th}}{\alpha_{th}} \ (\%)$$

Where α_{exp} and α_{th} are respectively the experimental and theoretical ratio between the area of the quadruplet (CH) divided by the area of the doublet (CH_3). Therefore, Δ should be as close to zero as possible.

The repetition time was chosen long enough for quantitative conditions (TR > 5.T1), and for each pulse sequence the final value is the average of three successive experiments. Before repeating the sequence, the carrier frequency is readjusted to the water frequency in order to exclude frequency instabilities from the measurement of trueness. The evaluation is first performed in static conditions, *i.e.,* inside an NMR tube, then at flow rates of 0.8 mL/min and 2.0 mL/min.

Table 1. Trueness of the solvent suppression methods for a sample of alanine at 0.2 mol/L in H_2O. The evaluation is first performed in static conditions, *i.e.,* inside an NMR tube, then at flow rates of 0.8 mL/min and 2.0 mL/min. For each flow rate, the first column gives the parameter Δ, the second one is the standard deviation (SD) evaluated on three experiments.

	0,0 mL/min		**0,8 mL/min**		**2,0 mL/min**	
	Δ	SD	Δ	SD	Δ	SD
WET-180-NOESY	1.80%	2.9%	3.00%	2.8%	4.50%	5.4%
WET-CP	26.1%	4.8%	32.1%	3.0%	28.53%	8.5%
WET-180	8.11%	2.1%	6.91%	4.3%	3.00%	6.0%
Sat-NOESY	9.01%	2.8%	23.12%	5.4%	14.71%	5.4%

Table 1 gives the ratio obtained for each method on the alanine sample. WET-180, Sat-NOESY and WET-180-NOESY provide ratios close to the expected value as long as the experiments are performed in a tube. Especially the WET-180-NOESY approach delivers quantitative spectra, illustrated by a Δ of 1.80% with a good repeatability: 2.9 % (table 1). On the contrary, the WET-CP is not quantitative, even in static conditions. This could be explained by the strong baseline distortions which were found difficult to correct. The same experiments performed on a flowing sample highlight the weakness of the Sat-NOESY sequence, which no longer yields quantitative spectra. The failure of Sat-NOESY on a moving liquid is not so surprising since the saturated spins of the solvent are refreshed by unsaturated ones in the course of the experiment, making the saturation far less efficient. Moreover, the frequency drift occurring through the experiment reduces the efficiency and the selectivity of the pre-saturation. More generally, this result can be extended for all the suppression methods relying on the Sat block during the preparation step. On the contrary, the performances of the WET-CP, WET-180 and WET-180-NOESY are not significantly affected by the flow, even in the challenging case of lactate (Table 2). The WET blocks, relying on soft pulses instead of a long continuous wave, are characterized by a short preparation step compared to the Sat blocks and are therefore less sensitive to the refreshment of the solvent spins even at high regime. This result highlights the suitability of the different WET blocks on flowing liquids, which confirms previously reported results in the field of NMR hyphenated with chromatography.[15] Like in the static

experiments, the WET-180-NOESY approach yields again the best trueness with a good repeatability.

While WET-180 and WET-180-NOESY appear well-suited for on-flow applications on common samples, it is interesting to evaluate their potential through a more challenging case. Table 2 shows a similar evaluation performed on the lactate sample. In this case, only the WET-180-NOESY method delivers a reasonable trueness. Moreover, this result is extended for a flowing sample at low and high flow rates with a good repeatability (Table 2).

Table 2. Trueness of the solvent suppression methods for a sample of lactate at 0.2 mol/L in H_2O. The evaluation is first performed in static conditions, *i.e.,* inside an NMR tube, then at flow rates of 0.8 mL/min and 2.0 mL/min. For each flow rate, the first column gives the parameter Δ, the second one is the standard deviation (SD) evaluated on three experiments.

	0.0 mL/min		**0.8 mL/min**		**2.0 mL/min**	
	Δ	SD	Δ	SD	Δ	SD
WET-180-NOESY	3.60%	2.7%	4.80%	2.5%	8.41%	4.0%
WET-CP	68.5%	7.2%	58.3%	4.5%	61.0%	5.2%
WET-180	49.3%	4.5%	46.0%	3.6%	33.6%	8.2%
Sat-NOESY	74.5%	8.7%	61.6%	9.5%	54.1%	7.3%

3-4 Robustness versus frequency variations.

Besides trueness, evaluating the impact of the frequency instabilities is particularly relevant for on-flow NMR, since the carrier frequency is likely to become more unstable in this situation. A drift from –6 to + 6 Hz (*i.e.,* from -0.14 to 0.14 ppm) is commonly observed in our on-flow set up, which is potentially impacting at 43 MHz. We evaluated the robustness through seven experiments varying the carrier frequency from -6 to 6 Hz. For each value of the difference between the water resonance and the carrier frequency (Δ_f), we measured the robustness via the parameter ΔS_f computed as follows:

$$\Delta S_f = 100 \, . \, \frac{S_{\Delta f} - S_0}{S_0}$$

where S_0 is the ratio of the area between the doublet and the quadruplet when the water signal is on resonance, and $S_{\Delta f}$ the value of this ratio when the frequency is shifted. ΔS_f should remain as close as possible to zero if the method is robust.

The values of ΔS_f measured with the different methods are plotted in Figure 5 for the alanine and lactate samples. Since we observed a dramatic increase in ΔS_f with the Sat-NOESY, the results obtained with this method are not shown on the graphs. This conclusion is not so surprising since it is well-known that the pre-saturation is highly sensitive to the frequency variations, which is particularly critical at low field. On the contrary, the results obtained on the sample of Alanine show an acceptable robustness (lower than 6.5 %) with the use of the WET-180 and WET-180-NOESY sequences (figure 5a). It can be noted that WET-CP is more sensitive to the frequency variations than the other WET blocks. This is illustrated by values of ΔS_f over 10% for variations Δ_f superior to 4 Hz. For the more challenging case of lactate (Figure 5b), the robustness dramatically decreases for all the methods. Nonetheless, the WET-180 method offers the best robustness whereas WET-CP becomes unsuitable.

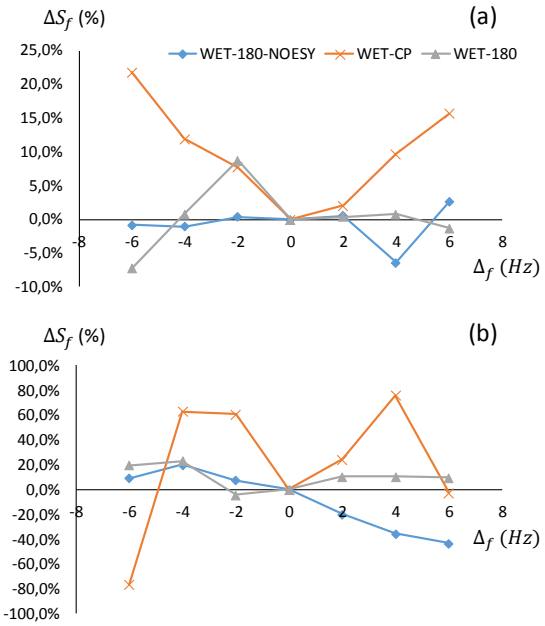

Figure 5. Robustness versus frequency variations. Evolution of the integral ratio between the quadruplet and the doublet as a function of the relative position of the carrier frequency, on a sample of alanine (a) and lactate (b) at 0.2 mol/L in H_2O.

Conclusion

The reduced spectral width associated with benchtop NMR, combined to the frequent use of non-deuterated solvents, requires suitable methods to efficiently suppress the high and broad solvent signal. This article highlights the inability of the common saturation blocks to strongly reduce the solvent peak at low field without impacting protons resonating close to the solvent signal. Moreover these common methods become unsuitable for on-line applications such as chemical process monitoring. The gradient coil included in our hardware opens new prospects to suppress the solvent peak, relying on more modern and sophisticated sequences for solvent suppression. The evaluation of these methods in term of residual solvent signal, trueness and robustness sheds light on the particular efficiency of a WET-180 preparation combined with a NOESY block, resulting in a WET-180-NOESY pulse sequence. A special trade-off concerns the monitoring of exchangeable protons in equilibrium with the solvent. In such a situation, both WET and excitation sculpting schemes could be used with different features. More generally, the recent methods using gradient-pulses provide a real toolbox for the solvent suppression while being suitable with flowing systems. Besides modern gradient-based methodologies such as diffusion experiments or Ultrafast NMR,[8, 9] the results presented in this article form a new argument towards the systematic implementation of a gradient coil in the hardware of benchtop spectrometers.

4. Experimental section

4.1 Benchtop spectrometer

The experiments were performed on a Spinsolve from Magritek, working at a frequency of 43.62 MHz via a permanent magnet based on a Hallbach design.[34] This equipment includes a gradient coil along the B_0-axis (*i.e.*, along the transverse plane of the NMR tube) which can generate a maximum field gradient of 0.16 T/m and operated through the Prospa Software. The spectrometer enables experiments without deuterated solvents thanks to a built-in external fluorine lock system.

4.2 Samples

Lactate and alanine were dissolved in H_2O, yielding a concentration of 0.2 mol/L. The samples were either analyzed in a 5 mm NMR tube, or placed in a flask and flowed to the NMR spectrometer by a peristaltic pump at a rate of 0.8 or 2 mL.min^{-1} through a by-pass system consisting of an NMR flow-cell and PEEK tubing for a total volume of 3.8 mL.

4.3 Suppression methods

The duration of the hard pulses was tuned at 6.35 µs to provide a 90° flip angle at 0 dB, which corresponds to a power of 39.37 kHz. It should be noted that the RF power values mentioned in the following description are only approximations due to the non-linearity of the RF amplifier in our hardware. The carrier frequency was adjusted to the water frequency. All the spectra were recorded with 4 scans including 2 dummy cycles for experiments performed inside the NMR tube, then 2 scans without dummy cycles for flowing samples. For each evaluated method, a series of three experiments was achieved with a dwell-time of 500 µs and an identical receiver gain fixed at 34 dB. Each spectrum was calibrated via the chemical shift of the doublet at 1.2 ppm for alanine and 1.3 ppm for lactate. The selective pulses (required for certain blocks) were designed with a Gaussian shape with a truncation level at 1% of the maximum value. The repetition time TR was fixed at 18 s to reach quantitative conditions, *i.e.*, $TR > 5.T_1$ for experiments taking place inside the NMR tube. As the longitudinal rate is reduced in presence of a flowing liquid, the repetition time is therefore adjusted according to the residence time so that $TR > 5.T_1^{flow}$. In practice the values of the effective relaxation rate T_1^{flow} are computed thanks to the equation given in section 2. With an inner diameter of 4 mm for the flow-cell, TR is fixed respectively at 11.5 s and 6.5 s for 0.8 and 2.0 mL/min flow rates, respectively.

4.3.1 Sat block

The pre-saturation was achieved by a continuous wave at the water resonance frequency during all the recovery period and with a RF power of 278 Hz.

4.3.2 Sat-180

The inversion was achieved by a hard 180° pulse, which was toggled on and off together with a change of 180° in the receiver phase. The water was previously saturated thanks to the same pre-saturation as in the previous block.

4.3.3 NOESY blocks

The water was saturated during the recovery delay as described in 4.3.1. The mixing time of the NOESY block was fixed at 6 ms, without pre-saturation during this mixing step.

4.3.5 WET blocks

The four Gaussian selective pulses were applied with a RF power of 1011, 1047, 832, 1189 Hz and a length of 82 ms. These values were experimentally adjusted in order to obtain the minimal residual solvent signal. The gradient spoilers (trapezoidal shape) were applied for 2.2 ms with the following power: 85.0, 42.5, 21.3, and 10.6 % of the maximum strength.

4.3.6 WET-180 blocks

The four Gaussian selective pulses were applied with a RF power of 1086, 1047, 832, 412 Hz. The last soft pulse was followed by a 180° hard pulse. These values were experimentally adjusted in order to obtain the minimal residual solvent signal. The gradient spoilers (trapezoidal shape) were applied for 2.2 ms with the following power: 85.0, 42.5, 21.3, and 10.6 % of the maximum strength.

4.3.7 ES-Sel blocks

The refocusing 180° selective pulse was a Gaussian pulse of 82 ms with a RF power of -1217 Hz. The refocusing gradients (trapezoidal shape) were applied for 2.0 ms with the following strength: 57 and 28.5 % of the maximum power.

4.4 Data Processing and analysis

The FIDs were processed in Mnova (MestreLab Research) with an exponential apodization (line broadening of 0.2 Hz). A baseline correction was achieved through a Whitthaker smoother correction provided by Mnova. For each series of experiments the spectra were

manually aligned, then displayed together as a stacked plot so that the same regions were used for peak integrations.

Acknowledgments

The authors warmly acknowledge Magritek, in particular Ernesto Danieli, Juan Perlo and Andrew Coy, for their strong support. We also thank Michel Giraudeau for linguistic assistance. This project was funded by Région Pays de la Loire (Grant RésoNantes).

References

1. K. Singh and B. Blümich, *TrAC Trend Anal. Chem.*, DOI: http://dx.doi.org/10.1016/j.trac.2016.02.014.
2. B. Blümich, *TrAC Trends Anal. Chem.*, DOI: http://dx.doi.org/10.1016/j.trac.2015.12.012.
3. F. Dalitz, M. Cudaj, M. Maiwald and G. Guthausen, *Prog. Nucl. Magn. Reson. Spectrosc.*, **2012**, *60*, 52-70.
4. V. Sans, L. Porwol, V. Dragone and L. Cronin, *Chem. Sci.*, **2015**, *6*, 1258-1264.
5. M. V. Silva Elipe and R. R. Milburn, *Magn. Reson. Chem.*, **2015**, DOI: 10.1002/mrc.4189.
6. S. K. Kuster, E. Danieli, B. Blumich and F. Casanova, *Phys. Chem. Chem. Phys.*, **2011**, *13*, 13172-13176.
7. E. Danieli, J. Perlo, A. L. L. Duchateau, G. K. M. Verzijl, V. M. Litvinov, B. Blümich and F. Casanova, *ChemPhysChem*, **2014**, *15*, 3060-3066.
8. B. Gouilleux, B. Charrier, E. Danieli, J.-N. Dumez, S. Akoka, F.-X. Felpin, M. Rodriguez-Zubiri and P. Giraudeau, *Analyst*, **2015**, *140*, 7854-7858.
9. B. Gouilleux, B. Charrier, S. Akoka, F.-X. Felpin, M. Rodriguez-Zubiri and P. Giraudeau, *TrAC Trends Anal. Chem.*, DOI: http://dx.doi.org/10.1016/j.trac.2016.01.014.
10. T. Parker, E. Limer, A. D. Watson, M. Defernez, D. Williamson and E. K. Kemsley, *TrAC, Trends Anal. Chem.*, **2014**, *57*, 147-158.
11. W. Jakes, A. Gerdova, M. Defernez, A. D. Watson, C. McCallum, E. Limer, I. J. Colquhoun, D. C. Williamson and E. K. Kemsley, *Food Chem.*, **2015**, *175*, 1-9.
12. R. d. O. R. Ribeiro, E. T. Mársico, C. d. S. Carneiro, M. L. G. Monteiro, C. C. Júnior and E. F. O. d. Jesus, *J. Food Eng.*, **2014**, *135*, 39-43.
13. S. Davies, C. Bauer, P. Barker and R. Freeman, *J. Magn. Reson.*, **1985**, *64*, 155-159.
14. D. I. Hoult, *J. Magn. Reson.*, **1976**, *21*, 337-347.
15. S. H. Smallcombe, S. L. Patt and P. A. Keifer, *J. Magn. Reson. Ser. A*, **1995**, *117*, 295-303.
16. N. Bloembergen and R. V. Pound, *Phys. Rev.*, **1954**, *95*, 8-12.
17. V. V. Krishnan and N. Murali, *Prog. Nucl. Magn. Reson. Spectrosc.*, **2013**, *68*, 41-57.

18. H. Mo and D. Raftery, *J. Biomol. NMR*, **2008**, *41*, 105-111.
19. H. Mo and D. Raftery, *J. Magn. Reson.*, **2008**, *190*, 1-6.
20. R. J. Ogg, P. B. Kingsely and J. S. Taylor, *J. Magn. Reson. Ser. B*, **1994**, *104*, 1-10.
21. S. Zhang, X. Yang and D. G. Gorenstein, *J. Magn. Reson.*, **2000**, *143*, 382-386.
22. A. Bax, *J. Magn. Reson.*, **1985**, *65*, 142-145.
23. O. Beckonert, H. C. Keun, T. M. D. Ebbels, J. Bundy, E. Holmes, J. C. Lindon and J. K. Nicholson, *Nat. Protocols*, **2007**, *2*, 2692-2703.
24. R. T. McKay, *Concept. Magn. Reson.*, **2011**, *38A*, 197-220.
25. M. Piotto, V. Saudek and V. Sklenár, *J. Biomed. NMR*, **1992**, *2*, 661-665.
26. T. L. Hwang and A. J. Shaka, *J. MAgn. Reson. Ser. A.*, **1995**, *112*, 275-279.
27. S. Grzesiek and A. Bax, *J. Am. Chem. Soc.*, **1993**, *115*, 12593-12594.
28. R. W. Adams, C. M. Holroyd, J. A. Aguilar, M. Nilsson and G. A. Morris, *Chem. Commun.*, **2013**, *49*, 358-360.
29. D. A. Foley, A. L. Dunn and M. T. Zell, *Magn. Reson. Chem.*, **2016**, *54*, 451-456..
30. L. R. Hirschel and L. F. Libelo, *J. Appl. Phys.*, **1961**, *32*, 1404-1405.
31. D. W. Arnold and L. E. Burkhart, *J. Appl. Phys.*, **1965**, *36*, 870-871.
32. A. Nordon, C. A. McGill and D. Littlejohn, *Analyst*, **2001**, *126*, 260-272.
33. P. Giraudeau, V. Silvestre and S. Akoka, *Metabolomics*, **2015**, *11*, 1041-1055.
34. E. Danieli, J. Perlo, B. Blümich and F. Casanova, *Angew. Chem. Int. Edit.*, **2010**, *49*, 4133-4135.

3.3. Commentaries and perspectives

According to this study the best analytical performance is reached by the application of a WET-180 block following by a NOESY excitation. Thereafter, this WET-180-NOESY experiment has often been used for solvent suppression unless a single-scan experiment is strictly required. In such a situation, WET-180 or WET-CP would be appropriate. So far, this methodological development has been a precious help to deal with the use of non-deuterated solvents, especially in flow measurements whereby the solvent line is even broader due to the out-flow effect (see section A.3). Pulse programs of and scripts necessary to perform WET-180-NOESY are available in Appendix 8. Nonetheless, some practical considerations should be kept in mind regarding the efficiency of the method:

i. The present WET-180-NOESY sequence relies on selective Gaussian pulses with a length of 82 ms. It turns out that the signals are unperturbed as long as they are shifted by 40 Hz or more from the solvent frequency. Otherwise, a calibration procedure is required to maintain the trueness of the measurement. Another way would be the use of more selective pulses, but at the cost of a longer suppression block, whose efficiency can be hampered by longitudinal relaxation of the solvent.

ii. The article shows an acceptable robustness of the WET-180-NOESY with frequency drifts < 4 Hz. In practice, we have noticed that more important drifts can be encountered in the course of time, in particular in flow measurements. In such a case, the frequency of selective pulses has to be adjusted to balance the drift.

iii. Even if the central line of the solvent signal is well suppressed, the ^{13}C satellite lines remain unperturbed by the solvent suppression method. The latter is a real source of overlaps as the ^{13}C – ^{1}H coupling constants are not negligible at all with respect to the spectral width in frequency at low-field (figure). Obviously the situation can be overcome by a decoupling, but unfortunately there is not a ^{13}C channel available in our benchtop system.

Further methodological works would be relevant to make this solvent suppression method even more versatile. Hitherto, only the case of a protonated solvent involving a single peak has been considered. In some situations, for examples in the field of reaction monitoring, widely used solvent as methanol complicates the situation by the presence of two huge peaks in the NMR spectra. So far, we have dealt with this case by applying successive WET-180 blocks to suppress one by one the lines of the solvent. This approach is limited by the longitudinal relaxation of the suppressed signals (the typical length of the WET-180 block is about 330 ms) and a relative poor performance is obtained. An appealing solution would be to perform a multi WET-180 that irradiate the different lines of the protonated solvent within the same block. This solution involves the design of multi-band selective pulses in the Prospa interface. Some efforts towards that direction are currently performed.

A last perspective relates to the band selective (or pseudo-2D) experiments. When the situation becomes more complex with the use of solvent exhibiting several multiplets, one may wonder if would be more judicious to select only the signal of interest by a suppression / reconstruction approach. Thus, alongside with the solvent suppression methods, we are currently investigating the potential of 1D selective TOCSY (1D Sel TOCSY). This experiment selectively excite a signal of interest and recovers the signal of the coupling partners through spin-locking while other resonances are undetected. This is an interesting solution to extract a whole spin-system from an overcrowded spectrum. As a proof of concept, we investigated this methodology on a synthetic metabolic mixture diluted in protonated water via the pulse-sequence proposed in figure C.11. The result of this band selective method is shown in figure C.12. It could be noted that we benefit from the gradient coil to achieve the selection step through a double pulse field gradient echo (DPFGE) leading to a cleaner phase than the selection by a 90° soft pulse. The comparison between figure C.12a and 12b highlights the promising potential of this approach.

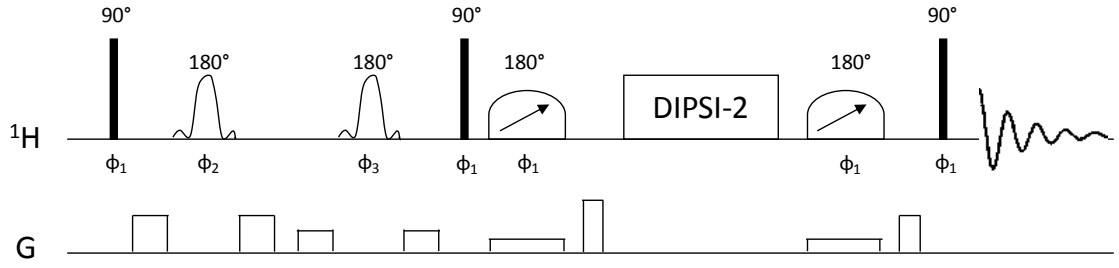

Figure C.11. Scheme of the 1D Sel TOCSY. The suppression step is achieved with a DPFGE whose selective pulse are either Gaussian cascade (Q3) or selective chirp pulses. The spin lock is a DIPSI-2 flanked by zero quantum filters (ZQF). This filter suppress undesirable zero quantum signals, which impact the phase of the signals.

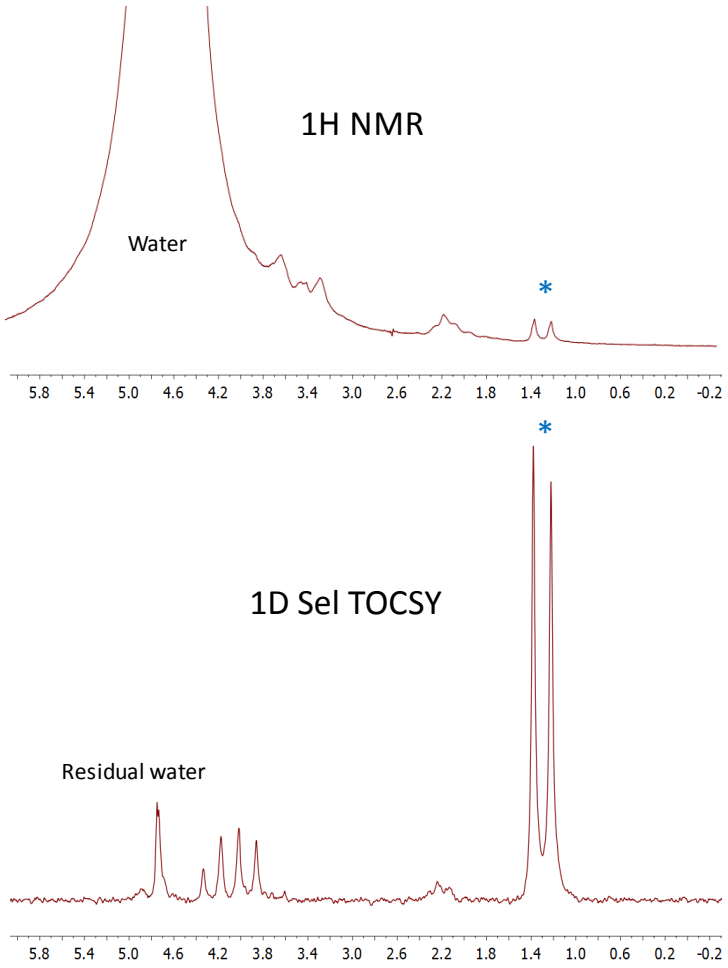

Figure C.12. **(a)** ^{1}H NMR spectra of a synthetic metabolic mixture in non-deuterated water recorded in 12 scans separated by a repetition time of 6 s. **(b)** 1D selective TOCSY spectra obtained with the pulse-sequence in figure C.11 after selection of the doublet of lactate (signal with an asterisk). The spectra was recorded in 64 scans with a repetition time of 6 s. The selective pulses for the selection were chirp pulses with a duration of 50 ms and a band width of 60 Hz. The isotropic mixing duration was 50 ms and the ZQF consisted of chirp pulses with a duration of 30 ms and a band width of 3500 Hz applied together with a gradient at 11.6 % of the maximum value.

D. Applications for Reaction monitoring and Food screening

In this part, we present applications, based on the methodological development described in Part C, in the field of reaction monitoring and food screening. The present part is built as a compendium of articles – each one being followed by a summary and commentaries – which have been published or submitted during this three-year PhD

1. Reaction monitoring and Process control

1.1. In-situ monitoring by UF 2D NMR at 43 MHz

1.1.1. Context

Following the implementation of UF 2D NMR on our 43 MHz compact spectrometer, we wanted to take advantage of fast 2D acquisitions in a practical case. Reaction monitoring, which potentially leads to complex ^{1}H spectra of mixtures, is a relevant testing ground to evaluate the capabilities of UF 2D NMR at low-field.

The organic chemists positioned in the "ResoNantes" project proposed to monitor a Heck-Matsuda coupling reaction. This choice of this chemical reaction offers interesting features. This type of Pd-coupling reaction has a growing interest within the synthetic community. In an analytical point of view, this reaction involved 1D spectra with numerous overlaps whereby there is no isolated signal to easily monitor the progress of the reaction. Moreover, gas formation and the presence of a metallic catalyst complicates even more the NMR monitoring.

Real-time reaction monitoring by ultrafast 2D NMR on a benchtop spectrometer

Boris Gouilleux, Benoît Charrier, Ernesto Danieli, Jean-Nicolas Dumez, Serge Akoka, François-Xavier Felpin, Mireia Rodriguez-Zubiri and Patrick Giraudeau

(Original research article)

Analyst, 140 (2015) 7854-7858.

Abstract

Reaction monitoring is widely used to follow chemical processes in a broad range of application fields. Recently, the development of robust benchtop NMR spectrometers has brought NMR under the fume hood, making it possible to monitor chemical reactions in a safe and accessible environment. However, these low-field NMR approaches suffer from a limited resolution leading to strong peak overlaps, which can limit their application range. Here, we propose an approach capable of recording ultrafast 2D NMR spectra on a compact spectrometer and to follow in real time a reaction in the synthetic chemistry laboratory. This approach –whose potential is shown here on a Heck-Matsuda reaction– is highly versatile; the duration of the measurement can be optimized to follow reactions whose timescale ranges between a few tens of seconds to a few hours. It makes it possible to monitor complex reactions in non-deuterated solvents, and to confirm in real time the molecular structure of the compounds involved in the reaction while giving access to relevant kinetic parameters.

Introduction

Reaction monitoring based on analytical spectroscopies provides essential kinetic and speciation information in a variety of application fields, from organic and inorganic synthesis to biochemistry and bioengineering.[1, 2] It is therefore a determining tool to deeply understand reaction mechanisms. The development of accessible, powerful and robust analytical methods is highly important to characterize in real time the molecular compounds involved in such processes. Among spectroscopic technics, NMR has the great advantage of being non-specific, non-destructive; it does not require prior knowledge on the analyzed compounds and delivers both structural and quantitative information. High field NMR (HF NMR) has been widely used in organic and pharmaceutical applications for monitoring chemical processes, either directly inside the NMR tube[3-5] or by using flow cells.[6-10]

Yet, the high analytical performance of HF NMR is associated with an expensive instrumentation, a high monetary and environmental cost, and the need for specific facilities which are barely compatible with the working environment of the synthetic chemistry laboratory, contrary to other techniques such as UV Vis, FTIR or Raman spectroscopy. However, low field NMR spectroscopy (LF NMR) has recently been brought under the hood through the development of a new generation of benchtop spectrometers relying on non-cryogenic magnets. These spectrometers have the advantage of being relatively inexpensive, practical, transportable and eco-friendly. During the last few years, the quality of the ^{1}H spectra recorded with these compact spectrometers has been greatly improved, particularly in terms of sensitivity and stability. These developments enabled the successful application of benchtop NMR to monitor reactions “on the fly”.[11-13] However, LF NMR suffers from intrinsic drawbacks vis-à-vis its HF counterpart, particularly in terms of low spectral resolution. The low magnetic field inevitably leads to a reduced dispersion of frequencies, generating numerous peak overlaps. Moreover, the real-time identification of chemical compounds is further complicated by the strong couplings commonly encountered in LF NMR. So far, resolution losses and peak overlapping have limited the application range of LF NMR to the monitoring of relatively simple reactions where the peaks of interest are well isolated.

2D NMR experiments[14, 15] are well-known to offer an efficient way of discriminating resonances while delivering invaluable structural information. A number of 2D pulse-sequences have already been developed on some benchtop spectrometers to take advantage

of this methodology at low field.[12] Unfortunately 2D NMR is affected by a long acquisition duration, arising from the need to sample the indirect dimension through the repetition of numerous experiments. As a fundamental consequence, conventional 2D NMR is not adapted to study samples whose composition evolves in the course of time,[16] unless time-resolved schemes based on non-uniform sampling (NUS) are employed.[17] In this context, ultrafast (UF) NMR, which is capable of acquiring 2D spectra within a single scan,[18] offers an attractive way to circumvent this drawback. Therefore, the implementation of UF NMR on a benchtop spectrometer would be a powerful analytical tool to monitor chemical reactions directly inside the synthetic chemistry laboratory and in real time. While UF NMR is now recognized as a powerful reaction monitoring tool at high field,[16, 19-24] it has never been reported on a benchtop spectrometer, as it requires a specific hardware. In fact, UF experiments rely on a spatial encoding scheme, which is also used in many other liquid-state NMR experiments, but has never been shown at low field.

In this article, we report the first spatially encoded NMR experiment on a compact benchtop spectrometer, using a permanent magnet based on a Hallbach design.[25, 26] This spectrometer includes a gradient coil along the B_0-axis which is efficient enough to meet the criteria to implement the UF methodology. Thanks to this device, the first UF spectra recorded on a benchtop spectrometer are shown, and the promising potential of this new analytical tool is demonstrated on the real-time monitoring of a Heck-Matsuda coupling reaction,[27] through UF COSY spectra recorded in real time during the chemical process.

Results and discussion

First UF spectra on a benchtop NMR spectrometer

The UF approach relies on the design of a spatially dependent evolution period. In order to perform this spatial encoding, a magnetic field gradient –applied together with frequency-swept pulses– is necessary to induce a position-dependent resonance frequency, and also to refocus spatially-encoded magnetizations during a detection scheme based on echo-planar spectroscopic imaging (EPSI).[28] The benchtop product (designed by Magritek, Aachen, Germany, a version of the commercial Spinsolve benchtop spectrometer) includes a gradient coil designed for pulsed-gradient spin echo diffusion measurements. By implementing an

appropriate pulse sequence, this gradient coil provides a robust and strong enough magnetic field gradient to achieve these UF features. Here, we implemented and optimized a constant time and phase-modulated spatial encoding pulse sequence based on a double spin echo scheme.[29] A combination of bipolar gradients based on EPSI was also implemented during the detection period. Further information about the pulse-sequence and detailed parameters are available in the ESI.

As a proof of concept, we acquired an initial UF COSY spectrum in 400 ms on a model sample at 43 MHz (Fig. 1B). The quality of this spectrum and the good match with the expected spectrum (numerical simulation shown in Fig. 1C) highlight the suitability of UF experiments at low field and the technical performance of the benchtop prototype. As the value of coupling constants is not negligible compared to the resolution, the coupling-patterns are visible along the vertical dimension for the low-field spectrum (Fig. 1B and C), while they are not observed at 400 MHz (Fig. 1E and F). The comparison of 1D (Fig. 1A and 1B) and 2D spectra (Fig. 1D and 1E) at low and high field shows that field-induced resolution losses are far less important for UF COSY experiments than for 1D pulse-acquire ^{1}H spectra. This is mainly explained by the fact that the UF experiments used in the present study, which are based on a "constant time" encoding, are intrinsically decoupled along the horizontal (or ultrafast) dimension,[31] i.e., they are "singly pure-shift" sequences.[32] Thanks to this feature, UF experiments provide a valuable discrimination of resonances at low field. The major drawback is the relatively low sensitivity, since the experimental limit of detection (LOD) decreases from typically 0.1 mol/L at 400 MHz[19] to 1 mol/L at 43 MHz for a one scan acquisition. However, this sensitivity loss is far less critical than what could be expected from the difference of one order of magnitude between magnetic fields. This is due in part to the probe design, but also to the fact that UF experiments are characterized by the need to compromise between resolution, sensitivity and spectral width.[19] At low field, the spectral widths are much smaller, which considerably alleviates this compromise. Still, the single-scan limit of detection is quite high, but when the timescale of the targeted reaction is compatible with an acquisition duration between a few seconds and a few minutes, the single-scan LOD can be increased by signal averaging while avoiding t_1-noise. This hybrid approach has shown great potential at high field for a variety of applications.[33] A detailed evaluation of the analytical performance of UF experiments at low field will be carried out in further studies.

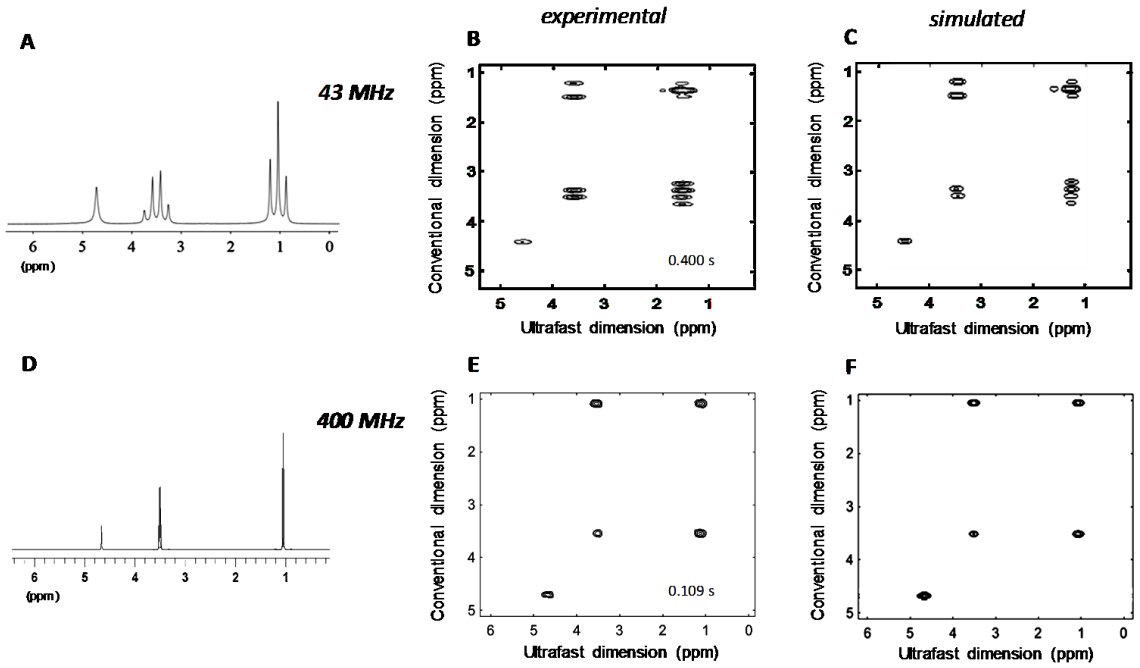

Fig 1. Comparison of low-field and high-field ultrafast 2D and 1D spectra on a model sample. Top line: 1D ^{1}H spectrum **(A)**, experimental **(B)** and simulated **(C)** UF COSY spectra obtained at 43 MHz. Bottom line: same spectra obtained at high field (400 MHz) **(D-F)**. All the experimental spectra were recorded on a sample of ethanol in D_2O (40/60: v/v). The "ultrafast" axis refers to the spatially[30]-encoded dimension (without Fourier transformation) whereas the "conventional" axis represents the direct dimension. The simulations **(C and F)** were performed thanks to a simulation platform that we recently introduced.[30]

Real-time reaction monitoring by UF NMR

We evaluate here the potential of benchtop UF 2D NMR through the monitoring of a Pd-catalyzed Heck-Matsuda reaction[27] (Fig. 2A). This variant of the Heck coupling uses aryl diazonium salts as highly reactive aryl halide surrogates and allows reaction at room temperature under ligand- and base-free conditions.[34] The Heck-Matsuda reaction has recently found a growing interest among the synthetic community,[35-39] especially since their hazardous character was overcome by a bicatalytic strategy[40, 41] or a continuous-flow approach.[42, 43]

The sequential diazonium formation-coupling reaction, depicted in Fig. 2A, is performed directly inside an NMR tube with an initial concentration of 0.36 mol/L for the limiting starting material: 4-methyl-2-nitroaniline (1). In this reaction, the aniline **(1)** dissolved in methanol first reacts with *t*-BuONO and $MeSO_3H$ to form a diazonium salt. The latter is then coupled with the olefin **(2)** in the presence of $Pd(OAc)_2$ as the catalyst, in order to produce the styrene **(3)**. The experiment was designed to keep the mixture as homogenous as possible (the detailed procedure is available in the ESI). It is important to notice that thanks to an external lock system, our experiments were carried out in a non-deuterated solvent. This reduces the cost of the monitoring and allows to avoid unwanted potential isotopic effects that could affect reaction rates in deuterated solvents.

UF COSY spectra are well-suited to monitor in real time this chemical reaction, as they deliver well-resolved cross-peaks, both for the product **(3)** and for the limiting starting material **(1)** (Fig. 2C-E). The starting material in excess **(2)** is also visible. Note that the reaction could not be studied through 1D spectra because the reactant and product peaks were overlapped between them and with the strong non-deuterated solvent peak. In order to optimize the sensitivity of the targeted peaks relatively to the reaction timescale, the number of scans was set to 36 with a recovery time of $1.25 \cdot T_1$,[44] leading to the acquisition of a COSY spectrum every 2.6 min. In addition, J-modulation effects, arising from the constant time nature of the spatial encoding, play a central role in the sensitivity and can be predicted thanks to numerical simulations.[30] These effects were therefore finely tuned for the cross-peaks of interest by adjusting the total time spent in the transverse plane. In this procedure, the sensitivity was optimized simultaneously for the limiting reactant **(1)** and the product **(3)**. The reactant in excess was not considered in this optimization.

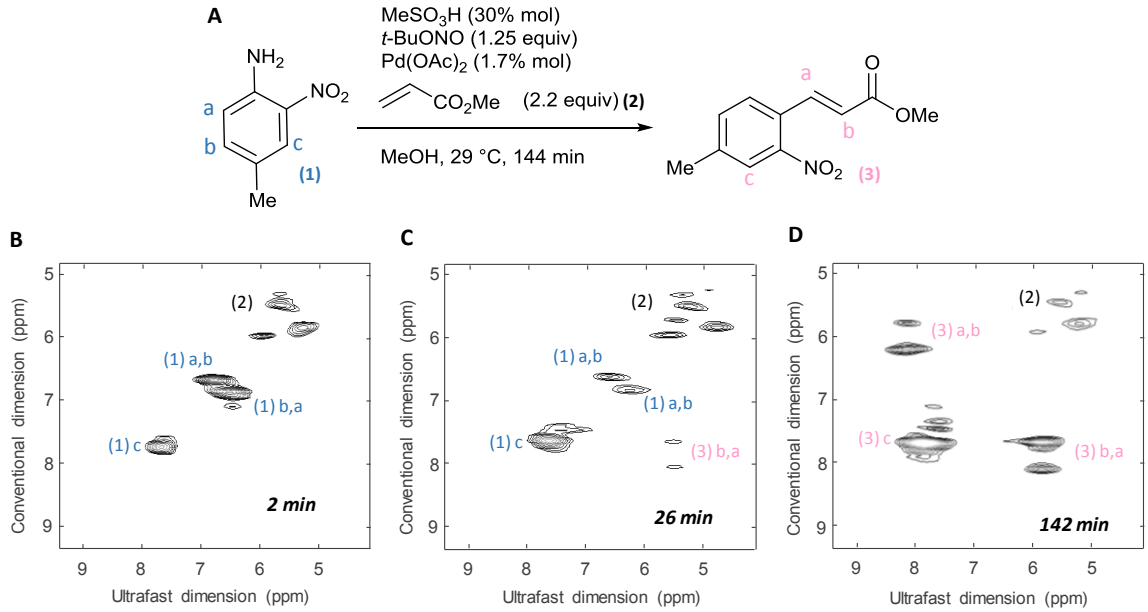

Fig. 2. Scheme of the one pot Heck-Matsuda reaction in the multicomponent mode **(A)**. The reaction was followed for 144 min with an initial concentration of 0.36 mol/L for the limiting starting material (1), at 29°C directly inside the NMR tube. The reaction was monitored through 55 UF COSY spectra recorded with 36 scans every 2.6 minutes, for instance: at 2 min **(B)**, 26 min **(C)** and 142 min **(D).** The observable cross-peaks which have been relevant for the monitoring are assigned for each spectrum.

The kinetic curves recorded from the time-evolution of 2D peak volumes are shown in Fig. 3A. These curves depict the two chemical processes involved in the reaction very well. The decreasing blue curve matches with the initial conversion of **(1)** into a diazonium salt. After the aniline is consumed (at *ca.* 20 min), the coupling reaction starts, leading to the final styrene **(3)** (increasing pink curve). Relevant kinetic parameters, namely the rate constants of the two consecutive processes, can be extracted thanks to a mono-exponential fitting of the corresponding time domains (Fig. 3B and C). The trend of the curves and the rate constants reveal that the coupling reaction is the rate-limiting step of the process with respect to the diazonium formation. In a qualitative point of view, this result is consistent with previous studies performed at high-field,[42] which highlight that the use of an electron-poor aniline leads to a quick conversion into a diazonium salt, thereby making the coupling process the rate-limiting step.

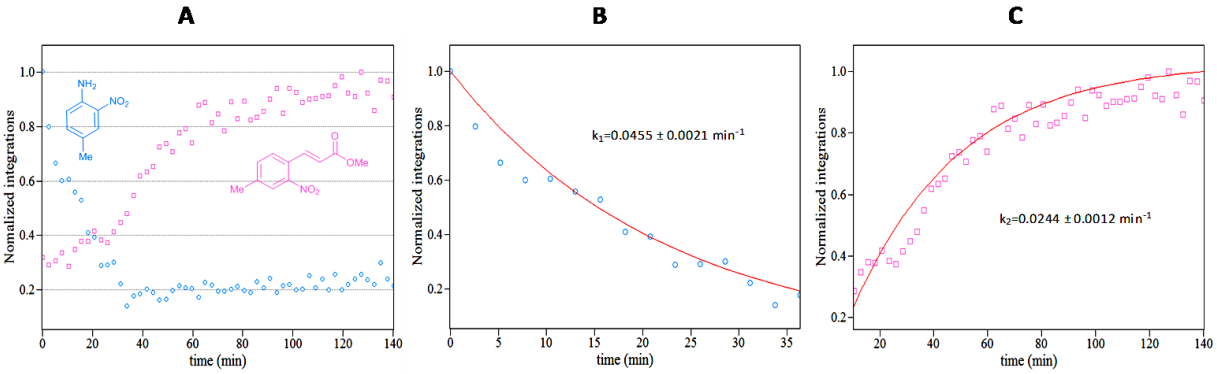

Fig. 3. Kinetics from the reaction monitoring **(A)** showing the evolution of normalized 2D peak volumes as the reaction progresses. These volumes were calculated from the cross-peaks (1) a,b and (3) b,a, matching respectively with the starting material and the final product. Blue open circles show the consumption of aniline and the pink open squares show the formation of the final styrene. The curves were obtained thanks to 55 UF COSY spectra recorded every 2.6 min. Kinetic constants can be extracted through exponential fitting of the 2D peak volumes in the relevant time domains, i.e. from 0-to 40 min for the consumption of aniline **(B)** and from 20 to 140 min for the production of the final styrene **(C)**

Conclusions

This paper demonstrates the potential of benchtop ultrafast 2D NMR. This new analytical approach extends the reaction monitoring toolkit for a broad community of synthetic chemists, making real-time 2D NMR directly available under the fume hood. When concentration allows it, the duration of the 2D measurement can be optimized to follow reactions whose timescale ranges between a few tens of seconds to a few hours. The ability of the UF 2D NMR to discriminate overlapping resonances is particularly valuable at low field where the frequency dispersion is significantly reduced. From the NMR point of view, this first report of spatially-encoded NMR experiments on a benchtop spectrometer could open the way to a number of developments for in-lab analysis of liquid-state samples, including other homo- or heteronuclear UF pulse sequences, pure-shift experiments or diffusion-based measurements, thereby also providing a higher number of accessible correlation peaks and resolution improvements. The potential and the suitability of UF NMR on a benchtop spectrometer have been shown through the real-time monitoring of a Heck-Matsuda reaction, leading to kinetic results which are consistent with the literature. This first application could open the way to a broad range of applications in synthetic chemistry, including the on-flow monitoring of chemical processes, a research avenue that we will explore in the near future.

Acknowledgements

The authors warmly acknowledge Magritek, in particular Juan Perlo and Andrew Coy, for their strong support. We also thank Nicolas Oger and Laetitia Rouger (CEISAM) and Stefano Caldarelli (ICSN) for discussions, as well as Michel Giraudeau for linguistic assistance. This project was funded by Région Pays de la Loire (Grant RésoNantes).

Notes and References

1. J. Workman, M. Koch and D. Veltkamp, *Anal. Chem.*, 2007, **79**, 4345-4364.
2. J. Workman, M. Koch, B. Lavine and R. Chrisman, *Anal. Chem.*, 2009, **81**, 4623-4643.
3. F. Susanne, D. S. Smith and A. Codina, *Org. Process Res. Dev.*, 2012, **16**, 61-64.
4. I. M. Clegg, C. M. Gordon, D. S. Smith, R. Alzaga and A. Codina, *Anal. Methods*, 2012, **4**, 1498-1506.
5. T. R. Hoye, B. M. Eklov, T. D. Ryba, M. Voloshin and L. J. Yao, *Org. Lett.*, 2004, **6**, 953-956.
6. M. Maiwald, H. H. Fischer, Y.-K. Kim, K. Albert and H. Hasse, *J. Magn. Reson.*, 2004, **166**, 135-146.
7. M. A. Bernstein, M. Štefinović and C. J. Sleigh, *Magn. Reson. Chem.*, 2007, **45**, 564-571.
8. M. Khajeh, M. A. Bernstein and G. A. Morris, *Magn. Reson. Chem.*, 2010, **48**, 516-522.
9. A. C. Barrios Sosa, R. T. Williamson, R. Conway, A. Shankar, R. Sumpter and T. Cleary, *Org. Process Res. Dev.*, 2011, **15**, 449-454.
10. D. A. Foley, C. W. Doecke, J. Y. Buser, J. M. Merritt, L. Murphy, M. Kissane, S. G. Collins, A. R. Maguire and A. Kaerner, *J. Org. Chem.*, 2011, **76**, 9630-9640.
11. S. K. Küster, E. Danieli, B. Blümich and F. Casanova, *PCCP*, 2011, **13**, 13172-13176.
12. V. Sans, L. Porwol, V. Dragone and L. Cronin, *Chem. Sci.*, 2015, **6**, 1258-1264.
13. M. V. Silva Elipe and R. R. Milburn, *Magn. Reson. Chem.*, 2015, DOI: 10.1002/mrc.4189, n/a-n/a.
14. W. P. Aue, E. Bartholdi and R. R. Ernst, *J. Chem. Phys.*, 1976, **64**, 2229-2246.
15. J. Jeener, *Lecture presented at Ampere International Summer School II, Basko Polje, Yugoslavia*, 1971.
16. R. Boisseau, U. Bussy, P. Giraudeau and M. Boujtita, *Anal. Chem.*, 2015, **87**, 372-375.
17. R. Dass, W. Koźmiński and K. Kazimierczuk, *Anal. Chem.*, 2015, **87**, 1337-1343.

18. L. Frydman, T. Scherf and A. Lupulescu, *Proc. Natl. Acad. Sci. USA*, 2002, **99**, 15858-15862.
19. P. Giraudeau and L. Frydman, *Annu. Rev. Anal. Chem.*, 2014, **7**, 129-161.
20. A. Herrera, E. Fernández-Valle, R. Martínez-Álvarez, D. Molero, Z. D. Pardo, E. Sáez and M. Gal, *Angew. Chem. Int. Edit.*, 2009, **48**, 6274-6277.
21. A. Herrera, E. Fernandez-Valle, E. M. Gutiérrez, R. Martinez-Alvarez, D. Molero, Z. D. Pardo and E. Saez, *Org. Lett.*, 2010, **12**, 144-147.
22. L. H. K. Queiroz Junior, P. Giraudeau, F. A. B. dos Santos, K. T. Oliveira and A. G. Ferreira, *Magn. Reson. Chem.*, 2012, **50**, 496-501.
23. Z. D. Pardo, G. L. Olsen, M. E. Fernández-Valle, L. Frydman, R. Martínez-Álvarez and A. Herrera, *J. Am. Chem. Soc.*, 2012, **134**, 2706-2715.
24. A. Herrera, E. Fernández-Valle, R. Martínez-Álvarez, D. Molero-Vílchez, Z. D. Pardo-Botero and E. Sáez-Barajas, *Magn. Reson. Chem.*, 2015, DOI: 10.1002/mrc.4240, n/a-n/a.
25. E. Danieli, J. Perlo, B. Blümich and F. Casanova, *Angew. Chem. Int. Edit.*, 2010, **49**, 4133-4135.
26. E. Danieli, J. Perlo, B. Blümich and F. Casanova, *Phys. Rev. Lett.*, 2013, **110**, 180801.
27. K. Kikukawa and T. Matsuda, *Chem. Lett.*, 1977, **6**, 159-162.
28. P. Mansfield and P. G. Morris, *NMR imaging in biomedicine*, Academic Press, New-York, 1982.
29. P. Pelupessy, *J. Am. Chem. Soc.*, 2003, **125**, 12345-12350.
30. B. Gouilleux, L. Rouger, C. Benoît, I. Kuprov, S. Akoka, J.-N. Dumez and P. Giraudeau, *ChemPhysChem*, 2015, DOI: 10.1002/cphc.201500514R1.
31. P. Giraudeau and S. Akoka, *J. Magn. Reson.*, 2008, **192**, 151-158.
32. R. W. Adams, L. Byrne, P. Kiraly, M. Foroozandeh, L. Paudel, M. Nilsson, J. Clayden and G. A. Morris, *Chem. Commun.*, 2014, **50**, 2512-2514.
33. S. Akoka and P. Giraudeau, *Magn. Reson. Chem.*, 2015, in press, DOI: 10.1002/mrc.4237.
34. F.-X. Felpin, K. Miqueu, J.-M. Sotiropoulos, E. Fouquet, O. Ibarguren and J. Laudien, *Chem. Eur. J.*, 2010, **16**, 5191-5204.
35. F.-X. Felpin, L. Nassar-Hardy, F. Le Callonnec and E. Fouquet, *Tetrahedron*, 2011, **67**, 2815-2831.
36. N. Oger, M. d'Halluin, E. Le Grognec and F.-X. Felpin, *Org. Process Res. Dev.*, 2014, **18**, 1786-1801.
37. A. Roglans, A. Pla-Quintana and M. Moreno-Mañas, *Chem. Rev.*, 2006, **106**, 4622-4643.
38. J. G. Taylor, A. V. Moro and C. R. D. Correia, *Eur. J. Org. Chem.*, 2011, **2011**, 1403-1428.
39. F. Mo, G. Dong, Y. Zhang and J. Wang, *Org. Biomol. Chem.*, 2013, **11**, 1582-1593.
40. F. L. Callonnec, E. Fouquet and F.-X. Felpin, *Org. Lett.*, 2011, **13**, 2646-2649.

41. N. Oger, F. Le Callonnec, D. Jacquemin, E. Fouquet, E. Le Grognec and F.-X. Felpin, *Adv. Synth. Catal.*, 2014, **356**, 1065-1071.
42. N. Oger, E. Le Grognec and F.-X. Felpin, *J. Org. Chem.*, 2014, **79**, 8255-8262.
43. N. Oger, E. Le Grognec and F.-X. Felpin, *Org. Chem. Front.*, 2015, **2**, 590-614.
44. P. Schanda, *Prog. Nucl. Magn. Reson. Spectrosc.*, 2009, **55**, 238-265.

Supporting information for manuscript

Real-time reaction monitoring by ultrafast 2D NMR on a benchtop spectrometer

Boris Gouilleux[a], Benoît Charrier[a], Ernesto Danieli[b], Jean-Nicolas Dumez[c], Serge Akoka[a], François-Xavier Felpin[a,d], Mireia Rodriguez-Zubiri[a] and Patrick Giraudeau[a,d]*

a. CEISAM CNRS, UMR6230, Université de Nantes, BP 92208. 2 rue de la Houssinière, 44322 Nantes (France).

b. Institut für Technische Chemie und Makromolekulare Chemie, RWTH Aachen University. Worringerweg 1, 52074 Aachen (Germany).

c. CNRS UPR2301, Institut de Chimie des Substances Naturelles. 1 avenue de la Terrasse, 91198 Gif-sur-Yvette Cedex (France)

d. Institut Universitaire de France. 1 rue Descartes 75005, Paris Cedex 05 (France)

*To whom correspondence should be addressed:patrick.giraudeau@univ-nantes.fr.

1. Ultrafast NMR experiments

1.1 Spectrometers

1.2 Experiment at high field

1.3 Experiments at low field

2. Numerical simulations

2.1 Simulation of UF COSY at 400 MHz

2.2 Simulation of UF COSY at 43 MHz

3. Procedure of the Heck-Matsuda reaction

4. References

1. Ultrafast NMR experiments

1.1 Spectrometers

400 MHz spectrometer. The spectra shown in Fig. 1A and B were recorded on a Bruker Avance I 400 spectrometer operated with Topspin 2.1, at a frequency of 400.13 MHz with a 5 mm dual probe equipped with a z-axis gradient generating a maximum field gradient of 0.80 T/m.

43 MHz benchtop spectrometer. The experiments performed at low-field were recorded on a Spinsolve from Magritek working at a frequency of 43.62 MHz, equipped with a gradient coil along the B_0-axis (i.e. along the transverse plane of the NMR tube) which can generate a maximum field gradient of 0.16 T/m and operated with the Prospa Software.

1.2 Experiment at high-field

UF COSY single scan. The experiment at 400.13 MHz presented in Fig. 2B was recorded in 109 ms with the homemade pulse sequence of Figure S1, consisting in a spatial encoding followed by a hard 90° pulse as mixing period and by echo-planar detection. The spatial encoding was performed in a constant time phase-modulated fashion based on a double spin echo scheme,[1] with two 15 ms smoothed chirp pulses (i.e. TE=30 ms) swept over a 13 kHz range. The amplitude of the encoding gradients Ge was adapted to obtain a frequency dispersion equivalent to the frequency sweep of the pulses, corresponding to 2.28% of the maximum gradient strength available. During the acquisition, 128 pairs of bipolar gradient pulses were applied (90% of maximum strength, 294.4 µs each, separated by a 20 µs delay). Conventional coherence-selection gradients were also used. The spectrum was processed using a home-written routine in Matlab, including an optimized Gaussian apodization in the spatially-encoded dimension[2] and a sine-bell apodization in the FT dimension. All the presented spectra are displayed with the indirect domain called “ultrafast dimension” since it results from specific ultrafast features, whereas the direct dimension arising from conventional evolution during the detection period is called “conventional dimension”.

1.3 Experiment at low-field

UF COSY single scan. The experiment at 43.62471 MHz presented in Fig. 2E was recorded in 400 ms with the homemade pulse sequence of Figure S1, consisting in a spatial encoding followed by a hard 90° pulse as mixing period and by echo-planar detection. The spatial encoding was performed in a constant time phase-modulated fashion based on a double spin echo scheme, with two 30 ms smoothed chirp pulses (i.e. TE=60 ms) swept over a 3.5 kHz range. The amplitude of the encoding gradients Ge was adapted to obtain a frequency dispersion equivalent to the frequency sweep of the pulses, corresponding to 11.6% of the maximum gradient strength available. A delay t_{mix} of 42 ms was added prior to the spatial encoding step in order to optimize the effects of J-modulation arising from the constant time nature of the double spin-echo encoding.[3] During the acquisition, 128 pairs of bipolar gradient pulses Ga were applied (85% of maximum strength, 1280.4 µs each). The desired coherence selection was obtained as described in Figure S1. The spectrum was processed using a home-written routine in Prospa, including an optimized Gaussian apodization in the spatially-encoded dimension and a sine-bell apodization in the FT dimension. All the presented spectra are displayed with the indirect domain called “ultrafast dimension” since it results from specific ultrafast features, whereas the direct dimension arising from conventional evolution during the detection period is called “conventional dimension”.

Fast hybrid UF COSY. The UF spectra COSY for the reaction monitoring (Fig. 2B-D) were recorded in 146 s (i.e. 36 scans) with the homemade pulse sequence of Figure S1. The sequence was similar to the previous UF COSY with the following features. The spatial encoding was performed by combining two 45 ms smoothed chirp pulses (i.e. TE=90 ms) swept over a 3.5 kHz range with encoding gradients Ge fixed at 9.00% of maximum gradient strength. The detection was then achieved with 128 pairs of bipolar gradient pulses Ga at 85% of maximum strength (1280 µs each). The desired coherence-selection was obtained thanks to both a standard four step phase cycling and selecting gradient pulses. The spectrum was processed in the same way as previously described.

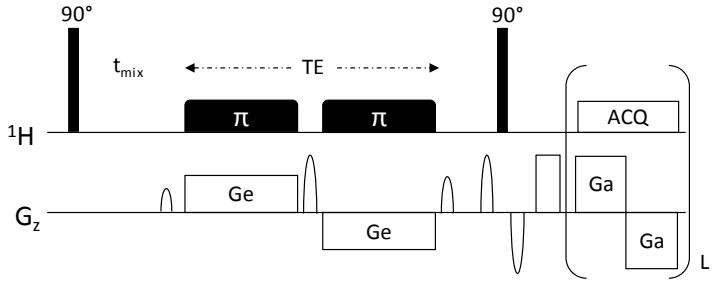

Supplementary figure S1. Pulse sequence of the UF COSY achieved with a constant time and phase-modulated spatial encoding.

2. Numerical simulations

The simulations shown in Fig. 1C and F were performed thanks to a simulation platform that we recently introduced,[3] based on the Fokker-Planck theory module implemented in version 2.0 of Spinach library.[4]
All the simulated spectra are displayed with the indirect domain called "ultrafast dimension" since it results from specific ultrafast features, whereas the direct dimension arising from conventional evolution during the detection period is called "conventional dimension".

2.1 Simulation of UF COSY at 400 MHz

The spectrum presented in Fig. 1F was simulated with the following features. Acquisition parameters: 512 points separated by a dwell time of 0.575 µs were used to compute the UF dimension whereas the conventional one was obtained with 128 loops in the detection block. The acquisition gradients were fixed at 0.800 T/m. For the encoding parameters, encoding gradients of 0.020 T/m were applied while the π-chirp pulses were performed by a WURST pulse built with 1000 points, sweeping a bandwidth of 13 kHz in 15 ms. The second chirp of the double spin echo is flanked by two crushers. The CTP was completed in the same way as in supplementary figure S1 via gradient pulses at 0.48 T/m. The length of the sample was fixed at 1.5 cm and the Liouvillian propagation was performed over 500 z-positions. Here a B_0 field of 9.416 T was considered and ideal pulses were assumed. The simulated 2D FID was then processed thank to a home-written procedure in Matlab: a sinusoidal apodization for the conventional dimension while a Gaussian apodization was applied in the UF dimension, including zero filling in both dimensions.

2.2 Simulation of UF COSY at 43 MHz

The spectrum presented in Fig. 1C was simulated with the following features. Acquisition parameters: 256 points separated by a dwell time of 5.000 µs were used to compute the UF dimension whereas the conventional one was obtained with 128 loops in the detection block. The acquisition gradients were fixed at 0.117 T/m. For the encoding parameters, encoding gradients of 0.016 T/m were applied while the π-chirp pulses were performed by a WURST pulse built with 1000 points, sweeping a bandwidth of 3.5 kHz in 30 ms. The second chirp of the double spin echo is flanked by two crushers. The CTP was completed in the same way as in supplementary figure S1 via gradient pulses at 0.48 T/m. The length of the sample was fixed at 0.5 cm and the Liouvillian propagation was performed over 500 z-positions. Here a B_0 field of 1.010 T was considered and ideal pulses were assumed. The simulated 2D FID was then processed thanks to a home-written procedure in Matlab: a sinusoidal apodization for the conventional dimension while a Gaussian apodization was applied in the UF dimension, including zero filling in both dimensions.

3. Procedure of the Heck-Matsuda reaction

t-BuONO (0.317 mmol, 38 µL) was added to a solution of aniline (0.252 mmol, 38.8 mg) in MeOH (0.450 mL). The resulting mixture was stirred and transferred into an NMR tube. Methyl acrylate (0.555 mmol, 50 µL) and palladium acetate (1.7 mol%, 1.1 mg) in MeOH (0.200 mL) were added to the solution. The bicatalytic reaction was then initiated by adding methanesulfonic acid (30 mol%, 5 µL). The NMR tube was stirred and inserted inside the benchtop NMR at 29°C for 144 min.

4. References

1. P. Pelupessy, *J. Am. Chem. Soc.*, 2003, **125**, 12345-12350.
2. P. Giraudeau and S. Akoka, *Magn. Reson. Chem.*, 2011, **49**, 307-313.
3. B. Gouilleux, L. Rouger, C. Benoît, I. Kuprov, S. Akoka, J.-N. Dumez and P. Giraudeau, *ChemPhysChem*, 2015, DOI: 10.1002/cphc.201500514R1.
4. H. J. Hogben, M. Krzystyniak, G. T. P. Charnock, P. J. Hore and I. Kuprov, *J. Magn. Reson.*, 2011, **208**, 179-194.

1.1.3. Summary and perspectives

The results presented above highlight the ability of LF UF 2D NMR to monitor the progress of a chemical reaction. Relying on resolved cross-peaks, this proof of concept offers an alternative to the use of deconvolution and/or chemometric supports that are often applied when reactive mixtures lead to overcrowded spectra.

Moreover, as the UF pulse-sequences are demanding for the gradient coil, a question concerning the robustness of the hardware could be opened. In this study a series of 55 UF 2D spectra, with 32 scans for each, was recorded without an appreciable reduction of the NMR performance thereby demonstrating the reliability of the gradient coil.

Beyond these results, the use of an NMR tube as reactor to probe a chemical reaction is stringent regarding the experimental conditions: stirring, controlled atmosphere, temperature regulation (see section A.2.1.2). Thus, investigating the potential of this spatially encoded method in a continuous flow mode, for instance within a bypass system, is an important perspective to assess the versatility of UF 2D NMR on a benchtop system.

This perspective, among other things, is explored in the next article, which portrays the analytical performance and promising applications of ultrafast NMR at low magnetic field.

1.2. UF 2D NMR at 43 MHz: Analytical performance, On-line monitoring and screening

Ultrafast 2D NMR on a benchtop spectrometer: applications and perspectives.

Boris Gouilleux, Benoît Charrier, Serge Akoka, François-Xavier Felpin, Mireia Rodriguez-Zubiri and Patrick Giraudeau

(Original article)

TrAC Trends in Analytical Chemistry, 83, Part A (2016) 65-75.

Abstract

Benchtop NMR spectrometers are associated with significant resolution losses, as peak overlaps become ubiquitous at low field. 2D spectroscopy offers an appealing solution to this issue. However 2D NMR is associated with long experimental times which are ill-suited for high-throughput applications such as real-time reaction monitoring or rapid screening. The first implementation of ultrafast (UF) 2D NMR on a benchtop spectrometer –including B_0 gradients– was recently reported, making it possible to record 2D spectra in a single –or at most a few– scans. In the present review, we investigate the analytical performance of UF 2D NMR at low field (43 MHz) and its application potential in two complementary research fields: real-time reaction monitoring and rapid screening. UF 2D spectroscopy at low field appears to be a powerful complement to existing analytical methods, and paves the way towards a number of developments in the field of spatially-encoded NMR at low field.

List of abbreviations

2D	Two-dimensional
COSY	COrrelation SpectroscopY
EPSI	Echo-Planar Spectroscopic Imaging
FTIR	Fourier Transform InfraRed
GLY	Glycerol
HF	High Field
HPLC	High Performance Liquid Chromatography
LF	Low Field
LOD	Limit Of Detection
NMR	Nuclear Magnetic Resonance
PUFA	Poly-Unsaturated Fatty Acids
RSD	Relative Standard Deviation
UF	Ultrafast
UFA	Unsaturated Fatty Acids
SNR	Signal-to-Noise Ratio

1. Introduction

Nuclear magnetic resonance (NMR) spectroscopy is one of the most powerful analytical tools, with applications in a broad range of domains, from the elucidation of (bio)chemical structures, to pharmaceutical, biomedical or food sciences. In the pursuit of a better sensitivity and spectral resolution, modern instruments are based on stronger and stronger magnetic fields generated by huge supra-conducting magnets. The amazing performance reached by these high field (HF) spectrometers is therefore associated with an expensive equipment and with the need for cryogenic fluids, involving a high monetary and environmental cost. Moreover, the incompatibility of this technology with harsh environments requires dedicated NMR laboratories, as well as a specialized staff to operate the spectrometers. Taken together, these economic and practical drawbacks have often kept NMR spectroscopy away from production and industrial sites.

Recently a new generation of low-field (LF) spectrometers, more compact, relatively inexpensive and cryogen-free, has brought NMR spectroscopy as close as possible to the production settings such as synthetic chemistry laboratories. Nowadays these so-called "benchtop NMR" spectrometers relying on permanent magnets, deliver ^{1}H spectra with a sufficient quality to enable promising applications in different fields such as chemical reaction monitoring [1-5] or screening applications [6-9].

However, the use of a low magnetic field is associated with a drastically reduced frequency dispersion as the static magnetic field B_0 decreases, leading to highly overlapped resonances. In addition to this overlapping issue, strong couplings are commonly encountered in LF NMR since the values of the coupling constants become comparable to the chemical shift dispersion. As a consequence, the identification and quantification of chemical compounds is far more complicated, and the resolution losses emerge as a limiting factor to extend the scope of LF NMR. In this context, NMR methods bringing a spectral resolution enhancement are particularly relevant in the low-field framework. By spreading the peaks over a 2D map, two-dimensional (2D) experiments [10, 11] provide this advantage while delivering invaluable chemical insights on the analyzed compounds. Several homo- and hetero-nuclear 2D pulse-sequences have recently been developed on some benchtop instruments to take advantage of these assets at low field [2].

Nonetheless, the advantages of 2D NMR are associated with an intrinsic long acquisition duration, arising from the need to sample the frequencies involved in the indirect dimension through numerous 1D experiments in a time-incremented fashion. This long duration makes conventional 2D NMR unsuitable to study samples whose composition evolves in the course of the 2D sampling [12]. Beyond the subsequent time constraints, these conventional 2D experiments are not well adapted to reaction monitoring, which is a fundamental application of benchtop NMR. In order to alleviate this time constraint, Ultrafast (UF) NMR, which yields a whole homo- or hetero-nuclear 2D spectrum within a single scan [13], appears to be a natural candidate. At high field, UF 2D NMR has been applied to a variety of situations where the experiment duration is critical, from the real-time monitoring of chemical or biochemical processes [14] to the coupling with other analytical techniques such as HPLC [15] or Dynamic Nuclear Polarization [16], but also to high-throughput quantitative metabolomics [17, 18]. Hence the development of the UF methodology on a benchtop spectrometer could generate a relevant analytical tool for numerous low-field applications. Although UF NMR is nowadays well established as a powerful analytical tool [19], its implementation at low field is not straightforward since it requires a specific hardware, *i.e.* a powerful gradient coil which is not yet routinely available on benchtop spectrometers. Very recently, we reported the first UF COSY NMR experiment on a low-field instrument [20]. The spectrometer used is a prototype version of the commercial 43 MHz Spinsolve (Magritek, Aachen, Germany), which includes a gradient coil along the B_0-axis designed for pulsed-gradient spin echo diffusion measurements.

This article aims at emphasizing the promising potential of UF experiments at low-field, as well as discussing the perspectives that could arise from this new analytical tool. The paper focuses on the COSY experiment, which is the most widely applied UF pulse sequence, and also the only one reported at low field so far. The first part describes the principle and basics of UF NMR, in order to provide an overview of the key features and characteristics of this generic approach. We also report the first evaluation of the analytical performance of UF NMR at low field. We then focus on the potential applications of this methodology in two domains where benchtop spectrometers appear particularly promising: reaction monitoring and screening analysis.

2. Principle of UF NMR

The main feature of the UF methodology is the replacement of the t_1-incremented period in the conventional 2D NMR scheme by a spatially-dependent evolution period. To this end, the sample is virtually divided in several slices, which undergo different evolution periods according to their positions, all within a single scan (Figure 1).

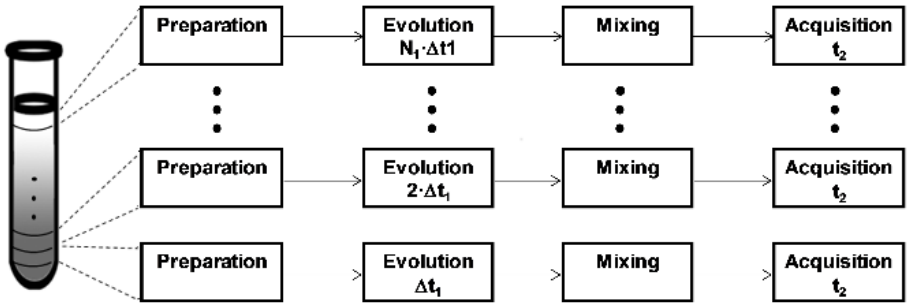

Figure 1. Principle of UF 2D NMR. The experiment can be visualized as subdividing the sample into numerous slices that simultaneously undergo different experiments with incremented t_1 delay.

This spatial encoding is commonly performed in a continuous fashion by applying a magnetic field gradient G_e together with a linear frequency-swept pulse (chirp pulses), so that the spins located at different z positions are excited at different times $t(z)$. A constant time spatial encoding scheme is generally used [21]. After a 90° conventional excitation, two successive chirp pulses applied with bipolar gradients induce a linear dephasing φ proportional to both the Larmor frequency Ω_i of the spins and their position z in the sample: $\varphi(z) = C \cdot \Omega_i \cdot z$, where C is an adjustable constant depending on the spatial-encoding pattern [21]. After a conventional mixing period, a whole 2D NMR spectrum can be retrieved from the encoded information if the spin evolution during the detection period t_2 is collected in a way that refocuses the linear dephasing obtained through the spatial encoding step. To this end, an acquisition gradient G_a is applied while the receiver is open, leading to a train of echoes in the k space, where k is a wave number depending on the acquisition gradient: $k = \gamma_a \int_0^t G_a(t')dt'$ (γ_a is the gyromagnetic ratio of the detected nuclei). These echoes arise when the refocusing induced by the acquisition gradient exactly compensates the dephasing φ

previously provided by the spatial encoding step, i.e. $k = -C \cdot \Omega_i$. This series of echoes resembles a 1D spectrum though obtained without Fourier transformation corresponding to the first dimension of the UF spectrum, often called “ultrafast dimension”. The second dimension is then obtained through the application of an Echo-Planar Spectroscopic Imaging (EPSI) block during the detection. In this scheme, a train of bipolar gradient pairs enables to map the spatial dimension k and the time domain t_2 along a zig-zag trajectory. This leads to a series of mirror-image 1D spectra with respect to the spatial dimension while the system evolves in t_2 under the influence of classical NMR parameters such as J-couplings, chemical shifts and transverse relaxation. After rearrangement of these series of sub-spectra, followed by a Fourier transformation, this t_2 evolution yields the second dimension (often called “conventional dimension”) so that a complete 2D spectrum is obtained in a single scan. For more details on the methodology and on the recent methodological developments which have significantly enhanced its performance, readers are referred to recent reviews on the subject [19, 22].

By implementing this methodology with parameters properly adapted to a low-field spectrometer, we recently reported the first experiment based on an optimized constant time phase-modulated experiment at 43 MHz (Figure 2) [20]. To illustrate this concept, we recorded a UF COSY spectrum in a single scan (0.4 s) on a sample of ethanol as a model compound. The quality of the spectrum shown in Figure 2 highlights the suitability of the UF NMR experiments at low field, and the performance of the hardware. Since the values of coupling constants become non-negligible at low field compared to the frequency dispersion, the coupling patterns are visible along the conventional dimension, while they are usually not observed at higher field because of insufficient resolution. The main drawback is the low sensitivity, however, this sensitivity loss is far less critical than what could be expected from the difference of one order of magnitude between magnetic fields. This is due in part to the probe design, but also to the fact that UF experiments are characterized by the need to compromise between resolution, sensitivity and spectral width [19]. In LF NMR, this compromise becomes more flexible as the spectral width is reduced. Moreover, the single-scan limit of detection is clearly high, but when the timescale of the targeted application is compatible with an acquisition duration from a few seconds to a few minutes, the single-scan LOD can be significantly increased by signal accumulation while avoiding t_1-noise commonly encountered

in the conventional 2D experiments. This hybrid approach, which has already shown its great interest at high field [23] should significantly enlarge the application perspectives of UF at low field. Note that it is still compatible with dynamic sample evolutions, since a complete 2D matrix is recorded at each scan –contrary to conventional 2D NMR– resulting in a final spectrum showing the average sample composition over the overall experiment time.

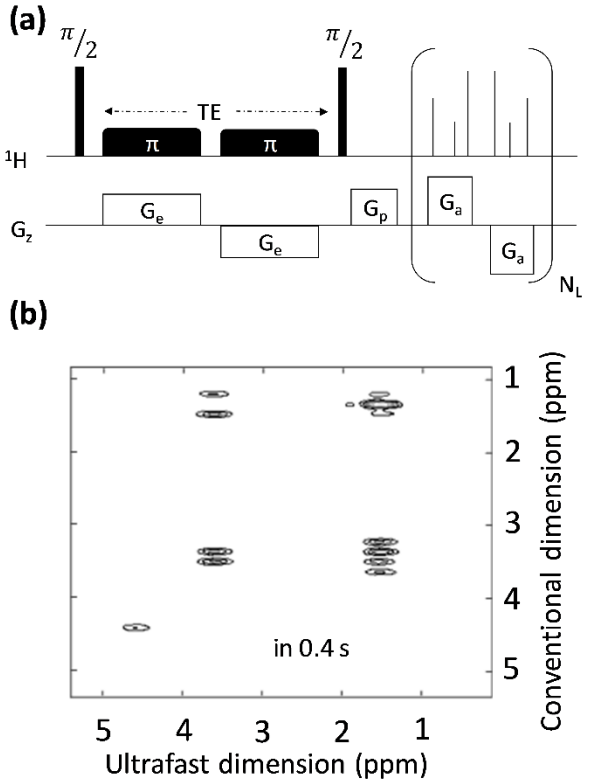

Figure 2. UF 2D COSY pulse sequence (a) and corresponding single-scan spectrum (b) of a sample of ethanol in D_2O, recorded in 0.4 s on a 43 MHz benchtop spectrometer. The ”ultrafast” axis refers to the spatially-encoded dimension (without Fourier transformation) whereas the ”conventional” axis represents the direct dimension. TE: duration of spatial encoding; G_e: amplitude of spatial encoding gradients; G_p: amplitude of pre-acquisition gradient; G_a: amplitude of acquisition gradient; N_L: number of loops for the EPSI scheme applied during the signal detection.

3. Analytical performance.

This section aims at providing an evaluation of the analytical performance of UF NMR at low field, so that potential users can figure out what kind of applications can be expected from this methodology. As mentioned above, the high LOD of the single-scan acquisition is not compatible with most applications such as reaction monitoring with realistic concentrations. Therefore, our analytical evaluation is based on UF COSY spectra recorded in 12 scans, leading to a total acquisition duration of 48 s. This duration remains very short compared to the typical duration of conventional 2D acquisitions and yields a LOD lower than 0.5 mol.L^{-1} that is more suitable for applications. The ester 3-bromo-ethylpropionate was chosen as a model compound, and five samples were prepared at different concentrations from 0.5 to 4 mol.L^{-1} in acetone-d_6. Figure 3 provides a qualitative comparison of the UF and conventional COSY spectra recorded at 43 MHz (Figure 3a and 3b) and at 400 MHz (Figure 3c and 3d). The comparison between UF (Figure 3a and 3c) and conventional spectra (Figure 3b and 3d) at low and high field shows that field-induced resolution losses are far less important for UF COSY experiments than for its conventional counterpart. Indeed, at 43 MHz some of the 2D peaks are almost overlapped in the conventional spectrum while it is not the case for the UF COSY. This is mainly due to the fact that these UF experiments, relying on a “constant time” encoding [21], are intrinsically decoupled along the ultrafast dimension [24], like any “singly pure-shift” experiment [25]. Thanks to this feature, UF experiments provide an attractive way to discriminate the resonances at low field. To go further, this valuable methodology is now evaluated through quantitative analytical criteria.

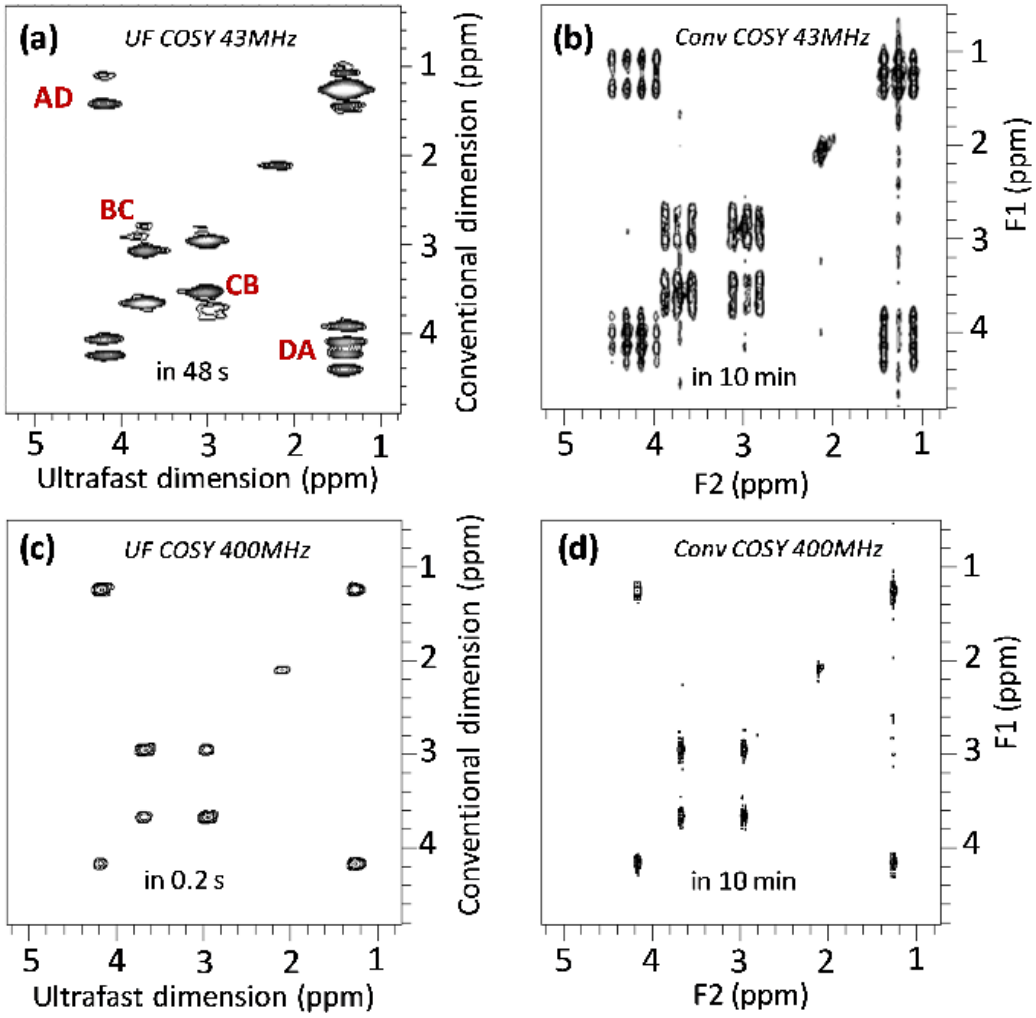

Figure 3. 2D COSY spectra recorded on a 1 mol.L^{-1} 3-bromo-ethylpropionate sample in acetone-d_6. (a) and (c) show the UF 2D spectra recorded with 12 and 1 scans at 43 MHz and 400 MHz, respectively, with the pulse sequence of Figure 2a. (b) and (d) show conventional COSY spectra recorded in 10 minutes with conventional pulse sequences.

The repeatability was evaluated for each sample by recording five experiments successively. Here the 2D peak volumes are considered without any normalization, so that the measured variations reflect all possible sources of irreproducibility. The results, presented in Table 1, are compared to those obtained with the same sample and in identical experiments at high field.

Table 1. Analytical performance of UF COSY experiments recorded in 12 scans (48 s) on 3-bromo-ethylpropionate samples in various concentrations and at two different fields (43 and 400 MHz). The repeatability is evaluated by the relative standard deviation (RSD) on the 2D peak volumes from five successive experiments. The linearity is determined after linear regression from the graph showing average 2D peak volumes as a function of the concentration. Peak labels correspond to the assignments indicated in Figure 2.

Cross-peaks			**AD**	**DA**	**BC**	**CB**
43 MHz	Repeatability (RSD)	4,0 M	1,19%	0,41%	0,33%	0,78%
		3,0 M	2,07%	0,25%	1,13%	0,34%
		2,0 M	3,95%	1,00%	2,81%	0,61%
		1,0 M	11,17%	2,57%	2,98%	2,67%
		0,5 M	6,06%	5,56%	6,10%	6,71%
	Linearity (R^2)		0.9714	0.9893	0.9823	0.9906
400 MHz	Repeatability (RSD)	4,0 M	7,74%	7,37%	8,07%	8,18%
		3,0 M	5,18%	4,73%	5,24%	5,31%
		2,0 M	2,12%	1,86%	2,15%	2,06%
		1,0 M	5,03%	4,12%	5,13%	5,34%
		0,5 M	3,34%	3,37%	3,51%	3,67%
	Linearity (R^2)		0.9911	0.9947	0.9921	0.9921

At low field, the repeatability mainly depends on the concentration, *i.e.* on the signal-noise ratio (SNR). The RSD is in general higher when the concentration decreases. Yet, the repeatability does not exceed 3% for most of the peaks at 1 mol.L^{-1}. The situation is quite different at high field where the worst repeatability is obtained at the highest concentration. Here, the SNR is not a limiting factor for such highly concentrated samples, and the lower repeatability for the most concentrated samples is probably explained by radiation damping effects –which can be suppressed if needed by appropriate methods [26]. But on the whole,

Table 1 results show that the repeatability of UF COSY at low field is comparable to the one measured at high field.

The method linearity was also evaluated from the 2D peak volumes measured on the five model samples. Five spectra were recorded, and for each concentration the average peak volume was calculated. The high coefficients of determination highlight the good linearity of the UF COSY both at high and low fields, with a slightly higher performance at high field.

Figure 4 gives a more precise idea of the SNR values that can be measured as a function of concentration, but also as a function of the experiment time –directly related to the number of scans. As expected, the SNR evolves linearly with concentration, while evolving with the square root of the number of scans when signal averaging is carried out.

In conclusion, the analytical performance (in terms of repeatability and linearity) appears similar to that of identical experiments at high field. The limit of detection is of course higher for LF UF, but can be decreased at a reasonable time cost when several scans are recorded. These results open the way to promising analytical applications, while highlighting the concentration limits of the method.

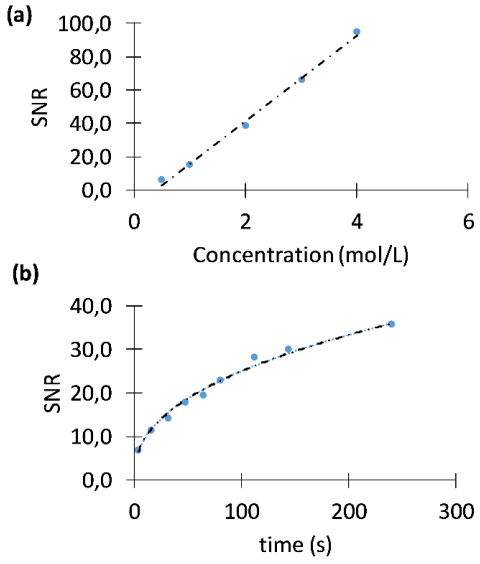

Figure 4. Typical SNR determined from UF COSY spectra on model 3-bromo-ethylpropionate samples in acetone-d_6. (a) SNR as a function of concentration for a 48 s experiment recorded with 12 scans. (b) SNR as a function of the experiment time measured on a 1 mol.L^{-1} sample. The SNR was computed on the signal CB as followed: S(CB)/σ(noise), where S(CB) is the amplitude of the peak CB and σ(noise) the standard deviation of the noise evaluated on an area of (F1 x F2) = (0.65 ppm x 1.14 ppm) centered at (F1 ; F2) = (4.6 ppm ; 3.0 ppm).

4. Reaction monitoring

Reaction monitoring performed through analytical spectroscopies yields essential kinetic and speciation information which could be determinant in numerous applications such as organic and inorganic synthesis, and for chemical engineering [27]. The development of accessible, powerful and robust analytical methods is therefore important to identify and quantify, in real time, the compounds involved in chemical processes. NMR spectroscopy has the advantage of being non-specific and non-destructive; moreover it requires no prior knowledge on the analyzed compounds. Furthermore, it delivers invaluable structural and quantitative information. HF NMR has been widely used in organic and pharmaceutical applications for monitoring chemical processes, either directly inside the NMR tube [28-30] or by using flow cells [31-35]. In spite of the valuable analytical insights, NMR remains less used than other more accessible spectroscopies such as FTIR or Raman, since it generally requires sophisticated and customized monitoring systems set up in dedicated laboratories.

It is against this background that benchtop NMR has emerged as a promising processing analytical tool; however its applicability is reduced by a lower performance compared to its HF counterpart. So far, resolution losses and overlapping issues have limited the application range of LF NMR to the monitoring of relatively simple reactions where the peaks of interest are well isolated, unless deconvolution tools are employed [3-5]. In this context, the potential of UF 2D NMR seems worth exploring.

We recently reported the suitability of this methodology through the monitoring of a Pd-catalyzed Heck-Matsuda reaction (Figure 5a) performed in the NMR tube [36]. This variant of the Heck coupling uses aryl diazonium salts as highly reactive aryl halide surrogates, and provides reactions in mild conditions under ligand- and base-free conditions [37]. Moreover, this reaction has recently found a growing interest, especially since its hazardous character was alleviated by a bicatalytic strategy [38, 39] and/or a continuous-flow approach [40, 41].

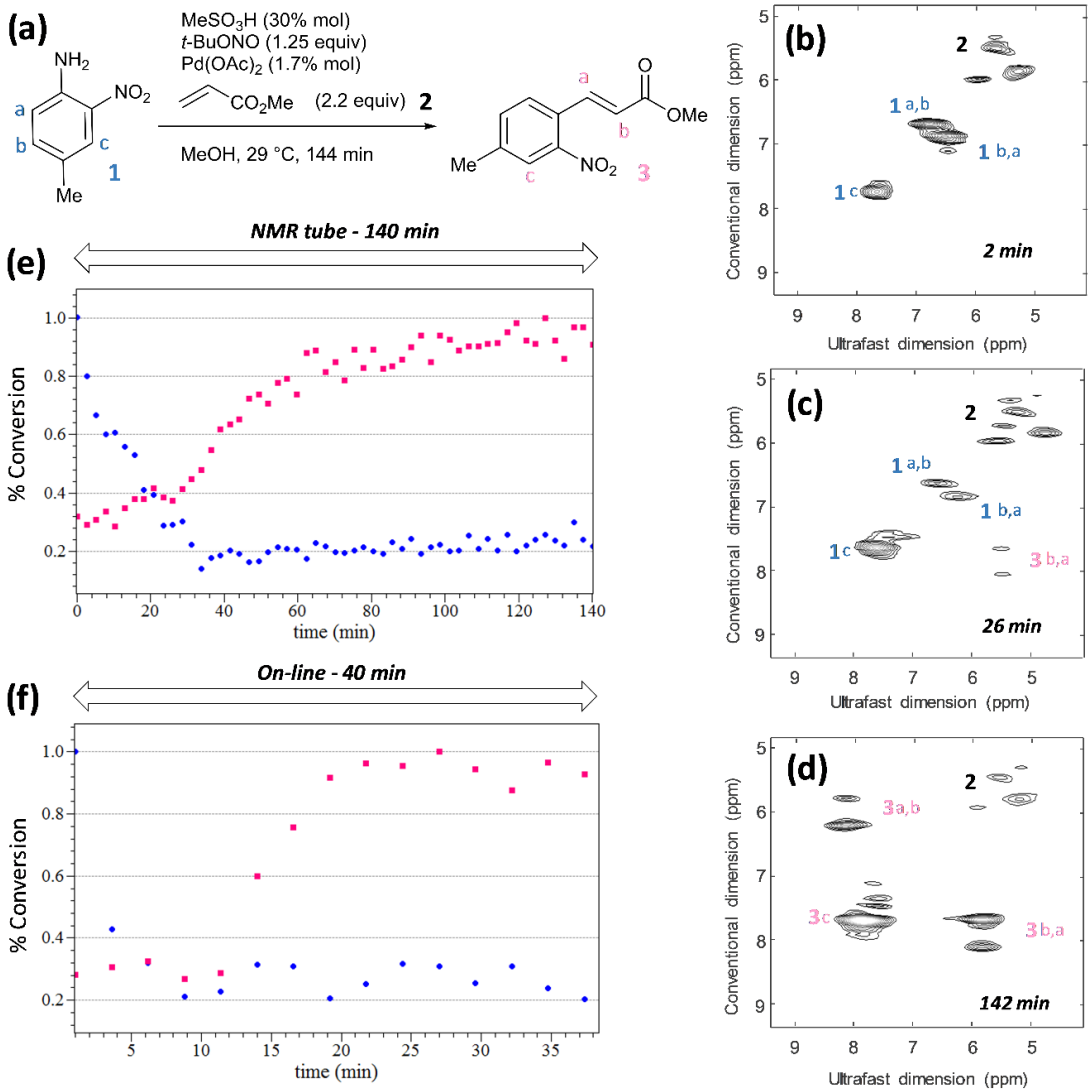

Figure 5. Scheme of the one pot Heck-Matsuda reaction in the multicomponent mode (a). The reaction was followed at 29 °C for 144 min with an initial concentration of 0.36 mol/L for the limiting starting material **1**. The reaction was followed either in the NMR tube or on-flow with mechanical stirring. (b, c, d) show UF COSY spectra recorded with 36 scans in 2.6 minutes at different times (2 min, 26 min and 142 min, respectively) in the course of the in tube monitoring. For the in tube and on-flow monitoring, 55 and 15 successive spectra were respectively recorded every 2.6 min. (e, f) show the evolution of normalized 2D peak volumes as the reaction progresses, for the "in tube " (e) and on-flow settings (f). These volumes were calculated from the cross peaks **1** a,b and **3** b,a indicated in Figure 2, corresponding to the starting material and the final product, respectively. The blue open circles show the consumption of aniline and the pink open squares show the formation of the final styrene. Figures (a-e) reproduced from (Gouilleux et al., Analyst 2015, DOI: 10.1039/C5AN01998B) with permission from The Royal Society of Chemistry.

In this reaction, the aniline **1** dissolved in methanol first reacts with *t*-BuONO and $MeSO_3H$ to form a diazonium salt. The latter is then coupled with methyl acrylate **2** in the presence of $Pd(OAc)_2$ as a catalyst, in order to produce the styrene **3**. The experiment must be designed to keep the mixture as homogeneous as possible in order to avoid disruption of the NMR

acquisition. It is important to notice that thanks to an external lock system, experiments are carried out in a non-deuterated solvent. This reduces the cost of the monitoring and allows to avoid unwanted potential isotopic effects that could affect reaction rates in deuterated solvents.

The Heck-Matsuda reaction represents a well-suited model reaction to assess the relevance of the UF approach at 43 MHz. Indeed, this reaction provides relatively crowded resonances in the aromatic region, justifying the need for multi-dimensional experiments. Moreover, the reaction conditions –use of a metallic catalyst and gas formed during the coupling reaction– form a challenging example. Here, in view of the relatively low SNR obtained in a single scan, the experiment duration was adapted to the reaction timescale (36 scans with a recovery time of $1.25 \cdot T_1$, leading to the acquisition of a COSY spectrum every 2.6 min). As previously reported, the sensitivity was optimized through the optimization of J-modulation effects [42]. The 2D UF spectra shown in Figure 5 highlight how this methodology can deliver time-dependent and spectrally resolved cross peaks, both for the product **3** and for the limiting starting material **1** (Figure 5b, 5c, 5d). The starting material in excess **2** is also visible on the spectra.

In this preliminary work, the reaction monitoring was performed directly inside an NMR tube in mild conditions, *i.e.* 29 °C, with an initial concentration of 0.36 $mol.L^{-1}$ for the limiting starting material. The kinetic curves recorded from the time-evolution of 2D peak volumes are shown in Figure 5e. These curves depict the two chemical processes involved in the Heck-Matsuda reaction very well. The decreasing blue curve matches with the initial conversion of **1** into the corresponding diazonium salt. After the aniline is consumed (at ca. 20 min), the coupling reaction starts, leading to the final styrene **3** (increasing pink curve). The trend of the curves and the rate constants (as determined in Ref. [20]) reveal that the coupling reaction is the rate-limiting step of the process with respect to the diazonium formation.

Although this reaction monitoring achieved inside an NMR tube already provides relevant kinetic information, the experimental conditions remain strongly limited: stirring is impossible, the temperature cannot be adjusted and the spectral quality is highly sensitive to potential heterogeneities. On the contrary, an on-flow monitoring through a bypass system allows to monitor the reaction in a vessel with a greater flexibility regarding the experimental conditions: regulated temperature, mechanical stirring, inert atmosphere etc. We therefore

decided to carry out the same reaction, but monitored in an on-flow fashion. In this case, the reaction takes place inside a conventional flask, which is connected to the benchtop spectrometer thanks to a bypass system. A peristaltic pump generates a continuous flow to refresh the sensitive volume of the magnet with the reactive mixture in the course of the chemical process (Figure 6).

Yet, this setup raises further questions about the recorded UF spectra, such as the robustness of the spatial encoding performed on a flowing mixture, as reported for online HPLC-UF NMR coupling [43]. Fortunately, in the Spinsolve Benchtop spectrometer, the gradient-axis used for the spatial encoding is perpendicular to the flow-cell, therefore reducing the sensitivity of the UF experiments to the flow. The spins located in a given sample slice can be considered as undergoing the same magnetic field gradient during the whole pulse sequence. Moreover, compared to the "in tube" monitoring, the mixture homogeneity is less critical, even though special care should be given to avoid that precipitates (here, from the diazonium salt) obstruct the capillary of the bypass system. To compare the results of the on-flow experiment to the previously reported "in tube" monitoring, the reaction was performed, while stirring, with identical concentrations (0.36 $mol.L^{-1}$) and at the same temperature (29 °C). The reaction mixture flowed continuously from the flask to the spectrometer at a rate of 2 $mL.min^{-1}$. This value allows to minimize the time spent by the mixture outside the flask while avoiding some hardware issues such as a significant drift of the carrier frequency which was observed at higher rates. NMR parameters and optimizations –as described in Ref. [20]– were kept unchanged, yielding COSY spectra every 2.6 minutes. The kinetic curves obtained with this experimental setup are displayed in Figure 5f. As for the monitoring carried out inside the tube, the curves highlight the two chemical processes, *i.e* the diazonium conversion followed by the Pd-coupling. However, a major difference is the significantly shorter time-scale of the Heck-Matsuda reaction when monitored in an on-flow setting. The plateau is reached at about 40 min, versus 140 min for the "in tube" monitoring. Here, after only 3.6 min, around 60% of the aniline is already consumed and almost 80% of the final styrene is obtained in approximatively 17 min. This fast kinetics could be attributed to: i) stirring, which is missing when the reaction takes place in the NMR tube. This result is consistent with recently reported results [44]; ii) the time spent by the solution in the by-pass system (*ca.* 40% of the reaction

time). Inside the tubing, the reaction is carried out in a continuous-flow fashion involving different kinetics than inside the reactor.

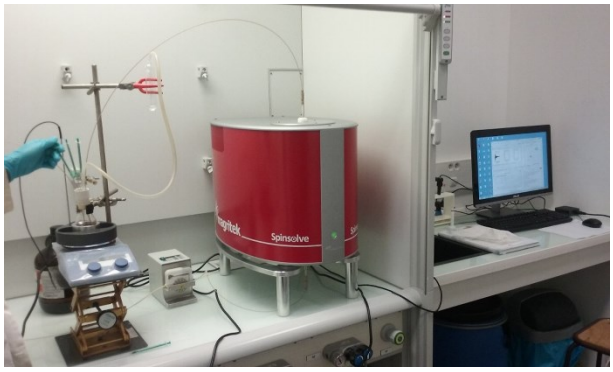

Figure 6. Picture of the experimental setting for the on-flow monitoring of chemical reactions under the fume hood.

5. Screening applications

Although the real-time monitoring of fast chemical processes is probably the most obvious application of UF 2D NMR, another potentially promising utilization of fast 2D experiments at low field relates to screening analysis. Indeed, relevant results about adulteration and authentication issues were recently reported using benchtop spectrometers in different fields, from food matrices - e.g. honey [7], edible oils [6], meat [8] - to sexual enhancement and weight loss dietary supplements [9]. In this section we focus on the potential of UF NMR at low field for screening analysis applied to a long-standing concern: the screening of the edible oils. In particular, olive oil, which is a mixture of tri, di, and mono-glycerides, is considered as one of the best sources of fatty acids and natural antioxidants. Its nutritional properties and its excellent taste make olive oil a high-value product that is related to numerous frauds and adulterations [45]. High-resolution ^{1}H NMR has been widely used in this context for assessing quality and detecting quality adulteration. Moreover, a recent article extended this background to LF NMR.[6] This study emphasized the ability of benchtop NMR to detect the adulteration of olive oils through the addition of cheaper substitutes. 1D spectra recorded in 10 min at 60 MHz and combined with a chemometric approach, enabled to detect hazelnut

oil into an olive oil sample at the level of 11.2% w/w. This result encouraged us to investigate the potential of fast 2D experiments to improve the screening performance.

Edible oil is formed of monounsaturated, polyunsaturated and saturated fatty acids, mainly in the form of esters with glycerol (triglycerides), which constitute more than 98% of the total content in the case of olive oil. The assignment of these components is significantly complicated by the overlapped resonances commonly encountered at 43 MHz (Figure 7). Hopefully, numerous fully assigned high-field ^{1}H spectra of edible oils are reported in the literature, which facilitates the identification of major peaks [46, 47]. An assignment of the visible signals is proposed in Figure 7 –which compares the LF and HF spectra of the same sample– where some of them are particularly interesting for the present study. The olefinic peak A at 5.26 ppm, arising from protons involved in a double bound, refers to the total number of unsaturated bounds, regardless of whether these are provided by mono- or polyunsaturated chains. The two peaks at 5.20 and 4.23 ppm respectively match with the -CH- and -CH_2- groups of the glycerol backbones in the triglycerides. Finally, the peak D located at 2.70 ppm arises from the diallylic CH_2 protons of the polyunsaturated chains (see Figure 7c).

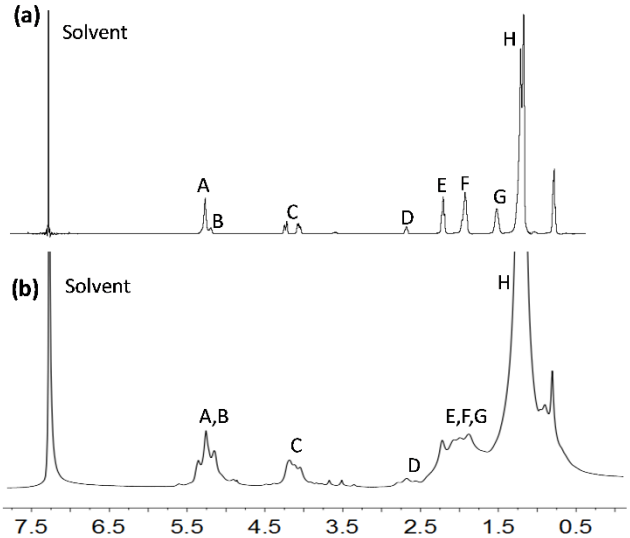

(c)

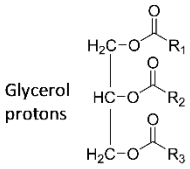

peak	δ (ppm)		components
A	5,26	*H*C=C*H*	All unsaturated fatty acids
B	5,20	*H*C−OCOR	Glycerols
C	4,23	*H*$_2$C−OCOR	Glycerols
D	2,70	HC=CHC*H*$_2$CH=CH	Polyunsaturated fatty acids
E	2,23	C*H*$_2$COOH	All acyl chains
F	1,96	C*H*$_2$CH=CH	All unsaturated fatty acids
G	1,55	C*H*$_2$CH$_2$COOH	All acyl chains
H	1,23	$[CH_2]_n$	All acyl chains

Figure 7. 1D 1H NMR spectra of a peanut oil sample (60% in chloroform v/v) recorded at 400 MHz (a) and 43 MHz (b). (c) shows the generic structure of triglycerides, which form the major constituents of edible oils, together with the assignment of main signals based on the literature.

A convenient way for screening the edible oil at low field is to consider ratios between integrated peaks that reflect the relative concentration of unsaturated fatty acids (noted UFA),

polyunsaturated fatty acids (PUFA) and glycerol (GLY) in the oil sample. In practice, a relevant ratio is obtained by dividing the signal C at 4.23 ppm arising from the -CH_2- protons GLY by the signal A at 5.26 ppm referring to UFA. Although the authors of Ref. [6]. used this criterion to screen different edible oils through 1D spectra, this procedure at low field suffers from a measurement bias, since the resonance at 5.20 ppm (peak B) matching with the CH group of the glycerol is totally collapsed with the olefinic peak A (Figure 7b). In this example, 2D experiments constitute an attractive way to circumvent this overlapping issue, and UF spectroscopy potentially provides a convenient way for such rapid screening. The UF 2D spectra shown in Figure 8, recorded on different oils in 2.4 min, highlight how the UF COSY experiments overcome the overlapping issue by delivering very well resolved correlation peaks. It is therefore possible to properly determine peak ratios without measurement bias in a short experimental time. It is even possible to discern different oils by a simple visual inspection in the case of peanut, sunflower and olive oils (Figure 8), as the intensity of the PUFA cross-peaks increases from the olive to the sunflower oil. We evaluated this promising benefit via a more quantitative approach based on the ratios of integrated peaks. UF COSY experiments were performed on a panel of 14 oil samples from 5 different sources: olive, peanut, corn, sunflower and hazelnut. 36 scans, i.e. 2.4 min, were enough to obtain a SNR higher than 20 for the peaks of interest. J-modulation was tuned to reach a compromise in sensitivity for the cross-peaks of interest arising from UFA, PUFA and GLY. The screening was first based on the ratio GLY / UFA previously reported, and a complementary ratio PUFA / UFA was also determined, reflecting the proportion of polyunsaturated acids in the sample. This ratio could not be accurately determined in 1D because of peak overlaps with the acyl chain signals. A series of 5 UF COSY spectra was acquired for each sample and average peak volume ratios were calculated. The two ratios were plotted in a 2D graph, showing the relevance of this approach to discriminate different sources of edible oils (Figure 8d). The complementarity of the two ratios is clearly visible in the 2D plot, where the group of olive oils appears well separated from the groups of corn and sunflower oils based on the PUFA / UFA criteria, while the ratio GLY / UFA separates olive from peanut and hazelnut oils.

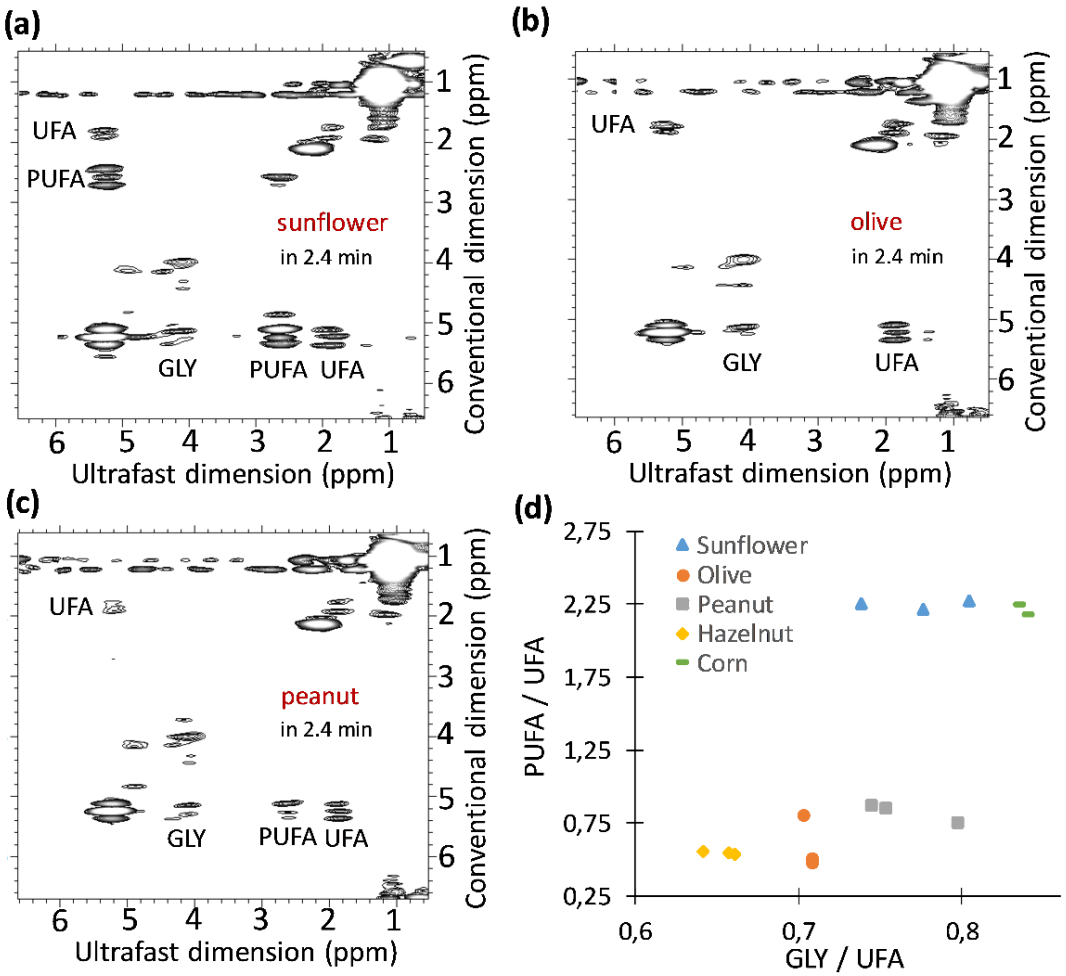

Figure 8. 2D UF COSY spectra of sunflower (a), olive (b) and peanut (c) oil samples (60% in chloroform v/v) recorded in 2.4 minutes at 43 MHz with the pulse sequence of Figure 2. (d) shows the PUFA/UFA versus GLY/UFA 2D peak ratios, enabling the group separation of 14 edible oil samples from different origins. UFA and PUFA were calculated by the sum of theirs symmetric resonances; for GLY only the peak located under the diagonal was taken into account.

Naturally, this study does not allow to accurately assess the intra-group variability due to the limited number of samples. Yet, this positive result highlights the relevancy of developing UF 2D NMR on a benchtop spectrometer for screening applications. This urges to investigate, in the near future, further developments along this direction, such as combining UF NMR at low field with chemometrics to build an efficient and rapid screening tool

6. Conclusion

This article presents some of the main features and application perspectives of ultrafast 2D NMR and its hybrid variants at low field. The excellent analytical performance that can be achieved in a few tens of seconds, and the promising results obtained in the fields of on-flow reaction monitoring and rapid screening, show that this approach can be a powerful complement to existing analytical methods. UF 2D spectroscopy should therefore help increasing the general applicability of benchtop spectroscopy in a variety of situations where the sample complexity generates spectral overlaps –an omnipresent case at low field.

More generally, these first spatially-encoded NMR experiments on a benchtop spectrometer could open the way to a number of developments for a fast analysis of liquid-state samples, including other homo- or heteronuclear UF pulse sequences, pure-shift experiments or diffusion-based measurements. In particular, heteronuclear pulse sequences would give access to a better separation of resonances, albeit at a sensitivity cost. In view of these perspectives, implementing a gradient coil on benchtop spectrometers is likely to become a standard option on low-field spectrometers.

7. Material and methods

7.1 Spectrometers

400 MHz spectrometer. The experiments performed at high field were recorded on a Bruker Avance III 400 spectrometer operated with Topspin 2.1, at a frequency of 400.13 MHz with a 5 mm BBFO+ probe equipped with a z-axis gradient coil generating a maximum field gradient of 0.90 $T.m^{-1}$.

43 MHz benchtop spectrometer. The experiments performed at low field were recorded on a Spinsolve from Magritek working at a frequency of 43.62 MHz via a permanent magnet based on a Hallbach design [48, 49]. This equipment includes a gradient coil along the B_0-axis (i.e. along the transverse plane of the NMR tube) which can generate a maximum field gradient of 0.16 $T.m^{-1}$ and operated with the Prospa Software. The spectrometer allows to work without deuterated solvents thanks to a built-in external fluorine lock system.

7.2 Analytical performance

7.2.1 Model samples

Five samples of commercial 3-bromo-ethylpropionate were prepared in acetone-d_6 at different concentrations: 0.5, 1, 2, 3 and 4 mol.L^{-1}.

7.2.2 UF 2D NMR experiments

All the UF spectra are displayed with the indirect domain called “ultrafast dimension” since it results from specific ultrafast features, whereas the direct dimension arising from conventional evolution during the detection period is called “conventional dimension”. The acquisition and processing parameters are given below for each experiment.

UF COSY single scan at 43 MHz recorded on the ethanol sample. The UF single scan experiment presented in Figure 2b was recorded in 400 ms with the homemade pulse sequence described in Figure 2a, with two 30 ms chirp pulses (*i.e.* TE = 60 ms) swept over a 3.5 kHz range. The amplitude of the encoding gradients G_e was adapted to obtain a frequency dispersion equivalent to the frequency sweep of the pulses, corresponding to 11.6% of the maximum gradient strength available. A delay t_{mix} of 42 ms was added prior to the spatial encoding step in order to optimize the effects of J-modulation arising from the constant time nature of the double spin-echo encoding.[42] During the acquisition, 128 pairs of bipolar gradient pulses G_a were applied (85% of maximum strength, 1280.4 µs each). The desired coherence selection was obtained as described in Figure 2a. The spectrum was processed using a home-written routine in Prospa, including an optimized Gaussian apodization in the spatially-encoded dimension [50] and a sine-bell apodization in the FT dimension.

Fast hybrid COSY at 43 MHz recorded on the model samples. The UF experiment presented in Figure 3a was recorded in 12 scans, *i.e. in* 48 s, with the homemade pulse sequence described in Figure 2a, with two 40 ms chirp pulses (*i.e.* TE = 80 ms) swept over a 3.5 kHz range. The amplitude of the encoding gradients G_e was adapted to obtain a frequency dispersion equivalent to the frequency sweep of the pulses, corresponding to 11.6% of the

maximum gradient strength available. A delay t_{mix} of 27 ms was added prior to the spatial encoding step in order to optimize the effects of J-modulation. Processing were performed as previously mentioned.

UF COSY at 400 MHz recorded on the model samples. The UF experiment presented in Figure 3c was recorded in a single scan, *i.e.* in 0.2 s, with the homemade pulse sequence described in Figure 2a, with two 15 ms smoothed chirp pulses (i.e. TE = 30 ms) swept over a 3.5 kHz range. The amplitude of the encoding gradients G_e was adapted to obtain a frequency dispersion equivalent to the frequency sweep of the pulses, corresponding to 11.6% of the maximum gradient strength available. A delay t_{mix} of 77 ms was added prior to the spatial encoding step so that the magnetizations spend the same time in the transverse plane as in the LF experiments. The spectrum was processed using a home-written routine in Topspin, including an optimized Gaussian apodization in the spatially-encoded dimension and a sine-bell apodization in the FT dimension.

7.2.3 Conventional (Conv) 2D NMR experiments

Conv COSY at 43 MHz. The UF experiment presented in Figure 3c was recorded in 10 min via the commercial routine "QuickCOSY" pulse sequence proposed within the Spinsolve software. The indirect domain was sampled through 256 t_1 increments (1 scan each), with each FID containing 8192 points separated by a dwell time of 200 µs. The processing was then automatically performed in MNOVA (Mestrelab Research), including sinusoidal apodization in the two dimensions, followed by a 2D FT to obtain the final spectrum.

Conv COSY at 400 MHz. The UF experiment presented in Figure 3c was recorded in 10 min via the commercial routine pulse-sequence "cosygpqf". The indirect domain was sampled through 256 increments (1 scan each), with each FID containing 2400 points separated by a dwell-time of 208 µs. The processing was performed under Topspin 2.1, including sinusoidal apodization in the two dimensions, followed by a 2D FT to obtain the final spectrum.

7.3 Reaction monitoring

7.3.1 Procedures for the Heck-Matsuda reaction

Monitoring performed inside the NMR tube. *t*-BuONO (0.317 mmol, 38 µL) was added to a solution of aniline (0.252 mmol, 38.8 mg) in MeOH (450 µL). The resulting mixture was stirred and transferred into an NMR tube. Methyl acrylate (0.555 mmol, 50 µL) and palladium acetate (1.7 mol%, 1.1 mg) in MeOH (200 µL) were added to the solution. The bicatalytic reaction was then initiated by adding methanesulfonic acid (30 mol%, 5 µL). The NMR tube, containing finally a 700 µL solution, was stirred and inserted inside the benchtop NMR at 29 °C for 144 min.

On-line monitoring procedure. The starting aniline (3.60 mmol, 547.4 mg) was dissolved in MeOH (8.0 mL) inside a 50 mL round-bottom flask. The mixture was stirred for at least 30 min until a homogeneous solution was obtained. The mixture was flowed by the peristaltic pump at a rate of 2 mL/min through the by-pass system consisting of an NMR flow-cell and PEEK tubing for a total volume of 3.8 mL. Then, *t*-BuONO (4.50 mmol, 540 µL), methyl acrylate (7.92 mmol, 713 µL) and palladium acetate (1.7 mol%, 13.5 mg) in MeOH (700 µL) were successively added to the reaction mixture. The bicatalytic reaction was then initiated by adding methanesulfonic acid (30 mol%, 70 µL). The final 10 mL volume of reactive mixture was regulated at 29 °C while stirring for about 40 min.

7.3.2 UF COSY experiments

Fast hybrid UF COSY at 43 MHz. The UF COSY spectra for both reaction monitorings (Figure 6) were recorded in 146 s (*i.e.* 36 scans) with the homemade pulse sequence of Figure 2a with the following features: the spatial encoding was performed by combining two 45 ms chirp pulses (*i.e.* TE = 90 ms) swept over a 3.5 kHz range with encoding gradients Ge fixed at 9.00% of the maximum gradient strength. The detection was then achieved with 128 pairs of bipolar gradient pulses Ga at 85% of the maximum strength (1280 µs each). The desired coherence-selection was obtained thanks to both a standard four step phase cycling and gradient pulses. The spectrum was processed in the same way as described for the LF experiments (7.2.2).

7.4 Screening applications

7.4.1 Oil samples

14 samples of edible oils from 5 different sources: olive, hazelnut, sunflower, peanut and corn were purchased from various supermarkets. For each sample, 600 µL of oil was dissolved in 400 µL of non-deuterated chloroform inside a 5 mm NMR tube.

7.4.2 UF COSY experiments

Fast hybrid UF COSY at 43 MHz. The UF COSY spectra (Figure 8) were recorded in 146 s (*i.e.* 36 scans) with the homemade pulse sequence of Figure 2a with the following features: the spatial encoding was performed by combining two 30 ms chirp pulses (*i.e.* TE = 60 ms) swept over a 3.5 kHz range with encoding gradients Ge fixed at 11.6% of the maximum gradient strength. The detection was then achieved with 128 pairs of bipolar gradient pulses Ga at 85% of the maximum strength (1280 µs each). The desired coherence-selection was obtained thanks to both a standard four step phase cycling and gradient pulses. The spectrum was processed in the same way as previously described for the LF experiments.

7.5 Data processing for ultrafast acquisition

All the data recorded in an ultrafast fashion were processed thanks to a home-written routine implemented in Topspin and Prospa. The first step of this routine consists in splitting and rearranging the echoes detected during the successive positive/negative acquisition gradients, leading to two mirror-image S(k, t_2) maps. A sine-bell apodization in the t_2 dimension is applied, followed by a FT (in magnitude mode) yielding two symmetric S(k, F2) maps. These maps are then added after reversing one of them along the ultrafast dimension (i.e. along k), leading to a 2D spectrum. Finally, a Gaussian apodization in the spatially encoded domain [50] is applied.

Acknowledgements

The authors warmly acknowledge Magritek, in particular Ernesto Danieli, Juan Perlo and Andrew Coy, for their strong support. We also thank Michel Giraudeau for linguistic assistance. This project was funded by Région Pays de la Loire (Grant RésoNantes).

References

[1] S.K. Kuster, E. Danieli, B. Blumich, F. Casanova, High-resolution NMR spectroscopy under the fume hood, Phys. Chem. Chem. Phys., 13 (2011) 13172-13176.
[2] V. Sans, L. Porwol, V. Dragone, L. Cronin, A self optimizing synthetic organic reactor system using real-time in-line NMR spectroscopy, Chem. Sci., 6 (2015) 1258-1264.
[3] M.V. Silva Elipe, R.R. Milburn, Monitoring chemical reactions by low-field benchtop NMR at 45 MHz: pros and cons, Magn. Reson. Chem., DOI 10.1002/mrc.4189(2015) n/a-n/a.
[4] F. Dalitz, M. Cudaj, M. Maiwald, G. Guthausen, Process and reaction monitoring by low-field NMR spectroscopy, Prog. Nucl. Magn. Reson. Spectrosc., 60 (2012) 52-70.
[5] E. Danieli, J. Perlo, A.L.L. Duchateau, G.K.M. Verzijl, V.M. Litvinov, B. Blümich, F. Casanova, On-Line Monitoring of Chemical Reactions by using Bench-Top Nuclear Magnetic Resonance Spectroscopy, ChemPhysChem, 15 (2014) 3060-3066.
[6] T. Parker, E. Limer, A.D. Watson, M. Defernez, D. Williamson, E.K. Kemsley, 60 MHz 1H NMR spectroscopy for the analysis of edible oils, TrAC, Trends Anal. Chem., 57 (2014) 147-158.
[7] R.d.O.R. Ribeiro, E.T. Mársico, C.d.S. Carneiro, M.L.G. Monteiro, C.C. Júnior, E.F.O.d. Jesus, Detection of honey adulteration of high fructose corn syrup by Low Field Nuclear Magnetic Resonance (LF 1H NMR), J. Food Eng., 135 (2014) 39-43.
[8] W. Jakes, A. Gerdova, M. Defernez, A.D. Watson, C. McCallum, E. Limer, I.J. Colquhoun, D.C. Williamson, E.K. Kemsley, Authentication of beef versus horse meat using 60 MHz 1H NMR spectroscopy, Food Chem., 175 (2015) 1-9.
[9] G. Pagès, A. Gerdova, D. Williamson, V. Gilard, R. Martino, M. Malet-Martino, Evaluation of a Benchtop Cryogen-Free Low-Field 1H NMR Spectrometer for the Analysis of Sexual Enhancement and Weight Loss Dietary Supplements Adulterated with Pharmaceutical Substances, Anal. Chem., 86 (2014) 11897-11904.
[10] J. Jeener, Lecture presented at Ampere International Summer School II, Basko Polje, Yugoslavia, DOI (1971).
[11] W.P. Aue, E. Bartholdi, R.R. Ernst, Two-dimensional spectroscopy. Application to nuclear magnetic resonance, J. Chem. Phys., 64 (1976) 2229-2246.
[12] R. Boisseau, U. Bussy, P. Giraudeau, M. Boujtita, In Situ Ultrafast 2D NMR Spectroelectrochemistry for Real-Time Monitoring of Redox Reactions, Anal. Chem., 87 (2015) 372-375.
[13] L. Frydman, T. Scherf, A. Lupulescu, The acquisition of multidimensional NMR spectra within a single scan, Prod. Natl. Acad. Sci. USA, 99 (2002) 15858-15862.

[14] A. Herrera, E. Fernández-Valle, R. Martínez-Álvarez, D. Molero-Vílchez, Z.D. Pardo-Botero, E. Sáez-Barajas, Monitoring organic reactions by UF-NMR spectroscopy, Magn. Reson. Chem., 53 (2015) 952-970.
[15] L.H.K. Queiroz, D.P.K. Queiroz, L. Dhooghe, A.G. Ferreira, P. Giraudeau, Real-time separation of natural products by ultrafast 2D NMR coupled to on-line HPLC, Analyst, 137 (2012) 2357-2361.
[16] J.-N. Dumez, J. Milani, B. Vuichoud, A. Bornet, J. Lalande-Martin, I. Tea, M. Yon, M. Maucourt, C. Deborde, A. Moing, L. Frydman, G. Bodenhausen, S. Jannin, P. Giraudeau, Hyperpolarized NMR of plant and cancer cell extracts at natural abundance, Analyst, 140 (2015) 5860-5863.
[17] A. Le Guennec, I. Tea, I. Antheaume, E. Martineau, B. Charrier, M. Pathan, S. Akoka, P. Giraudeau, Fast determination of absolute metabolite concentrations by spatially-encoded 2D NMR: application to breast cancer cell extracts, Anal. Chem., 84 (2012) 10831-10837.
[18] T. Jézéquel, C. Deborde, M. Maucourt, V. Zhendre, A. Moing, P. Giraudeau, Absolute quantification of metabolites in tomato fruit extracts by fast 2D NMR, Metabolomics, 11 (2015) 1231-1242.
[19] P. Giraudeau, L. Frydman, Ultrafast 2D NMR: An Emerging Tool in Analytical Spectroscopy, Annu. Rev. Anal. Chem., 7 (2014) 129-161.
[20] B. Gouilleux, B. Charrier, E. Danieli, J.-N. Dumez, S. Akoka, F.-X. Felpin, M. Rodriguez-Zubiri, P. Giraudeau, Real-time reaction monitoring by ultrafast 2D NMR on a benchtop spectrometer, Analyst, DOI 10.1039/c5an01998b(2015).
[21] P. Pelupessy, Adiabatic single scan two-dimensional NMR spectroscopy, J. Am. Chem. Soc., 125 (2003) 12345-12350.
[22] A. Tal, L. Frydman, Single-scan multidimensional magnetic resonance Prog. Nucl. Magn. Reson. Spectrosc., 57 (2010) 241-292.
[23] S. Akoka, P. Giraudeau, Fast hybrid multi-dimensional NMR methods based on ultrafast 2D NMR, Magn. Reson. Chem., 53 (2015) 986-994.
[24] P. Giraudeau, S. Akoka, Sources of sensitivity losses in ultrafast 2D NMR, J. Magn. Reson., 192 (2008) 151-158.
[25] M. Foroozandeh, R.W. Adams, P. Kiraly, M. Nilsson, G.A. Morris, Measuring couplings in crowded NMR spectra: pure shift NMR with multiplet analysis, Chem. Commun., 51 (2015) 15410-15413.
[26] K. Bayle, M. Julien, G.S. Remaud, S. Akoka, Suppression of radiation damping for high precision quantitative NMR, J. Magn. Reson., 259 (2015) 121-125.
[27] J. Workman, M. Koch, B. Lavine, R. Chrisman, Process Analytical Chemistry, Anal. Chem., 81 (2009) 4623-4643.
[28] F. Susanne, D.S. Smith, A. Codina, Kinetic Understanding Using NMR Reaction Profiling, Org. Process Res. Dev., 16 (2012) 61-64.
[29] I.M. Clegg, C.M. Gordon, D.S. Smith, R. Alzaga, A. Codina, NMR reaction monitoring during the development of an active pharmaceutical ingredient, Anal. Methods, 4 (2012) 1498-1506.
[30] T.R. Hoye, B.M. Eklov, T.D. Ryba, M. Voloshin, L.J. Yao, No-D NMR (No-Deuterium Proton NMR) Spectroscopy: A Simple Yet Powerful Method for Analyzing Reaction and Reagent Solutions, Org. Lett., 6 (2004) 953-956.
[31] M. Maiwald, H.H. Fischer, Y.-K. Kim, K. Albert, H. Hasse, Quantitative high-resolution on-line NMR spectroscopy in reaction and process monitoring, J. Magn. Reson., 166 (2004) 135-146.

[32] M.A. Bernstein, M. Štefinović, C.J. Sleigh, Optimising reaction performance in the pharmaceutical industry by monitoring with NMR, Magn. Reson. Chem., 45 (2007) 564-571.
[33] M. Khajeh, M.A. Bernstein, G.A. Morris, A simple flowcell for reaction monitoring by NMR, Magn. Reson. Chem., 48 (2010) 516-522.
[34] D.A. Foley, C.W. Doecke, J.Y. Buser, J.M. Merritt, L. Murphy, M. Kissane, S.G. Collins, A.R. Maguire, A. Kaerner, ReactNMR and ReactIR as Reaction Monitoring and Mechanistic Elucidation Tools: The NCS Mediated Cascade Reaction of α-Thioamides to α-Thio-β-chloroacrylamides, J. Org. Chem., 76 (2011) 9630-9640.
[35] A.C. Barrios Sosa, R.T. Williamson, R. Conway, A. Shankar, R. Sumpter, T. Cleary, A Safe and Efficient Synthetic Route to a 2,5-Dimethyl-1-aryl-1H-imidazole Intermediate, Org. Process Res. Dev., 15 (2011) 449-454.
[36] K. Kikukawa, T. Matsuda, Reaction of diazonium salts with transition metals. I. Arylation of olefinswith arenediazonium salts catalyzed by zero valent palladium, Chem. Lett., 6 (1977) 159-162.
[37] F.-X. Felpin, K. Miqueu, J.-M. Sotiropoulos, E. Fouquet, O. Ibarguren, J. Laudien, Room-Temperature, Ligand- and Base-Free Heck Reactions of Aryl Diazonium Salts at Low Palladium Loading: Sustainable Preparation of Substituted Stilbene Derivatives, Chem. Eur. J., 16 (2010) 5191-5204.
[38] F.L. Callonnec, E. Fouquet, F.-X. Felpin, Unprecedented Substoichiometric Use of Hazardous Aryl Diazonium Salts in the Heck-Matsuda Reaction via a Double Catalytic Cycle, Org. Lett., 13 (2011) 2646-2649.
[39] N. Oger, F. Le Callonnec, D. Jacquemin, E. Fouquet, E. Le Grognec, F.-X. Felpin, Heck–Matsuda Arylation of Olefins Through a Bicatalytic Approach: Improved Procedures and Rationalization, Adv. Synth. Catal., 356 (2014) 1065-1071.
[40] N. Oger, E. Le Grognec, F.-X. Felpin, Continuous-Flow Heck–Matsuda Reaction: Homogeneous versus Heterogeneous Palladium Catalysts, J. Org. Chem., 79 (2014) 8255-8262.
[41] N. Oger, E. Le Grognec, F.-X. Felpin, Handling diazonium salts in flow for organic and material chemistry, Org. Chem. Front., 2 (2015) 590-614.
[42] B. Gouilleux, L. Rouger, B. Charrier, I. Kuprov, S. Akoka, J.-N. Dumez, P. Giraudeau, Understanding J-Modulation during Spatial Encoding for Sensitivity-Optimized Ultrafast NMR Spectroscopy, ChemPhysChem, 16 (2015) 3093-3100.
[43] L.H.K. Queiroz Junior, D.P.K. Queiroz, L. Dhooghe, A.G. Ferreira, P. Giraudeau, Real-time separation of natural products by ultrafast 2D NMR coupled to on-line HPLC, Analyst, 137 (2012) 2357-2361.
[44] D.A. Foley, A.L. Dunn, M.T. Zell, Reaction monitoring using online vs tube NMR spectroscopy: seriously different results, Magn. Reson. Chem., DOI 10.1002/mrc.4259(2015) n/a-n/a.
[45] P. Dais, E. Hatzakis, Quality assessment and authentication of virgin olive oil by NMR spectroscopy: A critical review, Anal. Chim. Acta, 765 (2013) 1-27.
[46] R. Sacchi, F. Addeo, L. Paolillo, 1H and 13C NMR of virgin olive oil. An overview, Magn. Reson. Chem., 35 (1997) S133-S145.
[47] L. Del Coco, S.A. De Pascali, V. Iacovelli, G. Cesari, F.P. Schena, F.P. Fanizzi, Following the olive oil production chain: 1D and 2D NMR study of olive paste, pomace, and oil, Eur. J. Lipid. Sci. Tech., 116 (2014) 1513-1521.
[48] E. Danieli, J. Perlo, B. Blümich, F. Casanova, Small Magnets for Portable NMR Spectrometers, Angew. Chem. Int. Edit., 49 (2010) 4133-4135.

[49] E. Danieli, J. Perlo, B. Blümich, F. Casanova, Highly Stable and Finely Tuned Magnetic Fields Generated by Permanent Magnet Assemblies, Phys. Rev. Lett., 110 (2013) 180801.
[50] P. Giraudeau, S. Akoka, Sensitivity and lineshape improvement in ultrafast 2D NMR by optimized apodization in the spatially encoded dimension, Magn. Reson. Chem., 49 (2011) 307-313.

1.2.1. Summary and commentaries

The results presented in this articles gives an overview of the potential and limits of UF 2D NMR on a benchtop spectrometer. A first important feature was the evaluation of the analytical performance of UF COSY at 43 MHz in terms of signal-to-noise-ratio, repeatability and linearity. Based on a series of five successive 12-scans UF COSY experiments on a small molecules at 1 M, the standard deviation remains lower than 3 % with a linearity higher than 0.98 for most of the 2D peaks.

Concerning the sensitivity, UF COSY spectra recorded in 36 scans (*i.e.* 2.4 min) were sufficient to monitor a Heck-Matsuda coupling reaction with an initial concentration of 360 mM for the limiting starting materials. By delivering a whole 2D spectrum at each scan, the choice of the UF experiment duration is only a compromise between sensitivity and time resolution. This is in contrast to what happens in conventional 2D NMR where a minimal duration (about 10 min) is necessary to encode properly the indirect dimension, no matter the concentration. Next, another feature is the suitability of UF 2D NMR in a continuous flow mode since the spatial encoding is performed along an orthogonal direction to the flow. This is a crucial property in the case of on/in-line monitoring.

Now the nature of the insights yielded by such a monitoring should be discussed. As its conventional counterpart, UF 2D NMR does not provide directly quantitative information so that absolute concentrations of the followed compounds cannot be obtained. A prior calibration is required to do this. Yet, the good repeatability and linearity provided by UF 2D NMR at 43 Hz are sufficient to probe the progress of a chemical reaction and to extract kinetic parameters. In this article, UF COSY gave access to the reactive constant rates and the variations of the 2D-peak volumes in the course of the time, giving a faithful description of the two-step nature of the studied reaction. To go further in fundamental studies as the

elucidation of reaction mechanism, the ability to probe transient species is a determining point. In HF NMR, UF experiments offers such a vista as reviewed in section A.4.3. However, this potential should be tempered at 43 MHz where the sensitivity hampers the detection of short-lived intermediates.

1.3. In-line benchtop NMR monitoring in flow chemistry

1.3.1. Context

Hitherto, we have dealt with the potential of UF 2D NMR for real-time monitoring. Besides the UF methodology, the gradient-based solvent suppression methods described in part C.3 also provided promising applications in this field. In the following research article, WET-180 NOESY experiments were applied in the frame of an in-line process control whereby the benchtop spectrometer was integrated within a flow chemistry setting.

Oxidative Neutralization of Mustard-Gas Simulants in an On-Board Flow Device with In-Line NMR Monitoring

Baptiste Picard, Boris Gouilleux, Thomas Lebleu, Jacques Maddaluno, Isabelle Chataigner, Maël Penhoat, François-Xavier Felpin, Patrick Giraudeau and Julien Legros

(Original communication)
Angewandte Chemie, 129 (2017) 7676-7680.

Abstract

The fast and effective neutralization of the mustard gas simulant 2-chloroethyl ethyl sulfide (CEES) using a simple and portable continuous flow device is reported. Neutralization takes place through a fully selective sulfoxidation by a stable source of hydrogen peroxide (alcoholic solution of urea–H_2O_2 adduct/$MeSO_3H$ freshly prepared). The reaction progress can be monitored with an in-line benchtop NMR spectrometer, allowing a real-time adjustment of reaction conditions. Inherent features of millireactors, that is, perfect control of mixing, heat and reaction time, allowed the neutralization of 25 g of pure CEES within 46 minutes in a 21.5 mL millireactor (tR=3.9 minutes). This device, which relies on affordable and nontoxic reagents, fits into a suitcase, and can be deployed by police/military forces directly on the attack site.

The use of chemical weapons by terrorist groups has become a plausible threat since several chemical warfare agents (CWA) are currently available to perpetrators, including mustard compounds with the simplest bis(2-chloroethyl) sulfide as prominent member.[1, 2] This blister agent is wellknown under common names such as mustard agent, yperite or HD; this viscous liquid is used as a weapon through dispersion by spraying or explosion, hence the denomination “mustard gas”. The extreme toxicity of HD is due to the equilibrium with the strongly electrophilic episulfonium form, which also makes it carcinogenic (Scheme 1). Conventional processes for the destruction of large quantities of mustard agents (e.g. shells from World War I, Syrian stockpiles) require highly secure sites, specifically dedicated for this purpose. The neutralization/destruction of chemical warfare agents is generally conducted under harsh conditions, that is, direct pyrolysis, hydrolysis in strongly basic solutions or transformations with aggressive oxidants.[3–6] The limited solubility of HD in water explains the poor efficiency of the hydrolysis path. In contrast, oxidation has to be regarded as the method of choice to neutralize this CWA, at least if the process retained is very selective toward the sulfoxide, since overoxidation affords a highly toxic sulfone (Scheme 1).

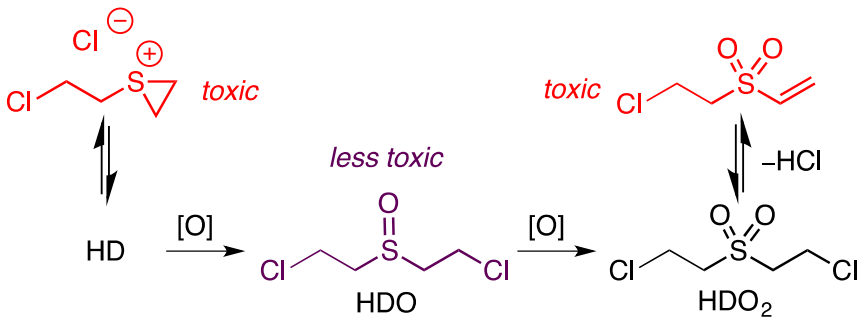

Scheme 1. Oxidation of mustard gas yperite (HD) into the corresponding sulfoxide (HDO) and sulfone (HDO_2).

In recent years, the academic community has made progresses towards the implementation of highly selective sulfoxidation of HD simulants with peroxides, singlet oxygen, hypochlorite, for instance, in the presence of metal promoters (including polyoxometallates and metal–organic frameworks) or in microemulsion media.[7–17] However, most of these protocols are unsuited for large scales or use in real situation.

Considering that the terrorist threat would most likely embody the form of a small and concealable chemical bomb introduced into a densely populated area, the possibility of intervening directly on site represents a decisive advantage. Therefore, the deployment of robust and transportable equipment allowing a rapid and selective oxidation of mustard gas is of utmost importance. Continuous flow devices fulfil all these requirements: they are compact systems which allow high control on reaction time as well as on heat and mass transfer, and the process can be easily up-scaled without optimization of new conditions.[18, 19] Moreover, hazardous chemicals such as oxidants are easily handled in a flow system,[20–24] and it offers the possibility of automation and inline analysis.[25–27] Herein we show that the fast neutralization of sulfur mustard simulants can be achieved by fully selective oxidation in a flow apparatus monitored by an in-line 1H NMR low-field instrument (Scheme 2).

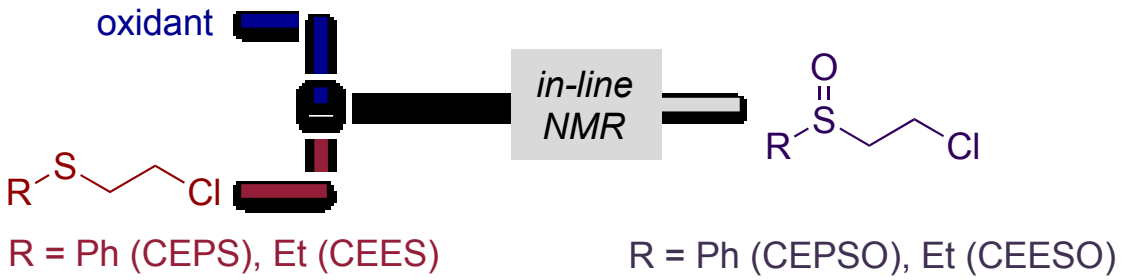

Scheme 2. An integrated flow system with in-line NMR monitoring for the sulfoxidation of mustard simulants chloroethyl phenyl sulfide (CEPS) and chloroethyl ethyl sulfide (CEES).

The toolbox of organic chemists overflows with oxidants, among which hydrogen peroxide is certainly one of the most convenient to use, especially under its UHP form (urea-H2O2 adduct; m.p. 908C), a very stable solid, hence transportable, source of anhydrous hydrogen peroxide. Whereas H2O2 generally requires the assistance of a promoter for efficient oxygen transfer, it has been shown that the simple use of hexafluoroisopropanol (HFIP) as solvent was able to efficiently activate the oxidant;[28–31] this activation is mostly due to an increase of the electrophilicity of peroxide oxygen through strong H-bonding with the solvent.[31, 32] Notably, Bégué and co-workers reported that complete oxidation of various sulfides into sulfoxides was attained within only 5 minutes reaction time.[28] Hence, a preliminary

experiment involving mustard gas simulants (CEPS and CEES) and a solution of UHP (2 equiv) in HFIP was run in a classical batch setup (Scheme 3).

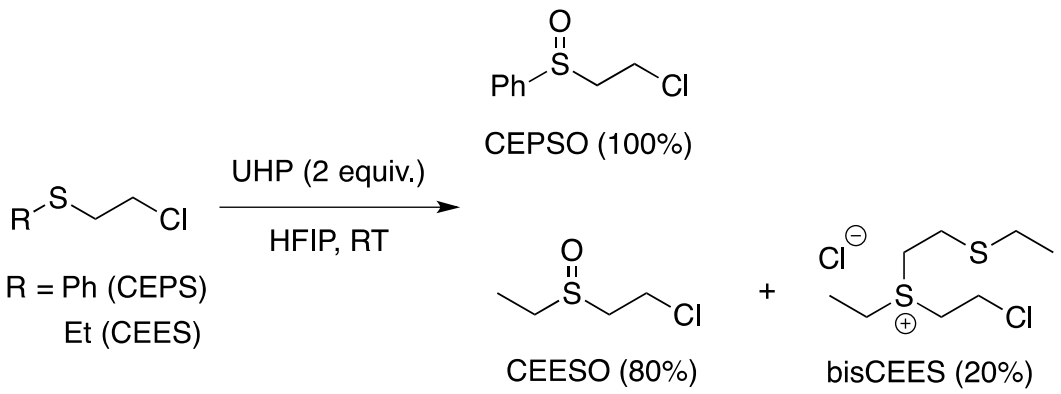

Scheme 3. Oxidation of half-mustards CEPS and CEES with UHP in HFIP

Full conversion of both substrates rapidly occurred and CEPS underwent fully selective sulfoxidation (CEPSO). However CEES, the closest analogue of the real warfare agent HD,[33] was converted into sulfoxide CEESO (80%), along with 20%of a dimeric sulfonium salt (bisCEES), whose formation has already been described, among several products, during hydrolysis.[34] A blank NMR experiment was then performed by diluting CEES in pure HFIP and after only 5 minutes, the dimeric sulfonium salt (bisCEES), was formed selectively. The possible reversible dimerization of the bisCEES in the presence of UHP was evaluated on a benchmark test, but unfortunately, after 15 days of stirring the dimeric sulfonium salts remained very stable. Thus, to avoid this competitive and irreversible dimerization affording a compound of unknown toxicity, we switched to the less polar solvent methanol,[35, 36] in the presence of methanesulfonic acid as proton donor to dissociate/activate UHP. Actually, CEES proved to remain stable in a MSA/methanol mixture for hours in the absence of oxidant. These new conditions (methanol/MSA/UHP) were implemented in a two-stream flow reactor shown on Figure 1. Neat CEES (23.36 mL, 0.2 mol), was pumped at a flow rate of 0.5 mLmin_1 and met in a T-shaped mixer a solution of UHP (1.3 equiv), MSA (2.6 equiv) in MeOH (30 equiv) pumped at a flow rate of 5 mLmin_1. The resulting stream entered in a PFA tubing reactor (ID=1.6 mm, L=10.7 m, V=21.5 mL) with a residence time of t_R=3.9 minutes. The reactor outlet was then collected into a bottle containing 40 mL of 10% (w/w) aqueous NaHSO3. Therefore,

a simple extraction afforded the corresponding sulfoxide CEESO in >99% yield. Similar results (conditions and yield) were obtained with CEPS.[37, 38]

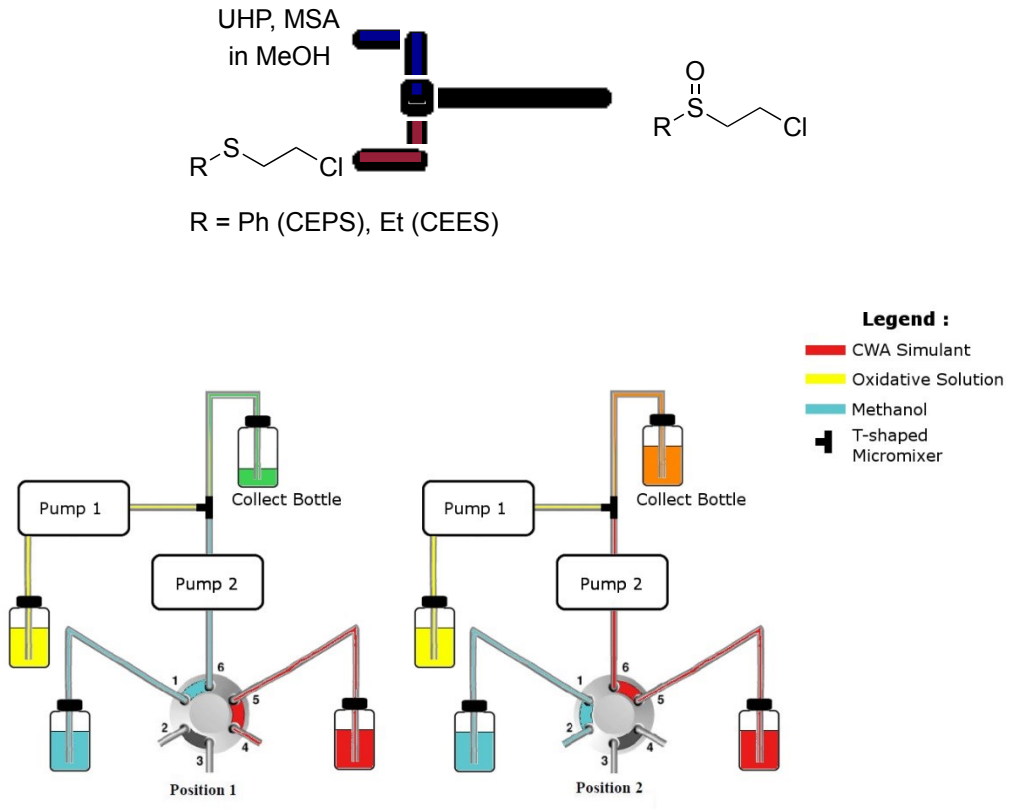

Figure 1. Continuous flow set-up for the oxidation of half-mustards CEPS and CEES with UHP/MSA in methanol. See supporting information for details.

These developments can be supported by the implementation of in-line analytical methods capable of monitoring the reaction on the fly. This enables the real-time characterization of reaction products, kinetic studies and the optimization of the reaction conditions. Obviously, high-field NMR spectrometers are not portable, but recent years have witnessed the use of compact NMR spectrometers for these purposes, either under a by-pass configuration [39–42] or within a flow chemistry platform.[43]We incorporated such a low-field NMR system within our continuous flow system in order to evaluate the residence time tR at which the maximal conversion of CEES into the sulfoxyde CEESO is achieved (Figure 2). However, performing the reaction with short t_R (less than 1 minute) in our setup involved high flow rates, which significantly impact the sensitivity and the resolution of the NMR experiments. A first feature—commonly called “inflow effect”—is the continuous replenishment of the excited spins by unexcited ones. The latter must spend a sufficient time within the pre-polarization

volume to reach their full thermal polarization. When the flow rate is too high, the saturated spins are refreshed by non-polarized ones leading to a loss of sensitivity.[44–46] Another feature involved by flow NMR— known as "outflow effect"—makes the use of high-flow regimes even more problematic. When the receiver is open during the detection of a flowing sample, some polarized and excited spins leave out the sensitive volume before the end of the acquisition.[44, 46] This phenomenon leads to a reduction of the effective transverse relaxation time and involves a significant line-broadening. Here, these limitations were circumvented by finely tuning the flow system, consisting in reducing the reactor volume and previously dissolving the neat CEES in methanol (further details are available in the Supporting Information). Thanks to this optimization, it was possible to assess the conversion rate on a range of t_R from 16.2 to 100.8 s without exceeding a flow rate of 3 mL.min^{-1}, which is an acceptable flow regime in our NMR flow system regarding the aforementioned limitations. The benchtop NMR spectrometer employed in this study (Spinsolve from Magritek) works at 43.62 MHz, relies on a permanent magnet and works without deuterated solvents.[47] This reduces the cost of the monitoring and avoids undesired isotopic effects.

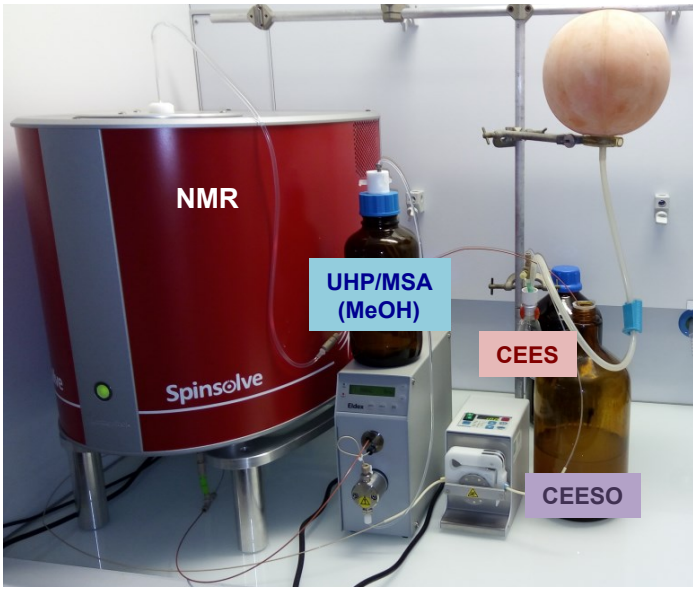

Figure 2. Continuous flow system including a benchtop NMR spectrometer directly connected to the outlet of the reactor

The downside of using non-deuterated methanol is the overlap between the huge solvent signal and the resonances of interest. This drawback became even more critical at high flow rates (e.g. 3 $mL.min^{-1}$) due to the inherent line broadening occurring with flowing samples.[44, 45] To outmatch this limitation, we implemented a tailored NMR pulse sequence capable of suppressing multiple solvent resonances at low magnetic field under flow conditions. The experiment combined a continuous presaturation with a WET-180-NOESY Scheme that we recently described (see the Supporting Information for pulse sequence and parameters).[46] The WET-180 block,[48] added during the preparation step, combines a train of selective shaped pulses applied together with gradient spoilers to selectively disperse the longitudinal component of the solvent magnetization. The Scheme includes a hard 180° pulse directly after the last selective pulse with a modification of the flip angle providing a narrower residual solvent signal with a cleaner phase. This block was followed by a NOESY excitation with a two-step phase cycling leading to a reduction of the faraway solvent effect and a flatter baseline close to the residual solvent signal.[49] As a result of the efficient solvent signal suppression, the CEESO peak at 3.8 ppm could be detected and monitored through the flow reaction. The experiments were carried out at decreasing flow rates, that is, at increasing residence times. The overlapping triplets at 1.25 ppm—arising from the overlaps between the methyl groups of CEES and CEESO—progressively turned into a simple triplet matching with the disappearance of CEES (Figure 3). The conversion rate as a function of t_R was monitored by computing the ratio between the peak area of the signals at 3.8 and 1.25 ppm for each kinetic point. Figure 3 displays the percentage of sulfoxide computed for six different residence times: full conversion is reached within 67 s, stressing the efficiency of the neutralization method.

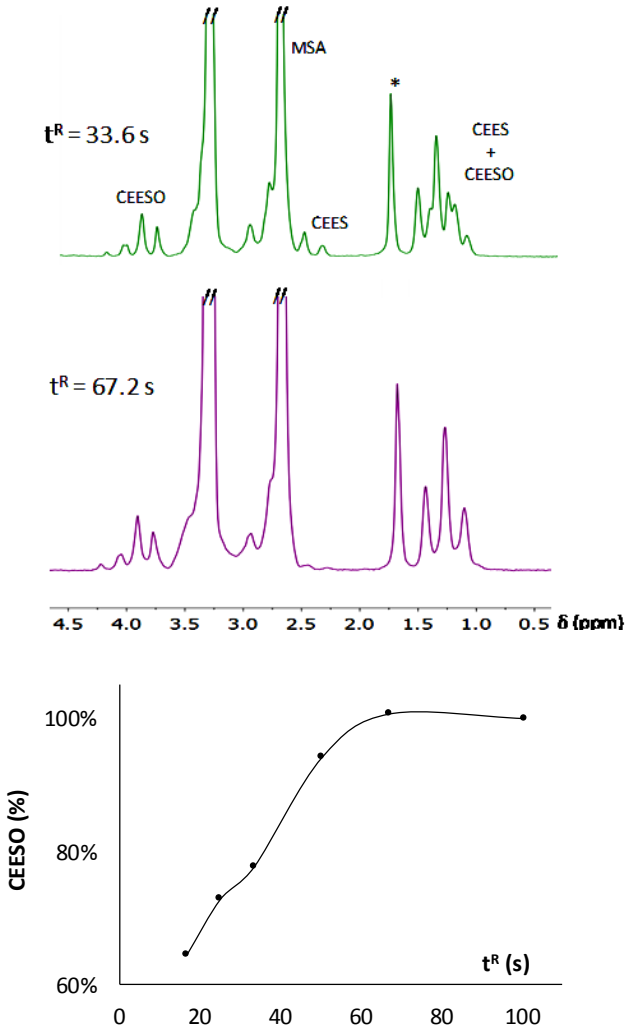

Figure 3. Neutralization of CEES monitored by an in-line NMR system. (Top and middle) two NMR spectra recorded at different t^R. Note that the peak with a * corresponds to a ^{13}C satellite line from the residual solvent signal at 3.3 ppm. (Bottom) Percentage of CEESO as a function of the residence time.

In conclusion, we have implemented a simple and mobile device allowing fast neutralization of mustard gas simulants. The neutralization occurs through complete and fully selective sulfoxidation (>99%) in a millitube reactor using a handy oxidizing system (an alcoholic mixture of highly stable urea-H_2O_2 adduct and methane sulfonic acid) that can be readily prepared on demand for on site operation. Intensification at multi-gram scale has been performed and showed full reproducibility: 25 g of neat half-mustard CEES have been neutralized within 46 minutes, and kilogram scale could be reached by using adequate pumps without any further changes. When optimized, an in-line real-time monitoring of the reaction efficiency is possible thanks to tailored spectroscopic methods on a benchtop NMR spectrometer. In practice, our mobile device could be embarked in a vehicle for field

intervention: the toxic agent would be directly pumped from the suspicious gear into the millireactor and neutralized on site.[50]

Acknowledgements

The authors gratefully acknowledge support from the CNRS « Attentats Recherche » program. J.L. is grateful to Dr M. De Paolis and Dr I. Decostaire for fruitful discussions. The authors from Normandie Université also thank the Labex SYNORG (ANR-11-LABX-0029), the Région Normandie (MicroChim Project and CRUNCh network) and the European France (Manche)–England cross-border cooperation program INTERREG IV A "AI-CHEM CHANNEL" co-financed by ERDF for support. The authors from the University of Nantes acknowledge the Région Pays de la Loire (grant RésoNantes) for financial support. FXF and PG are members of the Institut Universtaire de France (IUF).

Keywords: chemical warfare agent • hydrogen peroxide • oxidation • benchtop NMR spectrometry • continuous flow

[1] O. Meier, SWP Comments 2016, 23, 1–4.

[2] R. Weitz, Syria and Beyond: The Future of the Chemical Weapons Threat, Proliferation Papers, No. 51, December 2014.

[3] Y. C. Yang, J. A. Baker, J. R. Ward, Chem. Rev. 1992, 92, 1729 – 1743.

[4] B. M. Smith, Chem. Soc. Rev. 2008, 37, 470 – 478.

[5] K. Kim, O. G. Tsay, D. A. Atwood, D. G. Churchill, Chem. Rev. 2011, 111, 5345 – 5403.

[6] Y. J. Jang, K. Kim, O. G. Tsay, D. A. Atwood, D. G. Churchill, Chem. Rev. 2015, 115, PR1 – PR76.

[7] F. M. Menger, A. R. Elrington, J. Am. Chem. Soc. 1991, 113, 9621 – 9624.

[8] F. M. Menger, M. J. Rourk, Langmuir 1999, 15, 309 – 313.

[9] F. Gonzaga, E. Perez, I. Rico-Lattes, A. Lattes, New J. Chem. 2001, 25, 151 – 155.

[10] G.W. Wagner, L. R. Procell, Y.-C. Yang, C. A. Bunton, Langmuir 2001, 17, 4809 – 4811.

[11] C. R. Ringenbach, S. R. Livingston, D. Kumar, C. C. Landry, Chem. Mater. 2005, 17, 5580 – 5586.

[12] I. A. Fallis, P. C. Griffiths, T. Cosgrove, C. A. Dreiss, N. Govan, R. K. Heenan, I. Holden, R. L. Jenkins, S. J. Mitchell, S. Notman, et al., J. Am. Chem. Soc. 2009, 131, 9746 – 9755.

[13] F. Carniato, C. Bisio, R. Psaro, L. Marchese,M. Guidotti, Angew. Chem. Int. Ed. 2014, 53, 10095 – 10098; Angew. Chem. 2014, 126, 10259 – 10262.

[14] Y. Liu, A. J. Howarth, J. T. Hupp,O. K. Farha, Angew. Chem. Int. Ed. 2015, 54, 9001 – 9005; Angew. Chem. 2015, 127, 9129 – 9133.

[15] G.W. Wagner, L. R. Procell, D. C. Sorrick, G. E. Lawson, C. M. Wells, C. M. Reynolds, D. B. Ringelberg, K. L. Foley, G. J. Lumetta, D. L. Blanchard, Ind. Eng. Chem. Res. 2010, 49, 3099 – 3105.

[16] A. J. Howarth, C. T. Buru, Y. Liu, A. M. Ploskonka, K. J. Hartlieb, M. McEntee, J. J. Mahle, J. H. Buchanan, E. M. Durke, S. S. Al-Juaid, et al., Chem. Eur. J. 2017, 23, 214 – 218.

[17] M. Grandcolas, A. Louvet, N. Keller, V. Keller, Angew. Chem. Int. Ed. 2009, 48, 161 – 164; Angew. Chem. 2009, 121, 167 – 170.

[18] K. S. Elvira, X. C. i Solvas, R. C. R.Wootton, A. J. deMello, Nat. Chem. 2013, 5, 905 – 915.

[19] S. V. Ley, D. E. Fitzpatrick, R. M. Myers, C. Battilocchio, R. J. Ingham, Angew. Chem. Int. Ed. 2015, 54, 10122 – 10136; Angew. Chem. 2015, 127, 10260 – 10275.

[20] J. Sedelmeier, S. V. Ley, I. R. Baxendale,M. Baumann, Org. Lett. 2010, 12, 3618 – 3621.

[21] F. Lvesque, P. H. Seeberger, Org. Lett. 2011, 13, 5008 – 5011.

[22] A. B. Leduc, T. F. Jamison, Org. Process Res. Dev. 2012, 16, 1082 – 1089.

[23] X. Liu, K. F. Jensen, Green Chem. 2013, 15, 1538 – 1541.

[24] M. Peer, N.Weeranoppanant, A. Adamo, Y. Zhang, K. F. Jensen, Org. Process Res. Dev. 2016, 20, 1677 – 1685.

[25] S. S. Zalesskiy, E. Danieli, B. Blümich, V. P. Ananikov, Chem. Rev. 2014, 114, 5641 – 5694.

[26] D. C. Fabry, E. Sugiono, M. Rueping, React. Chem. Eng. 2016, 1, 129 – 133.

[27] A. M. R. Hall, J. C. Chouler, A. Codina, P. T. Gierth, J. P. Lowe, U. Hintermair, Catal. Sci. Technol. 2016, 6, 8406 – 8417.

[28] K. S. Ravikumar, J.-P. Bgu, D. Bonnet-Delpon, Tetrahedron Lett. 1998, 39, 3141 – 3144.

[29] K. Neimann, R. Neumann, Org. Lett. 2000, 2, 2861 – 2863.

[30] J. Legros, B. Crousse, D. Bonnet-Delpon, J. Bgu, Eur. J. Org. Chem. 2002, 3290 – 3293.

[31] D. Vuluga, J. Legros, B. Crousse, A. M. Z. Slawin, C. Laurence, P. Nicolet, D. Bonnet-Delpon, J. Org. Chem. 2011, 76, 1126 – 1133.

[32] A. Berkessel, J. A. Adrio, D. Hüttenhain, J. M. Neudçrfl, J. Am. Chem. Soc. 2006, 128, 8421 – 8426.

[33] J. Lavoie, S. Srinivasan, R. Nagarajan, J. Hazard. Mater. 2011, 194, 85 – 91.

[34] S. Y. Bae, M. D. Winemiller, J. Org. Chem. 2013, 78, 6457 – 6470.

[35] C. Reichardt, Chem. Rev. 1994, 94, 2319 – 2358.

[36] C. Laurence, J. Legros, A. Chantzis, A. Planchat, D. Jacquemin, J. Phys. Chem. B 2015, 119, 3174 – 3184.

[37] Same results were obtained with ethanol as solvent.

[38] The full selectivity relies on a favorable reaction rate for the sulfoxidation with respect to the sulfonation under these specific conditions provided to stop the reaction at a short residence time of 3.9 minutes: increasing temperature (40 8C), UHP amount (2.6 equiv) or residence time (8 minutes) afforded 5–10% sulfone.

[39] E. Danieli, J. Perlo, A. L. L. Duchateau, G. K. M. Verzijl, V. M. Litvinov, B. Blümich, F. Casanova, ChemPhysChem 2014, 15, 3060 – 3066.

[40] M. H. M. Killner, Y. Garro Linck, E. Danieli, J. J. R. Rohwedder, B. Blümich, Fuel 2015, 139, 240 – 247.

[41] C. A. McGill, A. Nordon, D. Littlejohn, Analyst 2002, 127, 287 – 292.

[42] B. Gouilleux, B. Charrier, S. Akoka, F.-X. Felpin, M. Rodriguez- Zubiri, P. Giraudeau, TrAC Trends Anal. Chem. 2016, 83, 65 – 75.

[43] V. Sans, L. Porwol, V. Dragone, L. Cronin, Chem. Sci. 2015, 6, 1258 – 1264.

[44] F. Dalitz, M. Cudaj, M. Maiwald, G. Guthausen, Prog. Nucl. Magn. Reson. Spectrosc. 2012, 60, 52 – 70.

[45] A. Nordon, C. A. McGill, D. Littlejohn, Analyst 2001, 126, 260 – 272.

[46] B. Gouilleux, B. Charrier, S. Akoka, P. Giraudeau, Magn. Reson. Chem. 2017, 55, 91 – 98.

[47] E. Danieli, J. Perlo, B. Blümich, F. Casanova, Angew. Chem. Int. Ed. 2010, 49, 4133 – 4135; Angew. Chem. 2010, 122, 4227 – 4229.

[48] H. Mo, D. Raftery, J. Biomol. NMR 2008, 41, 105 – 111.

[49] R. T. Mckay, Concepts Magn. Reson. Part A 2011, 38, 197 – 220.

[50] “Mustard gas” is often used in the presence of additives to make it viscous or solid. In this case, methanol should be first introduced inside the gear by an additional pump/tubing to solubilise the CWA.

Supporting information for manuscript

Oxidative Neutralization of Mustard-Gas Simulants in an On-Board Flow Device with In-Line NMR Monitoring

Baptiste Picard,[a] Boris Gouilleux,[b] Thomas Lebleu,[a] Jacques Maddaluno,[a]
Isabelle Chataigner,[a] Maël Penhoat,[d]
François-Xavier Felpin,[b,c]* Patrick Giraudeau[b,c]* and Julien Legros*[a]

[a] B. Picard, Dr. T. Lebleu, Dr. J. Maddaluno, Prof. I. Chataigner, Dr. J. Legros
COBRA, Normandie Univ, INSA Rouen, UNIROUEN, CNRS
76000 Rouen, France
E-mail: julien.legros@univ-rouen.fr

[b] B. Gouilleux, Prof. F.-X. Felpin, Dr. P. Giraudeau
CEISAM CNRS, UMR6230, Université de Nantes, BP 92208
2 rue de la Houssinière, 44322 Nantes, France
E-mail: patrick.giraudeau@univ-nantes.fr; E-mail: fx.felpin@univ-nantes.fr

[c] Prof. F. –X.Felpin, Dr. P. Giraudeau
Institut Universitaire de France
1 rue Descartes, 75005 Paris

[d] Dr. M. Penhoat
Université de Lille, CNRS, USR 3290, MSAP, Miniaturisation pour la Synthèse l'Analyse et la Protéomique,
F-59000 Lille, France

General information

Procedure for the synthesis of bisCEES and characterization

General procedure for the synthesis of samples of sulfones $CEPSO_2$ and $CEESO_2$ and characterization

General procedure for the oxidative neutralization of CWA simulants under flow conditions and characterization

The WET-180-NOESY pulse sequence

Examples of low-field NMR spectra recorded under flow conditions

Experimental procedure for in-line NMR monitoring of oxidative neutralization of CEES under flow conditions

High-field NMR Spectra

General information. CWA simulants (CEES and CEPS), urea-H_2O_2 adduct (UHP) and methane sulfonic acid (MSA) were purchased from Sigma Aldrich and used as provided; solvents were purchased from VWR (except HFIP, which was purchased from Fluorochem) and used without further purification. When required, purifications by column chromatography were performed on silica gel 40–63 µm (Macherey – Nagel) with cyclohexane/ethyl acetate as eluent and monitored by UV light (CEPS derivatives) or GC/MS (CEES derivatives).

All fluidic tubing, connections, adapters were manufactured by IDEX Health and Science, valves were manufactured by Rheodyne. Syringe pumps were manufactured by Harvard apparatus (Pump 11 Elite) and used for small to medium scale experiments (<10mL) with Hamilton glass syringes. A peristaltic pump was used for the inline NMR experiments instead of a piston pump to supress CWA priming.

High field ^{1}H NMR studies were realised on a 300 MHz Bruker Spectrospin spectrometer. Chemical shifts (δ) are given in regard to TMS using solvent as internal reference, *J* coupling constants are given in Hertz. Low resolution mass spectra and gas chromatograms were acquired on a Shimadzu QP2010 hybrid ionisation apparatus (HP5-MS stationary phase, l=30m, d=0.25mm, film thickness=0.25µm). Infrared spectra were recorded on a Perkin Elmer ATR universal sampler 100 spectrum. Melting points were observed on a Stuart SMP10 capillary bench. Elemental analyses were run on a Thermo Flash 2000.

All reactions were conducted at room temperature (23 °C) except if noted otherwise, with no particular precautions with regard to residual moisture and air. However due to the acute toxicity of CWA simulants, reactions were carried out under closed atmosphere in a very well ventilated fume hood. All glassware and materials in contact of simulants were immersed in a bleach bath under the fume hood for one day before further washing and/or disposal.

Procedure for the synthesis of bisCEES

CEES (214 mg, 1.7 mmol) was dissolved in HFIP (2 mL), stirred for 5 min and the reaction mixture was directly analyzed.

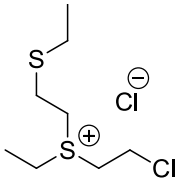

^{1}H NMR (300 MHz, HFIP): δ = 3.99 (dd, J=4.7, 2.1, 2H), 3.85 – 3.52 (m, 4H), 3.45 (q, J=7.4, 2H), 3.07 (m, 2H), 2.69 (q, J=7.4, 2H), 1.59 (t, J=7.4, 3H), 1.34 (t, J=7.4, 3H).[2]
^{13}C NMR (75 MHz, HFIP): δ = 43.9 (CH_2), 42.4 (CH_2), 36.8 (CH_2), 36.4 (CH_2), 26.1 (CH_2), 25.8 (CH_2), 12.7 (CH_3), 7.5 (CH_3).[2]
HRMS: Calcd m/z : ([M-Cl]$^+$ ^{35}Cl) 213.0538 ([M-Cl]$^+$ ^{37}Cl) 215.0509; **Found:** 213.0540 (+0.9 ppm) 215.0509 (0 ppm) by Direct Introduction ESI.

[2] Performed with a coaxial insert filled with C_6D_6.

General procedure for the synthesis of samples of sulfones $CEPSO_2$ and $CEESO_2$

$KMnO_4$ (9.4 mmol, 1.5 g) is dissolved in a water/acetonitrile mixture (1:3 v/v ratio, 20 mL) in a 50-mL round bottomed flask. The CWA simulant (0.5 mmol) is then added. The medium is then cooled to 0 °C by an ice bath, and concentrated sulfuric acid (1.1 mL, 20 mmol) is added dropwise (Caution is advised when adding the acid to keep the medium cold during addition, to avoid explosive manganese heptoxyde formation). After 17 h, the reaction is quenched with an aqueous solution of sodium bisulfite (40% w/w) until full discoloration. The resulting mixture is extracted with DCM and concentrated to afford an NMR pure product.

$CEESO_2$: Starting from CEES (63 mg), $CEESO_2$ was obtained directly as a pale yellow liquid (64 mg, 80% yield).

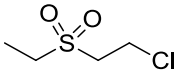

^{1}H NMR (300 MHz, $CDCl_3$) δ =3.91 (t, J=6.8, 2H), 3.40 (t, J=6.8, 2H), 3.12 (q, J=7.5, 2H), 1.43 (t, J=7.5, 3H).

^{13}C NMR (75 MHz, $CDCl_3$) δ = 54.3 (CH_2), 49.1 (CH_2), 36.0 (CH_2), 6.7 (CH_3).

IR ν (cm^{-1}) = 1296 (SO_2), 1117 (SO_2), 878 (C – Cl).

HRMS calcd m/z: 156.00118 ($[M]^{+\cdot}$ for ^{35}Cl) and 157.99823 ($[M]^{+\cdot}$ for ^{37}Cl); **Found:** 156.00153 and 157.99863 by GC/HRMS (Electron ionization)

$CEPSO_2$: Starting from CEPS (62 mg), $CEPSO_2$ was obtained after column chromatography (cyclohexane/AcOEt, 70:30) as white crystals (77 mg, 75% yield); mp: 46 °C.

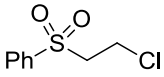

^{1}H NMR (300 MHz, $CDCl_3$): δ = 7.97 – 7.89 (m, 2H), 7.69 (m, 1H), 7.61 (m, 2H), 3.80 – 3.71 (m, 2H), 3.57 – 3.50 (m, 2H).

^{13}C NMR (75 MHz, $CDCl_3$): δ = 138.8 (C), 134.5 (CH), 129.7 (CH, 2C), 128.3 (CH, 2C), 58.2 (CH_2), 35.7 (CH_2).

IR ν (cm^{-1}) = 1294 (SO_2), 1151 (SO_2), 753 (C-H Ar), 685 (C–Cl),

El Anal: Calculated for $C_8H_9ClSO_2$: C, 46.95; H, 4.43; S, 15.67. Found: C, 46.70; H, 4.50; S, 15.87.

General procedure for the oxidative neutralization of CWA simulants under flow conditions

UHP (0.53 mol, 50 g) is diluted in methanol (500 mL) in the presence of MSA (1.05 mol, 100g) in a 1 L bottle equipped with a pressure regulating cap. The bottle is hand-shaked and cooled down for 5 minutes under open atmosphere (later referenced as “the oxidative solution”) and is pumped at a 5mL/min flow rate. The neat CWA (0.5 mL/min) is pumped directly from the commercial bottle through a rubber septum equipped with a needle for pressure equilibration. The fluidic device is composed of 2 Idex Laboratories 5969 Optos 1SIP piston

pumps (P1 and P2); a 2 position, 6 way valve standing between the bottle and P2; a mixing subsection; a main reactor subsection and finally a collection bottle filled with 40 mL of 10% (w/w) aqueous $NaHSO_3$ for peroxide quenching purpose.

- The mixing subsection (in black) is composed of an inox T-shaped micromixer, 1/16 in (1.56 mm) O.D., 0.02 in (0.058 mm) I.D., equipped with three 12 cm inox tubings (1/16 in O.D., 0.02 in I.D.) and a female adapter on each side. Total swept volume for mixer and adapter V = 97.24 µL. The two opposite sides of the mixer are connected to the pumps by two 1/16 in O.D., 0.02in I.D. PEEK tubings (each around 50 cm long), while the last is connected to the main reactor.
- The main reactor is made of a 10.7 m long PFA tubing 1/8in (3.13 mm) O.D., 1/16 in (1.56 mm) I.D., for a swept volume of V = 20.6 mL, for a total volume of 20.7 mL if accounting for the mixing subsection.

P1 is primed and is pumping through the cap and a filter directly into the oxidant bottle. The 6 way valve is put in position 1 to prime methanol (blue) into the line and P2 *via* syringe. On the same position, the CWA line (red) is primed *via* way 4 up to the valve level. The reactor is then flushed with methanol and the oxidative solution by action of the two pumps with valve on position 1.

After 5 minutes of reactor flushing, the valve is put in position 2, and now pumps the CWA simulant into the reactor. The pumping proceeds until the CWA bottle is empty, and until the line no longer contains any liquid. The valve is switched back to position 1 as soon as this happens and the pumping carries on for another 10 minutes, in order to recover the material still in reactor. The resulting solution is collected in a 2.5 L glass bottle, and after completion of the reaction, is extracted dichloromethane (3×0.5 L) and concentrated in vacuo to afford the corresponding sulfoxide.

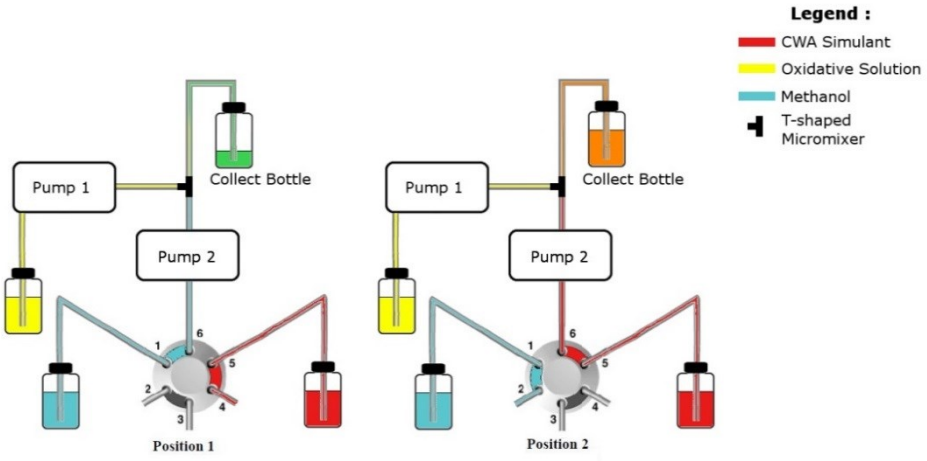

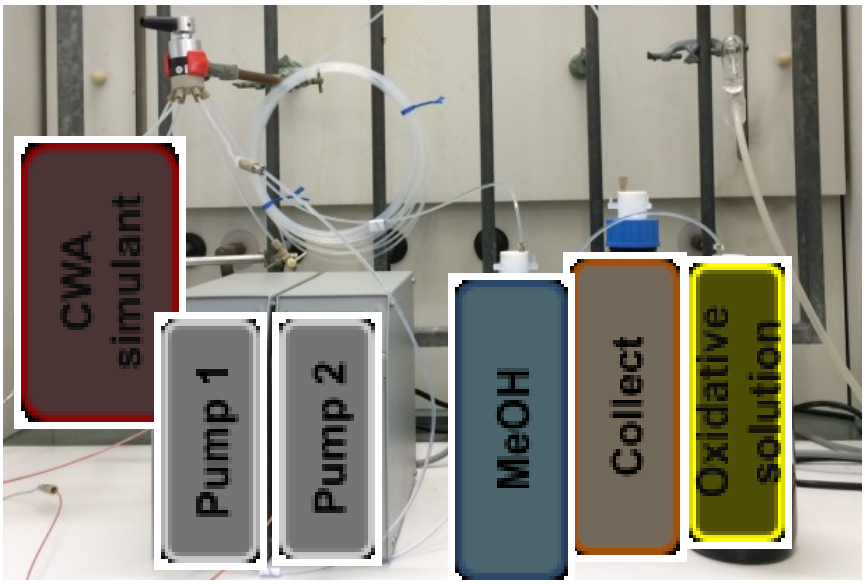

CEESO: Starting from CEES (25 g, 23.36 mL, 0.2 mol), CEESO was obtained as a slightly reddish oil (27.5 g, 98%).
^{1}H NMR (300 MHz, $CDCl_3$) δ = 4.11 – 3.79 (m, 2H), 3.20 – 2.95 (m, 2H), 2.95 – 2.63 (m, 2H), 1.54 – 1.14 (m, 3H).
^{13}C NMR (75 MHz, $CDCl_3$) δ = 54.2 (CH_2), 46.1 (CH_2), 37.0 (CH_2), 6.8 (CH_3).
HRMS calcd m/z: 141.01409 ($[M+H]^+$ with ^{35}Cl) and 143.0111 ($[M+H]^+$ with ^{37}Cl). Found : 141.01355 (-3.80ppm), 143.01036 (-5.45ppm) by GC/HRMS (tBuH Chemical Ionisation)
IR ν (cm^{-1}) = 1047 (SO), 863 (C-Cl).

CEPSO: Starting from CEPS (29.35 g, 25 mL, 0.17 mol), CEPSO was obtained as a white powder (31.1 g, 97%); mp: 33 °C.

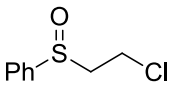

^{1}H NMR (300 MHz, $CDCl_3$) δ = 7.72 – 7.66 (m, 2H), 7.65 – 7.54 (m, 3H), 4.02 (m, 1H), 3.70 (m, 1H), 3.21 (m, 2H).
^{13}C NMR (75 MHz, $CDCl_3$) δ = 142.9 (C), 131.5 (CH), 129.6 (CH, 2C), 124.0 (CH, 2C), 59.4 (CH_2), 36.8 (CH_2).
El Anal Calculated for C_8H_9ClSO: C, 50.93; H, 4.81; S, 16.99. Found: C, 50.64; H, 4.80; S, 16.50.
IR ν (cm^{-1}) = 1040 (SO), 690 (C-Cl), 744 (C-H Ar).

The WET-180-NOESY pulse sequence

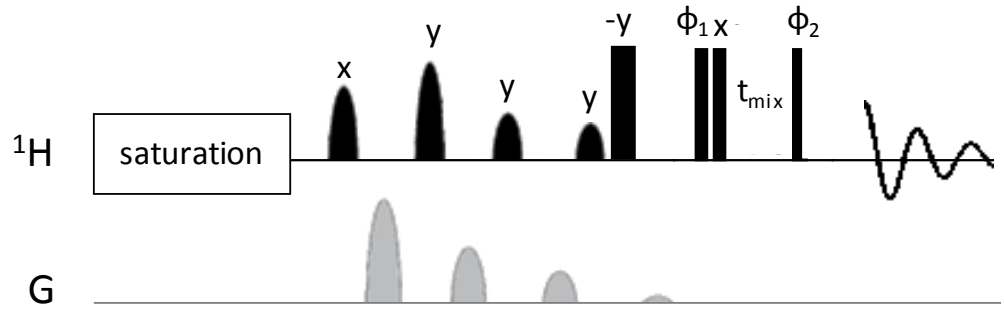

This pulse sequence combines a pre-saturation block (at 5.37 ppm) added prior to a WET-180-NOESY scheme. Narrow and large rectangles represent 90° and 180° hard pulses. The first four pulses match with the train of selective Gaussian pulses involved in the WET-180 block, with a γB_1 power of 1086, 1047, 832 and 412 Hz, respectively. These pulses impact selectively the signal of the methanol at 3.3 ppm. The grey symbols represent the spoiler gradients, which were applied for 2 ms with the following power: 85.0, 42.5, 21.3 and 10.6% of the maximum strength. The mixing time t_{mix} of the 1D-NOESY block was fixed to 6 ms. The phase cycles are: $\phi_1 = x, -x$ and $\phi_2 = x, -x$.

Examples of low-field NMR spectra recorded under flow conditions

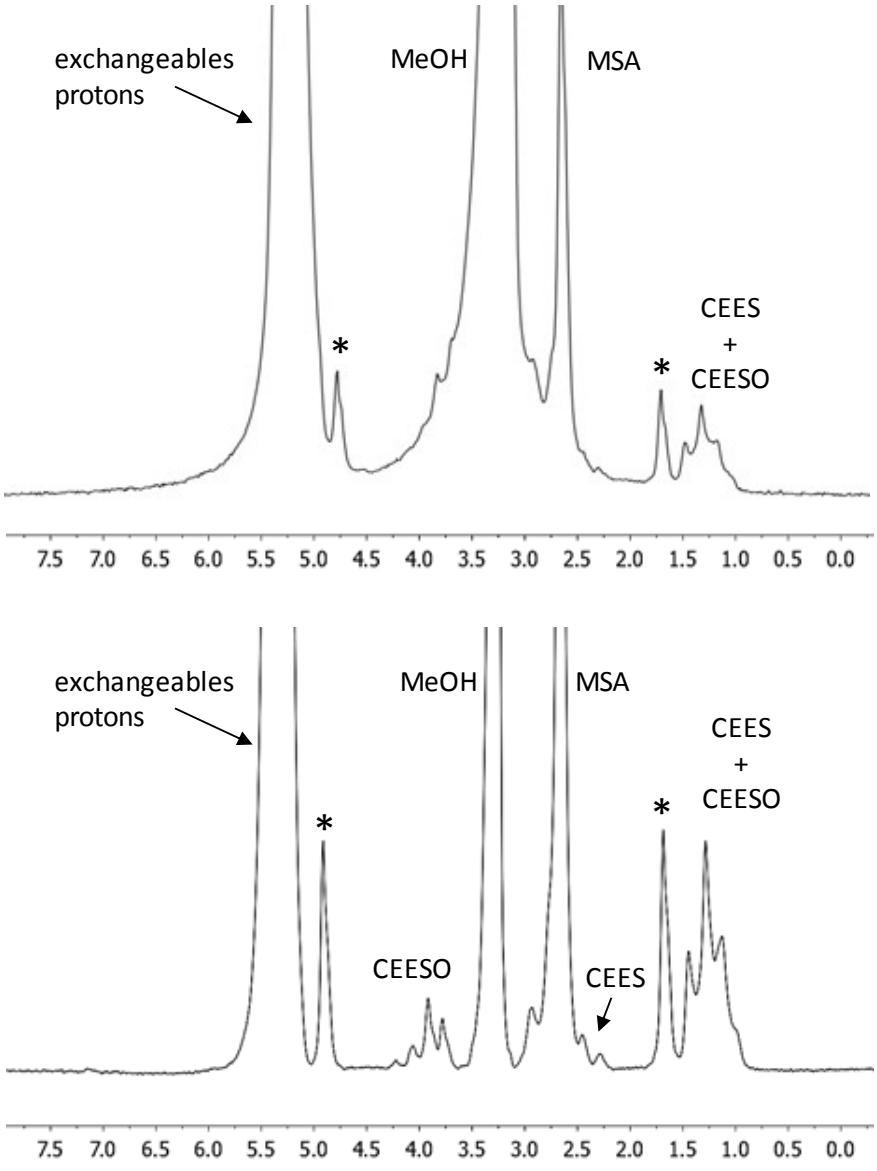

Low-field NMR spectra recorded on the reactive mixture with a flow rate at 3 $mL.min^{-1}$. On the top, conventional 1D spectrum. The asterisks * match with the ^{13}C satellites lines arising from the methanol resonance and MSA refers to methane sulfonic acid. The signals of interest are severely overlapped by the huge methanol signal at 3.3 ppm. On the bottom, low-field spectrum on the same mixture obtained with the WET-180-NOESY experiment. Thanks to this pulse sequence, the CEESO peak at 3.8 ppm can be efficiently detected through the flow reaction.

Experimental procedure for in-line NMR monitoring of oxidative neutralization of CEES under flow conditions

The procedure was performed according to the "General procedure for the oxidative neutralization of CWA simulants under flow conditions" except that CEES was dissolved in methanol (0.85 M). Total flow rate was increased from 0.5 to 3.0 mL min^{-1} according to the following Table :

Flow rate Φ (mL min^{-1})			t^R (min)	t^R (s)
Φ_{CEES}	$\Phi_{Oxidant}$	Φ_{Total}		
0.04	0.46	0.5	1.68	100.8
0.06	0.69	0.75	1.12	67.2
0.08	0.92	1.0	0.84	50.4
0.12	1.38	1.5	0.56	33.6
0.17	1.83	2.0	0.42	25.2
0.25	2.75	3.0	0.28	16.8

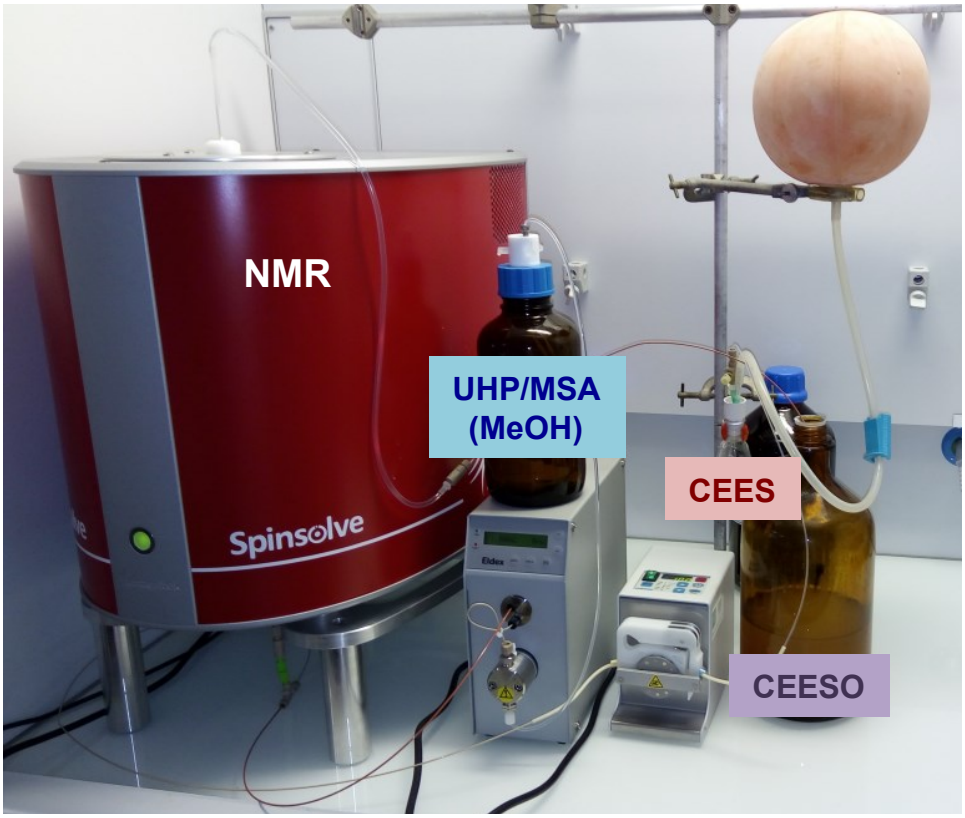

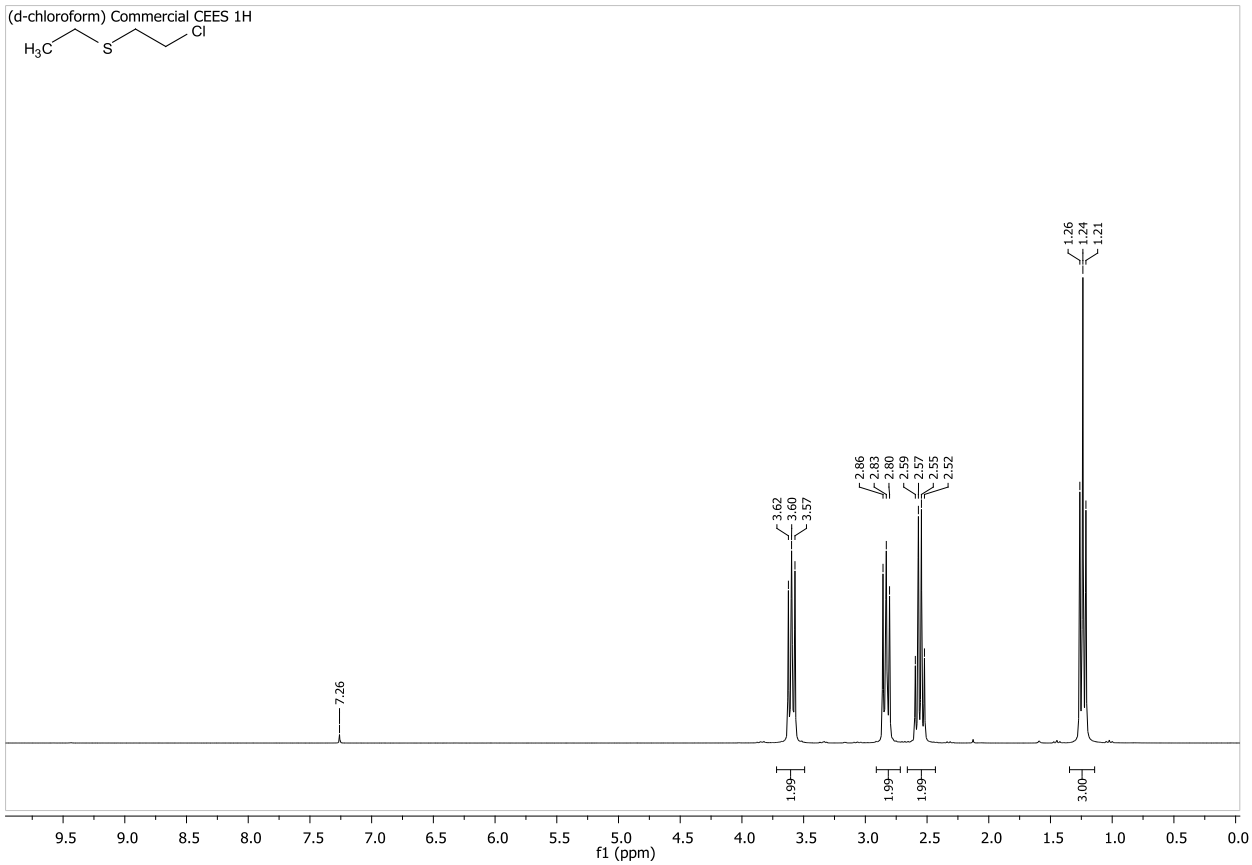
(d-chloroform) Commercial CEES 1H
H3C
S
Cl
7.26
3.62
3.60
3.57
2.86
2.83
2.80
2.59
2.57
2.55
2.52
1.26
1.24
1.21
1.99
1.99
1.99
3.00
f1 (ppm)

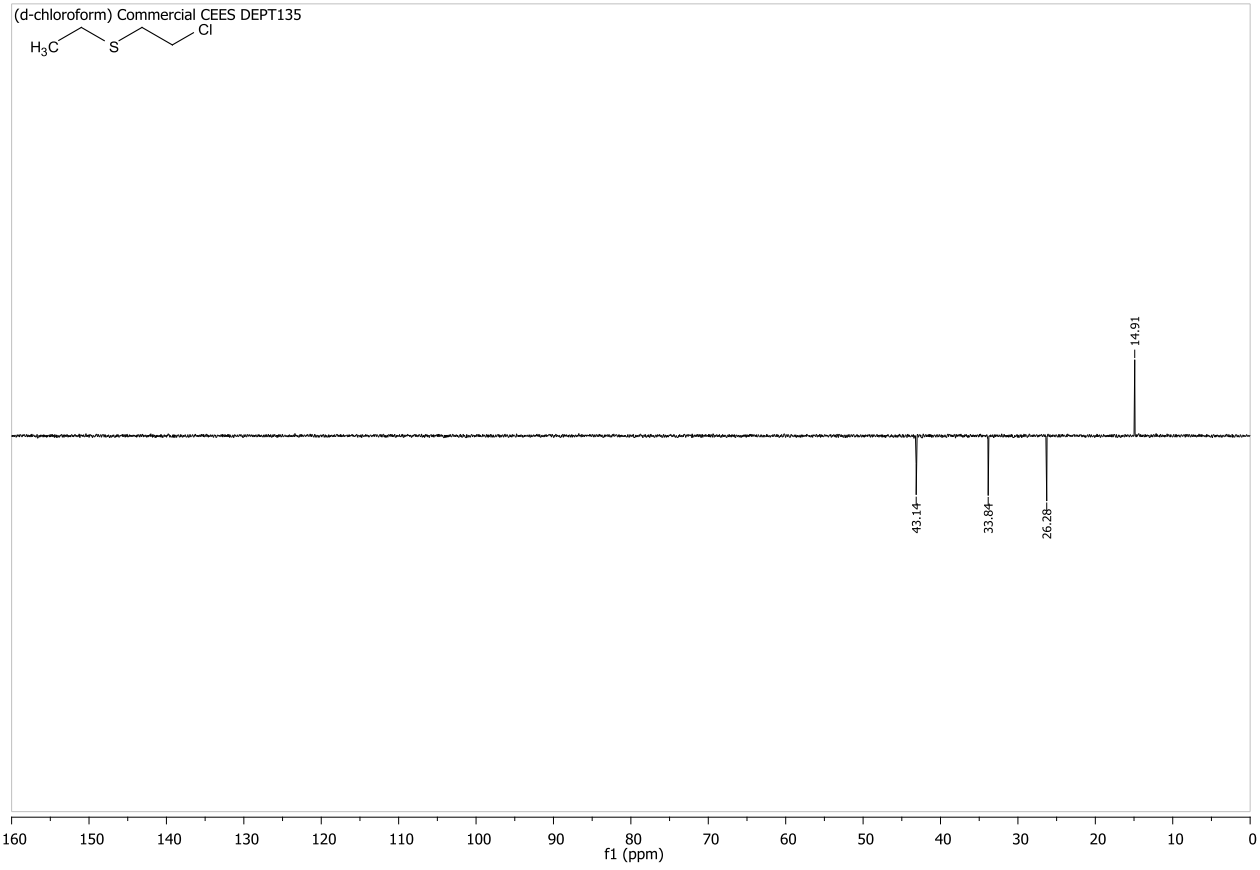
(d-chloroform) Commercial CEES DEPT135
H3C
S
Cl
14.91
43.14
33.84
26.28
f1 (ppm)

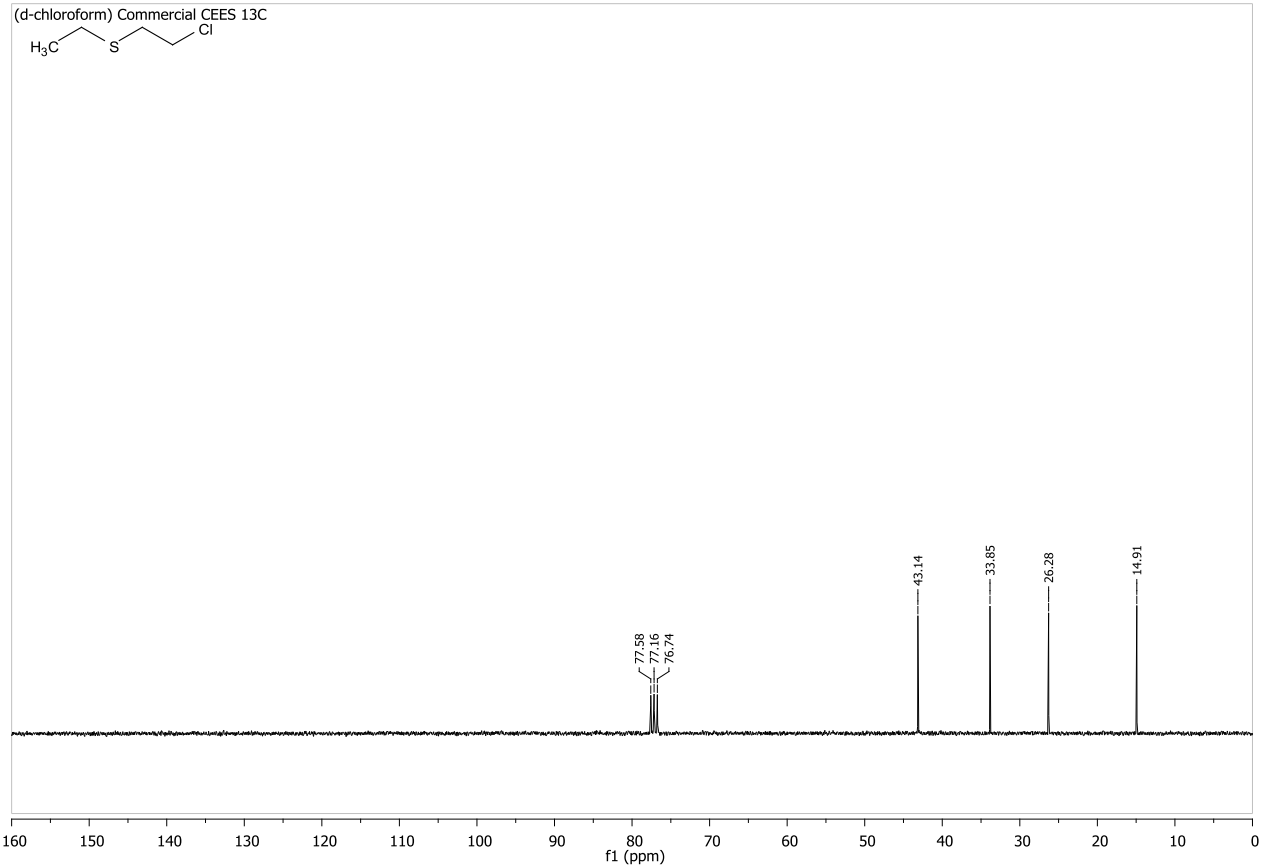
(d-chloroform) Commercial CEES 13C
H3C
S
Cl
77.58
77.16
76.74
43.14
33.85
26.28
14.91
160
150
140
130
120
110
100
90
80
70
60
50
40
30
20
10
0
f1 (ppm)

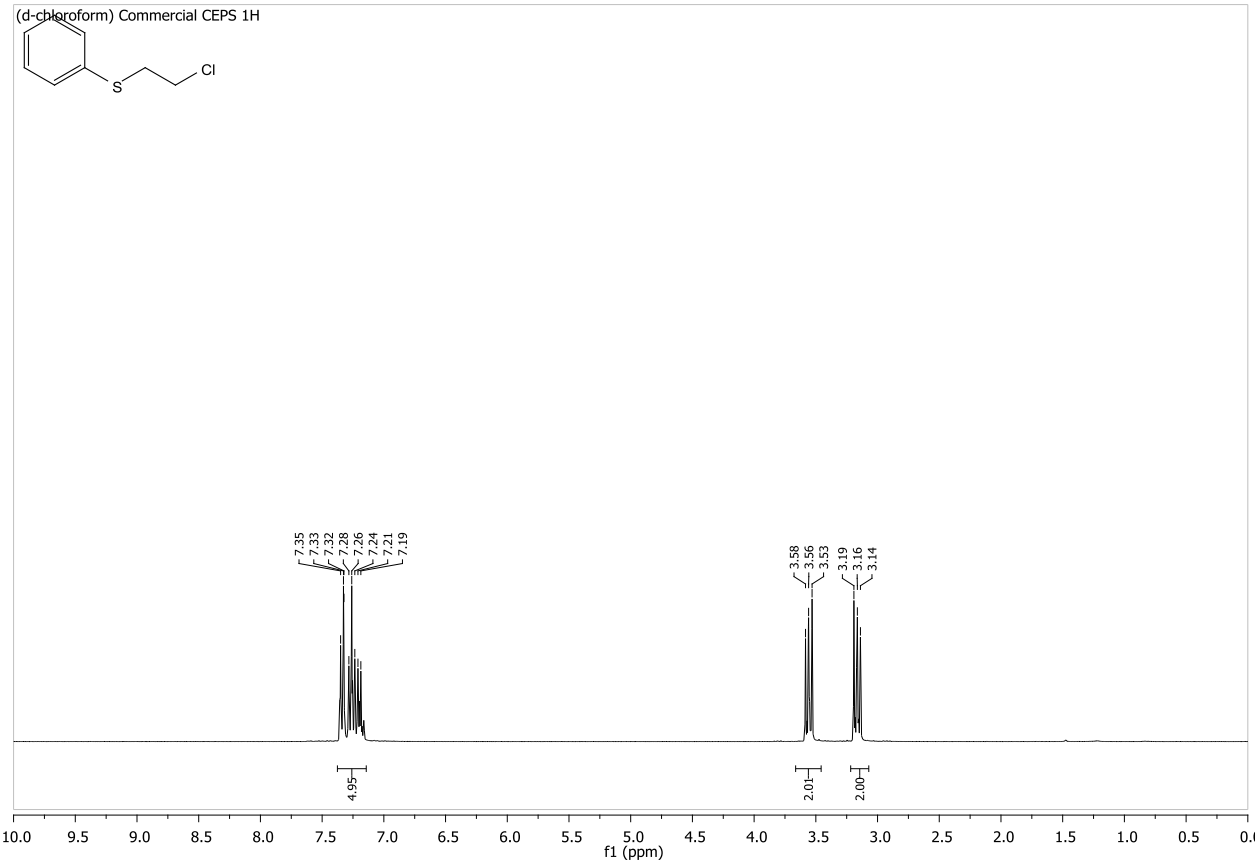
(d-chloroform) Commercial CEPS 1H
Cl
S
7.35
7.33
7.32
7.28
7.26
7.24
7.21
7.19
3.58
3.56
3.53
3.19
3.16
3.14
4.95
2.01
2.00
f1 (ppm)

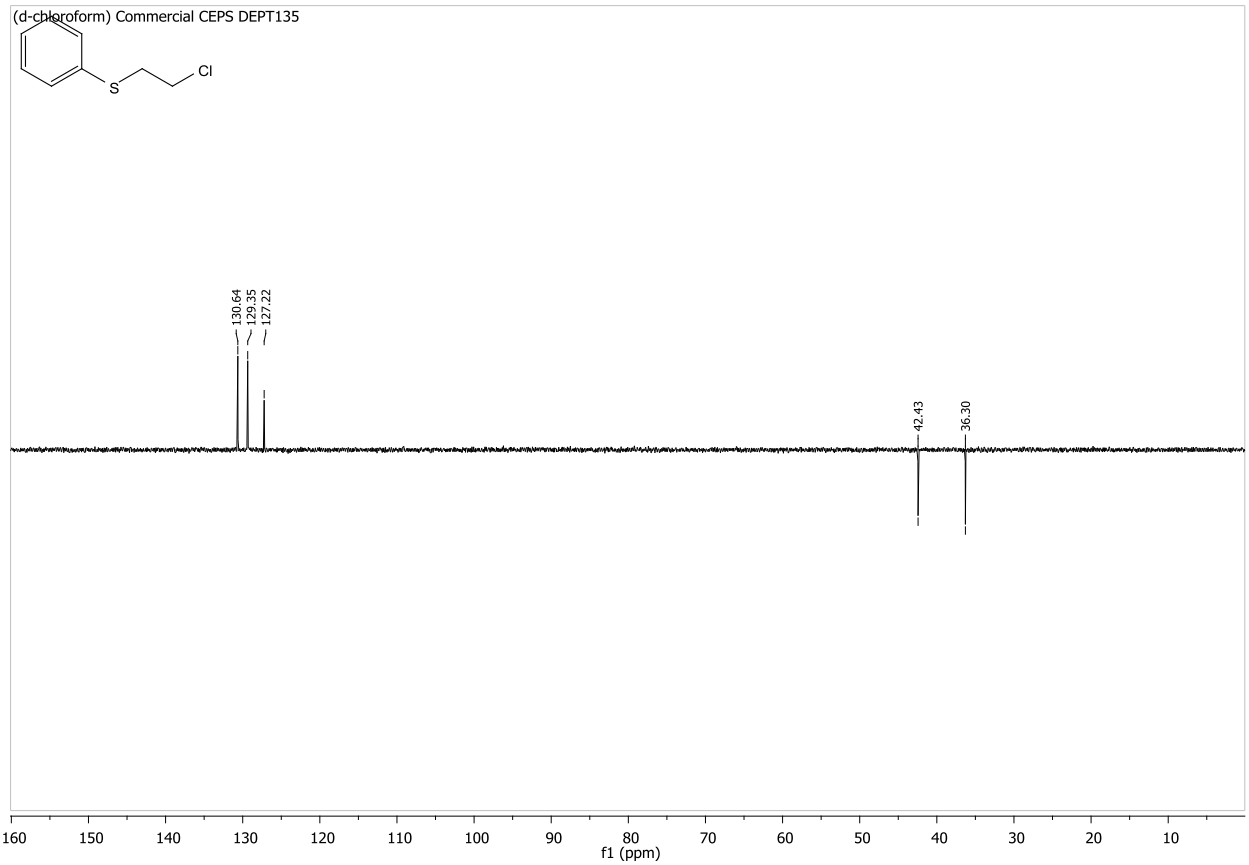
(d-chloroform) Commercial CEPS DEPT135
Cl
S
130.64
129.35
127.22
42.43
36.30
f1 (ppm)

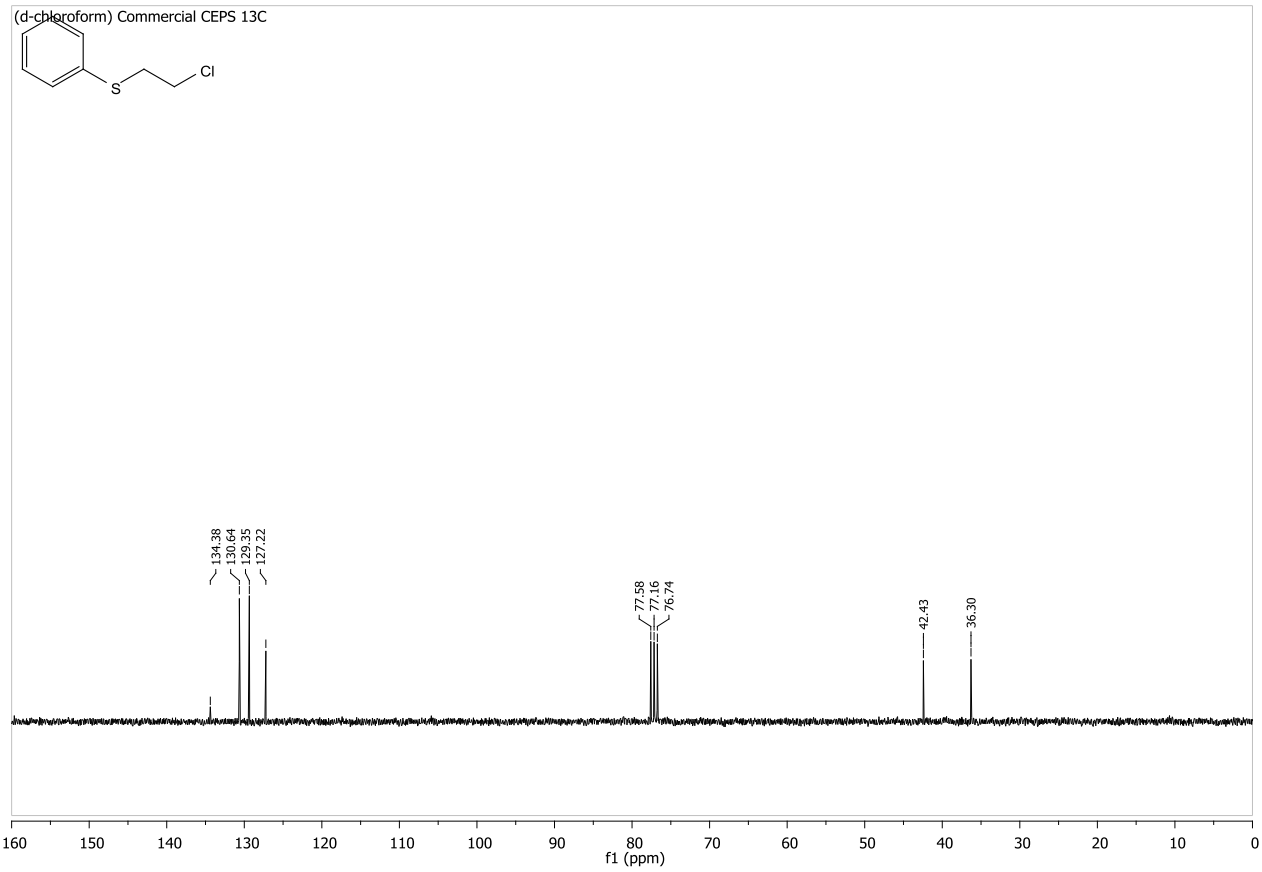
(d-chloroform) Commercial CEPS 13C
S
Cl
134.38
130.64
129.35
127.22
77.58
77.16
76.74
42.43
36.30
160
150
140
130
120
110
100
90
80
70
60
50
40
30
20
10
0
f1 (ppm)

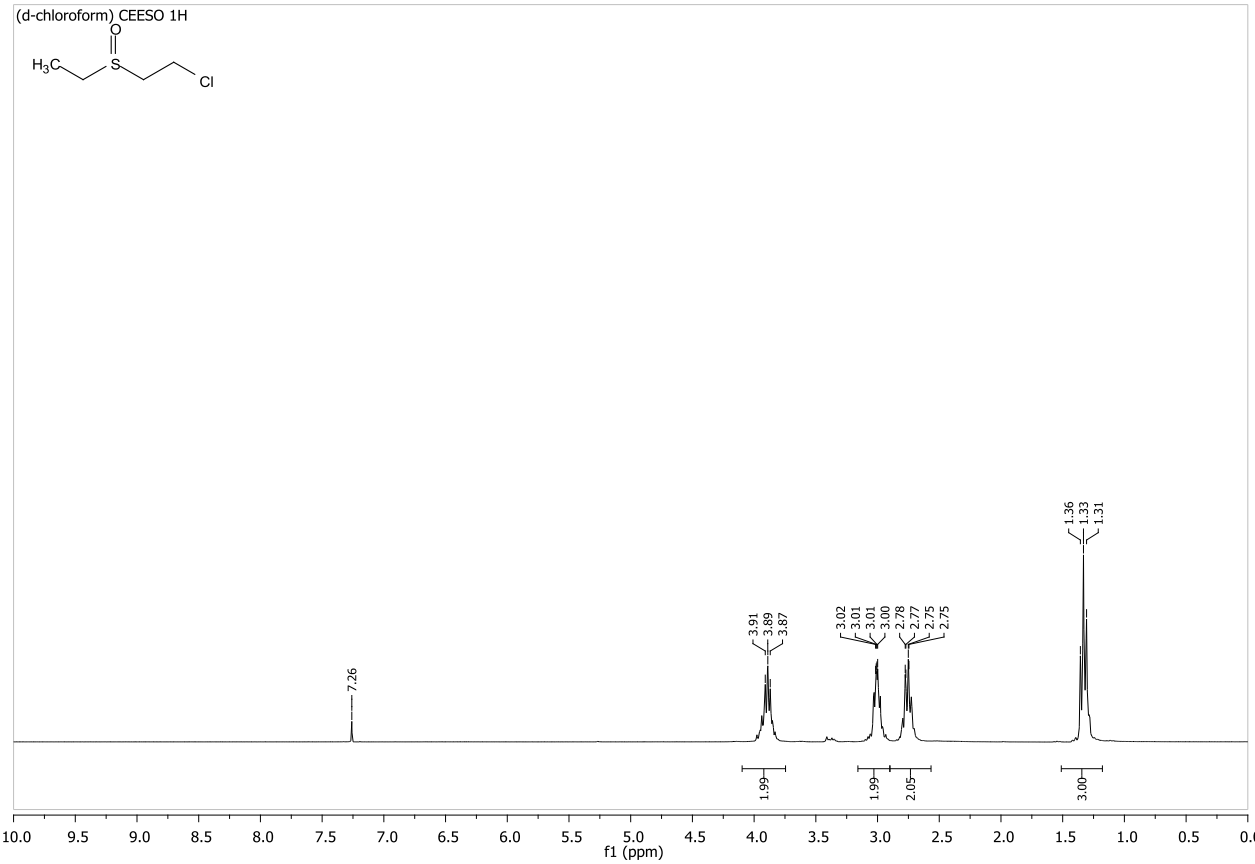
(d-chloroform) CEESO 1H
O
H3C
S
Cl
7.26
3.91
3.89
3.87
3.02
3.01
3.01
3.00
2.78
2.77
2.75
2.75
1.36
1.33
1.31
1.99
1.99
2.05
3.00
10.0 9.5 9.0 8.5 8.0 7.5 7.0 6.5 6.0 5.5 5.0 4.5 4.0 3.5 3.0 2.5 2.0 1.5 1.0 0.5 0.0
f1 (ppm)

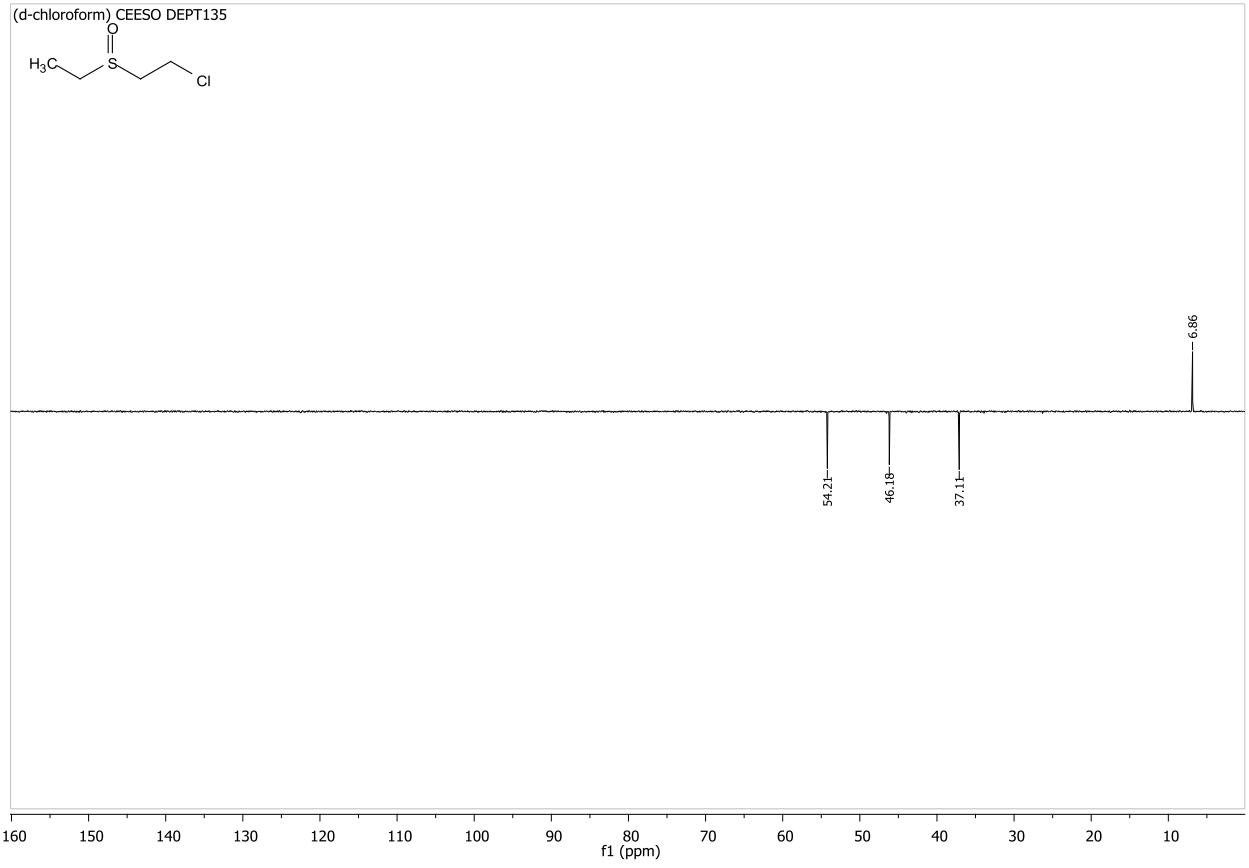
(d-chloroform) CEESO DEPT135
O
H3C
S
Cl
6.86
54.21
46.18
37.11
160 150 140 130 120 110 100 90 80 70 60 50 40 30 20 10
f1 (ppm)

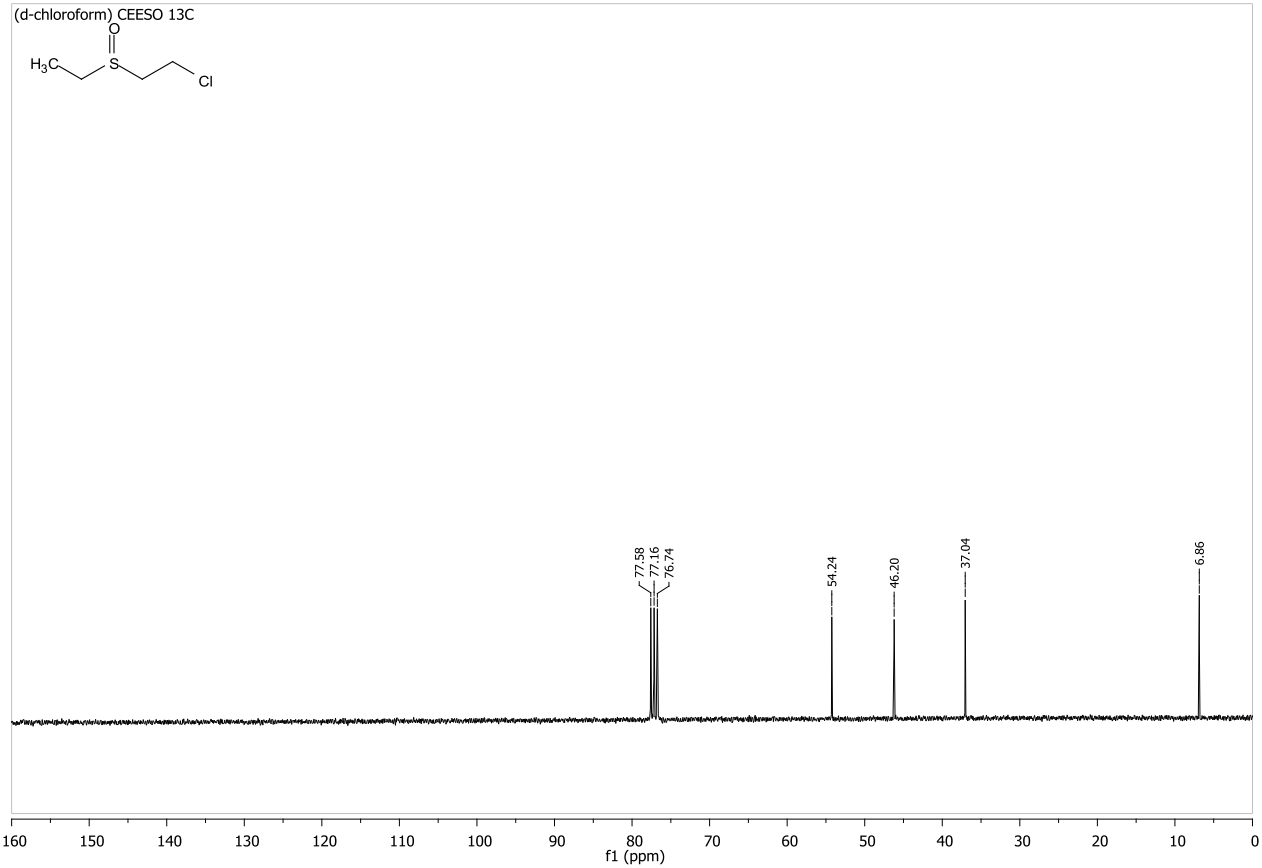
(d-chloroform) CEESO 13C
O
H3C
S
Cl
77.58
77.16
76.74
54.24
46.20
37.04
6.86
160
150
140
130
120
110
100
90
80
70
60
50
40
30
20
10
0
f1 (ppm)

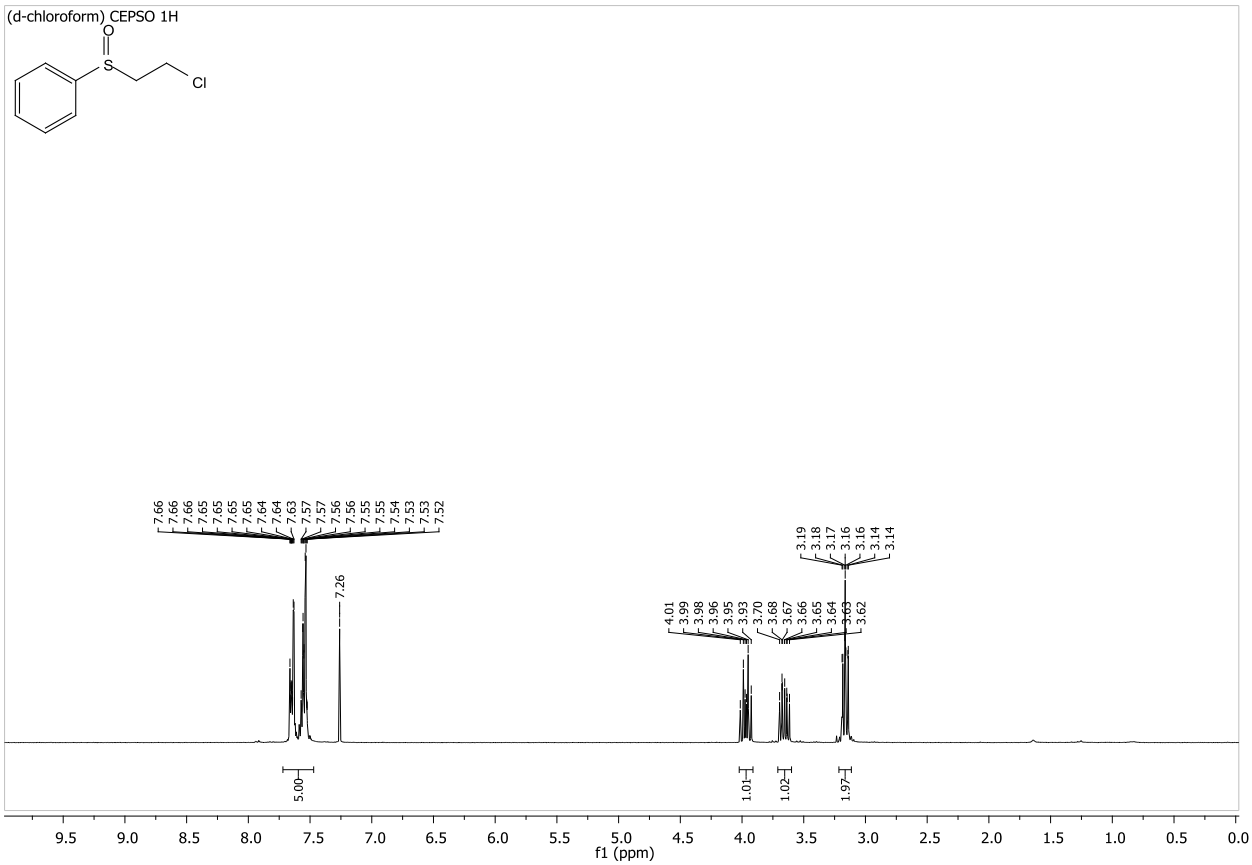
(d-chloroform) CEPSO 1H
O
S
Cl
7.66
7.66
7.66
7.65
7.65
7.65
7.64
7.64
7.63
7.57
7.57
7.56
7.56
7.55
7.55
7.54
7.53
7.53
7.52
7.26
4.01
3.99
3.98
3.96
3.95
3.93
3.70
3.68
3.67
3.66
3.65
3.64
3.63
3.62
3.19
3.18
3.17
3.16
3.16
3.14
3.14
5.00
1.01
1.02
1.97
9.5
9.0
8.5
8.0
7.5
7.0
6.5
6.0
5.5
5.0
4.5
4.0
3.5
3.0
2.5
2.0
1.5
1.0
0.5
0.0
f1 (ppm)

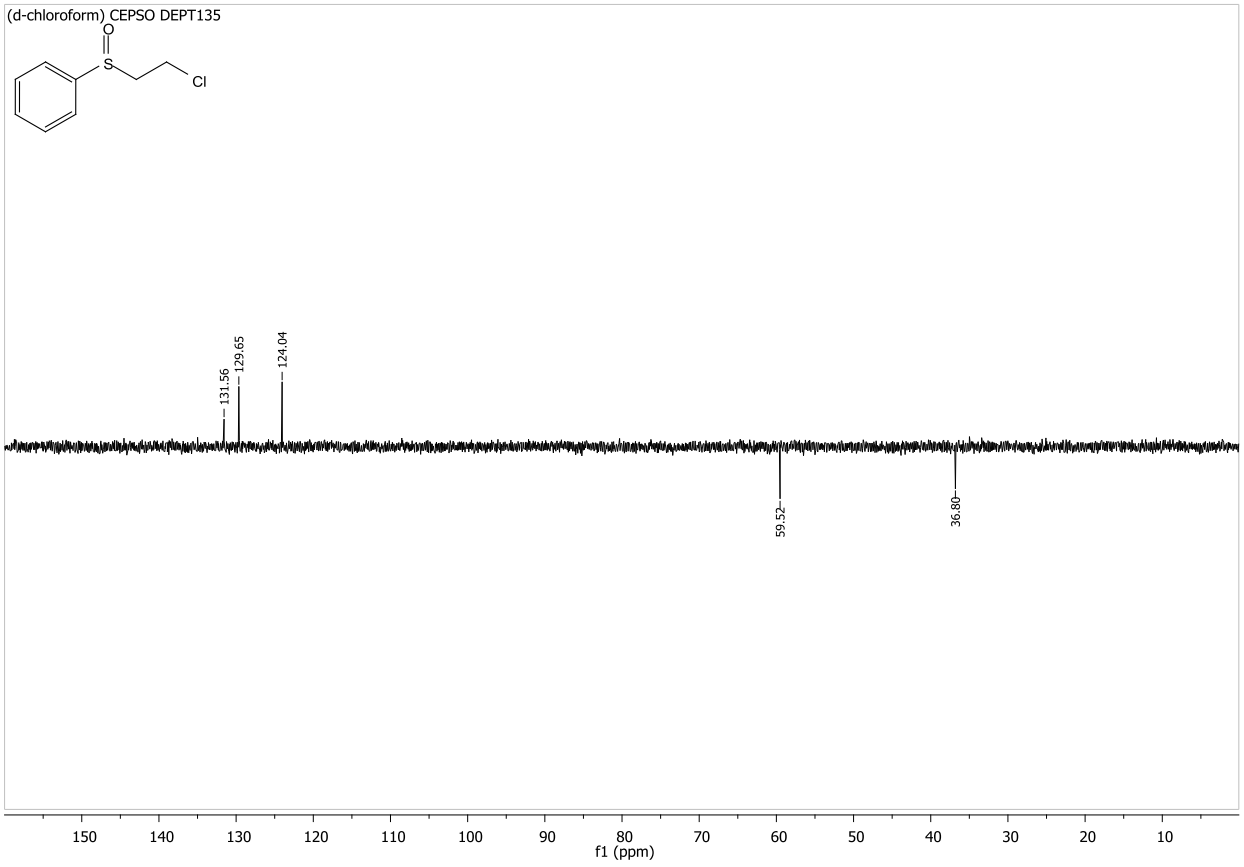
(d-chloroform) CEPSO DEPT135
O
S
Cl
131.56
129.65
124.04
59.52
36.80
150
140
130
120
110
100
90
80
70
60
50
40
30
20
10
f1 (ppm)

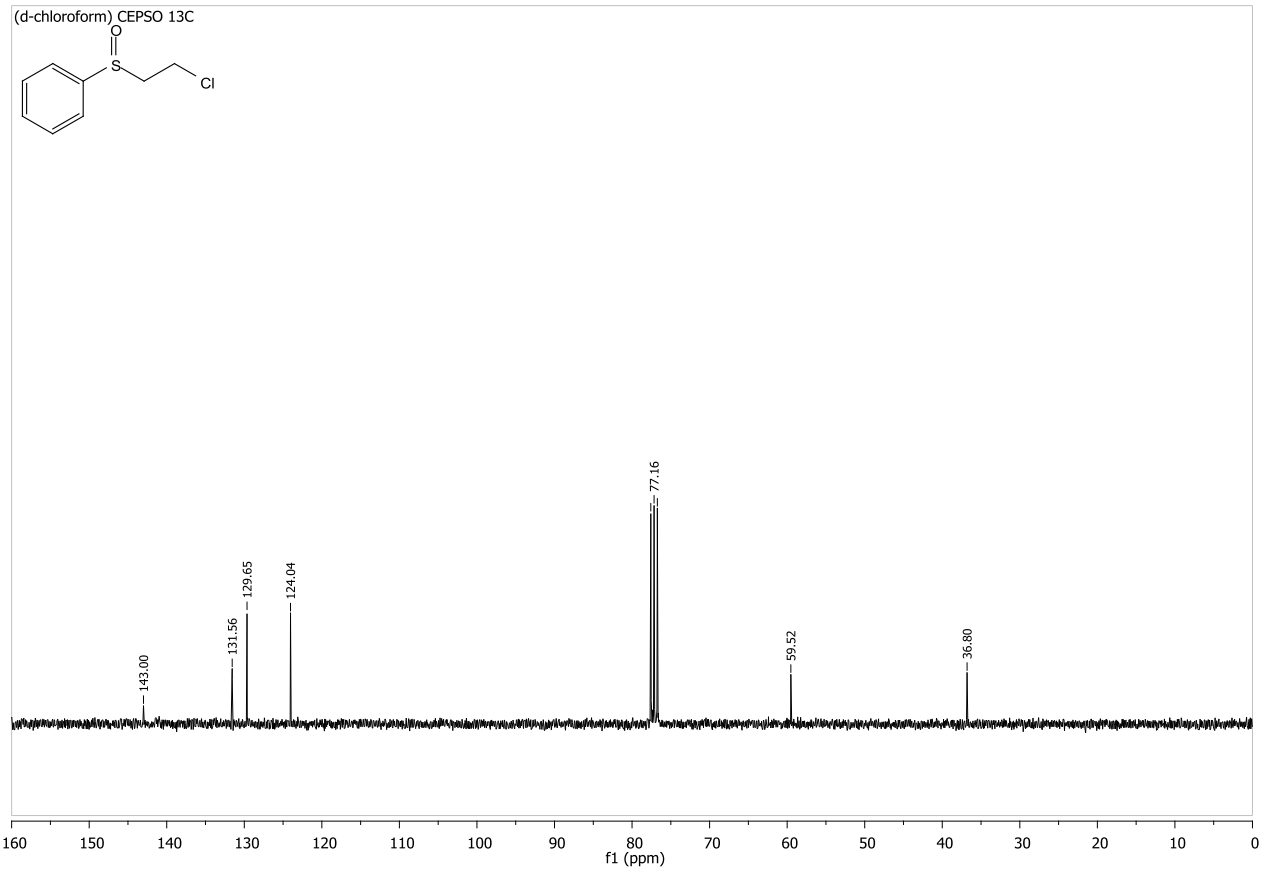
(d-chloroform) CEPSO 13C
O
S
Cl
143.00
131.56
129.65
124.04
77.16
59.52
36.80
160
150
140
130
120
110
100
90
80
70
60
50
40
30
20
10
0
f1 (ppm)

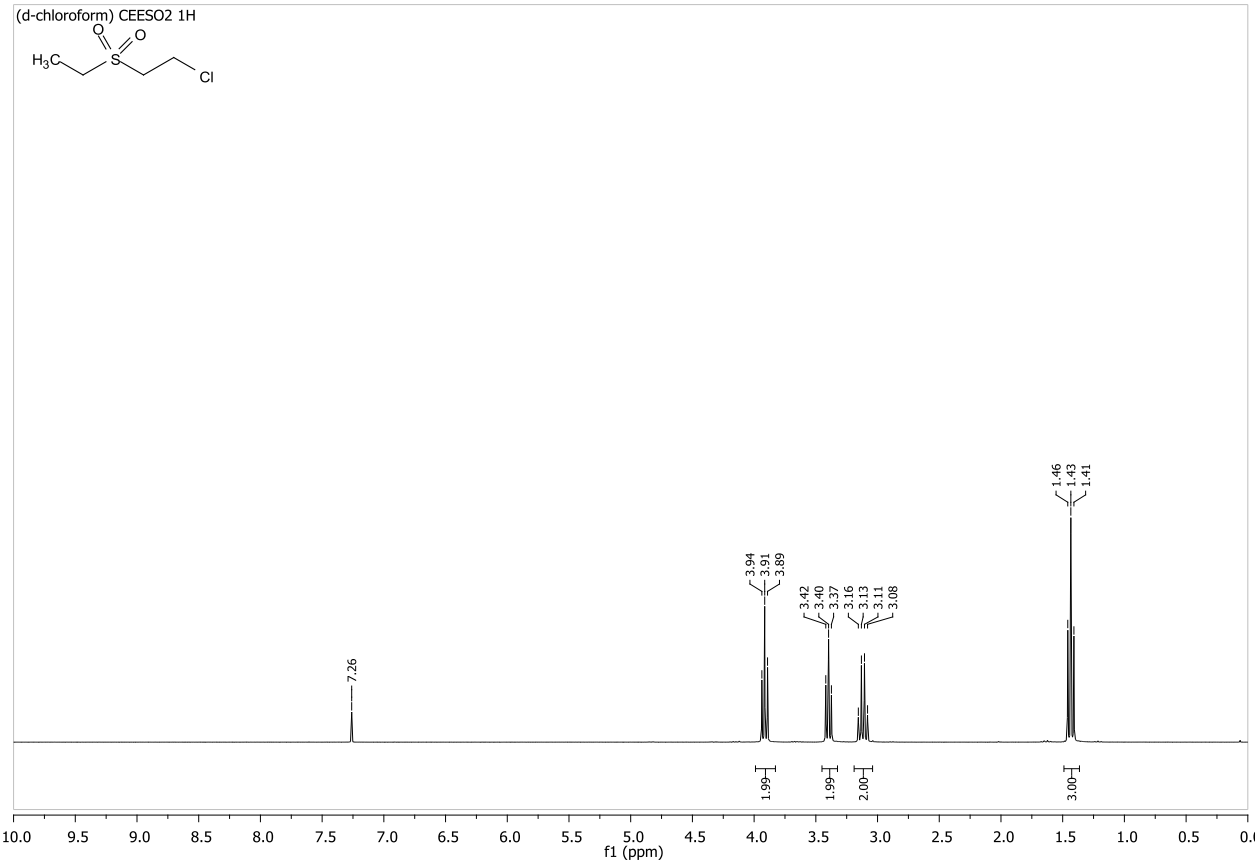
(d-chloroform) CEESO2 1H
H3C
S
O
O
Cl
7.26
3.94
3.91
3.89
3.42
3.40
3.37
3.16
3.13
3.11
3.08
1.46
1.43
1.41
1.99
1.99
2.00
3.00
f1 (ppm)

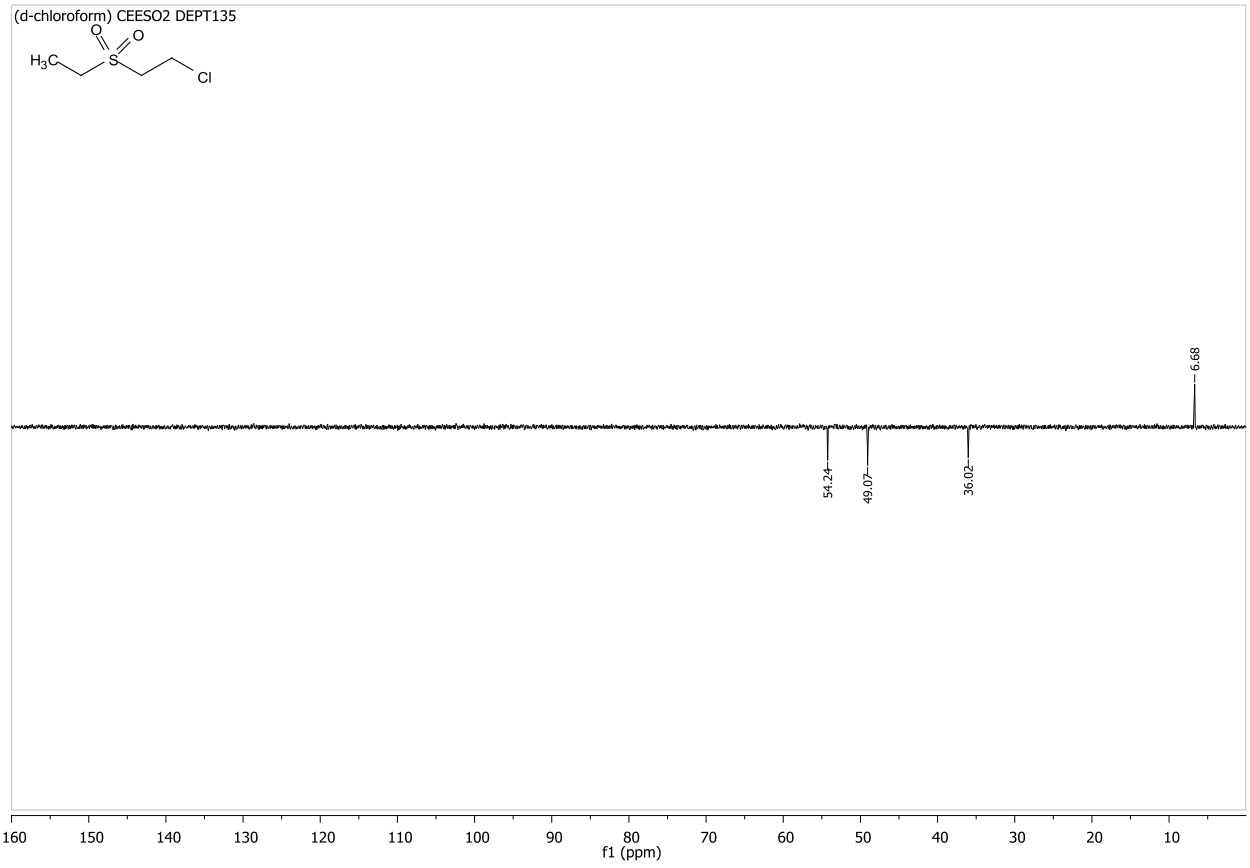
(d-chloroform) CEESO2 DEPT135
H3C
S
O
O
Cl
6.68
54.24
49.07
36.02
f1 (ppm)

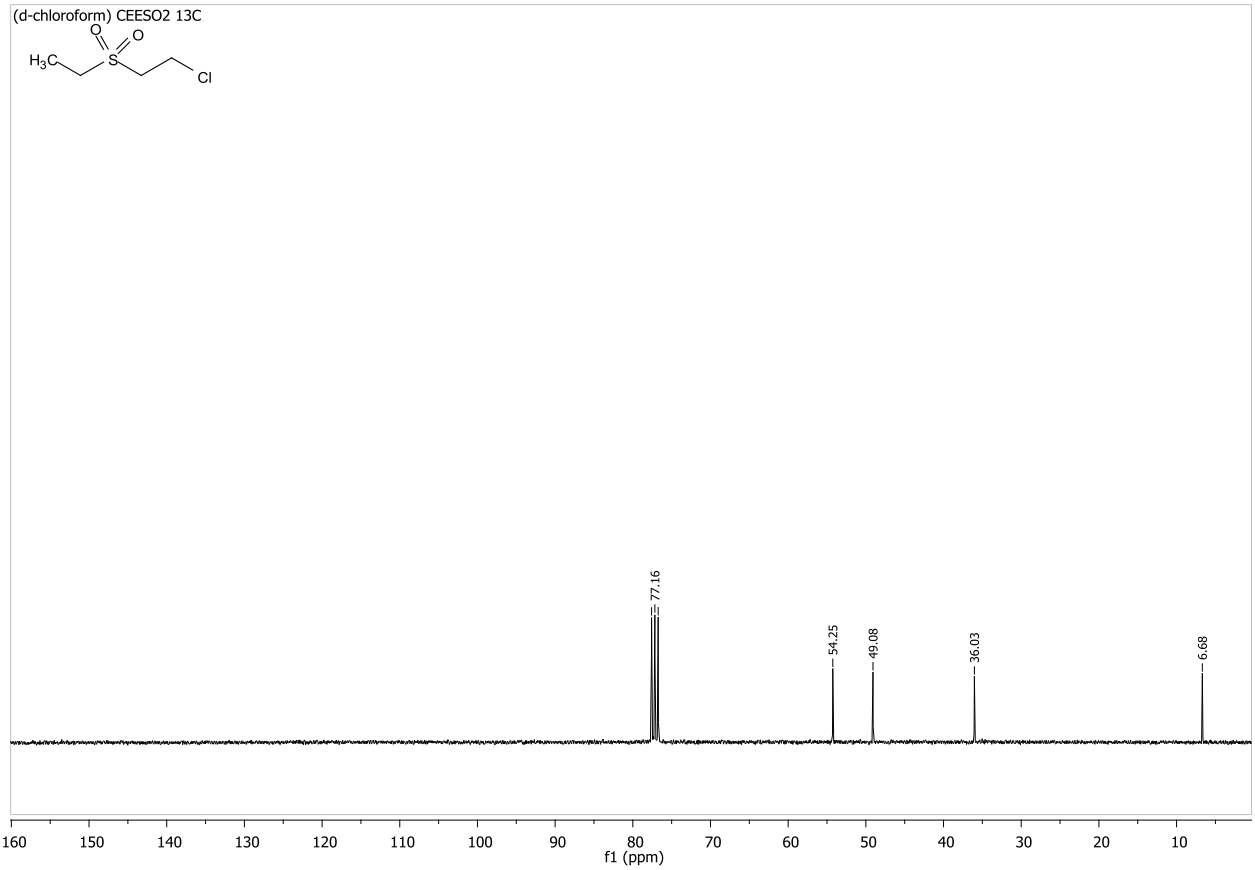
(d-chloroform) CEESO2 13C
O
O
H3C
S
Cl
77.16
54.25
49.08
36.03
6.68
160
150
140
130
120
110
100
90
80
70
60
50
40
30
20
10
f1 (ppm)

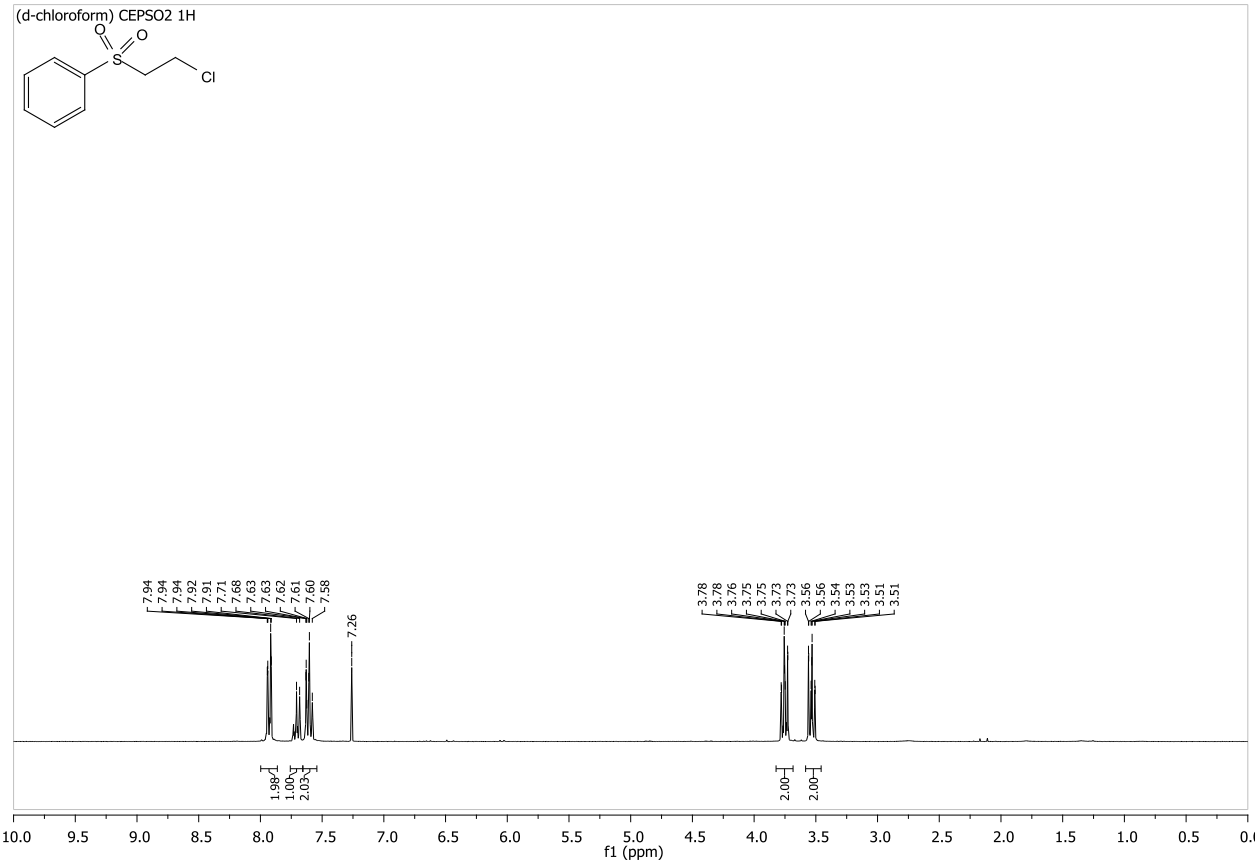
(d-chloroform) CEPSO2 1H
O
O
S
Cl
7.94
7.94
7.94
7.92
7.91
7.71
7.68
7.63
7.63
7.62
7.61
7.60
7.58
7.26
3.78
3.78
3.76
3.75
3.75
3.73
3.73
3.56
3.56
3.54
3.53
3.53
3.51
3.51
1.98
1.00
2.03
2.00
2.00
10.0
9.5
9.0
8.5
8.0
7.5
7.0
6.5
6.0
5.5
5.0
4.5
4.0
3.5
3.0
2.5
2.0
1.5
1.0
0.5
0.0
f1 (ppm)

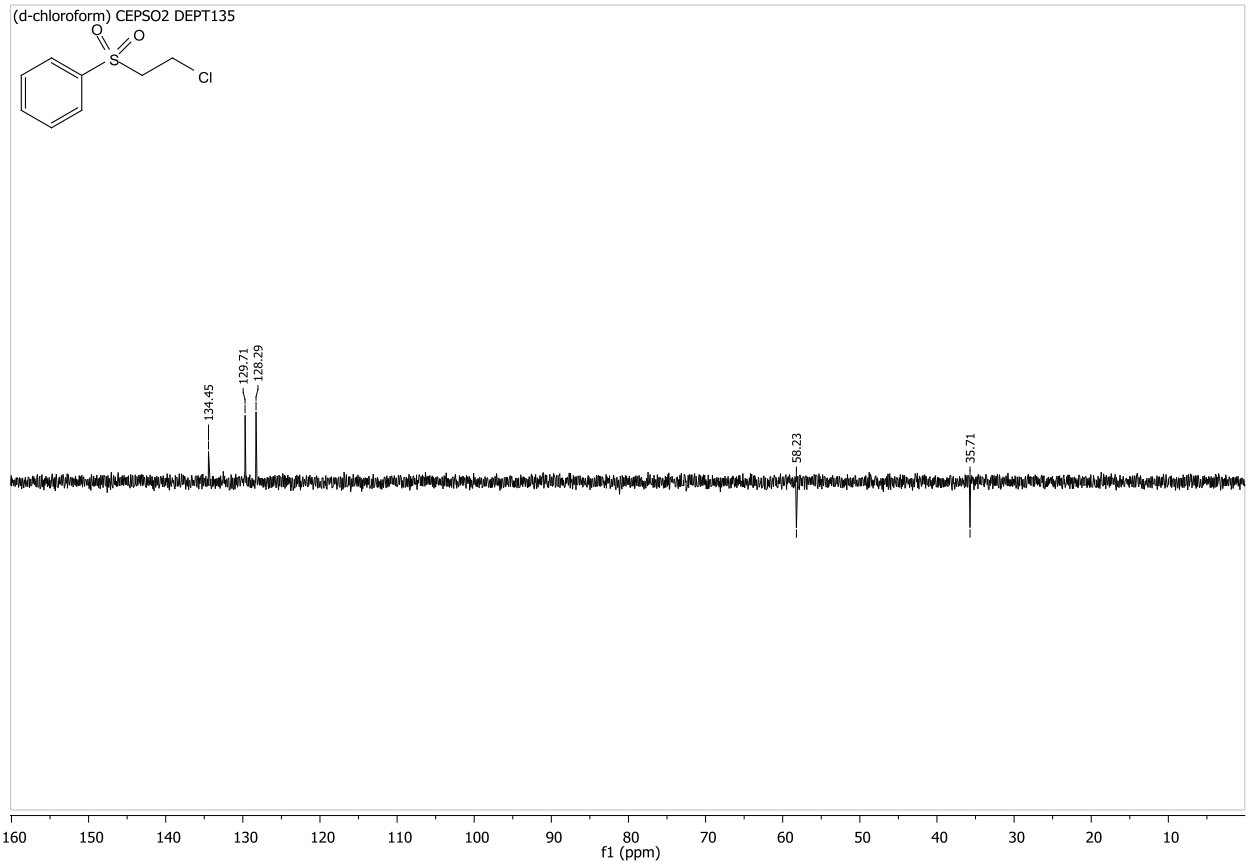
(d-chloroform) CEPSO2 DEPT135
O
O
S
Cl
134.45
129.71
128.29
58.23
35.71
160
150
140
130
120
110
100
90
80
70
60
50
40
30
20
10
f1 (ppm)

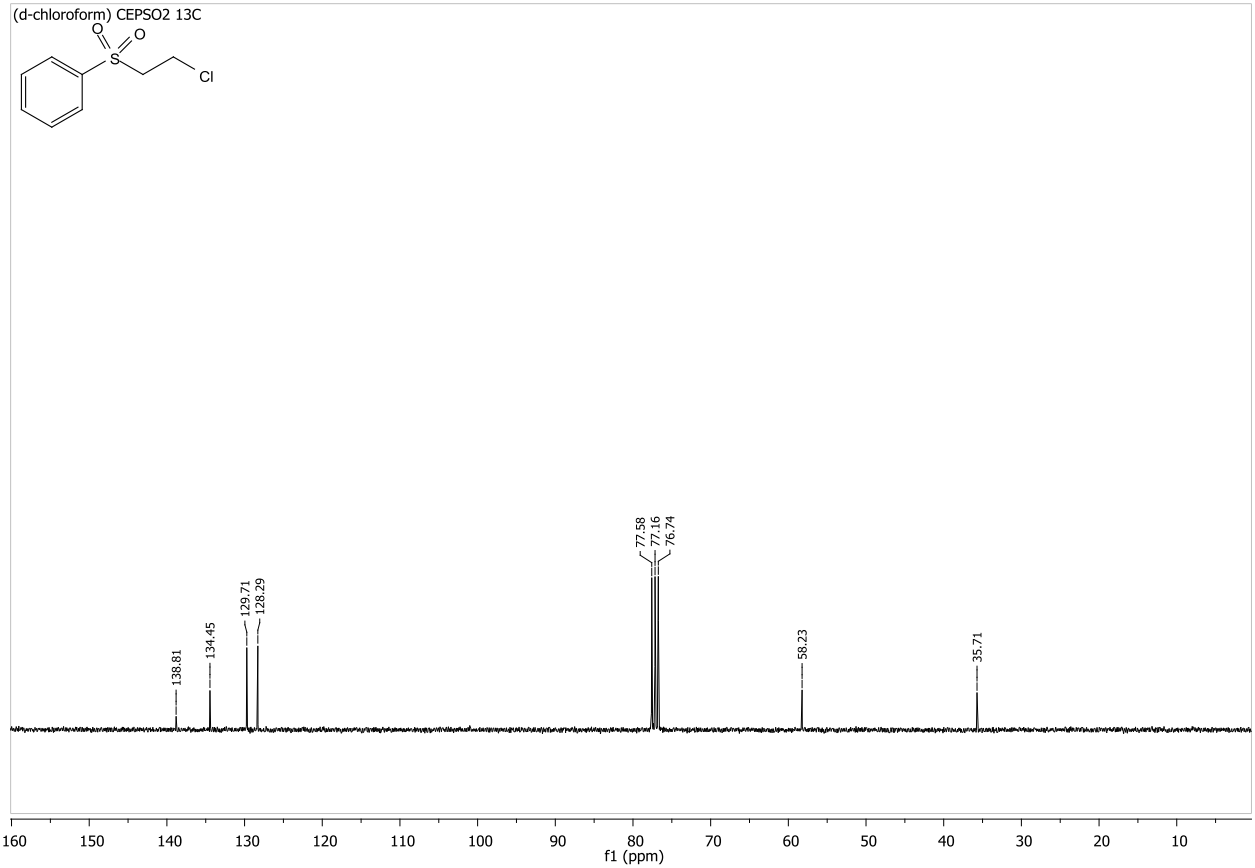
(d-chloroform) CEPSO2 13C
O
O
S
Cl
138.81
134.45
129.71
128.29
77.58
77.16
76.74
58.23
35.71
160
150
140
130
120
110
100
90
80
70
60
50
40
30
20
10
f1 (ppm)

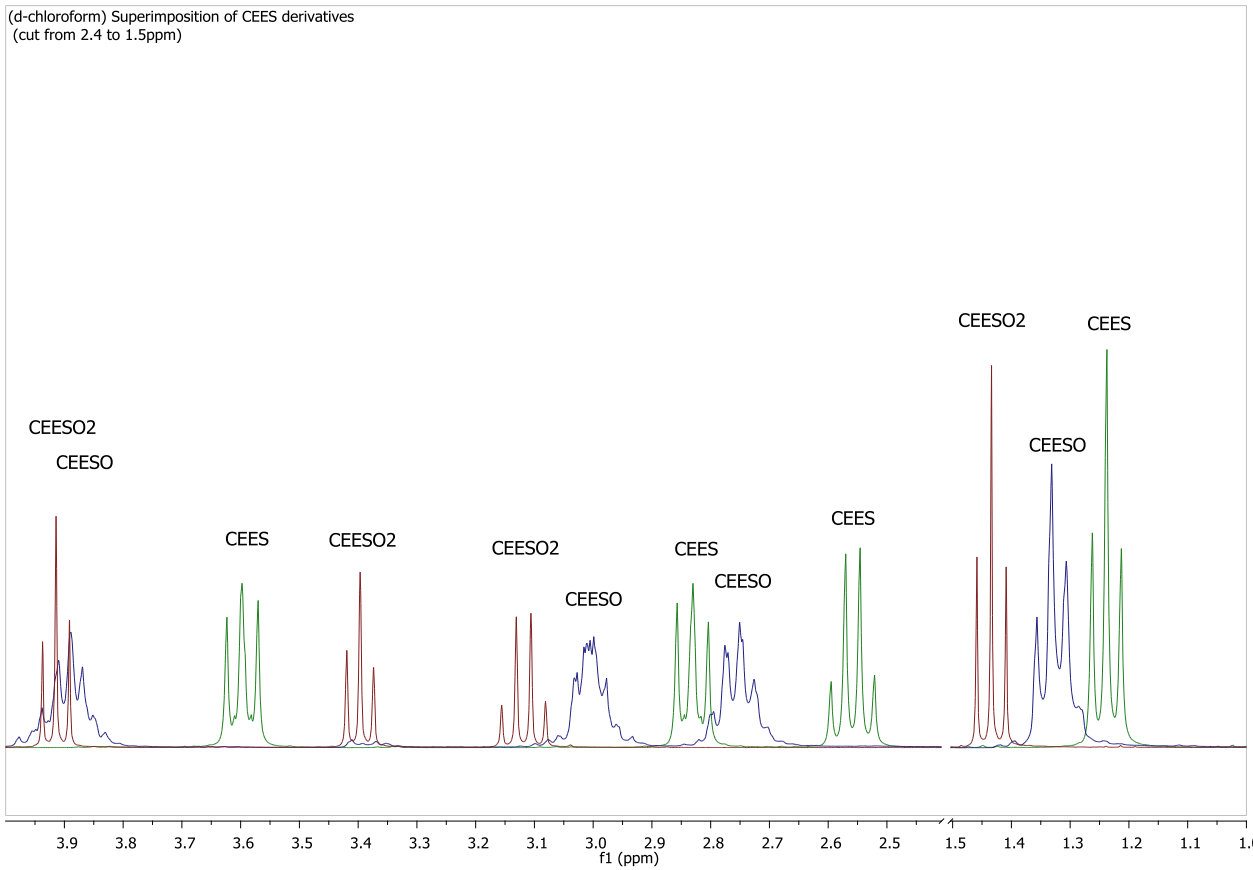
(d-chloroform) Superimposition of CEES derivatives
(cut from 2.4 to 1.5ppm)
CEESO2
CEESO
CEES
CEESO2
CEESO2
CEESO
CEES
CEESO
CEES
CEESO2
CEESO
CEES
3.9
3.8
3.7
3.6
3.5
3.4
3.3
3.2
3.1
3.0
2.9
2.8
2.7
2.6
2.5
1.5
1.4
1.3
1.2
1.1
1.0
f1 (ppm)

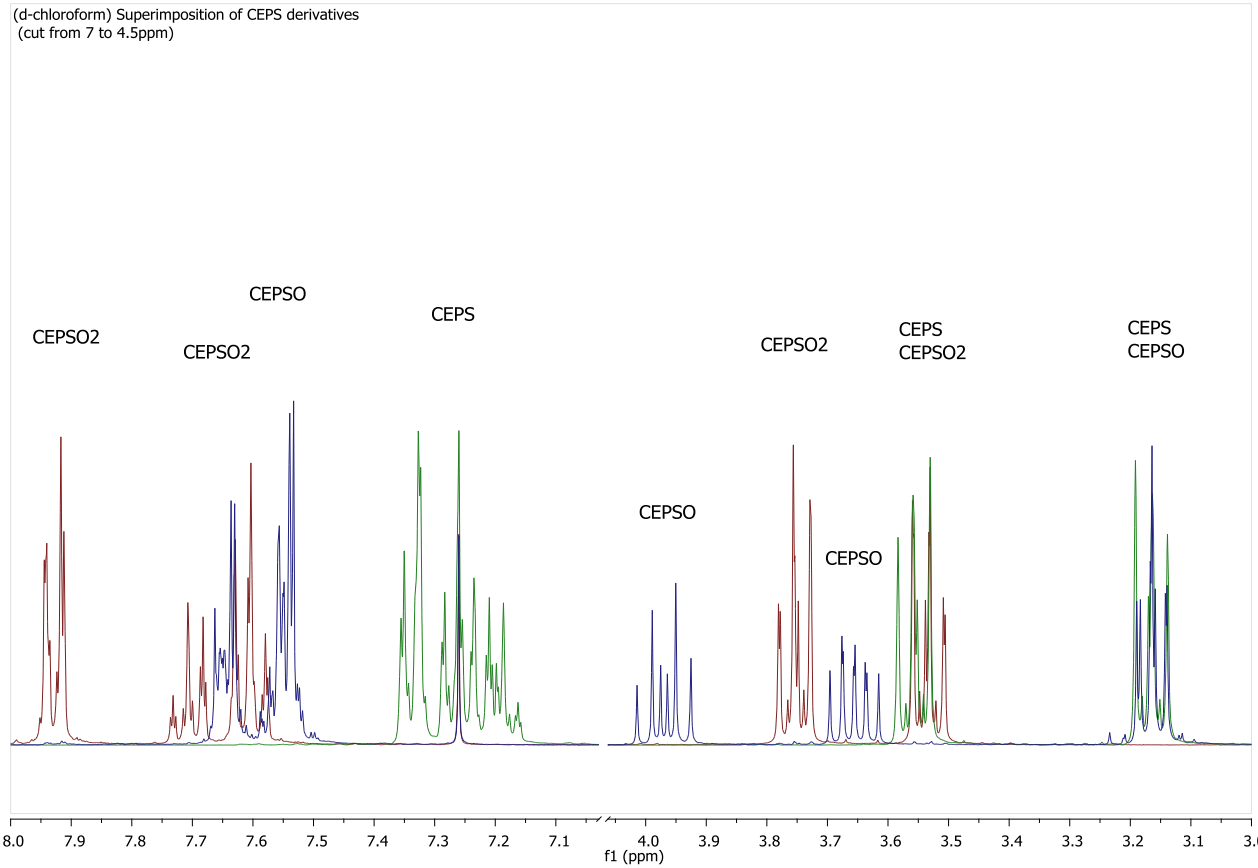
(d-chloroform) Superimposition of CEPS derivatives
(cut from 7 to 4.5ppm)
CEPSO2
CEPSO2
CEPSO
CEPS
CEPSO
CEPSO2
CEPS
CEPSO2
CEPS
CEPSO
8.0
7.9
7.8
7.7
7.6
7.5
7.4
7.3
7.2
7.1
4.0
3.9
3.8
3.7
3.6
3.5
3.4
3.3
3.2
3.1
3.0
f1 (ppm)

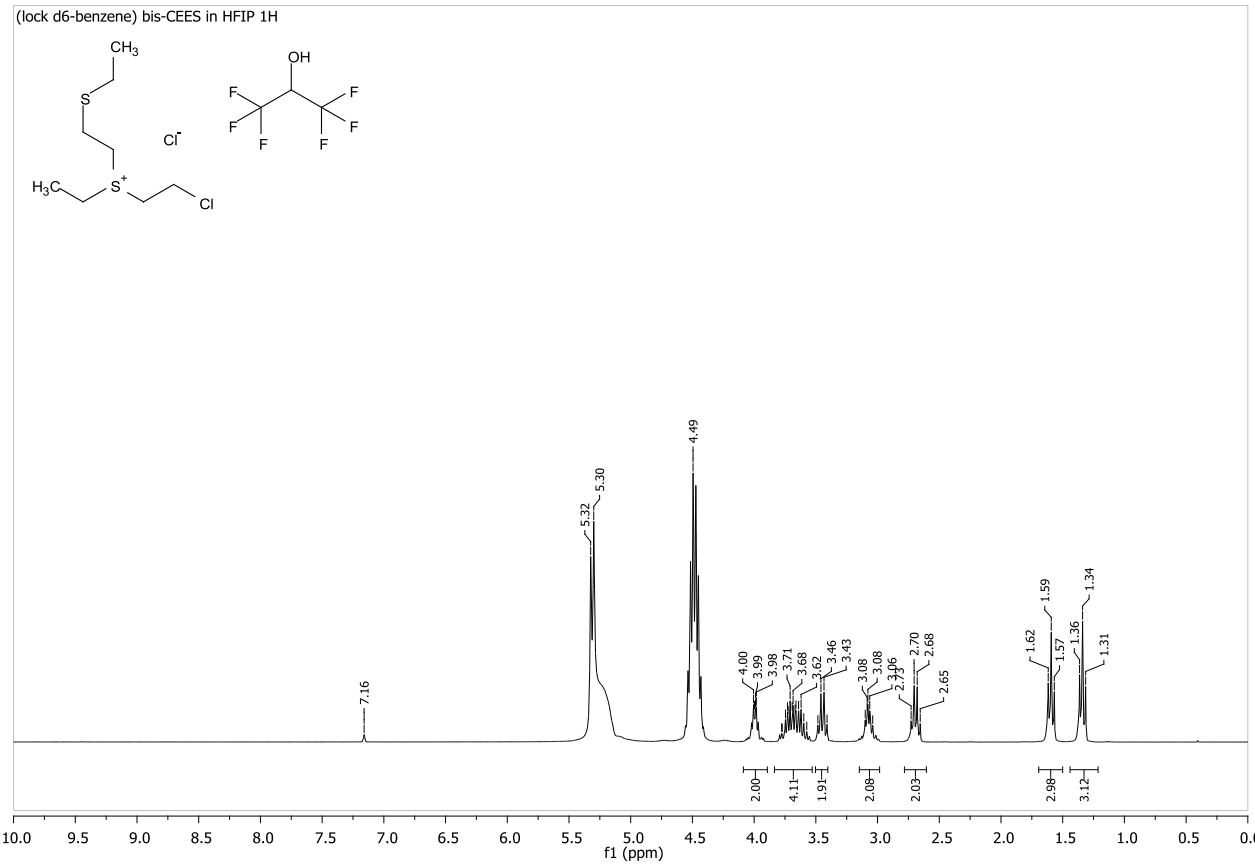
(lock d6-benzene) bis-CEES in HFIP 1H
CH3
S
Cl-
H3C
S+
Cl
OH
F
F
F
F
F
F
7.16
5.32
5.30
4.49
4.00
3.99
3.98
3.71
3.68
3.62
3.46
3.43
3.08
3.08
2.70
2.68
2.65
1.62
1.59
1.57
1.36
1.34
1.31
2.00
4.11
1.91
2.08
2.03
2.98
3.12
f1 (ppm)

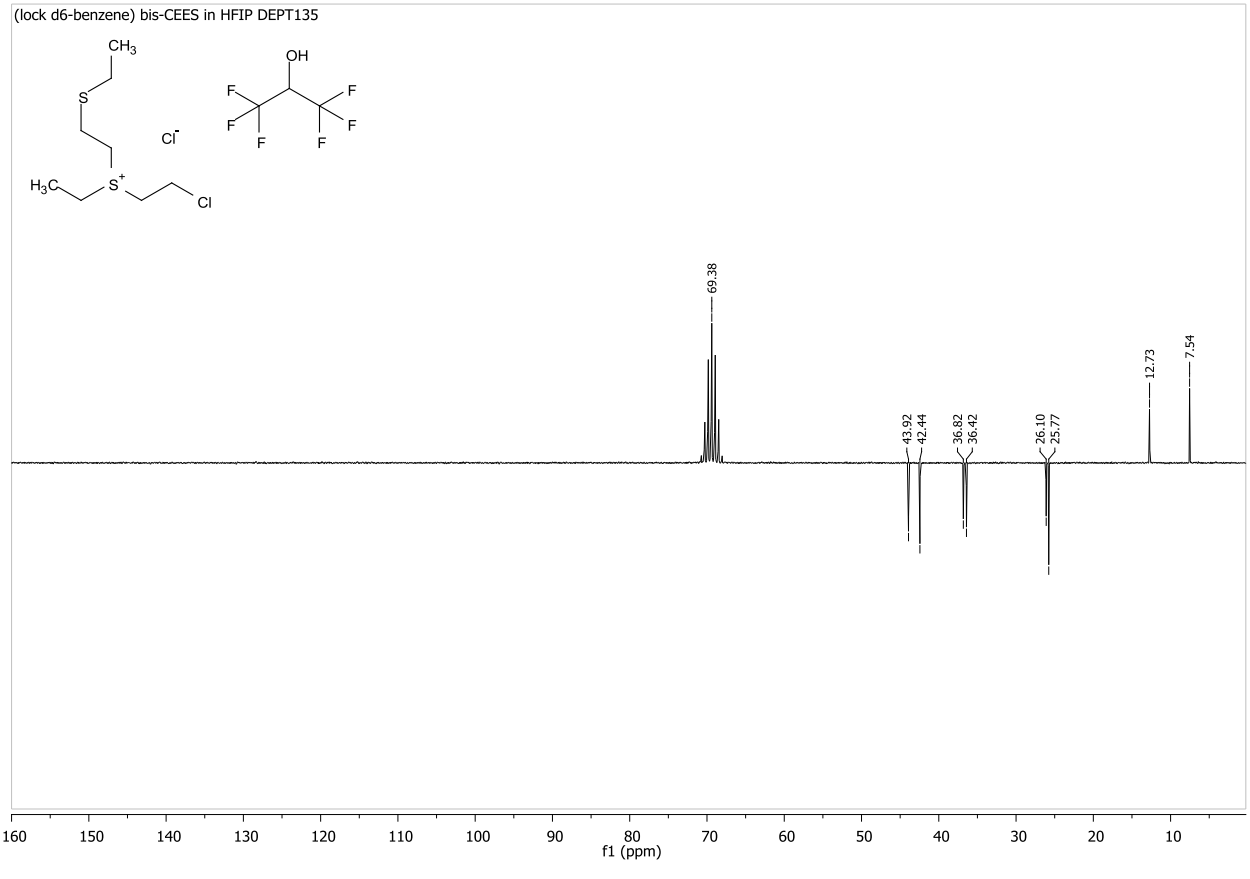
(lock d6-benzene) bis-CEES in HFIP DEPT135
CH3
S
Cl-
H3C
S+
Cl
OH
F
F
F
F
F
F
69.38
43.92
42.44
36.82
36.42
26.10
25.77
12.73
7.54
f1 (ppm)

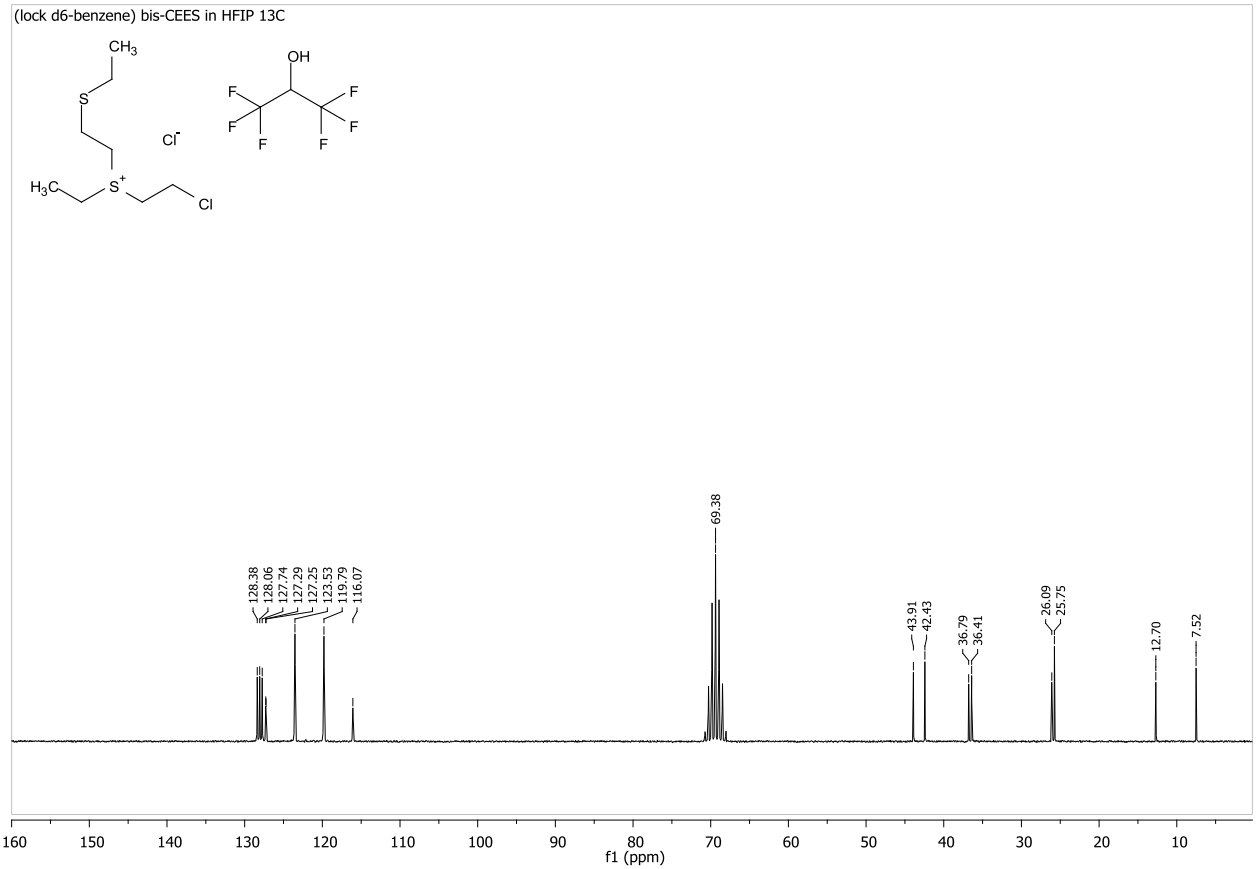
(lock d6-benzene) bis-CEES in HFIP 13C
CH3
S
Cl-
H3C
S+
Cl
OH
F
F
F
F
F
F
128.38
128.06
127.74
127.29
127.25
123.53
119.79
116.07
69.38
43.91
42.43
36.79
36.41
26.09
25.75
12.70
7.52
160
150
140
130
120
110
100
90
80
70
60
50
40
30
20
10
f1 (ppm)

1.3.3. Summary and Perspectives

This application highlights one more time the ability of benchtop NMR to monitor a chemical process in flow chemistry. The use of WET-180-NOESY enabled the quantification of the multiplet of interest at 3.8 ppm, which was obscured in standard ^{1}H spectra by the methyl group of the non-deuterated solvent.

Another manner to cope with the peak-overlap between this signal of interest and the solvent would be deconvolution. It should be noted that this method can be hindered by the inherent line-broadening associated with the increase of the flow rate leading to severe overlaps. This situation is well illustrated by low field spectra in the supplementary information document where the spectra were recorded with a flow rate of 3 $mL.min^{-1}$. Moreover, in this kinetic study, the different residence times were obtained by changing the flow regime. In turn, for each kinetic point, the line widths become different making the line-fitting methods even more tedious. In such flow kinetic study, applying a solvent suppression method to overcome the overlap with a solvent line seems to be a more practical and versatile approach.

2. Rapid screening and authentication

2.1. Context

In the research article in section D.1.2 a first investigation was conducted to evaluate the potential of UF COSY at 43 MHz to quickly screen samples of edible oils. It turned out that the UF spectra exhibited well-resolved correlation peaks matching with the unsaturated and polyunsaturated fatty chains of triglycerides. By computing several ratios between 2D-peaks volumes, edible oils from different botanical origins were distinguished. To pursue this endeavor, we felt it relevant to combine such UF COSY spectra with multivariate statistical tools. In addition, the following research article describes the potential of these fast 2D acquisitions in order to detect adulteration of olive oil samples with hazelnut oil, a long standing concern in food authentication.

High-throughput authentication of edible oils with benchtop ultrafast 2D NMR

Boris. Gouilleux, Jérémy Marchand, Benoît Charrier,

Gérald Stanislas Remaud and Patrick Giraudeau

(Original research article accepted to Food. Chem.)

Abstract

We report the use of an ultrafast 2D NMR approach applied on a benchtop NMR system (43MHz) for the authentication of edible oils. Our results demonstrate that a profiling strategy based on fast 2D NMR spectra recorded in 2.4 min is more efficient than the standard 1D experiments to classify oils from different botanical origins, since 1D spectra on the same samples suffer from strong peak overlaps. Six edibles oils with different botanical origins (olive, hazelnut, sesame, rapeseed, corn and sunflower) have been clearly discriminated by PCA analysis. Furthermore, we show how this approach combined with a PLS model can detect adulteration processes such as the addition of hazelnut oil into olive oil, a common fraud in food industry.

1. Introduction

Edible vegetable oils are widely used in cooking at home and in the food industry and represent an important part in our daily diet. They provide nutritional components such as fatty acids, but also phytosterols, tocopherols, phenolic compounds, vitamins, and volatile organic compounds (Zhang, Li, Sun, Wang, Xu, Wang, et al., 2014). The detection of adulteration of high priced oils with cheaper substitutes is a longstanding concern, both for economic and safety reasons (Moore, Spink, & Lipp, 2012). The main compounds in vegetable oils are triglycerides (~ 95 %), composed of fatty acids, whose fatty chains can be saturated or poly-mono unsaturated depending on the botanical origin. In turn, characterizing this fatty acid profile is a relevant approach to screen and classify the different varieties of edible oils (Jabeur, Zribi, Makni, Rebai, Abdelhedi, & Bouaziz, 2014; Lee, Su, Lee, & Lin, 2013; Zhang, et al., 2014). Over the past years, a large panel of analytical techniques have been engaged for this purpose such as gas chromatography (GC) (Aparicio & Aparicio-Ruíz, 2000; Bosque-Sendra, Cuadros-Rodríguez, Ruiz-Samblás, & de la Mata, 2012), mass spectrometry (MS) (Vaclavik, Cajka, Hrbek, & Hajslova, 2009), vibrational spectroscopies (Nunes, 2014) and fluorescence spectroscopy (Ge, Chen, Liu, & Zhao, 2014; Poulli, Mousdis, & Georgiou, 2007; Tan, Li, Jiang, Tang, Wang, Shi, et al., 2017). Moreover, high-field NMR (HF-NMR) has proven to be an efficient tool to determine the fatty acid profile in a simple and quick manner without the need of complex sample preparations (Castejón, Fricke, Cambero, & Herrera, 2016; Castejón, Mateos-Aparicio, Molero, Cambero, & Herrera, 2014; Knothe & Kenar, 2004). Hitherto, several methodologies – in a one or multidimensional fashion – relying on different nucleus (^{1}H, ^{13}C, ^{31}P) have been widely investigated and reviewed (Dais & Hatzakis, 2013; Sacchi, Addeo, & Paolillo, 1997). Despite its high performance, HF-NMR is not generally regarded as a candidate technique for routine applications compared to the aforementioned ones due to practical and economic reasons. By contrast, low-field NMR spectroscopy (LF-NMR) – relying on benchtop spectrometers based on permanent magnets – is relatively inexpensive and does not require cryogenic fluids. This emerges as a relevant alternative as a low-cost and accessible screening tool. Obviously, low-field instruments provide NMR spectra with a reduced performance in terms of sensitivity and spectral resolution. LF NMR spectra of edible oils suffer from numerous peak overlaps making the accurate characterization of the fatty acids profile far more difficult. Therefore, a screening approach considering the most

abundant fatty acids to characterize the overall lipid fingerprint is preferred. Such a profiling approach – nowadays popular in food authentication (Cubero-Leon, Peñalver, & Maquet, 2014; Trimigno, Marincola, Dellarosa, Picone, & Laghi, 2015) – combined with chemometric tools was recently investigated, highlighting the potential of LF-NMR spectroscopy in the detection of vegetable oil adulteration (Parker, Limer, Watson, Defernez, Williamson, & Kemsley, 2014). Yet, the high degree of spectral overlap can confuse the subsequent statistical analysis and limit the discrimination power. An appealing solution to overcome this limit is the use of two-dimensional NMR (2D-NMR) experiments, which spread the signal over a 2D plane. The price to pay for this resolution enhancement is a long experiment duration - from tens of minutes to several hours - required to record a whole 2D interferogram. This drawback hampers the use of 2D methods in the context of high-throughput analysis in food screening applications. At high field, the last two decades have witnessed strong efforts to speed up 2D NMR experiments via different strategies (Rouger, Gouilleux, & Giraudeau, 2016). Among them, Ultrafast 2D NMR (UF 2D NMR) is a generic approach, which enables the acquisition of a whole 2D spectrum within a single scan, i.e., in a fraction of second (Frydman, Scherf, & Lupulescu, 2002). This dramatic reduction of the experiment duration relies on a one-step spatial encoding performed instead of the time consuming repetition of the t_1-evolution delay. In spite of a low intrinsic sensitivity, this UF method has undergone significant improvements and is nowadays a well-recognized analytical tool (Giraudeau & Frydman, 2014; Le Guennec, Giraudeau, & Caldarelli, 2014; Le Guennec, Tea, Antheaume, Martineau, Charrier, Pathan, et al., 2012), which has been recently implemented on a benchtop NMR system (Gouilleux, Charrier, Danieli, Dumez, Akoka, Felpin, et al., 2015). While sub-second experiments are barely sensitive enough for low-field applications, we demonstrated that sub-molar limits of detection could be reached within a few tens of seconds, which makes this approach compatible with the analysis of concentrated food products such as edible oils (Gouilleux, Charrier, Akoka, Felpin, Rodriguez-Zubiri, & Giraudeau, 2016). In this article, we evaluate the potential of this UF 2D NMR approach on a low field NMR spectrometer (43 MHz) for the rapid screening of several vegetable oils: olive (EVO), hazelnut (HNO), sesame (SSO), rapeseed (RO), corn (CO) and sunflower (SO) oils. The benefit in terms of discrimination power of this fast 2D approach is discussed in comparison with results obtained via conventional ^{1}H NMR experiments. Furthermore, an application to the detection of adulteration of EVO with HNO is presented.

2. Material and Methods

2.1. Edible oil samples and storage

Twenty three vegetable oils of different brands were purchased from local groceries in Nantes, France. These edible oils included: eight different extra virgin olive oils (EVO), four hazelnut oils (HNO), three sunflower oils (SO), two corn oils (CO), three sesame oils (SSO) and three rapeseed oils (RO). Further details regarding the typical composition of these oil samples are mentioned in supplementary table S1. These different varieties of edible oils are characterized by a significant difference of fatty acid composition. Olive and hazelnut oils are rich in saturated and especially in mono-unsaturated fatty chains (e.g. oleic acid) in contrast to sunflower and corn oils, which mainly contain poly-unsaturated chains (e.g. linoleic acid) while sesame and rapeseed provide an intermediate fatty acid composition. These characteristics are well described in the literature (Kamal-Eldin & Andersson, 1997; Kostik, Memeti, & Bauer, 2013; Ramos, Fernández, Casas, Rodríguez, & Pérez, 2009).

2.2. Sample preparation

All the samples were stored in the dark at room temperature before analysis. Roughly 350 mg of vegetable oil was dissolved in 400 µL of non-deuterated chloroform (HPLC grade) in a 5 mL flask. After stirring, the sample was transferred into a 5 mm-diameter NMR tube and directly analyzed. The addition of chloroform serves two purposes: first, it reduces the viscosity of the oil samples thus increasing the transverse relaxation rate of the motionless glyceric protons, leading to sharper peaks, next, it provides a reference ppm value, allowing a chemical-shift scale to be properly attached to each spectrum. The choice of the concentration is an optimum between sensitivity and viscosity.

2.3. Benchtop NMR spectrometer

The experiments performed at low field were recorded on a Spinsolve from Magritek working at a frequency of 43.62 MHz via a permanent magnet based on a Hallbach design (Ernesto Danieli, Perlo, Blümich, & Casanova, 2010; E. Danieli, Perlo, Blümich, & Casanova, 2013). This equipment includes a gradient coil along the B0-axis (i.e. along the transverse plane of the

NMR tube) which can generate a maximum field gradient of 0.16 $T.m^{-1}$ and is operated with the Prospa Software. The spectrometer allows to work without deuterated solvents thanks to a built-in external fluorine lock system.

2.4. 1D NMR experiments

The 1D spectra were recorded in 16 scans for a total experiment duration of 2.4 min. The flip angle of 90° was achieved by a pulse length of 6.9 µs at 0 dB. The FIDs were recorded with 8 K points and a dwell-time of 200 µs, leading to a detection time of 1.64 s. The 1D data were processed in Mnova (Mestrelab Research) with the following features. The number of points was increased to 16 K by zero-filling to improve the digital resolution. All spectra experienced an automatic phase correction (some data required manual adjustments) and an automatic base-line correction via the Wittaker-smoother algorithm available in Mnova was applied. The signal of the chloroform at 7.26 ppm was used for ppm-scaling and the spectra were normalized by the total area (after excluding the solvent region) to cope with the unavoidable evaporation of the solvent. The resulting ^{1}H spectra are rearranged as a stacked plot and are realigned automatically.

2.5. Ultrafast 2D NMR experiments

The UF experiments were recorded in 2.4 min – 72 scans with a repetition time of 2 s – with the homemade pulse sequence described in supplementary information (figure S1). In spite of the capability of yielding a 2D UF spectrum in a single scan, signal accumulation was required to reach a sufficient sensitivity to ensure a reasonable repeatability of the experiment. Two 25 ms chirp pulses (i.e., a spatial encoding time TE of 50 ms) swept over a 3.5 kHz range were considered for the spatial encoding. This value of TE provides a good compromise between resolution, spectral width and J-modulated sensitivity losses (Gouilleux, Rouger, Charrier, Kuprov, Akoka, Dumez, et al., 2015). The amplitude of the encoding gradients Ge was adapted to obtain a frequency dispersion equivalent to the frequency sweep of the pulses, corresponding to 11.6% of the maximum gradient strength available. During the acquisition, 128 pairs of bipolar gradient pulses Ga were applied (85% of maximum strength, 1280.4 µs each). The desired coherence selection was obtained as described in figure S1. All the data recorded in an ultrafast fashion were processed thanks to a home-written routine

implemented in Prospa software, which is explained in details in supplementary information. The Prospa scripts necessary to perform UF COSY experiments and process the subsequent data are also available as supplementary materials. The 2D spectrum was finally plotted in magnitude mode so that no phase corrections were needed.

2.6. Chemometric analysis

The multivariate analyses were performed using the software SIMCA-P +12. (Umetrics Inc, Kinnelon NJ). The classification of the six varieties of vegetables was achieved by PCA analysis. For the 2D approach, twenty three experiments and thirteen 2D-peaks were considered. Thereby, the observations and the normalized 2D-peak volumes were rearranged into a 23 X 13 matrix. The matrix content was preprocessed through generalized log transformation and Pareto scaling before calculation. This log transformation reduces the impact of the high dynamic range between the very high diagonal peak 1 and the other ones. In practice, an optimized separation of the groups was obtained by suppressing the contribution of two variables (peak 9 and 13) resulting on a final 23 X 11 matrix. Indeed, peaks 9 and 13 arise mainly from the correlation between acyl protons E and those from aliphatic chains C (see figure 1 for proton labels). These scalar correlations are shared with all the fatty chains so that they do not provide valuable insights for the discrimination. Concerning the study based on 1D experiments, two different approaches have been here evaluated. The first one relies on six integration regions: [4.72, 6.28 ppm]; [3.61, 4.62 ppm]; [2.49, 3.24 ppm]; [1.68, 2.48 ppm]; [0.98, 1.66 ppm] and [0.53, 0.98 ppm] whose values reflects the composition of the sample in terms of SFA, UFA and PUFA. In practice, the best separation was yielded by deleting the contribution of the last integration region at [0.53, 0.98 ppm] leading to a final 23 X 5 matrix. The second one seeks to fully exploit the spectral information through a standard bucket integration with a width of 0.04 ppm. The bucket integration was performed from 0.03 to 6.23 ppm (the solvent region was previously excluded). The width of the buckets was thin enough to reflect the complexity of the signals. Afterwards, the buckets from empty regions, i.e., [0.03 ; 1.03 ppm] ; [3.23 ; 4.33 ppm] ; [4.69 ; 5.29 ppm] ; [5.93 ; 6.23 ppm], were excluded leading to a 23 X 79 matrix. The same procedure as for 2D including log transformations and Pareto scaling was applied in both 1D approaches. The quantification of the adulteration rate was performed thanks to a Partial Least Squares (PLS) model. The explained variances of the

model were evaluated by R^2X and R^2Y while the prediction ability was measured with Q^2 calculated by cross-validation. Finally, the model was further assessed by a 20-cycle permutation test.

3. Results and discussion

3.1 1D and Ultrafast 2D NMR spectra

Figure 1a shows an example of 1D NMR experiment performed on a sample of pure vegetable oil in chloroform. Clearly, at 43 MHz, the resulting spectrum suffers from numerous overlaps so that the assignment of the signals becomes overly complicated. Numerous fully assigned high-field 1H NMR spectra of vegetable oils are reported in the literature (Castejón, Mateos-Aparicio, Molero, Cambero, & Herrera, 2014; Sacchi, Addeo, & Paolillo, 1997), which facilitate the identification of major peaks as proposed in Figure 1d. Some of them are particularly interesting to characterize the fatty acid fingerprint. The olefinic peak I at 5.26 ppm, arising from protons involved in a double bound, corresponds to the total number of unsaturated bounds, regardless of whether these are provided by mono- or polyunsaturated chains. Thus, this signal is labeled UFA (Unsaturated Fatty Acids). The two peaks H and G at 5.20 and 4.23 ppm respectively match with the -CH- and -CH_2- groups of the glycerol backbones (GLY) in the triglycerides. It should be noticed that in such 1D experiment the contribution of the resonance H is entirely overlapped with the UFA signal. Furthermore, the signal F located at 2.70 ppm matches with the diallylic CH_2 protons of the polyunsaturated chains; it is labeled PUFA (Poly Unsaturated Fatty acids). The quantification of these relevant signals: UFA, PUFA and GLY constitutes a key factor to screen the fatty acid composition of the different vegetable oils. However, this 1D NMR approach involves significant measurement bias due to the inherent low spectral resolution (figure S2). The integration of the UFA signal is disturbed by the overlaps with the peak H from the glycerol backbones and the presence of the 13C satellite line of the solvent peak. In addition, the relevant PUFA signal is severely overlapped. 2D NMR experiments form an attractive way to overcome this overlapping issue. The UF 2D spectrum shown in figure 1b, recorded in 2.4 min, highlights how the UF COSY experiment circumvents the peak-overlaps by delivering well-resolved correlation peaks. It is therefore possible to

properly integrate, for instance, UFA, PUFA and GLY signals without measurement bias within a reasonable experimental time (figure 1b). It is even possible to discern different edible oils by a simple visual inspection, as the intensity of the PUFA cross peaks increases from olive or hazelnut oil to the corn, sunflower or sesame oil (figure S3). It should be highlighted that recording a conventional 2D spectrum in such a short time would not have been possible; in addition the "pure shift" character of the UF experiments in the horizontal dimension provides an additional resolution enhancement which is particularly interesting at low field.

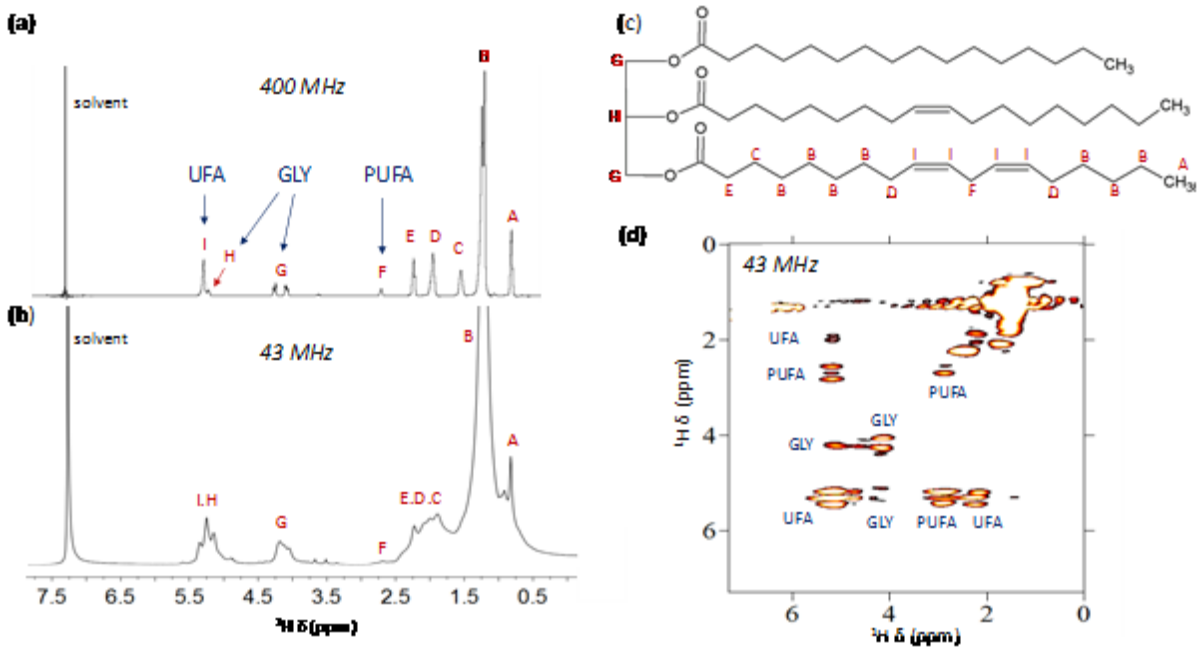

Figure 1: 1D ^{1}H NMR spectra of a vegetable oil sample in chloroform recorded at 400 MHz **(a)** and 43 MHz **(b)**, together with the structure and nomenclature used for the glycerol and fatty acids protons **(c)**. **(d)** Ultrafast 2D NMR spectrum recorded in 2.4 min on the same oil sample.

Beyond the resolved signals related to UFA, PUFA and GLY, a chemometric analysis of the UF COSY spectra should consider all the peaks present on the 2D spectrum. Among the different signals, only the 2D peaks with a minimal signal to noise ratio (SNR) of 20 are retained to ensure a sufficient repeatability of the 2D experiments. Figure 2 shows the 13 selected peaks together with their SNR and the associated peak volume repeatability. The repeatability is evaluated by the relative standard deviation (RSD) obtained on a series of five experiments. Each of these thirteen 2D-peaks are measured with a SNR over 30 and RSD below 10 %.

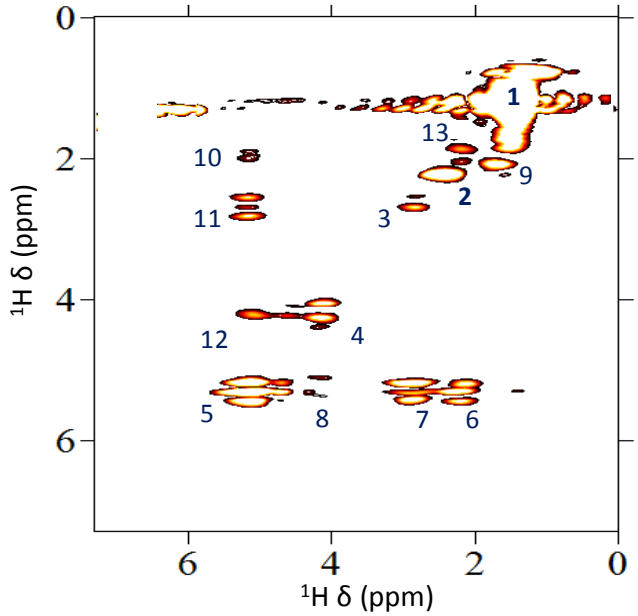

2D-Peak	SNR	Average 2D-peak volumes	RSD %
1	1533	1969300	2.6
2	123	126870	0.3
3	35	52383	8.0
4	50	129387	1.6
5	192	287745	2.6
6	49	88055	1.2
7	75	134465	8.0
8	22	57747	1.4
9	52	54737	0.7
10	21	35961	1.1
11	35	73906	6.0
12	34	59472	2.5
13	30	32351	1.7

Figure 2: On the left, UF 2D spectrum recorded in 2.4 min on a sunflower oil sample in non-deuterated chloroform. The numbers on the spectrum indicate the 2D-peaks whose volumes were considered as variables for the multivariate analysis. On the right, the table indicates the signal noise ratio (SNR), the average 2D peak volumes as well as the relative standard deviation (RSD) in % on 2D peak volumes. The RSD was based on a series of five successive UF 2D NMR experiments.

3.2. Classification of the vegetable oils

UF COSY experiments were performed in 2.4 min on a panel of twenty three edible oil samples from different sources: olive, hazelnut, sunflower, corn, rapeseed and sesame. A series of three UF COSY spectra was acquired for each sample. The average 2D-peak volume for each of the thirteen signals was computed and finally normalized by the sum of all the peak volumes. The twenty three experiments and the normalized volumes were rearranged into a matrix, then submitted to PCA. The matrix content was preprocessed through generalized log transformation and Pareto scaling. In order to assess the potential benefit of this 2D-approcah compared to standard ^{1}H NMR, both 1D procedures described in section 2.6 were applied on the same sample panel. The detailed processing in terms of calibration, phase and base-line correction is mentioned in section 2.4. A series of three 1D acquisitions was performed for each oil sample and the mean values for each integration were further considered for the multivariate analysis. Figure 3 displays the results provided by the PCA from the 2D and 1D

data. From the score plot of the 2D data (figure 3a), a high level of separation is obtained. The two principal components together explain 98.3 % of the total variance, with the first one explaining 94.7 %. These edible oils are clearly classified into six groups, among which a first cluster consisting of olive and hazelnut oils is far from another one including sunflower, rapeseed, sesame and corn oils. From the 1D data, slightly different results are obtained depending on the procedure (figure 3b versus 3c). The approach based on the five chosen integration regions provides a PCA analysis whose two components explain 98.4 % of the variance, from which 96.3 % is explained by the first one. With the method relying on a regular bucketing, the two components explain 92.6 % of the variance, from which 70.2 % is explained by the first one. Although the PCA obtained with 1D data provides this overall cluster separation it is apparently not possible to graphically distinguish varieties with similar composition such as corn and sunflower oils, and the distinction between olive and hazelnut oils is also reduced. It is also interesting to note that the procedure based on a 0.04-ppm width bucketing does not enable the separation between sesame and rapeseed oil samples (figure 3c). In conclusion, this method does not provide a better discrimination compared to the wider integrations. Overall, whatever the 1D procedure, the comparison of the score plots in figure 3 highlights the higher discrimination power of the 2D NMR methodology compared to its 1D counterpart. Furthermore, it is worth exploring the variables distribution related to this chemometric analysis. According to the loading plot (figure S4), the variables which contribute the most to the first component are the volumes of peaks 7, 11, 3 and 1 with loading values of 0.52, 0.51, 0.47 and -0.15, respectively. Bearing in mind that signals 11, 7 and 3 are associated with the presence of PUFA, these loading values are consistent with the variance of linoleic acid concentration in the different edible oils. In addition, a discrimination based on the concentration of saturated fatty acids (SFA) is clearly associated with the intensity of peak 1.

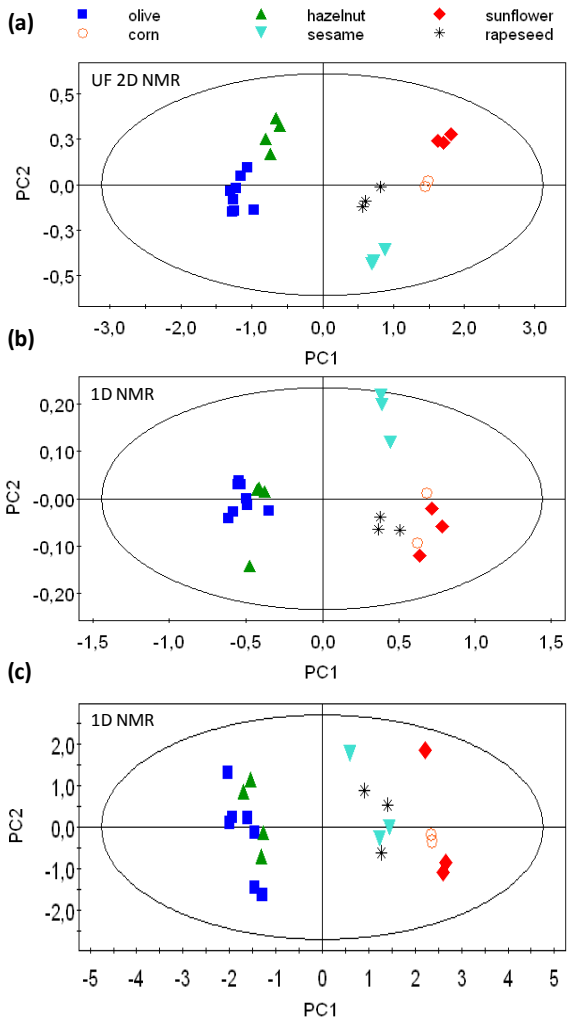

Figure 3: PCA analysis on 23 edible oils samples from different botanical origins. **(a)** score plot from data obtained with UF 2D NMR experiments, **(b)** with standard 1D experiments and a variable bucketing approach (5 wide integration regions), **(c)** with standard 1D experiments and a constant bucketing approach (0.04 ppm width). Both 1D and 2D spectra were recorded in 2.4 min.

3.3. Adulteration of olive oil with hazelnut oil

This efficient discrimination of six varieties of edible oils highlights the potential of fast 2D benchtop NMR as a versatile tool to cope with adulteration issues. To illustrate this capability, we focused on the adulteration of olive oil samples with hazelnut oil. Due to their similar fatty acid compositions, this form of adulteration is a challenging analytical issue and a long standing concern as evidenced by the numerous related articles and reviews (Dais & Hatzakis, 2013; Parker, Limer, Watson, Defernez, Williamson, & Kemsley, 2014; Poulli, Mousdis, & Georgiou, 2007; Vaclavik, Cajka, Hrbek, & Hajslova, 2009). To mimic this adulteration, blended samples were obtained by spiking four different olive oil samples with three distinct hazelnut

oils. In total, nineteen samples were prepared with different rates of adulteration from 0 % to 100 % (w/w). A two-component PLS regression was used to model the percentage (w/w) of hazelnut oil present in each sample. Fourteen mixtures were used for calibration and five other mixtures were used as a validation set for the PLS model. Figure. 4a shows how the PLS calibration model correlates the observed and estimated values of HNO % from the UF 2D NMR spectra recorded at 43 MHz. The difference between the real and the predicted rates of adulterant is relatively small for adulteration over 20 % (w/w) and becomes more significant for mixtures with a 10 % rate of adulteration. The regression coefficient reaches 0.9895, highlighting a good linearity of the model, and the root mean square error (RMSE) is 3.67 %. This two-component model is then characterized by a R^2X of 0.950 and a R^2Y of 0.990. The predictive ability is indicated by a Q^2 of 0.972, calculated by a cross-validation procedure. The developed PLS model was further evaluated by a 20-cycle permutation test where both R^2 and Q^2 were systematically calculated. For each re-ordered models, the values of R^2 and Q^2 remain significantly lower than those provided by the original model and the R^2 intercept and the Q^2 intercept are 0.152 and –0.236, respectively (figure S5). This provides evidence of the non-randomness of the estimated adulterant concentration. Moreover, to assess the prediction ability on a real case, the PLS calibration model was used to predict the levels of adulteration on unknown blended samples obtained with olive and hazelnut oils from different sources than the ones considered for the calibration set. Figure. 4b shows the fit between the real and the estimated values on this validation set. This fit is characterized by a regression coefficient of 0.9801 and a RMSEP of 6.27 %. These results highlight the reasonable capacity of this approach to evaluate the percentage of hazelnut oil into olive samples.

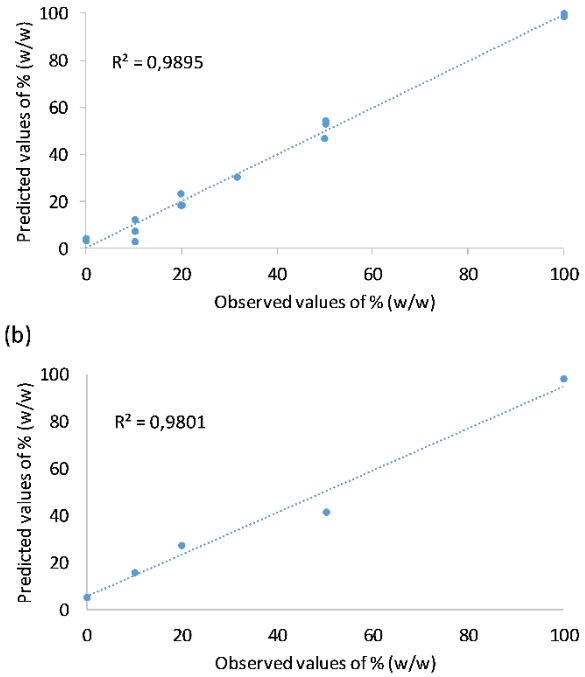

Figure 4: **(a)** PLS calibration model for the relationship between observed and predicted percentages (w/w) of HNO into EVO samples. **(b)** Correlations between observed and predicted percentages (w/w) of HNO into EVO samples for the validation set.

4. Conclusion

Based on the results of this article, ultrafast 2D NMR - applied on a benchtop NMR device - provides a real benefit for the authentication of edible oils with different botanical origins compared to a 1D NMR approach. The PCA analysis highlights the clear discrimination of olive, hazelnut, sesame, rapeseed, corn and sunflower oils. Moreover, this approach combined with a chemometric technique as PLS enables the detection of hazelnut oil into olive oil with a regression coefficient of 0.9801 and a reasonable RMSEP of 6.27 % w/w. As a fast approach (2.4 min), this spatially encoded 2D experiment is thereby compatible with high-throughput analysis, leading to a practical and rapid screening tool. Furthermore, the performance of the method could be further improved in the future with the constant improvement of the magnetic field strength and homogeneity of benchtop NMR spectrometers.

Disclosure Statement

The authors disclose any actual or potential conflict of interest.

Acknowledgments

The authors warmly acknowledge Magritek, in particular Ernesto Danieli, Juan Perlo and Andrew Coy, for their strong support. This project was funded by Région Pays de la Loire (Grant RésoNantes).

References

Aparicio, R., & Aparicio-Ruíz, R. (2000). Authentication of vegetable oils by chromatographic techniques. Journal of Chromatography A, 881(1–2), 93-104.

Bosque-Sendra, J. M., Cuadros-Rodríguez, L., Ruiz-Samblás, C., & de la Mata, A. P. (2012). Combining chromatography and chemometrics for the characterization and authentication of fats and oils from triacylglycerol compositional data—A review. Analytica Chimica Acta, 724, 1-11.

Castejón, D., Fricke, P., Cambero, M., & Herrera, A. (2016). Automatic 1H-NMR Screening of Fatty Acid Composition in Edible Oils. Nutrients, 8(2), 93.

Castejón, D., Mateos-Aparicio, I., Molero, M. D., Cambero, M. I., & Herrera, A. (2014). Evaluation and Optimization of the Analysis of Fatty Acid Types in Edible Oils by 1H-NMR. Food Analytical Methods, 7(6), 1285-1297.

Cubero-Leon, E., Peñalver, R., & Maquet, A. (2014). Review on metabolomics for food authentication. Food Res Int., 60, 95-107.

Dais, P., & Hatzakis, E. (2013). Quality assessment and authentication of virgin olive oil by NMR spectroscopy: A critical review. Anal. Chim. Acta, 765, 1-27.

Danieli, E., Perlo, J., Blümich, B., & Casanova, F. (2010). Small Magnets for Portable NMR Spectrometers. Angew. Chem. Int. Edit., 49(24), 4133-4135.

Danieli, E., Perlo, J., Blümich, B., & Casanova, F. (2013). Highly Stable and Finely Tuned Magnetic Fields Generated by Permanent Magnet Assemblies. Phys. Rev. Lett., 110(18), 180801.

Frydman, L., Scherf, T., & Lupulescu, A. (2002). The acquisition of multidimensional NMR spectra within a single scan. Prod. Natl. Acad. Sci. USA, 99, 15858-15862.

Ge, F., Chen, C., Liu, D., & Zhao, S. (2014). Rapid Quantitative Determination of Walnut Oil Adulteration with Sunflower Oil Using Fluorescence Spectroscopy. Food Analytical Methods, 7(1), 146-150.

Giraudeau, P., & Frydman, L. (2014). Ultrafast 2D NMR: An Emerging Tool in Analytical Spectroscopy. Annu. Rev. Anal. Chem., 7, 129-161.

Gouilleux, B., Charrier, B., Akoka, S., Felpin, F.-X., Rodriguez-Zubiri, M., & Giraudeau, P. (2016). Ultrafast 2D NMR on a benchtop spectrometer: Applications and perspectives. TrAC Trends in Analytical Chemistry, 83, Part A, 65-75.

Gouilleux, B., Charrier, B., Danieli, E., Dumez, J.-N., Akoka, S., Felpin, F.-X., Rodriguez-Zubiri, M., & Giraudeau, P. (2015). Real-time reaction monitoring by ultrafast 2D NMR on a benchtop spectrometer. Analyst, 140(23), 7854-7858.

Gouilleux, B., Rouger, L., Charrier, B., Kuprov, I., Akoka, S., Dumez, J.-N., & Giraudeau, P. (2015). Understanding J-Modulation during Spatial Encoding for Sensitivity-Optimized Ultrafast NMR Spectroscopy. ChemPhysChem, 16(14), 3093-3100.

Jabeur, H., Zribi, A., Makni, J., Rebai, A., Abdelhedi, R., & Bouaziz, M. (2014). Detection of Chemlali Extra-Virgin Olive Oil Adulteration Mixed with Soybean Oil, Corn Oil, and Sunflower Oil by Using GC and HPLC. Journal of Agricultural and Food Chemistry, 62(21), 4893-4904.

Kamal-Eldin, A., & Andersson, R. (1997). A multivariate study of the correlation between tocopherol content and fatty acid composition in vegetable oils. J. Am. Oil Chem. Soc, 74(4), 375-380.

Knothe, G., & Kenar, J. A. (2004). Determination of the fatty acid profile by 1H-NMR spectroscopy. European Journal of Lipid Science and Technology, 106(2), 88-96.

Kostik, V., Memeti, S., & Bauer, B. (2013). Fatty acid composition of edible oils and fats. J. Hygien. Eng. Design, 4, 112-116.

Le Guennec, A., Giraudeau, P., & Caldarelli, S. (2014). Evaluation of Fast 2D NMR for Metabolomics. Analytical Chemistry, 86(12), 5946-5954.

Le Guennec, A., Tea, I., Antheaume, I., Martineau, E., Charrier, B., Pathan, M., Akoka, S., & Giraudeau, P. (2012). Fast Determination of Absolute Metabolite Concentrations by Spatially Encoded 2D NMR: Application to Breast Cancer Cell Extracts. Analytical Chemistry, 84(24), 10831-10837.

Lee, W.-J., Su, N.-W., Lee, M.-H., & Lin, J.-T. (2013). Assessment of authenticity of sesame oil by modified Villavecchia Test and HPLC-ELSD analysis of triacylglycerol profile. Food Research International, 53(1), 195-202.

Moore, J. C., Spink, J., & Lipp, M. (2012). Development and Application of a Database of Food Ingredient Fraud and Economically Motivated Adulteration from 1980 to 2010. Journal of Food Science, 77(4), R118-R126.

Nunes, C. A. (2014). Vibrational spectroscopy and chemometrics to assess authenticity, adulteration and intrinsic quality parameters of edible oils and fats. Food Research International, 60, 255-261.

Parker, T., Limer, E., Watson, A. D., Defernez, M., Williamson, D., & Kemsley, E. K. (2014). 60 MHz 1H NMR spectroscopy for the analysis of edible oils. TrAC, Trends Anal. Chem., 57, 147-158.

Poulli, K. I., Mousdis, G. A., & Georgiou, C. A. (2007). Rapid synchronous fluorescence method for virgin olive oil adulteration assessment. Food Chemistry, 105(1), 369-375.

Ramos, M. J., Fernández, C. M., Casas, A., Rodríguez, L., & Pérez, Á. (2009). Influence of fatty acid composition of raw materials on biodiesel properties. Bioresour. Technol., 100(1), 261-268.

Rouger, L., Gouilleux, B., & Giraudeau, P. (2016). Fast n-Dimensional Data Acquisition Methods. In Reference Module in Chemistry, Molecular Sciences and Chemical Engineering): Elsevier.

Sacchi, R., Addeo, F., & Paolillo, L. (1997). 1H and 13C NMR of virgin olive oil. An overview. Magn. Reson. Chem., 35(13), S133-S145.

Tan, J., Li, R., Jiang, Z.-T., Tang, S.-H., Wang, Y., Shi, M., Xiao, Y.-Q., Jia, B., Lu, T.-X., & Wang, H. (2017). Synchronous front-face fluorescence spectroscopy for authentication of the adulteration of edible vegetable oil with refined used frying oil. Food Chemistry, 217, 274-280.

Trimigno, A., Marincola, F. C., Dellarosa, N., Picone, G., & Laghi, L. (2015). Definition of food quality by NMR-based foodomics. Curr Opin Food Sci, 4, 99-104.

Vaclavik, L., Cajka, T., Hrbek, V., & Hajslova, J. (2009). Ambient mass spectrometry employing direct analysis in real time (DART) ion source for olive oil quality and authenticity assessment. Analytica Chimica Acta, 645(1–2), 56-63.

Zhang, L., Li, P., Sun, X., Wang, X., Xu, B., Wang, X., Ma, F., Zhang, Q., & Ding, X. (2014). Classification and Adulteration Detection of Vegetable Oils Based on Fatty Acid Profiles. Journal of Agricultural and Food Chemistry, 62(34), 8745-8751.

Supplementary material

Table S1. Information regarding the vegetable oil samples used in this study. SFA: saturated fatty acid, MUFA: mono-unsaturated acid, PUFA: poly-unsaturated, nd: non-documented

		Distribution in grams for 100 g of edible oil		
Botanical origins	refined	SFA	MUFA	PUFA
olive	no	nd	nd	nd
	no	18,0	71,0	11,0
	no	14,0	69,0	9,0
	no	nd	nd	nd
	no	14,0	nd	nd
	no	14,6	78,8	6,6
	no	12,0	80,0	8,0
	no	13,0	73,0	6,0
hazelnut	no	10,0	80,0	10,0
	nd	nd	nd	nd
	nd	8,0	80,0	12,0
	nd	9,7	74,7	15,6
sunflower	no	nd	nd	nd
	no	11,0	25,0	56,0
	no	nd	nd	nd
corn	nd	nd	nd	nd
	yes	nd	nd	nd
sesame	no	16,0	40,0	37,0
	no	15,0	41,0	44,0
	no	16,0	42,0	42,0
rapeseed	no	8,0	61,0	31,0
	no	7,0	57,0	28,0
	no	7,0	57,0	28,0

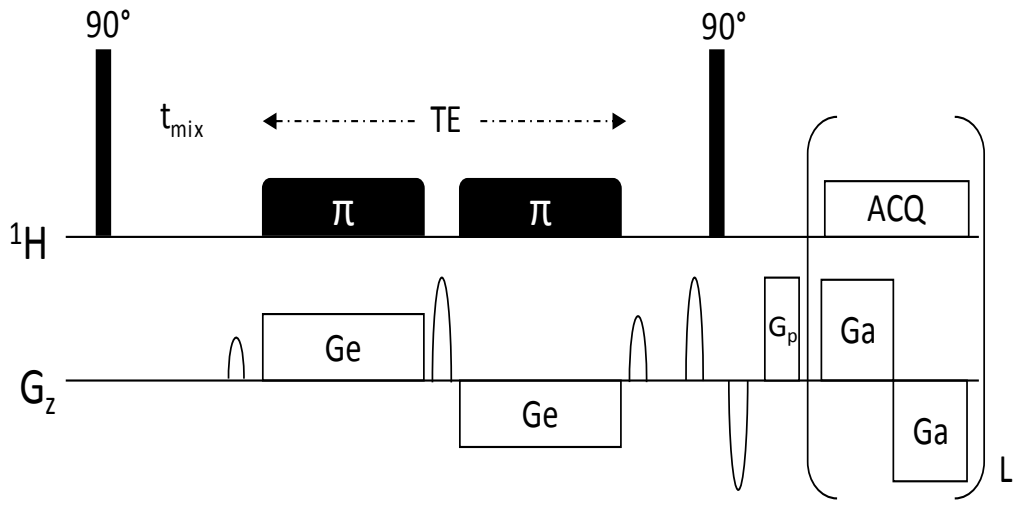

Figure S1: Pulse sequence of the Ultrafast 2D NMR experiment. The narrow filled rectangles correspond to the 90° hard pulses and the large filled boxes to the linearly frequency swept pulses. The open shaped symbols represent crushing and coherence selection gradients. TE: duration of spatial encoding; t_{mix}: delay for tuning the J-modulation effect; Ge: amplitude of spatial encoding gradients; Gp: amplitude of pre-acquisition gradient; Ga: amplitude of acquisition gradients; L: number of loops for the EPSI (Echo Planar Spectroscopic Imaging) scheme applied during the signal detection.

Principle of the home-written routine for processing Ultrafast 2D NMR data

The first step of this routine consists in splitting and rearranging the echoes detected during the successive positive/negative acquisition gradients, leading to two mirror-image S(k, t2) maps. A sine-bell apodization in the t2 dimension is applied, followed by a FT (in magnitude mode) yielding two symmetric S(k, F2) maps. These maps are then added after reversing one of them along the ultrafast dimension (i.e. along k), leading to a 2D spectrum. Finally, a Gaussian apodization in the spatially encoded domain is applied (Giraudeau & Akoka, 2011).

Prospa pulse program of UF constant-time phase-modulated COSY

```
#####################################################################
#   Ultrast Constant time phase-modulated COSY
#
#   Written by Boris Gouilleux - CEISAM - University of Nantes
#####################################################################


procedure(pulse_program,dir,mode)


# Interface description (name, label, x, y, ctrlType, varType)

   interface = ["b1Freq",      "B1 Frequency (MHz)",          "0","0",   "tbwv",   "float,[0.5,50]",
                "repTime",     "Repetition time (ms)",        "0","2",   "tbwv",   "float,[20,1e8]",
                "O1",          "Offset (Hz)",                 "0","4",   "tbwv",   "float,[-1e6,1e6]",

                "90Amplitude", "90 amplitude (dB)",           "1","0",   "tb",     "float,[-72,0]",
                "pulseLength", "Pulse length (us)",           "1","1",   "tb",     "float,[1,500]",
                "dmix",        "mixing delay (ms)",           "1","2",   "tb",     "float,[0,1000]",

                "gAmpExc",     "Excitation gradient(%)",      "2","0",   "tb",     "float,[-30,30]",
                "pulseLengthChirp",  "Pulse length chirp (us)","2","1",   "tb",     "float,[10,500000]",
                "ChirpAmplitude",    "amplitude chirp (dB)",  "2","2",   "tb",     "float,[-72,0]",
                "ChirpBandWidth",    "bandwidth chirp (kHz)", "2","3",   "tb",     "float,[0,100000]",
                "nwurst",            "Wurst power (int)",     "2","4",   "tb",     "integer,[1,100]",

                "n2",             "number of loops",          "3","0",   "tb",     "integer,[1,10000]",
                "gAmpAcq",     "Acquisition gradient(%)",     "3","1",   "tb",     "float,[-90,90]",
                "dph",          "prephasing delay (us)",      "3","2",   "tb",     "float,[-2000,2000]",
                "nprephasing",     "Gprephasing (%)",         "3","3",   "tb",     "float,[-2000,2000]",
                "nfolding",        "Gfolding (%)",            "3","4",   "tb",     "float,[-2000,2000]",

                "gAmpAcqComp",   "Acq. grad. comp",           "4","0",   "tb",     "float,[0.9,1.0]",
                "gSlopeComp",    "Slope comp",                "4","1",   "tb",     "float,[0,0.8]"
                ]

  tabs = ["Pulse sequence","Acquisition","Processing+Display","File Settings"]


# Relationships between pulse-sequence and GUI parameters
   relationships =
                     ["a1 = 90Amplitude",
                     "d1 = pulseLength",
                     "d2 = pulseLength*2",
                     "w1 = dmix*1000",

                     "d200=5.0",
                     "n200 = round(pulseLengthChirp/d200)",
                     "(t1,t2) =
UF_CT_PM_COSY:getAmpandFreqTable(b1Freq,O1,ChirpAmplitude,ChirpBandWidth,n200,
nwurst)",
                     "n11a = 0",
                     "d300 = 2",
                     "gradRamp = 200",
                     "gAmpExc = gAmpExc*0.01",
                     "gAmpAcq = gAmpAcq*0.01",
                     "nprephasing = nprephasing*0.01",
                     "nfolding = nfolding*0.01",
                     "n300 = round(gradRamp/d300)",
                     "n12e =  round(gAmpExc*32768)",
                     "n12a =  round(gAmpAcq*32768)",
                     "n12aMinus = -n12a",
                     "n12eMinus = -n12e",
                     "n12prephasing = round(nprephasing*32768)",
                     "n12folding = round(nfolding*32768)",
                     "n12c = round(0.65*32768)",
                     "n12cMinus = -n12c",
                     "n12ctp = round(0.80*32768)",
                     "n12ctpMinus = -n12ctp",
```

```
                    "n1 = nrPnts",
                    "totPnts = 2*n2*nrPnts",
                    "totTime = acqTime",
                    "d55 = acqTime*1000 + rxLat+50",
                    "d54 = d55/2+dph",
                    "t9 =
UFCosyBen:getGradAcqTable(n2,gAmpAcq,gAmpAcqComp,gSlopeComp)"
                     ]

# These parameters will be changed between experiments
   variables = [""]

# x and y spacing between controls
   dim = [155,26]

# Pulse sequence

   initpp(dir) # Reset internal parameter list

   #CT-spatial encoding by double spin-echo

   pulse(mode,a1,p1,d1)

   wait(w1)

   gradramp(n11a,n12c,n300,d300)
   delay(800)                        #crusher
   gradramp(n12c,n11a,n300,d300)

   gradramp(n11a,n12e,n300,d300)
   chirprf(mode,t1,t2,p2,n200,d200) # combine positive gradient + 180 chirp
   gradramp(n12e,n11a,n300,d300)

   delay(20)

   gradramp(n11a,n12c,n300,d300)
   delay(1200)                        #crusher
   gradramp(n12c,n11a,n300,d300)

   gradramp(n11a,n12eMinus,n300,d300)
   chirprf(mode,t1,t2,p2,n200,d200)   # combine negative gradient + 180 chirp
   gradramp(n12eMinus,n11a,n300,d300)

   gradramp(n11a,n12c,n300,d300)
   delay(400)                         #crusher
   gradramp(n12c,n11a,n300,d300)

   delay(20)

   #Mixing period

   gradramp(n11a,n12folding,n300,d300)
   delay(d54)                           #folding gradient
   gradramp(n12folding,n11a,n300,d300)

   gradramp(n11a,n12ctp,n300,d300)
   delay(1200)                         #CTP gradient performed by gradient coil
   gradramp(n12ctp,n11a,n300,d300)

   pulse(mode,a1,p3,d1)                  # mixing 90

   gradramp(n11a,n12ctpMinus,n300,d300)
   delay(1200)                         #CTP gradient performed by gradient coil
   gradramp(n12ctpMinus,n11a,n300,d300)

   gradramp(n11a,n12prephasing,n300,d300)
   delay(d54)                             #prephasing gradient
   gradramp(n12prephasing,n11a,n300,d300)
```

```
   #Acquisition performed by EPI block

   setindex(t9,0)
   loop(l1,n2)
   gradramp(n11a,n12a,n300,d300)
   acquire("append",n1,d55)
   gradramp(n12a,n11a,n300,d300)
   delay(200)
   gradramp(n11a,t9,n300,d300)
   acquire("append",n1,d55)
   gradramp(t9,n11a,n300,d300)
   delay(200)

   incindex(t9)

  endloop(l1)

### WARNING: DO NOT DELETE THE FOLLOWING LINE ########

gradoff() # set to zero value the current in gradient coil.
          # Include this line in all pulse sequences

   lst = endpp() # Return parameter list


# Phase cycle
   phaseList = [0,1,2,3; # 90 phase
                0,0,0,0; # chirp phase
                0,0,0,0; # 90 phase mixing
                0,1,2,3] # Acquire phase


endproc(lst,tabs,interface,relationships,variables,dim,phaseList)
```

Prospa procedure to generate WURST Chirp pulses

```
procedure(getAmpandFreqTable,b1Freq,O1,ChirpAmplitude,ChirpBandWidth,n200,nwurst)


fOut  = matrix(2*n200)
fInsingle = matrix(n200)

for k = 0 to 2*n200-1 step 2

    fIn = (b1Freq+O1/10^6d)+ (k-n200)/(2*n200)*ChirpBandWidth/10^3d

 if k == 2*n200-2
   fIn = (b1Freq+O1/10^6d)
 endif

    fInsingle[k/2] = single(fIn)

    DDSFword = round((fIn * 2^32d )/1000d)

    fOut[k]  = single((DDSFword & 0xFFFF0000)/(2^16)) # DDS freq
    fOut[k+1] = single(DDSFword & 0x0000FFFF)

next k

ampOut = matrix(n200)
ampOut = ampOut + 1*keaRun:convertTxGain(ChirpAmplitude)

x=[-0.5:(1/n200):(0.5-1/n200)]
nw=50
wurst = 1-abs((sin(pi*x))^nw)
ampOut = ampOut.*wurst

ampOut[n200-1] = 0
```

Prospa procedure for gradient offset compensation

```
procedure(getGradAcqTable,n2,gAmpAcq,gAmpComp,gSlopeComp)

taux = [0:1:n2-1]/(n2-1)

tsqrt = sqrt(taux)*n2*gSlopeComp


tOut=matrix(n2)
tOut = tOut - round(gAmpComp*0.01*gAmpAcq*32768) + tsqrt

(y,x) = max(tOut)
if(mag(y)>=32000); message

endproc(tOut
```

Prospa routine to automatically process and to display UF data

```
procedure(processing,guipar,plotting)

assignlist(guipar)

      Ta=totTime/1000 # in s
      scan=nrScans
      Ga_per=gAmpAcq     #acquisition gradient percentage
      Tchirp=pulseLengthChirp/1000000   #in s

      curplot("1d",1,1)
      (t,sumData)=getplotdata("1d")

      multiplot("1d",3,1)
      curplot("1d",1,1)
      plot(sumData)

      sumData=sumData*scan
      pr size(sumData)

      1dzfFactor=4 #factor of zero filling in the conventionnal dim (1)
      2dzfFactor=2 #factor of zero filling in the uf dim (2)
      SI1=n2*1dzfFactor #number of points in the conventional dim (1)
      SI2=nrPnts*2dzfFactor #number of points in the uf dim (2)


      #Fourier Transform of FID in order to filter the profile
      gradProfile  = ft(sumData)
      pr totPnts
      #filterGate
      filterGate = matrix(totPnts)
      profileBandwidth = 22000
      filterGate[(totPnts
profileBandwidth)/2:(totPnts+profileBandwidth)/2]=1
      gradProfile = gradProfile.*filterGate

      #Gaussian apodization
      x=[0:1:totPnts-1]
      p1=totPnts/2
      p2=0.00015                                  #tune UF apodisation
      gaussianFlt=exp(-(x-p1)^2*p2^2)
      gradProfile = gradProfile.*gaussianFlt

      #Inversed fourrier transform with zero filling of UF dim
      sumData = ift(zerofill(gradProfile,2*n2*SI2,"sides"))


      if(plotting=="yes")
      curplot("1d",2,1)
      plot(filterGate)
      hold("on")
      plot(gaussianFlt)
      curplot("1d",3,1)
      plot(gradProfile)
      endif

      #Building (k,t2) maps
      evenEcho = cmatrix(n2,SI2)
```

```
      oddEcho = cmatrix(n2,SI2)

      for k = 0 to n2-1
         for q = 0 to SI2-1
            evenEcho[k,q] = sumData[(2*k)  *SI2+q]
            oddEcho[k,q]  = sumData[(2*k+1)*SI2+q]
         next q
      next k

      # Reverse odd echos matrix
       oddEcho = reflect(oddEcho,"horiz")

assign("oddEcho",oddEcho,"global")
assign("evenEcho",evenEcho,"global")


      #Correction Ga/-Ga offset

      evenProj = submatrix(cumsum(mag(evenEcho),"x"),0,0,0,SI2-1)
      oddProj = submatrix(cumsum(mag(oddEcho),"x"),0,0,0,SI2-1)
      (evenMax,x,evenPos) = max(evenProj)
      (oddMax,x,oddPos) = max(oddProj)
      offset = evenPos-oddPos
      ref=50
      ref_min=ref-10
      ref_max=ref+10

      pr "The index of maximum of even sum-projection = $evenPos$\n"
      pr "The index of maximum of odd sum-projection = $oddPos$\n"
      pr "Index Offset between odd/even maps = $offset$\n"

      if(offset > ref_min & offset < ref_max)
      delta=offset
      pr "Odd versus Even shift within the standard range \nshift of
$offset$ index \n"
      else
      delta=ref
      pr "Odd versus Even shift out of range\nreference shift $ref$ is
therefore used \n"
      endif

      # FT 2D parameters and apodization along the Fourier dimension
      2dfltr = "none"
      1dfltr = "sinebell"
      2dft = "none"
      1dft = "FTEcho"
      magnitude = "yes"

      fft:2d("oddEcho","oddFT",SI1,SI2,1dfltr,2dfltr,1dft,2dft,magnitude)
      fft:2d("evenEcho","evenFT",SI1,SI2,1dfltr,2dfltr,1dft,2dft,magnitude)
      oddFT=eval("oddFT")
      evenFT=eval("evenFT")

      spec2DAll = evenFT+shift(oddFT,0,delta)
      spec2DAll = trans(spec2DAll)
      spec2DAll = reflect(spec2DAll,"vert")
      Echo = trans(Echo)
      Echo = reflect(Echo,"vert")

      Ga=Ga_per*0.16
      SWuf=(2.67e8*Ga*Ta*0.005)/(2*3.14*4*Tchirp)
```

```
       SWuf=SWuf/(b1Freq+(O1*1e-6))
       pr "SWuf=$SWuf$\n"
       SWconv = (1 / (2*Ta)) / (b1Freq+(O1*1e-6))
       pr "SWconv=$SWconv$\n"

       axis1=[0, SWuf]
       axis2=[0, SWconv]

      if(plotting=="yes")
       multiplot("2d",1,2)
       curplot("2d",1,1)
       image(spec2DAll,axis1,axis1)
       contour(15,2)
       draw2d("true")
       curplot("2d",2,1)
       image(mag(Echo))
       endif

endproc(Echo,spec2DAll,axis1,axis2)
```

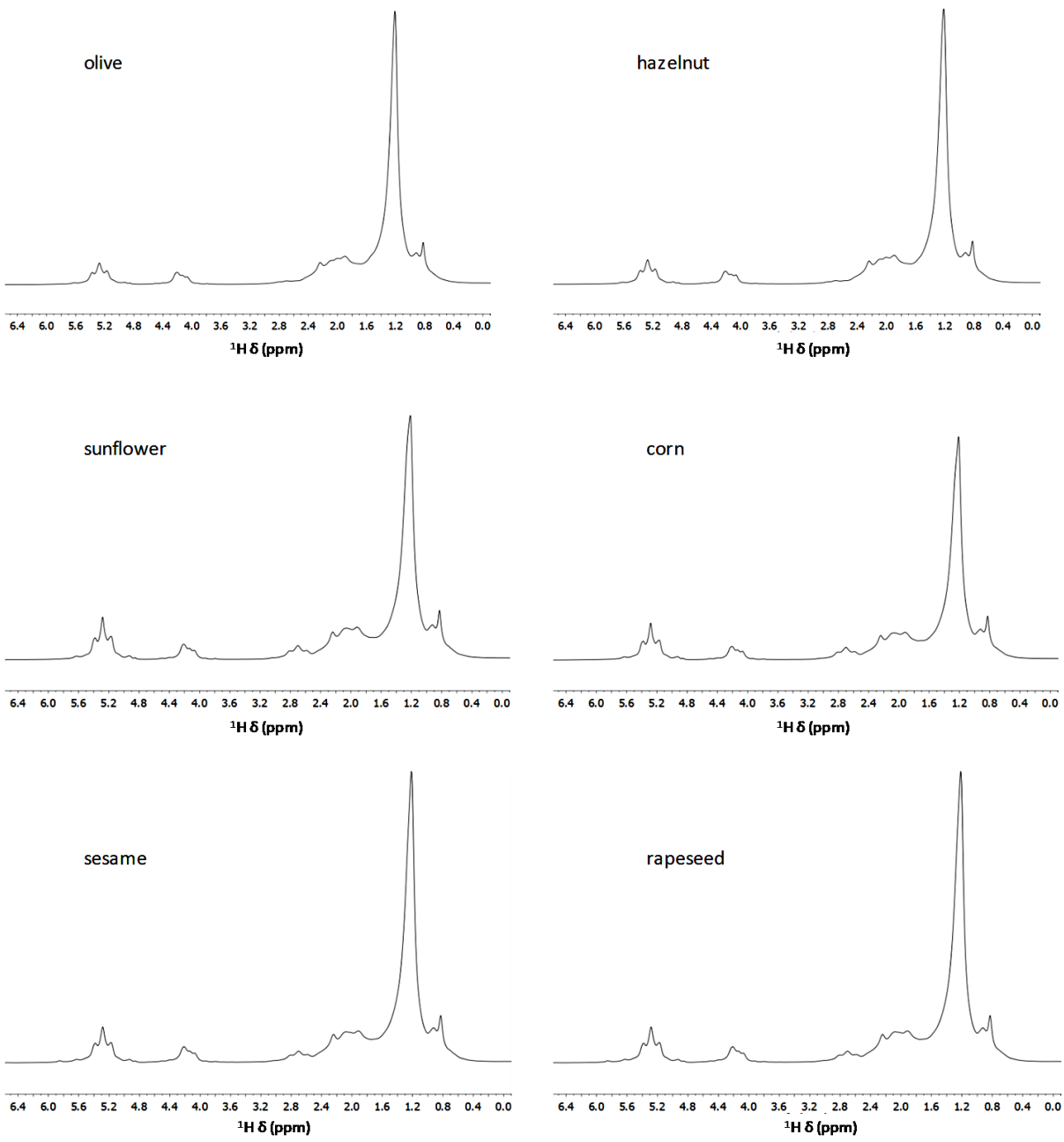

Figure S2. 1D ^{1}H NMR spectra of different types of vegetable oils recorded at 43 MHz with parameters and processing described in section 2.4.

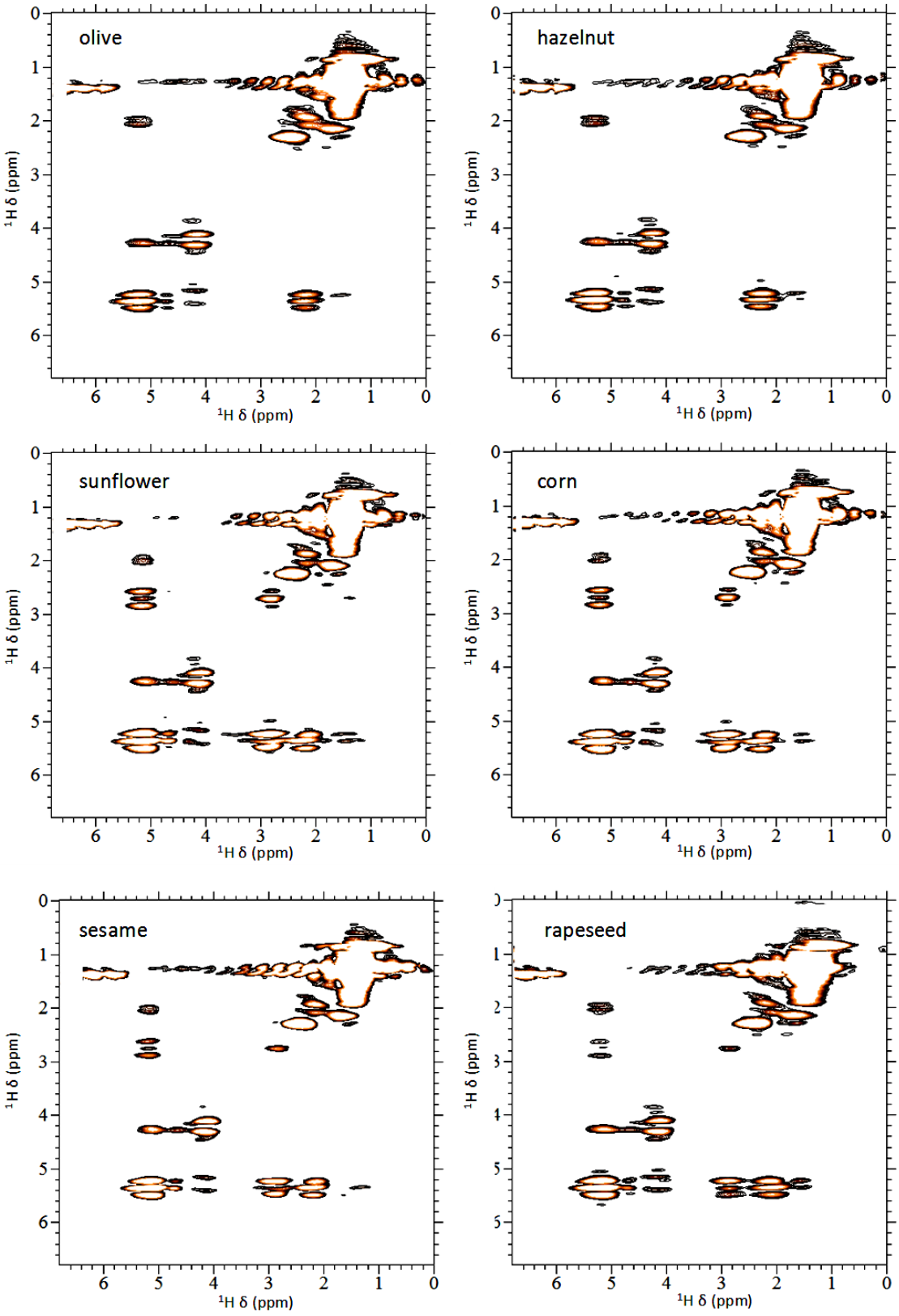

Figure S3. UF COSY spectra of different varieties of vegetable oils recorded at 43 MHz in 2.4 min. Parameters are given in section 2.5.

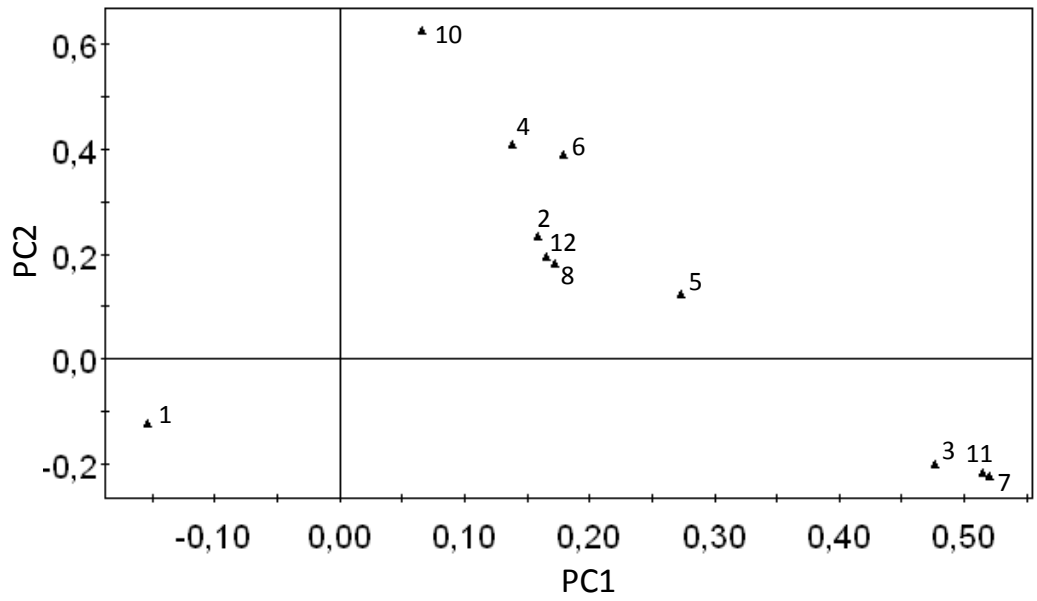

Figure S.4. Loading plot of the PCA analysis carried out with the UF COSY data.

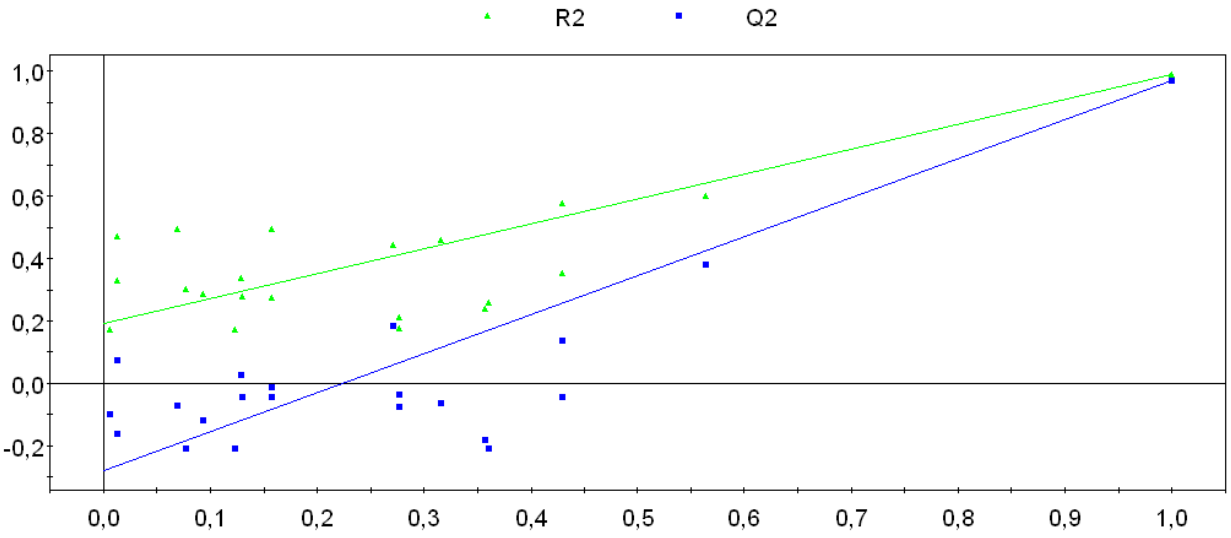

Figure S5: Validation of the PLS model by a 20-permutation test. R^2 (green) and Q^2 (blue) scores yielded for each permutation are displayed. R^2 and Q^2 intercepts are 0.193 and –0.279 respectively.

References

Giraudeau, P., & Akoka, S. (2011). Sensitivity and lineshape improvement in ultrafast 2D NMR by optimized apodization in the spatially encoded dimension. *Magn. Reson. Chem., 49*, 307-313.

General conclusion and perspectives

The driving force of this thesis has been to improve the current analytical performance of benchtop NMR through the implementation of gradient-based methods on a 43 MHz compact NMR spectrometer equipped with a gradient coil.

A first methodological development has been related to UF 2D NMR, capable of delivering a whole 2D spectra in single or at most a few scans. A theoretical study of this spatially encoded experiment has led to J-controlled UF 2D NMR, which enables a sensitivity enhancement of UF COSY in a variety of situations. This optimization is suitable for all UF sequence based on a constant time spatial encoding. In this vein, a similar work has been achieved to yield a sensitivity-optimized UF DQS that has proved to a relevant tool for quantitative 2D applications. Furthermore, it is possible to take advantage of the J-modulation effect to measure accurately tiny J-coupling constants. Such an approach has enabled sub-Hertz measurements of $J_{Li\text{-}Li}$ from lithium aggregates by recording a series of UF COSY experiments performed with different encoding times.

Following these developments, UF 2D NMR has been then implemented at low-field. Departing from the first ultrafast 2D spectrum obtained at 43 MHz, a significant effort has been geared towards the improvement of the line-shape and the sensitivity. As a result, analytical evaluations have highlighted the high performance of the method in terms of repeatability and linearity. These analytical properties form an interesting starting point for benchtop NMR applications.

In collaboration with organic chemists, the monitoring of a Pd-catalytic reaction has been carried out through UF COSY experiments in different manners: either directly inside the NMR tube or within a bypass system where UF data have been collected in a continuous flow mode. The robustness of the hardware has made it possible to acquire series of UF experiments without appreciable decrease of the performance. Obviously, the inherent low sensitivity of UF NMR – arising from its single-scan nature and from the need to open the receiver together with the application of readout gradients – requires signal averaging to reach a sufficient signal-to-noise-ratio. To summarize the current capabilities, UF COSY spectra recorded in 2.4

min are sufficient to probe the progress of the Pd-coupling reaction and to extract kinetic parameters with a starting concentration of 360 mM.

Besides this promising potential in reaction monitoring, UF 2D NMR at 43 MHz has been applied to the high-throughput authentication of food samples. 2D Spectra recorded in 2.4 min provide a real benefit for screening edible oils with different botanical origins compared to a 1D ^{1}H approach. Relying on a standard deviation lower than 3% for most of the 2D-peak volumes, the UF data are well-supported by chemometric tools in order to detect adulteration of olive oil.

Alongside with the potential of UF NMR, the presence of a robust and powerful gradient coil has enabled the implementation of efficient and versatile solvent suppression methods such as WET blocks or excitation sculpting. This methodological development has been consistent with practical issues encountered in benchtop NMR such as the use of non-deuterated solvents. The combination of a WET-180 preparation block with a 1D NOESY scheme provides an efficient solvent suppression in static as well as in flowing conditions. . The potential of this method has been highlighted through the in-line benchtop NMR monitoring of the neutralization of a mustard gas within a flow device. WET-180-NOESY has enabled the detection and the integration of a signal of interest, which is obscured in a standard 1D ^{1}H spectrum. Further methodological developments in the design of multi-bands selective excitations would be a relevant improvement extending the use of the WET-180-NOESY experiment for solvent exhibiting several lines.

Beyond the results described in the present manuscript, these first spatially-encoded NMR experiments on a benchtop spectrometer could open the way to a number of developments for a fast analysis of liquid-state samples, including other homo- or heteronuclear UF pulse sequences. Furthermore, the opportunity to apply pulse field gradients at LF could become a cornerstone in the implementation of valuable methods to cope with the overcrowded 1D spectra arising from mixtures or medium-sized molecules. One could think about pure-shift NMR [1, 2], which yields a helpful homonuclear decoupling leading to a high resolution enhancement. Another source of further developments relies on diffusion-based methods, which are of great assistance to discriminate different analytes within a mixture [3]. Moreover, this diffusion-based methodology could be even dramatically speeded up thanks to a spatial encoding, as recently suggested at high field [4].

In view of these perspectives, implementing a gradient coil on benchtop spectrometers is likely to become an appealing option. Present and future developments combined with the high versatility of benchtop NMR systems should also pave the way to the study of more advanced real-time processes. These include self-optimizing synthetic organic reactors [5] as well as the on-line monitoring of biochemical processes [6].

[1] K. Zangger, Pure shift NMR, Prog. Nucl. Magn. Reson. Spectrosc., 86 (2015) 1-20.
[2] L. Castañar, Pure shift 1H NMR: what is next?, Magn. Reson. Chem., 55 (2017) 47-53.
[3] C.S. Johnson Jr, Diffusion ordered nuclear magnetic resonance spectroscopy: principles and applications, Prog. Nucl. Magn. Reson. Spectrosc., 34 (1999) 203-256.
[4] L. Guduff, I. Kuprov, C. van Heijenoort, J.-N. Dumez, Spatially encoded 2D and 3D diffusion-ordered NMR spectroscopy, Chem. Commun., 53 (2017) 701-704.
[5] V. Sans, L. Porwol, V. Dragone, L. Cronin, A self optimizing synthetic organic reactor system using real-time in-line NMR spectroscopy, Chem. Sci., 6 (2015) 1258-1264.
[6] D. Kreyenschulte, E. Paciok, L. Regestein, B. Blümich, J. Büchs, Online monitoring of fermentation processes via non-invasive low-field NMR, Biotechnol. Bioeng., 112 (2015) 1810-1821.

.

Complete list of publications and communications

Journal publications

11) "Ultrafast 2D NMR: Methods and applications"

B.Gouilleux, L. Rouger and P. Giraudeau

Accepted to Annu. Rep. NMR Spectrosc.

10) "High-throughput authentication of edible oils with benchtop ultrafast 2D NMR"

B. Gouilleux, J. Marchand, B. Charrier, G. S. Remaud and P. Giraudeau

Accepted to Food Chem.

9) "Oxidative Neutralization of Mustard-Gas Simulants in an On-Board Flow Device with In-Line NMR Monitoring"

B. Picard, B. Gouilleux, T. Lebleu, J. Maddaluno, I. Chataigner, M. Penhoat, F.-X. Felpin, P. Giraudeau and J. Legros

Angew. Chem. Int. Ed., **2017**, 56, 7568-7572

8) "2D ^{7}Li Ultrafast CT-COSY: a new tool for the rapid measurement of tiny homonuclear lithium scalar couplings"

G. Hamdoun, B. Gouilleux, M. Sebban, G. Barozzino-Consiglio, A. Harrison-Marchand, P. Giraudeau,

J. Maddaluno and H. Oulyadi

Chem. Commun., **2017**, 53, 220-223

7) "Gradient-based solvent suppression methods on a benchtop spectrometer"

B. Gouilleux, B. Charrier, S. Akoka and P. Giraudeau

Magn. Reson. Chem., **2017**, 55, 2, 91-98

6) "Ultrafast double-quantum NMR spectroscopy with optimized sensitivity for the analysis of mixtures"

L. Rouger, B. Gouilleux, M. Pourchet-Gellez, J.-N. Dumez and P. Giraudeau

Analyst, **2016**, 141, 1686-1692.

5) "Ultrafast 2D NMR on a benchtop spectrometer: Applications and perspectives"

B. Gouilleux, B. Charrier, S. Akoka, F.-X. Felpin, M. Rodriguez-Zubiri and P. Giraudeau

TrAC Trends Anal. Chem., **2016**, 83, Part A, 65-75

4) "Ultrafast Multidimensional NMR: Principles and recent applications"

B. Gouilleux, L. Rouger and P. Giraudeau

eMagRes **2016**, 5, 913-922.

3) "Fast n-dimensional data acquisition methods"

L. Rouger, B. Gouilleux and P. Giraudeau

Encyclopedia of Spectroscopy and Spectrometry 3rd Edition (Lindon, Tranter and Koppenaal, Eds.) **2016,** DOI: 10.1016/B978-0-12-409547-2.12107-9.

2) "Real-time reaction monitoring by ultrafast 2D NMR on a benchtop spectrometer"

B. Gouilleux, B. Charrier, E. Danieli, J.-N. Dumez, S. Akoka, F.-X. Felpin, M. Rodriguez-Zubiri and P. Giraudeau

Analyst, **2015**, 140, 7854-7858.

1) "Understanding J-Modulation during Spatial Encoding for Sensitivity-Optimized Ultrafast NMR Spectroscopy"

B. Gouilleux, L. Rouger, B. Charrier, I. Kuprov, S. Akoka, J.-N. Dumez and P. Giraudeau

ChemPhysChem, **2015**, 16, 3093-3100.

Oral communications

The speaker is underlined

9) "Benchtop Ultrafast 2D NMR for high-throughput authentication of food samples"

B. Gouilleux, J. Marchand, B. Charrier, G. S. Remaud and P. Giraudeau

EUROMAR 2017, Warsaw, Poland, (July 2017)

8) "Gradient pulses on a benchtop spectrometer: new perspectives for low-field NMR"

B. Gouilleux, B. Charrier, S. Akoka, F.-X. Felpin, M. Rodriguez-Zubiri and P. Giraudeau

Journée RMN du Grand Bassin Parisien, Rennes, France (September 2016)

7) "Ultrafast NMR on a benchtop spectrometer: reaction monitoring and rapid screening"

B. Gouilleux, B. Charrier, S. Akoka, F.-X. Felpin, M. Rodriguez-Zubiri and P. Giraudeau

SMASH 2016, La Jolla, USA, (September 2016)

6) "Ultrafast 2D NMR on a benchtop spectrometer: a promising tool for on-line monitoring and rapid screening"

B. Gouilleux, B. Charrier, S. Akoka, F.-X. Felpin, M. Rodriguez-Zubiri and P. Giraudeau

EUROMAR 2016, Aarhus, Denmark, (July 2016), Wiley prize for Magnetic Resonance in Chemistry

5) "Ultrafast 2D NMR on a 43 MHz compact spectrometer"

B. Gouilleux, B. Charrier, S. Akoka, F.-X. Felpin, M. Rodriguez-Zubiri and P. Giraudeau

Journées de l'école doctorale 3MPL, Ecole des Mines de Nantes, France (June 2016)

4) "Ultrafast double-quantum NMR spectroscopy with optimized sensitivity: a new tool for the quantitative analysis of complex mixtures"

L. Rouger, B. Gouilleux, M. Pourchet-Gellez, J.-N. Dumez and P. Giraudeau

Journée RMN du Grand Bassin Parisien, Thiais, France (January 2016)

3) "J-controlled Ultrafast 2D NMR"

B. Gouilleux, L. Rouger, B. Charrier, M. Levitt, I. Kuprov, S. Akoka, J.-N. Dumez and P. Giraudeau

EUROMAR 2015, Prague, Czech Republic, (July 2015)

2) "Simulations numériques en RMN 2D ultrarapide : optimisation de la modulation-J et amélioration de la sensibilité"

B. Gouilleux, L. Rouger, B. Charrier, E. Baguet, M. Levitt, I. Kuprov, S. Akoka, J.-N. Dumez and P. Giraudeau

GERM 2015 Sète, France, (May 2015)

1) "Ultrafast double-quantum NMR spectroscopy"

A. Le Guennec, L. Rouger, B. Gouilleux, I. Kuprov, M.H. Levitt, S. Akoka, S. Caldarelli, P. Giraudeau and J.-N. Dumez

ENC, 2015, Pacific Grove, USA (April 2014)

Poster presentations

The speaker is underlined

9) "Benchtop NMR with gradients: new methods and applications"

B. Gouilleux, B. Charrier, S. Akoka, F.-X. Felpin, M. Rodriguez-Zubiri and P. Giraudeau

ENC 2017, Pacific Grove, USA (March 2017)

8) "New applications and perspectives on benchtop spectrometer equipped with a gradient coil"

B. Charrier, B. Gouilleux, S. Akoka, F-X. Felpin, M. Rodriguez-Zubiri and P. Giraudeau

GERM 2016, Lisbonne, Portugal (April 2016)

7) "Ultrafast NMR at 43 MHz: Applications and perspectives"

B. Gouilleux, B. Charrier, S. Akoka, F-X. Felpin, M. Rodriguez-Zubiri and P. Giraudeau

ENC 2016, Pittsburgh, USA (April 2016)

6) “Ultrafast Double Quantum NMR Spectroscopy with optimized sensitivity: a new tool for the quantitative analysis of complex mixtures”

L. Rouger, B. Gouilleux, M. Pourchet-Gellez, J.-N. Dumez and P. Giraudeau

ENC 2016, Pittsburgh, USA (April 2016)

5) ”Sensitivity enhancement in ultrafast NMR by optimizing J-modulation effects”

B. Gouilleux, L. Rouger, B. Charrier, M. Levitt, I. Kuprov, S. Akoka, J.-N. Dumez and P. Giraudeau

SMASH 2015, Baveno, Italy (September 2015)

4) “UF-DQS optimization through theoretical description and numerical simulations”

L. Rouger, B. Gouilleux, M. Pourchet-Gellez, I. Kuprov, M.H. Levitt, J.-N. Dumez and P. Giraudeau

SMASH 2015, Baveno, Italy (September 2015)

3) ”Amélioration de la sensibilité des expériences ultrarapides par simulations numériques”

B. Gouilleux, L. Rouger, B. Charrier, M. Levitt, I. Kuprov, S. Akoka, J.-N. Dumez and P. Giraudeau

Journées de l’école doctorale 3MPL, University of Mans, France (June 2015)

2) “Ultrafast DQS: a new tool for fast quantitative analysis in complex mixtures”

L. Rouger, B. Gouilleux, M. Pourchet-Gellez, I. Kuprov, M.H. Levitt, J.-N. Dumez and P. Giraudeau

Journées de l’école doctorale 3MPL, University of Mans, France (June 2015)

1) “Ultrafast DQS: theoretical analysis and numerical simulations”

L. Rouger, B. Gouilleux, M.H. Levitt, I. Kuprov, J.-N. Dumez and P. Giraudeau

GERM 2015 Sète, France, (May 2015)

Appendix

Appendix 1: Further applications in J-controlled UF 2D NMR

Appendix 2: Prospa pulse program of UF CT PM COSY

Appendix 3: Prospa procedure to generate WURST Chirp pulses

Appendix 4: Prospa procedure for gradient offset compensation

Appendix 5: Prospa routine to automatically process and to display UF data

Appendix 6: Prospa script to generate selective Gaussian pulses

Appendix 7: Prospa pulse program of WET-180-NOESY

Appendix 1: Further applications in J-controlled UF 2D NMR

Further applications arising from the control of J-modulation in UF NMR have been mentioned in section C.1.3. This work has led to two research articles presented in this appendix, in which I have contributed as second author.

The first one entitled "Ultrafast double-quantum NMR spectroscopy with optimized sensitivity for the analysis of mixtures" is based on a similar study of J-modulation to enhance the sensitivity of DQS experiments performed in a ultrafast fashion. This optimized UF DQS sequence, developed by Laetitia Rouger during her PhD thesis, enables a better peak-separation compared to its COSY counterpart since it provides a larger spectral width along the ultrafast dimension (double quantum evolution during the spatial encoding). Moreover, due to the DQ coherence transfer pathway, this experiment limits significantly the signal of uncoupled spins, which potentially leads to huge diagonal peaks in UF COSY spectra. As a result, UF DQS is an interesting analytical tool to probe samples involving severe overlaps and high dynamic ranges. The article presents both theoretical and numerical investigations of J-modulation during the spatial encoding to improve the sensitivity. Afterwards, the potential of this methodology is highlighted through the quantification of taurine in homemade and commercial energy drinks.

The second article exploits J-modulation for the accurate measurements of ^{7}Li-^{7}Li small scalar coupling constants in order to deliver structural insights of the aggregation state of n-BuLi/MeLi complexes. Such a study is an important concern in organometallic chemistry as the aggregation state impacts significantly the reactivity of these Li complexes. Usually obtained through arrayed data of constant-time 2D experiments, the ^{7}Li-^{7}Li coupling constants are hereby determined by a series of UF COSY experiments allowing a dramatic reduction of the total experiment time. Besides the relevance of this application in organic chemistry, this article shows the capability of recording UF 2D spectra with "exotic" nuclei such as ^{7}Li.

Analyst

PAPER

View Article Online
View Journal | View Issue

Cite this: *Analyst*, 2016, **141**, 1686

Ultrafast double-quantum NMR spectroscopy with optimized sensitivity for the analysis of mixtures†

Laetitia Rouger,[a,b] Boris Gouilleux,[a] Mariane Pourchet-Gellez,[a] Jean-Nicolas Dumez*[c] and Patrick Giraudeau*[a,d]

Received 13th January 2016,
Accepted 4th February 2016

DOI: 10.1039/c6an00089d

www.rsc.org/analyst

Ultrafast (UF) 2D NMR enables the acquisition of 2D spectra within a single-scan. This methodology has become a powerful analytical tool, used in a large array of applications. However, UF NMR spectroscopy still suffers from the need to compromise between sensitivity, spectral width and resolution. With the commonly used UF-COSY pulse sequence, resolution issues are compounded by the presence of strong auto-correlation signals, particularly in the case of samples with high dynamic ranges. The recently proposed concept of UF Double Quantum Spectroscopy (DQS) allows a better peak separation as it provides a lower spectral peak density. This paper presents the detailed investigation of this new NMR tool in an analytical chemistry context. Theoretical calculations and numerical simulations are used to characterize the modulation of peak intensities as a function of pulse-sequence parameters, and thus enable a significant enhancement of the sensitivity. The analytical comparison of UF-COSY and UF-DQS shows similar performances, however the ultrafast implementation of the DQS approach is found to have some sensitivity advantages over its conventional counterpart. The analytical performance of the pulse sequence is illustrated by the quantification of taurine in complex mixtures (homemade and commercial energy drinks). The results demonstrate the high potential of this experiment, which forms a valuable alternative to UF-COSY spectra when the latter are characterized by strong overlaps and high dynamic ranges.

Introduction

NMR spectroscopy is an essential analytical tool in a wide array of applications such as structure elucidation of organic or biological analytes, quantitative analysis or *in vivo* spectroscopy. Two-dimensional experiments[1,2] are particularly informative, and when associated with analytical procedures such as calibration or standard addition they become an efficient tool for the quantitative analysis of complex mixtures of small molecules.[3–7] The classic acquisition strategy of 2D NMR spectra, however, does suffer from long experiment durations. This is due to the requirement to repeat the same sub-experiment multiple times, with an incremented delay, to sample the indirect time dimension (t_1). This long experiment duration –from ten minutes to several hours– is not compatible with high-throughput analysis, the study of unstable samples or the coupling with on-flow techniques. Moreover, it makes conventional 2D NMR spectroscopy sensitive to hardware instabilities in the course of the experiment.[8] Such instabilities may lead to significant additional noise-like features, the so-called "t_1 noise", which affects the precision of quantitative analysis. This is particularly critical when the samples contain analytes whose concentrations are spread over a large range of values, as the signals of low-concentrated analytes can be hidden in the noise ridges generated by the high-concentrated ones.

Several strategies have been developed to overcome this major time limitation.[9] For example, the inter-scan delay can be optimized together with the radio-frequency (RF) pulse angles.[10] Several "non-uniform sampling" (NUS) strategies have also been proposed, which consist of collecting only a randomly selected subset of t_1 increments and use non-Fourier signal processing methods.[11–13] Other developments are based on alternatives to time encoding, such as Hadamard spectroscopy.[14,15]

A decade ago, a generic multidimensional approach was designed by Frydman and co-workers, which makes it possible to acquire 2D NMR spectra within a single scan.[16,17] In this so-called "ultrafast" (UF) method, the incremented evolution period (t_1) is replaced by a spatial encoding scheme, based on a combination of bipolar gradients and linearly frequency-

[a]*Université de Nantes, UMR CNRS 6230 CEISAM, Nantes, France. E-mail: patrick.giraudeau@univ-nantes.fr*
[b]*MFP Michelin, Clermont-Ferrand, France*
[c]*Institut de Chimie des Substances Naturelles, CNRS UPR2301, Univ. Paris-Sud, Université Paris-Saclay, Gif-sur-Yvette, France. E-mail: jeannicolas.dumez@cnrs.fr*
[d]*Institut Universitaire de France, Paris, France*

†Electronic supplementary information (ESI) available: Theory: Propagation of the density matrix, Fig. S1: β-modulation for an AMX spin system, Fig. S2: conventional "constant-time" COSY and "constant-time" DQS spectra of a metabolite mixture, Fig. S3: conventional CT-DQS pulse sequence. See DOI: 10.1039/c6an00089d

swept pulses,[18] and the acquisition is carried out with an MRI-inspired strategy.[19,20] The sensitivity and resolution of UF NMR have been significantly improved during the last decade thanks to several methodological developments, and UF NMR spectroscopy is nowadays applied in a variety of fields such as real-time monitoring, metabolomics, or coupled techniques like chromatography or dissolution dynamic nuclear polarization (DNP).[21] UF NMR has been applied recently to the quantitative analysis of complex mixtures, showing a precision and an accuracy of a few percent.[22]

In spite of its high potential, ultrafast 2D NMR still suffers from the need to compromise between sensitivity, spectral widths and resolution.[23,24] However, when the targeted applications are compatible with experiment durations of a few seconds to a few minutes, spatial-encoding-based techniques still form a valuable alternative to conventional 2D NMR. Such "hybrid" approaches remain faster than conventional experiments and address the main limitations of the UF approach. For example, the sensitivity limit of UF experiments can be pushed forward by the use of signal averaging. For a similar experiment duration, this approach is more repeatable than conventional 2D NMR.[22] In a complementary approach, the spectral widths –for a given resolution– can be increased by the use of "interleaving".[17,25]

The question of resolution is particularly acute in UF-COSY –one of the most widely used UF experiments. Indeed, the presence of intense auto-correlation ("diagonal") peaks can impede the analysis of such spectra, particularly when signals of interest are close to the diagonal, or for samples with large dynamic ranges. This limitation affects the trueness and precision of quantitative analysis, as recently highlighted in the case of plant extracts where signals from sugars are heavily overlapped.[26] The recently introduced UF-DISSECT pulse sequence leads to the acquisition of a homonuclear correlation 2D spectra, with diagonal peak suppression.[27] Multiple-quantum spectroscopy[28–32] is another valuable method to circumvent this overlap issue, as the lower density of peaks in multiple-quantum spectra leads to a better peak separation and removes the strong diagonal peaks, thus lowering the dynamic range.[33,34] Double-quantum spectroscopy (DQS) is particularly interesting for the quantitative analysis of complex mixtures, since it provides the same information as COSY while considerably reducing peak overlap.[35] Recently, the possibility to record double-quantum NMR spectra in an ultrafast fashion has been demonstrated.[36] An added benefit of UF multiple-quantum experiments is that the artifacts arising from the interleaving procedure, which can affect the quantification in cases where they overlap the peaks of interest, are fewer and weaker, with no need for specific post-processing.[25] In order to turn this UF-DQS experiment into an analytical tool, an in-depth understanding of the experiment is essential to maximize the resulting sensitivity.

In this paper, we show how the recent concept of UF-DQS can be turned into an accurate analytical approach for the quantitative analysis of mixtures. First, we exploit a combined experiment, theory and simulation approach[37] to provide a full mechanistic description of the UF-DQS pulse sequence and assess the parameters that govern its sensitivity. We then compare experimentally the sensitivity of UF-DQS to that of conventional and ultrafast methods that are currently used for quantitative 2D NMR. Finally, we assess its quantitative performance, with the quantification of taurine in a homemade and a commercial energy drink. The UF-DQS experiment emerges as a promising analytical tool for the quantitative analysis of complex mixtures.

Methods

Numerical simulations

In all simulations, a B_0 field of 9.40 T m^{-1} was considered and ideal pulses were assumed. Spatial encoding was performed by using a CT spatial encoding scheme, that is, double spin echo with smoothed chirp encoding pulses. Those pulses were defined with 1000 points, with a WURST envelope, sweeping a bandwidth of 11 kHz in 15 ms. Excitation gradients of 0.013 T m^{-1} and 0.016 T m^{-1} were applied for the alanine sample and the AMX spin system respectively. The CTP was completed as shown in Fig. 1. Acquisition gradients were fixed at 0.654 T m^{-1} for the alanine sample and 0.484 T m^{-1} for the AMX spin system. 512 points separated by a dwell time of 0.55 μs were used to compute the indirect dimension, whereas the direct one was obtained with 128 loops in the detection block. The sample length was fixed at 1.6 cm and the simulation was performed with 500 grid points in the z direction. The simulated 2D FID was processed in the same way as the experimental

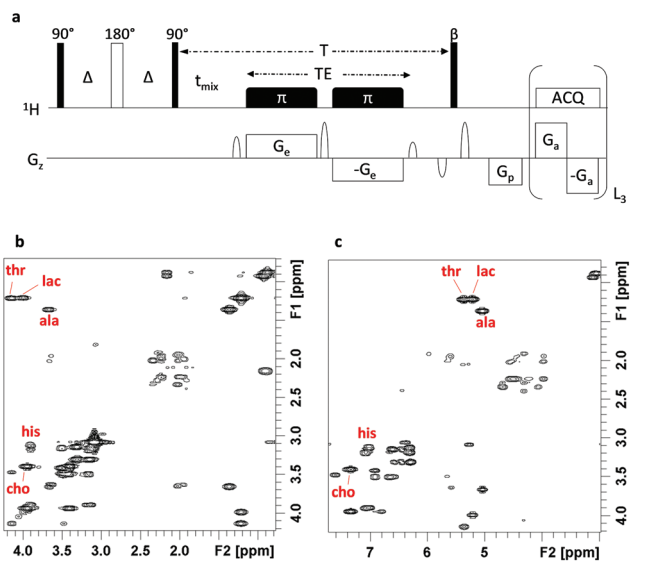

Fig. 1 (a) UF-DQS pulse sequence ($\Delta = 1/4J_{H-H}$). (b) UF-COSY and (c) UF-DQS spectra of a metabolite mixture recorded on a 700 MHz spectrometer equipped with a cryoprobe. The two spectra were recorded in four interleaved scans to increase the observable spectral width, 28 and 46 scans for UF-COSY and UF-DQS respectively, resulting in acquisition times of 10 min and 16 min, using a double-quantum buildup delay Δ = 35.7 ms.

data: a sinusoidal apodization was applied in the direct dimension and a spatial Gaussian apodization was applied in the indirect dimension.[38] Zero filling was applied in both dimensions.

Sample preparation

The experimental UF-DQS spectra of alanine (Ala, Fig. 3) were recorded on a 100 mmol L^{-1} alanine sample in D_2O. The metabolite mixture related to Fig. 1 was prepared with five metabolites: Ala, threonine (Thr), lactate (Lac), histidine (His) and choline (Cho), dissolved in a mixture of phosphate buffer (pH 7) and D_2O (2.4 mL; 37.5/62.5 v/v) leading to a concentration of 50 mmol L^{-1} for each metabolite. A stock solution of homemade energy drink (spectra shown in Fig. 4) was prepared, consisting of 41.63 mg of taurine (Tau), 434.04 mg of glucose and 644.2 mg of sucrose dissolved in 10 mL of water. Each sample used in the standard addition procedure contains 650 μL of this stock solution, 150 μL of D_2O and graded amounts of Tau (0 mg, 3.03 mg, 6.20 mg, 9.82 mg and 12.15 mg). For the standard addition procedure performed on commercial energy drink, each sample contained 650 μL of this drink, 150 μL of D_2O and graded amounts of Tau (0 mg, 3.31 mg, 6.31 mg, 9.49 mg and 12.05 mg).

NMR spectrometry

Experimental NMR spectra of the alanine sample, of the homemade and of the commercial energy drinks were recorded at 298 K on a Bruker 400 Avance I spectrometer, at a frequency of 400.13 MHz with a 5 mm dual+ $^1H/^{13}C$ probe equipped with *z*-axis gradients. NMR spectra recorded on the metabolite mixture were performed at 298 K on a Bruker Avance III spectrometer equipped with a cryogenic probe $^1H/^{13}C$ and *z*-axis gradients, at a frequency of 700.28 MHz.

UF experiments

For all UF experiments, spatial encoding was performed by using a CT spatial encoding scheme, that is, double spin echo with 15 ms smoothed chirp encoding pulses. The sweep range for the encoding pulses was set to 10 kHz for the Ala sample, 7 kHz for the homemade and commercial energy drinks, and 20 kHz for the metabolic mixture. The amplitude of the encoding gradients was adapted to obtain a frequency dispersion equivalent to the frequency range of the pulses: G_e = 0.012 T m^{-1}; 0.009 T m^{-1}; 0.022 T m^{-1} respectively. Coherence-selection gradients were added, flanking the reading pulse (amplitude ratios: −1 : 2 for UF-DQS and −1 : 1 for UF-COSY). The acquisition gradient parameters were set as follows: 0.646 T m^{-1} for the sample of Ala, 0.404 T m^{-1} for the homemade and commercial energy drinks and 0.325 T m^{-1} for the metabolite mixture. For all the experiments, the detecting block used 128 detection gradient pairs. The duration of acquisition gradients was T_a = 274.4 μs for the Ala sample as for homemade and commercial energy drinks, and T_a = 266.6 μs for the metabolite mixture. For UF-DQS experiments, the double-quantum buildup delay was set to $\Delta = 1/4{\cdot}J_{H-H}$ (34.5 ms for Ala and an average value of 35.7 ms for the metabolite mixture and both homemade and commercial energy drinks). UF-DQS spectra of Ala were recorded in 1 minute with 16 scans. Both UF-COSY and UF-DQS spectra of energy drinks were recorded in 4 minutes with 45 scans. All spectra of the metabolite mixture were recorded in four interleaved scans to increase the observable spectral width, with 28 and 46 scans for UF-COSY and UF-DQS respectively, resulting in acquisition times of 10 and 16 minutes equivalent to those of conventional 2D experiments (see below). The specific processing of the UF spectra was performed with Matlab by using the same method as the one described for the simulated spectra.

Conventional experiments

Conventional experiments performed on the metabolite mixture used a CT scheme, the time spent in the transverse plane being set to 34.8 ms as for UF experiments. In order to reach the desired spectral widths, COSY spectra were acquired with 93 t_1 increments, and DQS spectra with 150 t_1 increments. Other experimental parameters (CTP, spectral widths) are similar to those used in ultrafast experiments. A sinusoidal apodization was performed in both dimensions on COSY spectra, whereas a Gaussian apodization was used in both dimensions for DQS spectra.

Results and discussion

The UF-DQS pulse sequence

The pulse sequence for ultrafast double-quantum NMR is shown in Fig. 1. During the preparation period, multiple quantum coherences are generated thanks to a spin-echo block flanked by 90° pulses. The evolution consists of a "constant-time" (CT) phase-modulated spatial encoding, implemented with a pair of 180° chirp pulses applied during alternating gradients. The CT nature of this scheme is due to the identical time spent in the DQ state by all spins regardless of their position along the *z*-axis. The final "mixing" pulse converts the multiple-quantum coherence back into observable magnetization, prior to acquisition with an Echo Planar Spectroscopic Imaging (EPSI) scheme.

Double-quantum 2D spectra display pairs of correlation peaks for J-coupled spins. Fig. 1(b and c) shows examples of UF-COSY and UF-DQS spectra recorded on a model metabolite mixture. The direct dimension is displayed vertically, and the indirect one is horizontal. In the UF-COSY spectrum, single-quantum frequency offsets are measured in each dimension. In contrast, in the UF-DQS spectrum, single-quantum frequency offsets are measured in the direct dimension only, and in the indirect dimension double-quantum frequency offsets are measured, *i.e.* the sum of two offsets.

Analysis and optimization

The UF-DQS pulse sequence involves several parameters that have a subtle effect on the resulting spectra and govern in part its analytical potential. In particular, because of the "constant-time" nature of the spatial encoding block, the duration of the

evolution period, T has a strong impact on peak amplitudes and in turn sensitivity, as commonly found in UF NMR.[37,39] Here we extend the framework developed for UF-COSY to assess this influence using theory and simulation.

The case of an AMX system (*i.e.*, a system of 3 weakly coupled spins $I = 1/2$), where X is coupled to spins A and M, is of particular interest, as it is the minimal set of spins that displays a modulation of correlation-peak intensities by the J coupling interaction during the encoding period. Analytical expressions can be obtained, using a product-operator calculation, for the intensity of the correlation peaks in the double-quantum spectrum of such AMX system (details of the calculation are available in ESI†). For the peak located at $[\Omega_A; \Omega_A + \Omega_X]$, the peak intensity can be written:

$$S_{A;AX} \propto \cos(\beta/2)^2 \sin\beta \cos(\pi J_{MX} T) \quad (1)$$

where J_{MX} is the coupling constant between spins M and X. The J-dependence of DQS peaks is illustrated in Fig. 2. Using this knowledge, the duration of the evolution period, T, can be adjusted by the addition of a delay, t_{mix}, prior to the spatial encoding scheme, in order to maximize the intensity of the correlation peaks, as demonstrated in the case of UF-COSY.[37] In addition to J-modulation, eqn (1) shows the usual dependence of DQS peaks with respect to the flip angle of the final mixing pulse, β, resulting in optimal sensitivity with a 60° (resp. 120°) angle for the anti-echo (resp. echo) coherence transfer pathway. This dependence is reproduced in numerical simulations, as shown in Fig. S1.†

Analytical product-operator calculations become cumbersome when dealing with larger spin systems, and inadequate in the case of strong coupling. Numerical simulations are then an efficient approach to J-modulation. The Spinach simulation package[40] has been adapted to include the simulation of spatial encoding schemes.[37] This framework can first be assessed by comparing simulated results to analytical calculations for the AMX spin system. Fig. 2 shows an example from simulated DQS data; J-modulation can be obtained by integration of the peak volumes in simulated spectra obtained for a series of values of t_{mix}. As illustrated in Fig. 2, the effect of J-modulation matches very well with the analytical expressions obtained from theoretical calculations – simulations of beta-modulation are shown in Fig. S1.†

The results from simulations can be further validated by comparison to experimental data for a larger spin system. The example of alanine was selected here as it provides an A_3X spin system commonly encountered in small molecules. The J-modulations of the A_3X spin system from alanine (Fig. 3a and b) show a good match between experimental and simulated curves.

These results demonstrate that the numerical simulations performed with the Spinach package can be used to optimize the sensitivity of UF-DQS spectra of small molecules. As recently shown in the case of UF-COSY, predicting the effects

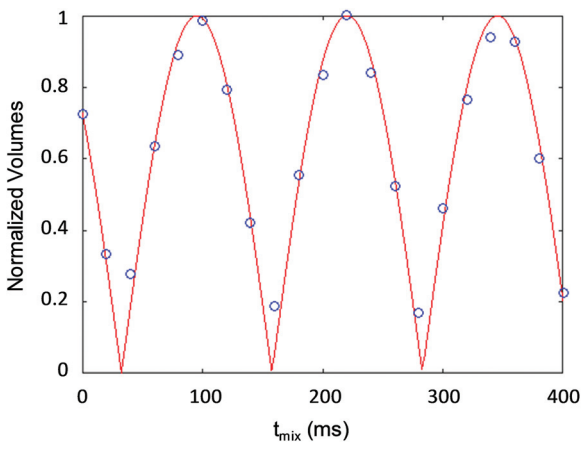

Fig. 2 Theoretical (solid line) and simulated (circles) J-modulation for an AMX spin system where spin M is coupled to spins A and X. J-modulation is studied for the peak located at $[\Omega_A; \Omega_A + \Omega_X]$. The curves are normalized to their maximum.

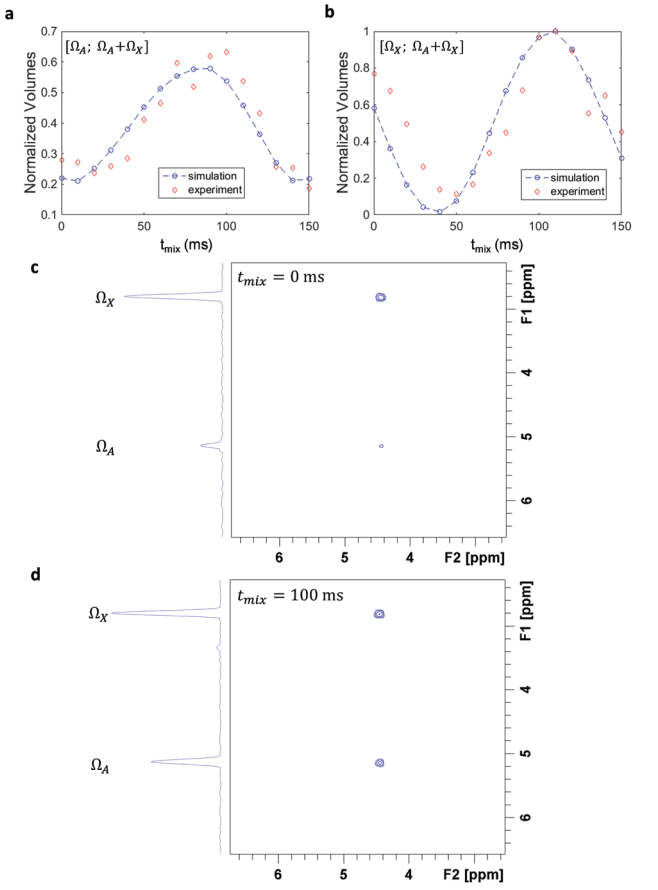

Fig. 3 Integrals of the simulated *versus* experimental signals as a function of t_{mix} for both peaks on the UF-DQS spectrum of alanine (a and b). 2D spectra and relative projections (c, d) show a significant increase in sensitivity when t_{mix} is set to the optimal value determined thanks to these J-modulation curves, *i.e.* 100 ms (d), compared to t_{mix} = 0 ms (c). All the spectra are recorded on a 400 MHz spectrometer equipped with a 5 mm dual+ $^1H/^{13}C$ probe; within 16 scans, resulting in an acquisition time of 1 min.

of J-modulation can indeed prevent unnecessary sensitivity losses.[37] Here, from the simulated and experimental J-modulation curves of the A_3X spin system from alanine, an optimum t_{mix} of 100 ms can be chosen as the best compromise between the J-modulations of the two peaks, leading to a sensitivity enhancement of about 50% for the peak located at $[\Omega_A;\Omega_A + \Omega_X]$ and 20% for the one at $[\Omega_X;\Omega_A + \Omega_X]$ (Fig. 3c and d). This significant sensitivity enhancement for both peaks allows a reduction of the limit of detection, non-negligible in the case of UF experiments for which sensitivity remains one of the major limitations.

The optimization of sensitivity for complex samples containing different spin systems will obviously require compromising between different coupling constants. An appropriate approach consists in avoiding situations in which some peaks are missing, whereas others have a maximum intensity under the influence of J-modulation effects. This strategy was recently described for UF-COSY,[37] as well as a multi-scan approach which consists in adding several spectra recorded with different t_{mix} values. These methods should be easily transposed to the case of UF-DQS.

Sensitivity considerations

The sensitivity of the UF-DQS approach should be compared to the one of related methods for quantitative 2D NMR, *i.e.* conventional DQS on the one hand, and UF-COSY on the other hand. In order to perform such comparison, UF-COSY and UF-DQS experiments and their conventional counterparts are performed on a metabolite mixture. Both UF and conventional experiments use a CT scheme. The time spent in the transverse plane is the same for all experiments, making the impact of J-modulation comparable in conventional and UF spectra. The spectral widths are identical between conventional and UF-COSY, as between conventional and UF-DQS. As the indirect spectral width is larger for DQS *vs.* COSY experiments, the two conventional approaches are compared with identical numbers of points per Hertz in the indirect dimension. For conventional experiments, it results in a longer experiment time for DQS *vs.* COSY (16 min *vs.* 10 min). UF spectra are recorded with a number of scans yielding the same overall duration as their conventional equivalent. Apodization functions are optimized to yield the best compromise between signal-to-noise ratio (SNR) and resolution, as previously described.[41] SNR measurements are performed in both direct and indirect dimensions and normalized by the root mean square of the experiment duration. The peaks considered for each metabolite in the UF spectra are indicated on Fig. 1b and c. The corresponding peaks are used in the conventional spectra (shown in ESI Fig. S2†). The DQS/COSY and UF/conventional relative sensitivity is calculated from the ratios of their respective SNR values, *i.e.* SNR^{DQS}/SNR^{COSY} and SNR^{UF}/SNR^{Conv} (Tables 1 and 2 respectively).

Considering SNR^{DQS}/SNR^{COSY} ratios, the nature of the more sensitive experiment between DQS and COSY appears to be peak dependent, both in conventional and in ultrafast experiments. This is explained in part by the different J-modulation effects in the two experiments, which were not optimized for a specific case. Still, on average no significant losses are observed using DQS, both in the conventional or UF cases. Regarding the SNR^{UF}/SNR^{Conv} ratios, the sensitivity effects are dimension-dependent. In the indirect dimension which is the limiting dimension in terms of sensitivity, SNR^{UF}/SNR^{Conv} ratios for COSY experiments show that the nature of the more sensitive experiment is peak-dependent. This is consistent with previous observations.[42]

On the contrary, for all metabolites, UF-DQS experiments appear to be more sensitive than their conventional counterparts in the indirect dimension. This feature may be explained by the large t_1-noise ridges observed on the conventional DQS spectra. In the direct dimension, conventional experiments are more sensitive, which is a well-known characteristic of UF 2D NMR.[21] Nevertheless, the sensitivity issues are mainly governed by the indirect dimension, as described recently.[42]

Overall, Tables 1 and 2 show that the sensitivity is similar for UF-COSY and UF-DQS, but that the sensitivity of UF-DQS experiments is noticeably higher than its conventional counterpart in the limiting dimension. UF-DQS appears as a powerful alternative to existing methods for the analysis of complex mixtures, especially when peak overlaps in COSY spectra prevent the accurate quantification of some analytes.

Table 1 SNR^{DQS}/SNR^{COSY} along the two dimensions of conventional (Conv.) and UF experiments, for the different metabolites observed in the spectra shown in Fig. 1

	Direct dimension		Indirect dimension	
	Conv.	UF	Conv.	UF
Thr	1.25 ± 0.13	1.05 ± 0.26	1.38 ± 0.54	2.58 ± 0.27
Lac	0.38 ± 0.09	1.67 ± 0.25	1.67 ± 0.41	3.28 ± 0.28
Ala	1.88 ± 0.11	1.06 ± 0.34	1.97 ± 0.41	2.36 ± 0.27
His	1.01 ± 0.16	0.79 ± 0.14	0.65 ± 0.22	1.08 ± 0.38
Cho	1.17 ± 0.13	0.53 ± 0.35	0.80 ± 0.22	0.78 ± 0.44

Table 2 SNR^{UF}/SNR^{conv} along the two dimensions of COSY and DQS experiments, for the different metabolites observed in the spectra shown in Fig. 1

	Direct dimension		Indirect dimension	
	COSY	DQS	COSY	DQS
Thr	0.18 ± 0.24	0.15 ± 0.16	0.78 ± 0.58	1.45 ± 0.17
Lac	0.15 ± 0.24	0.66 ± 0.13	1.38 ± 0.45	2.71 ± 0.21
Ala	0.27 ± 0.33	0.15 ± 0.13	1.72 ± 0.46	2.07 ± 0.18
His	0.25 ± 0.14	0.19 ± 0.16	0.63 ± 0.35	1.05 ± 0.27
Cho	0.62 ± 0.15	0.28 ± 0.35	5.36 ± 0.39	5.24 ± 0.30

Evaluation of the quantitative performance

In order to assess the quantitative performance of the UF-DQS approach, we consider here the quantification of taurine, a small-molecule analyte, in an energy drink. We consider both a homemade and a commercial sample; the homemade

sample of known true concentration (29.56 mM) is needed to evaluate the trueness of the quantitative method. Energy drinks usually contain highly concentrated sugars, which result in strong overlap and a high dynamic range in COSY spectra. This is illustrated in Fig. 4b for the homemade sample. The DQS approach is expected to overcome these two limitations. The UF-DQS spectrum of the homemade sample drink, shown in Fig. 4d, indeed has a lower density of peaks than the COSY spectrum and thus less overlap. In addition, the absence of auto-correlation peaks leads to a significant reduction of the dynamic range. An additional benefit is the absence, in these interleaved experiments, of artefactual "ghost" peaks.[36]

Quantification is performed here with a standard addition procedure, an approach commonly used to obtain accurate quantitative results from 2D NMR spectra.[22,35,43] The standard addition approach ensures that the trueness of the result does not depend on peak-specific parameters such as J-modulation.

Here, to ensure accurate results, all spectra are recorded in 4 minutes using 45 scans. Such signal averaging yields sufficient SNR even for the sample containing the lowest amount of taurine. The resulting standard addition curves are shown in Fig. 4c and e.

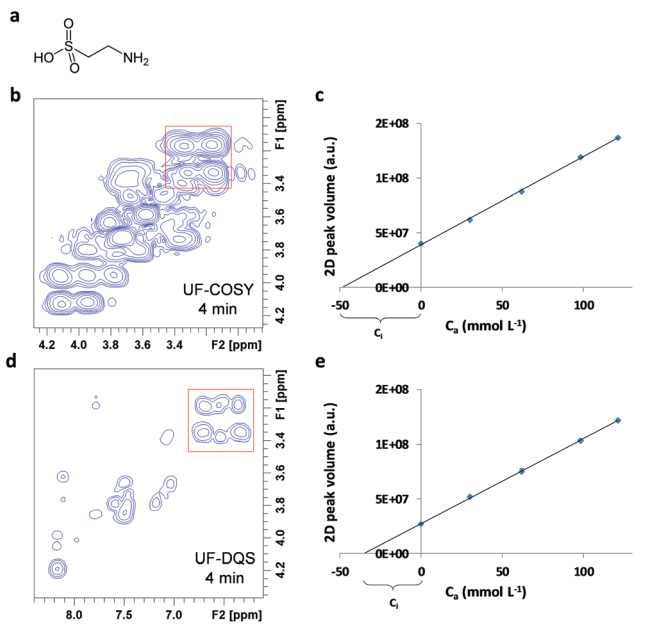

Fig. 4 Quantification of taurine (a) in a homemade energy drink by a standard addition procedure. The latter is performed using both UF-COSY –spectrum shown in (b) and corresponding standard curve in (c) – and UF-DQS experiments –spectrum shown in (d) and corresponding standard curve in (e). The 2D peak volume is plotted as a function of the added concentration C_a. C_i represents the initial taurine concentration. The signals arising from taurine are indicated in both spectra (red square). All the spectra are recorded on a 400 MHz spectrometer equipped with a 5 mm dual+ $^{1}H/^{13}C$ probe; within 45 scans, resulting in an acquisition time of 4 min, thus allowing a sufficient SNR for quantification even for the sample containing the lowest amount of taurine.

Table 3 Analytical properties of UF-COSY and UF-DQS pulse sequences in the quantification of taurine in a homemade energy drink by a standard addition procedure. True concentration in taurine: 29.56 mM

	UF-COSY	UF-DQS
Linearity (R^2)	0.9991	0.9998
Precision (RSD)	0.82%	2.09%
Trueness ($[tau]_{calc}$)	47.52 mM	29.96 mM
Error	60.8%	1.4%

The analytical properties –linearity, precision and trueness– of the UF-DQS pulse sequence are compared to those obtained from UF-COSY in Table 3.

Even though a good linearity and precision are obtained for both sequences, the trueness of the method is far better using the UF-DQS pulse sequence than UF-COSY. The high error on the determination of concentration in UF-COSY is a clear sign of bias, which is most likely explained by the strong overlap between the signals of interest and the neighbouring peaks from glucose (Fig. 4b). On the contrary, these peaks do not overlap with the taurine signals on the UF-DQS spectrum (Fig. 4d) thanks to the spectral simplification obtained through double-quantum spectroscopy, leading to a strong reduction of the error on concentration (1.4%).

The same procedure is performed on the commercial energy drink RedBull. The indicative value of concentration in taurine given by the supplier is 32.2 mM. By the use of UF-DQS, the calculated concentration (27.88 mM) is close to this indicative value, whereas by the use of UF-COSY the calculated concentration reaches 52.17 mM. These results are in agreement with the discrepancies in terms of trueness between UF-COSY and UF-DQS determined by the study of our homemade energy drink.

These results highlight the usefulness of the UF-DQS pulse sequence for cases where UF-COSY spectra are characterized by high dynamic ranges and strong overlaps.

Conclusions

The detailed characterization of the recently introduced UF-DQS NMR methods provides an in-depth understanding of its properties and a clear illustration of its analytical potential. Theory and simulation studies make it possible to fine-tune experimental parameters: t_{mix}, the delay placed prior to the spatial encoding step, and β, the angle achieved by the mixing pulse. As we demonstrate in the case of an example small-molecule, these optimizations can lead to a significant enhancement of the sensitivity of UF-DQS experiments, thus lowering the limit of detection.

Sensitivity considerations and evaluation of the analytical performance show comparable results between UF-COSY and UF-DQS, however the latter appear to be far more sensitive than its conventional counterpart in the indirect dimension which governs the sensitivity limitations.

As illustrated by the quantification of taurine in energy drinks by a standard addition procedure, the UF-DQS experiment yields more accurate results than UF-COSY (one of the most widely used ultrafast pulse sequences) in cases of high dynamic ranges and overlaps in the UF-COSY spectrum, thanks to the absence of auto-correlation peaks and lower density of peaks in this type of spectra. UF-DQS is thus expected to become a useful component of the NMR toolbox for the analysis of complex mixtures.

Acknowledgements

We warmly thank Prof. Malcolm H. Levitt and Dr. Ilya Kuprov (University of Southampton) for fruitful discussions. We also acknowledge Michel Giraudeau for linguistic assistance.

Notes and references

1 J. Jeener, *Lecture presented at Ampere International Summer School II*, Basko Polje, Yugoslavia, 1971.
2 W. P. Aue, E. Bartholdi and R. R. Ernst, *J. Chem. Phys.*, 1976, **64**, 2229–2246.
3 I. A. Lewis, S. C. Schommer, B. Hodis, K. A. Robb, M. Tonelli, W. Westler, M. Sussman and J. L. Markley, *Anal. Chem.*, 2007, **79**, 9385–9390.
4 K. Hu, T. P. Wyche, T. S. Bugni and J. L. Markley, *J. Nat. Prod.*, 2011, **74**, 2295–2298.
5 P. Giraudeau, *Magn. Reson. Chem.*, 2014, **52**, 259–272.
6 P. Giraudeau and S. Akoka, *Adv. Bot. Res.*, 2013, **67**, 99–158.
7 K. Bingol and R. Brüschweiler, *Anal. Chem.*, 2014, **86**, 47–57.
8 G. A. Morris, *J. Magn. Reson.*, 1992, **100**, 316–328.
9 L. Rouger, B. Gouilleux and P. Giraudeau, in *Encyclopedia of Spectroscopy and Spectrometry*, ed. J. C. Lindon, G. E. Tranter and D. Koppenaal, Elsevier, 3rd edn., 2016, in press, DOI: 10.1016/B978-0-12-409547-2.12107-9.
10 P. Schanda and B. Brutscher, *J. Am. Chem. Soc.*, 2005, **127**, 8014–8015.
11 A. S. Stern, K.-B. Li and J. C. Hoch, *J. Am. Chem. Soc.*, 2002, **124**, 1982–1993.
12 H. Barkhuijsen, R. De Beer, W. M. M. J. Bovée and D. Van Ormondt, *J. Magn. Reson.*, 1985, **61**, 465–481.
13 J. C. Hoch, *J. Magn. Reson.*, 1985, **64**, 436–440.
14 E. Kupce and R. Freeman, *J. Magn. Reson.*, 2003, **162**, 158–165.
15 E. Kupce and R. Freeman, *J. Magn. Reson.*, 2003, **162**, 300–310.
16 L. Frydman, T. Scherf and A. Lupulescu, *Prod. Natl. Acad. Sci. U. S. A.*, 2002, **99**, 15858–15862.
17 L. Frydman, A. Lupulescu and T. Scherf, *J. Am. Chem. Soc.*, 2003, **125**, 9204–9217.
18 Y. Shrot and L. Frydman, *J. Chem. Phys.*, 2008, **128**, 052209.
19 P. Mansfield, *J. Phys. C: Solid State Phys.*, 1977, **10**, 55–58.
20 A. Tal and L. Frydman, *Prog. Nucl. Magn. Reson. Spectrosc.*, 2010, **57**, 241–292.
21 P. Giraudeau and L. Frydman, *Annu. Rev. Anal. Chem.*, 2014, **7**, 129–161.
22 A. Le Guennec, I. Tea, I. Antheaume, E. Martineau, B. Charrier, M. Pathan, S. Akoka and P. Giraudeau, *Anal. Chem.*, 2012, **84**, 10831–10837.
23 Y. Shrot and L. Frydman, *J. Chem. Phys.*, 2009, **131**, 224516.
24 P. Pelupessy, L. Duma and G. Bodenhausen, *J. Magn. Reson.*, 2008, **194**, 169–174.
25 L. Rouger, B. Charrier, M. Pathan, S. Akoka and P. Giraudeau, *J. Magn. Reson.*, 2014, **238**, 87–93.
26 T. Jézéquel, C. Deborde, M. Maucourt, V. Zhendre, A. Moing and P. Giraudeau, *Metabolomics*, 2015, **11**, 1231–1242.
27 A. Banerjee and N. Chandrakumar, *J. Chem. Phys.*, 2014, **140**, 231103.
28 A. Wokaun and R. R. Ernst, *Mol. Phys.*, 1979, **38**, 1579–1601.
29 A. Wokaun and R. R. Ernst, *Chem. Phys. Lett.*, 1977, **52**, 407–412.
30 G. Bodenhausen, *Prog. Nucl. Magn. Reson. Spectrosc.*, 1980, **14**, 137–173.
31 T. J. Norwood, *Prog. Nucl. Magn. Reson. Spectrosc.*, 1992, **24**, 295–375.
32 L. Braunschweiler, G. Bodenhausen and R. R. Ernst, *Mol. Phys.*, 1983, **48**, 535–560.
33 G. N. Manjunatha Reddy and S. Caldarelli, *Anal. Chem.*, 2010, **82**, 3266–3269.
34 B. Baishya and N. Suryaprakash, *J. Phys. Chem. A*, 2007, **111**, 5211–5217.
35 E. Martineau, I. Tea, S. Akoka and P. Giraudeau, *NMR Biomed.*, 2012, **25**, 985–992.
36 A. Le Guennec, P. Giraudeau, S. Caldarelli and J.-N. Dumez, *Chem. Commun.*, 2015, **51**, 354–357.
37 B. Gouilleux, L. Rouger, B. Charrier, I. Kuprov, S. Akoka, J.-N. Dumez and P. Giraudeau, *ChemPhysChem*, 2015, **16**, 3093–3100.
38 P. Giraudeau and S. Akoka, *Magn. Reson. Chem.*, 2011, **49**, 307–313.
39 C. Wu, M. Zhao, S. Cai, Y. Lin and Z. Chen, *J. Magn. Reson.*, 2010, **204**, 82–90.
40 H. J. Hogben, M. Krzystyniak, G. T. P. Charnock, P. J. Hore and I. Kuprov, *J. Magn. Reson.*, 2011, **208**, 179–194.
41 E. Martineau, P. Giraudeau, I. Tea and S. Akoka, *J. Pharm. Biomed. Anal.*, 2011, **54**, 252–257.
42 M. Pathan, S. Akoka, I. Tea, B. Charrier and P. Giraudeau, *Analyst*, 2011, **136**, 3157–3163.
43 P. Giraudeau, *Magn. Reson. Chem.*, 2014, **52**, 259–272.

ChemComm

COMMUNICATION

View Article Online
View Journal | View Issue

Cite this: *Chem. Commun.*, 2017, 53, 220

Received 31st October 2016,
Accepted 28th November 2016

DOI: 10.1039/c6cc08744b

www.rsc.org/chemcomm

2D ^{7}Li Ultrafast CT-COSY: a new tool for the rapid measurement of tiny homonuclear lithium scalar couplings†

G. Hamdoun,[a] B. Gouilleux,[b] M. Sebban,[a] G. Barozzino-Consiglio,[a] A. Harrison-Marchand,[a] P. Giraudeau,[bc] J. Maddaluno[a] and H. Oulyadi*[a]

The measurement of small homonuclear $^{2}J_{^{7}Li-^{7}Li}$ scalar couplings relying on constant time (CT) COSY NMR suffers from strong time limitations. We describe the first Ultrafast CT COSY experiment on lithium 7, which provides a considerable acceleration in the study of the aggregation state and dynamics of *n*-BuLi/MeLi complexes.

Because they behave as both versatile bases and potent nucleophiles, organolithium derivatives are regarded as routine reagents in organic synthesis. However, these highly polar species tend to oligomerize in solution to form flexible aggregates of which reactivity can vary significantly and interfere with the envisaged applications. Practically, chemists seldom check the aggregation state of their reagents before handling because accessing this information is perceived as complex and tedious. Thus, organolithium reagents are employed, in most cases, empirically and their behaviour is seen as a black box requiring multiple experiments, fine-tuning of the reaction conditions and, often, unexplained addition of metallic salts of various kinds.

High-resolution NMR spectroscopy is the technique most frequently used to characterize the structures of organolithium derivatives directly in solution.[1–8] This analysis gives a straight access to primary data such as the spin–spin[6,7] Li–X (X: ^{13}C, ^{15}N) coupling constant and the multiplicity of the X nucleus,[9–15] affording valuable clues about the structure of the aggregates adopted by the R–Li systems in solution. However, when lithium derivatives such as ^{15}N unlabelled lithium amides, lithium alkoxides or lithium enolates are at stake, the multiplicity of nucleus X and the Li–X coupling constant are generally not observed, and the information provided by all conventional NMR experiments remains insufficient to conclude about the structure and aggregation of these compounds. In this context, that is not uncommon, a simple access to homonuclear Li–Li couplings becomes of fundamental importance.[4]

In practice, the identification of the ^{6}Li homonuclear scalar coupling has been resolved in a conventional 1D ^{6}Li NMR spectrum in only one case,[16] this measurement being prevented by the signal line-widths in most cases.

Among the various homonuclear 2D NMR experiments used to detect and measure scalar spin–spin coupling, one can mention the CT-COSY,[17] DQF-COSY[18] and INADEQUATE[16,19] experiments. With regards to lithium 6 nuclei, the INADEQUATE experiment is certainly the most commonly employed for ease of use and appreciable time saving in its 1D version.[4,19,20] However, measuring $^{2}J_{^{6}Li-^{6}Li}$ scalar coupling remains difficult because of line broadening due to dynamic exchanges and may result in a poor estimate of the real value of the coupling constant. Moreover, the relatively long duration of the mixing period ($1/4J$) ($\approx$1.25 s) in this experiment also causes a strong attenuation leading to an extremely poor signal-to-noise ratio.

Experiments with ^{6}Li generally profit from the smaller line-width of ^{6}Li as compared to ^{7}Li signals, but the larger ^{7}Li homonuclear couplings (factor 2.64 due to the ratio $\gamma(^{7}Li)/\gamma(^{6}Li)$) are an attractive feature of ^{7}Li experiments. Information about small ^{7}Li homonuclear scalar coupling constants can be obtained by manipulating the time evolution of scalar couplings. Typically, we recently published a study based on the CT–COSY NMR experiment, from which $^{2}J_{^{7}Li-^{7}Li}$ coupling constants were obtained using different scalar J-coupling evolution times and by fitting the signal intensity ratio as a function of this J-evolution time.[17] But the major limitation of this methodology is the long experiment time (several hours) required to record the associated arrayed 2D spectra. A long time is indeed necessary to acquire each 2D FID $s(t_1, t_2)$, due to the repetition of numerous transients with incremented delays. Moreover, this limitation is amplified by the need to record series of 2D spectra with an incremented constant-time period. The most evident consequence is the timetable constraint, but a more fundamental limitation is the sensitivity to temporal instabilities leading to noise ridges along the F_1 dimension. Moreover, the long experiment duration makes 2D NMR experiments unsuitable

[a] *Normandie Univ, UNIROUEN, INSA Rouen, CNRS, COBRA (UMR 6014 & FR 3038), 76000 Rouen, France*
[b] *CEISAM, Université de Nantes, UMR CNRS 6230, 2 rue de la Houssinière, 44322 Nantes, France*
[c] *Institut Universitaire de France, 1 rue Descartes, 75005, Paris, France*

† Electronic supplementary information (ESI) available. See DOI: 10.1039/c6cc08744b

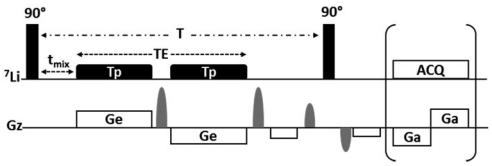

Fig. 1 Pulse sequence of UF CT-COSY. TE = duration of spatial encoding, T_p = duration of adiabatic pulse, T = total time in the transverse plane, t_{mix} = variable mixing time to tune the J-modulation, Ge = spatial encoding gradient, Ga = acquisition gradient, ACQ = acquisition. The curved grey shapes indicate coherence-selection gradients.

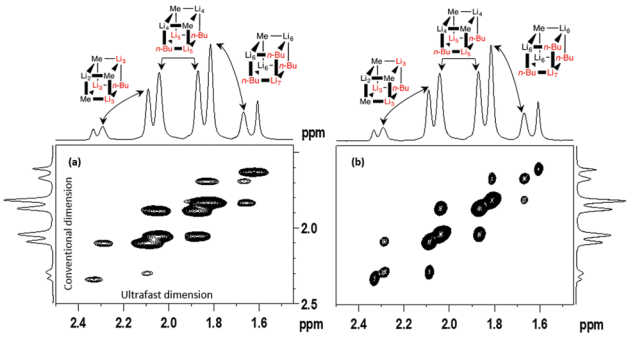

Fig. 2 (a) 2D ^{7}Li UF CT-COSY and (b) conventional 2D ^{7}Li COSY spectra obtained at 194 MHz on the 1 : 1 *n*-BuLi/MeLi solution in THF-d_8 at 185 K. The conventional spectrum was acquired with 128 t_1 increments and four scans for each FID separated by a 10 s recycling delay, involving a total time of 1 h 35 min. The Ultrafast spectrum was recorded in a single scan (0.34 s) with a spatial encoding duration TE of 100 ms.

for unstable lithiated samples that evolve during the acquisition and also require keeping the NMR probe at low temperature for extensive periods of time.

For a fast and easy measuring of $^2J_{^7Li-^7Li}$ coupling constants, Ultrafast (UF) NMR spectroscopy is an appealing alternative to reduce by several orders of magnitude the time required to carry out the 2D CT-COSY experiment.[21,22] In this method, the incrementation of the evolution period t_1 is replaced by a spatial encoding which is decoded during the detection period by an echo planar spectroscopic imaging (EPSI)[23] detection scheme (Fig. 1) allowing the acquisition of a 2D spectrum in a sub-second duration.

Over the last ten years, the performance of UF experiments has been greatly enhanced by numerous methodological developments, which have made UF NMR applicable to a wide range of analytical situations such as quantitative metabolomics[24] or real-time reaction monitoring.[25] UF NMR is characterized by specific peculiarities and limitations which have been widely described,[26] but when the sample concentration allows single-scan acquisitions, it is the fastest among the family of accelerated 2D NMR experiments.[27] The first detection of quadrupolar nuclei by UF 2D NMR has been reported very recently on the example of deuterium (I = 1),[28] but UF 2D NMR has never been exploited for nuclei with larger quadrupolar moments such as Lithium 7 (I = 3/2).

In this paper, we report on the first examples of 2D ^{7}Li UF CT-COSY spectra from lithiated samples and on the usefulness of 2D UF CT-COSY NMR experiments for the characterization and quantitative estimation of the lithium coupling constants on various complexes of *n*-BuLi/MeLi as a model mixture.

The study begins with a 1 : 1 *n*-BuLi/MeLi solution in THF-d_8 at 185 K,[29] which corresponds to typical experimental conditions for these reagents. The ^{7}Li NMR spectrum of 1 : 1 *n*-BuLi/MeLi solution in THF-d_8 at 185 K reveals the presence of eight separate signals corresponding to a statistical distribution of mixed tetramers with the following formula: $(n\text{-BuLi})_{4-n}(\text{MeLi})_n$ (with n between 0 and 4).

The assignment of the ^{7}Li signals refers to the work by F. Paté *et al.*,[30] and shows that each mixed aggregate is characterized by two signals in the ^{7}Li NMR spectrum (Fig. 2).

The ^{7}Li UF CT-COSY spectra are recorded thanks to the pulse sequence described in Fig. 1. This experiment includes a spatial encoding step achieved by a pair of linear frequency-swept pulses with a duration T_p applied together with a bipolar excitation gradient Ge, whose value is fixed to provide a dispersion in Hz equivalent to the frequency sweep of the pulses. The resulting signal is then decoded by an EPSI block consisting in a train of bipolar gradients Ga. Both power and duration of Ga are set according to the required spectral widths. Further details on acquisition and processing parameters are available in ESI.†

The resulting 2D ^{7}Li UF CT-COSY NMR spectrum (Fig. 2a) shows the same correlation peaks as those observed on the conventional one at the following (F_2; F_1) positions: 2.29 ppm and 2.09 ppm, 2.04 ppm and 1.86 ppm, 1.81 ppm and 1.67 ppm. These values are typical of a homonuclear weak scalar coupling between the lithium signals belonging to the same mixed aggregates Li_2/Li_3 $(n\text{-BuLi})_3(\text{MeLi})_1$, Li_4/Li_5 $(n\text{-BuLi})_2(\text{MeLi})_2$ and Li_6/Li_7 $(n\text{-BuLi})_1(\text{MeLi})_3$, respectively.

The resolution of the UF spectrum is lower in F_2 owing to intrinsic characteristics of spatial encoding, but is similar in F_1. The asymmetric appearance of peak intensities for correlated signals of $(n\text{-BuLi})_3(\text{MeLi})_1$ and $(n\text{-BuLi})_1(\text{MeLi})_3$ complexes on each side of the diagonal should be noted; this effect is expected because such signals undergo different J-modulation effects in A_3X spin systems as recently described by B. Gouilleux *et al.* (see below).[31] These effects also explain the missing diagonal peak in the UF spectrum.

This comparison sheds light on the great potential of this UF approach as it provides similar information while considerably reducing the experiment duration (0.34 s *versus* 1 h 35 min). This time saving is particularly relevant in this study, which requires the time-consuming acquisition of a series of 2D NMR experiments with different J-coupling evolution times. Still, specific features of the UF approach should be taken into account such as the compromise between sensitivity, spectral width and resolution. These aspects have been widely described for ^{1}H UF NMR,[32–34] and similar effects should be expected here. However, some usual limitations of UF NMR become less critical in the case of ^{7}Li. First, the impact of translational diffusion[35,36] is much reduced since the spectra are recorded at low temperature (T = 185 K). Second, the small spectral width of ^{7}Li makes the compromise between resolution and spectral width much less critical than for ^{1}H.

A significant source of sensitivity losses that the UF experiment shares with its conventional counterpart is the *J*-modulation arising from the constant-time nature of the spatial encoding step.[31] A theoretical description of this effect applied to a system of two coupled spins was already proposed by Wu *et al.*,[37] who established an expression for the density matrix at the beginning of detection, which showed a *J*-modulation that was different for the diagonal peaks (cosine modulation: $\cos((2 \times I)\cdot\pi\cdot J\cdot T)$) and cross-peaks (sine modulation: $\sin((2 \times I)\cdot\pi\cdot J\cdot T)$). This modulation – depending on the scalar coupling constant J, on the total time spent in the transverse plane T and on the nature of the spins-system – can lead to sensitivity losses and even to missing spectral peaks for samples including different spins-systems. But as described by B. Gouilleux *et al.*,[31] this *J*-modulation can also be controlled by adding a delay (t_{mix}) prior to the spatial encoding step to tune this total time $T = (TE + t_{mix})$ spent in the transverse plane. Due to the trigonometric nature of this *J*-modulation, there is an optimal T value, which maximizes the sensitivity for a given spin-system.

Here, this effect was optimized by recording a series of 2D ^{7}Li UF CT-COSY spectra on the mixture of $(n\text{-BuLi})_{4-n}(\text{MeLi})_n$ with different t_{mix} values ranging from 0 to 0.16 s (Fig. S1, ESI†). From these spectra, an optimum delay t_{mix} of 0.05 s can be chosen in order to optimize the overall sensitivity and avoid missing peaks.

Recently, we showed that the 2D CT-COSY technique in ^{7}Li observation was an excellent method to accurately measure scalar $^2J_{^7\text{Li}-^7\text{Li}}$ couplings, regardless of the complexity and resolution of the ^{7}Li NMR spectrum. The remarkable efficiency of this method for extracting small $^2J_{^7\text{Li}-^7\text{Li}}$ was demonstrated, for the first time, on a 1 : 1 *n*-BuLi/MeLi model solution in THF-d_8 with a total experimental time of $\approx$24 h.[17] Here, our aim is to test the ability of the UF CT-COSY experiment, as a constant time approach, to predict homonuclear ^{7}Li–^{7}Li scalar coupling constant in a much shorter time.

By performing a series of 2D ^{7}Li UF CT-COSY experiments with different T values and then by graphically plotting the ratio of the cross peak volumes I_c *versus* the diagonal peak volumes I_d as a function of T, it is possible to determine $^2J_{^7\text{Li}-^7\text{Li}}$ from the simulation of the experimental graph as a tangent function of eqn (1). The discontinuity in the plot of the tangent function at $T = 1/(6J_{\text{Li}-\text{Li}})$ contributes to the precision in the measurement of $^2J_{^7\text{Li}-^7\text{Li}}$.[38]

$$\frac{I_c}{I_d} = A\ \tan(3\pi J_{\text{Li}-\text{Li}} T) \qquad (1)$$

In the case of 1 : 1 *n*-BuLi/MeLi complexes, ^{7}Li–^{7}Li scalar couplings measured from the conventional 2D CT-COSY experiments were very small and discontinuities in the graph showing I_c/I_d *versus* T were attained for about 300–400 ms. Unfortunately, such constant time delays lead to large sensitivity losses in the 2D ^{7}Li UF CT-COSY spectrum and no peaks could be detected for these values. These SNR losses were attributed to the transverse relaxation effect of the lithium nuclei. This observation is consistent with experimental measurements of T_2, which show that the average lifetime of the ^{7}Li signals in the transverse plane would be around 220 ms (Table S1, ESI†).

An approach that could avoid this complication involves the incrementation of the time duration of the adiabatic pulse T_p instead of the free evolution period t_{mix}. This idea is based on recent theoretical investigations of relaxation effects in the rotating frame during adiabatic pulses.[39,40] These works revealed that the relaxation rates $R_{1\rho}$ and $R_{2\rho}$ can be significantly decreased when increasing T_p while the time-bandwidth product of the pulse remains constant.

Fig. S2 (ESI†) shows several 2D ^{7}Li UF CT-COSY spectra obtained from a solution of 1 : 1 *n*-BuLi/MeLi in THF-d_8 at 185 K with a spatial encoding delay "T_p" ranging from 50 ms to 215 ms.

While for the 2D ^{7}Li UF CT-COSY experiments with an incremented t_{mix} delay, an almost total loss of signal occurs at a time $T = (TE + t_{mix})$ around 250 ms (Fig. S1, ESI†), incrementing the length of the adiabatic pulse T_p results in a significantly enhanced lifetime in the transverse plane – greater than 440 ms (Table 1). The significant long life lithium signals due to an adiabatic pulse makes the 2D ^{7}Li UF CT-COSY experiment well suited for the measurement of very weak homonuclear Li–Li scalar coupling. Still, 64 scans were necessary to obtain a sufficient SNR for peak integration, resulting in an experiment time of about 12 min, which remains much shorter than the duration required to record the conventional spectrum (1 h 35 min).

The 2D ^{7}Li UF CT-COSY sequence was run for 15 spatial encoding adiabatic pulse delays "T_p" ranging from 50 ms to 200 ms on a 1 : 1 *n*-BuLi/MeLi solution in THF-d_8 at 185 K. 64 scans were recorded for each experiment for a total experimental time of $\approx$3 h (*versus* $\approx$24 h if a conventional experiment was used). All the 2D ^{7}Li UF CT-COSY spectra were processed with the same parameters as described previously and the resulting data (ratio of the integrals as a function of "TE") were then processed with GraphPad® software in order to obtain a graph representing the variation of the intensity ratio of the correlation peaks and diagonal peaks for the $(n\text{-BuLi})_3(\text{MeLi})_1$ and $(n\text{-BuLi})_1(\text{MeLi})_3$ tetrameric structures as a function of TE (Fig. 3). The resulting graph can be fitted to extract the active coupling for each cross-peak.

Fig. 3 shows the correlation peak to diagonal peak intensity ratio plotted against TE for the Li_6–Li_7, Li_2–Li_3 pairs. The curve is adjusted using the function $A\tan(3\pi J_{\text{Li}-\text{Li}}\text{TE})$ where A is a scaling factor to account for misrepresentation of intensities in integrals.

The derived J splittings for $(n\text{-BuLi})_3(\text{MeLi})_1$ and $(n\text{-BuLi})_1(\text{MeLi})_3$ tetramers lithium signals were 0.558 ± 0.005 Hz and 0.475 ± 0.005 Hz, respectively. These values, in perfect agreement with those obtained by the standard 2D CT-COSY method,[17] highlight the effectiveness of the 2D ^{7}Li UF CT-COSY approach, if the delay of the encoding adiabatic pulse is incremented, in the measurement of very weak ^{7}Li–^{7}Li scalar coupling, with a total experiment time divided by eight.

Table 1 Signal-to-noise ratio (SNR) and cross peak-to-diagonal peak ratio (I_c/I_d) of the $(n\text{-BuLi})_1(\text{MeLi})_3$ complex as a function of TE for the 2D ^{7}Li UF CT-COSY, acquired with variable T_p

TE (s)	0.11	0.17	0.21	0.25	0.26	0.33	0.37	0.40	0.44
I_c/I_d	0.17	0.40	0.63	1.11	2.72	2.26	0.85	0.54	0.12
SNR	2934	1484	619	400	360	226	184	120	110

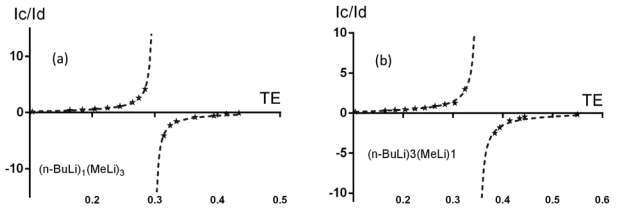

Fig. 3 Variations of integration ratios I_c/I_d as a function of TE for (a) $(n\text{-BuLi})_1(\text{MeLi})_3$, (b) $(n\text{-BuLi})_3(\text{MeLi})_1$ aggregates.

In the present work, we have demonstrated the usefulness of the UF CT-COSY experiments for the case of quadrupolar nuclei such as ^{7}Li. Moreover, it is the first time that UF experiments are performed at low temperature. Therefore, this technique can certainly be regarded as a tool worthy of being added to existing NMR toolbox for the determination of mixed-aggregates arrangements in the field of organolithium chemistry.

We have also presented a robust and fast method for the assignment and determination of homonuclear splitting in cases where scalar couplings cannot be extracted because of the signal linewidths, due to the large quadrupole moments of the ^{7}Li nucleus. Our strategy was to increment the length of the adiabatic pulse instead of the t_{mix} delay to describe modulation of signal intensities by the spin–spin J-coupling. This led to a greater lifetime of lithium signals in the transverse plane, allowing easier measurements of weak $^2J_{^7\text{Li}-^7\text{Li}}$ homonuclear couplings, as illustrated in the case of a mixed tetramers $(n\text{-BuLi})_{4-n}(\text{MeLi})_n$. This approach may still show limitations in cases where the species at hand are structurally and dynamically inhomogeneous. In this case, different cluster sizes could coexist or interconvert and some signals of interest may decrease faster than others under transverse relaxation.

Still, we believe that the 2D ^{7}Li UF CT-COSY experiment can be extended to other systems in which lithium cations are in close interaction. Work towards this goal is in progress.

This work has been partially supported by Rouen University, CNRS, INSA Rouen, ERDF and the Labex SynOrg (ANR-11-LABX-0029). We thank the Région Normandie for its support to this research through the CRUNCh network.

Notes and references

1 L. M. Seitz and T. L. Brown, *J. Am. Chem. Soc.*, 1967, **89**, 1602.
2 H. L. Lewis and T. L. Brown, *J. Am. Chem. Soc.*, 1970, **92**, 4664.
3 F. W. Wehrli, *J. Magn. Reson.*, 1978, **30**, 193.
4 H. Günther, *J. Braz. Chem. Soc.*, 1999, **10**, 241.
5 A. C. Jones, A. W. Sanders, M. J. Bevan and H. J. Reich, *J. Am. Chem. Soc.*, 2007, **129**, 3492.
6 D. Li, I. Keresztes, R. Hopson and P. G. Williard, *Acc. Chem. Res.*, 2009, **42**, 270.
7 H. J. Reich, *Chem. Rev.*, 2013, **113**, 7130.
8 A. Harrison-Marchand and F. Mongin, *Chem. Rev.*, 2013, **113**, 7470.
9 P. I. Arvidsson and Ö. Davidsson, *Angew. Chem., Int. Ed.*, 2000, **39**, 1467.
10 T. Koizumi and O. Kikuchi, *Organometallics*, 1995, **14**, 987.
11 R. D. Thomas, R. M. Jensen and T. C. Young, *Organometallics*, 1987, **6**, 565.
12 J. Granander, R. Sott and G. Hilmersson, *Chem. – Eur. J.*, 2006, **12**, 4191.
13 R. Sott, J. Granander and G. Hilmersson, *J. Am. Chem. Soc.*, 2004, **126**, 6798.
14 W. Bauer, W. R. Winchester and P. V. R. Schleyer, *Organometallics*, 1987, **6**, 2371.
15 A. Corruble, D. Davoust, S. Desjardins, C. Fressigné, C. Giessner-Prettre, A. Harrison-Marchand, H. Houte, M.-C. Lasne, J. Maddaluno, H. Oulyadi and J.-Y. Valnot, *J. Am. Chem. Soc.*, 2002, **124**, 15267.
16 O. Eppers, H. Günther, K.-D. Klein and A. Maercker, *Magn. Reson. Chem.*, 1991, **29**, 1065.
17 G. Hamdoun, M. Sebban, V. Tognetti, A. Harrison-Marchand, L. Joubert, J. Maddaluno and H. Oulyadi, *Organometallics*, 2015, **34**, 1932.
18 D. Moskau, W. Frankmölle, O. Eppers, H.-E. Mons and H. Günther, *Proc. – Indian Acad. Sci., Chem. Sci.*, 1994, **106**, 1471.
19 O. Eppers, T. Fox and H. Günther, *Helv. Chim. Acta*, 1992, **75**, 883.
20 H. Oulyadi, C. Fressigné, Y. Yuan, J. Maddaluno and A. Harrison-Marchand, *Organometallics*, 2012, **31**, 4801.
21 B. Gouilleux, L. Rouger and P. Giraudeau, *eMagRes*, 2016, **5**, 913.
22 L. Frydman, T. Scherf and A. Lupulescu, *Proc. Natl. Acad. Sci. U. S. A.*, 2002, **99**, 15858.
23 P. Mansfield, *Magn. Reson. Med.*, 1984, **1**, 370.
24 T. Jézéquel, C. Deborde, M. Maucourt, V. Zhendre, A. Moing and P. Giraudeau, *Metabolomics*, 2015, **11**, 1231.
25 A. Herrera, E. Fernández-Valle, R. Martínez-Álvarez, D. Molero-Vílchez, Z. D. Pardo-Botero and E. Sáez-Barajas, *Magn. Reson. Chem.*, 2015, **53**, 952.
26 P. Giraudeau and L. Frydman, *Annu. Rev. Anal. Chem.*, 2014, **7**, 129.
27 L. Rouger, B. Gouilleux and P. Giraudeau, in *Encyclopedia of Spectroscopy and Spectrometry*, ed. G. E. Tranter and D. W. Koppenaal, Academic Press, Oxford, 3rd edn, 2017, p. 588, DOI: 10.1016/B978-0-12-409547-2.12107-9.
28 P. Lesot, P. Berdague and P. Giraudeau, *Chem. Commun.*, 2016, **52**, 2122.
29 A temperature less than 200 K is required to reach a sufficient level of resolution for lithium 7 spectrum of *n*-BuLi/MeLi (1 : 1), but we chose to work at 185 K, that is, in conditions which the lithium nuclei undergo a slow intra-aggregate exchange.
30 F. Paté, H. Oulyadi, A. Harrison-Marchand and J. Maddaluno, *Organometallics*, 2008, **27**, 3564.
31 B. Gouilleux, L. Rouger, B. Charrier, I. Kuprov, S. Akoka, J.-N. Dumez and P. Giraudeau, *ChemPhysChem*, 2015, **16**, 3093.
32 Y. Shrot and L. Frydman, *J. Chem. Phys.*, 2009, **131**, 224516.
33 P. Pelupessy, L. Duma and G. Bodenhausen, *J. Magn. Reson.*, 2008, **194**, 169.
34 Z. Wei, L. Lin, Q. Ye, J. Li, S. Cai and Z. Chen, *J. Chem. Phys.*, 2015, **143**, 024201.
35 Y. Shrot and L. Frydman, *J. Chem. Phys.*, 2008, **128**, 164513.
36 P. Giraudeau and S. Akoka, *J. Magn. Reson.*, 2008, **192**, 151.
37 C. Wu, M. Zhao, S. Cai, Y. Lin and Z. Chen, *J. Magn. Reson.*, 2010, **204**, 82.
38 F. Tian, P. J. Bolon and J. H. Prestegard, *J. Am. Chem. Soc.*, 1999, **121**, 7712.
39 M. Shalom, J. S. Dennis and G. Michael, *Curr. Anal. Chem.*, 2008, **4**, 8.
40 S. Mangia, T. Liimatainen, M. Garwood and S. Michaeli, *J. Magn. Reson. Imaging*, 2009, **27**, 1074.

Appendix 2: Prospa pulse program of UF CT PM COSY

```
#####################################################################
#   Ultrast Constant time phase-modulated COSY
#
#   Written by Boris Gouilleux - CEISAM - University of Nantes
#####################################################################


procedure(pulse_program,dir,mode)


# Interface description (name, label, x, y, ctrlType, varType)

   interface = ["b1Freq",      "B1 Frequency (MHz)",          "0","0",   "tbwv",   "float,[0.5,50]",
                "repTime",     "Repetition time (ms)",        "0","2",   "tbwv",   "float,[20,1e8]",
                "O1",          "Offset (Hz)",                 "0","4",   "tbwv",   "float,[-1e6,1e6]",

                "90Amplitude", "90 amplitude (dB)",           "1","0",   "tb",     "float,[-72,0]",
                "pulseLength", "Pulse length (us)",           "1","1",   "tb",     "float,[1,500]",
                "dmix",        "mixing delay (ms)",           "1","2",   "tb",     "float,[0,1000]",

                "gAmpExc",     "Excitation gradient(%)",      "2","0",   "tb",     "float,[-30,30]",
                "pulseLengthChirp",  "Pulse length chirp (us)","2","1",   "tb",     "float,[10,500000]",
                "ChirpAmplitude",    "amplitude chirp (dB)",  "2","2",   "tb",     "float,[-72,0]",
                "ChirpBandWidth",    "bandwidth chirp (kHz)", "2","3",   "tb",     "float,[0,100000]",
                "nwurst",            "Wurst power (int)",     "2","4",   "tb",     "integer,[1,100]",

                "n2",               "number of loops",        "3","0",   "tb",     "integer,[1,10000]",
                "gAmpAcq",     "Acquisition gradient(%)",     "3","1",   "tb",     "float,[-90,90]",
                "dph",          "prephasing delay (us)",      "3","2",   "tb",     "float,[-2000,2000]",
                "nprephasing",     "Gprephasing (%)",         "3","3",   "tb",     "float,[-2000,2000]",
                "nfolding",        "Gfolding (%)",            "3","4",   "tb",     "float,[-2000,2000]",

                "gAmpAcqComp",   "Acq. grad. comp",           "4","0",   "tb",     "float,[0.9,1.0]",
                "gSlopeComp",    "Slope comp",                "4","1",   "tb",     "float,[0,0.8]"
                ]

  tabs = ["Pulse sequence","Acquisition","Processing+Display","File Settings"]


# Relationships between pulse-sequence and GUI parameters
   relationships =
                     ["a1 = 90Amplitude",
                     "d1 = pulseLength",
                     "d2 = pulseLength*2",
                     "w1 = dmix*1000",

                     "d200=5.0",
                     "n200 = round(pulseLengthChirp/d200)",
                     "(t1,t2) =
UF_CT_PM_COSY:getAmpandFreqTable(b1Freq,O1,ChirpAmplitude,ChirpBandWidth,n200,
nwurst)",
                     "n11a = 0",
                     "d300 = 2",
                     "gradRamp = 200",
                     "gAmpExc = gAmpExc*0.01",
                     "gAmpAcq = gAmpAcq*0.01",
                     "nprephasing = nprephasing*0.01",
                     "nfolding = nfolding*0.01",
                     "n300 = round(gradRamp/d300)",
                     "n12e =  round(gAmpExc*32768)",
                     "n12a =  round(gAmpAcq*32768)",
                     "n12aMinus = -n12a",
                     "n12eMinus = -n12e",
                     "n12prephasing = round(nprephasing*32768)",
                     "n12folding = round(nfolding*32768)",
                     "n12c = round(0.65*32768)",
                     "n12cMinus = -n12c",
                     "n12ctp = round(0.80*32768)",
                     "n12ctpMinus = -n12ctp",
```

```
                    "n1 = nrPnts",
                    "totPnts = 2*n2*nrPnts",
                    "totTime = acqTime",
                    "d55 = acqTime*1000 + rxLat+50",
                    "d54 = d55/2+dph",
                    "t9 =
UFCosyBen:getGradAcqTable(n2,gAmpAcq,gAmpAcqComp,gSlopeComp)"
                     ]

# These parameters will be changed between experiments
   variables = [""]

# x and y spacing between controls
   dim = [155,26]

# Pulse sequence

   initpp(dir) # Reset internal parameter list

   #CT-spatial encoding by double spin-echo

   pulse(mode,a1,p1,d1)

   wait(w1)

   gradramp(n11a,n12c,n300,d300)
   delay(800)                        #crusher
   gradramp(n12c,n11a,n300,d300)

   gradramp(n11a,n12e,n300,d300)
   chirprf(mode,t1,t2,p2,n200,d200) # combine positive gradient + 180 chirp
   gradramp(n12e,n11a,n300,d300)

   delay(20)

   gradramp(n11a,n12c,n300,d300)
   delay(1200)                        #crusher
   gradramp(n12c,n11a,n300,d300)

   gradramp(n11a,n12eMinus,n300,d300)
   chirprf(mode,t1,t2,p2,n200,d200)   # combine negative gradient + 180 chirp
   gradramp(n12eMinus,n11a,n300,d300)

   gradramp(n11a,n12c,n300,d300)
   delay(400)                         #crusher
   gradramp(n12c,n11a,n300,d300)

   delay(20)

   #Mixing period

   gradramp(n11a,n12folding,n300,d300)
   delay(d54)                           #folding gradient
   gradramp(n12folding,n11a,n300,d300)

   gradramp(n11a,n12ctp,n300,d300)
   delay(1200)                         #CTP gradient performed by gradient coil
   gradramp(n12ctp,n11a,n300,d300)

   pulse(mode,a1,p3,d1)                  # mixing 90

   gradramp(n11a,n12ctpMinus,n300,d300)
   delay(1200)                         #CTP gradient performed by gradient coil
   gradramp(n12ctpMinus,n11a,n300,d300)

   gradramp(n11a,n12prephasing,n300,d300)
   delay(d54)                             #prephasing gradient
   gradramp(n12prephasing,n11a,n300,d300)
```

```
   #Acquisition performed by EPI block

   setindex(t9,0)
   loop(l1,n2)
   gradramp(n11a,n12a,n300,d300)
   acquire("append",n1,d55)
   gradramp(n12a,n11a,n300,d300)
   delay(200)
   gradramp(n11a,t9,n300,d300)
   acquire("append",n1,d55)
   gradramp(t9,n11a,n300,d300)
   delay(200)

   incindex(t9)

  endloop(l1)

### WARNING: DO NOT DELETE THE FOLLOWING LINE ########

gradoff() # set to zero value the current in gradient coil.
          # Include this line in all pulse sequences

   lst = endpp() # Return parameter list


# Phase cycle
   phaseList = [0,1,2,3; # 90 phase
                0,0,0,0; # chirp phase
                0,0,0,0; # 90 phase mixing
                0,1,2,3] # Acquire phase


endproc(lst,tabs,interface,relationships,variables,dim,phaseList)
```

Appendix 3: Prospa procedure to generate WURST Chirp pulses

```
procedure(getAmpandFreqTable,b1Freq,O1,ChirpAmplitude,ChirpBandWidth,n200,nwurst)


fOut  = matrix(2*n200)
fInsingle = matrix(n200)

for k = 0 to 2*n200-1 step 2

    fIn = (b1Freq+O1/10^6d)+ (k-n200)/(2*n200)*ChirpBandWidth/10^3d

 if k == 2*n200-2
   fIn = (b1Freq+O1/10^6d)
 endif

    fInsingle[k/2] = single(fIn)

    DDSFword = round((fIn * 2^32d )/1000d)

    fOut[k]  = single((DDSFword & 0xFFFF0000)/(2^16)) # DDS freq
    fOut[k+1] = single(DDSFword & 0x0000FFFF)

next k

ampOut = matrix(n200)
ampOut = ampOut + 1*keaRun:convertTxGain(ChirpAmplitude)

x=[-0.5:(1/n200):(0.5-1/n200)]
nw=50
wurst = 1-abs((sin(pi*x))^nw)
ampOut = ampOut.*wurst

ampOut[n200-1] = 0
```

Appendix 4: Prospa procedure for gradient offset compensation

```
procedure(getGradAcqTable,n2,gAmpAcq,gAmpComp,gSlopeComp)

taux = [0:1:n2-1]/(n2-1)

tsqrt = sqrt(taux)*n2*gSlopeComp


tOut=matrix(n2)
tOut = tOut - round(gAmpComp*0.01*gAmpAcq*32768) + tsqrt

(y,x) = max(tOut)
if(mag(y)>=32000); message

endproc(tOut)
```

Appendix 5: Prospa routine to automatically process and to display UF data

```
procedure(processing,guipar,plotting)

assignlist(guipar)

      Ta=totTime/1000 # in s
      scan=nrScans
      Ga_per=gAmpAcq     #acquisition gradient percentage
      Tchirp=pulseLengthChirp/1000000   #in s

      curplot("1d",1,1)
      (t,sumData)=getplotdata("1d")

      multiplot("1d",3,1)
      curplot("1d",1,1)
      plot(sumData)

      sumData=sumData*scan
      pr size(sumData)

      1dzfFactor=4 #factor of zero filling in the conventionnal dim (1)
      2dzfFactor=2 #factor of zero filling in the uf dim (2)
      SI1=n2*1dzfFactor #number of points in the conventional dim (1)
      SI2=nrPnts*2dzfFactor #number of points in the uf dim (2)


      #Fourier Transform of FID in order to filter the profile
      gradProfile  = ft(sumData)
      pr totPnts
      #filterGate
      filterGate = matrix(totPnts)
      profileBandwidth = 22000 #en nb de points pour l instant
      filterGate[(totPnts-
profileBandwidth)/2:(totPnts+profileBandwidth)/2]=1
      gradProfile = gradProfile.*filterGate

      #Gaussian apodization
      x=[0:1:totPnts-1]
      p1=totPnts/2
      p2=0.00015                                  #tune UF apodisation
      gaussianFlt=exp(-(x-p1)^2*p2^2)
      gradProfile = gradProfile.*gaussianFlt

      #Inversed fourrier transform with zero filling of UF dim
      sumData = ift(zerofill(gradProfile,2*n2*SI2,"sides"))


      if(plotting=="yes")
      curplot("1d",2,1)
      plot(filterGate)
      hold("on")
      plot(gaussianFlt)
      curplot("1d",3,1)
      plot(gradProfile)
      endif

      #Building (k,t2) maps
      evenEcho = cmatrix(n2,SI2)
```

```
      oddEcho = cmatrix(n2,SI2)

      for k = 0 to n2-1
         for q = 0 to SI2-1
            evenEcho[k,q] = sumData[(2*k)  *SI2+q]
            oddEcho[k,q]  = sumData[(2*k+1)*SI2+q]
         next q
      next k

      # Reverse odd echos matrix
       oddEcho = reflect(oddEcho,"horiz")

assign("oddEcho",oddEcho,"global")
assign("evenEcho",evenEcho,"global")

processing = "2"

      #Correction Ga/-Ga offset

      evenProj = submatrix(cumsum(mag(evenEcho),"x"),0,0,0,SI2-1)
      oddProj = submatrix(cumsum(mag(oddEcho),"x"),0,0,0,SI2-1)
      (evenMax,x,evenPos) = max(evenProj)
      (oddMax,x,oddPos) = max(oddProj)
      offset = evenPos-oddPos
      ref=50
      ref_min=ref-10
      ref_max=ref+10

      pr "The index of maximum of even sum-projection = $evenPos$\n"
      pr "The index of maximum of odd sum-projection = $oddPos$\n"
      pr "Index Offset between odd/even maps = $offset$\n"

      if(offset > ref_min & offset < ref_max)
      delta=offset
      pr "Odd versus Even shift within the standard range \nshift of
$offset$ index \n"
      else
      delta=ref
      pr "Odd versus Even shift out of range\nreference shift $ref$ is
therefore used \n"
      endif

      # FT 2D parameters and apodization along the Fourier dimension
      2dfltr = "none"
      1dfltr = "sinebell"
      2dft = "none"
      1dft = "FTEcho"
      magnitude = "yes"

if(processing == "1")
      #shift odd matrix to the offset value and Sum both matrix
      Echo = evenEcho+shift(oddEcho,0,delta)
      assign("all",Echo,"global")

      #Perform 2D FT on the final map
      fft:2d("all","allft$scan$",SI1,SI2,1dfltr,2dfltr,1dft,2dft,magnitude)
      spec2DAll = eval("allft$scan$")
endif
```

```
if(processing == "2")
      fft:2d("oddEcho","oddFT",SI1,SI2,1dfltr,2dfltr,1dft,2dft,magnitude)
      fft:2d("evenEcho","evenFT",SI1,SI2,1dfltr,2dfltr,1dft,2dft,magnitude)
      oddFT=eval("oddFT")
      evenFT=eval("evenFT")

      spec2DAll = evenFT+shift(oddFT,0,delta)
endif

      spec2DAll = trans(spec2DAll)
      spec2DAll = reflect(spec2DAll,"vert")
      Echo = trans(Echo)
      Echo = reflect(Echo,"vert")

      Ga=Ga_per*0.16
      SWuf=(2.67e8*Ga*Ta*0.005)/(2*3.14*4*Tchirp)
      SWuf=SWuf/(b1Freq+(O1*1e-6))
      pr "SWuf=$SWuf$\n"
      SWconv = (1 / (2*Ta)) / (b1Freq+(O1*1e-6))
      pr "SWconv=$SWconv$\n"

      axis1=[0, SWuf]
      axis2=[0, SWconv]

     if(plotting=="yes")
      multiplot("2d",1,2)
      curplot("2d",1,1)
      image(spec2DAll,axis1,axis1)
      contour(15,2)
      draw2d("true")
      curplot("2d",2,1)
      image(mag(Echo))
      endif

endproc(Echo,spec2DAll,axis1,axis2)
```

Appendix 6: Prospa script to generate selective Gaussian pulses

```
procedure(getAmpand_Phase_Table,a2,n100)

#gaussiand shaped amplitude table
ampOut = matrix(n100)
ampOut = ampOut + 1*keaRun:convertTxGain(a2)
x=[0:1:n100-1]
p1=n100/2
p2=0.000259
gaussianShape = exp(-(x-p1)^2*p2^2)
ampOut = ampOut.*gaussianShape
gammaB1max=max(ampOut)
tronc=min(ampOut)
ampOutRec = matrix(n100)+gammaB1max

#Constant phase table
phaseOut = matrix(n100)

# Report the shaped pulse features

#sgauss = integvector(xtime,real(ampOut))
#srect = integvector(xtime,real(ampOutRec))
sgauss=sum(ampOut)
srect=sum(ampOutRec)
ampRatio=sgauss/srect  # Amplitude ratio between the shaped pulse
and the linked gate
troncLevel=(tronc/gammaB1max)*100 # Troncature level in %

pr "ampRatio: $ampRatio$ \n "
pr "gammaB1max: $gammaB1max$ \n"
pr "troncature level: $troncLevel$% \n"

endproc(ampOut, phaseOut)
```

Appendix 7: Prospa pulse program of WET-180-NOESY

```
#############################################################
#
# WET-180-NOESY
# Solvent suppression sequence including WET-180 and NOESY-1D blocks
# Need the 2-steps phase cycling for improving the baseline
# Further information in Magn. Reson. Chem. 2016
#
# Written by Boris Gouilleux - CEISAM - University of Nantes -
FRANCE
#
#############################################################

procedure(pulse_program,dir,mode)

# Interface description (name, label, x, y, ctrl, vartype)

   interface = ["b1Freq",     "B1 Frequency (MHz)",           "0","0", "tbw","freq",
                "offFreq",    "Offset Frequency (Hz)",        "0","1", "tbw","float",
                "repTime",    "Repetition time (ms)",         "0","2", "tbw","reptime",
                "90Amplitude","Hard pulse amplitude(dB)",     "1","0", "tbw","pulseamp",
                "pulseLength","90° Pulse length (us)",        "1","1", "tbw","pulselength",
                "dummyCycle", "Dummy scans",                  "1","2", "tbw","float",
                "SelAmp1",    "Soft pulse amplitude1 (dB)",   "2","1", "tbw","pulseamp",
                "SelAmp2",    "Soft pulse amplitude2 (dB)",   "2","2", "tbw","pulseamp",
                "SelAmp3",    "Soft pulse amplitude3 (dB)",   "2","3", "tbw","pulseamp",
                "SelAmp4",    "Soft pulse amplitude4 (dB)",   "2","4", "tbw","pulseamp",
                "SoftLength", "Soft pulse length (ms)",       "2","0", "tbw","float,[0.1,10000]",
                "mixDur",     "Mixing dealy (ms)",            "3","0","tbw",  "float",
                "gradAmp",    "Gradient Power(%)",            "3","1","tbw","float,[0,90]",
                "gradDur",    "Gradient length(ms)",          "3","2","tbw","float,[0.1,20]"
                ]


# Relationships to determine remaining variable values
   relationships = ["n1 = nrPnts",
                    "O1 = offFreq",
                    "a1 = 90Amplitude",
                    "d1 = pulseLength",
                    "d2 = 2*d1",
                    "a2 = SelAmp1",
                    "a3 = SelAmp2",
                    "a4 = SelAmp3",
                    "a5 = SelAmp4",
                    "w1 = mixDur*1000",
                  # Generate the shaped pulses
                    "d100 = 5",
                    "d11=SoftLength*1000",
                    "n100 = d11/d100",
                    "(t11,t21) = WET_180_NOESY_1D:getAmpand_Phase_Table(a2,n100)",
                    "(t12,t22) = WET_180_NOESY_1D:getAmpand_Phase_Table(a3,n100)",
                    "(t13,t23) = WET_180_NOESY_1D:getAmpand_Phase_Table(a4,n100)",
                    "(t14,t24) = WET_180_NOESY_1D:getAmpand_Phase_Table(a5,n100)",
                  #-------------------------------
                  # Gradient features. By default the power of the next gradient is
the half of the previous one
                  # Trapezoidal shape, max power is reached smoothly: in 100 us, to
avoid overshooting
                    "gradRamp = 100",
                    "d300 = 2",
                    "n300 = round(gradRamp/d300)",
                    "n11a = 0",
                    "n121a = round((gradAmp/100)*32768)", # *32768 for conversion
```

```
                    "n122a = n121a/2",
                    "n123a = n122a/2",
                    "n124a = n123a/2",
                    "d5 = gradDur*1000",
                  # -------------------------------
                    "shiftPnts=0",
                    "totPnts = nrPnts",
                    "totTime = acqTime"
                   ]

# Define the tabs and their order

   tabs = ["Pulse_sequence","Acquisition","Processing_Display_Std","File_Settings"]

# These parameters will be changed between experiments
   variables = [""]

# x and y spacing between controls
   dim = [190,26]

# Pulse sequence
   initpp(dir) # Reset internal parameter list

   delay(100)

# -----------Prepartion: WET-180 block-----------------------

   shapedrf(mode,t11,t21,p1,n100,d100)
   delay(50)
   gradramp(n11a,n121a,n300,d300)
   delay(d5)
   gradramp(n121a,n11a,n300,d300)
   delay(1000)

   shapedrf(mode,t12,t22,p2,n100,d100)
   delay(50)
   gradramp(n11a,n122a,n300,d300)
   delay(d5)
   gradramp(n122a,n11a,n300,d300)
   delay(1000)

   shapedrf(mode,t13,t23,p3,n100,d100)
   delay(50)
   gradramp(n11a,n123a,n300,d300)
   delay(d5)
   gradramp(n123a,n11a,n300,d300)
   delay(1000)

   shapedrf(mode,t14,t24,p4,n100,d100)
   delay(120)
   pulse(mode,a1,p5,d2)                # 180° hard pulse
   delay(6)
   gradramp(n11a,n124a,n300,d300)
   delay(d5)
   gradramp(n124a,n11a,n300,d300)
   delay(1000)

# ----------End of the preparation step----------------------

# -------------Excitation: NOESY block-----------------------

   pulse(mode,a1,p6,d1)          # 1st 90° hard pulse
   delay(10)
   pulse(mode,a1,p7,d1)          # 2nd 90° hard pulse
   delay(50)
   wait(w1)                      # Mixing delay
   delay(50)
   pulse(mode,a1,p8,d1)          # 3rd 90° hard pulse
```

```
   delay(20)

# ----------End of the excitation step----------------------

   acquire("overwrite",n1)      # Acquisition


   lst = endpp(mode) # Return parameter list

# Phase cycle list
  phaseList  = [0,0;   # WET Pulse phase
                1,1;   # WET Pulse phase
                1,1;   # WET Pulse phase
                3,3;   # WET Pulse phase
                1,1;   # 180° hard pulse
                0,2;   # 1st 90° hard pulse
                0,0;   # 1st 90° hard pulse
                0,0;   # 1st 90° hard pulse
                0,2]   # Acquire phase

endproc(lst,tabs,interface,relationships,variables,dim,phaseList)
```

UNIVERSITE BRETAGNE LOIRE

UNIVERSITÉ DE NANTES

Thèse de Doctorat

Boris GOUILLEUX

Développements méthodologiques sur un appareil RMN de paillasse avec des gradients de champ magnétique. Nouvelles perspectives pour la spectroscopie RMN à bas champ.

Gradient-based methods on a benchtop spectrometer. New perspectives for low-field NMR spectroscopy

Résumé

La RMN à haut champ, basée sur des aimants supraconducteurs, est caractérisée par une instrumentation onéreuse et encombrante qui limite son utilisation dans les environnements de production. Le récent renouveau des aimants permanents a engendré des spectromètres RMN de paillasse qui permettent la réalisation d'expériences RMN directement sous la hotte du chimiste. L'objectif de cette thèse est d'améliorer la performance analytique de ces nouveaux spectromètres à bas champ.
Dans cette optique, nous avons implémenté pour la première fois la RMN 2D Ultrarapide (UF) ainsi que des méthodes modernes de suppression du signal du solvant sur un spectromètre de paillasse opérant à 43 MHz équipé d'une bobine de gradient de champ magnétique. Suite à plusieurs optimisations, la RMN 2D UF à bas champ délivre des spectres 2D en un temps fortement réduit de qualité tout à fait intéressante. En parallèle, le développement des méthodes de suppressions permet dorénavant d'appréhender l'utilisation de solvant non-deutérés sur des échantillons statiques ou en flux.
Ces travaux ont débouché sur de nouvelles opportunités pour la RMN à bas champ. Plusieurs suivis de réactions, réalisés en ligne et en temps réel, ont été menés à bien sur diverses réactions comme le couplage de Heck-Matsuda, la neutralisation de mimes de gaz moutardes ou encore la synthèse d'un composé naturel par chimie en flux. Par ailleurs, la RMN 2D UF à bas champ a été appliquée avec succès pour discriminer des huiles alimentaires en fonction de leurs origines botaniques. Cette méthodologie 2D, compatible avec des analyses à haut débit, démontre une amélioration notable par rapport à la RMN 1D.

Mots clés
RMN de paillasse – RMN à bas champ – RMN 2D Ultrarapide – Suppression de solvant – Suivi de réaction – RMN en flux – Authentification

Abstract

High-field NMR based on superconducting magnets involves an expensive and bulky equipment, which has hampered the use of NMR in harsh environments. A new generation of benchtop NMR spectrometers, compact and cryogen free, has brought NMR spectroscopy under the chemist's fume-hood and as close as possible to production sites. The driving force of this PhD project is to improve the analytical performance of these benchtop NMR systems.
We report here the first implementation of Ultrafast (UF) 2D NMR- a method yielding 2D NMR spectra in a single scan- as well as modern gradient-based solvent suppression methods on a 43 MHz benchtop spectrometer, including a B_0-gradient coil. Substantial optimizations have led to UF experiments at low-field (LF) with a reasonable performance while the acquisition duration is reduced by one order of magnitude. Then, the presence of non-deuterated solvents –commonly used in LF NMR– has been tackled by the development of suppression methods both in static and flowing conditions.
This methodological effort has opened new opportunities for benchtop NMR applications. Several on- and in-line real-time monitorings have been performed on different types of chemical reactions: Heck-Matsuda coupling reaction, oxidative neutralization of mustard-gas simulants or even the synthesis of a natural product in flow-chemistry. Besides applications to process monitoring, UF 2D NMR at 43 MHz has been successfully applied to discriminate the botanical origins of a panel of edible oils. This fast 2D approach has provided a better classification than standard 1D experiments while remaining compatible with high-throughput analysis.

Key Words
Benchtop NMR – Low-field NMR spectroscopy – Ultrafast 2D NMR – Solvent suppression – Reaction monitoring – Flow NMR - Authentication